17th INTERNATIONAL CONGRESS of the Geological Society of Greece

BULLETIN OF THE GEOLOGICAL SOCIETY OF GREECE, SP. PUBL.

EXTENDED ABSTRACT 251

V_{S30} Estimation from P-Wave Seismograms: Exploring a Frequency-Domain Approach for Stations Located in Sedimentary Basins

Pappa E[1]., Papazachos C[1]., Chatzis N[1].

[1]*Geophysical Laboratory, Aristotle University of Thessaloniki, P.O. Box 352-1, GR-54124, Thessaloniki, GREECE*

Introduction

Earthquakes are natural phenomena, often with significant impacts on the human infrastructure. Understanding the factors that influence seismic motion at a specific location is crucial for reducing earthquake risk. These factors include the earthquake source (e.g., magnitude and rupture mechanism), the propagation path (e.g., geometrical spreading and anelastic attenuation), as well as local site effects.

The later factor, local site effects, can play a critical role, as they can amplify seismic motion and significantly influence the level of ground shaking. One of the most common approaches to assess local site effects involves calculating the time-averaged shear wave velocity down to 30 meters, V_{S30}, (e.g., EN1998-1, NEHRP97, etc.). However, reliably estimating V_{S30} is not always straightforward. Traditional methods such as borehole drilling, or geophysical measurements, including refraction, MASW (Multichannel Analysis of Surface Waves), and microtremor measurements (e.g., Chatzis et al., 2018, Chatzis et al., 2022), require significant time, human resources, and funding. Meanwhile, proxy methods, like those based on slope or terrain (e.g., Wald and Allen, 1997) often introduce significant errors. This highlights the need for simple, cost-effective, and reliable methodologies.

Ni et al. (2014) proposed a promising approach, the P-wave seismogram method, to estimate the time-averaged shear wave velocity down to a depth z (V_{SZ}) at a station's location using seismic records. This methodology has been extensively validated using small to moderate magnitude earthquakes (**M**2–4) across various regions, including Central and Eastern North America (Kim et al., 2016), Texas, Oklahoma, and Kansas (Zalachoris et al., 2017), California (Li and Rathje, 2023), Japan (Miao et al., 2018, Kang et al., 2020), and Korea (Kim et al., 2020). It has also been applied to larger earthquakes (**M**4.0–5.5) near the Anchorage Basin in Alaska (Skarlatoudis et al., 2022) and microearthquakes ($-1.1 \leq M_L \leq 1.7$) in the Pohang Basin, South Korea (Lee et al., 2022). In all cases, the method demonstrated a good correlation between estimated and reference (*in situ*) V_{S30} values, verifying its potential as a reliable tool.

Greece, one of Europe's most seismically active countries, has a dense seismic network covering both inhabited and remote areas. However, reliable V_{S30} data is unavailable for many of the stations' locations, making it a critical area of study. Pappa et al. (2025) applied the P-wave seismogram method to two accelerometric arrays in Greece and found a strong correlation with reference values, after employing a standard bandpass filter (0.2–40 Hz) and making appropriate corrections for the effect of the ray parameter and earthquake magnitude on V_{SZ}. In this study, we applied the same methodology to test its applicability at seven stations, those with the most extensive datasets, from the arrays already used by Pappa et al. (2025). However, we deliberately chose not to apply the bandpass filter to assess whether the method performs reliably without it. Our findings revealed that the results were not satisfactory, with all stations showing a bias with respect to reference values, typically exceeding 50%, especially in basin areas (low V_{S30} sites). To address this issue, we explored an alternative approach, by considering the same data in the frequency domain instead of the time domain. This modification significantly reduced the method errors, offering a potential pathway to improve the reliability of the P-wave seismogram method in estimating V_{S30} values for noisy sites, especially for stations located in basin sites.

The P-wave seismogram Method and its Frequency Domain Adapting

Most earthquakes originate within the crust, where seismic waves travel with relatively high velocities. In contrast, seismic stations are often located on near surface, lower-velocity media. Due to Snell's law, the incident angle of incoming P and SV waves at the free surface is smaller than their takeoff angle at the source. This phenomenon results in a stronger P wave on the vertical component and a weaker P wave on the radial component (Figure 1a). The softer the medium, the weaker the P wave contribution to the radial component. Consequently, the ratio of the radial to vertical component amplitudes increases as the soil becomes stiffer. Conversely, the SV reflections from an surface impinging P-wave are generally stronger on the radial component, even in softer sites, as the SV polarization is perpendicular to the ray path. Theoretical arguments (Aki and Richards, 2002; Ni et al., 2014) have shown that the amplitude ratio of the radial (U_R) to vertical (U_Z) components of the incident P wave is reliable indicator of the near surface shear-wave velocity (Vs):

$$\frac{U_R}{U_Z} = \frac{-2V_S\, p\, cosj U_R}{1-2p^2{V_S}^2\, U_Z} = \frac{-2V_S\, p\, cosj}{1-2p^2{V_S}^2} \quad (1)$$

Where, p, is the ray parameter for plane waves:

$$p = \frac{sinj}{V_S} \left(= \frac{sini}{V_P}\right) \quad (2)$$

By combining equations (1) and (2) to eliminate the angle j, the time-averaged shear wave velocity down to a depth z, V_{SZ}, can be estimated as a function of U_R/U_Z and p (Li et al. 2014):

$$V_{SZ} = \frac{1}{\sqrt{2}p}\left[1 - \left(\frac{1}{1+(\frac{U_R}{U_Z})^2}\right)^{\frac{1}{2}}\right]^{\frac{1}{2}} \quad (3)$$

The depth z to which the estimated V_{SZ} corresponds is roughly equal to the dominant wavelength of the S-wave:

$$z = \tau_p V_{SZ}^{Pseis} \quad (4)$$

where τ_p is the duration of the source time function, e.g. duration of the P-wave pulse.

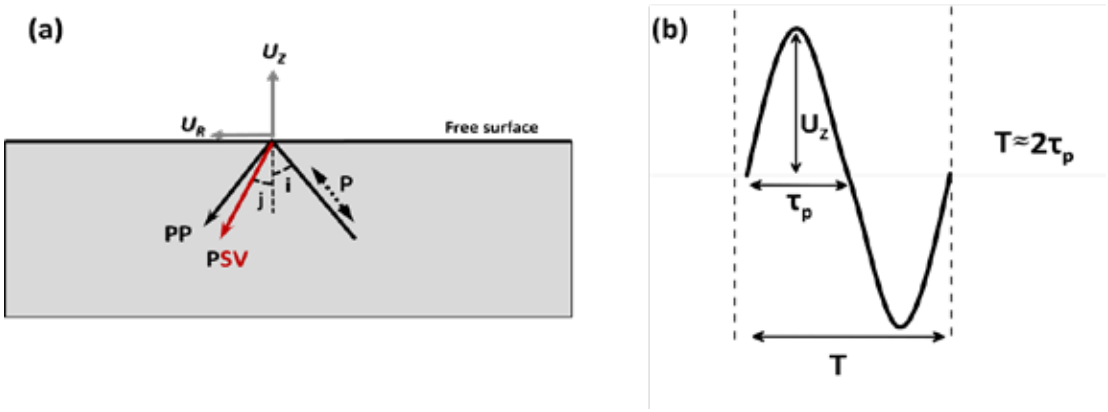

Figure 1. (a) Interaction between an incident P wave and a free surface. The vertical and horizontal components of the P wave result from the superposition of the incident P wave, the reflected P wave, and the S wave generated at the free surface. (b) Schematic representation of a simplified single wave time series, illustrating the source time function (τ_p), the period (T), and their durations.

The application of Fast Fourier Transform (FFT) analysis for the U_R/U_Z estimation section offers several advantages over traditional time-domain analysis, allowing for a more detailed investigation of signal characteristics. In the frequency domain, a signal is represented by independent frequency components, whereas in the time domain, the signal is described by a single waveform that contains the sum of all frequency-dependent contributions.
Figure (1b) presents a schematic first P wave pulse. The source time function used in equation (4) corresponds to the duration of the first pulse, τ_P. If we consider that this waveform is dominated by a characteristic frequency, the duration of this wavetrain should correspond to this dominant wave period. Thus, the period of the first P wave should be approximately twice the source time function, τ_P. The Discrete Fourier Transform (DFT) of the signal shown in Fig.1b includes a minimum (first) frequency component after the zero-frequency, which is determined by the duration of the signal, since this first frequency component is the inverse of the total signal duration. By analyzing the DFT amplitudes, we can better understand the characteristics of the seismic signal, which may be less evident in the time domain. Additionally, this approach allows us to identify and retain only the records where the signal in both components (R and Z) is above the noise level.

Site Selection and Data Processing
Several previous studies have applied the P-wave method using hundreds of stations, with or without reliable reference velocity profiles. In contrast, we focused in two specific arrays and a total of seven stations, selecting those with the most extensive dataset. These arrays are located in sedimentary basins, which are of particular interest due to the significant amplification of seismic motion often observed in such areas. Additionally, the arrays are situated in earthquake-prone regions with well-established velocity profiles (Raptakis et al., 2000; Theodoulidis et al., 2018,

Cushing et al., 2020), making them ideal for testing the methodology.
The first array, EUROSEISTEST, is located in the epicentral area of the 1978 **M**6.5 earthquake in the Mygdonia Basin, which caused severe damage in the neighboring city of Thessaloniki (Papazachos and Papazachou, 2003). The basin spans 5.5 km in the NNW-SSE direction and consists of Quaternary deposits, with a maximum bedrock depth of 200 m, where gneiss was identified (Raptakis et al., 2000). The second array, ARGONET, is located in the Koutavos Basin on the island of Cephalonia, near the Cephalonia Transform Fault Zone (CTFZ). This array was established as part of the SINAPS project (Berg-Thierry et al., 2017). The basin consists of a range of geological formations, including Cretaceous limestones (below 90 m depth, as indicated by borehole data), Upper Pliocene marly sandy limestones and claystones, Pleistocene lithological clays, and Holocene clays and silty sands (Theodoulidis et al., 2018).
From the EUROSEISTEST array, we selected five stations (BUT, GRA, PRO, STC, TST), while from the ARGONET array two surface stations (CK0, CKWP) were chosen for further processing. Among these seven stations chosen, CKWP and PRO are located on bedrock sites, while the others are situated on soft sediments. We utilized all available data, i.e. records of regional earthquakes recorded by the two networks, spanning from 1994 to 2020. The only restriction applied to the dataset was to reject data with ray parameter values p<0.1s/km, as Pappa et al. (2025) demonstrated that the use of smaller p values leads to a systematic bias of the near-surface velocity results.
For the first P-arrival we manually picked the maximum amplitudes of both the radial and vertical components. We opted not to rely on automatic pickers, even though they could expedite the process, as they can introduce errors, especially in noisy signals. We also chose not to apply any filters (highpass, lowpass, or bandpass) in order to preserve the original information contained in the initial P-wave arrivals and examine the method robustness to noise, since we aimed to test the method without applying any a priori filtering. For each waveform, we performed baseline corrections and identified the maximum values of the initial P-wave pulse (indicated between the red dotted lines in Figures 2a and 2b) in both radial and vertical components to calculate the U_R/U_Z ratio.

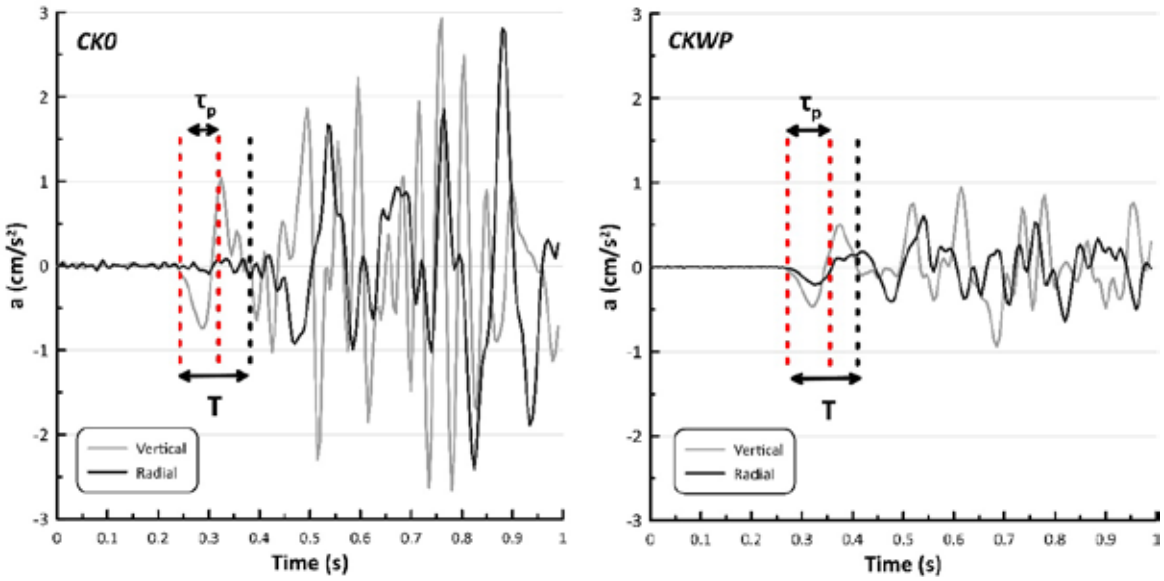

Figure 2. Example of a record at (a) CK0 and (b) CKWP stations for the arrival of the first P wave from the same local earthquake. The source time function, τ_P, and the duration, T, of the corresponding first period are also depicted.

We also extracted the arrival time of the earthquake at the station, the ending time of the first pulse, as well as the end time of the first period (see examples in Figures 2a and 2b). Figure 2a shows a waveform from station CK0, located in soft sediments, where the vertical component is much larger than the radial component. Figure 2b, from station CKWP (located on bedrock), shows a smaller difference between the radial and vertical components, which is attributed to the higher velocity of the near-surface structure.
Once the U_R/U_Z was estimated, we proceeded with the p estimation for each waveform using the TauP toolkit (Crotwell et al., 1999), implemented in ObsPy (Beyreuther et al., 2010). We used the epicentral distance, focal depth, and a local 1D P and S velocity model for each station, derived from the 3D tomographic model of Papazachos and Nolet (1997). As already mentioned, we kept only data with a ray parameter p≥0.1s/km. Since U_R/U_Z and p are known, we applied Equation (3) to estimate V_{SZ} for each record. However, since V_{S30} values are most widely used, we used the V_{SZ}-to-V_{S30} conversion equations from Boore et al. (2011) to assess V_{S30} values for each recording station. To apply

these equations, we first estimated the depth z corresponding to each V_{SZ} value using Equation (4). The duration of the first P-wave pulse was used as τ_p. Unlike Lee et al. (2022), who used an average value for τ_p, we opted to use the specific τ_p for each record to more accurately estimate the correspnding depth samples by the P-pulse wavetrain. The corresponding median V_{S30} values, noted as $V_{S30}^{Original}$, showed significant deviations, involving values with a ~ 50% relative bias (BUT, GRA, PRO, STC, TST) compared to the reference values, increasing to over 80% for stations CK0 and CKWP.

In an attempt to improve these results, we tested the possibility of computing the U_R/U_Z in the frequency domain, where we could more easily identify frequencies where the signal was above the noise level. This approach appears to be promising, especially since most of the stations used in this study were located in soft soil sediments, for which the radial components are more prone to noise compared to rock sites, potentially leading to erroneously larger U_R/U_Z values. For this reason, we applied the Fast Fourier Transform (DFT) to each waveform with a duration equal to the dominant period, T, and selected only those with an SNR in the radial component greater than or equal to 1.2 for the first (lower) frequency. This SNR threshold was applied to the radial component because stations in soft soil often exhibit weak P-wave arrivals, making them susceptible to noise. In the frequency domain, the U_R/U_Z ratio was calculated as the amplitude of the radial component divided by the amplitude of the vertical component at the first frequency. Figures 3a and 3b show examples of how the picking was done in the frequency domain for indicative records from the CK0 and CKWP stations, respectively. The subsequent processing steps, namely from the ray parameter estimation up to the V_{S30} calculation, noted as V_{S30}^{FFT} for this application, remained the same as in case of U_R/U_Z processing in time domain.

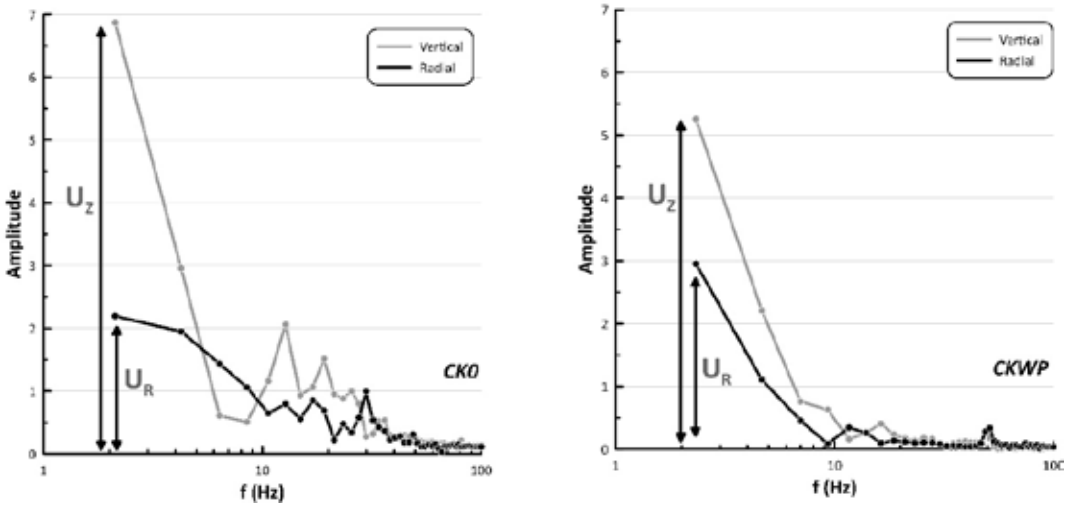

Figure 3. Example of waveform amplitude spectra at (a) CK0 and (b) CKWP stations for the first P wave and a duration equal to the dominant period (see Fig.2). The amplitude of the two components, used for U_R/U_Z estimation, is also depicted.

Results

The results of the V_{S30} estimations using both the time-domain and frequency-domain (FFT) approaches are summarized in Table 1. For stations CK0 and CKWP, the time-domain methodology ($V_{S30}^{Original}$) produced significantly overestimated values, with CK0 showing the largest deviation from the reference values (V_{S30}^{ref}). Applying the FFT-based approach reduced the overestimation across all stations, yielding lower V_{S30}^{FFT} values that were closer to the reference ones. Despite this improvement, all stations still exhibited some degree of overestimation with the FFT approach, except for station GRA, where the methodology failed to provide an improvement. The exclusion of waveforms due to low signal-to-noise ratio (SNR < 1.2) in the radial component has a different impact, depending on the recording station. CK0 had the highest exclusion rate (21%), while PRO and CKWP had no data rejections. Other stations, such as STC (2%), BUT (5.7%), and TST (6.7%), had minimal rejection rates, reflecting the overall improved data quality in the FFT-based analysis.

Figure 4 illustrates these findings: in Figure 4a we present the comparison of time-domain results with reference V_{S30} values, showing a pronounced overestimation compared to the reference, with most points lying far from the 1:1 line. On the contrary, the FFT-based results (Figure 4b) demonstrate a much better agreement with the reference values.

Table 1. V_{S30} median values, estimated from the P-wave Seismogram method with a time domain U_R/U_Z picking procedure, $V_{S30}^{Original}$, and frequency domain approach V_{S30}^{FFT} for SNR in the radial component greater than 1.2. For comparison, we also present the reference V_{S30}^{ref} values from local velocity profiles estimated from active and passive seismic methods.

Station	$V_{S30}^{Original}$ (km/s)	V_{S30}^{FFT} (km/s)	V_{S30}^{ref} (km/s)
CK0	1.05	0.48	0.24
CKWP	1.44	0.87	0.79
BUT	0.43	0.29	0.26
GRA	0.4	0.46	0.23
PRO	1.24	1.23	0.83
STC	0.54	0.52	0.35
TST	0.35	0.32	0.22

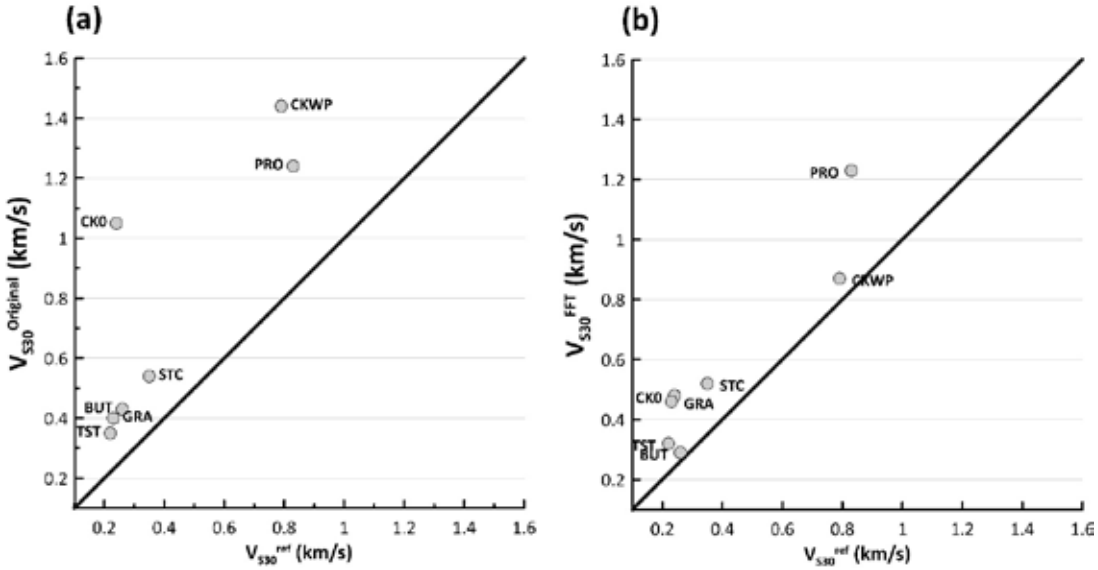

Figure 4. Plot of (a) $V_{S30}^{Original}$ and (b) V_{S30}^{FFT} as a function of V_{S30}^{ref} of each station, estimated from various active and passive seismic methods. The 1:1 line is also presented.

Conclusions

We have processed seven selected stations from two seismic arrays (EUROSEISTEST and ARGONET) located in sedimentary basins with well-documented velocity profiles and a large number of seismic records from regional earthquakes. These stations were chosen to test and refine the P-wave seismogram method for estimating V_{S30} values, focusing on both time-domain and frequency-domain approaches. Specifically, the use of FFT and imposing an SNR threshold on the radial component significantly reduced errors for most stations, bringing the estimated V_{S30}^{FFT} values closer to the reference values. However, the station GRA remains an exception, with noisy waveforms likely contributing to larger errors. This highlights the critical role of the picking process, which is particularly sensitive to noise, especially for stations in soft-soil conditions.

CK0, one of the noisiest stations, presented challenges in the time-domain approach, where its U_R/U_Z ratio was highly exaggerated. After applying the frequency-domain methodology, only 78 waveforms (less than 50% of the total dataset) were retained due to the SNR filter, leading to much better results. Similarly, other stations, especially those in ARGONET, benefited significantly from the frequency-domain approach, with notable improvements in V_{S30} estimates. The results also suggest that the softer the formation at a station's location, the lower the U_R/U_Z ratio tends to be, consistent with theoretical expectations. Stations such as BUT, which have a reference V_{S30}^{ref} value close to the V_{S30}^{FFT}, exhibited a median U_R/U_Z of ~0.11, whereas GRA, with noisier data, showed a higher median U_R/U_Z of ~0.16.

In conclusion, the proposed frequency-domain approach can enhance the reliability of V_{S30} estimations, particularly in noisy environments or soft-soil conditions. However, challenges are still present regarding the handling of noisy data, such as at GRA, where an additional refinement of the proposed approach may be necessary. The findings underscore the potential of frequency-domain analysis to improve site condition assessment, but additional investigation is needed to address the remaining discrepancies and optimize the approach for broader applications.

Acknowledgements
We would like to thank D. M. Boore for sharing with us the unpublished coefficients for V_{SZ} to V_{S30} conversion equations.

References

Aki, K., and P. G. Richards, (2002). Quantitative Seismology, University Science Books, Sausalito CA, 700.

Aristotle University of Thessaloniki. (1993). EUROSEISTEST Strong Motion Network [Data set]. International Federation of Digital Seismograph Networks. https://doi.org/10.7914/SN/EG

Berge-Thierry, C., A. Svay, A. Laurendeau, T. Chartier, V. Perron, C. Guyonnet-Benaize, E. Kishta, R. Cottereau, F. Lopez-Caballero, F.Hollender, B. Richard, F. Ragueneau, F. Voldoire, F. Banci, I. Zentner, N. Moussallam, M. Lancieri, P. Y. Bard, S. Grange, S. Erlicher and N. Theodoulidis (2017). Toward an integrated seismic risk assessment for nuclear safety improving current French methodologies through the SINAPS@ research project, Nucl. Eng. Des. 323 185–201.

Beyreuther, M., R. Barsch, L. Krischer, T. Megies, Y. Behr, and J. Wassermann (2010). ObsPy: A Python toolbox for seismology SRL 81 530–533.

Boore, D. M., E. M. Thompson, and H. Cadet (2011). Regional correlations of VS30 and velocities averaged over depths less than and greater than 30 meters, Bull. Seism. Soc. Am. 101 3046–3059.

Chatzis N., C. Papazachos, N. Theodoulidis, N. Klimis, M. Anthymidis (2018). 1D VS MODELS BY SINGLE-STATION NOISE DATA INVERSION AND JOINT INTERPRETATION WITH INDEPENDENT DATA, 16th European conference on earthquake engineering, Thessaloniki 18-21 June.

Chatzis N., C. Papazachos, N. Theodoulidis, P. Hatzidimitriou, G. Vougioukalakis, M. Paulatto, B. Heath, E. Hooft, D. Troomey, M. Anthymidis, C. Ventouzi (2022). Metamorphic bedrock geometry of Santorini using HVSR information and geophysical modeling of ambient noise and active-source surface-wave data. J. Volcanol. Geotherm. Res. 432 107692.

Crotwell, H. P., and T. J. Owens (1999). The TauP Toolkit: Flexible Seismic Travel-Time and Raypath Utilities, SRL 70 154–160.

Cushing, E. M., F. Hollender, D. Moiriat, C. Guyonnet-Benaize, N. Theodoulidis, E. Pons-Branchu, S. Sépulcre, P. Y. Bard, C. Cornou, A. Dechamp, A Mariscal, and Z. Roumelioti (2020). Building a three dimensional model of the active Plio-Quaternary basin of Argostoli (Cephalonia Island, Greece): An integrated geophysical and geological approach, Eng. Geol. 2265 105441

EN 1998-1 (2004). Eurocode 8: Design of structures for earthquake resistance – Part 1: General rules, seismic actions and rules for buildings, European Union Regulation 305/2011, Directive 98/34/EC, Directive 2004/18/EC

Kang, S., B. Kim, H. J. Park, and J. Lee. (2020). Automated procedure for estimating VS30 utilizing P-wave seismograms and its application to Japan, Eng. Geol. 264 105388.

Kim, B., Y. M. A. Hashash, E. M. Rathje, J. P. Stewart, S. Ni, P. G. Somerville, A. R. Kottke, W. J. Silva, and K. W. Cambell (2016). Sub-surface shear wave velocity characterization using P-wave seismograms in Central and Eastern North America, Earthq. Spectra 32 143–169.

Kim, J., B. Kim, and H. Cho (2020). Shear Wave Velocity Estimation in Korea Using P-Wave Seismograms, KSCE J. Civ. Eng. 24 3650–3658. J. Seismol

Lee, J., K. H. Kim, S. Y. Kang, M. Son, & B. Kim. (2022). Shear-wave velocity map for Pohang Basin, South Korea, based on the P-wave seismogram method, Earthq. Spectra 38 2162–2182.

Li, Z., S. Ni, & P. Somerville (2014). Resolving shallow shear-wave velocity structure beneath station CBN by waveform modeling of the Mw 5.8 mineral, Virginia, earthquake sequence, Bull. Seism. Soc. Am. 104 944–952.

Li, M., and E. M. Rathje (2023). Evaluation of the P-wave seismogram approach to estimate VS30 in California, Earthq. Spectra 39 454-477.

Miao, Y., Y. Shi, and S. Y. Wanga (2018). Estimating near-surface shear wave velocity using the p-wave seismograms method in Japan, Earthq. Spectra 34 1955–1971.

NEHRP (1997). Recommended Provisions for Seismic Regulations for New Buildings (FEMA 273), Washington, DC, Federal Emergency Management Agency.

Ni, S., Z. Li, and P. Somerville (2014). Estimating subsurface shear velocity with radial to vertical ratio of local P Waves, SRL 85 82–90.

Papazachos, B. C., and C. Papazachou (2003). The earthquakes of Greece, Ziti Editions (3rd Edition), 288.

Papazachos, C., and G. Nolet (1997). P and S deep velocity structure of the Hellenic area obtained by robust nonlinear inversion of travel times, J. Geophys. Res. Solid Earth 102 8349–8367.

Pappa, E., C. Papazachos, N. Chatzis, I. Grendas, N. Theodoulidis, and P. Triantafyllidis (2025). Analyzing the stability of P-wave Seismogram method for estimating VS30: Insights from two accelerometer arrays in Greece, BSSA (accepted for publication).

Raptakis, D., F. J. Chávez-García, K. Makra, and K. Pitilakis (2000). Site effects at Euroseistest-I. Determination of the valley structure and confrontation of observations with 1D analysis, Soil Dyn. Earthq. Eng. 19 1-22.

Skarlatoudis, A. A., H. K. Thio, and P. G. Somerville (2022). Estimating shallow shear-wave velocity profiles in Alaska using the initial portion of P waves from local earthquakes, Earthq. Spectra 38 1076–1102.

Theodoulidis, N., F. Hollender, A. Mariscal, D. Moiriat, P. Y. Bard, A. Konidaris, M. Cushing, K. Konstantinidou, and Z. Roumelioti. (2018). The ARGONET (Greece) seismic observatory: An accelerometric vertical array and its data, SRL 89 1555–1565.

Wald, D. J., and T. I. Allen (2007). Topographic slope as a proxy for seismic site conditions and amplification, Bull. Seismol. Soc. Am. 97 1379–1395.

Zalachoris, G., E. M. Rathje, and J. G. Paine (2017). VS30 Characterization of Texas, Oklahoma, and Kansas using the P-wave seismogram method, Earthq. Spectra 33 943–961.

17th INTERNATIONAL CONGRESS of the Geological Society of Greece

BULLETIN OF THE GEOLOGICAL SOCIETY OF GREECE, SP. PUBL.

EXTENDED ABSTRACT 252

Preliminary results of High-Resolution Microgravity Monitoring During the 2025 Santorini Unrest

Paraskevas M.[1,2], Katsafados I.[1,2], Anastasiou D.[1], Tsakiri M[1]., Nomikou P[3]., Synolakis C[4].

(1) Hellenic Military Geographical Service, john.katsafados@gmail.com
(2) National Technical University of Athens
(3) National and Kapodistrian University of Athens
(4) University of Southern California and Academy of Athens

Research Highlights

- Gravity changes during early 2025 suggest renewed subsurface activity in Santorini.
-Integrated microgravity and GNSS monitoring reveal localized mass redistributions.

Introduction

The Santorini volcanic complex is well known around the globe, largely due to the catastrophic Bronze Age eruption (~1600 BCE), possibly contributing to the collapse of the Minoan civilization (Bruins et al 2008, Friedrich 2000; Pyle 1990). The last eruption occurred in 1950, after which the volcano remained dormant. Between January 2011 and February 2012, significant unrest was recorded, characterized by seismicity, ground uplift of approximately 14 cm, and changes in fumarolic gas compositions (Newman et al. 2012; Parks et al. 2012; Tassi et al. 2013; Tarchini et al. 2019). After this unrest period, gravity surveys were conducted by the National Technical University of Athens (NTUA) in 2012 and 2014. The processing of these datasets indicated the injection of approximately 330 billion kg of basaltic magma at a depth of ~3 km, north of Nea Kameni, and highlighted concurrent changes in the hydrothermal regime (Paraskevas et al, 2023).
Beginning in August 2024, preliminary GNSS and InSAR observations indicated renewed ground uplift, marking the onset of a new phase of geophysical unrest (Paraskevas et al. 2023). Since late January 2025, Santorini has experienced a significant seismic swarm, centered primarily offshore between Santorini and Amorgos islands. Over 50,000 earthquakes have been recorded from January 31, 2025 to April 8, 2025 (Margarita Segou, British Geological Survey, pers. comm) , several exceeding magnitudes 4.0, with the largest event reaching M 5.3 on February 10, 2025(National Observation of Athens). These developments triggered a targeted gravity survey conducted from 7 to 13 February 2025.

Methods

Between February 7 and 13, 2025, a high-resolution gravity survey was carried out at Santorini, during which a total of 865 gravity measurements were collected at 137 established stations distributed across Santorini (96 stations), Nea Kameni (18 stations), Thirasia (8 stations), and Anydros (15 stations). All measurements were referenced to a fixed base station (ID 2000) located in Santorini, with a calibrated absolute gravity value of 979992.9261 mGal. Data processing was conducted using a least squares adjustment approach, incorporating 677 gravity observations to resolve 137 unknown station values, resulting in 540 degrees of freedom. The initial variance factor (σ^2) of 0.225 and the maximum residual of 0.0394 mGal indicated an overestimation of the observational errors. Consequently, a rescaling of weights and standard deviations was applied, yielding robust absolute gravity values for each of the 137 stations referenced to the Santorini base station. Following the derivation of these absolute gravity values, Free-Air and Complete Bouguer anomaly maps were produced according to the methodology thoroughly detailed by Paraskevas et al. (2024). Subsequently, offshore gravity measurements from the PROTEUS project (Hooft et al. 2015) were integrated with the new onshore data, enabling the generation of updated and comprehensive Free-Air and Complete Bouguer gravity anomaly maps for the Santorini volcanic complex and its surroundings

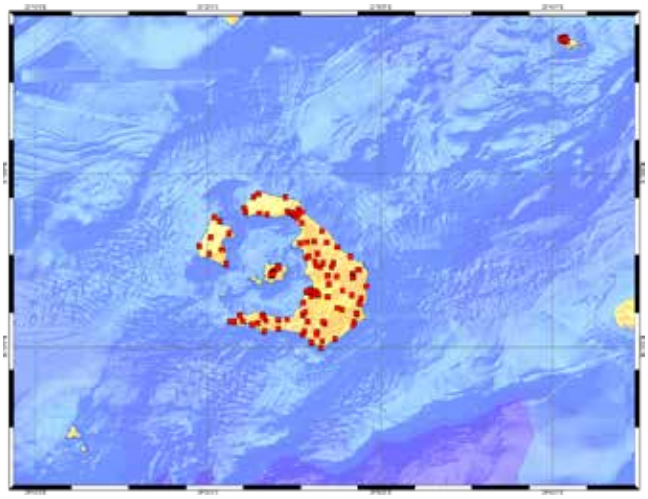

Figure 1 – 137 Gravity stations measured from 7 to 13 Feb 25

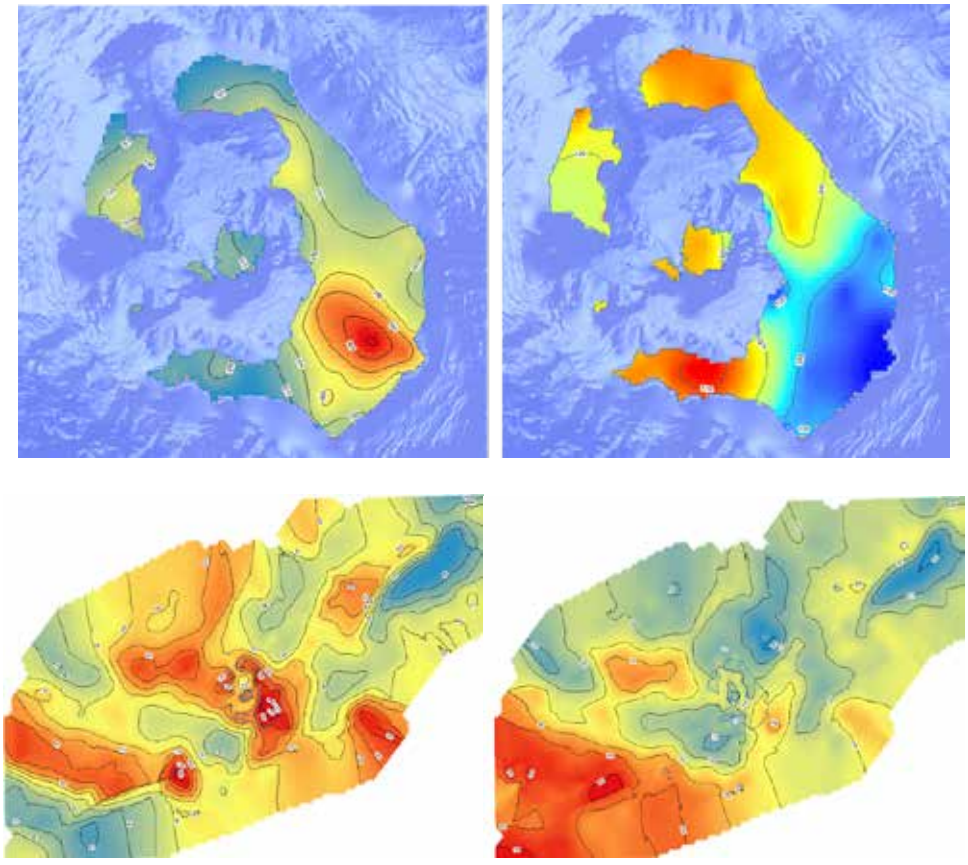

Data Analysis

Out of the 137 stations surveyed in 2025, 93 stations had previously been measured in either 2012 or 2014, providing a baseline for temporal gravity comparisons. At these 93 stations, absolute gravity values from the current study were directly compared with those earlier measurements. Subsequently, gravity effects associated with ground deformation were isolated and removed using GNSS and InSar-derived displacement data, allowing for the calculation of residual spatiotemporal gravity variations within the study area. The results of this comparative analysis are illustrated in Figure 4. These preliminary results indicate the presence of a subsurface mass deficit beneath the Santorini volcanic system during the period of measurements, primarily focused in the area of Nea Kameni and extending northwestward towards Kolumbo. Additionally, statistically significant gravity variations highlight a notable subsurface mass redistribution within the broader Santorini volcanic complex.

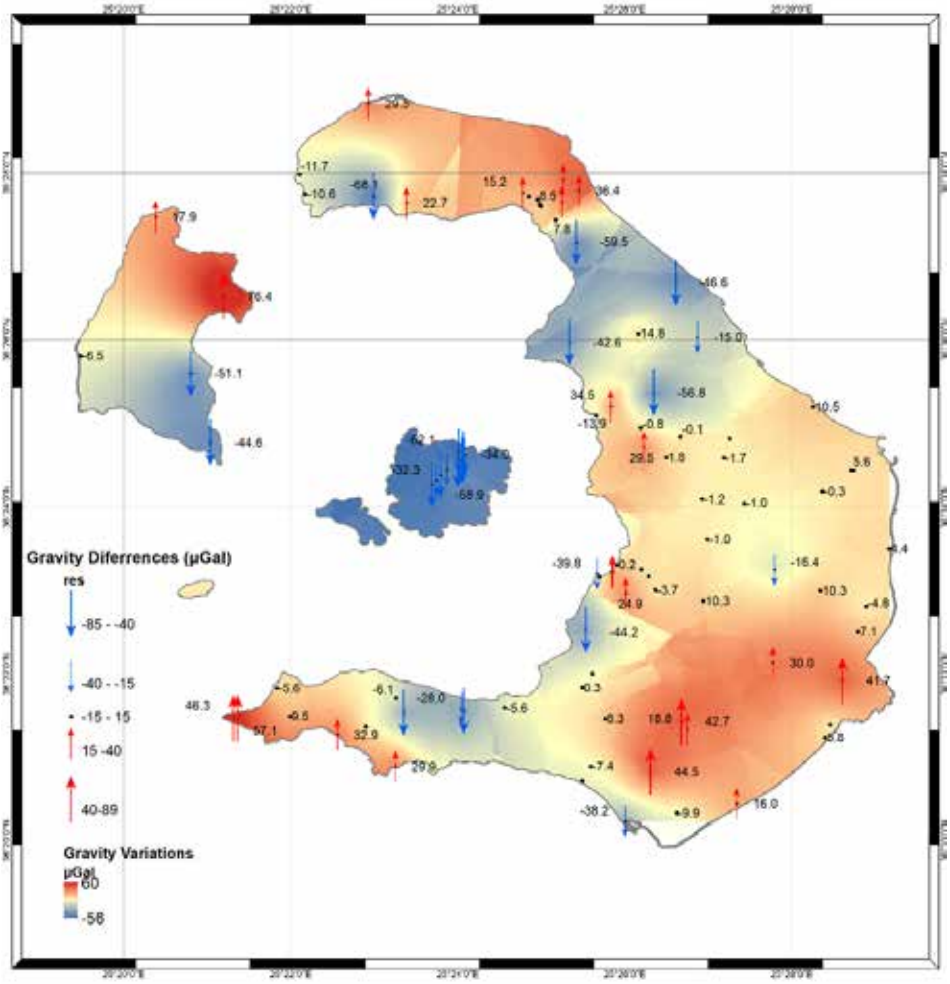

Figure 4 – Spatiotemporal Gravity changes from 2025 to 2012 or 2014

Conclusions

The high-resolution microgravity measurements conducted between February 7 and 13, 2025, provide critical insights into the ongoing geophysical unrest at the Santorini volcanic complex. The comparative analysis of gravity data collected in 2025 against previous measurements from 2012 and 2014 reveals statistically significant spatiotemporal gravity variations, indicative of substantial subsurface mass redistribution processes. The observed mass deficit, predominantly beneath Nea Kameni and extending northwest toward Kolumbo, strongly suggests changes in the volcanic and hydrothermal systems. These preliminary findings highlight the importance of integrating gravity monitoring with GNSS and InSAR deformation analyses, underscoring their collective capability to enhance our understanding and monitoring of volcanic unrest. Continued monitoring and multidisciplinary analyses are recommended to refine interpretations and provide timely updates on potential volcanic hazards.

References

Bruins H.J., MacGillivray, J.A., Synolakis C.E., Benjamini C., Keller J., Kisch H.J, Klugel A, van der Plicht, J., 2008, Geoarchaeological tsunami deposits at Palaikastro (Crete) and the Late Minoan IA eruption of Santorini, Journal of Archeological Sciences 35 , 191– 212, doi:10.1016/j.jas.2007.08.017.

Friedrich, W.L. 2000. Fire in the Sea: The Santorini Volcano and the Lost Atlantis. Cambridge University Press, Cambridge.

Hooft E. E. E., ToomeyD. Nomikou P., 2015: PROTEUS: Plumb in reservoirs of the Earth under Santorini.MGL1521Cruise report 2015,website:https://pages.uoregon.edu/emilie/PROTEUS/

Newman, A.V., Stiros, S., Feng, L., Psimoulis, P., Moschas, F., Saltogianni, V., Jiang, Y.,Papazachos, C., Panagiotopoulos, D.G., Karagianni, E. and Vamvakaris, D., 2012. Recent geodetic unrest at Santorini Caldera, Greece, Geophys. Res. Lett., 39, L06309, doi:10.1029/2012GL051286..

Paraskevas M.,Paradissis D., Raptakis C., Nomikou P., Hooft, E., Bejelou K. (2021). Gravity observations on Santorini island (Greece): Historical and recent campaigns. Contributions to Geophysics and Geodesy. 51. 24. 10.31577/congeo.2021.51.1.1.

Paraskevas M. (2024). Πεδίο Βαρύτητας Ελλαδικού Χώρου με έμφαση στην περιοχή της Σαντορίνης, Μάρτιος 2024, PhD Thesis(in Greek). http://dx.doi.org/10.13140/RG.2.2.11448.76807

Paraskevas M., Paradissis D., Hooft E., Nomikou P., Spatiotemporal gravity changes at the Santorini Volcanic complex and their interpretation, Quaternary Science Advances, Volume 13,2024, 100140, ISSN 2666-0334, https://doi.org/10.1016/j.qsa.2023.100140.

Parks, M.M., Moore, J., Papanikolaou, X., Biggs, J., Mather, T.A., Pyle, D.M., Raptakis, C., Paradissis, D., Hooper, A., Parsons, B. and Nomikou, P., 2015. From quiescence to unrest - 20 years of satellite geodetic measurements at Santorini volcano, Greece, Journal of Geophysical Research (Solid Earth), 120, 1309-1328, doi: 10.1002/2014JB011540.

Pyle, D.M. and Elliott, J.R., 2006. Quantitative morphology, recent evolution and future activity of the Kameni islands volcano, Santorini, Greece, Geosphere 2, 253-268

Tarchini, L., Carapezza, M.L., Ranaldi, M. 2019. Fluid geochemistry contribution to the interpretation of the 2011–2012 unrest of Santorini, Greece. Tectonics 38, no. 2: 552–575.

Tassi, F., Vaselli, O., Papazachos, C.B., Giannini, L., Chiodini, G., Vougioukalakis, G.E., Panagiotopoulos, D. 2013. Geochemical and isotopic changes in fumarolic and submerged gas discharges during the 2011–2012 unrest at Santorini caldera (Greece). Bulletin of Volcanology 75: 711.

17th INTERNATIONAL CONGRESS of the Geological Society of Greece

BULLETIN OF THE GEOLOGICAL SOCIETY OF GREECE, SP. PUBL.

EXTENDED ABSTRACT 253

Stone bridges. Resilience to catastrophic phenomena

Paschos Panagiotis
Dr Geologist
Hellenic Survey of Geology and Mineral Exploration (H.S.G.M.E.), Regional Branch of Epirus, Eleonas, 48100 Preveza. Greece

Introduction / Background

Epirus, being an integral part of Greece with the complex geodynamic evolution that remains active until today, is characterized by the diversity of relief elements, featuring a set of successive mountain ranges with rapid and abrupt altitude changes and a dense hydrographic network.

Numerous settlements, endowed with abundant natural resources (water, food) and protected throughout history, evolved within this environment. Due to the mountainous nature of the area, the construction of bridges was of paramount significance, as it facilitated the free movement of inhabitants from one place to another.

This presentation describes the results of the project: Recording stone bridges in the Region of Epirus that face problems from catastrophic phenomena. The project is implemented by EAGME, with funding from the Public Investment Program.

In the Region of Epirus, there are several stone bridges as a result of the intense relief and the multifaceted dissection of the hydrographic network. These bridges are architectural monuments of exceptional aesthetics and are part of the cultural identity of the region. However, the action of catastrophic phenomena (earthquakes, floods, landslides) but in some cases also human intervention result in the deterioration of these monuments. The fact of the collapse of the Plaka Bridge is an example to avoid similar incidents.

The bridges were constructed from blocks of limestone and sandstone, which are common building materials in the area.

The bridges' foundation positions were chosen so as to ensure their stability and durability against the flooding phenomena of the streams and rivers.

They were located at narrow passages where the cross-section of the stream was confined.

Stone bridges receive the entire volume of water during flood conditions, as well as large quantities of accumulated debris from mud, stones and wood, along with all sorts of objects/materials that were discarded on the slopes and the beds of torrents and rivers.

The hydraulic restriction regarding the amount of water that has to pass only through the bridges' arches creates an increase in water velocity that is accompanied, in some cases, by erosion of the riverbed and damage to the bridge pedestal.

High rainfall is a frequently occurring phenomenon in the area of Epirus. Sometimes recorded extremely high rainfall that takes place in the region

Considering that due to the lithology of the catchment area (flyschic background with limited infiltration) all these quantities of water accumulate abruptly and flow downstream, forming flood conditions.

With this specific project, the bridges that have been affected and are at risk from the ongoing action of the destructive phenomena are recorded in cooperation with Municipalities of Epirus and in collaboration with the Service of Modern Monuments and Technical Works of Epirus, North Ionian and West Macedonia.

The identification, prevention and minimization of the corrosive processes affecting the foundation platforms, especially during flooding conditions, as well as the submission of proposals for their mitigation, constitute determining factors as far as the bridges' protection is concerned.

The procedures and actions that will be launched, after the completion of the project, to remove the risk and restore the possible damage to the bridges, will require combined interventions and collaborations of several scientific specialties and specialized technicians. This will create, in addition to preservation, a turnover and the creation of jobs. Through this project, knowledge will be enriched for minimizing the consequences of the action of the destructive phenomena.

Stone bridges constitute part of the cultural heritage of Greece and most of them have been designated, by legislative regulations, as protected monuments. Responsible for their protection is the Service of Modern Monuments and Technical Works of Epirus, North Ionian and West Macedonia, whereas the local authorities play a crucial role in the implementation of protection measures and monitoring.

Figure 1. Panoramic view of the bridge. Damage from vegetation and erosion to the foundation can be seen.

Figure 2. Detail of erosion in the foundation pedestal.

References

Αράπογλου Μιχάλης, 1981. Γεφύρια του Ζαγορίσιου χώρου, Δελτίο Κέντρου Ερευνών Ζαγορίου, τεύχος 1,

Βλαχοστέργιος Ι., Λύτρα Α., Παπαχριστοδούλου Γ., 2013. Τα πετρογέφυρα της Ηπείρου, Φωτογραφικό άλμπουμ, ΥΝΜ&ΤΕ Ηπείρου, 213 σελ.

Γκράσσος Γεώργιος,2007. Τα πέτρινα τοξωτά γεφύρια της Ελλάδας, Κέντρο Περιβαλλοντικής Εκπαίδευσης Μακρινίτσας, ISBN: 978-960-98043-9-4

Μαντάς Σπύρος, 2020. Γεφυρογραφία της Πίνδου και των Όμορων περιοχών, 5 Τόμοι, Περιφερειακό ταμείο Ανάπτυξης Ηπείρου. Αρχείο γεφυριών Ηπειρωτικών. Ιωάννινα.

Τσομπανάκης Δ., Δημουβγία Α. 2019. Καταγραφή και μελέτη των πέτρινων γεφυριών της Περιφερειακής ενότητας Κοζάνης, Διεύθυνση τεχνικών έργων ΠΕ Κοζάνης, 48 σελ.

17th INTERNATIONAL CONGRESS of the Geological Society of Greece

BULLETIN OF THE GEOLOGICAL SOCIETY OF GREECE, SP. PUBL.

EXTENDED ABSTRACT 254

Mineralogy and Geochemistry of the polymetallic nodules of the Clarion Clipperton Zone, NE Pacific.

Passali N[1]., Sakellaris G.A. [1], Melfou M[1]., Papadopoulou L. [1], Kantiranis N. [1]
(1) Faculty of Geology, Aristotle University of Thessaloniki, 54124 Thessaloniki, Greece, npassali@geo.auth.gr

Abstract
The Clarion Clipperton Zone (CCZ), located in the Northeast Pacific Ocean between the Hawaii islands and Mexico, is a region known for its polymetallic nodules. These nodules are iron and manganese-rich concretions formed of concentric layers of hydroxides and are found on the ocean floor, at depths ranging from 3500 to 6500 meters. They contain valuable metals such as nickel, copper, cobalt, and rare earth elements, making them a potential resource for various high-tech applications. This study focuses on the mineralogical and geochemical analysis of polymetallic nodules collected from the eastern part of the CCZ. X-ray Diffraction (XRD) and Scanning Electron Microscopy (SEM) with EDS techniques were used to investigate the mineral composition, morphology and textures of these nodules. Special attention is given to key minerals such as manganese oxides, todorokite, and birnessite, which serve as indicators of growth processes as well as concentric layering patterns and compositions to identify the specific environmental and geochemical conditions under which these formed.

Introduction
The existence of manganese (Mn) or polymetallic nodules has been known since the early 19th century but it was during the Challenger expedition of 1873–1876 that they were recognized for their significance as metal resources. It was only after World War II that the nodules became focus of detailed research, due to their unique ability to absorb important metals from seawater and form valuable ore deposits. However, the exploration and interest in their potential economic use diminished, due to technical, economic and environmental challenges. In recent years, the interest in the polymetallic nodules has revived, as they can be important source of nickel, copper, cobalt, and rare earth metals. These elements are essential for the continuous advancement of high technologies, the transition to green energy systems, and the development of efficient energy storage systems.
Manganese, ferromanganese and polymetallic nodules are metal-rich concretions found on the deep ocean floor, in depths ranging from 3500 to 6500 meters. Their size ranges from a few millimeters to several centimeters and exhibit irregular shapes. Structurally they consist of multiple, concentric micron-thick layers that form around a core, growing in an extremely slow rate over millions of years. The central core, may either be of biogenetic origin such as shark tooth, or of sedimentary origin such as sand grains, and rock fragments.
Manganese nodules form over millions of years through two main processes: hydrogenetic and diagenetic growth. In the hydrogenetic growth process, the minerals precipitate directly from oxic seawater and their mineralogy is dominated by vernadite (δ-MnO□) and amorphous δ-FeOOH phase (Halbach et. al., 1988). Their composition is characterized by low Mn/Fe ratio (≤3) and relatively low concentrations of Ni and Cu. Hydrogenetic nodules are found commonly in seamounts and on their slopes. When nodules grow diagenetically, the metals precipitate from the sediment pore water under oxic conditions. The Mn/Fe ratio is between 3 and 10 and Ni and Cu concentrations are significantly higher. Todorokite, -a phyllomanganate mineral, and birnessite are the most common Mn-minerals. Nodules that form through the influence of both processes are named as mixed-type nodules and are characteristic of the CCZ (Halbach et al., 1981).
This research work investigates several polymetallic nodules from the CCZ with focus on their internal structures, mineralogy and mineralogical textures in micron-scale. The primary objective is to classify the nodules based on their formation processes (hydrogenic or diagenetic).

Geological Setting of the Clarion Clipperton Zone
The Clarion Clipperton zone is a vast segment of the Pacific Oceanic Plate located in the northeastern Pacific Ocean. It covers an area of approximately 5 million square kilometers, which is equivalent to the size of continental Europe.

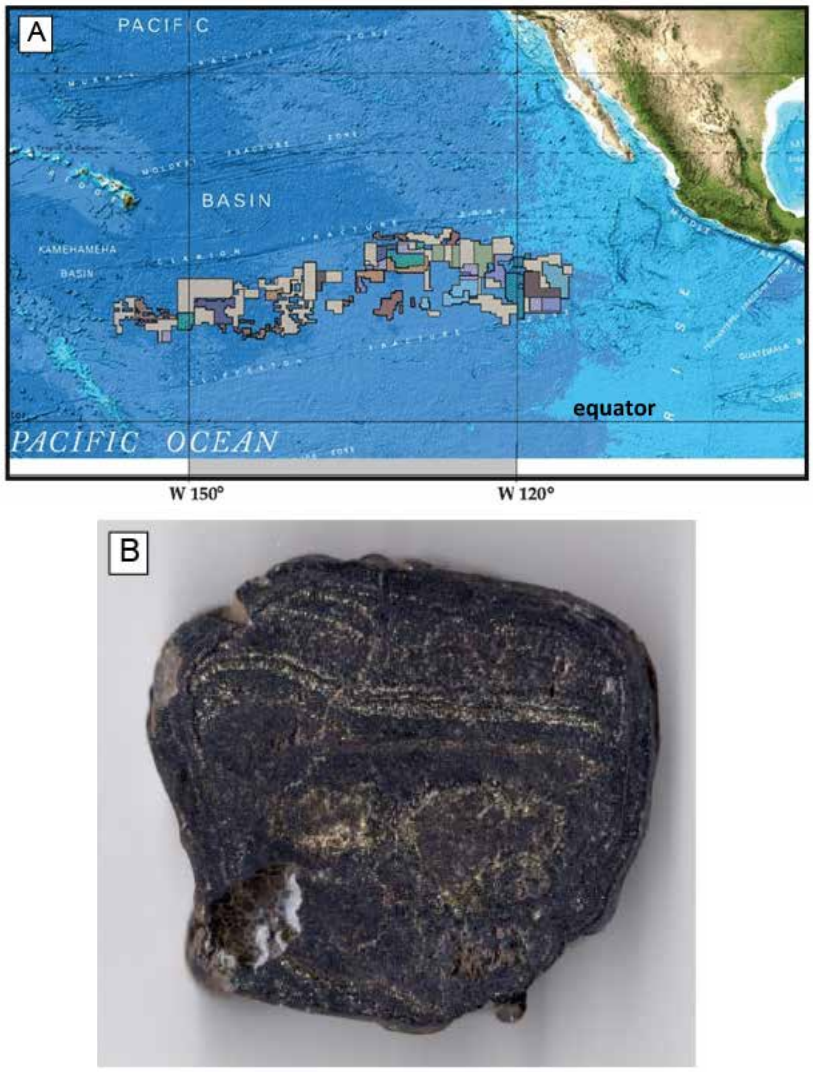

Figure 1. A) Map showing the location of the Clarion Clipperton Zone and the numerous exploration areas (Abramowski et al., 2021). B) Polished slab of a typical polymetallic nodule from the CCZ studied in this work.

The depth is relatively uniform and ranges from 4000 meters to the southeast up to 5000 meters in the northwest. The CCZ lies between of two major fracture zones: The Clarion to the north and the Clipperton to the south. The seabed of the CCZ is predominately composed of basaltic abyssal hills covered by layers of siliceous and calcareous sediments (Parianos et al., 2021). The abyssal hills are the result of normal faulting at mid-ocean ridges, that formed horst and graben structures, indicative of the extensional tectonic regime during opening of the Pacific Ocean. Other occurring geomorphological features include volcanic knolls, seamounts, and lava outcrops.

Samples and Methodology

Approximately 3 kilograms of individual polymetallic nodules were made available for this study by the AllSeas Group S.A. X-ray Diffraction (XRD) was used for the identification and characterization of mineral phases based on their crystallographic structure. The nodules were first heated at 140ºC for 24h and then crushed powdered in homogenous samples and finally pressed into holders. The X-ray Diffractometer used is D8 ADVANCE BRUKER. Polished thin sections were prepared for microscopic examination using a Zeiss Axioscope 40 Pol, and by backscattered electron imaging with a JEOL JSM-6390LV scanning electron microscope (SEM) equipped with INCA 300 energy-dispersive X-ray Spectroscopy (EDS). All sample preparation and analytical procedures were carried out in the laboratory facilities of the Mineralogy-Petrology-Economic Geology at the Department of Geology, Aristotle University of Thessaloniki.

Results

Nodule mineralogy: The XRD analysis revealed that the main mineral phases found in most samples are a) todorokite $Mn_6O_{12}(H_2O)_4$, b) birnessite $MnO_2(H_2O)$, c) manganese dioxide MnO_2 or vernadite (and/or hydroxide), d) goethite FeO(OH), e) quartz SiO_2, f) baryte $BaSO_4$, and, g) ilmenite $FeTiO_3$ (Figure 2). Other aluminosilicates observed are illite $(K,H_3O)(Al,Mg,Fe)_2(Si,Al)_4O_{10}(OH)_2\ nH_2O$, smectite (and probably zeolite), and detrital anorthite $(Ca,Na)_x(Al,Si)_xSi_2O_8$.

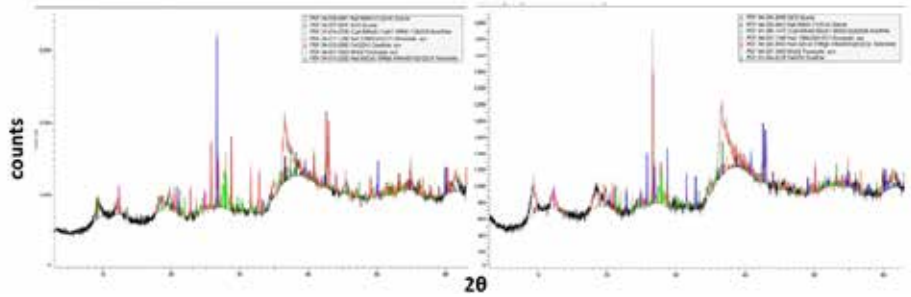

Figure 2. Typical X-ray powder diffractograms from two samples (No.205, No.104). Peak positions indicate the main minerals identified as listed in the legend box.

Manganoan mineral textures and chemistry:

a) MnO_2 and $Mn(OH)_2$: In BSE imaging vernadite is the brightest mineral after barite and ilmenite found as finely crystalline, botryoidal, or in dendritic structures (Figure 3, 4). It contains > 70 wt % MnO_2 and significant amounts of Fe, Ni and Cu as well as impurities of Si, Al, Na and Mg.

b) Todorokite and Birnessite: These form concentric zones where todorokite is slightly brighter than birnessite because it incorporates higher levels of heavier metal cations (Ni, Cu) in its structure. However, these are difficult to distinguish because of the incorporation of various amounts (or impurities) of clay minerals. They both contain commonly more than 40% MnO_2, Fe, Ni and Cu up to 10% in total (oxides), and locally very high amounts of Si and Al.

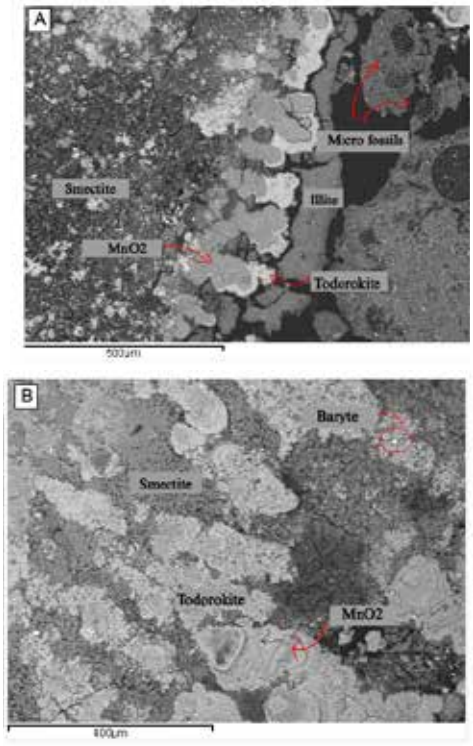

Figure 3. BSE high resolution images of: A) sample CCZ101 showing the different layers and microfossils (possibly radiolaria). B) sample CCZ206 showing the dendritic structures of the manganoan oxides, bright white are baryte crystals.

SEM analyses revealed three distinct types of layers based on texture and composition (labeled as 1-3):
Layer Type 1: These layers exhibit low reflectivity and appear dense with columnar growth. Energy Dispersive Spectroscopy (EDS) spot analyses show Mn/Fe ratios ranging from 0.53 to 4.24, and Ni+Cu contents between 0.16 and 2.55 wt %. These layers are indicative of the hydrogenetic growth process.
Layer Type 2: These layers show high reflectivity and are the most dominant in the nodules, with characteristic dendritic, porous growth patterns. These dendritic zones contribute to the high porosity of the nodules. EDS spot analyses reveal Mn/Fe ratios ranging from 1 to 30, with Ni+Cu contents averaging 3.9 wt %, reaching a maximum of 6.5 wt %. These layers are characteristic of the diagenetic growth process.
Mixed Layer Type 3: These layers have low reflectivity and a columnar growth pattern, with Mn/Fe ratios ranging from 3 to 11 and Ni+Cu contents ranging from 1 to 4.6 wt %. These layers represent a transitional type from Layer Type 1 to Layer Type 2.

Elemental Distribution:
The element map shown in Figure 4 illustrates the distribution of the critical metals in different layers of the nodule. Iron, Ni, Cu, and Mg show a similar distribution pattern to Mn, indicating that these metals are absorbed by the layered and tubular structure of the phyllomanganate minerals, such as birnessite and todorokite, respectively. Areas enriched with Si and Al correspond to the non-crystalline aluminosilicates (e.g., smectite).

Aluminosilicates:
The chemical composition of the aluminosilicates in the nodules varies widely, including smectites, illite, and their manganous varieties. These aluminosilicates are primarily deposited directly on the seafloor or form through early diagenetic processes.

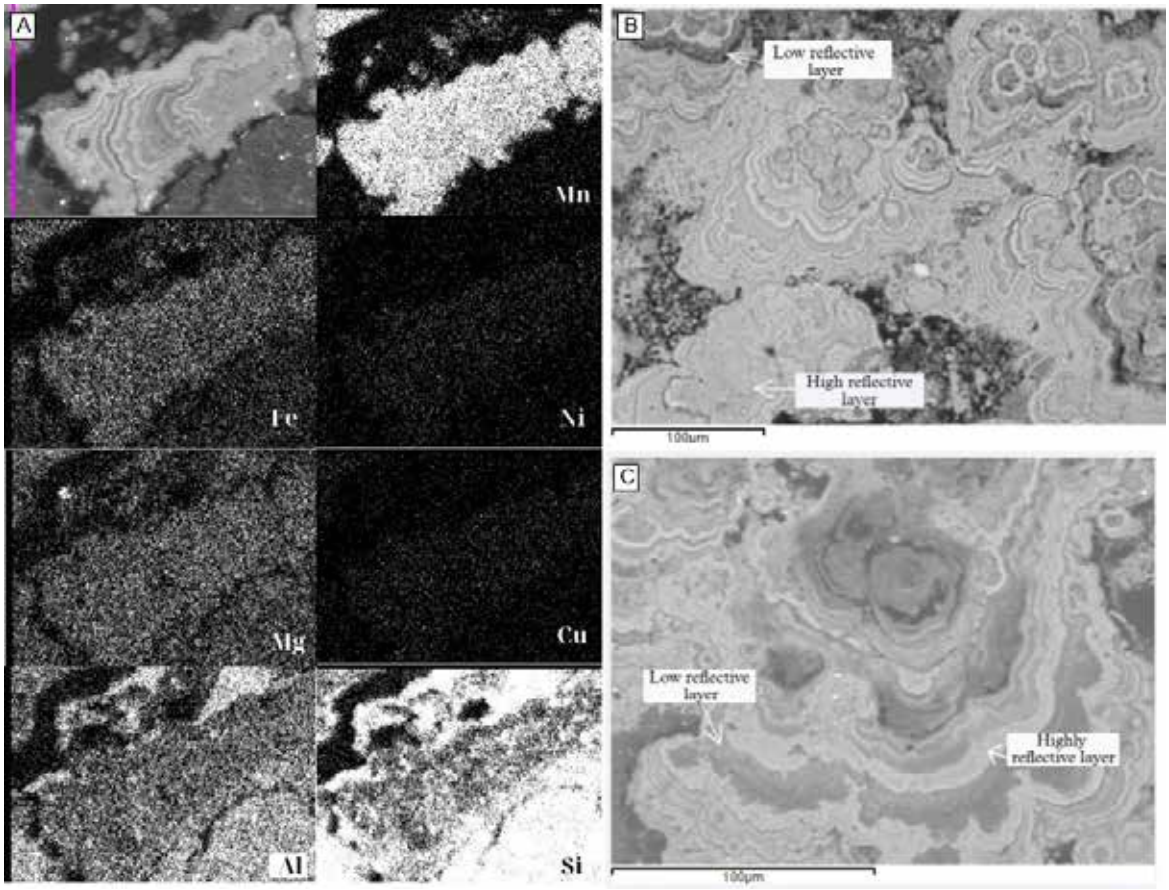

Figure 4. A) SEM-EDS elemental mapping images showing the distribution of metals in the high-manganese layers (sample CCZ203). B) BSE images of concentric layers of types 1 to 3. The higher the reflectivity intensity, the greater the manganese content.

Discussion and conclusions

The polymetallic manganese nodules of the Clarion-Clipperton Zone (CCZ) consist of macroscopically distinguishable layers, which include fine-grained, partially crystallized clays (e.g., smectite, illite) containing detrital quartz, plagioclase, ilmenite, and abundant visible microfossils. These layers alternate with metal-rich layers primarily composed of vernadite, todorokite, and birnessite. Baryte, in the form of small acicular crystals, is a common accessory mineral.

The phyllomanganates are not present as pure phases; rather, they incorporate significant amounts of substituted cations such as Fe, Ni, Mg, and Cu, as well as impurities from surrounding sediments. These impurities result in elevated concentrations of SiO□, Al□O□, and trace metals (e.g., Ti), contributing to the complex compositions of the manganese minerals. Additionally, manganese-rich clays, most likely Mn-smectite (e.g., Mn-nontronite), were identified in the nodules.

These aluminosilicates are typical clay minerals, primarily deposited directly on the seafloor (e.g., smectite) or formed through early diagenetic processes (e.g., illite). The detrital material, such as quartz and ilmenite, accumulated from the erosion of basaltic rocks and was transported by deep ocean currents. Based on the mineralogy and textures observed, the manganese minerals in the nodules formed through both hydrogenetic and diagenetic growth processes. The presence of dendritic todorokite, enriched in Ni, Cu, and Mg, suggests these metals are concentrated within its tunnel structure, while the higher Mn/Fe ratios (compared to birnessite) indicate a diagenetic origin. The Ni, Cu, and Mn metals may have originated from multiple sources, including terrestrial influx and hydrothermal activity associated with the East Pacific Rise (Piper et al., 1981).

Minerals such as vernadite (MnO□) and birnessite, which contain higher Fe, Ca, and Na, likely precipitated directly from oxic seawater during hydrogenetic growth due to their layered structure. The presence of baryte in the nodules further supports the diagenetic processes involved, likely precipitating from sulfate-rich pore waters enriched in barium released from biogenic material (e.g., radiolarians) or organic degradation. Baryte formation may have occurred alongside todorokite. In conclusion, the nodules from this part of the CCZ exhibit a mixed-type hydrogenetic-diagenetic growth pattern, consistent with the observations of Halbach et al. (1981).

Acknowledgements

We express our sincere gratitude to AllSeas S.A. and particularly Mr. Wouter Duijnstee for their generous provision of the samples used in this study.

References

Abramowski T., Urbanek M., 3 Baláž P. (2021). Structural Economic Assessment of Polymetallic Nodules Mining Project with Updates to Present Market Conditions, Minerals 2021, 11(3), 311.

Baturin, G. N. (1987). The Geochemistry of Manganese and Manganese Nodules in the Ocean. In G. N. Baturin (Ed.), *Sedimentology and Petroleum Geology* (pp. 1–166). Dordrecht: D. Reidel Publishing Company.

Dekov, V. M., Rouxel, O., Gu´eguen, B., Wegorzewski, A. V., Khripounoff, A., & Menot, L. (2021). Mn-micronodules from the sediments of the Clarion-Clipperton zone (Pacific Ocean): Origin, elemental source, and Fe-Cu-Zn-isotope composition. *Chemical Geology*, *580*, 120388. [Journal Article]

Halbach, P. (1986). Processes controlling the heavy metal distribution in Pacific ferromanganese nodules and crusts. *Geologische Rundschau*, *75*(1), 235–247.

Halbach, P., Friedrich, G., & Stackelberg, U. (1988). *The Manganese Nodule Belt of the Pacific*. Stuttgart: Enke Verlag.

Hein, J.R. (2016). Manganese Nodules. In J. Harff, M. Meschede, S. Petersen, & J. Thiede (Eds.), *Encyclopedia of Marine Geosciences* (pp. 408–412).

Hüneke, H., & Mulder, T. (Eds.) (2011). *Deep-sea sediments* (Developments in Sedimentology, 63). Amsterdam: Elsevier.

Parianos, J., & Madureira, P. (2021). Geomorphology of the Clarion Clipperton Zone, tropical North Pacific Ocean. *Journal of Maps*, *17*(2), 901–909.

Piper, D.Z., & Williamson, M.E. (1981). Mineralogy and Composition of Concentric Layers Within a Manganese Nodule from the North Pacific Ocean. *Marine Geology*, *40*, 255–268. [Journal Article]

Wegorzewski, A. V. (2015). *Geochemical and mineralogical investigations of fine growth structures of ferromanganese nodules from the Clarion and Clipperton Zone, Pacific Ocean* [Dissertation]. Gottfried Wilhelm Leibniz Universität Hannover.

17th INTERNATIONAL CONGRESS of the Geological Society of Greece

BULLETIN OF THE GEOLOGICAL SOCIETY OF GREECE, SP. PUBL.

EXTENDED ABSTRACT 255

A Pilot Study of Erosion in the Mavro Lithari Beach, part of the Highly Urbanized Coastal Zone of the Eastern Saronic Gulf, through the use of drone technology

Paschali Patouchi Adamantia[1], Ioannis P. Panagiotopoulos[1], Dimitrios Vandarakis[2]

(1) Faculty of Geology and Geoenvironment, School of Science, National and Kapodistrian University of Athens, University Campus, Zografou, Greece, adama_paschali_patouhi@yahoo.com

(2) Hellenic Centre for Marine Research, Institute of Oceanography, Anavyssos, Greece

Introduction

On the basis of aerial photographs collected from seasonal drone flights between May and November 2023, a shoreline retreat of 1-2 m in the central part of Mavro Lithari beach was observed, which can be characterized not very significant in comparison to other places of the Saronic Gulf.

Beaches are dynamic geomorphic systems that are in constant evolution and can be affected by a number of human and natural factors leading to erosion. Specifically, the increase in coastal population, combined with climate change, have disturbed the annual balance of erosive and reserve processes (it has become negative in the majority of cases), so that erosion is now a permanent regime even within an annual cycle of beach evolution, especially when human populations occupy the active part of the beach and create conditions of 'coastal squeeze'. Such conditions are now the norm in highly urbanized coastal areas.

In Greece, coastal erosion threatens more than 30% of its coastlines, making it one of the country's most important environmental problems. In particular, the coastal areas of Attica face significant environmental and aesthetic degradation due to excessive urbanization, due to the artificial transport of sediment from the hinterland to the coast (with the transported sediment subject to erosion) and due to the development of facilities and structures to serve tourism and trade (Belibassakis and Karathanasi, 2017). Human interventions and coastal erosion lead to ecosystem degradation and the destruction of shorelines that are important paleo-indicators of a beach's changes while protecting it from further erosion (Koutsomichou et al, 2009).

Regarding the Saronic Gulf and the phenomenon of its coastal erosion, this seems to be linked to human interventions, to climatic factors, to the change in sea level and at the same time to the tectonics that characterizes the Gulf. The Gulf is characterized by moderate seismicity, with the northern and western Gulf margins exhibiting high magnitude historical and recent earthquakes, associated with the presently active N-S extensional tectonic regime (Foutrakis and Anastasakis, 2020). The basin of the Gulf forms a complex neotectonic structure in the NW edge of the inner, modern, Hellenic volcanic arc, while a relatively shallow underwater ridge at its central portion demarcates the eastern from the western part of the basin (Kolaiti and Mourtzas, 2016). This central platform implies the existence of a NNE–SSW trending rupture zone, which is probably the offshore extension of a large thrust belt dominating the adjacent onshore areas (Drakatos et al., 2005).

For the study of erosion and the short- and long-term assessment of changes in a coastline, drone technology has become particularly effective. According to Joyce et al. (2023), drone technology is well suited to providing data in coastal environments and offers flexible timeframes that sequentially cover continuous changes in coastal dynamics; it can be applied to a variety of data types while offering better spatial resolution than that offered by other modes of survey (such as aircraft and satellites), as drones move at lower altitudes and therefore closer to the area of interest. In addition, their data can be combined with free satellite data to produce high fidelity images, which can then be used to build digital terrain models (DEMs and DTMs) and surface models (DSMs). Of course, drone technology presents its own challenges when using it in research, a topic that is beyond the scope of this research.

Objectives

The aim of this research is to investigate, using drone technology, the extent of erosive processes in the highly urbanized coastal zone of the Eastern Saronic Gulf, by determining the extent of horizontal shoreline displacement at the touristic beach of Mavro Lithari within two consecutive seasons - spring and autumn - of 2023. Understanding the size and dynamics of the active part of a beach is crucial for the sustainable environmental management of the wider coastal zone, although each beach due to its particular physiographic features may show smaller or larger deviations from the general morphological trend of the wider coastal area.

Methods

The collection of high-resolution images from the beach of Mavro Lithari in the two different seasons of 2023 (spring and autumn) was carried out using a rotor-wing UAS, the 'DJI Matrice 210 RTK' model series (Figure 1). This drone is one of the most suitable for coastal monitoring, and thanks to its RTK antenna equipment it shows great stability in flight, even in conditions with strong winds. Moreover, this type of drone can support different types of sensors and, therefore, can be applied in a variety of research fields (Vandarakis et all., 2016). At the same time, 14 Ground Control Points (GCPs) were selected for the georeferencing of the

collected aerial photographs, 7 points for the flight that took place in the spring season and additional 7 points for the autumn flight. In general, the use of GCPs (these are black and white targets of 25 cm × 25 cm., see Figure 1) plays an important role in maximizing the positional accuracy of the collected aerial photographs.
Therefore, the methodology followed was based on the use of drone technology for the collection of high-resolution aerial photographs and their processing through the Pix4D Mapper software in order to compose two orthophoto maps, one for the spring period (early May 2023) and one for the autumn period (late November 2023). Thus, the overall processing of the recorded data, led to the conversion of the orthophotomosaic into a format of two maps with all the necessary elements (such as orientation, scale, background and description of details), using ArcGIS Pro software. At the end, a combined, also, map was created that included both seasonal orthophotos in order to achieve a comparison of the results of the two flights performed (Figure 2).

Figure 1: The DJI Matrice 210 RTK drone and one of the seven GCPs

Results

Based on the acquisition and processing of the data collected, the orthophotos and the corresponding maps that were produced, the combined map showed the shoreline change between the two seasons (Figure 2). The comparison of the two seasonal orthophoto maps indicated an obvious shoreline retreat in the central part of Mavro Lithari beach, by the end of autumn, of 1-2 m. This calculation has not been influenced by the negligible error values (absolute and relevant), as showed in the comparative data of Table 1. The retreat of 1-2 m is an expected seasonal (probably) temporary retreat of the shoreline, as the physiography of the Saronic Gulf does not favor the development of frequent extreme wave conditions, while Mavro Lithari beach has not been subject to much human intervention in the active sedimentation zone, as the case is in other coastal areas of the Saronic Gulf (e.g. Ormos Faliros, Alimos, Glyfada), which present much more significant erosion processes.

Absolute camera position and orientation uncertainties (sigma) for the May 2023 orthophotomosaic

	X(m)	Y(m)	Z(m)	Omega(degrees)	Phi(degrees)	Kappa(degrees)
Mean	0,064	0,046	0,123	0,034	0,033	0,009
Sigma	0,013	0,016	0,011	0,014	0,010	0,002

Relevant camera position and orientation uncertainties (sigma) for the May 2023 orthophotomosaic

	X(m)	Y(m)	Z(m)	Omega(degrees)	Phi(degrees)	Kappa(degrees)
Mean	0,022	0,023	0,031	0,060	0,032	0,011
Sigma	0,005	0,008	0,015	0,026	0,013	0,002

Absolute camera position and orientation uncertainties (sigma) for the November 2023 orthophotomosaic

	X(m)	Y(m)	Z(m)	Omega(degrees)	Phi(degrees)	Kappa(degrees)
Mean	0,343	0,364	0,577	0,176	0,169	0,155
Sigma	0,054	0,071	0,034	0,008	0,005	0,003

Relevant camera position and orientation uncertainties (sigma) for the November 2023 orthophotomosaic

	X(m)	Y(m)	Z(m)	Omega(degrees)	Phi(degrees)	Kappa(degrees)
Mean	0,020	0,022	0,027	0,062	0,031	0,012
Sigma	0,004	0,006	0,012	0,025	0,013	0,003

Table 1. Absolute and relevant camera position and orientation uncertainties

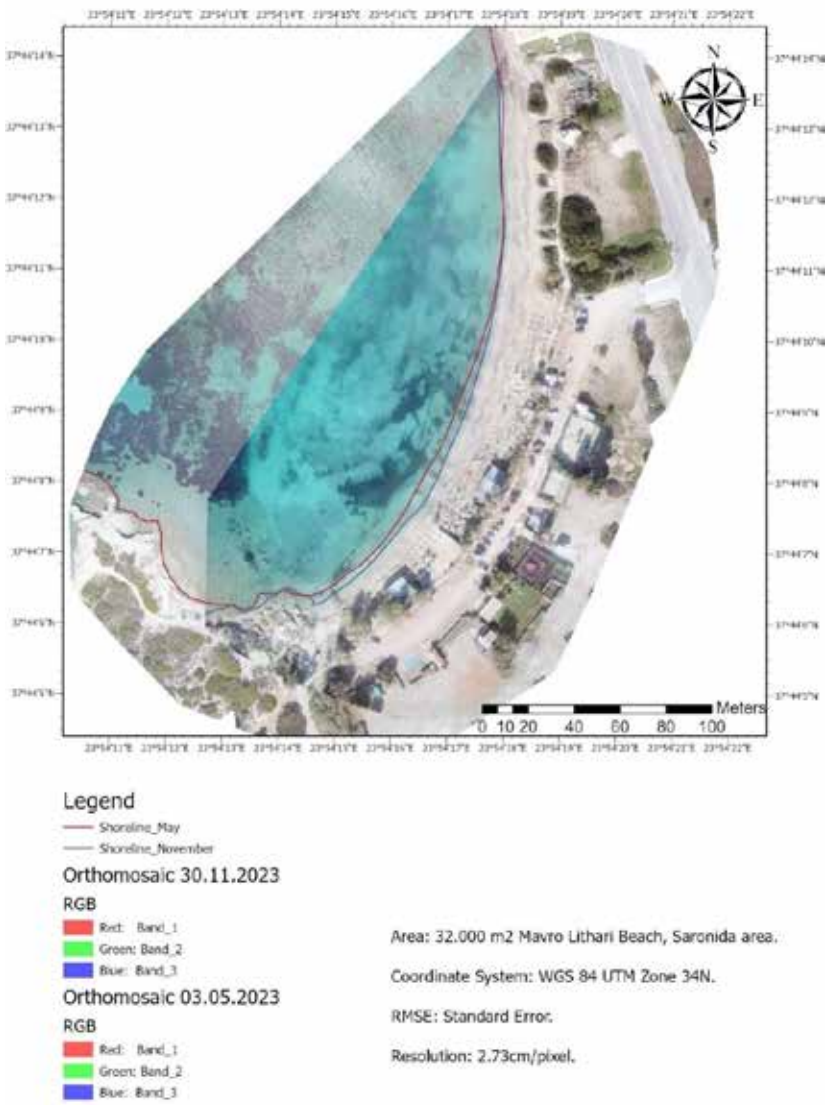

Figure 2: Combination of the two seasonal orthophotomosaics for the beach of Mavro Lithari

Discussion and Conclusions

The orthophotos produced by the two flights of the DJI Matrice 210 RTK drone showed that the shoreline in the central part of the study area receded by 1-2 m. It is considered that this shoreline shift probably represents a seasonal, temporary situation, as the beach of Mavro Lithari has not been subjected to significant human interventions (which are an erosional factor), while at the same time it is part of a bay whose general physiography favors only a small frequency of extreme wave conditions. Regarding the uncertainties of the determined erosion amplitude at Mavro Lithari beach, as calculated by the relevant Pix4D software of the two flights, they show very low error values, so the 1-2 m shoreline retreat is realistic and indicative of the degree of receding of a natural beach in the Eastern Saronic Gulf, albeit probably seasonally.

These results seem particularly interesting if we compare them with other studies for the Saronic Gulf. For example, Skilodimou et al. (2021) state that in the last 76 years the coastline has been enhanced by 40% in terms of extension (e.g. through earth filings, technical works, artificial structures) and the 60% of its total length is artificial, 29% includes rocky shores and the remaining part consists of beaches. The largest interventions have been made in Ormos Faliro (287%), Alimos (256%) and Glyfada (194%), areas with a higher coastal erosion. For comparative purposes, Figure 3 shows the artificial extension (tens to hundreds of meters) of various shorelines in the Eastern Saronic Gulf, which is the main factor of coastal erosion in the region. In our case, with the measurements showing a much smaller erosive area compared to the above-mentioned areas of the Saronic Gulf, this can be interpreted due to the physiography of the Mavro Lithari beach and the fewer human interventions (or absence of them).

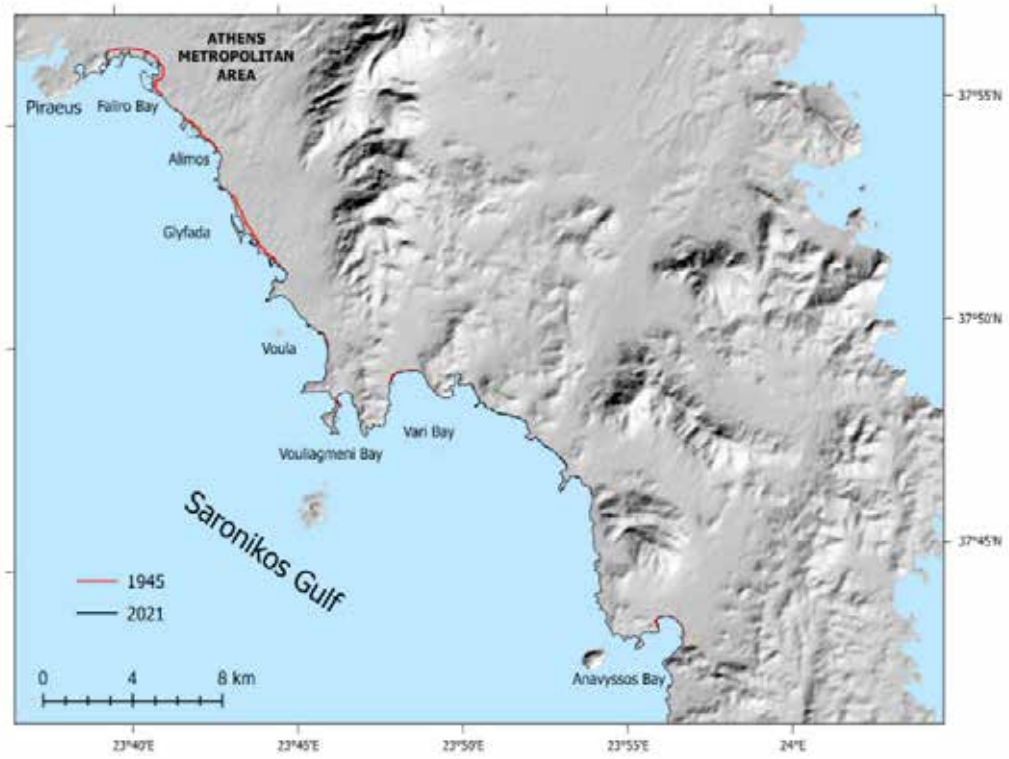

Figure 3: Shoreline changes in the northwest of the studied beach of Black Lithari (red arrow) which has undergone intense changes over the last decades (from Skilodimou et al., 2021)

The results of the research also highlight that drone technology is a very useful and versatile tool, which can produce very high resolution orthophotos and thus accurately capture the changes of coastlines in different regions of the planet at regular intervals, thus contributing significantly to the study of the phenomenon of coastal erosion, which is critical for humanity.

To conclude the discussion, our research has some limitations: a) the measurements were made between 3 May and 30 November 2023, so they cannot capture inter-annual changes; b) the research would be more complete if there were data related to the quality of sediments and rocks in the area as well as wave and wind data.

References

Belibassakis, K.A., Karathanasi, F.E., 2017. Modelling nearshore hydrodynamics and circulation under the impact of high waves at the coast of Vakia in Saronic-Athens Gulf. Oceanologia 59, 350-364.

Drakatos, G., Karastathis, V., Makris, J., Papoulia, J., Stavrakakis, G., 2005. 3D crustal structure in the neotectonic basin of the Gulf of Saronikos (Greece). Tectonophysics 400, 55–65.

Foutrakis, M.P., Anastasakis, G., 2020. Quaternary continental shelf basins of Saronikos Gulf, Aegean Sea. Geo-Marine Letters, 40, 629–647.

Guerrera, F., Martín-Martín, M., Tramontana, M., Nimon, B., Kpémoua K.E., 2021. Shoreline changes and coastal erosion: The case study of the Coast of Togo (Bight of Benin, West Africa Margin). Geosciences 11, Article No 40.

Joyce, K.E., Fickas, K.C., Kalamandeen, M., 2023. The unique value proposition for using drones to map coastal ecosystems. Cambridge Prisms: Coastal Futures 1, e6, 1-10.

Kolaiti, E., Mourtzas, N.D., 2016. Upper Holocene sea level changes in the West Saronic Gulf, Greece, Quantenary International, 401, 71-90.

Koutsomichou, I., Poulos, S., Evelpidou, N., Anagnostou, C., Chionis, G., Vassilopoulos, A., 2009. The role of beachrock formations in the evolution of embayed coastal zones of Attica (Greece) in relation to sea level rise. The case of Kalyvia beach zone. Geografia Fisica e Dinamica Quaternaria 32, 49-56.

Skilodimou, D.H., Antoniou, V., Bathrellos, D.G, Tsami, E., 2021. Mapping of coastline changes in Athens Riviera over the past 76 years' measurements. Water 13, Article No 2135.

Vandarakis, D., Pavlopoulos, K., Kapsimalis, V., 2016. Coastal geomorphological features and geoarchaeological potential of Kavouri Bay, Attica, Greece. 14th International Conference of the Geological Society of Greece, Thessaloniki, 25-27 May, Bulletin of the Geological Society of Greece, vol. L, pp. 265-273.

17th INTERNATIONAL CONGRESS
of the Geological Society of Greece

BULLETIN OF THE GEOLOGICAL SOCIETY OF GREECE, SP. PUBL.

EXTENDED ABSTRACT 256

Active Faulting in Santorini and the recent intra-caldera (2024-2025) seismic activity along the Kameni-Fira Fault line

Pavlides S.[1], Karastathis V.[2], Mouzakiotis E.[2], Sboras S.[2], Chatzipetros A.[1], Lazos I.[1]
(1) School of Geology, Aristotle University of Thessaloniki, Greece, pavlides@geo.auth.gr
(2) Institute of Geodynamics, National Observatory of Athens, Greece

This paper presents certain elements of the neotectonic and active structure of the Santorini island complex. The active structures consist of sets of primarily normal fault systems with right-lateral component in an *en échelon* pattern, trending at or around N30°E (Mountrakis et al., 1998). Another important and common feature on Santorini is the feeder dykes that are related with those faults. Along the major Columbo fault line, which appears to start at the southernmost tip of Therassia Island (Cape Trypiti) and stretch up to the Columbo submarine volcano and Anhydros Islet, they are primarily concentrated on the northern narrow part of the island, north of Mikros Prophitis Elias ridge.

The Fira normal fault is another active structure that is visible in the caldera walls. Significant tectonic evidence of recent activity may be seen on the Yialos Caldera cliff, including fractured and tilted late Quaternary volcanic layers, as well as new on-land tectonic scarps. A syn-depositional normal fault, it is a significant structure that deforms various volcanic lava layers, scoria, and pyroclastic flows. As evidenced by the microseismic activity during the 2011–2012 crisis and the one ongoing since the end of 2024, this fault is classified as active.

A large scarp of the same strike affects the relief along the fault-line and continues farther to the northeast on the island, even though volcanic material near the topmost part of the fault appears undeformed. It is thought to be a longer, seismically hazardous structure that follows the tectonic line of the Kameni volcano. The fault was modelled by using data from a UAV campaign, that allowed for the construction of a precise DTM (Figure 1, Pavlides & Chatzipetros, 2018). It shows that fault throw episodically declines upward on the caldera's highly steep inner escarpment, from 22 m at sea level to nearly 2 m at the highest point (Pavlides et al., 2025, this volume).

Two extensional contemporary stress phases have been documented, implying that the first is attributed to the tectonic stresses related to the well-established Aegean motion towards SSW, whereas the second, which gives rise to recent microseismicity of the area, is a local stress regime attributed to buoyancy forces relating to magmatic processes of the area (Pavlides & Tranos 2014). Therefore, the combination of these two stress regimes reflects the competition between the tectonic (lithospheric) and magmatic (local volcano-tectonic) forces, in a fault-dynamic regime that could be characterized as extensional-transtentional field.

During the 2024-2025 volcano-seismotectonic crisis, the Fira fault ("Kameni line") is activated producing a shallow sequence which slowly initiated in the beginning of late September 2024 and is still in progress. More than 200 eventst were recorded within the study region for this period and their hypocentres were calculated using the NonLinLoc earthquake location algorithm (Lomax et al., 2000) along with the local 1D velocity model proposed for the region by Dimitriadis et al. (2009). The NonLinLoc algorithm utilizes the equal-differential-time (EDT) likelihood function (Zhou, 1994; Font et al., 2004), which uses travel-time differences between observed and synthetic travel times for pairs of stations, resulting to a more robust calculation of the optimal hypocentral location, due to the fact that the 4-D problem (x,y,z, t) is reduced to a 3-D search over space (x,y,z). Furthermore, mispicked phase data can be identified by the methodology and excluded from the solution. Due to the large number of local seismographic stations at a very close proximity to the sequence, for most of the located events the horizontal error was as low as 0.5km, whereas the vertical (depth) error was between 0.8-1.2 km. The majority of the sequence's hypocentres is located at shallow depths (3-8 km). The strongest earthquake (ML 3.6) occurred on January 25, 2025. The moderately linear horizontal trend of the epicentres is main the characteristic of the sequence.

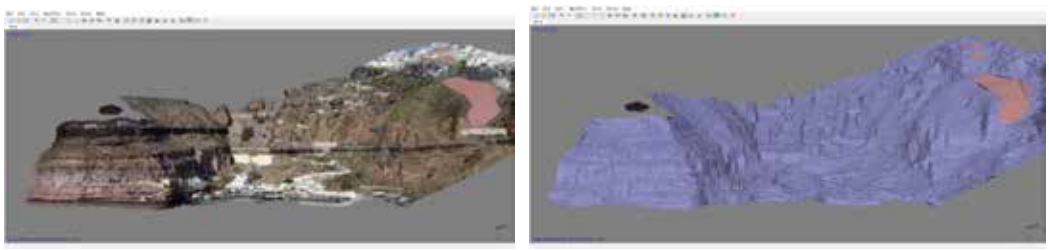

Figure 1. Digital Terrain Model of the Yialos cliff face, where the Fira fault is observed deforming the layers of lavas and pyroclastics. It was obtained through a targeted UAV campaign (Pavlides & Chatzipetros, 2018). Left image shows the outcrop photomosaic draped over the 3D model, which is shown at the right one.

The majority of earthquakes are thought to be caused solely by tectonic forces, specifically the Fira fault. If we additionally consider the estimation of the volume and depth of the magma intrusion, some of them are most likely caused by the volcanotectonic activity. More specifically, the Fira fault likely both facilitates the magma chamber's upward progress and marks it off to the south.

All evidence, both geological and seismological, indicate that the Fira fault is an active tectonic structure. Its activated length is estimated to about 6-8 km, corresponding to a moderate expected earthquake magnitude of Mw 5.5-6.0, as calculated from known empirical relationships (Wells & Coppersmith, 1994). The fault probably extends bilaterally, i.e. toward the NE, as shown by the seismic activity of the beginning of 2025, and toward the SW as well. Northward onward intracaldera tectonic structures formation example elucidates a swelling of the volcanic edifice.

References

Dimitriadis, I., Karagianni, E., Panagiotopoulos, D., Papazachos, C., Hatzidimitriou, P., Bohnhoff, M., ... & Meier, T. (2009). Seismicity and active tectonics at Coloumbo Reef (Aegean Sea, Greece): Monitoring an active volcano at Santorini Volcanic Center using a temporary seismic network. Tectonophysics, 465(1-4), 136-149.

Font, Y., Kao, H., Lallemand, S., Liu, C. S., & Chiao, L. Y. (2004). Hypocentre determination offshore of eastern Taiwan using the Maximum Intersection method. Geophysical Journal International, 158(2), 655-675.

Lomax, A., Virieux, J., Volant, P., & Berge-Thierry, C. (2000). Probabilistic earthquake location in 3D and layered models: Introduction of a Metropolis-Gibbs method and comparison with linear locations. Advances in seismic event location, 101-134.

Mountrakis, D., Pavlides, S., Chatzipetros, A., Meletlidis, S., Tranos, M., Vougioukalakis, G., & Kilias, A., 1998. Active deformation of Santorini. In: Casale et al. (Eds), The European laboratory volcanoes, European Commission, EUR 18161 EN, 13-22.

Pavlides, S. & Chatzipetros, A. (2018). The Fira fault (Santorini, Greece) from the French "Expédition de Morée (1829□38)" to modern scientific approach, *In:* Koukousioura, O. & Chatzipetros, A. *(Eds.),* Proceedings of the 9th International INQUA Workshop on Paleoseismology, Active Tectonics and Archeoseismology, Possidi, Greece, 25-27 June 2018, 218-220.

Pavlides, S. & Tranos, M. (2012). Fault geometry and kinematics of the broader Santorini area in relation to seismic activity and volcanism. Abst. VOLSAM2012.

PavlidesS., Sboras S., LazosI., Mouzakiotis E., & Karastathis V. (2025). The Fira fault, Santorini (Thera): morphotectonic, geomorphological and seismological evidence of fault activity, 17th International Congress of the Geological Society of Greece, Mytilene, Greece.

Zhou, H.W. (1994). Rapid three□dimensional hypocentral determination using a master station method. Journal of Geophysical Research: Solid Earth, 99(B8), 15439-15455.

17th INTERNATIONAL CONGRESS of the Geological Society of Greece

BULLETIN OF THE GEOLOGICAL SOCIETY OF GREECE, SP. PUBL.

EXTENDED ABSTRACT 257

The Fira fault, Santorini (Thera): morphotectonic, geomorphological and seismological evidence of fault activity

Pavlides S.[1], Sboras S.[2], Lazos I.[2], Mouzakiotis E.[2], Karastathis V.[2]

(1) School of Geology, Aristotle University of Thessaloniki, Thessaloniki, Greece, pavlides@auth.gr (2) Institute of Geodynamics, National Observatory of Athens, Athens, Greece

Introduction

The volcanic island of Santorini, *aka* Th(i)era, is located in the central part of the Hellenic Arc (or Hellenic Subduction Zone), in the South Aegean Sea, where the Nubian (African) and Eurasian tectonic plates converge (Figure 1; Pavlides *et al*., 2024 and references there in). Santorini has a rich geological history including recent tectonic and volcanic activity, particularly in the last century. The Fira Fault (*aka* Phera) is one of the most prominent active faults in Santorini (Figure 2). It outcrops on the eastern rim of the Caldera crossing the capital town of the island, in a NE-SW direction. Santorini's fault system includes numerous faults and fractures that contribute to its seismic activity, particularly around the caldera, which has been the focus of volcanic activity for thousands of years. The Fira Fault plays a key role in the ongoing geodynamic processes of the island. In addition to this fault, there are several other active faults around the caldera, including the "Kulumbo (or Columbo) line" and the "Kamenes line" (Pfeiffer, 2001), and others that create a complex tectonic pattern in the region (Figure 2; Mountrakis *et al*., 1998; see also Nomikou *et al*., 2021; Sakellariou *et al*., 2021).

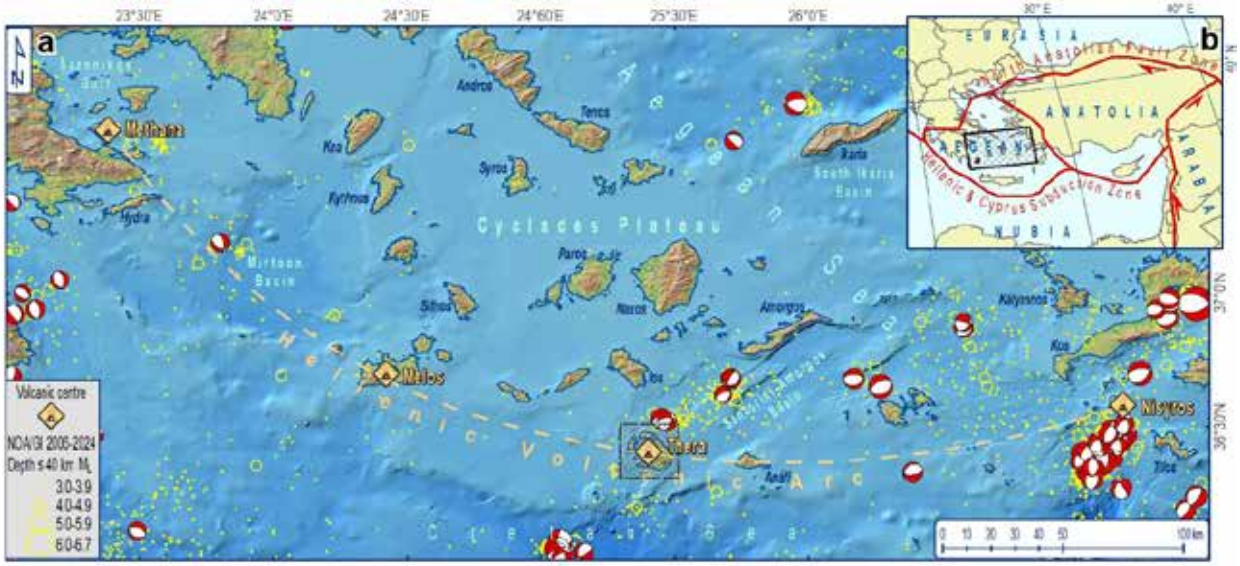

Figure 1. (a) Map of the South Aegean Sea showing seismicity (yellow circles; NOA/GI revised catalogue since 2006 for depths ≤ 40 km) and RCMT's focal mechanisms for depths ≤ 40 km (Pondrelli, 2002). The Hellenic Volcanic Arc is marked by an orange dashed line. Hatched frame indicates location of Thera as shown in Figure 2. (b) The tectonic plates boundaries in eastern Mediterranean Sea according to Bird (2003). Hatched frame indicates position of map (a).

Geodynamic & seismotectonic setting

The recent tectonic regime of the Aegean Sea is characterized by a regional extension deriving from the subducting slab's roll-back and retreat as the Hellenic Arc has been migrating southwards during the last 80 Myr (*e.g.* Le Pichon & Angelier, 1979; 1981; Jolivet *et al*., 2013; Barbot & Weiss, 2021; van der Stoel *et al*., 2024). This extension generates normal faults in the upper crust and rifting in the shallower part of the lithosphere (Jolivet *et al*., 2013). The extensional thinning of the crust facilitates the magma intrusion from the melting of the subducting slab and the emergence of the Methana, Melos, Santorini, Kolumbo and Nisyros volcanic centres which comprise the volcanic arc. The Santorini–Amorgos offshore basin is a crustal weakness zone in an overall right-lateral oblique-slip transtensional regime, representing a major structural boundary *(e.g.* Sakellariou & Tsampouraki-Kraounaki, 2019; Tsampouraki-Kraounaki *et al*., 2021).

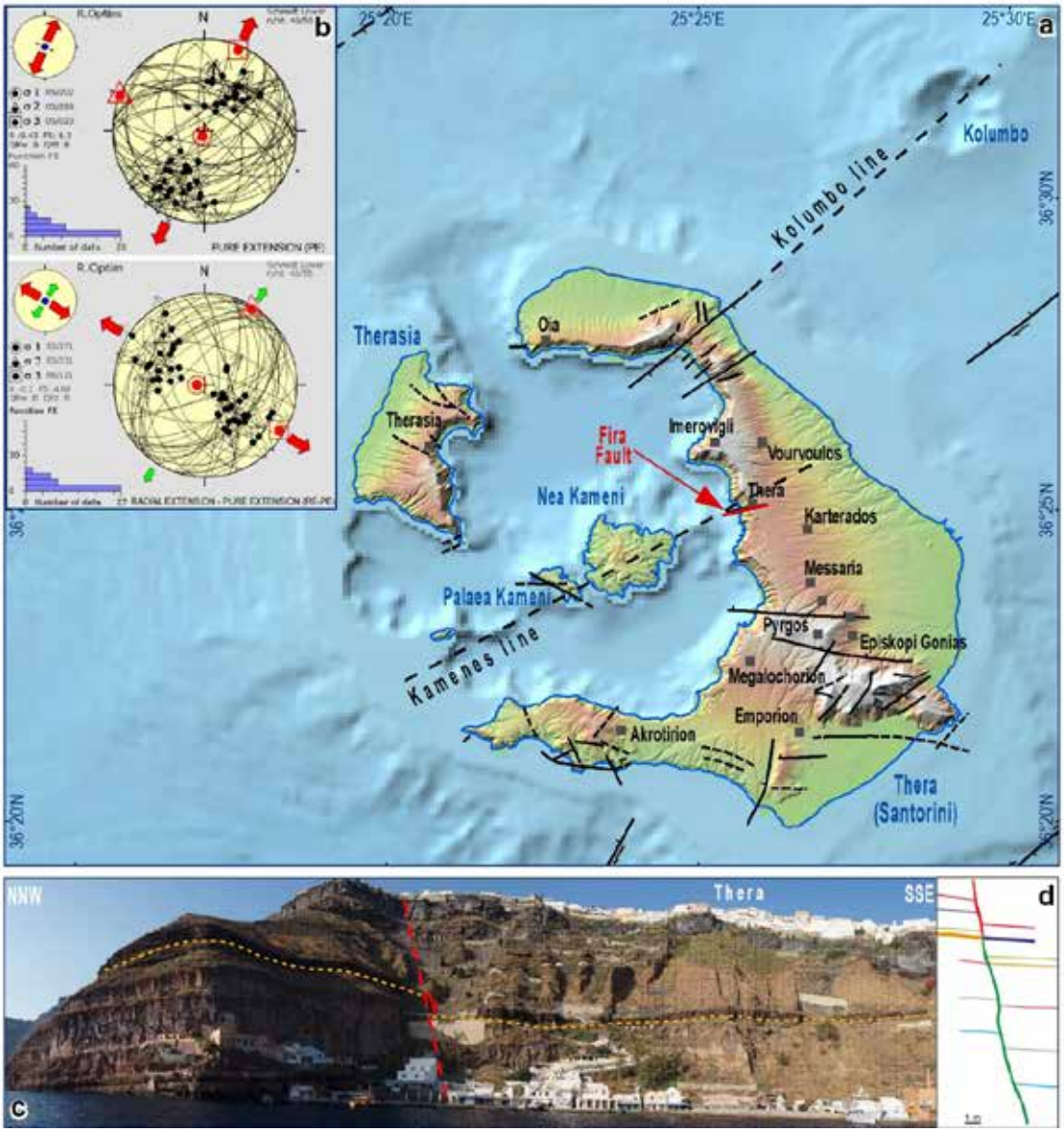

Figure 2. (a) Morphotectonic map of Santorini Island after Mountrakis *et al*. (1998). The "Kulumbo line" and "Kamenes Line" are modified from Pfeiffer (2001). (b) Meso-structural analysis of active faults on Santorini and surroundings showing two co-existing extensional stress fields: one (upper) due to pure tectonic forces (typical of the Aegean back-arc), and the other (lower) probably due to magmatic (local volcano-tectonic) forces (more radial extension). (c) Snapshot of a 3D image obtained from UAV depicting the inner caldera flank and the Fira fault cutting and downthrowing toward the SSE the lava layers (the most distinguishable layer is marked by a dashed orange line). (d) Sketch of the Fira fault and the displaced lava layers as shown in (c).

Santorini Island is an emergent remnant on the central and eastern flanks of a collapsed caldera. Its summit is preserved with over 50 active tectonic structures of the Middle Pleistocene to Holocene. Seafloor topography and subsurface fault data show a complex system of faulting from Christiana island to Amorgos island, with mainly NE trending normal and oblique faults in a right-stepping en echelon arrangement. A tectonic model demonstrating the occurrence of the volcanic centers at the fault segment boundaries is presented. In the case of Santorini – Amorgos Fault System, volcanic centers of Christiana Island, Thera – Kammeni and the submarine crater of Columbo are positioned in the boundaries of the right-stepping en echelon segments of normal and oblique faults. Fault segment boundaries comprise low strength multi-fractured parts of the upper crust, enabling insertion and ascendance of magma dykes. Possible interaction between volcanic activity and fault activation is also investigated based on the

early 20th century eruption activity in Kammeni islands and the 1956 double-earthquake event, as well as the 2011-12 volcanotectonic crisis. Dykes and fault swarms are the two main modes of brittle tectonics in the area. The active tectonic structures mainly consist of normal fault systems often in an *en-échelon* pattern. Reverse and right-lateral, or oblique-slip, faulting also occur in the area. Meso-structural analysis reveals the three main stress axes acting on Santorini and surrounding islets (Tranos & Pavlides, 2012; see also Tranos 2012): σ_1 in a NE–SW direction, σ_3 in a normal direction, and σ_2 in the third leading σ_2 direction. Santorini's tectonic structures are then probably the result of this stress field (Manning *et al*., 2020). Basaltic dykes, associated with neotectonic faulting, are another common feature in Santorini. They are aligned along the axial zone of the submarine caldera and are exposed on the marine cliffs, forming up to a 100-m wide rail on the caldera wall, concentrated on the northern narrow part of the island. The N30°E-trending arc (?) of Santorini and its orientation guide the spatial correlation in the dyke-fault system. This system is expected to be connected at depth because tensional fracturing is expected to occur in fissure eruptions and in the effects of ascending magma within the surrounding rocks (Mountrakis *et al*., 1998; Ruch *et al*., 2016). The orientation of the N30°E-striking structures, comprising mostly of normal and a few reverse faults restricted in the alpine basement, represent the local σ_3 axis. Northward, in the inner flank of the caldera, tectonic structures document a swelling of the volcanic edifice. The neotectonic map of Santorini in Figure 2 (Mountrakis *et al*., 1998) indicates the more recent tectonic structures and the active processes shaping the island's landscape. It shows the fault systems, including the Fira Fault and other fractures, which have been active in recent geologic and historical times. This map also highlights the zones of volcanic activity and deformation, which are critical for understanding the island's seismic hazards.
The faults that control the eruptive history of Santorini and changes of the magmatic chamber produce characteristic earthquake swarms. The 2011-2012 seismic crisis on Santorini is a typical example.

Morphotectonic study of the Fira fault

Neotectonic field studies on Santorini started in 1992-94 and were completed during 2016-22 (Figure 2; see Mountrakis *et al*., 1998; Pavlides & Chatzipetros, 2018). Among the on land mapped faults, the less studied is the Fira fault, named after the capital town of the Island. The fault has been a prominent feature of Fira cliff (Yalos harbour), and it has been described as a simple tectonic structure since the early French "Expédition de Morée (1829□38)". New airborne (UAV) and terrestrial (LiDAR) images were used to produce 2D and 3D photomosaics with photogrammetric methods so as to detect the location and map the Fira fault.
Meso-structural analyses, where the fault outcrops in accessible locations, indicate a normal dip-slip sense of movement with a right-lateral strike-slip component on an ENE-WSW (N60°E to70°E) striking fault. According to our 3D terrain model obtained from UAV images, on the very steep inner escarpment of the caldera, fault throw episodically decreases from 22 m at the sea level down to almost 2 m at the highest elevation where the Nomikos Conference Centre is built (Figure 2). At this point, the uppermost lava layer is affected suggesting a syn-depositional normal fault that deforms even the most recent volcanic lava layers and pyroclastic flow strata. This lava layer, which is also the last, 40-60 ka old, volcanic flow, documenting typical cooling fractures and tectonic open joints outcrop, has been vertically displaced. The episodic pattern of displacement can be interpreted as intermittent periods of possibly volcano-tectonic activity rather than simply tectonic. A non-typical fault scarp affecting the volcanics is detected in the urban area of Fira running subparallel to *i)* a longer "fault zone" which includes the known volcanic centres of Kamenes (Kamenes line), and *ii)* the large Amorgos-Thera seismic fault which produced the 1956 M7.5 earthquake (Kolumbo line). Due to its proximity to the "Kamenes line", the Fira fault can be considered as part of this line.
The Fira fault is classified as active, as it is documented not only from field observations, but also from the microseismic activity during the 2011□2012 volcano-tectonic crisis. Its activated length has estimated about 6 km, corresponding to moderate earthquake Ms 5.5 +_ , as calculated from known empirical relationships, while it is possibly extended both towards NE and SW.

Seismic Activity and the Volcanic Crisis of 2011-2012

During the 2011-2012 volcano-seismotectonic crisis, the Fira fault of the "Kamenes line" was activated producing a shallow sequence which slowly initiated in the beginning of late February 2011 and outburst in October of the same year (Kaviris et al., 2015). The strongest earthquake (M_L3.3) occurred on January 9, 2012; Five (5) earthquakes with $M_L \geq 3.0$ preceded and one followed the strongest shock.
The local seismicity for the period of interest was accurately located with the use of a local 1D velocity model proposed for the region by Dimitriadis *et al*. (2009), by applying the NonLinLoc -linear location algorithm (Lomax *et al*., 2000). The NonLinLoc algorithm utilizes the equal-differential-time (EDT) likelihood function (Zhou, 1994; Font *et al*., 2004),

which uses travel-time differences between observed and synthetic travel times for pairs of stations, resulting to a more robust calculation of the optimal hypocentral location, due to the fact that the 4-D problem (x,y,z, t) is reduced to a 3-D search over space (x,y,z). Furthermore, mispicked phase data can be identified by the methodology and excluded from the solution.

The majority of the sequence's hypocentres is concentrated at very shallow depths (2-6 km). The spatial distribution shows a quite well-formed cluster (cluster A in Figure 3 *left*) on the SW continuation of the Fira fault which moderately aligned along a NE-SW axis, *i.e.* parallel to the fault's strike. Two transverse profiles show the vertical extent of the sequence from ca. 1 km to 12 km depth (Figure 3 *right*). However, the density differs in the two profiles (Figure 3 *right*): in the profile B-B' it is much more concentrated than in profile A-A'. This also explains the moderately linear horizontal trend of the epicentres. In profile B-B', the density of hypocentres is much higher at depths shallower than 6 km. From this depth and deeper (down to 12 km), a much more linear, SSE steeply dipping trend can be observed, the upward continuation of which also marks the southern limit of the cluster. Thus, two sub-clusters can be distinguished: the shallow one, cluster A_1, down to the depth of 6 km, and the deeper one, cluster A_2, at depths between 6 and 12 km. Cluster A_2 is attributed to purely tectonic causes, and more particularly to the Fira fault. Cluster A_1 is probably due to the combined tectonic and volcanic (magmatic) activity if we also take into account the estimation of both volume and depth of the magma intrusion (Newman *et al*., 2012; Feuillet, 2013; Parks *et al*., 2012; 2015; Druitt *et al*., 2016). In more detail, the Fira fault probably restrains the magma chamber to the south and, at the same time, facilitates it movement.

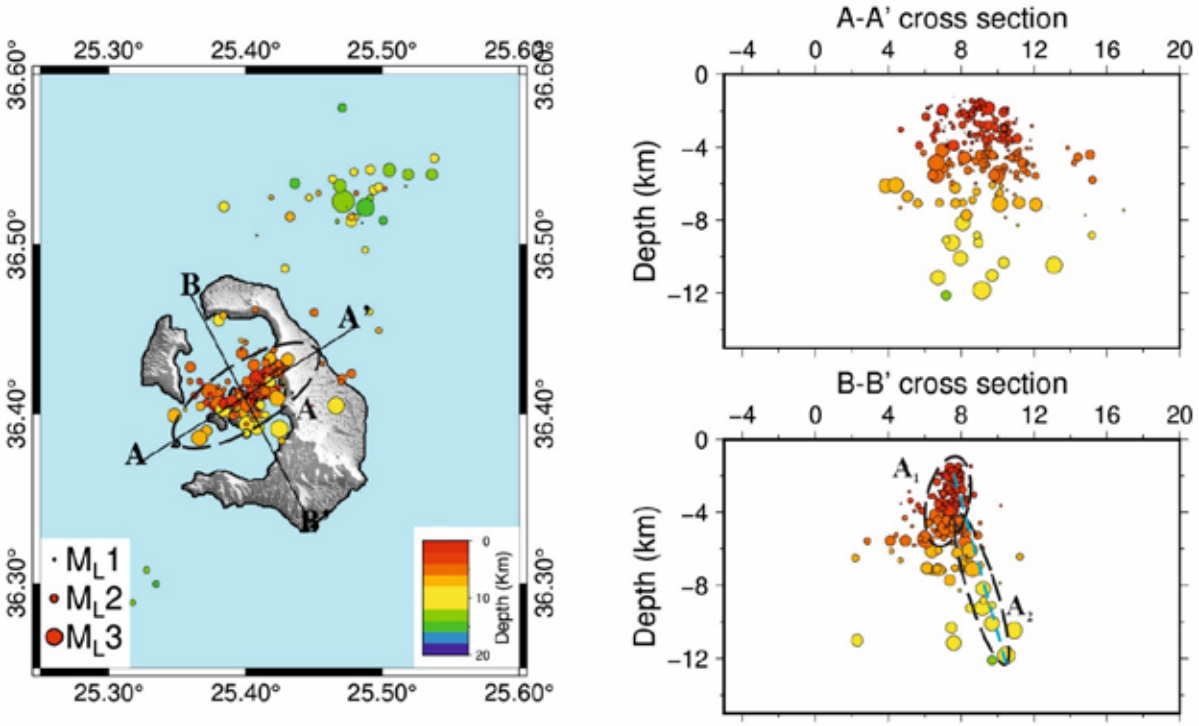

Figure 3. (Left) Relocated epicentres of the 2011-2012 crisis. The main cluster A is marked by a dashed ellipsis. A sparse concentration NE of Santorini Island is located under the Kolumbo submarine volcano. (Right) Vertical profiles of the 2011-2012 main cluster which is divided into two more sub-clusters (A_1 and A_2). The blue dashed line represents the Fira fault. The profile traces are shown on the left map.

The 2011-2012 volcanic crisis in Santorini was marked by increased seismic activity, volcanic unrest, and noticeable ground deformation. This period of volcanic crisis also involved:

- Ground deformation: There were reports of ground uplift, which is often associated with magma intrusion or movement beneath the surface (e.g. ISMOSAV, 2013). GPS measurements and InSAR images show both lateral extension and uplift, clearly suggesting inflation (Newman *et al*., 2012; Foumelis *et al*., 2013; Papoutsis *et al*., 2013; Saltogianni *et al*., 2014). This is typical in volcanic regions where magma rises and causes the earth's crust to stretch or deform.
- Magma intrusion: A magma intrusion of 10–25 million m^3 is estimated (Newman *et al*., 2012; Parks *et al*., 2012;

2015) at a depth of ca. 4 km (Druitt *et al*., 2016). This magma is suspected to be linked to the dyke systems beneath the island, contributing to the seismic events. A dyke system refers to a network of vertical or steeply inclined fractures filled with magma, often causing crustal deformation and triggering earthquakes.

Conclusions

The Fira normal fault shows significant tectonic evidence of recent activity such as fresh scarps and faulted and tilted late Quaternary volcanic strata. It has not been studied in depth.

- The Fira fault is a typical normal tectonic structure trending ENE-WSW, with a right-lateral oblique-slip sense of movement. It shows decreasing downthrow from the sea level to the top lava layer, indicating a syn-volcanic deposition fault growth.
- It is an active fault in the western part of the Santorini caldera rim, contributing to seismic hazard.
- It is a "segment" of sub-parallel, left stepping faults belonging to the larger fault zone of "Kamenes line", including the known volcanic centers. It is also subparallel to the 1956 earthquake great Amorgos-Thera fault. Its internal structure is complex (under investigation).
- The 2011-2012 volcanotectonic crisis was characterized by increased seismicity and ground deformation, linked to magma intrusion and fault activity, associated with the Fira fault. It was a segment of 6 km that was activated by a series of small-magnitude earthquakes, along the Kamenes volcanic line. It is believed to be longer.
- This known fault length corresponds to a minor or moderate earthquake.

Understanding these elements is crucial for monitoring and assessing the potential volcanic and seismic hazards in the region.

Acknowledgements

Bathymetric DTM data used in figures are obtained from the EMODnet Bathymetry (2022). On land DEM data derive from ALOS World 3D, 30-m DEM, v3.2 (Japan Aerospace Exploration Agency, 2021) and the National Cadastre and Mapping Agency S.A. (5-m resolution).

References

Barbot, S., Weiss, J. R., 2021. Connecting subduction, extension and shear localization across the Aegean Sea and Anatolia. Geophysical Journal International, 226(1), 422-445.

Bird, P., 2003. An updated digital model of plate boundaries. Geochemistry, Geophysics, Geosystems, 4(3), 1027.

Dimitriadis, I., Karagianni, E., Panagiotopoulos, D., Papazachos, C., Hatzidimitriou, P., Bohnhoff, M.,..., Meier, T., 2009. Seismicity and active tectonics at Coloumbo Reef (Aegean Sea, Greece): Monitoring an active volcano at Santorini Volcanic Center using a temporary seismic network. Tectonophysics, 465(1-4), 136-149.

Druitt, T. H., Mercier, M., Florentin, L., Deloule, E., Cluzel, N., Flaherty, T., Médard, E., Cadoux, A., 2016. Magma storage and extraction associated with plinian and interplinian activity at Santorini Caldera (Greece). Journal of Petrology, 57(3), 461-494.

Feuillet, N., 2013. The 2011–2012 unrest at Santorini rift: Stress interaction between active faulting and volcanism. Geophysical Research Letters, 40, 3532-3537.

Font, Y., Kao, H., Lallemand, S., Liu, C. S., & Chiao, L. Y., 2004. Hypocentre determination offshore of eastern Taiwan using the Maximum Intersection method. Geophysical Journal International, 158(2), 655-675.

Foumelis, M., Trasatti, E., Papageorgiou, E., Stramondo, S., Parcharidis, I., 2013. Monitoring Santorini volcano (Greece) breathing from space. Geophysical Journal International, 193(1), 161-170.

ISMOSAV - Institute for the Study and Monitoring of the Santorini Volcano, 2013. Current status of the volcano and proposal for monitoring continuation of the Santorini volcano during the year 2014. Final report of ISMOSAV for the 2013 Santorini volcano monitoring, 34 pp.

Kaviris, G., Papadimitriou, P., Kravvariti, Ph., Kapetanidis, V., Karakonstantis, A., Voulgaris, N., Makropoulos, K., 2015. A detailed seismic anisotropy study during the 2011–2012 unrest period in the Santorini Volcanic Complex. Physics of the Earth and Planetary Interiors, 238, 51-88.

Jolivet, L., Faccenna, C., Huet, B., Labrousse, L., Le Pourhiet, L., Lacombe, O.,…, Driussi, O., 2013. Aegean tectonics: Strain localisation, slab tearing and trench retreat. Tectonophysics, 597, 1-33.

Le Pichon, X., & Angelier, J., 1979. The Hellenic arc and trench system: a key to the neotectonic evolution of the eastern Mediterranean area. Tectonophysics, 60(1-2), 1-42.

Le Pichon, X., & Angelier, J., 1981. The Aegean Sea. Philosophical Transactions of the Royal Society of London, Series A, Mathematical and Physical Sciences, 300(1454), 357-372.

Lomax, A., Virieux, J., Volant, P., Berge-Thierry, C., 2000. Probabilistic earthquake location in 3D and layered models: Introduction of a Metropolis-Gibbs method and comparison with linear locations. Advances in seismic event location, 101-134.

Manning, S. W., Wacker, L., Büntgen, U., Bronk Ramsey, C., Dee, M. W., Kromer, B., Lorentzen, B., Tegel, W., 2020.

Radiocarbon offsets and old world chronology as relevant to Mesopotamia, Egypt, Anatolia and Thera (Santorini). Scientific Reports, 10(1), 13785.

Mountrakis, D., Pavlides, S., Chatzipetros, A., Meletlidis, S., Tranos, M., Vougioukalakis, G., Kilias, A., 1998. Active deformation of Santorini. In: Casale et al. (Eds), The European laboratory volcanoes, European Commission, EUR 18161 EN, 13-22.

Newman, A. V., Stiros, S., Feng, L., Psimoulis, P., Moschas, F., Saltogianni, V., Jiang, Y., Papazachos, C., Panagiotopoulos, D., Karagianni, E., Vamvakaris, D., 2012. Recent geodetic unrest at Santorini caldera, Greece. Geophysical Research Letters, 39(6), L06309.

Nomikou, P., Krassakis, P., Kazana, S., Papanikolaou, D., Koukouzas, N., 2021. The Volcanic Relief within the Kos-Nisyros-Tilos Tectonic Graben at the Eastern Edge of the Aegean Volcanic Arc, Greece and Geohazard Implication. Geosciences, 11(6), 231.

Papoutsis, I., Papanikolaou, X., Floyd, M., Ji, K. H., Kontoes, C., Paradissis, D., Zacharis, V., 2013. Mapping inflation at Santorini volcano, Greece, using GPS and InSAR. Geophysical Research Letters, 40(2), 267-272.

Parks, M. M., Biggs, J., England, P., Mather, T. A., Nomikou, P., Palamartchouk, K., Papanikolaou, X., Paradissis, D., Parsons, B., Pyle, D.M., Raptakis, C., Zacharis, V., 2012. Evolution of Santorini Volcano dominated by episodic and rapid fluxes of melt from depth. Nature Geoscience, 5(10), 749-754.

Parks, M. M., Moore, J. D., Papanikolaou, X., Biggs, J., Mather, T. A., Pyle, D. M., Raptakis, C., Paradissis, D., Hooper, A., Parsons, B., Nomikou, P., 2015. From quiescence to unrest: 20 years of satellite geodetic measurements at Santorini volcano, Greece. Journal of Geophysical Research: Solid Earth, 120(2), 1309-1328.

Pavlides, S., Chatzipetros, A., 2018. The Fira fault (Santorini, Greece) from the French “Expédition de Morée (1829□38)” to modern scientific approach. Proceedings of the 9th International INQUA Meeting on Paleoseismology, Active Tectonics and Archeoseismology (PATA), Possidi, Greece, 25-27 June 2018, 218-220.

Pavlides, S., Drakatos, G., Zouros, N., 2024. Active Tectonics and Seismicity in Greece. In: Darques, R., Sidiropoulos, G., Kalabokidis, K. (eds), The Geography of Greece. World Regional Geography Book Series, Springer, Cham, 431-444.

Pavlides, S. Tranos, M. 2012. Fault geometry and kinematics of the broader Santorini area in relation to seismic activity and volcanism. Abst. VOLSAM2012.

Pfeiffer, T., 2001. Vent development during the Minoan eruption (1640 BC) of Santorini, Greece, as suggested by ballistic blocks. Journal of Volcanology and Geothermal Research, 106 (3-4), 229-242

Pondrelli, S., 2002. European-Mediterranean Regional Centroid-Moment Tensors Catalog (RCMT) [Data set]. Istituto Nazionale di Geofisica e Vulcanologia (INGV).

Ruch, J., Wang, T., Xu, W., Hensch, M., Jónsson, S., 2016. Oblique rift opening revealed by reoccurring magma injection in central Iceland. Nature Communications, 7, 12352.

Sakellariou, D., Rousakis, G., Drakopoulou, P., Tsampouraki-Kraounaki, K., Morfis, I., Panagiotopoulos, I., Livanos, I., Loukaidi, V., Kyriakidou, C., Manta M., Lykousis, V., 2021. Geomorphology, Geological Structure, Active Tectonics, and Basin Formation in the Aegean Sea. In: Anagnostou, C.L., Kostianoy, A.G., Mariolakos, I.D., Panayotidis, P., Soilemezidou, M., Tsaltas, G. (eds) The Aegean Sea Environment. The Handbook of Environmental Chemistry, vol 127. Springer, Cham., 49-69.

Sakellariou, D., Tsampouraki-Kraounaki, K., 2019. Plio-Quaternary extension and strike-slip tectonics in the Aegean. In: Duarte, J. C. (ed), Transform plate boundaries and fracture zones, Elsevier, 339-374.

Saltogianni, V., Stiros, S. C., Newman, A. V., Flanagan, K., Moschas, F., 2014. Time□space modeling of the dynamics of Santorini volcano (Greece) during the 2011–2012 unrest. Journal of Geophysical Research: Solid Earth, 119(11), 8517-8537.

Tranos, M.D. 2012. Slip preference on pre-existing faults: a guide tool for the separation of heterogeneous fault-slip data in extensional stress regimes. Tectonophysics, 544-545, 60–74.

Tsampouraki-Kraounaki, K., Sakellariou, D., Rousakis, G., Morfis, I., Panagiotopoulos, I., Livanos, I., Manta, K., Paraschos, F., Papatheodorou, G., 2021. The Santorini-Amorgos Shear Zone: Evidence for Dextral Transtension in the South Aegean Back-Arc Region, Greece. Geosciences, 11(5), 216.

van der Stoel, J. M., Strak, V., Schellart, W. P., 2024. The role of subduction and gravitational collapse in driving extension in the Aegean Sea. Tectonophysics, 872, 230206.

Zhou, H. W., 1994. Rapid three□dimensional hypocentral determination using a master station method. Journal of Geophysical Research: Solid Earth, 99(B8), 15439-15455.

17th INTERNATIONAL CONGRESS of the Geological Society of Greece

BULLETIN OF THE GEOLOGICAL SOCIETY OF GREECE, SP. PUBL.

EXTENDED ABSTRACT 258

Geological routes on Ammouliani Island, northern Greece

Pegioudi E.[1], Chatzipetros A.[2]

(1) University of the Aegean, Mytilene, Greece, pegiou@hotmail.com (2) Department of Structural, Historical and Applied Geology, School of Geology, Aristotle University of Thessaloniki, Greece, ac@geo.auth.gr

Introduction

The study area is an island located west of Agio Oros (Mt. Athos) peninsula. It consists of basement rocks of Kerdilia and Vertiskos Units (Kockel et al., 1977), intruded by younger magmatic products. Ammouliani Unit is suggested as a new Unit, between Kerdilia and Vertiskos Units (Plougarlis & Tranos, 2015). Published geological maps featuring the island are: (1) Geological Map of Chalkidiki peninsula and the surrounding region, scale 1:100,000 (Kockel et al., 1977), (2) Geological Map of Greece, Ierissos Sheet. Scale 1:50,000 (Kockel et al., 1978), (3) Geology of Ammouliani Island (Northern Greece), scale 1:10,000 (Plougarlis & Tranos, 2015), (4) Geological Map of Greece, scale 1:500,000 (IGME). The pre-alpine basement rocks are characterized by a general ENE-WSW strike and generally intermediate to large angles of dip, mainly towards the WNW. The northern part of Ammouliani is characterized by the rocks of Kerdilia , Vertiskos, and Ammouliani Units. The southern part of the island consists of Ammouliani's granitoid, which is considered to be part of the Sithonia/Ouranoupoli-type granite (Papapavlou, 2021).

Objectives

The aim of this paper is to propose georoutes on Ammouliani Island, targeted to both the scientific community, as well as the general public. This enhances the potential of an alternative form of tourism in this area and suggests a different approach to the economic and cultural development of the island. It promotes geology as a multidisciplinary scientific field accessible to everyone. It encourages people to become familiar with this science and cultivate curiosity for their surroundings. The island's geology contributes to its unique character and beauty, which has been valued by tourists and the scientific community.

Methods

Pre-existing studies of the island and the wider area were collected and, their description of general geology was unified. Also, this work utilizes the 1:12.000 topographic map of the area from the Ierissos Sheet (1:50,000) of the Hellenic Army Geographical Service using the Quantum Geographical Information System (QGIS). A detailed geological study was carried out and confirmed the evidence of previous researchers who studied this island. Based on the most recent 1:10,000 scale map (Plougarlis & Tranos, 2015), the geological sections of the same scale, and visitor accessibility, decisions were made about possible geopaths that could be mapped and documented. Fieldwork along these geopaths was conducted and original structural data were acquired. They were exported and analyzed using the appropriate software for each product. A digital topographic map of the area and a Digital Elevation Model (DEM) were created, as well as digitized detailed geological maps. All data, as well as the results of the quantitative structural analysis of faults, folds, schistocity etc., were incorporated into an integrated GIS database, of which any query can produce various outcomes. Three geological trails were selected for presentation, the technical information of which is shown in Table 1. Their profile is generally gentle, with occasional small irregularities (Fig. 1). They are shown in the summary map of Fig. 2.

Table 1. Technical details of georoutes

Georoute	Max Altitude	Average Duration	Max Incline	Average Incline	Existing Road
1.1-1.5	74 m	1:05 h	32.6%	7%	Yes (1.1-1.2), No (1.2-1.6)
1.7-1.11	23 m	1:15 h	22.5%	6.2%	Yes
2	67 m	2:00 h	31.1%	7.3%	Yes
3	65 m	2:30 h	31.5%	7.4%	Yes

Figure 1. Georoutes elevation graph.

The purpose was to cover the geology of the entire island, showcasing specific sites, and ensuring convenient visitor access to existing roads. The rocks mentioned in each area are based on the already existing geological map of 1:10,000 scale (Plougarlis & Tranos, 2015). An effort was made to categorize them in geotopes according to the geology they highlighted.

Results and Conclusions

Georoute 1 focuses on Sithonia-type granite intrusions into the existing bedrock. Georoute 2 refers to the gneisses of the Kerdilia and Ammouliani Units. Georoute 3 focuses on the biotite-mica gneiss of the Vertiskos Unit, however, geosites of the Ammouliani Unit have also been chosen to be presented, so a comparison of the two types of lithology and their characteristics is achieved. Additionally, two locations of structural interest have been selected as Geosites 4.1 and 4.2 on Karagatsia Beach. The study refers to all the rocks mapped on the previously mentioned 1:10,000 scale geological map, except for the marbles of the Kerdilia Unit, which had limited outcrops in areas that are currently under building construction.

Georoute 1 (Fig. 3)

This route is 4.5 km long, crosses Ammouliani's gneissic granite and is divided into two branches in the middle of the hiking path, southeast of Agionissi Resort. The first branch (Georoute 1.1) passes from the southernmost part of the island and moves along Psili Rachi, reaches 74 m altitude, and ends before Turkolimano beach. The second branch (Georoute 1.2) continues the road in the northern part starting from Agionisi Resort, reaches an altitude of 24 m and has direction to the north-east part of the Island. The granite of this area is mentioned by Plougarlis (2011) as the Eocene granitoid of Ouranoupolis and Sithonia.

The route starts from Ormos Glastri (location 1.1). In this location, the separation of the granite body, which is a typical plutonite structure, is evident. The granitic bodies are produced by magma in its cooling stages. The exposure of a granitic body at its surface causes corrosion, disintegration, and deformation associated with the creation of the plutonite. The structure that develops in the igneous masses is shaped during its cooling conditions and the process of intrusion of the magmatic body from the moment it is finally consolidated. These later forms non-tectonic rock separations (Vidal Romaní, 2008). Those form outcrop along Georoute 1.1. At Georoute 1.2 the fault and the crustal-deformation phenomena are firstly presented at Plougarlis & Tranos (2015) map.

Georoute 2 (Fig. 4)

Georoute 2 is approximately 3.7 km long and crosses the rocks of the Kerdilia Unit, including the plagioclase-microcline gneiss, and the Ammouliani Unit. It represents an attempt to trace the path along cross section A-A', as outlined by the most recent geological mapping (Plougarlis & Tranos, 2015).

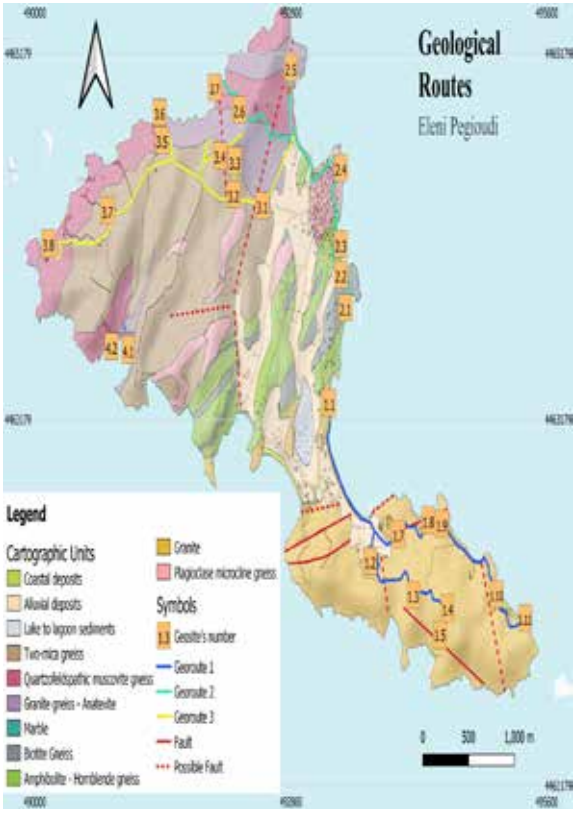

Figure 2. Geological Map of Ammouliani Island (modified from Plougarlis & Tranos, 2015) with the proposed georoutes and geosites

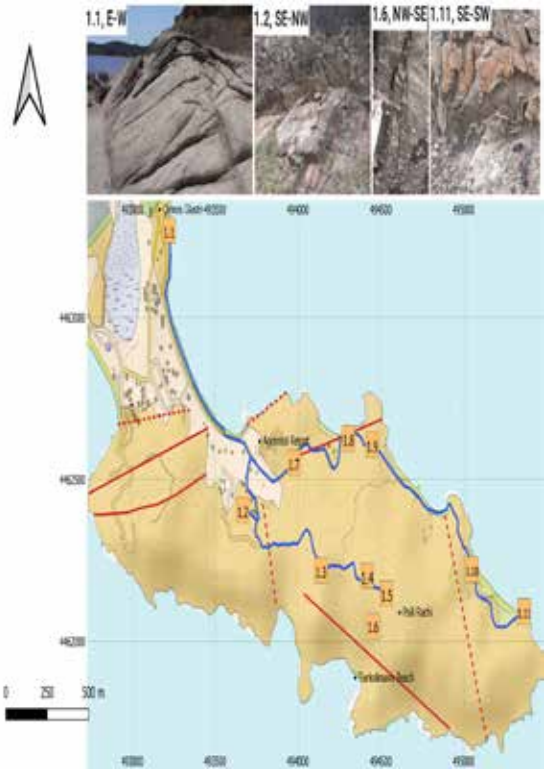

Figure 3. Georoute 1 at the southern side of the Island. Photos show a selection of geosites along the georoutes as well as the viewing orientation

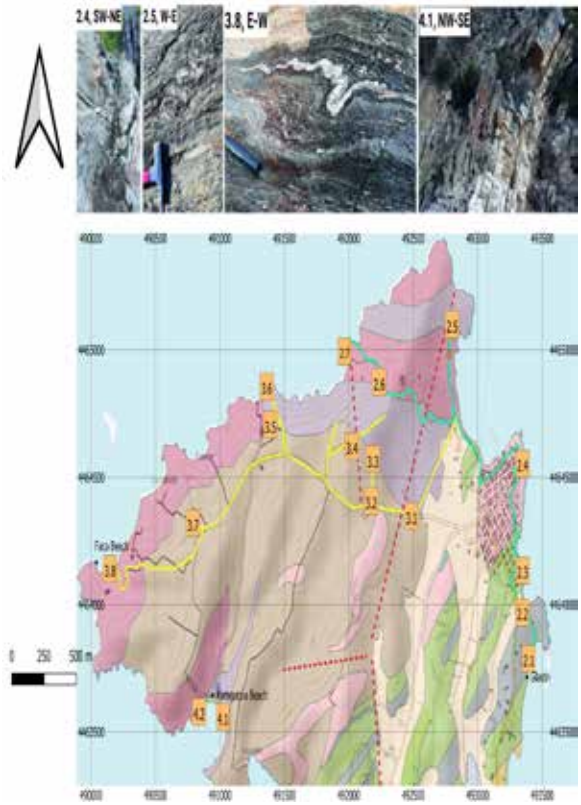

Figure 4. Georoutes 2,3,4 at the northern side of Ammouliani Island. Photos show a selection of geosites along the georoutes, as well as the viewing orientation.

Georoute 3 (Fig. 4)

This geological route is 5.2 km long and primarily features two-mica gneiss and its geological contacts with the Ammouliani Unit. The brownish two-mica gneiss belongs to the Vertiskos Unit and consists of quartz, plagioclase, muscovite, and biotite, with rare garnet, chlorite, and epidote occurrences. These gneisses are often interbedded with quartzofeldspathic muscovite gneiss of light brown-beige color, consisting of quartz, plagioclase, and muscovite. Additionally, muscovite-garnet gneisses appear as layers a few meters thick within the two-mica and quartzofeldspathic muscovite gneiss. Within the two-mica and quartzofeldspathic muscovite gneiss, augen gneisses with a variety of thickness that extending for several kilometers are observed, often showing features of intense shearing and mylonitization. Mineralogically, they consist of quartz, plagioclase, K-feldspar, muscovite, biotite, and in smaller amounts, hornblende and epidote.

Georoute 4 (Fig. 3)

An attempt was also made to trace two additional geological routes in the northwest part of the island; however, the flat geomorphology, the road network, cultivated olive groves, and vegetation inhibited exposure of rocks. However, there is information about Karagatsia Beach, which could be an interesting geological site, as its rocks belong to the Ammouliani Unit and are in contact with the Vertiskos Unit.

Discussion

The island, despite its small area, presents a variety of structures and lithological types. A multitude of kinematic indicators characterizes its entire range, while at the same time, it varies petrologically. Various types of rock deformation, such as faults, are quite new. Further studies of it may contribute to the disciplines of petrology, structural geology, stratigraphy, and neotectonics. Its small area and rich geology are suitable for developing geotourism for interested parties. Routes are easy to use for educational purposes, as they are short, have good accessibility, and are not physically demanding.

Acknowledgments

The first author would like to thank her family and friends for fieldwork assistance and georoute validation. The authors would like to thank an anonymous reviewer for their comments.

Reference

Kockel, F., Mollat. H. and Walther, H.W., 1977. Erlauterungen zur Geologischen Karte der Chalkidiki und angrenzender Gebiete 1:100.000 (Nord-Griechenland). Bundesanstalt fur Geowissenschaften und Rohstoffe, Hannover 119 pp

Kockel F, Mollat H and Antoniadis P (1978) Geological Map of Greece, Ierissos Sheet. Scale 1:50.000. Athens: Institute of Geology and Mineral Exploration of Greece.

Neofotistos, P. G., Tranos, M. D., & Heilbronner, R. (2020). Geology and deformation of the Serbo-Macedonian massif in the northern part of the Athos Peninsula, Northern Greece: Insights from two detailed cross-sections. Bulletin of the Geological Society of Greece, 56(1), 167. https://doi.org/10.12681/bgsg.22529

Papapavlou, K. (2021). Zircon U–Pb–Hf snapshots on the crustal evolution of the Serbo-Macedonian massif: new insights from Ammouliani island (Northern Greece). Geological Magazine, 158(11), 2079–2086. https://doi.org/10.1017/S0016756821000698

Papathanasoglou A. and Sagias I. (2017). Institutional Framework for Geosite Protection [in Greek], Environment and Law, 2017/4,628-636

Pazaras, G. (2016). Petrographic Study of metapelite from the Island Ammouliani, S. Chalkidiki [in Greek]. Bsc. Thesis, School of Geology, Aristotle University of Thessaloniki. http://geolib.geo.auth.gr/digeo/index.php/grelit/article/view/11270

Plougarlis, A. (2011). Geological and tectonic structure of Ammouliani Island (Peninsula Chalkidiki). Digital Library "Theofrastos", School of Geology, Aristotle University of Thessaloniki, 0(0). DOI 10.26262/heal.auth.ir.126766, https://ikee.lib.auth.gr/record/126766/

Plougarlis, A. P., & Tranos, M. D. (2015). Geology of Ammouliani Island (Northern Greece) – implications for the tectono-magmatic evolution of the Serbo-Macedonian Massif. Journal of Maps, 11(4), 552–560. https://doi.org/10.1080/17445647.2014.948504

Tranos, M., Kilias, A., & Mountrakis, D. (1993). Emplacement and deformation of the Sithonia granitoid pluton (Macedonia, Hellas). Bulletin of the Geological Society of Greece, 28, 195–210.

Vidal Romaní, J. R. (2008). Forms and structural fabric in granite rocks. Cadernos Do Laboratorio Xeoloxico de Laxe, 33.

Shapefile of coastlines for DEM creation in Global Mapper:
http://geodata.gov.gr/maps/?package=d59c2895-49c0-416f-a77e-122459cc8cac&resource=eb718a13-6e4a-45d6-9f9d-b3439d92a668&locale=en

Maps and other digital sources:

Army Geographical Service. (1970). Ierissos Sheet (Topographical Map). 1:50.000 Army Geographical Service.

Geological Map of Greece, scale 1:500,000 EAGME

17th INTERNATIONAL CONGRESS of the Geological Society of Greece

BULLETIN OF THE GEOLOGICAL SOCIETY OF GREECE, SP. PUBL.

EXTENDED ABSTRACT 259

Assessing Microplastic Pollution in Atzinolakas caves, Crete: Implications for Remote Karst Aquifers

Christos Pennos[1,2], Maria Perraki[3], Sofia Pechlivanidou[1], Rannveig Øvrevik Skoglund[4], Christos Salmas[4], Eleni Vasileiou[3], Yorgos Sotiriadis[5], Markos Vaxevanopoulos[6]

(1) School of Geology, Department of Physical Geography, Aristotle University of Thessaloniki, 54636 Thessaloniki, Greece cpennos@auth.gr

(2) Emil Racoviță Institute of Speleology, Romanian Academy, 400006 Cluj-Napoca, Romania

(3) School of Mining and Metallurgical Engineering, National Technical University of Athens, 15780 Zografou Campus-Athens, Greece

(4) Mineralogy-Geology Laboratory, Department of Natural Resources Management and Agricultural Engineering, Agricultural University of Athens, 11855 Athens, Greece

(4) Department of Geography, University of Bergen, Fosswinckels gt. 6, 5007 Bergen, Norway

(5) Proteas caving club, 54636 Thessaloniki, Greece

(6) Department Of History, Archaeology and Social Anthropology, University of Thessaly, Greece

Introduction

Over the last decade, microplastics (MPs) have increasingly attracted the attention of both the scientific community and the public. Microplastics are usually defined as plastic particles <1 mm but in a broader sense as all particles < 5 mm. A large proportion of MPs form unintentionally, for instance through the decomposition of larger pieces of plastic waste (i.e., secondary MPs). However, tiny fragments of synthetic or chemically modified natural polymers are also produced to be used as such or added to products (i.e., primary MPs). In 2022, the European Chemical Agency (ECHA) estimated that more than 42,000 tons of intentionally present microplastics are eventually released into the environment each year. The widespread presence of MPs, both in the terrestrial and marine environments, also in surface and groundwater has only been recently demonstrated (e.g., Yu et al., 2020, Drummond et al., 2022, Perraki et al, 2024), Microplastics have also been detected in the food chain, and eventually enter humans (De-la-Torre, 2020), highlighting their pervasive impact. In this study, we analyze water samples collected from two caves at the Atzinolakkas area of Lefka Ori in Crete, a uniquely remote location, to determine whether the water is contaminated by (MPs). We performed water sampling at three locations using glass vials to minimize contamination from external sources such as equipment or clothing. The sampling sites were selected to ensure maximum spatial coverage of the caves.

Setting

Our study area is in Atzinolakas (or Atzines), on the northern side of the Lefka Mountains in the Chania Prefecture of Crete (fig.1), approximately 2 km east of the Agio Pneuma summit (2262 m). The broader area hosts more than 1000 caves (Adamopoulos, 2013) including the two deepest caves in Greece, the Gourgouthakas and the Lion caves namely. These caves are part of a larger hydrological system that composes the recharge area of the Koiliaris drainage area (Lili et al, 2020) and that most probably discharges at the Stylos spring.

The karst system of the White Mountains comprises an autochthonous geotectonic unit (Plattenkalk nappe) and two allochthonous units: the Western Crete unit (Trypali limestones and phyllites) and the Arna unit (metamorphic schists). Within the alpine nappes, the Plattenkalk nappe exhibits a stratigraphic sequence, from base to top, as follows: a)karstified unbedded dolomites, b) dolomitic marbles, c) thinly bedded calcitic marbles intercalated with chert layers and nodules, d) metamarls and limeschists.

Although the geological composition of the area appears to be quite uniform, it shows both spatial and deep changes. Based on the observations made during the visits to the cave, black dolomites with brecciated textures are predominant in the wider region, especially south-west of the entrance to the Gourgouthakas cave. Surrounding the Gourgouthakas cave entrance, partially recrystallized and locally brecciated white limestones are observed. This lithological unit persists within the cave to a depth of 522 m below the cave entrance, where transitions to thick bedded to platy limestones occurs, the same succession continues to 850 m below the entrance. Between 646 and 670 meters, interbeds of green schist are encountered.

In climatic terms, the western part of Crete, and particularly the Lefka Ori, is characterized by significant winter precipitation, estimated at around 2331 mm (Agou et al, 2019). The winter low pressure associated with the North Atlantic Oscillation (NAO) typically originates in the Atlantic near the Strait of Gibraltar. These systems exhibit a

northeastward trajectory, generally skirting the Adriatic Sea. Consequently, significant rainfall is primarily confined to western Greece. As these frontal systems approach Greece from the west, they induce predominantly southwest winds over the Ionian and Aegean Sea, thereby advecting maritime air masses eastward (e.g. Pennos et al., 2018).

Figure 1. Topographic map of the broader study area. Red rectangle highlights the Atzinolakas caves (basemap: Google satellite; GGRS87).

Methods

The water samples were collected at three different locations in Gourgouthakas, Lion Cave and LO23 cave systems in August 2024 Gourgouthakas-Liontari caving expedition. Glass vials of 30 ml were used as sampling containers. To minimise the risk of contamination from external sources such as equipment or clothing the sampling group performed the sampling in the beginning of the expedition. In the Gourgouthakas Cave, the Marcel Waterfall was designated as the sampling site (fig.3a&e). In Lion Cave, dripwater was collected (fig. 3b&d) from a location situated above the first hotspot, minimizing the potential for external contamination. In LO23 Cave, the spring utilized to supply the expedition's water requirements served as the sampling point and a small stream with continuous flow was selected (fig.3c). Unfortunately, the sample obtained from Lion Cave was lost during transport as the vial broke. Concurrently with the MP sampling, in situ measurements of the electrical conductivity (EC) were carried out on water samples from the same sampling sites.

Samples were filtered using a filtration device, a mechanical pump (-100kbar) and filter membranes (Macherey-Nagel, 47 Ø and 0.45 μm pore size, REF: 65300045047). Before filtering the samples, we performed a cleaning round with double filtered de-ionized water, to ensure that the apparatus was cleaned to proceed with blank samples. A negative blank sample (BL1) was prepared prior to analysis. All filters were covered with glass Petri dishes and stored in a controlled environment in a closed laminar flow hood for 24h to dry. After filtration a second negative blank (BL2) was prepared and intentionally left uncovered to measure possible air contamination inside the laminar flow hood. Each surface was cleaned with 95% ethanol prior to analysis and cotton labware, and glassware were used during the whole procedure. No pretreatment protocol was applied.

Particles were quantified using a Leica Ivesta 3 stereoscope (x40-x63 optics) with a Leica Flexacam C3 attached at the Laboratory of Mineralogy and Geology, Department of Natural Resources Management and Agricultural Engineering, Agricultural University of Athens. The material was sorted based on its visual characteristics (size, color, shape, degradation degree) (Hidalgo-Ruiz et al., 2012) and classified as potential microplastics using the LASX image analysis software. The particle size was estimated based on the Feret min diameter.

Subsequently, μ-Raman analysis was performed on 10 suspect particles (24%) without further treatment, using a Renishaw inVia Reflex micro-Raman at the School of Mining and Metallurgical Engineering of the Technical University of Athens, Greece. The spectra were excited at room temperature with the 532 nm excitation wavelength of a diode laser, in the spectral range from 200 cm^{-1} to 2000 cm^{-1}. Spectra acquisition time was set to 10s, 1 accumulation cycle and laser power at 1%. The spectra were processed with the WIRE 3.4 software.

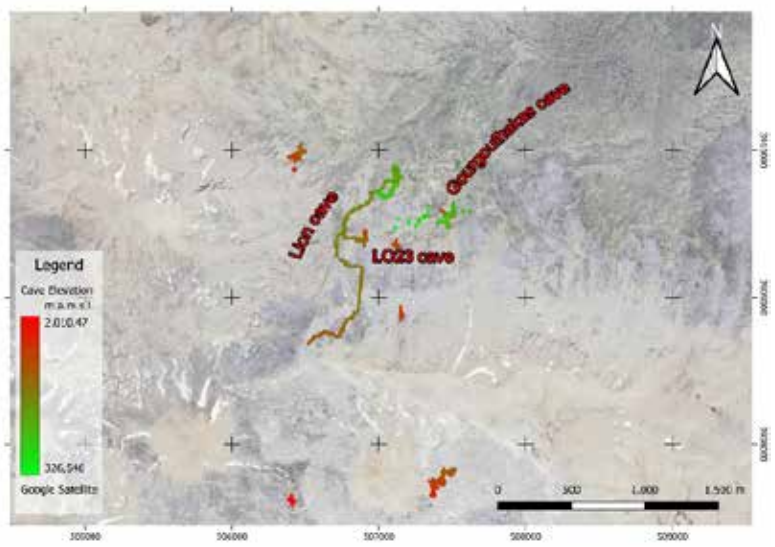

Figure 2. Map of the broader area with interpolated plan view of the caves. The color on the cave surveys represents the absolute elevation of the cave (cave data shared by Adamopoulos K.; GGRS87).

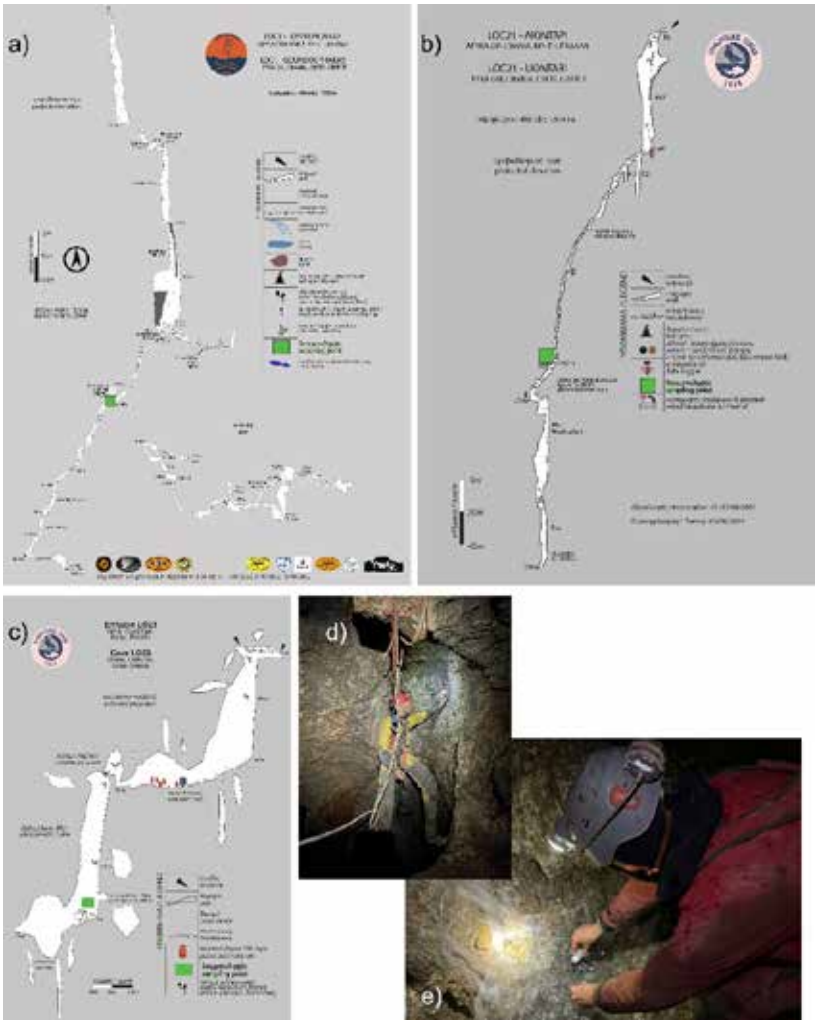

Figure 3. Extended projection of caves. a) Gourgouthakas cave, b) Lion cave, c) LO23 cave. d&e) collecting water samples in Lion and Gourgouthakas, respectively. Cave surveys are courtesy of Gourgouthakas expeditions.

Results

A total of 42 particles in the form of fibers and fragments were visually identified and classified as potential microplastics. Sample LOC1 contained 16 fibers and 4 fragments (fig.4). The predominant fiber color was blue (56.25%) followed by transparent (31.25%) and red (12.5%) (fig.5). Irregular fragments were only found in red color (100%). Regarding size, fibers in the LOC1 sample were distributed in 3 size classes namely, <500 μm (37.5%), 501-1000 μm (31.25%), > 1001 μm (31.25%), indicating a relative size homogeneity in their distribution. On the other hand, all fragments were measured with a size of <50 μm (100%). In the LO23 sample, a total of 22 particles were identified divided into 14 fibers and 8 fragments (fig. 6). Fibers were mostly transparent (71.43%) followed by blue (21.43%) and red (7.14%). Fragments were mainly blue (62.50%) but red, black and white colors were observed (12.5% each). Fibers were distributed in 3 size classes namely, <500 μm (50%), 501-1000 μm (35.7%), > 1001 μm (14.28%), with the <500 μm size class occupying 50% of the total fibrous material. Fragments were measured to be <50 μm (37.5%) and >51 (62.5%). Blank samples were also visually observed. BL1 had 2 fibers (transparent and black) and BL2 (opened Petri dish) had 2 white fragments and 1 blue fiber. Contamination was neither classified nor considered in the results. Raman spectroscopy of selected microplastic particles, revealed a very strong overlap of the MP peaks with the pigment peaks and in particular the indigo blue [547(s), 599(s), 939, 1010, 1147, 1252(s), 1297, 1310, 1365(vs), 1462, 1484, 1579(s), 1585, 1609, 1697 cm-1 (s)] and the copper phthalocyanine blue [peaks at 484, 594, 681(s), 748, 954(s), 1342(s), 1452(s) and 1529 cm-1 (vs)]. Besides, Raman peaks of polyethylene oxide (850, 1283, 1374cm-1) were also identified.

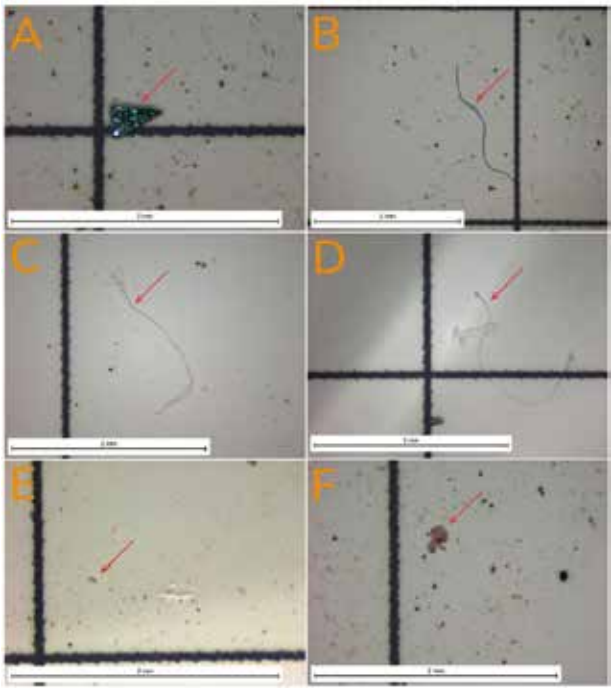

Figure 4. Particles identified as potential microplastics under the stereoscope in both samples: (A) black fragment, (B) blue fiber, (C, D) transparent fibers, (E, F) red fragments.

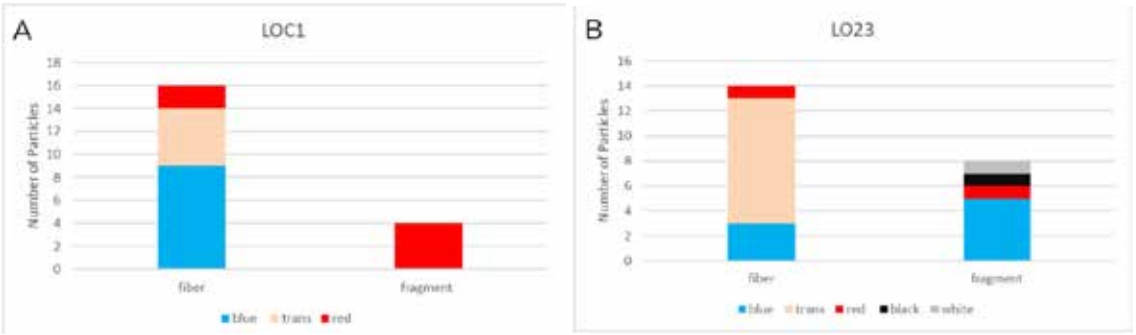

Figure 5. Total particle number of LOC1 (A) and LO23 (B) samples sorted by particle type and color, based on stereoscopical observations.

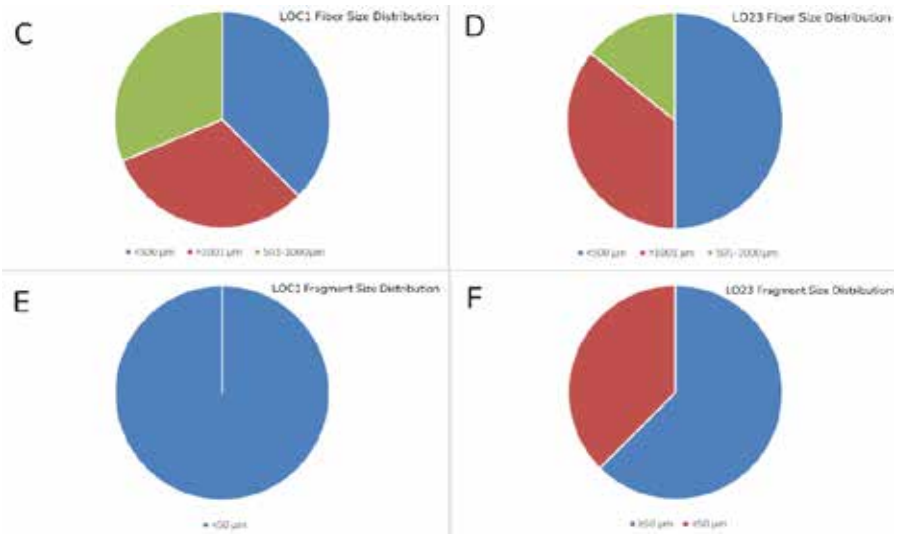

Figure 6: Distribution of fibers and fragments in LOC1 (C, E) and LO23 samples (D, F) based on stereoscopical observations.

The measurements on each sampling site showed similar EC values. In detail, in Gourgouthakas cave at the Marcel waterfall site the EC was 196 μS/cm at 9.6 °C, in Lion cave the EC of the drip water was 188 μS/cm at 9.3 °C. Finaly, the sample from LO23 exhibits EC of 180 μS/cm.

Discussion

Electrical conductivity measurements of the cave water samples exhibited values below the average reported for Greek karstic springs (Li Vigni et al., 2023). These low values of EC suggest a relatively short residence time within the karst aquifer and the recharge from the meteoric water. Despite the deep location of the sampling points within the karst massif, the observed low conductivity indicates rapid water percolation. This rapid flow likely occurs through high-permeability pathways, enabling swift infiltration and limited interaction with the limestone bedrock. Furthermore, the low water temperature recorded during mid-summer in the northern hemisphere strongly suggests a significant contribution from snowmelt, likely to originate from residual snow patches within the catchment area.

The presence of microplastics (MPs) in the collected samples suggests that it was transported to the sampling sites with infiltrating water. Given the remote location of the area above the caves and the minimal anthropogenic activities, a plausible transport mechanism for the MPs is proposed. Aeolian transport by westerly winds may have carried MPs from regions west of Crete, similar evidence was recorded recently to Mt. Tymfi's Alpine Lake (Salmas et al, 2024). These MPs could have subsequently precipitated snowfall during winter months. During summer, snowmelt would have introduced the MPs into the karst system, facilitating their rapid transport to the sampling points (fig. 7).

While this interpretation is based on limited data, it highlights the potential environmental hazard posed by aeolian-transported MPs and warrants further investigation.

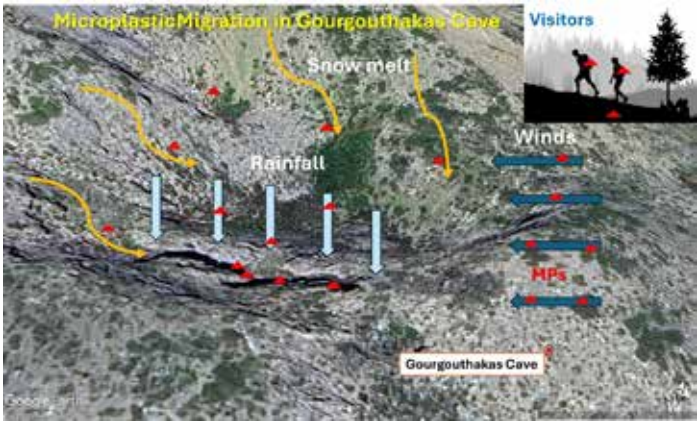

Figure 7: A schematic representation of the possible migration mechanism of microplastics in the Gourgouthakas cave.

Acknowledgements

The authors would like to thank the members of the Gourgouthakas – Liontari 2024 speleological expedition for helping us during our fieldwork and facilitating our stay. Keith Chatteraton is gratefully thanked for sacrificing his pair of clean socks to extract safely to surface the sample from Gourgouthakas cave. CP has been supported by the project titled “MP-Karst, Development of a methodological approach to detect Microplastics in Karstic environments” (code ΥΠ2ΤΑ-0554154) funded in the context of the call “Visiting Professors/Visiting Researchers” by the European Union - Next Generation EU. SP and RØS acknowledge support from the project “Comprehensive Assessment of Microplastics in Karst Environments / CAVE-MP” (MIS5224501) funded by EEA financial Mechanism for Bilateral funds 2014-2021.

References

Adamopoulos, K. 2013. 1000 and 1 caves in “Lefka Ori” massif, on Crete, Greece. 16th International congress of Speleology, Czech Republic, Brno.

Agou, V.D., Varouchakis, E.A. & Hristopulos, D.T. Geostatistical analysis of precipitation in the island of Crete (Greece) based on a sparse monitoring network. *Environ Monit Assess* **191**, 353 (2019). https://doi.org/10.1007/s10661-019-7462-8

Background Document to Committee for Risk Assessment (RAC) and Committee for Socio-economic Analysis (SEAC) Opinions on the on intentionally added microplastics, 10 December 2022

Drummond, J. D., Schneidewind, U., Li, A., Hoellein, T. J., Krause, S., & Packman, A. I. (2022). Microplastic accumulation in riverbed sediment via hyporheic exchange from headwaters to mainstems. Sci Adv, 8(2), eabi9305. https://doi.org/10.1126/sciadv.abi9305 Gabriel Enrique De-la-Torre, 2020. Microplastics: an emerging threat to food security and human health. J Food Sci Technol, 57(5):1601–1608

Hidalgo-Ruz, V., Gutow, L., Thompson, R. C., & Thiel, M. (2012). Microplastics in the Marine Environment: A Review of the Methods Used for Identification and Quantification. Environmental Science & Technology, 46(6), 3060–3075. https://doi.org/10.1021/es2031505

Li Vigni, L., Daskalopoulou, K., Calabrese, S., Brusca, L., Bellomo, S., Cardellini, C., Kyriakopoulos, K., Brugnone, F., Parello, F., & D’Alessandro, W. 2023. Hellenic karst waters: geogenic and anthropogenic processes affecting their geochemistry and quality. Sci Rep, 13(1), 11191. https://doi.org/10.1038/s41598-023-38349-6

Lilli, M. A., Efstathiou, D., Moraetis, D., Schuite, J., Nerantzaki, S. D., & Nikolaidis, N. P. 2020. A Multi-Disciplinary Approach to Understand Hydrologic and Geochemical Processes at Koiliaris Critical Zone Observatory. Water, 12(9). https://doi.org/10.3390/w12092474

Pennos, C., Styllas, M., Sotiriadis, Y., & Vaxevanopoulos, M. 2018. Ice Caves in Greece. In A. Persoiu & S. E. Lauritzen (Eds.), Ice Caves (pp. 385-397). Elsevier. https://doi.org/10.1016/b978-0-12-811739-2.00018-8

Yu, Q., Hu, X., Yang, B., Zhang, G., Wang, J., Ling, W., 2020. Distribution, abundance and risks of microplastics in the environment. Chemosphere Chemosphere 249, 126059.

Perraki, M.; Skliros, V.; Mecaj, P.; Vasileiou, E.; Salmas, C.; Papanikolaou, I.; Stamatis, G. Identification of Microplastics Using μ-Raman Spectroscopy in Surface and Groundwater Bodies of SE Attica, Greece. *Water* **2024**, *16*, 843. https://doi.org/10.3390/w16060843

Salmas, C., Alexopoulos, K., Kaspar, B., Skliros, V., Mecaj, P., Vasileiou, E., Papanikolaou, I., Perraki, M. & Papaioannou, H. First Evidence of Microplastics in Mt. Tymfi’s Alpine Lake (Dragonlake) in Greece, Using μ-Raman Spectroscopy. Extended abstract, 16th International GeoRAMAN Conference 24-27 September 2024, Rhodes, Greece

17th INTERNATIONAL CONGRESS of the Geological Society of Greece

BULLETIN OF THE GEOLOGICAL SOCIETY OF GREECE, SP. PUBL.

EXTENDED ABSTRACT 260

Investigating the failure characteristics of certain rock types using the Acoustic Emission technique.

D. Pepas[1], V. Marinos[1], P. Nomikos[2], C. Saroglou[1]
(1) School of Civil Engineering (NTUA), Athens, Greece, dimitris.pepas99@gmail.com
(2) School of Mining and Metallurgical Engineering (NTUA), Athens, Greece

Introduction / Background

In recent years, the Acoustic Emission (AE) method has seen significant advancement and usage in the field of rock mechanics for monitoring the gradual fracturing process and stress-induced damage due to crystal or grain sliding, crack growth and coalescence. The AE technique has been used both in laboratory and in-situ applications, especially in tunnels for studying the elastic wave propagation characteristics and acquiring parameters that can reflect the rock fabric and damage evolution process before the macroscopic rock failure. Acoustic Emissions consist of elastic sound waves that are transmitted from the interior of a localized source (etc. rock sample) during crack development. These elastic waves are the result of stored accumulated energy that suddenly releases during external loading. The resulting AE waves propagate through the rock and then captured from specialized surface piezoelectric sensors. The sensors convert the mechanical waves into electrical signals and record them as AE events (Hits) in specialized acquisition programs. Several parameters can be extracted from the raw data such as hits, amplitude, frequency, duration and energy of the AE signals.
According to literature, the AE method has been used in the laboratory for the determination of various values and factors such as (1) the AE activity regions (Boyce et al., 1981) and their connection with the main cracking stages, namely the crack coalescence (σ_{cc}), the crack initiation (σ_{ci}) and the crack damage (σ_{cd}) stages in the stress-strain diagram (Martin C.D., 1993), (2) the B-value factor whose reduction during the loading process provides insight on the gradual failure and the stability of the rock (C. H. Scholz, 1968) and has been used as a risk assessment tool in various civil projects (Gerd Manthei et al., 2018) and (3) the Felicity ratio (FR) after several loading cycles that can be used as a rock's quality index (Kallimogiannis, 2023). Outside the laboratory scale and into the deep tunnel construction, the already complex in-situ stress environment is redistributed during excavation causing microcrack and later macrocrack generation if the crack initiation load is exceeded. As such, AE monitoring has been utilized together with numerical simulations and laboratory AE tests in several underground mining and tunneling projects to examine the size of the excavation-disturbed zone (EDZ) (Stephen D. et. al., 1996), determine the rock mass strength parameters through back-analysis (M. Cai et. al., 2006) and predict hazards such as rockbursts (A. Hirata et. al., 2006), thermal induced dilation (J Hesser et. al., 2015) and ruptures of not-persistent joints (Shuting Miao et. al., 2024).
The failure mechanism and consequently the acoustic emission (AE) activity is strongly influenced by the rock's texture, mineralogical composition, and formation history (Gramberg, 1989). In particular, fine-grained monomineralic rocks tend to fail abruptly as σ_{cd} and σ_c almost occur simultaneously. In contrast, more ductile or plastic rocks exhibit lower AE activity, partly due to the deformability of clay minerals. Additionally, factors such as porosity and lamination significantly affect the microcrack development mechanism.

Objectives

In this study, the AE method was implemented during Uniaxial Compressive and Cyclic loading laboratory tests* in several rock types such as a Limestone both in intact and karst form from Revithousa island, a tectonized Mudshale from South Crete and a Trachyandesite from Poros island. The scope of this study is to examine if the determination of the above factors with the Acoustic Emission method can be utilized as a basic monitoring tool both inside the laboratory and in underground construction projects, providing greater insight into the rockmass behavior from the standard rock mechanic tests.
*All the tests were executed according to the ISRM standards in the laboratory of Engineering geology and Rock-mechanics (NTUA) in the School of Civil Engineering

Physical parameters

Before proceeding with the Uniaxial Compression Tests (UCS), itis necessary to obtain the rocks' physical parameters. Particularly, the density (pd, psat) and porosity (n%) of every rock type was determined using the saturation and caliper technique in at least three specimens. The results are given in **Table 1**. Some noteworthy findings include 1) the high density (2.77) and the inversely proportional low porosity (< 1%) of the intact Limestone indicative of its very high strength (Koukis et al., 1998) and 2) the high porosity (n=19%) of Trachyandesite which depicts the vesicular, but otherwise homogenous texture with albite, anorthite and biotite phenocrystals. These rocks' characteristics were also confirmed by measuring the primary-P and secondary- S ultrasonic wave velocity. In general, higher rock density facilitates faster propagation of sound waves. Finally, petrographic (via stereoscope) and if necessary XRD- analysis was conducted to derive the exact mineralogical composition of every rock.

Table 1. Physical properties (density and porosity) and ultrasonic wave velocity of every rock type.

Rock type	pdry	psat	ps	γdry	γsat	n	VP	VS
	*10^3 kg/m^3			kN/m^3		%	m/s	
Limestone (L)	**2.77**	2.77	2.79	27.2	27.2	**0.63**	6549	3945
Karstified Limestone (KL)	**2.53**	2.59	2.68	24.9	25.4	**5.49**	4197	2328
Trachyandesite (A)	**1.99**	2.18	2.45	19.5	21.4	**19.00**	3033	1769
Mudshale (S)	**2.62**	2.63	2.66	25.7	25.8	**1.57**	3749	2228

Experimental set-up for UCT tests

A servo-hydraulic load frame with a built-in load cell was used for loading the specimens under a constant stress rate (MPa/s). Axial and circumferential strain gauge extensometers were used for the strain measurement. The AE activity was recorded by two AE sensors connected via a signal pre-amplifier in the specialized AE data acquisition system. Full contact between the specimen and sensors was achieved using an ultrasonic gel couplant. Finally, HRC58 steel discs were positioned between specimen and load platens for minimizing the friction's influence in the AE signal. The exact sensor arrangement is presented in **Figure 1**.

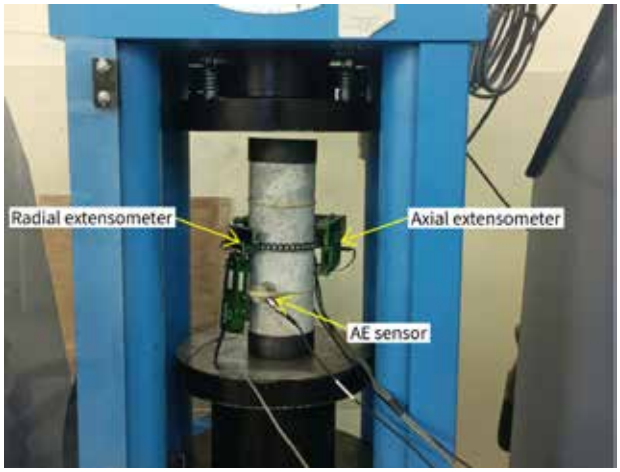

Figure 1. Experimental setup for the UCT-AE laboratory tests

Uniaxial Compressive Test with AE measurement (UCT-AE)

Before further examination, the first UCT results including strength, Young modulus and Poisson's ratio for every rock are presented in **Table 2**. Two sets of parameters (⊥ and //) were derived for Mudshale, based on the orientation of laminas with respect to the loading axis. The resulting stress-strain curves were divided into four microcracking stages, as presented in **Figure 2** (Martin CD et. al., 2001).

Table 2. Average values of strength and elastic parameters for every rock type.

Rock type	Limestone	Karstified Limestone	Trachyandesite	Mudshale (⊥ and //)	
σc (MPa)	106.5	31.0	20.2	54.6	23.8
E (GPa)	79.2	30.3	8.0	23.3	13.6
v	0.15	0.28	0.24	0.10	0.13

The brittle behavior of limestone is evident, as the elastic stage covers most of the loading range and is difficult to distinguish from the stable cracking stage. Also, the unstable cracking stage is presented just before failure within the final 5% and there is no post- failure stage. Karstified Limestone behaved similarly with a limestone breccia. The loading curve presents a clear distinction between the elastic and stable cracking stages, but from there the rock presents two different stages of severe cracking, the first one at around at 75% and the second at 98% of the total strength just before ultimate failure. In Trachyandesite, the microcrack coalescence was favored by the high porosity. Moreover, all failure stages are clearly visible. The Mudshale underwent the most significant deformation and failed by shearing along its laminations.

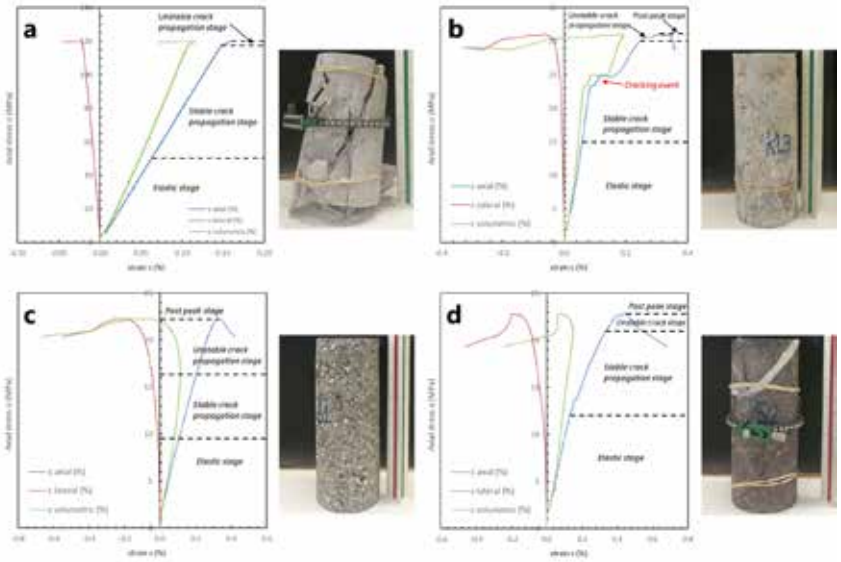

Figure 2. Distinction of microcracking stages along the stress–strain curve for every rock type. a) Limestone, b) karstified Limestone, c) Trachyandesite and d) Mudshale.

Microcracking stages determination with the AE method

Both microcracking stages (σci and σcd) were determined from the AE data by plotting the graph of the cumulative acoustic emission hits versus the axial stress (**see Figure 3**). Particularly, the microcracking stages correspond to the points of abrupt AE hit generation (i.e., where the slope of the curve suddenly increases). If the curve displays a continuous concave-up trend, precise determination becomes difficult. Therefore, the AE hit rate was employed as an alternative (Kallimogiannis, 2016). Moreover, AE activity is strongly influenced by the presence of pre-existing weak surfaces within each rock (e.g., veins, discontinuities). As such, it should be noted that the selection of the following values is subjective and relies on the user's experience.

Based on the results, the standard deviation for σ_{ci} is much lower (**see Table 3**), so it can be considered a more appropriate value for characterizing the mechanical behavior of the rock. The σ_{cd} is very close to the ultimate failure in the brittle rocks. On the other hand, the unstable cracking stage comes earlier in the porous or semi-plastic rocks, as they are slowly losing the ability to bear increasing loads. This microcrack generation and propagation is accompanied by increasing deformation (both axial and radial) and dilation.

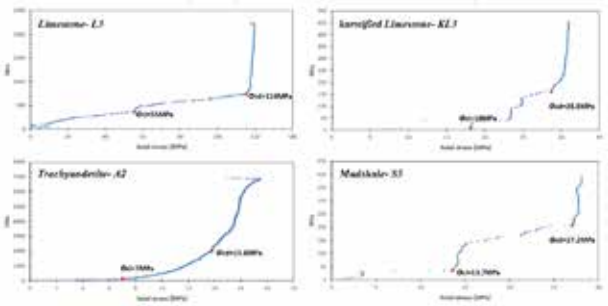

Figure 3. Examples of the produced AE hits vs stress curve for every rock type. The σ_{ci} and σ_{cd} values have been marked.

Table 3. Average values, % ultimate strength and St. deviation of the microcracking stages for every rock type.

Rock type (I.D)	σ_{ci}			σ_{cd}			σ_c	
	μ	% σ_c	St.dev	μ	% σ_c	St.dev	μ	St.dev
Limestone	55.7	52	9.0	97.8	92	29.8	106.5	37.9
Karstified Limestone	18.0	58	-	28.8	93	-	31.0	
Trachyandesite	9.5	47	2.3	15.5	77	2.1	20.2	2.5
Mudshale	15.9	49	3.6	27.5	84	11.7	32.8	18.9

B-value

Unlike the number of hits-stress relationship, the B- value accounts for the intensity of the AE waves (Hardy RH., 2003) and particularly it represents the relative proportion between weak and strong acoustic emission events that are produced under a specific load. B- values lower than one are indicative of intensive AE events that produce large-scale microfractures as the rock approaches failure. B- values larger than one mean that small-scale microfractures are dominant, so the rock has not experienced significant damage (Kallimogiannis, 2023).

All rocks display similar behavior (**see Figure 4**). Particularly, under low stress conditions, any microcracking event produce AE waveforms of low amplitude, resulting in higher B-values, ranging from 1.5 to 4. As the stress increases, crack propagation and coalescence occur, producing higher amplitude waves and therefore decreasing the B- value below one. The B- value decrement is more evident after the σci and σcd stresses are exceeded close to failure.

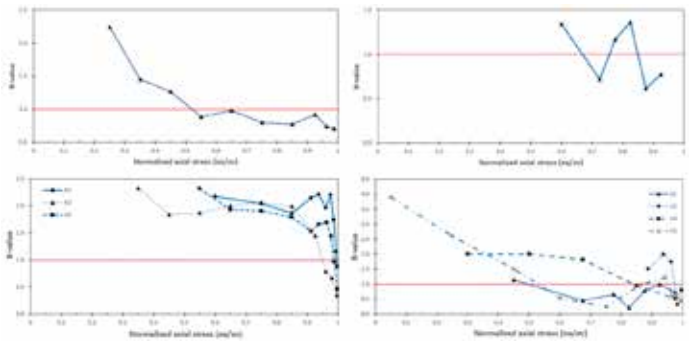

Figure 4. The B-value vs axial stress curve for every rock type. Notice that the B-value reduces after the main microcrack events. Limestone (top left), karstified Limestone (top right), Trachyandesite (below left), Mudshale (below right).

Cyclic Uniaxial Compressive Test with AE measurement. (CUCT-AE)

The rock specimens were repeatedly loaded, each cycle corresponding to a 10-20% increment towards the expected peak strength. The main objective was to study the rock damage accumulation in a damage “controlled” environment

(Eberhardt E. et. al., 1999). The results demonstrate that both axial and lateral strain curves move incrementally after each cycle (**see Figure 5**).

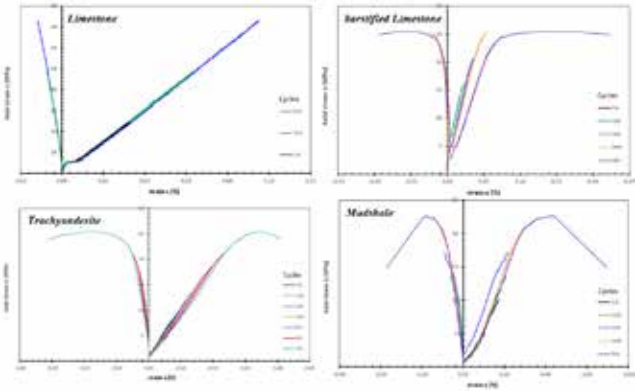

Figure 5. Combined stress–strain curves for every loading cycle.

This shift becomes more obvious as the stress approaches the σc and can be explained by microstructural damage accumulation. In particular, when microcracks generate in a preceding loading cycle, they partially close upon unloading. As such, during the following reloading phase, they extend at considerably lower stress level. Moreover, as most tensile microcracks generate along the specimen's length, lateral extension is the dominant deformation mechanism. The only exception belongs to Limestone in which the elastic phase has not yet passed, so no severe microcracking has yet occurred.

The acoustic emission (AE) method is employed in cyclic loading tests through the Felicity ratio. FR less than unity depicts the transition from the Kaiser effect (absence of AE events until the previously experienced stress on the material is exceeded (Lavrov, 2002) to the Felicity effect (presence of AE events before the previous cycle's peak stress) from which point, the damage that has been accumulated is irreversible. The Felicity ratio was calculated by dividing the stress in which the first AE activity was recorded, namely the AE onset stress with the maximum stress of the previous cycle. As illustrated in **Figure 6**, the FS value exhibits a gradual decline with increasing stress across all rock types.

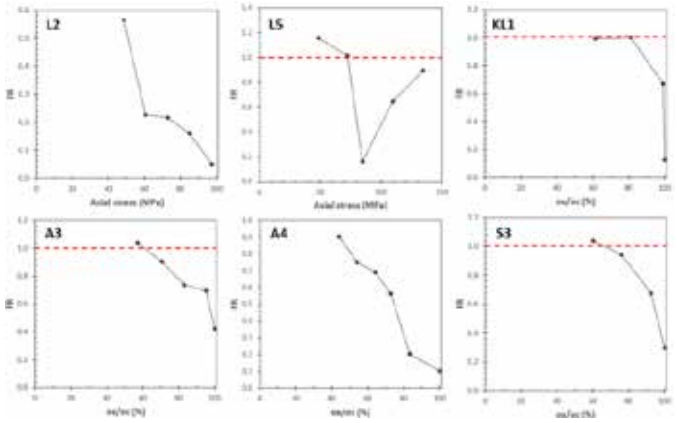

Figure 6. FR vs stress curve for every specimen. The red line marks the transition from the Kaiser to the Felicity effect.

Conclusions

This study highlights the application of acoustic emission (AE) monitoring across four different lithologies. Specifically, it was found that the crack initiation (σ_{ci}) and crack damage stress (σ_{cd}) occur earlier in porous and semi-plastic rocks and later in brittle rocks, relative to the unconfined compressive strength (UCS). Notably, σ_{ci} exhibits significantly lower variability, indicating its potential for use in estimating a more representative UCS through inverse analysis. Moreover, sudden reduction in the B-value reflects the intensity of microcracking activity which peaks near failure.

In damage-controlled UCS tests, the reactivation of microcracks is reflected in the progressive increase of deformation, irreversible strain and Poisson's ratio after each loading cycle. Furthermore, the Felicity Ratio (FR) emerges as a promising parameter for identifying both the onset and evolution of internal damage within the rockmass.
Consequently, the physical properties of rocks significantly influence both their failure behavior and their AE response. High-density rocks exhibit well-defined phases of intense microcracking, accompanied by elevated AE activity, while highly porous rocks tend to show continuous but less intense AE signals, indicative of a more distributed damage mechanism. In contrast, argillaceous rocks display limited AE activity, primarily due to the ductile behavior of their clay minerals, which inhibits microcrack formation. Collectively, these findings highlight the potential of the AE method to enhance understanding of rock failure processes and improve predictive modeling in geotechnical engineering.

Acknowledgements

The authors would like to thank the geotechnical company GeoTerra for providing the rock samples from various geotechnical projects in Greece and their support throughout the entire duration of the study. Special thanks to Geologists Tzivolias Efstratios, Varvadakis Manolis and Antoniou Anastasios.

References

A. Hirata, Y. Kameoka, and T. Hirano, 2006. Safety Management Based on Detection of Possible Rock Bursts by AE Monitoring during Tunnel Excavation. Rock Mech. Rock mechanics and Rock engineering 40 (6), 563–576. **[Journal Article]**

A. Lavrov, 2002. The Kaiser effect in rocks: Principles and stress estimation techniques. International Journal of Rock Mechanics & Mining Sciences 40, 151–171. **[Journal article]**

Boyce, 1981. Acoustic Emission Signatures of Various Rock Types in Unconfined Compression. **[Symposia paper, ASTM article]**

C. H. Scholz, 1968. The frequency-magnitude relation of microfracturing in rock and its relation to earthquakes. **[Book Chapter]**

Eberhardt, E., Stead, D., Stimpson, B., 1999. Quantifying progressive pre-peak brittle fracture damage in rock during uniaxial compression. Int. J. Rock Mech. Min. Sci., 36, 361–380. **[Journal article]**

Gerd Manthei, Katrin Plenkers, 2018. Review on In Situ Acoustic Emission Monitoring in the Context of Structural Health Monitoring in Mines. **[Journal Article]**

Hardy RH (2003), Acoustic Emission/ Microseismic Activity. Volume 1: Principles, Techniques and Geotechnical Applications, A.A. Balkema, The Netherlands. **[Book]**

ISRM. Suggested methods for Rock Characterization, Testing and Monitoring (1974-2006). **[Book]**

ISRM. Suggested methods for Rock Characterization, Testing and Monitoring (2006-1014). **[Book]**

J Hesser et. al., 2015. Measurements of Acoustic Emission and Deformation in a Repository of Nuclear Waste in Salt Rock, p. 551. **[Book chapter]**

J. Gramberg, 1989. A Non-Conventional View on Rock Mechanics and Fracture Mechanics. **[Book]**

Kallimogiannis V., 2016. Laboratory investigation on the impact of the fracturing degree on rock's wave velocity. **[MSc Thesis]**

Kallimogiannis V., 2023. Investigation of the mechanical properties and classification of weak carbonate fault rocks with application in western Lefkada island, Greece. **[Ph.D. thesis]**

Koukis G., Sabatakakis N, Tsiambaos G, 1998. ''Geotechnical properties of Greek limestones''. Proc. 8th Intern. Congress of IAEF, Vancouver, pp. 2883-2888. **[Symposia paper]**

M. Caia, , H. Moriokab, P.K. Kaisera, Y. Tasakac, et. al., 2006. Back-analysis of rock mass strength parameters using AE monitoring data. International Journal of Rock Mechanics & Mining Sciences 44, 538–549. **[Journal article]**

Martin C.D., 1993. Strength of Massive Lac du Bonnet Granite Around Underground Openings'. Ph.D. thesis, Department of Civil and Geological Engineering, University of Manitoba, Winnipeg, p. 278. **[PhD thesis]**

Martin CD, Christiansson R, Soderhall J, 2001. Rock stability considerations for siting and constructing a KBS-3 repository. Based on Experiences from .Aspo HRL, AECL's URL, Tunneling and Mining. **[Journal article]**

Shuting Miao et. al., 2024. Shear band evolution and acoustic emission characteristics of sandstone containing non-persistent flaws **[Journal Article]**

Stephen D. Falls et. al., 1996. Acoustic emission and ultrasonic-velocity methods used to characterize the excavation disturbance associated with deep tunnels in hard rock. **[Journal Article]**

Tsuyoshi Ishida, Joseph F. Labuz, Gerd Manthei, Philip G. Meredith, M.H.B. Nasseri, Koichi Shin, Tatsuya Yokoyama, Arno Zang, 2017. ISRM Suggested Method for Laboratory Acoustic Emission Monitoring **[Journal Article]**

X. Chang et. al., 2015. Acoustic Emission Technique to Detect Micro Cracking During Uniaxial Compression of Brittle Rocks, p. 465. **[Book chapter]**

17th INTERNATIONAL CONGRESS of the Geological Society of Greece

BULLETIN OF THE GEOLOGICAL SOCIETY OF GREECE, SP. PUBL.

EXTENDED ABSTRACT 261

Coal and Asbestos Mining-Induced Pulmonary Pathologies: Radiological Diagnosis and Associated Challenges

Argyrios Periferakis[1,2,3], Lamprini Troumpata[1], Aristodemos-Theodoros Periferakis[1,3], Konstantinos Periferakis[2,4]

(1) Department of Physiology, The "Carol Davila" University of Medicine and Pharmacy, 050474 Bucharest, Romania; (2) Akadimia of Ancient Greek and Traditional Chinese Medicine, 16675 Athens, Greece; (3) Elkyda, Research & Education Centre of Charismatheia, 17675 Athens, Greece; (4) Pan-Hellenic Organization of Educational Programs (P.O.E.P), 17236 Athens, Greece

Introduction

The majority of the first tools devised by Prehistoric men were made of stone; while it is reasonable to assume that a great many of these tools where made from rocks found lying around, at some point it seems inevitable that our ancestors would have to go about actively procuring the materials for their rudimentary tools and implements (Coulson, 2012). The oldest mine yet discovered is, most probably, that of Lion Cave in Swaziland, Africa, which is estimated to be about 30.000 years old (Dart & Beaumont, 1969). The first quarrying operation discovered is even older, and it is located in the Nile Valley, where numerous evidence for Palaeolithic flint and chert extraction is present (Vermeersch *et al.*, 1990). These are then the origins of mining and quarrying, an activity which grew steadily from the Bronze Age onwards (Coulson, 2012), and has influenced the course of history and civilisations (Periferakis *et al.*, 2019; Periferakis, 2021), being regarded as an integral part of the local heritage in certain places (Periferakis *et al.*, 2022).

However, neither mining nor quarrying are easy and danger-free tasks; in fact, they are rather laborious and potentially dangerous, especially in more primitive conditions. The recognition that mining is associated with specific pulmonary diseases has been made since the 16th century by Agricola (Ross & Murray, 2004). Since then, and especially after the 19th century, a systematic documentation of mining- and quarrying-related and induced occupational diseases is underway, revealing an ever-increasing number of pathologies and their associated mechanisms. Aside from increased awareness and potential of diagnostic techniques to identify such pathologies, the massive increase of the global mining and quarrying activities in the last two decades (Jasansky *et al.*, 2023) brings this problem even more to the foreground. Given that such occupational diseases represent a diverse and multifaceted issue, from the point of view of pathogenicity, diagnosis, and treatment, here we will focus on a brief overview of the radiographic evidence of pulmonary pathologies associated with coal and asbestos mining, and the associated diagnostic challenges. We have chosen coal and asbestos mining, as a wealth of data exist on the subject, and the relevant pathologies are associated specifically with these materials and are not generically caused by the mining conditions themselves.

Coal Miners' Pneumoconiosis (Black Lung Disease) and Other Pulmonary Pathologies

Coal deposits occur in coal-bearing strata, which can be found today in numerous locations worldwide. The Eurasia-China and the North America coal belts existing today were formed in the ancient supercontinent of Laurasia, while a third coal belt has formed across regions which were originally part of Gondwana. While coal from the Devonian age has been found, the majority of currently known deposits has formed during the Permian and Carboniferous ages; younger coal deposits from the Mesozoic and Cenozoic eras exist but there are fewer in number and less widespread (Wagner, 2020).

Ever since the industrial revolution, coal has been perhaps the most important source of energy, followed by oil as the 20th century progressed. Today, the major coal producing countries are China, the US, Australia, Indonesia and India, with a number of other countries also having significant resources (Wagner, 2020). Pneumoconiosis is most probably the oldest occupational disease, especially given the importance of mining and quarrying from a very early stage in human prehistory, as presented above. It is also the most prevalent occupational disease at a worldwide level (Wang et al., 2023). Coal mining-related pneumoconiosis has been identified since the 1830s, when miners presented with black sputa, breathlessness and coughing, and in autopsies, the lungs had a black pigmentation (Ronsmans & Nemery, 2022).

Pneumoconiosis is defined as a form of interstitial lung disease induced by particle inhalation, which leads to scarring and progressively diminished breathing capacity (Shekarian *et al.*, 2021). Regarding the pathophysiology of pneumoconiosis, this is determined by the interaction and deposition of the inhaled particles at the different levels of the respiratory system. As such, the smaller the particle, the more it will penetrate into the respiratory system, with

nanoparticles being the most dangerous and pathogenic

In coal mining the prolonged exposure to coal dust can lead to a particular form of pneumoconiosis, called coal workers' pneumoconiosis due to exposure to both coal and silica dust. The relevant forms of pneumoconiosis are anthracosis, silicosis and anthracosilicosis. In this context, particles with a 1-100 μm are characterised as dust, while particles below 1 μm are classified as the nano-sized fraction and are also damaging to the lungs when inhaled (Pan *et al.*, 2021); it is estimated that in mining enterprises, about 3% of the mined material will be converted to dust in the extraction process. About 40% to over 90% of dust in coal mines, at any moment, is pure coal. The particular characteristics of such dust and its relative pathogenicity depend both on the characteristics of the coal itself and on the mining methods and equipment used.

From a diagnostic perspective, the radiographic findings between the three forms are similar, with milder forms of the disease being confined to the upper parts of the lungs and presenting as small (< 1 cm) rounded opacities. The coalescence of these opacities into more massive forms is indicative of progressive massive fibrosis, a more severe form of this disease. Interestingly, in miners which are already suffering from rheumatoid arthritis, Caplan syndrome, i.e., rheumatoid pneumoconiosis, may occur. This presents as well-defined rounded nodules in the lung periphery, resembling rheumatoid nodules (Schreiber *et al.*, 2010). Anthracosis, in its mild and moderate forms, has COPD-like symptoms and a similar treatment scheme (Mirsadraee, 2014). Compared to asbestosis, it is usually less severe in the absence of comorbidities.

Other pulmonary pathologies, associated with dust inhalation in the context of coal mining are dust-related diffuse fibrosis, and some diseases of the airways such as emphysema and chronic bronchitis. Dust-related diffuse fibrosis is also, like pneumoconiosis, an interstitial lung disease, but radiographically appears as irregular opacities and presents difficulties in the differential diagnosis with idiopathic pulmonary fibrosis if an exposure history is not available (Petsonk *et al.*, 2013); it is more frequent in long-tenured coal miners compared to idiopathic pulmonary fibrosis prevalence in the general population (Laney & Weissman, 2014).

Notably, since the 1970s, due to legislation regulating the amounts of maximum permissible coal dust in mines, in major coal-producing countries, such as the US, and Australia, coal miners' pneumoconiosis incidence begun to decline. However, during the last decade, there has been an apparently unexplained increased in incidence, despite the improvement of working conditions and safety standards (Wang *et al.*, 2023). In the US, there also has been a constant incidence increase since the 1990s. In this resurgence, silica particles are implicated more than coal particles, and this may be attributable to a shift in mining methods as well as the stricter control of maximum allowed coal dust in mines compared to silica dust (Go *et al.*, 2023), although more research is required on this matter.

Pulmonary Pathologies Associated with Asbestos Exposure

The term asbestos is used to describe a group of silicate minerals, which form elongate thin fibers. These will release numerous microscopic fibers when tampered with or crashed. Their usual diameter is less than 1 μm and their length may range from several to hundreds of micrometres. Remarkably, even though the peak for asbestos demand is associated with the onset of the industrial age, such minerals have been known and used for over 5000 years (Ross & Nolan, 2003). Asbestos fibres have a number of very positive physicochemical properties, are especially durable to fire, and are very good insulators (Ross & Virta, 2001). From a mining and use perspective, chrysotile asbestos represents over 90% of the total mined asbestos (Ross & Virta, 2001).

From a mineralogical perspective, the term "asbestos" is used to refer to a family of fibrous silicate minerals, which occur in igneous and metamorphic settings. The asbestiform minerals can either be amphiboles or seprentines. The former group comprise grunerite $[(Fe_2^{2+})(Fe_5^{2+})(Si_8O_{22})(OH)_2]$, cummingtonite and its dimorph anthophyllite $[(Mg_2)(Mg_5)(Si_8O_{22})(OH)_2]$, crocidolite $[(Na_2)(Z_3^{2+}Fe_2^{3+})(Si_8O_{22})(OH,F,Cl)_2]$, tremolite, and actinolite $[Ca_2(Mg_{4.5-2.5}Fe_{0.5-2.5}(Si_8O_{22})(OH)_2)]$; anthophyllite is also known as amosite. About 90% of the total production of asbestos corresponds to crocidolite, with the rest comprising mostly chrysotile $[Mg_3(Si_2O_5)(OH)_4]$and amosite. All commercially exploitable asbestos minerals share a number of physical properties, i.e., (1) they occur as fibrous bundles, (2) these fibres have high tensile strength, (3) they have a high aspect (length:width) ratio, (4) they are flexible enough to be coiled. Due to their chemical composition, they are very stable in a variety of environments, have high thermal resistance, are not very biodegradable and are poor conductors of electricity. Other minerals which exhibit an asbestiform habit but do not exhibit all such properties are not classified as asbestos (Campbell *et al.*, 1977; Ross *et al.*, 1984; Hodgson, 1986; Skinner *et al.*, 1988).

Even though mining and use of asbestos have decreased in recent years, while safety standards and protective measures have gradually improved, there is a notable and quantifiable risk of development of asbestos-related diseases. A factor compounding the problem of correlating such pathologies with the original asbestos exposure is

the notable time lag between exposure and the manifestation of the pathology. This lag is commonly between 15 and 40 years (Luus, 2007). Exposure to asbestos can occur through a number of ways, via skin contact, ingestion, and inhalation; the first two are relatively harmless, or at least there is no significant evidence of severe asbestos-related pathologies in relation to these routes. Inhalation is the most dangerous avenue of exposure, being associated with severe pathologies (Luus, 2007).

Asbestos fibers, when inhaled, exhibit irritative, genotoxic and immunosuppressive properties. Respiratory mucosa irritation by asbestos fibers will lead to scar tissue formation, and finally benign fibrosis, effusions and plaques in the lung cavities (Pedley, 1930). Amphibole fibers are far more dangerous in that aspect given their chemical stability; chrysotile fibers can be removed relatively quickly while amphiboles may remain forever in their place of deposition (Bernstein & Hoskins, 2006). The induction of autoimmunity by asbestos fibers is not fully understood, although there is evidence indicating that they can suppress the activity of natural killer and pulmonary parenchymal cells, thus potentially leading to lung cancer (Sider *et al.*, 1987; Tsang *et al.*, 1988). Asbestos has also been found to damage the DNA and alter gene transcription and protein production (Sider *et al.*, 1987; Berry *et al.*, 2000); it seems that the genotoxic properties of asbestos fibers are proportional to their length, with the chrysotile fibers being longer and thus more dangerous (Keane *et al.*, 1999).

It is therefore clear that asbestos fibers can cause both benign and malignant lung pathologies. Regarding benign pathologies, there are asbestosis, effusions and plaques (Luus, 2007). Asbestosis represents one of the most characteristic pathologies associated with asbestos exposure and is, essentially, a bilateral interstitial pulmonary fibrosis, which preferentially affects the base of the lungs (Mossman & Churg, 1998). Amphibole fibers are the principal culprits in this case (Hessel *et al.*, 2005). The localization of asbestos-related fibrosis in specific lung regions leads to the development of plaques, which gradually limit lung functionality (Goldsmith, 1982; Cudgell & Kamp, 2004). The plaques themselves are benign but are associated with an increased cancer incidence (Sprince *et al.*, 1991). Effusions, i.e., lung collections in the lungs, which occur in association with asbestosis, plaque development and mesothelioma, can be either acute or chronic (Davies *et al.*, 1991) and can be potentially deadly. Amphibole fibers are again more responsible for this pathological aspect compared to chrysotile fibers (Davies *et al.*, 1991).

Clinical features of asbestosis comprise cough and dyspnea, while common signs are diminished breath sounds, limited chest expansion, finger clubbing, and cyanosis. The most severe complication and the usual cause of mortality is cor pulmonale (Kleinfeld, 1966). Localized fibrotic plaques may or may not impact lung function depending on a number of factors (Kerper *et al.*, 2015). In addition, the presentation of clinical effusions may vary from asymptomatic to difficulty in breathing, depending on its size and other comorbidities (Iyer *et al.*, 2019).

Mesothelioma is a type of cancer of the cell lining of the lungs and abdomen. It is often misdiagnosed as pneumonia (Peto *et al.*, 1999). Radiographically, mesothelioma presents as plaque-like or nodular pleural thickenings, which are concentric and unilateral. They may be associated with pleural effusions, with the tumor frequently extending into the lung fissures. Even though a simple chest radiograph is not enough to conclusively diagnose mesothelioma, it is highly suggestive in patients with a previous exposure history (Aziz, 2009). From a clinical perspective, most cases of mesothelioma present with chest pain and dyspnea; even with treatment, the prognosis is usually very poor (Berzenji & Van Schil, 2018). Asbestosis can subsequently lead to bronchogenic lung cancer (Luus, 2007). Bronchogenic carcinoma is the most frequently diagnosed pulmonary cancer and comprises a number of histopathological patterns. For its staging, a CT scan is necessary (Reddy & Reddy, 2022).

Discussion

As has been presented, both asbestos and coal mining are associated with a number of potentially severe pulmonary pathologies, which are mostly irreversible. While anthracosis and related pathologies are generally less severe than asbestosis and mesothelioma, they nevertheless correspond to a notable burden of disease (Lu *et al.*, 2021), especially given the prominence of coal mining relative to asbestos mining. The mortality and morbidity of such diseases is compounded by a frequent late diagnosis or misdiagnosis, especially if occupational exposure is not taken into account by medical personnel.

The diagnosis of occupational diseases associated with mining and quarrying, and their causative connection to these activities, is also important from a socioeconomic perspective, i.e., the possibility of workers to both demand safer working conditions and to claim compensation for such diseases from the owners of the enterprises where they work. While this may seem self-evident, it is not always the case. On one hand, in third world the countries working conditions in mines and quarries are not constrained by modern safety regulations and compensatory policies. But even in countries of the western world, there can be situations where the actual dangers are discounted. For example, in Britain in the early 20th century, anthracosis was considered eradicated in miners, thus leading to laxer safety regulations and the inability to claim compensation for this particular pathology; initial compensatory policies

of the period, both in the US and Britain were considered relevant only for miners suffering from silicosis (Ronsmans & Nemery, 2022). In the case of asbestos, exposure has rapidly decreased in countries where it has been banned, and it is only relevant in non-mining related contexts. In the EU, the first measures for reducing asbestos exposure were taken in the 1980s (Belackova *et al.*, 2022). Legislation to that effect has also been discussed and gradually implemented in the US around that time (Cohen, 1991). Even so, in spite of the known dangers inherent in asbestos mining and use, the global asbestos industry continues to thrive in certain countries, although globally the demand for asbestos has dropped after 2000 (Frank & Joshi, 2014).

For mesothelioma, a simple chest X-ray is a good screening test, but its non-specific findings may be confused with cases of lymphomas and metastatic carcinomas, or even benign asbestosis. Both CT and MRI scans are more useful in determining the disease and its extend, but the definitive diagnosis is always made after a biopsy (Aziz, 2009). A CT scan is also necessary for the staging of bronchogenic carcinoma (Reddy & Reddy, 2022), which in a chest X-ray usually appears as a peripheral mass (Sider, 1990). Likewise, screening for diseases associated with coal mining may be performed by radiography, although the fact that they may initially not manifest via specific signs and symptoms will most likely be associated with a delayed patient presentation, and thus diagnosis.

Even though coal miners' pneumoconiosis and asbestosis have histological differences, they both present as fibrotic pneumoconioses, and the differential diagnosis on imaging is not always simple. In principle, in pneumoconiosis we can identify diffusely distributed granular micronodules with a perilymphatic pattern, which may present central calcifications; these are often accompanied by hilar or mediastinal lymph node enlargement and may also associate emphysema. Conversely, in asbestosis we encounter dot-like opacities which are usually distributed to the inferior lobes with a reticular centrilobular pattern; it is usually associated with pleural effusions and plaques, as well as traction bronchiectasis and honeycomb fibrosis (Chong *et al.*, 2006).

Based on the aforementioned evidence, the particularities of coal mining and asbestos mining-related pulmonary pathologies, from a diagnostic perspective, have been briefly outlined. In considering the associated morbidity and mortality, and thus decrease in quality of life, it is evident that they represent a matter not only of medical, but also of socioeconomic significance (Yokoyama *et al.*, 2013; Deng *et al.*, 2022). Such aspects are highlighted also in other mining and quarrying-associated occupational diseases in scientific literature (Mandel *et al.*, 2016; Periferakis, 2020; Bonilla *et al.*, 2024). It is for these reasons that adequate enforcement of workplace regulations is necessary, along with the implementation of novel measures and technologies aimed at further improving the safety and hygiene of these occupational environments. Social support and financial assistance aimed at improving of the quality of life of affected miners must also be implemented, especially in communities where a significant part of the workforce is thus occupied. But, first and foremost, there is the need of timely diagnosis, of accurate and efficient screening methods, which will enable prompt diagnosis, therefore improving patient prognosis. Hopefully, future developments in imaging, surgical techniques and biomaterials (Nedelea *et al.*, 2024; Periferakis *et al.*, 2024) will improve care and treatment standards for such patients.

References

Aziz, F., 2009. Radiological Findings in a case of Advance staged Mesothelioma. Journal of Thoracic Disease, 1, 46-47.

Belackova, L., Verbeek, J.H., Hoving, J.L., van der Molen, D.G., Curti, S., Hulshof, C.T.J., Scheepers, P.T.J., Marinaccio, A., 2022. Legal banning of asbestos for preventing asbestos exposure. Cochrane Database of Systematic Reviews 2022, CD015106.

Bernstein, D.M., Hoskins, J.A., 2006. The health effects of chrysotile: current perspective based upon recent data. Regulatory toxicology and Pharmacology 45, 252-264.

Berry, G., Newhouse, M.L., Wagner, J.C., 2000. Mortality from all cancers of asbestos factory workers in east London 1933-80. Occupational and Environmental Medicine 57, 782-785.

Berzenji, L., Van Schil, P., 2018. Multimodality treatment of malignant pleural mesothelioma. F1000 Research 7, 1681.

Bonilla, J.S., Idrovo, A.J., Figueroa, H.H., 2024. Intoxication in a Colombian mercury mine: Aranzazu, 1948-1975. História, Ciências, Saúde-Manguinhos 31, e2024048.

Campbell, W.J., Blake, R.L., Brown, L.L., Cather, E.E., Sjoberg, J.J., 1977. Selected Silicate Minerals and Their Asbestiform Varieties. Mineralogical Definitions, Identification and Characterisation. U.S. Bureau of Mines.

Chong, S., Lee, K.S., Chung, M.J., Han, J., Kwon, O.J., Kim, T.S., 2006. Pneumoconiosis: Comparison of Imaging and Pathologic Findings. Radiographics 26, 59-77.

Cohen N., 1991. Regulation of in-place asbestos-containing material. Environmental Research 55, 97-106.

Coulson, M., 2012. The history of mining: The events, technology and people involved in the industry that forged the modern world. Harriman House Limited.

Cudgell, D.W., 2004. Kamp DW. Asbestos and Pleura. Chest 125,1103-1117.

Dart, R.A., Beaumont, P., 1969. Evidence of iron ore mining in Southern Africa in the Middle Stone Age. Current Anthropology 10, 127-128.

Davies, D., Andrews, M.I., Jones, J.S., 1991. Asbestos induced pericardial effusion and constrictive pericarditis. Thorax 46, 429-432.
Deng, Z., Tao, T.Y., Qiao, Q., 2022. Socioeconomic Status, Occupational Disease, and Psychological Well-Being: Evidence from People with Pneumoconiosis in China. Social Sciences 11, 28.
Frank, A.L., Joshi, T.K., 2014. The global spread of asbestos. Annals of Global Health 80, 257-262.
Go, L.H., Rose, C.S., Zell-Baran, L.M., Almberg, K.S., Iwaniuk, C., Clingerman, S., Richardson, D.L., Abraham, J.L., Cool, C.D., Franko, A.D., Green, F.H., 2023. Historical shift in pathological type of progressive massive fibrosis among coal miners in the USA. Occupational and Environmental Medicine 80, 425-430.
Goldsmith, J.R., 1982. Asbestos as a systemic carcinogen: the evidence from eleven cohorts. American Journal of Industrial Medicine 3, 341-348.
Hessel, P.A., Gamble, J.F., McDonald, J.C., 2005. Asbestos, asbestosis, and lung cancer: a critical assessment of the epidemiological evidence. Thorax 60, 433-436.
Hodgson, A.A., 1986. Scientific Advances in Asbestos, 1967 to 1985. Anjalena Publications.
Iyer, N.P., Reddy, C.B., Wahidi, M.M., Lewis, S.Z., Diekemper, R.L., Feller-Kopman, D., Gould, M.K., Balekian, A.A., 2019. Indwelling Pleural Catheter versus Pleurodesis for Malignant Pleural Effusions. A Systematic Review and Meta-Analysis. Annals of the American Thoracic Society 16, 124-131.
Jasansky, S., Lieber, M., Giljum, S., Maus, V., 2023. An open database on global coal and metal mine production. Scientific data 10, 52.
Keane, M.J., Stephens, J.W., Zhong, B.Z., Miller, W.E., Ong, T.M., Wallace, W.E., 1999. A study of the effect of chrysotile fiber surface composition on genotoxicity in vitro. Journal of Toxicology and Environmental Health Part A 57, 529-541.
Kerper, L.E., Lynch, H.N., Zu, K., Tao, G., Utell, M.J., Goodman, J.E., 2015. Systematic review of pleural plaques and lung function. Inhalation Toxicology 27, 15-44.
Kleinfeld, M., Messite, J., Shapiro, J., 1966. Clinical, radiological, and physiological findings in asbestosis. Archives of Internal Medicine 117, 813-819.
Laney, A.S., Weissman, D.N., 2014. Respiratory diseases caused by coal mine dust. Journal of Occupational and Environmental Medicine 56, S18-22.
Lu, C., Dasgupta, P., Cameron, J., Fritschi, L., Baade, P., 2021. A systematic review and meta-analysis on international studies of prevalence, mortality and survival due to coal mine dust lung disease. PLoS One 16, e0255617.
Luus, K., 2007. Asbestos: mining exposure, health effects and policy implications. McGill Journal of Medicine 10, 121-126.
Mandel, J.H., Alexander, B.H., Ramachandran, G., 2016. A review of mortality associated with elongate mineral particle (EMP) exposure in occupational epidemiology studies of gold, talc, and taconite mining. American Journal of Industrial Medicine 59, 1047-1060
Mirsadraee, M., 2014. Anthracosis of the Lungs: Etiology, Clinical Manifestations and Diagnosis: A Review. Tanaffos 13, 1-13.
Mossman, B.T., Churg, A., 1998. Mechanisms in the pathogenesis of asbestosis and silicosis. American Journal of Respiratory and Critical Care Medicine 157, 1666-1680.
Nedelea, D.G., Vulpe, D.E., Viscopoleanu, G., Radulescu, A.C., Mihailescu, A.A., Gradinaru, S., Orghidan, M., Scheau, C., Cergan, R., Dragosloveanu, S., 2024. Progressive Thoracolumbar Tuberculosis in a Young Male: Diagnostic, Therapeutic, and Surgical Insights. Infectious Disease Reports 16(5), 1005-1016.
Pan, L., Golden, S., Assemi, S., Sime, M.F., Wang, X., Gao, Y., Miller, J., 2021. Characterization of Particle Size and Composition of Respirable Coal Mine Dust. Minerals, 11, 276.
Pedley, F.G., 1930. Industrial Hygiene: Asbestosis. Canadian Public Health Journal 21, 576-577.
Periferakis, A., 2020. The Keramos Antimonite Mines in Chios Island, Greece: Mining History and Current Situation. News on Minerals 35, 5-21.
Periferakis, A., 2021. The emery of Naxos: A multidisciplinary study of the effects of mining at a local and national context. JournalNX: A Multidisciplinary Peer Reviewed Journal 7, 93-115.
Periferakis, A., Paresoglou, I., Paresoglou, N., 2019. The significance of the Lavrion mines in Greek and European Geoheritage. European Geologist 48, 24-27.
Periferakis, A., Periferakis, A.-T., Troumpata, L., Dragosloveanu, S., Timofticiuc, I.A., Georgatos-Garcia, S., Scheau, A.-E., Periferakis K., Caruntu, A., Badarau, I.A., Scheau, C., 2024. Use of Biomaterials in 3D Printing as a Solution to Microbial Infections in Arthroplasty and Osseous Reconstruction. Biomimetics 9, 154.
Periferakis, A., Periferakis, K., Periferakis, A.-T., 2022. The Geoheritage of Malta from Prehistory to the Present Day. Proceedings of the 16th International Congress of the Geological Society of Greece, Patra, Greece, p. 816-817.
Peto, J., Decarli, A., La Vecchia, C., Levi, F., Negri, E., 1999. The European mesothelioma epidemic. British Journal of Cancer 79, 666-672.
Petsonk, E.L., Rose, C., Cohen, R., 2013. Coal mine dust lung disease. New lessons from an old exposure. American Journal of Respiratory and Critical Care Medicine 187, 1178-1185.
Reddy, R., Reddy, S., 2022. Trends in Imaging Patterns of Bronchogenic Carcinoma: Reality or a Statistical Variation? A Single-Center Cross-Sectional Analysis of Outcomes. Medical Principles and Practice 31, 480-485.
Ronsmans, S., Nemery. B., 2022. Pneumoconiosis in Coal Miners: Anthracosilicosis after All?. Annals of the American Thoracic Society 19, 1451-1452.
Ross, M., Nolan, R.P., 2003. History of asbestos discovery and use and asbestos-related disease in context with the

occurrence of asbestos within ophiolite complexes, in: Dilek, Y., Newcomb, S., (Eds.), Ophiolite Concept and the Evolution of Geological Thought, 447-470.

Ross, M., Virta, R.L., 2001. Occurrence, production and uses of asbestos, in: Nolan, R.P., Langer, A.M., Ross, M., Wicks, F. J., Martin, R.F., (Eds.), The health effects of chrysotile asbestos—Contribution of science to risk-management decisions, 79-88.

Ross, M.H., Murray, J., 2004. Occupational respiratory disease in mining. Occupational Medicine (London) 54, 304-310.

Ross, M., Kuntze, R.A., Clifton, R.A., 1984. A Definition for Asbestos, in: B. Levadie, B. (Ed.), Definition for Asbestos and Other Health Related Silicates: A Symposium, 139-147.

Schreiber, J., Koschel, D., Kekow, J., Waldburg, N., Goette, A., Merget, R., 2010. Rheumatoid pneumoconiosis (Caplan's syndrome). European Journal of Internal Medicine 21, 168-172.

Shekarian, Y., Rahimi, E., Rezaee, M., Su, W.-C., Roghanchi, P., 2021. Respirable Coal Mine Dust: A Review of Respiratory Deposition, Regulations, and Characterization. Minerals 11, 696.

Sider, L., 1990. Radiographic manifestations of primary bronchogenic carcinoma. Radiologic Clinics of North America 28, 583-597.

Sider, L., Holland, E.A., Davis Jr, T.M., Cugell, D.W., 1987. Changes on radiographs of wives of workers exposed to asbestos. Radiology 164, 723-726.

Skinner, H.C.W., Ross, M., Frondel, C., 1988. Asbestos and Other Fibrous Materials, Oxford Press.

Sprince, N.L., Oliver, L.C., McLoud, T.C., Eisen, E.A., Christiani, D.C., Ginns, L.C., 1991. Asbestos exposure and asbestos-related pleural and parenchymal disease. American Review of Respiratory Disease 143, 822-828.

Tsang, P.H., Chu, F.N., Fischbein, A., Bekesi, J.G., 1988. Impairments in functional subsets of T-suppressor (CD8) lymphocytes, monocytes, and natural killer cells among asbestos-exposed workers. Clinical Immunology and Immunopathology 47, 323-332.

Vermeersch, P.M., Paulissen, E., Van Peer, P., 1990. Palaeolithic chert exploitation in the limestone stretch of the Egyptian Nile Valley. African Archaeological Review 8, 77-102.

Wagner, N.J., 2020. Geology of Coal, in: Alderton, D., Elias, S.A. (Eds.)., Encyclopedia of Geology, 2nd ed., vol. 5, 745-761.

Wang, H., Ye, Q., Chen, Y., Li, T., 2023. Epidemiology of coal miners' pneumoconiosis and its social determinants: An ecological study from 1949 to 2021 in China. Chinese Medical Journal Pulmonary and Critical Care Medicine 1, 46-55.]

Yokoyama, K., Iijima, S., Ito, H., Kan, M., 2013. The socio-economic impact of occupational diseases and injuries. Industrial Health 51, 459-461.

17th INTERNATIONAL CONGRESS of the Geological Society of Greece

BULLETIN OF THE GEOLOGICAL SOCIETY OF GREECE, SP. PUBL.

EXTENDED ABSTRACT 262

Mineralogical composition and mineral chemistry of the listvenite-hosted mineralization in Kato Vyrsini area, Thrace, Greece

Peristeridou E.[1], Melfos V.[1], Voudouris P.[2], Papapodoulou L.[1], Pršek J.[3], Kantiranis N.[1]

(1) School of Geology, Aristotle University of Thessaloniki, Thessaloniki, Greece, peristee@geo.auth.gr

(2) School of Geology and Geoenvironment, National and Kapodistrian University of Athens, Athens, Greece

(3) Faculty of Geology, Geophysics, and Environmental Protection, AGH UST University of Science and Technology, Kraków, Poland

Research highlights:

The study focuses on Ni-Co sulfides and arsenides, highlighting their association with hydrothermal processes and ultramafic protolith alteration in the listvenite-hosted mineralization of the Rhodope massif.

Introduction / Background

Hydrothermal alteration of peridotites or serpentinites from ophiolite complexes, remnants of the Neotethys oceanic lithosphere has formed listvenites either mineralized or non-mineralized in many places, including Kosovo, Greece, Turkey, Oman, and Iran. In Greece, listvenites have been reported in Tinos Island, Mount Oeta in Central Greece, Gerakini and Vavdos at Chalkidiki, and in Vyrsini at Komotini (Iliadis, 2006, Hinsken et al., 2017 and references therein). The term listvenitization is used to describe the range of carbonization processes, from carbonate-rich to silica-rich phases, caused by hydrothermal fluids enriched in CO_2. These rocks are typically composed of quartz, Ca-Fe-Mg carbonates, fuchsite, serpentine, talc, chlorite, relics of chromite, magnetite, sulfides, and arsenides (Boskabadi et al., 2020). They commonly occur in shear or fault zones that serve as pathways for hydrothermal fluids, facilitating CO_2 infiltration and subsequent metasomatism. Listvenites are important since they are commonly associated with lode gold mineralization, as well as enrichment in other precious and critical metals, such as Ag, Hg, Co, Ni, As, and Sb that have been formed under low temperature conditions (Boskabadi et al., 2020).

The transformation of peridotite to listvenite involves multiple stages, beginning with hydration to form serpentinite, followed by carbonation and metasomatism through the influx of CO_2 rich fluids (Boskabadi et al., 2020). This transition is gradual, evolving with increasing CO□, and involves intermediate stages characterized by the progressive replacement of serpentine or talc, leading to quartz-carbonate assemblages. Based on the modal proportions of quartz and carbonate, three types of listvenite lithologies can be classified: carbonate listvenites, silica-carbonate listvenites, and silica listvenites (Boskabadi et al., 2020).

The objective of this study is to present preliminary data on the mineral composition of the listvenite occurrences in the Kato Vyrsini region in the Rhodope massif, and to document the mineralization they host, which has not been studied in detail so far.

Geology

The study area is part of the Kechros metamorphic core complex, which belongs to the Rhodope Massif in northeastern Greece. The Kechros complex is the lowermost tectonic unit of the Rhodope domain, exhumed against the Kimi complex by extensional deformation of the low-angle Kechros detachment fault during Early Eocene (36-32 Ma) (Mposkos et al. 2013, Kounov et al., 2024). This terrain consists of both continental and oceanic lithologies, represented by orthogneisses, pelitic gneisses, and high-alumina metapelites, intercalated with schists, amphibolites, boudins of eclogites, and scarce marbles. The oceanic affinity lithologies are tectonically intercalated and comprise serpentinized peridotites with dykes of gabbroic pegmatites, diabases, rodingitic gabbros, and blocks of trondjemites (Iliadis 2006, Mposkos et al. 2013). The antigorite serpentinite at Vyrsini spans approximately 95 km^2 and is considered one of the largest ultramafic bodies in the Greek Rhodopes. Its boundaries are defined by two major tectonic structures: the Smigada dip slip fault, and the Ragada-Esochi low-angle fault in the northern and southern parts, respectively. Over a large area, these rocks have undergone intense serpentinization and subsequent silica-carbonate alteration forming the listvenite zones. The largest listvenite body in the region extends from NW of the Kato Vyrsini village to Akritas occupying an area of approximately 2.5 km^2 (Fig. 1).

Methods

A preliminary investigation of the mineralization hosted in the listvenites of the Kato Vyrsini region was carried out on polished and thin sections. Observations were made using a Leitz LaborLux 11 Pol dual reflected-transmitted light polarizing microscope equipped with a Levenhuk M base series digital camera. The analysis was complemented by SEM back-scattered electron imaging, and the chemical composition of the ore minerals was determined by JEOL JSM- 6390LV scanning electron microscope (SEM) (JEOL Ltd., Tokyo, Japan) equipped with an OXFORD INCA 300 energy dispersive system (EDS). All the analyses were performed in the School of Geology at Aristotle University of Thessaloniki.

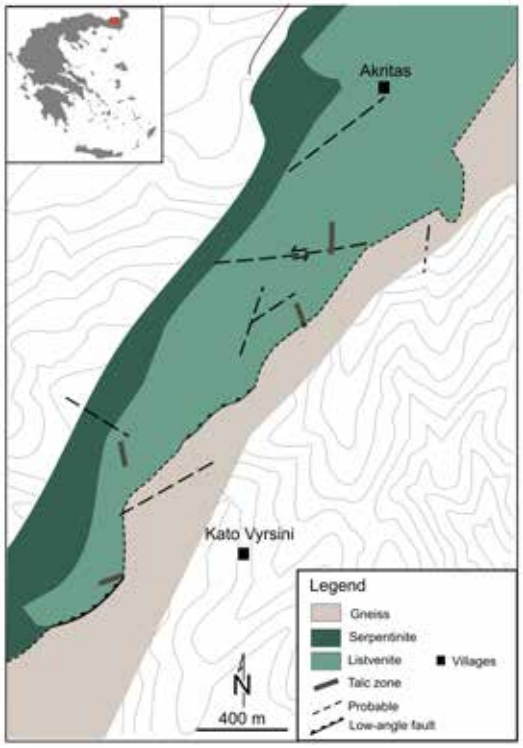

Figure 1. Simplified geological map of the area between Kato Vyrsini and Akritas (modified after Iliadis et al., 2006 and Kounov et al., 2024)

Results

In Kato Vyrsini, the listvenitization of serpentinite has resulted in the formation of three different rock types, each differing in mineralogy and the degree of metasomatism. These rock types include transitional rocks (Type I), carbonate-rich listvenite (Type II) and silica-rich listvenite (Type III) (Fig. 2a-c). Transitional rock types occur as lenses within the serpentinite body. They exhibit a greyish green color (Fig. 2a) and are characterized as magnesite-bearing serpentinite that contains over 70% serpentine along with magnesite and minor talc, chromite, magnetite, and hematite (Fig. 3a). Commonly, magnetite destabilized into hematite. Carbonate-rich listvenite is found adjacent to shear zones and is characterized by a green color (Fig. 2b). Its mineralogical composition is dominated by carbonate minerals, mainly dolomite, magnesite, with rare calcite, as well as quartz (Fig. 3b). It also contains chromite, which is often thinly rimmed by magnetite or ferri-chromite, and minor amounts of pyrite. Silica-rich listvenite, commonly referred to as “birbirite”, is formed along fault planes, indicating brittle deformation (Fig. 2c). It consists of a silicified mass with fine-grained quartz (Fig. 3c) and disseminated chromite, pyrite, marcasite, a Ni-sulfarsenide (gersdorffite), Ni-sulfides (vaesite, violarite), and minor rutile.

Figure 2. Hand specimen of different types of listvenite (a) Transition rock type (Type I), (b) Carbonate-rich listvenite (Type II), (c) Silica-rich listvenite (Type III) with mineralization

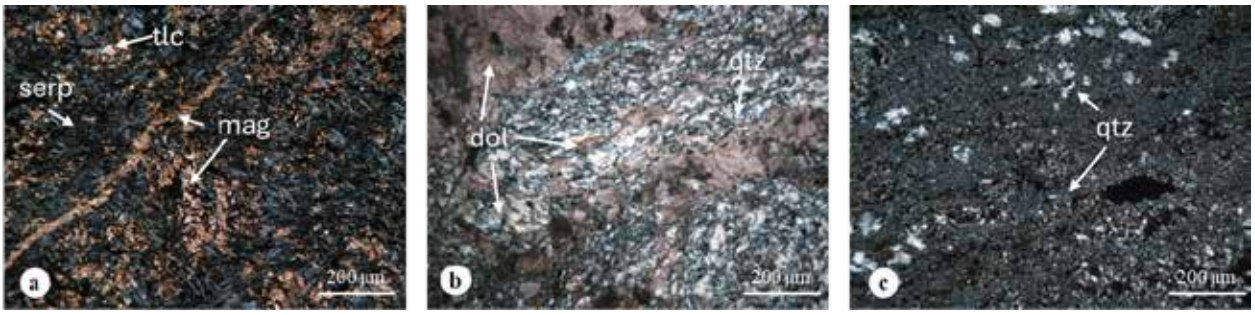

Figure 3. Microphotographs with closed-polarized light, of the different listvenite types (Type I-III) (a) Magnesite with fine-grained talc within a serpentine groundmass in Type I listvenite, (b) Dolomite with quartz in Type II listvenite, (c) Coarse- and fine-grained quartz in type III listvenite. Abbreviations: serp=serpentine, tlc=talc, mag=magnesite, dol=dolomite, qtz=quartz

Chromite appears with intense cataclastic texture in all listvenite types, with a decreasing extent from type I to type III, reaching sizes of up to 500 μm. In types I and II, chromite occurs within the carbonate mass and is commonly rimmed by magnetite or ferri-chromite (Figure 4a). In type III, it occurs as disseminated subhedral grains within the fine-grained matrix and appears more homogenous, without zoning. The chemical composition of chromite differs between the types II and III. When it is hosted in carbonate listvenites, it exhibits higher Cr_2O_3 contents, which decrease from the core to the outer rims, ranging from 45.98 to 49.56 wt.%. Similarly, MgO follows this trend, demonstrating contents of 6.67 wt.% in the core and 4.34 wt.% towards the rim. Conversely, Al_2O_3 ranges between 14.83 and 17.67 wt.% and increases towards the rims of the chromite crystals. Minor amounts of SiO_2 (up to 0.88 wt.%), V_2O_3 (up to 0.53 wt.%), ZnO (up to 0.96 wt.%) and NiO (up to 0.74 wt.%) are also present. Chromite in the silica-rich listvenites exhibits Fe content ranging from 24.6 to 52.01 wt.%, while Cr_2O_3 concentrations are lower compared to those in carbonate-rich listvenites, ranging from 40.74 to 44.05 wt.%. Additionally, there are minor contents in Al_2O_3 (0.7-0.91 wt.%) and MgO (0.66-1.16 wt.%). These chromites also contain TiO_2 ranging from 2.68-3.59 wt.%. Overall, the analyzed chromite grains in type III are characterized by a high chromite component, with a Cr# [Cr/(Cr+Al)] of 0.97, whereas those in Type II listvenites have a lower average Cr# of 0.67. Similarly, the average Fe# [$(Fe^{+2} / (Mg + Fe^{+2})$] value is 0.95 for chromites in silica listvenites and 0.72 for chromites in carbonate listvenites.

The abundance of magnetite decreases as the silica metasomatism increases, similar to chromite. Magnetite occurs as coarse- and fine-grained euhedral and subhedral grains, disseminated or massive, within the transitional listvenite and carbonate-rich listvenite. It commonly forms rims around chromite and occasionally it alters to hematite. It contains inclusions of Ni-bearing phases, such as violarite ($FeNi_2S_4$) (Fig. 4b). Variations in composition are observed within the same grains. In the cores, Fe content is lower and Cr decreases, while Ni is omnipresent (0.58–1.17 wt.%).

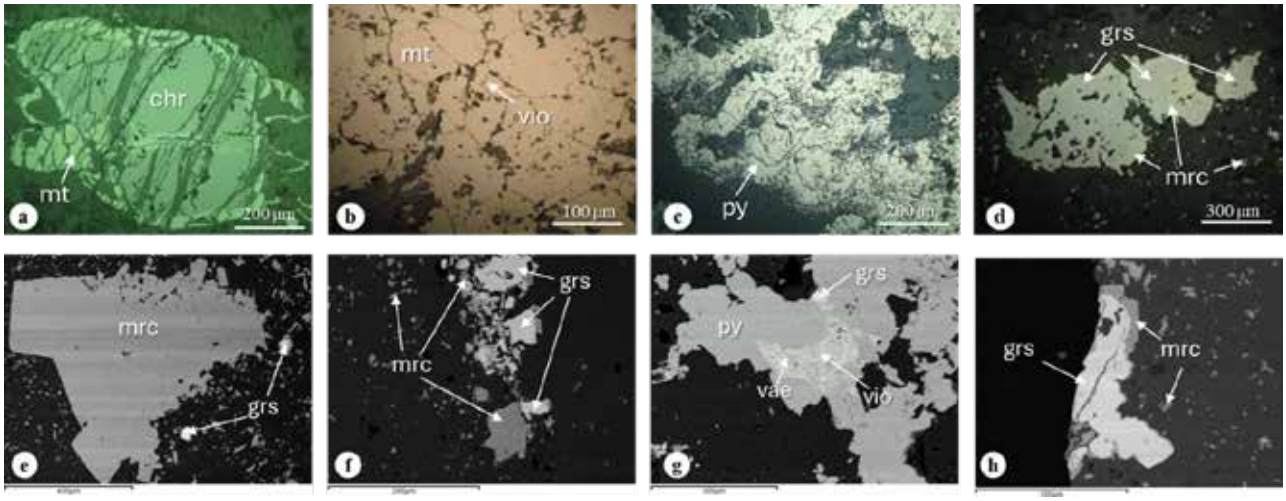

Figure 4. Microphotographs (a-d) and BSE images (e-h) of ore minerals in different listvenite types. (a) Chromite rimmed by magnetite. The microcracks are filled by serpentine (Type I listvenite), (b) Massive magnetite with violarite inclusion in Type II listvenite, (c) Oscillatory coarse-zoned pyrite in Type III listvenite, (d) Gersdorffite rimmed by marcasite in Type III, (e) Marcasite and gersdorffite with rims of marcasite in Type III listvenite, (f) Gersdorffite intergrown with marcasite in Type III listvenite, (g) Pyrite intergrown with Ni-phases (violarite and vaesite) in type III listvenite, (h) Gersdorffite with marcasite rim in Type III listvenite. Abbreviations: mt= magnetite, chr=chromite, vio=violarite, py=pyrite, grs=gersdorffite, mrc= marcasite, vae= vaesite.

Pyrite is present in listvenites of type II and III at Kato Vyrsini. Pyrite hosted within the carbonate-rich listvenites, exhibits a cataclastic texture and occurs as small subhedral to euhedral crystals, up to 20 μm in size. It is often oxidized to goethite while retaining the hexahedron crystal shape. In contrast, pyrite in the silica-rich listvenites forms significantly larger aggregates and is often associated with marcasite (Fig. 4c). The chemical composition of pyrite varies, with notable element concentrations. It contains up to 5.91 wt.% Ni, up to 1.91 wt.% As, up to 1.03 wt.% Ag and Zn, up to 0.87 wt.% Ti, up to 0.59 wt.% Sb, up to 0.47 wt.% Cu and up to 0.23 wt. % Co, many of which may be associated with micro-inclusions of other minerals. Iron content ranges from 35.48 to 43.09 wt.%, while S content ranges 54.82-59.16 wt.%. The average chemical composition can be expressed as $Fe_{0.87}Ni_{0.01}S_{2.11}$.

Gersdorffite is distributed within silicified listvenite (Type III) and occur as euhedral crystals up to 200 μm in size. These grains are often rimmed by marcasite or pyrite (Fig. 4d-h). Gersdorffite is the most widespread Ni-bearing phase of listvenites at Kato Vyrsini. The general chemical composition is NiAsS, with significant amounts of Fe and Co that can substitute for Ni, and minor amounts of Sb that can replace As. Gersdorffite from Kato Vyrsini contains 42.53-46.92 wt.% As and 27.89-36.01 wt.% Ni, 1.74-5.40 wt.% Fe, up to 3.28 wt.% Sb, 0.08-2.77 wt.% Co, and up to 0.53 wt.% Cu (Table 1). The average chemical formula is $(Ni_{0.9}Fe_{0.09}Co_{0.03})_{1.02}As_{0.99}S_{0.99}$.

Nickel sulfides are present in lower abundances and are represented by violarite and vaesite. Vaesite appears as anhedral grains interstitial to pyrite, alongside to violarite and gersdorffite in the silicified listvenites (Fig. 4g). Violarite is found in small grains associated with magnetite in the carbonate-rich listvenites. The average chemical composition of vaesite is $Fe_{0.2}Ni_{0.77}As_{0.02}S_2$, while violarite has a composition of $Fe_{0.99}Co_{0.01}Ni_{1.89}As_{0.03}S_4$. Violarite grains coexisting with magnetite are slightly richer in Ni and Co, contain no As, and exhibit a mean composition of $Fe_{0.75}Co_{0.06}Ni_{2.19}S_4$.

Table 1. Representative microanalyses (wt %) and calculated formulae of gersdorffite (1-6), vaesite (7-8), violarite (9-10) and pyrite (11-12) of the Kato Vyrsini listvenites

	1	**2**	**3**	**4**	**5**	**6**	**7**	**8**	**9**	**10**	**11**	**12**
Sb	0.33	0.9	bdl[1]	bdl	3.28	bdl	bdl	bdl	bdl	0.00	0.00	bdl
As	43.18	43.68	42.53	43.1	44.59	45.91	2.37	bdl	0.00	0.00	0.68	0.86
Zn	0.00	0.00	0.00	0.00	0.00	0.00	0.00	0.00	0.00	0.00	bdl	0.69
Ni	34.92	32.17	36.01	35.35	31.01	31.17	29.96	44.29	42.97	41.82	6.57	0.43
Co	0.49	0.53	0.19	0.08	0.47	1.62	0.16	bdl	1.25	1.08	bdl	0.15
Fe	2.81	4.15	1.92	2.32	1.88	2.4	15.13	3.25	13.19	14.51	39.42	45.55
S	19.19	18.86	19.47	19.71	18.90	19.15	52.52	52.35	42.35	42.42	53.44	53.24
Total	100.93	100.29	100.12	100.56	100.14	100.25	100.14	99.89	99.76	99.83	100.10	100.92
Chemical formula												
Sb	-	0.01	-	-	0.05	-	-	-	-	-	-	-
As	0.94	0.97	0.93	0.94	1.00	1.01	0.04	-	-	-	0.01	0.01
Zn	-	-	-	-	-	-	-	-	-	-	-	0.01
Ni	0.97	0.91	1.01	0.98	0.89	0.88	0.62	0.93	2.22	2.16	0.13	0.01
Co	0.01	0.01	0.01	-	0.01	0.05	-	-	0.06	0.06	-	-
Fe	0.08	0.12	0.06	0.07	0.06	0.07	0.33	0.07	0.72	0.79	0.85	0.98
S	0.98	0.97	1.00	1.00	0.99	0.99	2.00	2.00	4.00	4.00	2.01	1.99
Total	3.00	3.00	3.00	3.00	3.00	3.00	3.00	3.00	7.00	7.00	3.00	3.00

1: bdl: below detection limit

Discussion and Conclusions

The study of listvenites in the Kato Vyrsini area provides significant insights into their classification, mineralogical composition, and the associated mineralization processes. Based on mineralogical investigations, distinct types of listvenite were identified, differentiated by their dominant mineral assemblages. Serpentinization precedes listvenitization, as evidenced by the remnants of serpentine within the listvenite bodies, forming a transitional rock type (Type I). Type II (Carbonate-Rich Listvenites) forms during a subsequent phase of carbonation, characterized by the development of carbonate-dominated assemblages. Type III (Silica-Rich Listvenites) represents the most advanced stage, marked by intense silicification forming quartz-rich assemblages with disseminated Fe-Ni-S mineralization.

Most listvenites at Kato Vyrsini formed within or at the borders of serpentinized ultramafic rocks, along major tectonic zones (i.e. low-angle faults zones), which acted as pathways for hydrothermal fluids. However, some occurrences are associated with second order structures, such a small-scale cracks and high-angle faults, and also related to the porosity of highly altered serpentinized zones. A key aspect of listvenite-hosted ore formation in the study area is the role of a potential tectonic reactivation. Early-stage Mesozoic thrust faults were reactivated during Cenozoic

extension, and created low-angle detachment faults, enhancing fluid mobility and contributing to extensive alteration and mineralization, consistent with the tectonic regime observed in the Rhodope Massif (Melfos and Voudouris, 2017, Kounov et al., 2024). However, on the absence of age data, any genetic relationship between specific types of alteration and mineralization in the studied listvenites cannot be yet proven. We suggest here a scenario, where detachment faults facilitated deep circulation of CO_2-rich fluids, initiating carbonation reactions in the ultramafic protolith forming the transitional listvenite (Type I). As the system was uplifted the carbonate-rich fluids were substituted by silica-rich fluids and formed the carbonate-rich listvenite (Type II) and the silica-rich listvenite (Type III).
Chromite and magnetite occur in the least altered meta-ultramafic rocks. During listvenitization, these minerals are progressively replaced by newly formed mineral assemblages, especially sulfides, Ni-sulfarsenides, and Ni-arsenides. Pyrite and marcasite are the dominant sulfides, occurring in all types, and are accompanied by Ni-minerals, including gersdorffite, vaesite and violarite enriched in cobalt. The source of Ni and Co is attributed to the ultramafic protoliths, where they are hosted in silicates (primarily olivine or serpentine) or in magmatic sulfides that were destroyed during serpentinization and the subsequent hydrothermal alteration facilitated their leaching and mobilization (Kiefer et al., 2023). Although earlier studies in the Kato Vyrsini listvenites do not mention the presence of nickel minerals, they note attempts to explore nickel mineralization in the 1960s (Iliadis, 2006). This research shows that nickel mineralization is fairly common in the mineralization of the broader area.

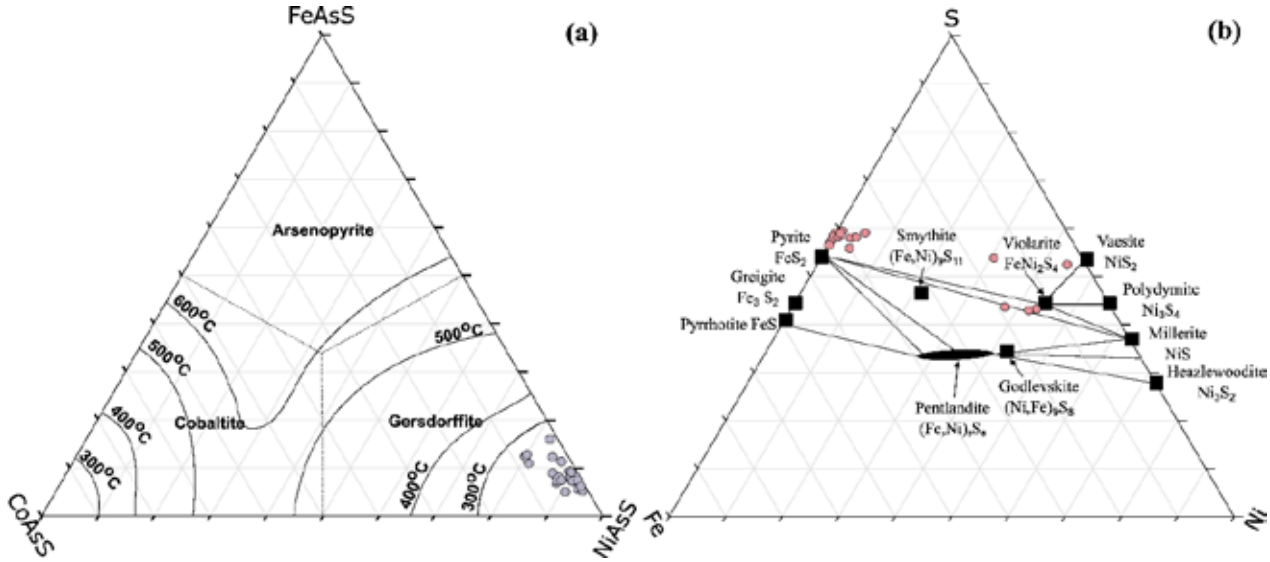

Figure 5. (a) Composition of gersdorffite in the FeAsS-CoAsS-NiAsS system. The solid lines contour the compositional fields of solid solutions in the system FeAsS-CoAsS-NiAsS at the specified temperatures (after Klemm, 1966), (b) Mineral stabilities in the ternary diagram Fe–Ni–S (after Schwarzenbach et al., 2014).

The ternary plot of gersdorffite analyses on the FeAsS-CoAsS-NiAsS system indicates formation temperatures between ~220-280 °C (Klemm, 1966, Mederski et al., 2021). Antimony, although not a common component of gersdorffite, was observed in grains coexisting with residual chromite within the listvenite mass. Correlation diagrams reveal a strong relationship (R^2=0.99) between Ni+Co+Fe and S+As+Sb (Fig. 6a), indicating that the elements behave in a coupled manner during mineral formation, transitioning to the gersdorffite-ullmannite series. Additionally, the substitution of Ni by Co is evident from the negative correlation between these elements in Fig. 6b. Iron, however, exhibits limited substitution for nickel (Fig. 6c), possibly due to the presence of a Fe-bearing phase intergrown with gersdorffite on a sub-microscopic scale, or due to the pyrite-marcasite rims around gersdorffite grains, creating observed irregularities. Figure 6d presents the correlation of R^2=0.67 of the couple substitution between Ni by Co and Fe.
Vaesite is intergrown with pyrite, gersdorffite and violarite. It typically forms at low temperatures through the replacement or remobilization of earlier Ni- and Co-bearing minerals. Vaesite is generally associated with the listvenitization of ultramafic rocks, where disulfides replace or overgrow older assemblages of sulfides (Schwarzenbach et al., 2014). Co- and Fe-bearing vaesite also contains more arsenic, while pyrite associated with vaesite exhibits higher cobalt concentrations. The same behavior is observed by the associated violarite. Violarite also forms intergrowths in magnetite with notable Ni and Co contents, suggesting formation at higher temperatures. Chemical analyses of vaesite and violarite indicate formation temperatures of ~230 °C consistent with phase relations in the Fe-S-Ni system (Fig. 5b) (Schwarzenbach et al., 2014).

The results of this study indicate that the Kato Vyrsini listvenites formed through complex processes involving hydrothermal fluids and tectonic activity. Further investigation is required to a more precise determination of the conditions that influenced their formation and mineralogical evolution.

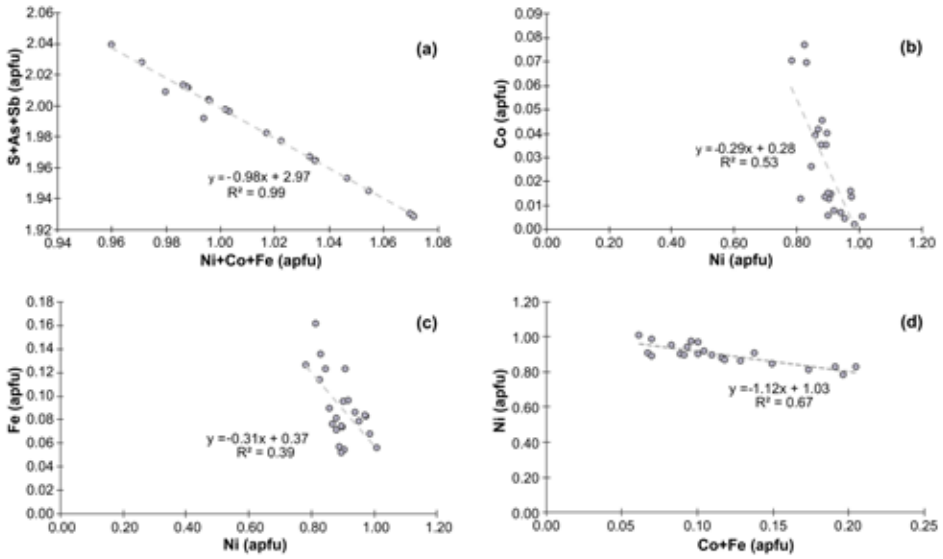

Figure 6. Plots showing substitution mechanisms in gersdorffite lattice: (a) S+As+Sb vs Ni+Co+Fe, (b) Co vs Ni, (c) Fe vs Ni, and (d) Ni vs Co+Fe

Acknowledgements

E. Peristeridou received a scholarship of excellence for PhD Candidates of the School of Sciences of Aristotle University of Thessaloniki, through the Special Account for Research Grants (S.A.R.G.) A.U.Th. in the context of the project 50186, No 673429-Excellence Scholarships for the Schools: Faculty of Engineering, School of Sciences, School of Agriculture – 2023. In addition, the research was funded by the Society of Economic Geologists Foundation (SEGF) and the SEG Canada Foundation (SEGCF) through the Student Research Grant Awards of 2024.

References

Boskabadi, A., Pitcairn, I. K., Leybourne, M. I., Teagle, D. A., Cooper, M. J., Hadizadeh, H., Bezenjani, R. N., & Bagherzadeh, R. M., 2020. Carbonation of ophiolitic ultramafic rocks: Listvenite formation in the Late Cretaceous ophiolites of eastern Iran. Lithos, 352, 105307.

Hinsken, T., Bröcker, M., Strauss, H., & Bulle, F., 2017. Geochemical, isotopic and geochronological characterization of listvenite from the Upper Unit on Tinos, Cyclades, Greece. Lithos, 282, 281-297.

Iliadis, A., 2006. Study of the ultrabasic rocks of Ano Vyrsini (Geology–Petrology–Metallogeny). PhD Thesis, National Technical University of Athens, Athens, 249p.

Kiefer, S., Ivan, P., Kaufmann, A. B., VĎAČNÝ, M., & Majzlan, J., 2023. Remobilization of Ni–Co–As and platinum-group elements by carbonate metasomatic alteration (listvenitization) of metaultramafic rocks from Dobšiná, Slovakia. Geologica Carpathica, 74(2), 139-153.

Klemm, D. D., 1966. Synthesen und Analysen in den Dreickdiagrammen FeAsS-CoAsS-NiAsS und FeS_2-CoS_2-NiS_2. Neues Jahrb. Mineral. Abh., 103, 205-255.

Kounov, A., & Gerdjikov, I., 2024. On the Rhodopean protoliths and their Middle Jurassic to Early Cretaceous evolution. A review. Geologica Balcanica, 53(1).

Mederski, S., Wojslaw, M., Prsek, S., Majzlan, J., Kiefer, S., & Asllani, B., 2021. A geochemical study of gersdorffite from the Trepça Mineral Belt, Vardar Zone, Kosovo. Journal of Geosciences, 66(2), 97-115.

Melfos, V., & Voudouris, P., 2017. Cenozoic metallogeny of Greece and potential for precious, critical and rare metals exploration. *Ore Geology Reviews*, *89*, 1030-1057.

Mposkos, E., Baziotis, I., Leontakianakos, G., & Barry, P. H.,2013. The metamorphic evolution of the high-pressure Kechros complex in East Rhodope (NE Greece): Implications from Na–Al-rich leucocratic rocks within antigorite serpentinites. *Lithos*, *177*, 17-33.

Schwarzenbach, E. M., Gazel, E., & Caddick, M. J., 2014. Hydrothermal processes in partially serpentinized peridotites from Costa Rica: evidence from native copper and complex sulfide assemblages. Contributions to Mineralogy and Petrology, 168, 1-21.

17th INTERNATIONAL CONGRESS of the Geological Society of Greece

BULLETIN OF THE GEOLOGICAL SOCIETY OF GREECE, SP. PUBL.

EXTENDED ABSTRACT 263

The geological structure of the Myrtoan Sea islets

Photiades A. [1], Kampolis I.[1,2], Vakalas I.[1,2], Deligiannakis G.[1,3]

(1) Hellenic Survey of Geology & Mineral Exploration, Acharnes, Greece, afotiadis@eagme.gr (2) National Technical University of Athens, Zografou, Greece (3) Agricultural University of Athens, Athens, Greece

Research Highlights

The previously unexplored geological structure of the Myrtoan Sea islets is briefly presented.

Myrtoan Sea stretches north to south between Spetses and Kithira Islands and east to west between Laconia Peninsula and Milos Island, comprising a subdivision of the Aegean Sea. It hosts a number of small islands (Antimilos, Ananes, Paximadi, Falconera and Velopoula) scattered on its marine territory, documenting the interesting, surficial geological structure of the area. With the scope of recording this local geology, the personnel of the Hellenic Survey of Geology and Mineral Exploration (HSGME) surveyed and mapped these islets in the framework of the project "Islets and rocky islets of the Aegean Sea" (2021-2025), supported by the National Funds Programme (NFP). This project attempted to shed light on the previously unexplored geological stratigraphy of the islets within the Myrtoan Sea, and place them in the context of the Hellenides belts.

The geology of the respective region can be distinguished in: a) the recent processes that took part at the northwestern segment of the active volcanic system of the South Aegean volcanic arc, b) the Mesozoic metamorphic basement of the Attic-Cycladic metamorphic complex and c) the Pelagonian realm. Each of these environments can be traced on the individual islets of the area. In the following sections, the stratigraphy description for each islet is given, starting from the most recent geological events and moving backwards in time.

Antimilos and Ananes Islets

Antimilos is situated almost 9 km northwest of Milos Island, whereas Ananes lies 22 km southwest of it. Both islets are part of the northwestern segment of the active South Aegean volcanic arc. The latter is comprised of a series of volcanic centers in a chain arrangement, that have produced a range of edifice-rich domes and lava flows with pyroclastic ejecta. The volcanic rocks vary from basaltic, through andesitic and dacitic, to rhyolitic compositions. They bear a typical calc-alkaline chemical composition associated with the active volcanic arc, triggered by the convergence of the African and Aegean plates. The volcanic activity initiated 3 million years ago (Ma) and remains active (Innocenti *et al.,* 1981). The tectonic regime of the area is characterized by a compressional phase during the Middle Miocene, followed by intense extensional stresses in the Pliocene (Angelier, 1979).

Antimilos Islet (Fig. 1) represents a large cone-shaped stratovolcano with steep-sided slopes, formed by an alternation of lava flow layers, composed mainly of dacite lava domes and subordinate andesite (Marinos, 1961) as well as pyroclastics. This volcano is characterized by explosive eruptions due to the high viscosity of the lava, suggesting a rhyolitic, dacitic and andesitic composition for the latter. The Antimilos rhyolitic activity (0.32 ± 0.05 Ma; Fytikas *et al.*, 1986) is coeval with the most recent eruptive phase on Milos.

Ananes Islets (Fig. 2) comprise a six-islet group, with the largest recording an altitude of 82 m, the intermediate 42 m, and the smallest ranging from 9 to a few meters. They consist mainly of highly-altered porphyritic andesitic lava flows, developed in dome structures, and their explosive and extrusive activities belong to the Milos Volcanic Field, dating back from 3.5 to 1.6 Ma (Late Pliocene-Early Pleistocene) (Fytikas *et al.,* 1986).

Paximadi Islet

Paximadi Islet is located 1,5 km southwest of Milos Island and consists of alpine and post-alpine lithologies. More particularly, Paximadi hosts the pre-volcanic metamorphic basement of the Attic-Cycladic Metamorphic Complex and on top of it, Neogene sediments lie unconformably. The metamorphic rock consists mainly of glaucophanitic schist and partly green schist, phyllite, metabasalt and quartz veins. It has undergone high-pressure (HP-LT) metamorphic facies in the Eocene and low-pressure (LP-LT) facies in the middle to late Miocene. Thus, it constitutes part of the Cyclades Blueschist unit (Grasemann *et al.,* 2018), and is identical to that of Milos Island.

Additionally, the Blueschist unit is subject to pervasive ductile deformation, possibly during the Paleocene-Eocene period, with a shearing direction towards south to southwest.

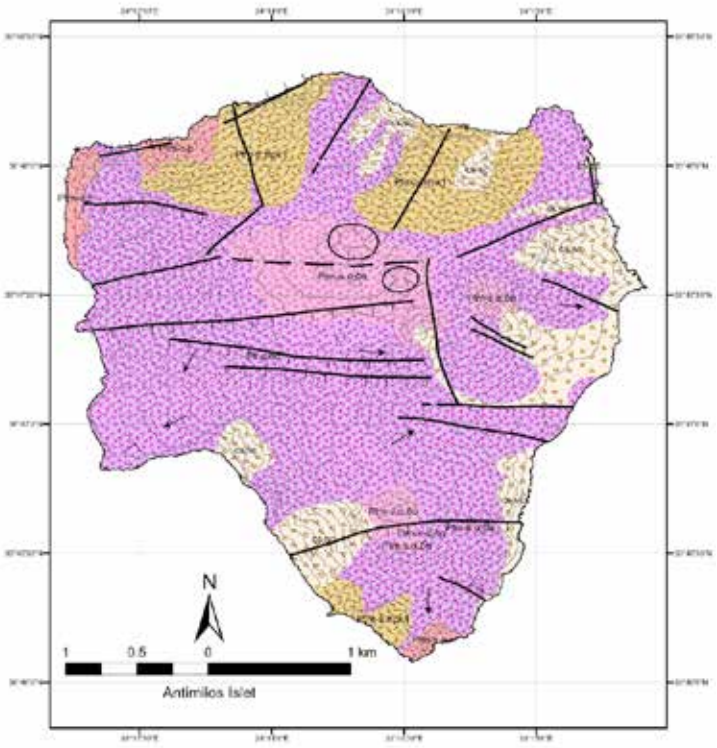

Figure 1. Geological map of Antimilos Islet. **cs,sc**: recent scree, **$Pt_{m\text{-}s}$.p**: pyroclastic-rhyolitic lavas, **$Pt_{m\text{-}s}$.πρκ1**: pyroclastic cones, **$Pt_{m\text{-}s}$.αδα**: mainly andesitic lavas , **Pt_{i}.α.δα**: mainly dacitic lavas.

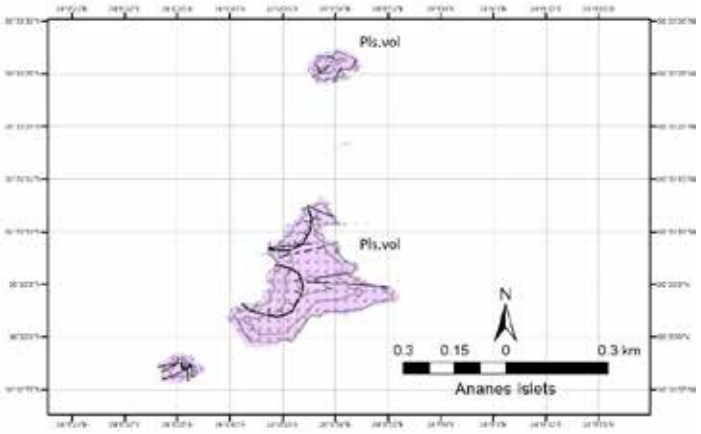

Figure 2. Geological map of Ananes Islet. **Pl_{s}.vol**: highly hydrothermally-altered volcanite.

Falconera, Velopoula and Karavia Islets

Falconera, Velopoula and Karavia Islets occupy the southeastern sector of the Pelagonian sensus lato (s.l.) geotectonic unit. Karavia comprises two islets where the larger one is delimited by faulted surfaces trending NW-SE and NE-SW, resulting in steeper and more vertical cliffs compared to the smaller one, lying southwestwards. It consists of limestone rich in Upper Permian-age fossils (determination by J. Bizon in Tataris 1988).

The main characteristic of the larger islets of Falconera and Velopoula is the outcropping of the ophiolitic unit that could be palaeotectonically related to a back-arc environment, as the ophiolitic and flyschoidal materials that fed the mélange of the Argolis tectonic units (Photiades *et al.,* 2024a). Moreover, the ophiolitic unit can be regarded as representative of a back-arc basin opening during the Middle to Late Jurassic (?), analogous to that of Guevgeli and

Skra ophiolite complexes that occur to the east of the Paikon volcanic arc (Saccani *et al.,* 2008).

Falconera resembles an elongated Z in shape (Fig. 3) and has a steep coastline controlled by NW-SE and NE-SW trending faults. Its name derives from the "Black Hawk" due to the dark color of its surface owing to the lithological composition of gabbro. The ophiolitic complex of Falconera consists of the crustal section of the ophiolitic sequence, lacking the mantle rock remnants, probably due to the sequence's emplacement onto the continental margin, as in the case of the post-flysch Upper Tectonic Unit with serpentinite mélange in Argolis (Photiades *et al.,* 2024a). Therefore, it only includes (from base to top): a) the lower members of the ophiolitic complex that outcrop towards the NW basal part of the islet and they are magmatically characterized by a basic cumulate sequence consisting of stratified-layered gabbro, b) an isotropic massive gabbro, dominated by cumulate intrusive coarse-grained rocks of hornblende-bearing gabbro, c) a sheeted dyke diabase complex system which is interconnected and magmatically overlain by a submarine extrusion lava cover, without any presence of red radiolarian chert. The lava cover comprises horizons of massive vesicular to porphyritic lava flows with acidic volcanic veins, which are successively derived from multiple underlying feeder veins (see geological section in Fig. 3).

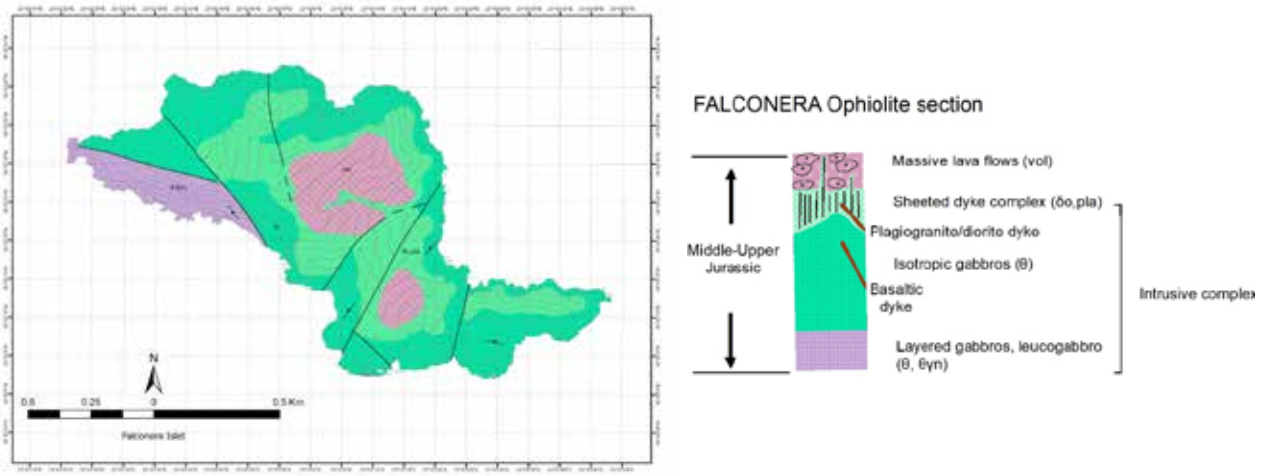

Figure 3. Geological map of Falconera Islet with its respective schematic stratigraphic column.

Velopoula is a 3-km long islet, bearing an elongated NW-SE steep ridge (Fig. 4). The presence of NW-trending faults contributes to the formation of its steep and weathered coasts. Ktenas (1924) mentions the outcropping of tuff, diorite, thick red jasper and Mesozoic carbonate at this islet.

Tectono-stratigraphically, Velopoula constitutes a nappe pile of the ophiolitic unit, thrusted on the Pelagonian continental margin, resulting from the compressional tectonic activity during the paleohellenic (eohellenic) phase as well as the post-flysch phase. The latter successively affected the neighboring Argolis Peninsula, too. Thus, from top to base, it comprises isotropic gabbro and tectonic slices of diabase intruded successively by quartz diorite, sub-ophiolitic mélange, red jasper succession, the carbonate platform and a basal volcano-sedimentary formation of Permo-Triassic age. Lithologically, the ophiolitic unit is homologous to the Falconera rocks. In general, Velopoula has undergone brittle deformation and low-grade, greenschist metamorphic conditions with recrystallizations.

The geological mapping of the above islets extending in the Myrtoan Sea between the Peloponnese and the Cyclades highlighted the following points: 1) The Upper Permian carbonate within the Karavia islets occurs as isolated blocks both in the Adheres-Argolis flyschoidal mélange of the internal Hellenides and in the imbricated Tertiary mélange unit between the Tripolis and Pindos Units in Peloponnese; 2) the Falconera and Velopoula ophiolite units can be regarded as representative as back-arc basin opening during the Middle to Late Jurassic (?), analogous to that of Guevgeli and Skra ophiolite complexes that obducted during late Jurassic-early Cretaceous times the continental margin of the internal Hellenides. Later, they were implicated by the post-Eocene continental collision of the Hellenides, leading to a non-metamorphic upper Cycladic Unit via a Miocene detachment over the Cycladic Blueschist Unit; and 3) Antimilos and Ananes volcanoes erupted during the Late Pliocene-Early Pleistocene, characterizing the Milos Volcanic Field on that subbasement.

The abovementioned geology of the islets at the Myrtoan Sea has been included in the geological sheet of Greece "Myrtoan Sea Islets", in scale 1:25000, edited by the HSGME (Photiades *et al.,* 2024b).

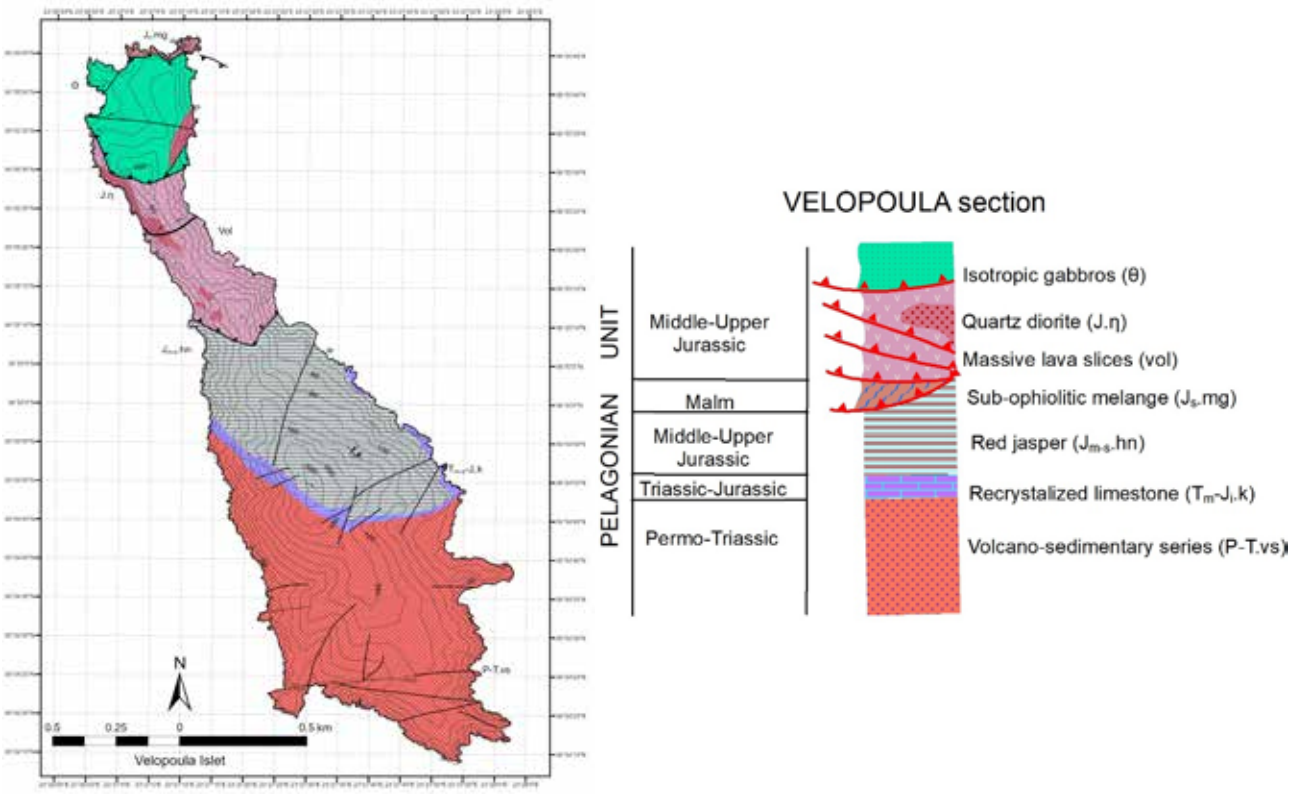

Figure 4. Geological map of Velopoula Islet with its respective schematic stratigraphic column.

Acknowledgements

The current work was carried out in the frame of the project “Islets and rocky islets of the Aegean Sea” (2021-2025), supported by the NFP.

References

Angelier, J., 1979. Recent Quaternary Tectonics in the Hellenic Arc: Examples of geological Observation on Lands. Tectonophysics, 52, 267-275.

Fytikas, M., Innocenti, F., Kolios, N., Manetti, P., Mazzuoli, R., Poli, G., Villari, L.,1986. Volcanology and petrology of volcanic products from the island of Milos and neighbouring islets. Journal of Volcanology and Geothermal Research, 28, 3–4, 297–317.

Grasemann, B., Huet, B., Schneider, D. A., Rice, A. H. N., Lemonnier, N., Tschegg, C., 2018. Miocene post-orogenic extension of the Eocene synorogenic imbricated Hellenic subduction channel: New constraints from Milos (Cyclades, Greece). GSA Bulletin, 130 (1–2), 238–262.

Innocenti, F., Manetti, P., Peccerillo, A., Poli, G., 1981. South Aegean Volcanic Arc: Geochemical Variations and Geotectonic Implications. Bulletin of Volcanology, Vol. 44-3, 377-391.

Ktenas, K., 1924. L’île de Bélopoula entre le Péloponnèse et les Cyclades. Société Géologique de France, séance 28 avril 1924, p.13-14.

Marinos, G.,1961. The Antimilos volcano in Aegean Sea. Bulletin of the Geological Society of Greece IV 1, 38-50.

Photiades, A., Deligiannakis, G., Vakalas, I., Carras, N., 2024a. Geological map of “TROIZINA sheet” in scale 1:50.000. Edited by HSGME, Athens.

Photiades, A., Kampolis, I., Vakalas, I., Deligiannakis, G., 2024b. Geological map of “MYRTOAN SEA ISLETS sheet” in scale 1:25.000. Edited by HSGME, Athens.

Saccani E., Bortolotti, V., Marroni, M., Pandolfi, L., Photiades, A., Principi, G., 2008. The Jurassic association of back-arc basin ophiolites and calk-alcaline volcanics in the Guevgueli complex (Northern Greece: implication for the evolution of the Vardar Zone). Ofioliti, 33, 2, 209-227.

Tataris, A., 1988. The Paleozoic of the Karavia islets, east of Lakonia (Aegean Sea). Bulletin of the Geological Society of Greece, 20, 2, 21-38.

17th INTERNATIONAL CONGRESS of the Geological Society of Greece

BULLETIN OF THE GEOLOGICAL SOCIETY OF GREECE, SP. PUBL.

EXTENDED ABSTRACT 264

Assessment of the exposure of coastal sectors of the Greek Mainland to hazards induced by climate change, using the Coastal Hazard Wheel

Poulos S.E.[1], Alexandrakis[2] G., Karditsa[3] S. Lesioti[1], F. Markozanes[1], Katritsis[1] I., and A. Kampanis[2] N.
(1) Laboratory of Physical Geography, Section of Geography and Climatology, Department of Geology and Geoenvironment, Panepistimioupolis-Zografou 15784, Attiki, Greece.
(2) Coastal & Marine Research Laboratory, Institute of Applied and Computational Mathematics, Foundation for Research and Technology-Hellas, 70013 Heraklion, Crete, Greece
(3) Department of Port Management and Shipping, National and Kapodistrian University of Athens, Psahcna, Evia, Greece

Introduction

Low-lying coasts such as beaches and lagoons are vulnerable to erosion and/or coastal flooding due to sea storms. A tool for the evaluation of the vulnerability of the coasts is the (CHW: Coastal Hazard Wheel), that is a universal coastal management framework (extended landwards to 200 m) for coastal classification, hazard information and adaptation guidance (Rosendahl Appelquist 2012; Appelquist & Halsnæs, 2015).

The coastal classification system is based on the bio geophysical components that are considered most important for the characteristics of a particular generic coastal environment; these are: (1) geological layout, (2) wave exposure, (3) tidal range, (4) flora/fauna, (5) sediment balance and (6) storm climate. Obviously, each generic coastal environment has a specific combination of these variables (Appelquist, 2012).)

The inherent hazard levels are defined as the hazards being an inherent part of the bio-geophysical properties of a coastal environment when exposed to the predicted changes in global climate over the coming decades. The inherent hazards covered by the CHW system are:

(a) ecosystem disruption that describes the possibility of a disruption of the current state of the coastal ecosystems under a changing climate

(b) gradual inundation, which describes the possibility of a gradual submergence of a coastal environment under a changing climate.

(c) salt water intrusion that describes the possibility of salty sea water penetrating into coastal surface waters and groundwater aquifers under a changing climate

(d) erosion and flooding, which describes the possibility of a sudden, abrupt and often dramatic inundation of a coastal environment caused by a short term increase in water level due to storm surge and extreme tides, under a changing climate

The purpose of the present study is to investigate the exposure of beach sectors from 4 different coastal areas of the Greek mainland The Kotychi lagoon, the Alfios River deltaic coast (north Kyparissiakos), the beach/dunes in the central Kyparissiakos coast and central part of the north coast of the Messiniakos Gulf, and four beaches from the coast of Attika (Figure 1).

Figure 1. **Beaches under investigation (a: West and Southwest Peloponnese, b: West Attica Coast)**

Methodology

The application of CHW requires quantification/categorization of the bio-geo-physical components, as it is described below (Mangor, 2004).

The geological layout categories include (i) sedimentary plain; (ii) barrier; (iii) delta/low estuary island; (iv) sloping soft rock coast; (v) flat hard rock coast; (vi) sloping hard rock coast; (vii) coral island; (viii) tidal inlet/sand; and (ix) spit/river mouth (e.g., Davis and Fitzgerald, 2004).

Regarding wave exposure, coasts are classified as: (i) Exposed Coasts when fetches >100 km, (ii) moderately exposed, when fetches are 10–100 km and (iii) protected costs when fetches <10 km, but can also be seen along larger waterbodies with shallow nearshore zones or mild onshore wind climates (Mangor 2004).

The effect of tidal range includes 3 main categories: (i) microtidal <2 m; (ii) meso-tidal 2-4 m; and (iii) macro-tidal >4 m (Masselink and Hughes, 2003).

The flora/fauna component includes nine different categories; (i) intermittent marsh; (ii) intermittent mangrove; (iii) marsh/tidal flat; (iv) mangrove; (v) marsh/mangrove; (vi) vegetated; (vii) not vegetated; (viii) coral and (ix) any. Moreover, the vegetated category is applied when more than 25 % of the sloping soft rock coast is covered with vegetation while the not vegetated category is used when less than 25 % is vegetated (Appelquist & Halsnæs, 2015).

The sediment balance includes the two main categories: (i) balance/deficit; and (ii) surplus for the low-lying ssoft coasts and other two special categories (i) no beach and (ii) beach that applies to the hard rock coastlines (Haslett, 2009).

Storm climate differentiates between locations (i) with and (ii) without tropical cyclone activity, irrespective of their frequency. In areas identified as being under tropical cyclone influence (i.e., 5°–15°N and 5°–15°S), the classification system assigns a “yes” to tropical cyclone activity, while it assigns a “no” to locations outside these regions. (Appelquist, 2012).

The CHW hazard levels are divided into four categories ranging from 1 (low hazard) to 4 (high hazard). (Rosendahl Appelquist & Halsnæs, 2015). Each generic coastal environment is assigned a specific inherent hazard level for each hazard type. In the CHW, this information is presented using a combined number and color code, providing users with a clear and comprehensive overview of the hazard profile for a given coastal environment (Figure 2).

Results and Discussion

The results refer to: (1) The coastal zone of Kotyki, which extends in front of the homonymous lagoon, (2) The deltaic coastline of the Alphios River, (3) The coastal zones of the Central Kyparissia Gulf and the central part of the Messinian Gulf coastline, which include dunes and develop in front of a coastal lowland plain and (4) Four pocket beaches along the coast of the Athinaiki Riviera.

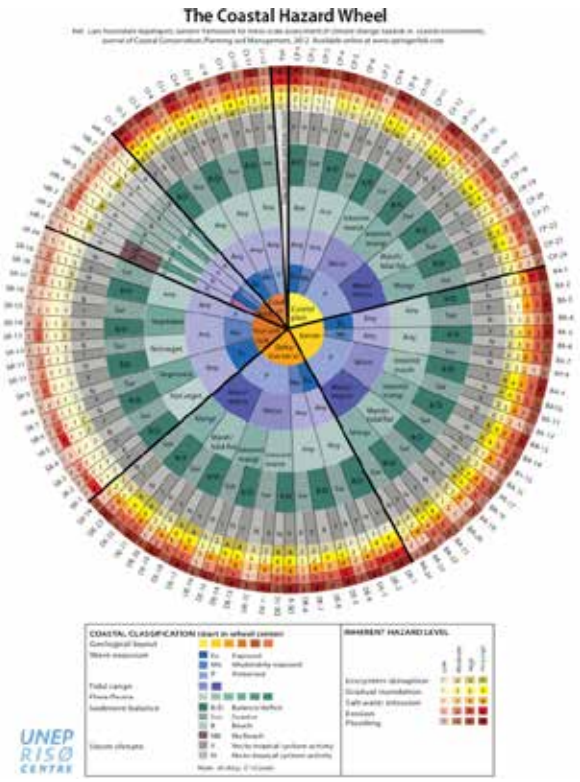

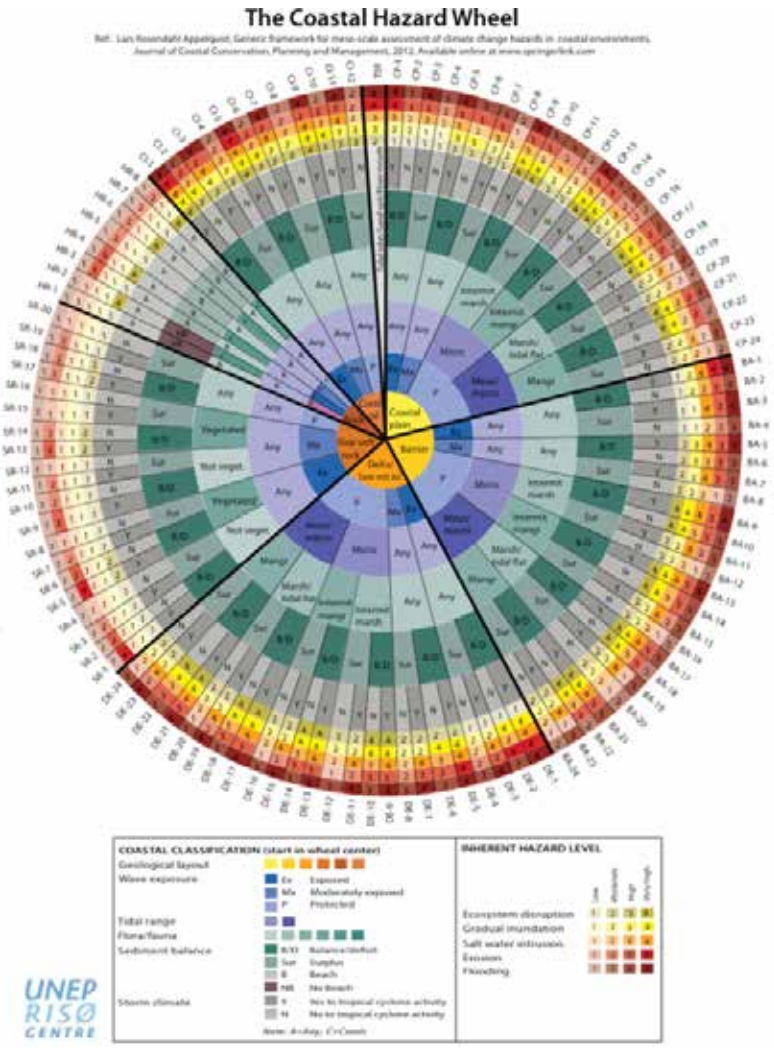

Figure 2. Coastal classification Wheel (abstracted from Rosendahl Appelquist & Halsnæs, 2015.

.

A. Kotychi Laggoon

Geological layout	Beach barrier	BA-5 (2-3-4-3-4)
Wave exposure	Moderate	Ecosystem disruption = Moderate (2)
Tidal range	Micro-tidal	Gradual inudation= High (3)
Flora/fauna	Swampy /not continous	Salt water intrusion= Very High (4)
Sediment balance	Deficit, beach presence	Erosion = High (3)
Storm (tropical) climate	No	Flooding= Very high (4)

B Alfios Delta

Geological layout	Delta	DE-2 (1-4-3-4-3)
Wave exposure	High	Ecosystem disruption = Small (1)
Tidal range	Micro-tidal	Gradual inudation= Very High (4)
Flora/fauna	Any	Salt water intrusion = High (3)
Sediment balance	Deficit, beach presence	Διαβρωση = Very High (4)
Storm (tropical) climate	No	Flooding= High (3)

C Central Kyparissiakos and Central Messiniakos Beaches (with dunes)

Geological layout	Coastal plain	CP-2 (1-2-2-3-3)
Wave exposure	High	Ecosystem disruption = Small (1)
Tidal range	Micro-tidal	Gradual inudation = Moderate (2)
Flora/fauna	Any	Salt water intrusion = Moderate (2)
Sediment balance	Balance	Erosion = High (3)
Storm (tropical) climate	No	Flooding= High (3)

D. Athinaiki Riviera

D.1. Kavouri and Anavyssos beaches

Geological layout	Coastal plain	CP-6 (2-3-2-3-3)
Wave exposure	Moderate	Ecosystem disruption = Moderate (2)
Tidal range	Micro-tidal	Gradual inudation = High (3)
Flora/fauna	Any	Salt water intrusion = Moderate (2)
Sediment balance	Balance	Erosion = High (3)
Storm (tropical) climate	No	Flooding= High (3)

D.2. Vouliagmeni and Varkiza beaches

Geological layout	Coastal plain	CP-2 (1-2-2-3-3)
Wave exposure	High	Ecosystem disruption = Small (1)
Tidal range	Micro-tidal	Gradual inudation = Moderate (2)
Flora/fauna	Any	Salt water intrusion = Moderate (2)
Sediment balance	Balance	Erosion = High (3)
Storm (tropical) climate	No	Flooding= High (3)

Discussion and Conclusions

According to the results on biodiversity threat, the threat is low (category 1) for groups B and C, and moderate (category 2) for groups A and D1. In the micro-tidal environment of Greece, the gradual inundation is moderate (category 2) for group C (dune beaches) and D2 (pocket beaches not exposed to high waves), high (category 3) for group B (deltaic coast) and D2 (pocket beaches exposed to high waves), and very high (category 4) for group A (coastal barrier in front of a lagoon). Regarding saltwater intrusion, it was assessed as moderate (category 3) for groups B, C, and D, and high for group A. The risk of erosion is high (category 3) in groups A, C, and D, and very high (category 4) in group B. Finally, the risk of coastal (marine) flooding is high (category 3) in groups B, C, and D, and very high (category 4) in group A. Therefore, the main factors controlling the variability of exposure to coastal hazards appear to be primarily related to the geological layout and exposure to wave activity, followed by sediment balance and the type of flora and fauna.

Acknowledgements

The authors S. Poulos, A. Karditsa, S. Lesioti, F. Markozanes acknowledge the project ATHINAIKI RIVIERA (P4-0325990) entitled: “Study for the development of smart infrastructure along the coastal front of Southwest Attica, with emphasis on the promotion of the natural and cultural reserve for the enhancement of tourist services”, Attica Regional Programme (2014-2020).

References

Appelquist, L. R. (2013). Generic framework for meso-scale assessment of climate change hazards in coastal environments. Journal of Coastal Conservation, 59-74.

Davis RA Jr, Fitzgerald DM (2004) Beaches and coasts. Blackwell Publishing

Haslett SK (2009) Coastal systems. Routledge Rosendahl

Mangor, K. (2004). Shoreline Management Guidelines.” DHI Water and Environment, 294p

Rosendahl Appelquist, L., & Halsnæs, K. (2015). The Coastal Hazard Wheel system for coastal multi-hazard assessment & management in a changing climate. Journal of coastal conservation, 19, 157-179.

17th INTERNATIONAL CONGRESS of the Geological Society of Greece

BULLETIN OF THE GEOLOGICAL SOCIETY OF GREECE, SP. PUBL.

EXTENDED ABSTRACT 265

Hydrogeological and hydrochemical investigations of Selinous basin region

Pyrgakis D. [1], Stavropoulou V.[1], Kaskani E.[1], Papailiopoulou M.[1], Pouliaris C. [1], Lampropoulou D.[2], Zagana E.[1], Chalikakis K.[3], Kazakis N.[1]

(1) University of Patras, Department of Geology, Laboratory of Hydrogeology, Patra, Greece, dpyrgakis@upatras.gr, vstavropoulou@ac.upatras.gr , up1074001@upatras.gr, m.papailiopoulou@ac.upatras.gr, christospouliaris@gmail.com, zagana@upatras.gr, kazakis@upatras.gr ,

(2) Aristotle University of Thessaloniki, Department of Chemistry, Environmental Pollution Control Laboratory, Thessaloniki, Greece, dlambro@chem.auth.gr

(3) UMR 1114 EMMAH (AU-INRAE), Avignon Université, 84029 Avignon, France; konstantinos.chalikakis@univavignon.fr

Introduction

Rock weathering constitute a major factor controlling the hydrochemical evolution of river basins (Wang et al., 2022; Zhou et al., 2021; M. Zhu et al., 2021). Carbonate weathering is typically the main source of ions, followed by silicate weathering (Wang et al., 2020; Zhou et al., 2021). Land use and land cover changes in the river basin can have a direct influence on the hydrological realm and water quality (Lima et al., 2014; Raj and Azeez, 2010; Wang et al., 2022). Deforestation and agricultural expansion can lead to changes in the water balance, water availability, and water quality (Lima et al., 2014; Wang et al., 2022). Conversely, afforestation can increase the buffering capacity and pH of streams (Burgess-Conforti et al., 2022).

River basins are dynamic systems shaped by diverse factors, including geology, land use, and human activities, all of which can significantly influence the hydrochemical properties of both surface water and groundwater. In karst regions, characterized by soluble rock formations such as limestone and dolomite, the interaction between surface water and groundwater is particularly intricate. This complexity arises from the unique hydrological pathways and chemical processes inherent to these environments, where water movement and composition are heavily influenced by the dissolution of the surrounding rock (Xiao et al., 2021). Kazakis et al. (2018) point out that a holistic approach combining hydrodynamic analysis, vulnerability assessment, and integrated management strategies is essential for the sustainable exploration, protection, and management of Greece's karst aquifers, ensuring their long-term viability as critical water resources.

Karst aquifers are renowned for their heterogeneity and rapid flow dynamics, which contribute to significant variations in water quality and chemical composition. Research indicates that the dominant hydrochemical type of karst groundwater typically features bicarbonate and sulfate ions, reflecting the dissolution of carbonate minerals and the impact of surrounding geological formations (Yu et al., 2023; H. Zhu et al., 2021). The hydrochemical facies of karst groundwater are influenced by factors such as recharge mechanisms, land use practices, and pollution sources. These complexities underscore the need for comprehensive hydrochemical analyses to better understand the interactions within these aquifer systems (Kshetrimayum, 2015). Karst aquifers are highly vulnerable to contamination due to their unique hydrological characteristics, such as well-developed conduit systems, which allow rapid pollutant transport with minimal natural filtration (Kazakis et al., 2015).

In summary, hydrochemical investigations in river basins and karst groundwater systems are important for evaluating water quality, understanding hydrological processes, and managing water resources effectively. The integration of hydrochemical analyses of main and trace elements provides a comprehensive framework for unraveling the complexities of these aquatic systems (Pacheco Castro et al., 2018).

Study area

The study area is located in northwest Peloponnese in western Greece. The NW Peloponnese region has been the focus of numerous geological and tectonic studies, shedding light on the area's rock formations and their evolution (Doutsos & Poulimenos, 1992; Poulimenos et al., 1993; Flotte et al., 2005; Ghisetti & Vezzani, 2005; Trikolas, 2008; Backert et al., 2010; Ford et al., 2016). Geologically, the rocks in this region are classified as part of the External Hellenides (Koukouvelas, 2019, and references therein), specifically including formations from the Pindos and Tripolis Units.

From a paleogeographic perspective, the sequences of the Pindos and Tripolis Units were deposited along the eastern passive margin of the Apulian microplate. This margin was bounded to the east by the Pindos Ocean. The External Hellenides were formed during the Tertiary period as a result of the closure of the Pindos Ocean and the subsequent continental collision between the Apulian and Pelagonian microplates during the Alpine orogeny. A significant portion of the broader study area is now covered by post-Alpine Neogene and Quaternary formations, including modern alluvial deposits linked to the opening of the Corinth Rift.

The Pindos Unit occupies the largest part of the study area and comprises Mesozoic deep-sea carbonate and siliceous sedimentary rocks with a total thickness of approximately 1200 meters. These rocks are overlain by a clastic flysch sequence of Paleocene–Oligocene age (Degnan & Robertson, 1998). Structurally, the Pindos Unit is composed of distinct formations arranged from lower to higher levels. At the base lies the Triassic Clastic Formation, characterized by alternating sandstones, clays, and argillaceous layers interbedded with tuffs, granites, and gabbros, reaching a total thickness of about 100 meters. Above this, the Drymos Limestone Formation consists of hemipelagic limestones interbedded with cherts and clays, with a maximum thickness of 300 meters. This is followed by the Radiolarite Formation, a sequence of glassy cherts, clayey horizons, and pink limestones dated to the Jurassic–Lower Cretaceous, with a maximum thickness of 350 meters.

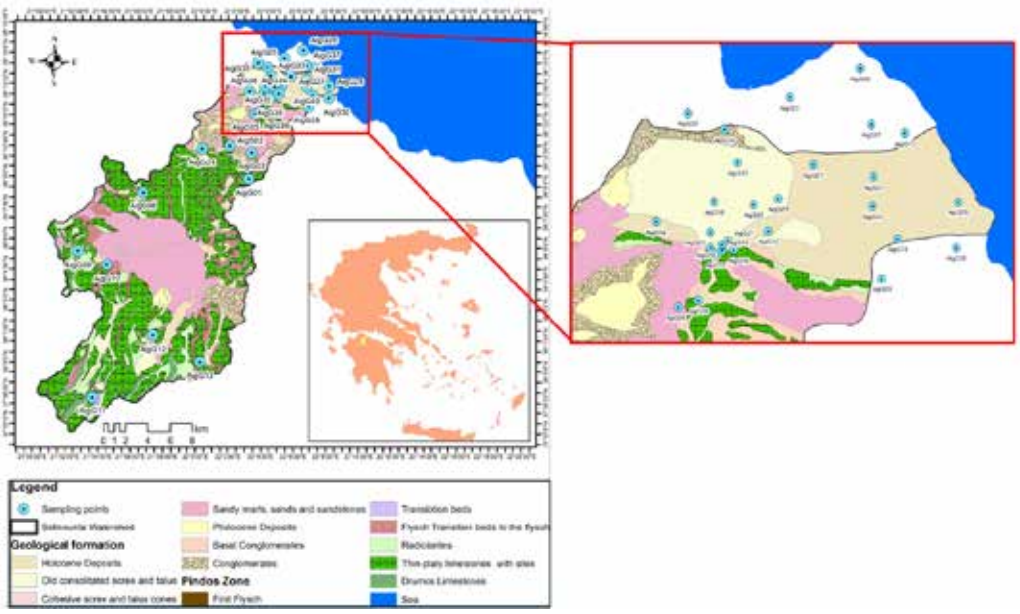

Figure 1: Geological map of the study area (modified by IGME geological maps)

The sequence continues with the Clastic Horizon, also known as the First Flysch, consisting of alternating sandstones and clays from the Lower Cretaceous, approximately 50 meters thick. Above this horizon lie the Upper Cretaceous Thin-Plated Limestones, containing cherts and reaching a thickness of 400 meters. Finally, the unit transitions into flysch deposits, including Transitional Flysch Layers and the Pindos Flysch Formation, composed of alternating sandstones, clays, and argillaceous layers of Paleocene–Oligocene age.

The Tripolis Unit, which underlies the Pindos Unit, has limited surface exposure within the broader study area. Its stratigraphy begins with a volcanic-sedimentary sequence of variable thickness, up to 400 meters, of Middle Triassic age, referred to as the “Tyros Beds.” Overlying this sequence is a thick carbonate succession, ranging from 3000 to 3500 meters, dating from the Triassic to the Eocene. This carbonate sequence is followed by a flysch sequence of Oligocene–Miocene age, which can be up to 1800 meters thick (Fleury, 1980; Jacobshagen, 1986). The Tripolis Unit includes dolomites and dolomitized limestones of Middle Triassic–Lower Jurassic age, neritic limestones with occasional dolomitic intercalations from the Upper Jurassic–Upper Cretaceous, and massive limestones rich in foraminifera of Paleocene–Middle Eocene age. These formations are capped by the flysch deposits of Oligocene–Lower Miocene age.

Hydrogeology

The flow of groundwater in porous media is influenced by the presence of faults (Knipe, 1997), which create boundaries with convergent and divergent flows, forming zones of drainage and recharge, respectively. Additionally, the depth of groundwater is a critical parameter for its protection. Greater depth offers a higher degree of protection from surface-originating pollutants, as contaminants must travel a longer distance to reach the saturated zone.

In the study area, groundwater level measurements were conducted to determine the direction of groundwater flow. Results indicate that groundwater flows in a southwest-northeast direction, from the mountainous region toward the coastal area. The highest hydraulic heads (64.87 m) are observed in the karstic aquifer, while the lowest are found in the coastal granular aquifer. Notably, no negative hydraulic heads were recorded in the study area.

Methodology

In this study, 40 water samples were collected from distinct sites, which included 7 springs, 2 surface water and 31 boreholes. From each sampling site, three separate water samples were collected and stored in thoroughly cleaned polyethylene bottles that had been acid-washed and rinsed. The first sample, with a volume of 1 liter, was designated for the analysis of anions, including (NO_3^-, NO_2^-, SO_4^{2-}, Cl^-, and F^-) and cations (Ca^{2+}, K^+, Mg^{2+}, and Na^+). The second sample, measuring 0.1 liters, was filtered using a Whatman 0.45 μm cellulose membrane and treated with 0.5 mL of ultrapure HNO_3 to analyze trace elements concentrations. Chemical calculations, such as the determination of saturation indices, were performed using PHREEQC version 3.0 (Appelo and Postma, 2004). The accuracy of the major element analyses was checked by using charge mass balance, and analyses were considered as acceptable when charge mass balance was less than 5%.

Results and Discussions

In Table 1 are presented the descriptive statistical parameters of the physicochemical characteristics, major elements, and trace elements for the 40 samples collected in the study area. Additionally, hydrochemical diagrams such as Piper and Durov were constructed for all samples collected during the investigation.

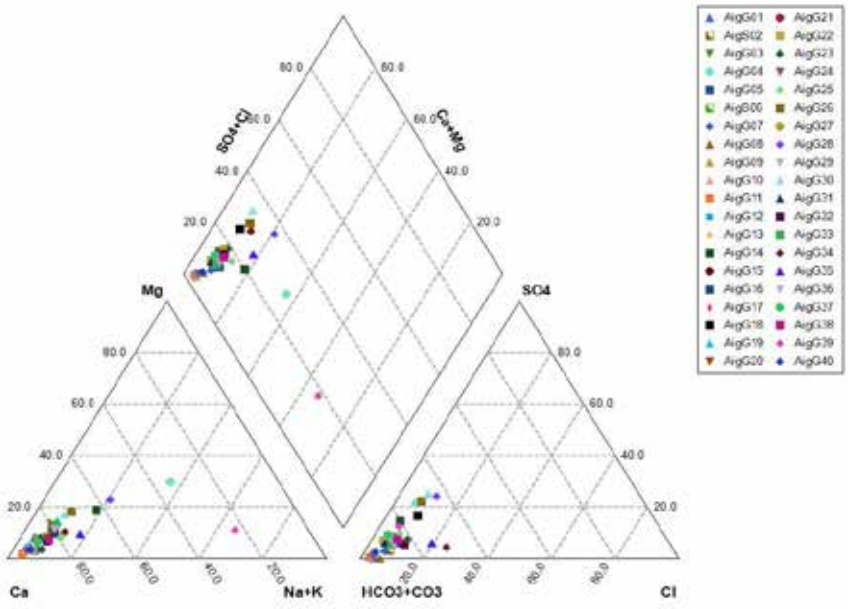

Figure 2. Piper diagram of samples in the study area

Piper diagram facilitates the identification of geochemical processes within a group of groundwater samples. The data from Selinountas river basin are shown in Figure 2. The results of ion exchange are particularly evident; when cation exchange occurs, the data points are projected parallel to the outer side of the diamond-shaped diagram. In contrast, when other reactions occur, the points deviate from the outer side. The dissolution of calcium carbonate is reflected in the movement of data points toward the calcium (Ca^{2+}) and bicarbonate (HCO_3^-) corners. The reduction of sulfate (SO_4^{2-}) shifts the points parallel to the anion axis, while the precipitation of calcium carbonate ($CaCO_3$) directs the points toward the sodium (Na^+), sulfate (SO_4^{2-}), and chloride (Cl^-) corners. The hydrochemical type Ca-HCO_3 represents the majority of the samples, and their chemical composition indicates rapid and shallow interactions with the geological formations of the area. Most waters in this category, primarily natural springs, exhibit low temperatures (Tw <20°C), although several boreholes show higher temperatures (Tw >20°C). Ca^{2+} concentrations range from 34.0 mg/L to 152.0 mg/L, with an average of 84.3 mg/L. Chloride (Cl^-) concentrations vary between 3.5 mg/L and 54.0 mg/L, with an average of 14.5 mg/L, which is typical for the study area.

The Mg^{2+}/Ca^{2+} ratio provides insights into the origin of water, the dissolution of subsurface minerals, and the geochemical processes that have occurred. In the study area, this ratio ranges from 0.017 to 0.86, with an average value of 0.14. All samples are associated with limestone and dolomitic aquifers. Specifically, the borehole samples AigG15 and AigG16 exhibit Mg^{2+}/Ca^{2+} values of 0.17 and 0.12, respectively. In regions dominated by limestone or dolomitic rocks, the Ca^{2+}/Cl^- ratio is typically high, as limestone contributes significant amounts of calcium to the water. Typical values may range from 0.5 to 10 or more, depending on the chloride concentration. In the study area, the samples show Ca^{2+}/Cl^- ratios ranging from 3.31 to 37.64, indicating calcium dominance resulting from the dissolution of carbonate rocks.

Table 1. Statistical parameters of chemical composition.

	Min	Max	Average	Std. Division
pH	7,37	8,05	7,76	0,16
T(°C)	14,20	27,80	20,75	2,89
ORP	-9,30	170,00	120,10	34,05
E.C (T°C)	213,00	1080,00	460,80	217,73
E.C (25°C)	239,00	1109,00	496,10	220,24
Ca^{2+}	34,00	152,00	84,34	28,71
Mg^{2+}	0,73	32,68	6,75	6,99
Na^{+}	2,60	110,00	14,40	20,16
K^{+}	0,30	5,00	1,47	1,04
HCO_3^{-}	134,20	446,52	269,28	87,67
SO_4^{2-}	0,00	132,00	24,15	32,26
F^{-}	0,00	1,51	0,16	0,28
Cl^{-}	3,50	54,00	14,52	12,02
NO_3^{-}	0,70	49,50	9,54	9,35
NO_2^{-}	0,00	0,04	0,01	0,01
NH_4^{+}	0,00	0,55	0,06	0,13
PO_4^{3-}	0,03	4,30	0,26	0,73
Li (μg/L)	0,54	43,55	4,69	7,99
B (μg/L)	0,00	327,57	15,01	65,70
Cr (μg/L)	0,00	3,5	1,2	0,7
Mn (μg/L)	0,29	599,82	20,33	94,13
Fe (μg/L)	9,60	720,51	46,71	110,61
Zn (μg/L)	0,00	217,66	21,32	38,47
Co (μg/L)	0,04	0,53	0,18	0,10
Cu (μg/L)	0,19	7,09	1,64	1,41
Sr (μg/L)	113,84	2261,52	434,01	398,41
Ba (μg/L)	9,59	114,46	61,30	21,63
U (μg/L)	0,03	0,85	0,22	0,14

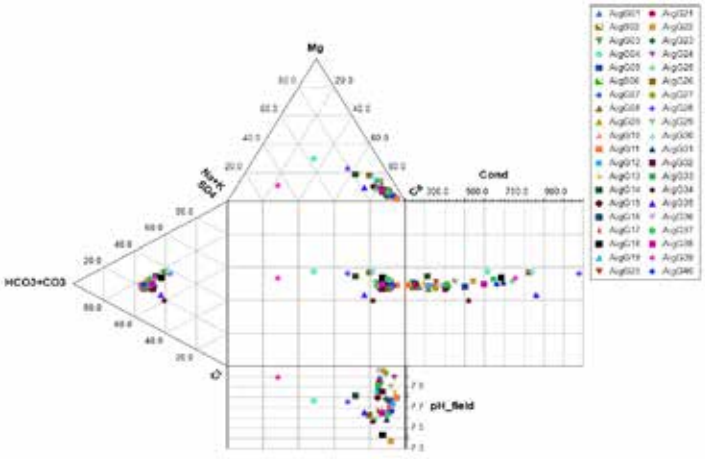

Figure 3. Durov diagram of samples in the study area.

The lithium (Li) concentrations of samples range from 0.5 to 43.5 μg/L, with an average value of 4.7 μg/L. The highest concentrations were recorded in boreholes AigG04 (43.5 μg/L), AigG28 (30.7 μg/L), and AigG39 (13.9 μg/L), while the remaining samples showed values between 0.5 μg/L and 5.9 μg/L. Boreholes Coca Cola AigG15 and AigG16 reported lithium concentrations of 3.8 μg/L and 4.1 μg/L, respectively. Chromium (Cr) concentrations range from 0.0 μg/L to 3.5 μg/L, which are below the drinking water limit (25.0 μg/L). Arsenic (As) concentrations were below the drinking water limit in all groundwater samples from the study area. Strontium (Sr) is found in natural waters at concentrations that depend on the geology of the area, with typical values reaching up to 2000 μg/L. In the analyzed samples, strontium concentrations range from 113.8 μg/L to 2261.5 μg/L, with the highest value recorded in sample AigG04. The average concentration is 434.0 μg/L. Generally, higher strontium concentrations are observed in waters that flow through limestone or dolomitic rocks, as well as in areas with geology rich in celestite ($SrSO_4$) or strontianite ($SrCO_3$) (Banner, 1995).

Iron (Fe) can be released to groundwater under specific conditions from minerals such as amphiboles, pyroxenes, ferromagnesian micas, iron sulfides, sandstones with oxides, carbonates, and clay minerals. The concentrations of Fe range from 9.6 μg/L to 720.5 μg/L, while the highest concentration occurs in sample AigG26 which was the only sample with concentration above drinking limit. Manganese (Mn) typically occurs alongside iron, enriching groundwater in acidic environments. Its sources include soils, sediments, and metamorphic rocks rich in micas and amphiboles. The drinking water limit for manganese is 50 μg/L, and samples from boreholes AigG26 and AigG29 exceed this limit.

Conclusion

In conclusion, the hydrochemical analysis of 40 water samples from the study area has provided significant insights into the quality and characteristics of the region's groundwater resources. The Ca-HCO□ hydrochemical type dominates in the water samples. The hydrochemical pattern of the samples suggests quick and shallow interactions with the region's geological formations. The parameters with concentration above the drinking limit are two (Fe and Mn), however the excess is limited only to two samples (AigG26 and AigG29).

Such concentrations might pose potential risks to human health. These results underscore the critical role of hydrogeological variability which shapes groundwater hydrochemical regime in river basins.

Acknowledgement

This paper is a part of Pyrgakis' PhD.

References

Appelo, C.A.J., Postma, D., 2004. Geochemistry, Groundwater and Pollution, 2nd ed. CRC Press, London. https://doi.org/10.1201/9781439833544

Banner, Jay.L., 1995. Application of the trace element and isotope geochemistry of strontium to studies of carbonate diagenesis. Sedimentology 42, 805–824. https://doi.org/10.1111/j.1365-3091.1995.tb00410.x

Burgess-Conforti, J.R., Moore Jr, P.A., Owens, P.R., Miller, D.M., Ashworth, A.J., Hays, P.D., Evans-White, M.A., Anderson, K.R., 2022. Relationships between land use and stream chemistry in the Mulberry River basin, Arkansas. River Research and Applications 38, 1031–1040. https://doi.org/10.1002/rra.3970

Degnan, P. J., Roberston, A.H.F. 1998. Mesozoic- Early Tertiary passive margin evolution of the Pindos Ocean (NW Peloponnese, Greece). Sedimentary Geology, 117, 33–70.

Dercourt, J. 1964. Contribution à l'étude géologique d'un secteur du Peloponnèse septentrional. Annales Géologiques des Pays Helléniques, 15, 1–418.

Doutsos, T., Poulimenos, G. 1992. Geometry and Kinematics of active faults and their seismotectonic significance in the Western Corinth-Patras rift (Greece). J. Struct. Geol., 14(6), 689-699.

Fleury, J. 1980. Les zones de Gavrovo-Tripolitza et du Pinde-Olonos (Grèce continentale et Péloponnèse du Nord). Evolution d'une plateforme et d'un bassin dans leur cadre alpin. (p. 651). France: Annales de la Société Géologique du Nord, 4.

Flotté, N. 2003. Caracterisation structurale et cinematique d'un rift sur detachement: Le rift de Corinthe-Patras, Grece. Thesis 197 pp., Universite de Paris-Sud.

Flotté, N., Sorel, D., Müller, C., Tensi, J. 2005. Along strike changes in the structural evolution over a brittle detachment fault: example of the Pleistocene Corinth–Patras rift (Greece). Tectonophysics, 403, 77–94, http://doi.org/10.1016/j.tecto.2005.03.015

Ford, M., Hemelsdael, R., Mancini, M., Palyvos, N. 2016. Rift migration and lateral propagation: evolution of normal faults and sediment-routing systems of the western Corinth rift (Greece). In: The Geometry of Normal Faults (Ed. by C. Childs, R.E. Holdsworth, C.A-L. Jackson, T. Manzocchi, J.J. Walsh, G. Yielding), Geol. Soc. London, Spec. Publ., 439.

Freeze, A., Cherry, J.A (1979). Groundwater. Prentice Hall, Englewood Cliffs.

Gawthorpe, R. L., Leeder, M. R., Kranis, H., Skourtsos, E., Andrews, J. E., Henstra, G. A., Mack, G, Muravchik, M., Turner, J., Stamatakis, M. 2018. Tectono-sedimentary evolution of the Plio-Pleistocene Corinth rift, Greece. Basin Research, 30, 448-479.

Ghisetti, F., Vezzani, L. 2005. Inherited structural controls on normal fault architecture in the Gulf of Corinth (Greece). Tectonics, 24, TC4016 doi: 10.1029/2004TC001696.

Jacobshagen, V. 1986. Geologie von Griechenland (p. 363). Berlin: Gebruder Borntraeger.

Kazakis, N., Oikonomidis, D. & Voudouris, K.S. (2015) Groundwater vulnerability and pollution risk assessment with disparate models in karstic, porous, and fissured rock aquifers using remote sensing techniques and GIS in Anthemountas basin, Greece. Environ Earth Sci 74, 6199–6209. https://doi.org/10.1007/s12665-015-4641-y

Kazakis, N., Chalikakis, K., Mazzilli, N., Ollivier, C., Manakos, A., & Voudouris, K. (2018). Management and research strategies of karst aquifers in Greece: Literature overview and exemplification based on hydrodynamic modelling and vulnerability assessment of a strategic karst aquifer. Science of the Total Environment, 643, 592-609.

Knipe, R.J., (1997) Juxtaposition and seal diagrams to help analyze fault seals in hydrocarbon reservoirs. American Association of Petroleum Geologists Bulletin 87, 185-197.

Kshetrimayum, K.S., 2015. Hydrochemical evaluation of shallow groundwater aquifers: a case study from a semiarid Himalayan foothill river basin, northwest India. Environ Earth Sci 74, 7187–7200. https://doi.org/10.1007/s12665-015-4697-8

Lima, Letícia S., Coe, M.T., Soares Filho, B.S., Cuadra, S.V., Dias, L.C.P., Costa, M.H., Lima, Leandro S., Rodrigues, H.O., 2014. Feedbacks between deforestation, climate, and hydrology in the Southwestern Amazon: implications for the provision of ecosystem services. Landscape Ecol 29, 261–274. https://doi.org/10.1007/s10980-013-9962-1

Pacheco Castro, R., Pacheco Ávila, J., Ye, M., Cabrera Sansores, A., 2018. Groundwater Quality: Analysis of Its Temporal and Spatial Variability in a Karst Aquifer. Groundwater 56, 62–72. https://doi.org/10.1111/gwat.12546

Poulimenos, G., Zelilidis, A., Kontopoulos, N., Doutsos, T. 1993. Geometry of trapezoidal fan deltas and their relationship to extensional faulting along the south-western active margins of the Corinth rift. Basin Res., 5, 179–192.

Raj, P.P.N., Azeez, P.A., 2010. Land Use and Land Cover Changes in a Tropical River Basin: A Case from Bharathapuzha River Basin, Southern India. Journal of Geographic Information System 02, 185. https://doi.org/10.4236/jgis.2010.24026

Wang, Q., Dong, S., Wang, H., Yang, J., Huang, H., Dong, X., Yu, B., 2020. Hydrogeochemical processes and groundwater quality assessment for different aquifers in the Caojiatan coal mine of Ordos Basin, northwestern China. Environ Earth Sci 79, 199. https://doi.org/10.1007/s12665-020-08942-3

Wang, Wanrui, Chen, Y., Wang, Weihua, Yang, Y., Hou, Y., Zhang, S., Zhu, Z., 2022. Assessing the Influences of Land Use Change on Groundwater Hydrochemistry in an Oasis-Desert Region of Central Asia. Water 14, 651. https://doi.org/10.3390/w14040651

Xiao, S., Zeng, C., Lan, J., Di, Y., He, J., Xiao, H., Wang, J., 2021. Hydrochemical Characteristics and Controlling Factors of Typical Dolomite Karst Basin in Humid Subtropical Zone. Geofluids 2021, 8816097. https://doi.org/10.1155/2021/8816097

Yu, D., Yu, J., Wu, D., Han, Y., Sun, B., Zheng, L., Chen, H., Liu, R., 2023. Isotopic and Hydrochemical Characteristics of the Changqing-Xiaolipu Water Resource, Jinan, Eastern China: Implications for Water Resources in the Yellow River Basin. Sustainability 15, 2439. https://doi.org/10.3390/su15032439

Zhou, B., Wang, H., Zhang, Q., 2021. Assessment of the Evolution of Groundwater Chemistry and Its Controlling Factors in the Huangshui River Basin of Northwestern China, Using Hydrochemistry and Multivariate Statistical Techniques. IJERPH 18, 7551. https://doi.org/10.3390/ijerph18147551

Zhu, H., Zhou, J., Liu, Z., Yang, L., Liu, Y., 2021. Hydrogeochemistry Evidence for Impacts of Chemical Acidic Wastewater on Karst Aquifer in Dawu Water Source Area, Northern China. International Journal of Environmental Research and Public Health 18, 8478. https://doi.org/10.3390/ijerph18168478

Zhu, M., Kuang, X., Feng, Y., Hao, Y., He, Q., Zhou, H., Chen, J., Zou, Y., Zheng, C., 2021. Hydrochemistry of the Lhasa River, Tibetan Plateau: Spatiotemporal Variations of Major Ions Compositions and Controlling Factors Using Multivariate Statistical Approaches. Water 13, 3660. https://doi.org/10.3390/w13243660

17th INTERNATIONAL CONGRESS of the Geological Society of Greece

BULLETIN OF THE GEOLOGICAL SOCIETY OF GREECE, SP. PUBL.

EXTENDED ABSTRACT 266

Assessment of natural and anthropogenic contamination of the sediments in the Sacca di Goro lagoon (Po river delta, northern Italy)

Rapti D.[1,2]

(1) University of Ferrara, Department of Chemical, Pharmaceutical and Agricultural Sciences, cpr@unife.it (2) New Energies And environment, spinoff company of Ferrara University, Ferrara, Italy

Abstract

The definition of heavy metal content in lagoon sediments plays a critical role in distinguishing between natural contamination (geohazard) and anthropogenic impact, and is essential for assessing the risk posed by these pollutants in the aquatic environment.

In particular, the Sacca di Goro lagoon, located in the Po River delta (Northern Italy), represents a significant area of interest due to its natural and economic value. Spanning an area of approximately 20 km², with an average depth of 1.5 meters and salinity levels of 29‰, the lagoon is not only crucial for its biodiversity but also plays a pivotal role in regional aquaculture, particularly for mussels and clams (Figure 1).

In this unique lagoon system, understanding the quality of the sea-bottom sediments is fundamental not only for the health and growth of cultivated species but also in addressing potential bioaccumulation problems of heavy metals that may impact both wildlife and human health. By evaluating the qualitative status of the sediments, we can develop effective strategies for sustainable environmental management and safeguard productive aquaculture activities while minimizing risks to the ecosystem.

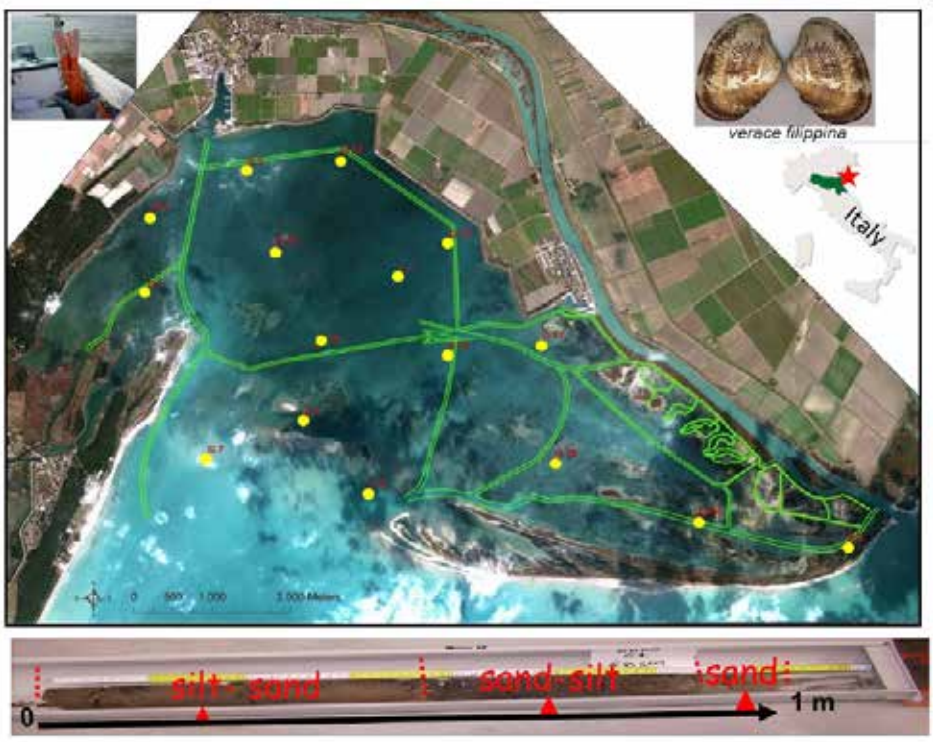

Figure 1: Location of the Sacca di Goro lagoon. The yellow circles represent the sampling points. Below, an example of a continuous core drilling. The green lines represent the sub-lagoon channels.

In the present study, fifteen continuous core drilling surveys were conducted, with depths ranging from 100 to 200 cm, distributed evenly across the lagoon area. A total of 70 sediment samples were collected and analyzed for grain size composition, organic matter content, and concentrations of various elements such as SiO_2, TiO_2, Al_2O_3, Fe_2O3, MgO, MnO, CaO, Na_2O, K_2O, P_2O_5, Ba, Ce, Co, Cr, La, Nb, Ni, Pb, Rb, Sr, Th, V, Y, Zn, Cu, Ga, Nd, S, and Sr. Furthermore, in selected samples, sediment toxicity was evaluated using the bacterial bioluminescence toxicity assay, which provides insight into the potential biological impact of the sediments.

The comprehensive dataset obtained from these analyses enabled us to achieve several important goals: i) defining the overall environmental quality of the sediments, ii) identifying areas with the highest contamination risks, iii) establishing a relationship between grain size distribution and chemical concentrations (Figure 2), and iv) emphasizing the local occurrence of natural pollution phenomena linked to metals such as chromium (> 50 ppm) and nickel (> 30 ppm), as well as human-induced contamination from lead (> 30 ppm) and copper (> 60 ppm).. Additionally, the toxicity results from the bioluminescence assay further clarified the potential harmful effects of these sediments on marine life.

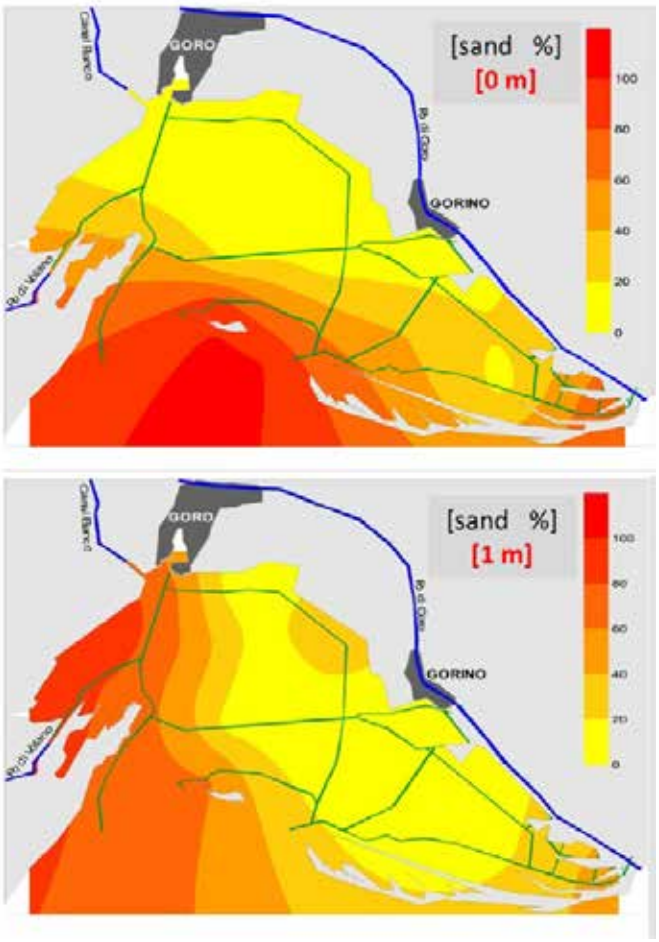

Figure 2: Example of the spatial distribution of sand content in the sediments at depths of 0 cm (lagoon bottom) and 100 cm.

This study provides valuable information for the formulation of effective management policies that can mitigate the risks posed by both natural and anthropogenic pollution, while ensuring the sustainable development of the aquaculture industry and the protection of the broader ecosystem in the Po River delta.

17th INTERNATIONAL CONGRESS of the Geological Society of Greece

BULLETIN OF THE GEOLOGICAL SOCIETY OF GREECE, SP. PUBL.

EXTENDED ABSTRACT 267

The role of hydrogeology in the sustainable exploration of shallow geothermal resources

Rapti D.[1,2]

(1) University of Ferrara, Department of Chemical, Pharmaceutical and Agricultural Sciences, Italy cpr@unife.it (2) New Energies And environment, spinoff company of Ferrara University, Ferrara, Italy

Abstract

Climate change, the diffusion of micropollutants in the atmosphere, as well as European energy and environmental policies, are driving the research and use of renewable and eco-sustainable energy resources to support the energy transition process.

The optimization of a geothermal exchange system requires a holistic approach that takes into account both the energy needs of the building and the hydrogeological, chemical, and thermophysical characteristics of the subsoil, as well as the presence of natural and legislative constraints.

In this context, a new dynamic closed-loop heat? exchanger designed for the exploitation of shallow geothermal resources has been installed at a test site in the alluvial Po plain (northern Italy). By means of *in situ* and laboratory tests, we collected data on:

a) sedimentary sequences and grain size, obtained through continuous core drilling and laboratory tests;

b) hydrogeological conditions and the local conceptual hydrogeological model up to a depth of 80 meters, assessed via pumping tests, measurement, and analysis of hydrodynamic data;

c) hydrochemical characteristics of the aquifer systems, determined through chemical and isotopic analyses (oxygen, deuterium, strontium);

d) thermo-physical monitoring, conducted via the implementation of a Distributed Thermal Response Test and laboratory measurements of thermal conductivity. Additionally, a monitoring system based on Distributed Fibre-Optic Temperature-Sensing (DTS) has been installed to better define underground temperature profiles under both natural and thermal solicitation conditions (Fig. 1).

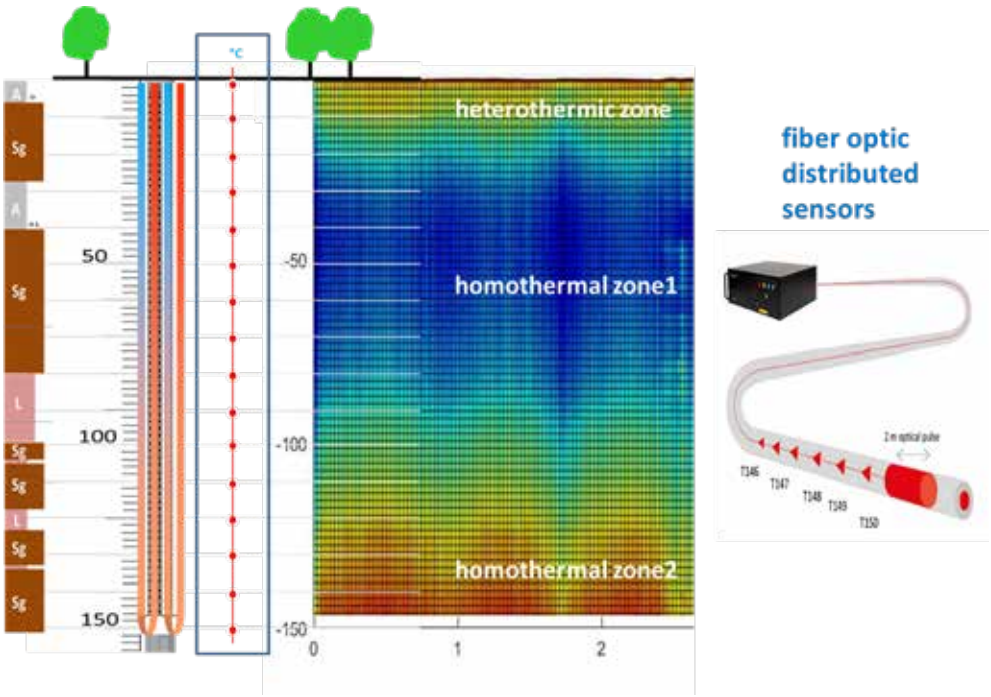

Figure 1. Results of the Distributed Fibre-Optic Temperature-Sensing (depth in meters; A: clay; Sg: sandy; L: silt).

By employing a comprehensive and holistic methodology, the integrated analysis of various data sets facilitated a rigorous characterization of the hydrodynamic and thermo-physical properties of the local aquifers. This characterization was further enhanced through the utilization of advanced numerical simulation models. Additionally,

the study assessed the subsoil's responses to the thermal stresses that could potentially be induced by a low-enthalpy geothermal plant with an approximate capacity of 350 kW. Finally, this analysis enabled us to assess the energy and environmental sustainability of these innovative dynamic closed-loop heat exchangers.

17th INTERNATIONAL CONGRESS of the Geological Society of Greece

BULLETIN OF THE GEOLOGICAL SOCIETY OF GREECE, SP. PUBL.

EXTENDED ABSTRACT 268

Liquefaction susceptibility in delta environments: the case of the Po delta area (northern Italy)

Rapti D.[1] Papathanassiou G.[2], Valkaniotis S.[2], Taftsoglou M.[3], Caputo R.[3]

(1) University of Ferrara, Department of Chemical, Pharmaceutical and Agricultural Sciences, Ferrara, Italy cpr@unife.it.

(2) Aristotle University of Thessaloniki, School of Geology, Thessaloniki, Greece

(3) University of Ferrara, Department of Physics and Earth Sciences, Ferrara, Italy.

Abstract

We know that, during a seismic event, liquefaction phenomena are not randomly distributed over an active or recent floodplain but are strongly dependent on the depositional evolution of the area like grain size of the sediments, depositional age shallow layering, and depth of the groundwater level. Recent unconsolidated sediments (Holocene age), deposited by fluvial or wave action, such as those found in paleo-channels and point bars in coastal areas, generally exhibit a higher frequency of liquefaction compared to sediments deposited under different conditions within the same floodplain and/or coastal zone.

Based on these considerations, Youd and Perkins (1978) proposed the division of geological units into four classes of liquefaction susceptibility: low, moderate, high, and very high. They also emphasized that water-saturated geological formations, such as river channels, floodplains, deltaic regions, and dunes, are generally characterized by a high to very high susceptibility to liquefaction.

The reliability of a liquefaction susceptibility map is heavily influenced by the investigation scale, as well as the density and accuracy of the geological, geomorphological, and hydrogeological data.

In this paper, an area of about 560 km², situated in the eastern sector of the Po River plain (northern Italy) within the Po River delta, including part of the modern delta, has been considered and analyzed in detail to examine the likelihood of geological units to liquefaction. To achieve this, a large variety of data has been considered. Lithological, chronological (14C data), geomorphological, hydrological, hydrogeological data, satellite imagery, modern and historical topographic maps, as well as historical and archaeological evidence, were integrated with data from continuous core drilling and penetrometer tests (Figure 1).

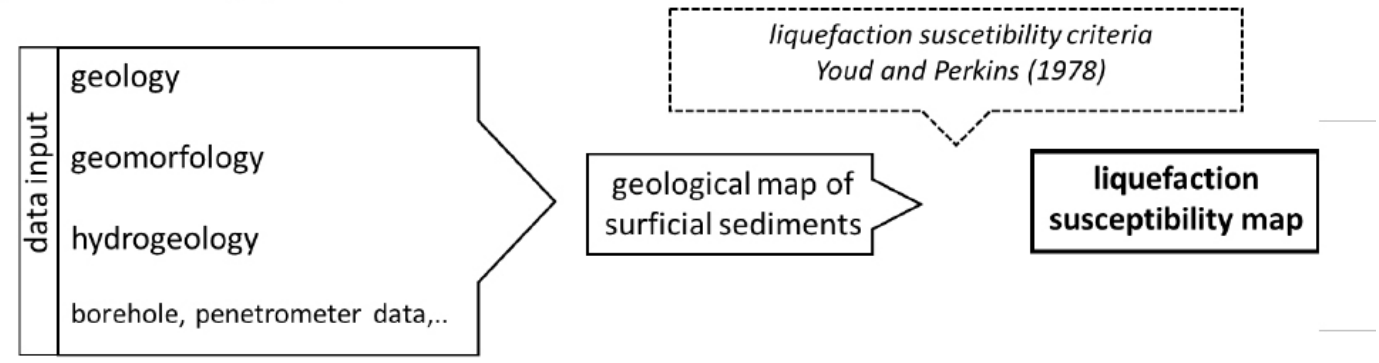

Figure 1. Flowchart showing the phases of the method applied in this study.

This integrated data analysis allowed us to define the liquefaction susceptibility map. Specifically, four classes were identified, corresponding to the following susceptibility levels:

a) *very high*, in the portion of the territory occupied by the floodplain of the main Po channel, which accounts for 4% of the overall area;

b*) high*, corresponding to 26% of the area, found in geological formations such as floodplains, channels, crevasse splays, abandoned channels, and coastal dunes;

c) *moderate*, covering approximately 20% of the territory, mainly characterized by beach barrier formations;

d) *non-susceptible features*, representing 50% of the territory, including marshes of interdistributary areas and brackish marshes and lagoons of the front delta plain, since they are fully infilled by clays, silty clays, and silts.

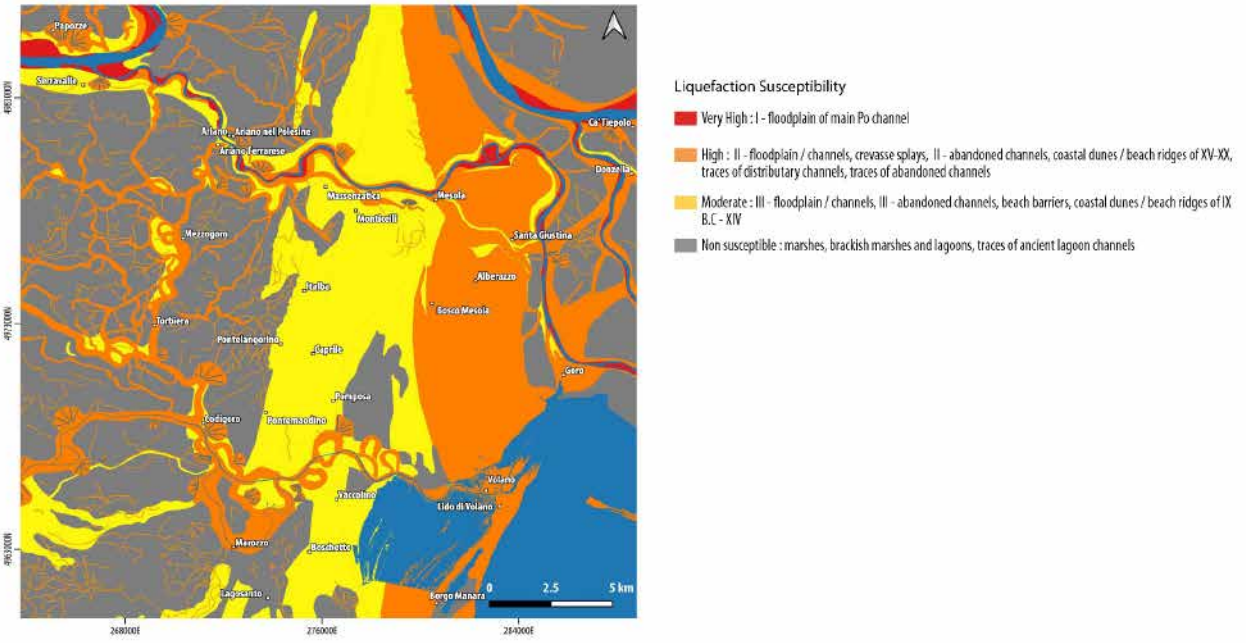

Figure 2. Liquefaction Susceptibility map of Po delta plain, based on the proposed refined classification of Youd and Perkins criteria (1978).

The obtained data could be used by public authorities to implement strategies and governance measures aimed at the sustainable management of the territory, considering the significant natural (a large portion of the area is included in the Natura 2000 protected areas network), environmental, cultural, and economic value of the Po Delta area.

References

Youd T.L., Perkins D.M., 1978. Mapping of Liquefaction induced Ground Failure Potential, J. Geotech. Eng. Div., 104, 433-446.

17th INTERNATIONAL CONGRESS of the Geological Society of Greece

BULLETIN OF THE GEOLOGICAL SOCIETY OF GREECE, SP. PUBL.

EXTENDED ABSTRACT 269

Investigation of legislation and tools for coastline demarcation: the coastline along the Kalamas delta in Thesprotia as a case study

Rapti Georgia[1], Tzoraki Ourania[2]

1 University of the Aegean, Mytilene, Greece, grapti@hotmail.com, 2 University of the AegeanMytilene, Greece

Introduction / Background

The purpose of this study is first to investigate the Greek legislation regarding the delimitation of the coastline and second compare the delimitation tools used internationally. In addition, the question arises whether the automatic coastline extraction tool SAET is feasible to be used for the delimitation of coastlines by a simple user.The region of Thesprotia was chosen as a case study, and specifically, a part of the coastline along the Kalamas River delta.
For the Greek state, in 21.06.1837 was the first time that the definition of the coastline was established and it was defined its common use (Skandali G. D.,2010). Since then, many laws have used for the definition, protection and the exploitation of the coastline and the shoreline. The table below attempts to summarize the differences between the basic laws regarding the definition and mapping of the coastline.

Table 1. Differences of the basic Greek laws regarding the determination and mapping of the coastline

Low	Coast-beach width	Determination of the coast	Mapping -drawing of the coastline	Scale	Comments
L.2344/1940	20m	Testimonies of witnesses and without appropriate tools	Topographic and elevation chart and relevant report	Not specified	
L. 2971/2001	50m	Drawn after anon siteinspection or as interpreted from aerial photographs by the committee as a polygonal line closest to the actual natural line, based on the country's trigonometric network	Drawing on a cadastral-elevational chart based on the country's trigonometric network, referring to a coastline of at least 500 m	1:1000	In case of error redefinition is allowed
Amendments to Law 2971/2001	50m	Photographic captures 2008-2009, Digitized Coastline using photo interpretative methods, with a minimum cartographic unit of 2m. (Cadastre s.a.)	Precision Digital ColorOrthophoto Maps withaltitudeinformation ina Digital Terrain Model (DTM) (inraster grid format) with,points dependenton the HellenicGeodetic Reference System 1987Drawing of thePreliminary CoastalBorderline(POA) based on ten thematic categoriesof boundary lines drawingcriteria.	1:1000	
L. 5092/2024	50m	From the orthophotographic backgrounds kept in the Greek Land Registry and in site inspection		1:1000	In overall the previous procedure is not modified

(F.E.K. – National Printing House,1940, F.E.K. – National Printing House,2001, F.E.K. – Joint Ministerial Decision 1089532/P.E./8205P.E./2005, 2005, National Printing House,2024)

With the help of the bibliographic review and the PRISMA Statement 2020 protocol,documents were extracted from the international bibliography Scopus, based on keywords.regarding the tools used for the delimitation of coastlines. A total number of 328studieswere selected, mainly published articles and conference proceedings, between the years 2000-2024 with the year 2022 presenting the largest number of studies. India appeared the country with the biggest involvement in studies and research on coastline detection and demarcation tools and also hadthe largest network of cooperation with other countries, followed by China and Italy.In almost half of the

studies, the coastline was demarcated due to integrated beach management because erosion and deposition had been observed. A large percentage concerned integrated management and monitoring. Other reasons were the detection of the coast, themonitoring of changes due to anthropogenic factors, or due to storms or for reasons of governance, or changes in the coastline due to tsunamis and due to changes in land use.Regarding the size, type and land use near the coasts, in numerous studiesthey were not mention but the next highest percentage involves small sandy beaches with multiple uses and close to urban areas.Most of the studies used a combination of data sources, followed by those that used Landsat, Sentinel and generally satellite images. In some of the studies the date source was not stated, while in others were used synthetic aperture radar, UAV/UAS or images from videos, cameras and mobile phones. Some chose SPOT, LIDAR, bathymetry. Among the less used are Global Navigation Satellite system (GNSS), Pléiades, QuickBird.

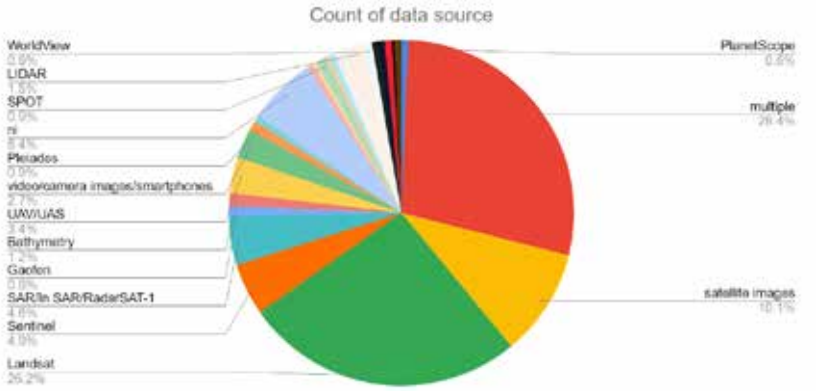

Figure 1. Data source used

Regarding the tools for coastline delineation in most studies, more than one tool was used, with the Digital Shoreline Analysis System (DSAS) and GIS being chosen quite often.In the table below we observe that the dominant tool for coastline delineation is the Digital Shoreline Analysis System (DSAS), while GIS is generally mentioned as a tool, some of the studies seems to have used some kind of model or an algorithm. Others used ENVI software, SAET, ERDAS and Convolutional Neural Networks, Google Earth Engine (GEE). Numerus studies used more than one coastal delineation tool, while SELI, AMBUR, SHOREX. CoastSat, CoastSnap, CLAHE, MATLAB, Pix4dMapper, Beachmeter, AgisoftPhotoscan, CET, ODSAS, Cliff DelineaTool, ArcMapCASSIE are also presented (Figure 2.)

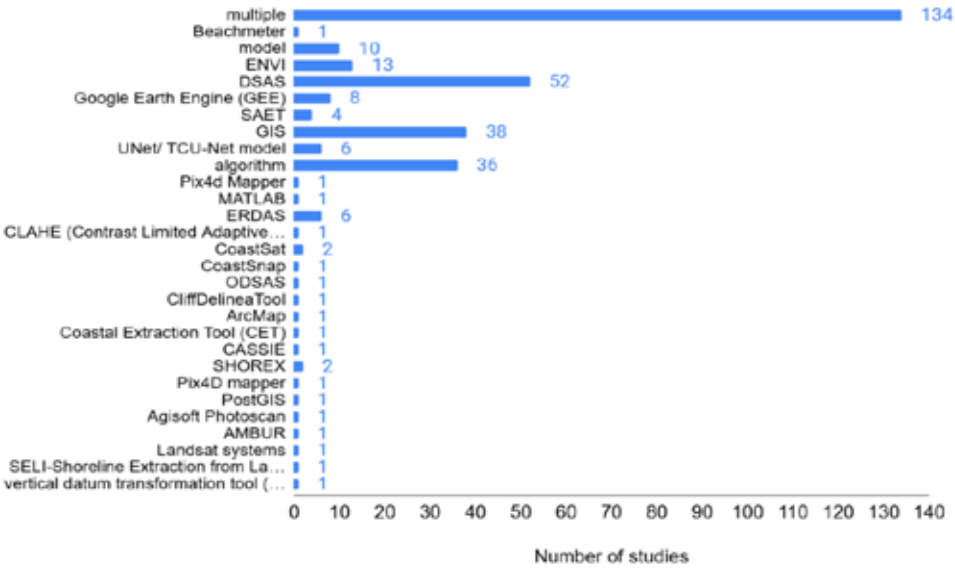

Figure 2. Shoreline extraction tools

In most studies, not just one coastal delineation method was chosen, but multiple, followed bythe segmentation and classification method.

Study area and storm events

The Kalamas River Delta is located on the coast of the Ionian Sea, in the region of Thesprotia (Epirus, northwestern Greece) and is one of the most important wetlands of western Greece. It has an area of approximately 85 km², and its shape corresponds to an “arc-shaped” delta and consists of two different mouths: one anthropogenic, active today, and the other located less than 10 km south (old estuary), which is now inactive and sheltered behind sandy beaches. In general, the front consists of sandy beaches and large sandy “tongues”. The construction of the dam in 1962 upstream of the delta as well as several works aimed at draining the land to facilitate cultivation and the construction of a river channel in 1951, have significantly changed the appearance of the delta. It should also be noted that the Kalamas River delta developed in the straits of Corfu, so it is protected from the strong currents that prevail in the Ionian Sea. (Chabrol et al., 2022, Epirus Water Resources Authority - EL05, (n.d.))

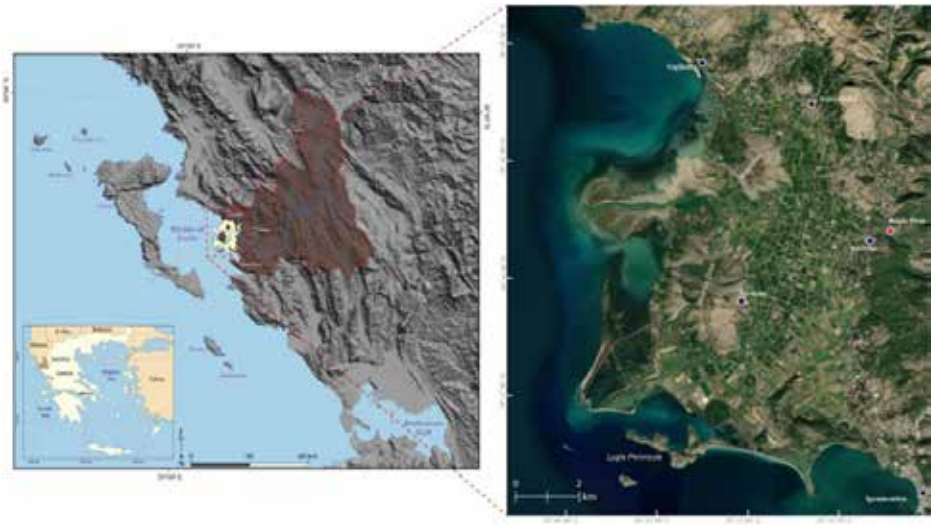

Figure 3. Study area (Chabrol et al., 2022)

Figure 4. Damage caused by the storm on 11/12/2021, (photos by author)

Figure 5. Damage caused by the storm on 06/01/2024 (photos by author)

Three storm events were selected because of the reported problems (erosion and flooding) in the area. The first one occurred 10-12 December 2021, the second one 6-7 January 2024 and the third 5-6 October 2024 (Cassandra storm). (meteo.gr, https://meteo.gr/article_view.cfm, https://www.cnn.gr/ellada/story/442473/kakokairia-cassandra-plimmyrisan-spitia-kai-katastimata-stin-ipeiro-xoris-reyma-stous-filiates.). In all three storm events strong southerly winds and a fairly high percentage of precipitation were the main characteristics. (https://www.in.gr/2024/01/06/greece/synagermos-gia-tin-kakokairia-ekspres-neo-ektakto-deltio-deite-xartes/, https://www.cnn.gr/ellada/story/442056/allazei-o-kairos-apo-paraskevi-me-tin-kakokairia-cassandra-na-xtypa-kerkyra-kai-ipeiro, meteo.gr)

Methodology

The Shoreline Analysis and Extraction Tool (SAET) software was developed within the framework of the European project ECFAS (European Coastal Flood Awareness System), with the aim of providing a solution to enhance the resilience of coasts to climate change and reduce the exposure of the population and infrastructure to risk.It was developed by the Geo-Environmental Cartography and Remote Sensing group of the University of Valencia (UniversitatPolitècnica de València, Spain) and is the work of Jesús Palomar Vázquez, Jaime Almonacid Caballer, Josep E. and is the intellectual property of the university SAET is a software developed in Python and focuses on the automatic extraction of coastlines from optical satellite images (Sentinel-2, Landsat-8 and Landsat-9). The main algorithm is based on the subpixel coastline detection approach, allowing the acquisition of the coastline before and after the storm, enabling comparison and the identification of the impact of storm erosion on beaches.(Palomar-Vázquez et al., 2023).

The first step for coastline delineation is the collection of satellite images, based on their coverage and acquisition date in relation to the storm. In our case, the study area is covered by a single Landsat scene and a Sentinel-2 tile. We then searched for the closest satellite images before and after the storm peak date (11/12/2021) by running SAET in “search only” mode and selected the images with the highest spatial resolution between (Landsat and Sentinel-2), so two Sentinel-2 images before and after the storm (12 November and 17 December) were selected, according to the criteria of the lowest possible cloud cover (up to 10%), the closest storm peak date (11 December). These two images were used as input to run SAET again, butthis time, in the “acquire” mode, and then in the “process” modeusing the AWEInsh water index for the segmentation method.Thus, two Sentinel-2 images were processed, resulting in the extractedcoastline.(Figure 6)The same procedure was followed for the following storms, for the one on January 6, 2024, Landsat images were selected, on 12/28/2023 and on 01/29/2004 (Figure 7) Finally, in the case of the Kassandra storm that hit the area on October 4,2024, 2 Landsat images were used on 09/01/2024 and 10/27/2024.(Figure 8)

Figure 6. Satellite-Derived Shorelines before and after the storm 11/12/2021 The coastline in green is the shoreline before the storm and the coastline in red is the shoreline after the storm.

Figure 7. Satellite-Derived Shorelines before and after the storm 06/01/2024 The coastline in green is the shoreline before the storm and the coastline in red is the shoreline after the storm.

Figure 8. Satellite-Derived Shorelines before and after the storm 04/10/2024 The coastline in green is the shoreline before the storm and the coastline in red is the shoreline after the storm.

Results

The analysis of the extracted coastlines for all three cases was done through the QGIS program, on a coastline length of approximately 2 kilometers, for each one separately. A single section of the coastline was selected in order to reduce the number of points to be compared of the coastlines obtained from SAET in order to make their analysis easier.These were then divided into 10 sections each.In the first storm in 2021, maximum erosion was observed at nine meters in some points but also deposition in some others with a maximum of eleven meters. It should be noted that erosion occurred on the largest part of the coastline. (Figure 9) In the second storm in January 2024(Figure 10), the greatest erosion observed was 15 meters, while the deposition reached 20 meters. In this case, the coastline, according to the analysis, showed total deposition after the storm.Finally, in the storm of October 2024 (Figure 11), the greatest erosion reached 15 meters, while the maximum deposition was 24 meters. In general, the storm left the coastline with erosion in most of its part.In some sections, the same phenomenon is observed in all 3 cases, which also agree with the damages that had been reported. The first two cases seem to have more similarities, while in the case concerning the storm Kassandra, the analysis also shows sections in which, while they showed deposition in the previous storms, after “Kassandra” they were eroded and vice versa.

Figure 9. Analysis of SDS before and after the storm in December2021 Dark blue indicates maximum erosion and yellow indicates maximum deposition.

Figure 10. Analysis of SDS before and after the storm in January 2024. Dark blue indicates maximum erosion and yellow indicates maximum deposition.

Figure 11 Analysis of SDS before and after the storm in October 2024. Dark blue indicates maximum erosion and yellow indicates maximum deposition.

Uncertainties

In the original SAET file, the area of interest is divided into 3 smaller beaches with a different code each, so the largest one was selected, with the code 2127.The beach areas were taken from the European zone dataset provided by the Earth Observation Service. Copernicus. Also, when applying the software in the “download” mode in order

toreceive satellite images from Sentinel, the error “Access token” occurred and it was not possible to overcome it by the specific user, while a request was made tobecome “online” again.In addition, it was not possible to produce SDS close to the dates of the events andin the three cases the time period before and after exceeds one month, while ideallyit should have been one day before and one day after the storm, we believe that this alsoaffected the results.It shouldbe noted that the cases selected for examination did not involve majorstorms.

Conclusions

Comparing the results, we observe that in all three cases, in most sections, the same phenomenon is observed, erosion or deposition, which is in agreement with the damages caused. The first two cases seem to have more similarities, while in the case of the storm Kassandra, the analysis also shows sections in which, while they presented deposition in the previous storms, after ̈Kassandra ̈they were eroded and vice versa.

The delineation of a coastline is now achieved:in a short time, almost automatically which reduces the error rate from the userand at low cost, since much of the data is freely available with a fairly high resolutionFor a given section of coastline after a coastal storm, SAET facilitates the selection of the closest satellite images in time to the analyzed events, ensures a sufficient level of coverage for the analysis of the coastline change, and automatically ‘downloads’ the images from the official satellite repositories, processes them and exports them to the location of the coastline. SAET: performs a tool for studying the impact and recovery of beach morphology in a coastal storm, but also in the case of anthropogenic interventions and long-term SDS, thus contributing to the effort to address and mitigate the effects of coastal and not only storms and to finding the most appropriate measures for their timely response.

References

Chabrol, A., Gonnet, A., Fouache, E., Pavlopoulos, K., &Lecoeur, C. (2022). Geomorphology of the Kalamas river delta (Epirus, Greece). Journal of Maps, 18(2), 276–287.

Palomar-Vázquez, J., Almonacid-Caballer, J., Eliseu Pardo-Pascual, J., & Sánchez-García, E. (2018).Proceedings of the 7 th International Conference on the Application of Physical Modelling in Coastaland Port Engineering and Science (Coastlab18) SHOREX: A NEW TOOL FOR AUTOMATIC ANDMASSIVE EXTRACTION OF SHORELINES FROM LANDSAT AND SENTINEL 2 IMAGERY.

Palomar-Vázquez, J., Pardo-Pascual, J. E., Almonacid-Caballer, J., & Cabezas-Rabadán, C. (2023).Shoreline Analysis and Extraction Tool (SAET): A New Tool for the Automatic Extraction ofSatellite-Derived Shorelines with Subpixel Accuracy. Remote Sensing 2023, Vol. 15, Page 3198,15(12), 3198.

Athanasakopoulou, M. (2019). Coastal zone. National legislative framework for coastal zone management. Coastal protection projects against erosion - The case of the Kalamaki region, Western Achaia. Faculty of Engineering Project Management (DCHT), MSc Thesis, Hellenic Open University, Patra.

Petrelis V. N. (2012 Investigating the estimation models of the coastline displacement, Faculty of Agricultural and Surveying Engineering, Ph.D. Thesis, National Technical university of Athens.

Skandali G. D. (2010). Development of a knowledge base in an object-oriented analysis environment of digital telescopic data for the purpose of automatic delineation of the coastal coastal zone, Faculty of Agricultural and Surveying Engineering, National Technical university of Athens.

Coastal Vulnerability and Shoreline Mapping - ECFAS. (n.d.). Retrieved September 26, 2024, from, https://www.ecfas.eu/public-deliverables/coastal-vulnerability-and-shoreline-mapping/.

meteo.gr: Severe weather until Sunday 12 December 2021. (n.d.-a). Retrieved December 18,2024, from https://meteo.gr/article_view.cfm?entryID=2041.

meteo.gr: New wave of bad weather until Friday 10 December. (n.d.). Retrieved December 18,2024, from https://meteo.gr/article_view.cfm?entryID=2040.

The weather changes from Friday with the bad weather Cassandra hitting Corfu and Epirus -CNN.gr. (n.d.). Retrieved January 16, 2025, from https://www.cnn.gr/ellada/story/442056/allazei-o-kairos-apo-paraskevi-me-tin-kakokairia-cassandra-na-xtypa-kerkyra-kai-ipeiro.

Epirus Water Resources Authority - EL05 – Flood Risk Management Plans. (n.d.). Retrieved September 29, 2024,from https://floods.ypeka.gr/sdkp-lap/maps-1round/sdkp-el05-1round/.

Storm «Cassandra»: Houses and shops flooded in Epirus - No electricity in Filiates - CNN.gr. (n.d.). Retrieved December 18, 2024, fromhttps://www.cnn.gr/ellada/story/442473/kakokairia-cassandra-plimmyrisan-spitia-kai-katastimata-stin-ipeiro-xoris-reyma-stous-filiates.

Bad weather alert - express: New emergency bulletin [maps] | in.gr. (n.d.). RetrievedDecember 18, 2024, from https://www.in.gr/2024/01/06/greece/synagermos-gia-tin-kakokairia-ekspres-neo-ektakto-deltio-deite-xartes/.

EMY - Home.. (n.d.). Retrieved December 18, 2024, from https://www.emy.gr/?area=forecast.

Joint Ministerial Decision 1089532/P.E./8205P.E./2005 - FEKB-595/4-5-2005 - AIGIALOS -PARALIA. (n.d.).

BANK OF LEGAL INFORMATION OF THE STATE ADMINISTRATION. (1946).

F.E.K. –National Printing House. (1940). https://search.et.gr/el/fek/?fekId=653170

F.E.K. – National Printing House. (2001). https://search.et.gr/el/fek/?fekId=230027

F.E.K. – National Printing House (2024). https://search.et.gr/el/fek/?fekId=763363

17th INTERNATIONAL CONGRESS of the Geological Society of Greece

BULLETIN OF THE GEOLOGICAL SOCIETY OF GREECE, SP. PUBL.

EXTENDED ABSTRACT 270

Remnants of oceanic crust of Edessa ophiolite (North Greece): Petrographic and geochemical characteristics

Rogkala A.[1], Petrounias P.[1], Giannakopoulou P.P.[1], Koutsovitis P.[1], Kalpogiannaki M.[2], Lampropoulou, P.[1], Tsikos H.[1]

(1) Department of Geology, University of Patras, Patras, Greece, krogkala@upatras.gr (2) Department of Geology and Geoenvironment, National and Kapodistrian University of Athens, Athens, Greece

Introduction

Ophiolites are fragments of oceanic lithosphere that have been tectonically emplaced along the continental margins in accretionary prisms during orogenic processes providing important insights regarding the petrogenetic activity within the oceanic lithospheric mantle beneath spreading centers in mid-ocean ridge (MOR) and suprasubduction zone (SSZ) settings (Dilek and Furnes, 2011, Ahmed, 2013, Dai *et al.*, 2013).These tectonic settings include oceanic spreading centres, hot spots, backarc and forearc basins (supra-subduction zone environments) as well as arcs and other extensional magmatic settings including those in association with plumes. Furthermore, they provide information about the magmatic, metamorphic and geotectonic processes that occurred in the oceanic crust and the upper mantle (Arai *et al.*, 2006, Uysal *et al.*, 2007). The mantle-derived ophiolites provide significant information for paleotectonic evolution of the oceanic lithosphere, partial melting processes, melt-rock interaction and melt fractionation of the uppermost mantle (Singh *et al.*, 2016). Specifically, the abyssal peridotites represent mantle residues produced by partial melting beneath MOR settings, whereas the highly depleted SSZ peridotites experience intense partial melting above a subduction zone.

The aim of the present study is to provide new petrographic and geochemical data of mafic rocks from the Edessa ophiolite complex, in order to shed light on their petrogenesis.

Geological setting

The ophiolitic complex of Edessa, comprises a series of oceanic crust and mantle fragments linking the Veria-Naousa ophiolite (Rogkala *et al.*, 2017) in the south with the Guevgeuli ophiolite (Giannakopoulou *et al.*, 2018) in the northeast (Figure 1). It represents remnants of oceanic lithosphere that was thrust out of one or more ocean basins during Upper Jurassic to Lower Cretaceous time (Michailidis, 1990).

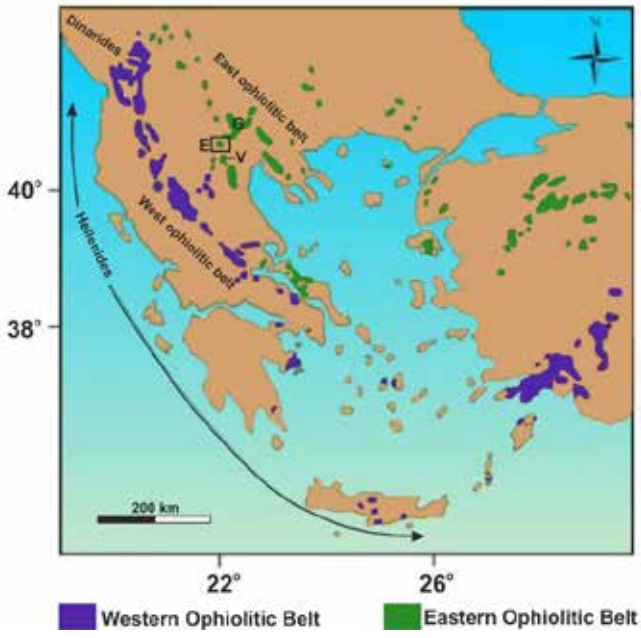

Figure 1. Distribution of ophiolites in the southernmost part of the Balkan Peninsula and Turkey (Rogkala *et al.*, 2019). Key to lettering: E = Edessa (also marked by the open square), G: Guevgeuli, V: Veria-Naousa.

The ophiolitic complex has been significantly affected by tectonically related emplacement mechanisms and it consists of several tectonic units (Pe-Piper and Piper, 2002, Saccani *et al.*, 2008). It includes lherzolites, serpentinised harzburgites

with high degree of serpentinisation, gabbros, diorites, diabasic sheeted dykes and pillow basalts. The serpentinised harzburgite is the dominant rock type amongst the ultramafics and encloses chromitites (Rogkala *et al.*, 2019). A sparse network of gabbroic and dioritic dykes crosscuts the serpentinised harzburgite. Massive diabase and basalt are thrust over serpentinised harzburgite and pass upwards into basaltic pillow-lava flows (Figure 2). A sparse network of rodingite dykes within the highly serpentinised harzburgites has also been identified. The ophiolitic rocks are unconformably overlain by Middle-Upper Cretaceous to Paleocene transgressive sediments (conglomeritic limestone, flysch).Other, non-ophiolitic volcanic rocks crop out to the eastern part of the ophiolite occurrence and they belong to the Almopias subzone (Vougioukalakis, 2002).

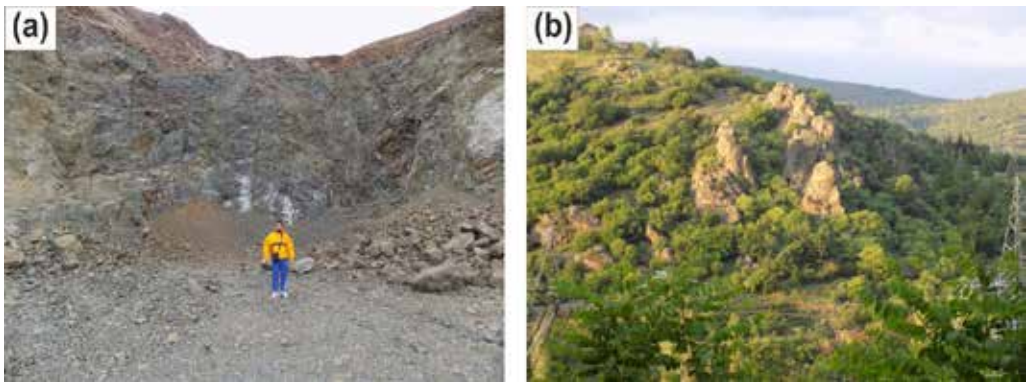

Figure 2. Mafic rocks from Edessa ophiolites: (a) Diabase, (b) Basalt.

Analytical methods

The textural characteristics of the samples were studied in polished-thin sections in a polarising microscope (Leitz Ortholux II POL-BK Ltd., Midland, ON, Canada) at the Department of Geology and scanning electron microscope (SEM) at the Laboratory of Electron Microscopy and Microanalysis, University of Patras. Whole-rock chemical analysis for major and trace elements was performed at Bureau Veritas Mineral Laboratories at Vancouver (Canada). Major element analysis was carried out using an XRF spectrometer and a sequential spectrometer (ICP-ES). Trace elements and rare earth elements were determined in totally digested samples by inductively coupled plasma-mass spectrometry (ICP-MS) in the same laboratory. Detection limits for major and trace elements range from 0.01 wt.% to 0.04 wt.% and from 0.01 ppm to 10 ppm, respectively. The analytical precision calculated by replicate analyses is better than 3% for most major elements and better than 5% for trace elements.

Results

Petrographic features

The Edessa mafic rocks comprise gabbroic (gabbros and less frequent diorites) and volcanics rocks (diabases and basalts). Diorites are moderately altered and they are fine to medium-grained rocks (Figure 3a). Their texture is granular but locally becomes porphyritic with subhedral to euhedral plagioclase phenocrysts. Sporadic, euhedral hornblende grains are enclosed within larger plagioclase crystals forming poikilitic textures. Gabbros are mainly comprised of clinopyroxene and plagioclase (Figure 3b). Ilmenite, magnetite, titanite and zircon are present in small amounts, less than 5% of the mode. Primary textures have been obliterated by alteration.

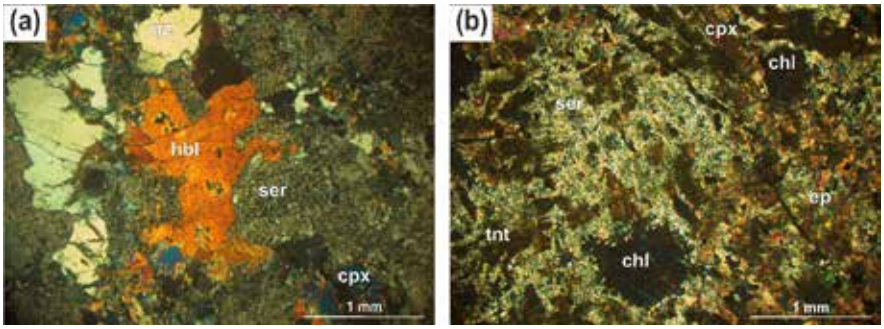

Figure 3. Photomicrographs of:(a) hornblende (hbl) crystal with irregular shape surrounded by sericitised (ser) plagioclase, quartz (qz) and clinopyroxene (cpx) in diorite, (b) subophitc texture in altered gabbro showing seriticised plagioclase (ser), clinopyroxene (cpx), chlorite (chl), epidote (ep) and titanite (tnt).

Diabase samples exhibit porphyritic, ophitic and subophitic textures. The mineral assemblage is similar to that of gabbros including clinopyroxene and subhedral plagioclase. In some cases the plagioclase is partially to completely altered to sericite (Figure 4a). Basalts display interwoven, porphyritic and microlitic textures (Figure 4b). Their primary assemblage includes plagioclase, clinopyroxene, magnetite, ilmenite and accessory zircon. They have suffered by a low-grade, oceanic alteration episode and by the development of quartz, epidote, chlorite, calcite and titanite, occurring in the groundmass and within joints or amygdules.

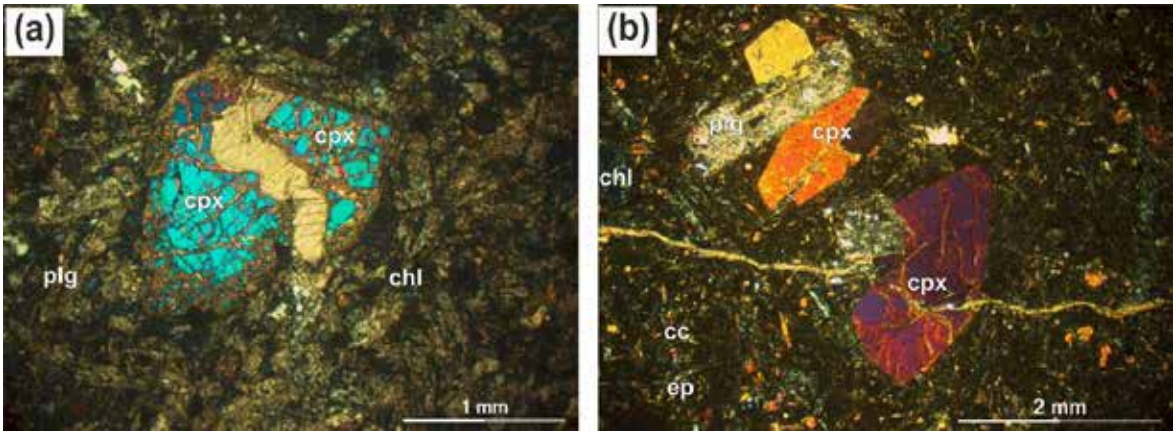

Figure 4. Photomicrographs of: (a) clinopyroxene (cpx) porphyroclast cross cutting by calcite (cc) and surrounding by plagioclase (plg), sericite (ser) and chlorite (chl) in diabase, (b) porphyritic texture in basalt showing clinopyroxene (cpx), plagioclase (plg), chlorite (chl), epidote (ep) and calcite veinlet.

Geochemical features

All the investigated mafic rock samples were moderately affected by alteration, resulting in the mobility of the large ion lithophile (LIL) elements (such as Na, K, Ca, Rb, Ba, Sr, Pb) and thus their measured values may not be able to define these rocks (Shervais, 1982). Therefore, we use only high field strength (HFS) elements (Ti, Nb, Y, Zr, Hf, Ta, REE) and transition elements (such as Y, V, Ni, Cu) for interpretation, as these elements are considered immobile during alteration and can effectively be used to describe the primary chemical features of rocks. Immobile-element ratios such as Zr/Ti and Nb/Y are commonly used to identify mafic, intermediate and acid rocks that they might have been variably altered (Winchester and Floyd, 1977, Pearce, 1996). In order to clarify the nature of the environment of mafic rocks, we have applied the Zr-Nb-Y diagram in the analyzed results. In this diagram, gabbro, basalt and diabase, except one sample (ED.110), are plotted in gabbro field, whereas the diorite clusters in the tonalite, a fact that supports the mafic character of the investigated samples (Figure 5).

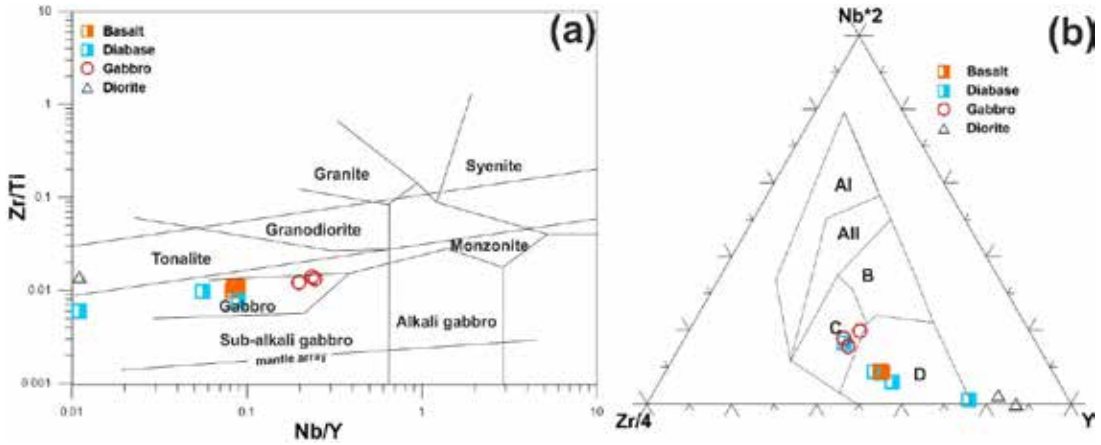

Figure 5. a. Binary classification diagram of Zr/Ti versus Nb/Y for the mafic rocks of Edessa ophiolites (Winchester and Floyd 1977; modified by Pearce 1996). b. Discrimination Nb-Zr-Y diagram (Meschede, 1986) (fields: AI = within-plate alkali basalts, AII = within-plate alkali basalts and within-plate tholeiites, B = E-type MORB, C = within-plate tholeiites and volcanic basalts, D = N-type and volcanic-arc basalts).

Basalts show remarkably high Ti and REE concentrations than the other mafic rock samples. The chondrite normalised REE patterns for diorite, gabbro, diabase and basalt are plotted individually and they show four distinct REE patterns (Figure 6). Though all studied samples show almost flat HREE pattern, gabbro shows highly fractionated LREE patterns relative to the HREE, with positive Eu anomalies, which implies plagioclase accumulation. These patterns are similar to E-MORB type represented from many ophiolitic complexes. Diabases present two subgroups. The first is enriched in LREE and depleted in HREE, similar to OIB-like lavas. The second is depleted in LREE and enriched in HREE, similar to the SSZ type. Basalt exhibits almost flat REE pattern without any LREE enrichment relative to HREE, which is similar to N-MORB type. Diorite shows totally depleted LREE pattern (SSZ type) with negative Eu anomaly, which implies removal of plagioclase.

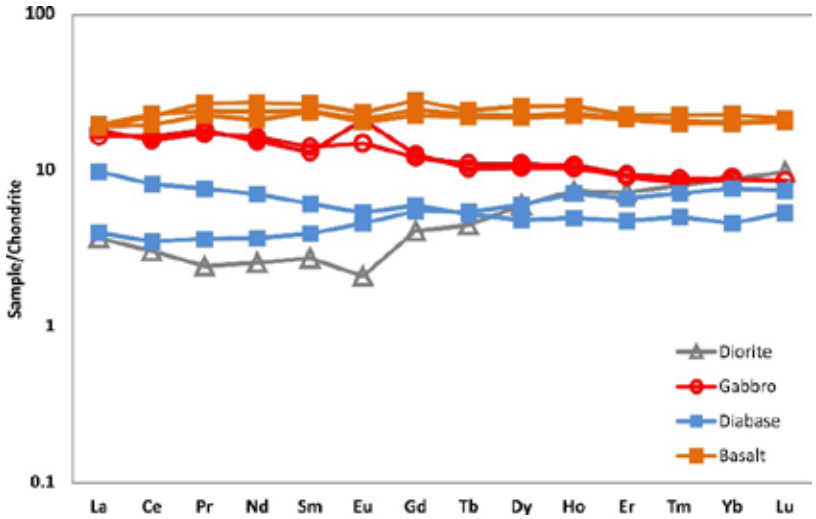

Figure 6. Chondrite-normalised REE patterns of the mafic rocks from the Edessa ophiolite. Normalising values are from McDonough and Sun (1995).

Conclusions

Based on these geological, petrographic and geochemical evidences, we suggest that mid ocean ridge (MOR) type mafic rocks (basalt and gabbro) from the Edessa ophiolite represent the section of older oceanic crust which was generated during the opening of the Axios Ocean. Conversely, diorite and partially diabase represent the younger oceanic crust which was formed at the forearc region by partial melting of the depleted mantle wedge modified by hydrous fluids released from the subducting oceanic slab.

Acknowledgements

We kindly thank Dr. A.K. Seferlis of the Laboratory of Electron Microscopy and Microanalysis, University of Patras for his assistance with the microanalyses and SEM micrographs. We kindly thank Dr. K. Hatzipanagiotou and Dr. B. Tsikoura for their assistance in the fieldwork, in the interpretation of the results and for their whole contribution of this study.

References

Ahmed, A.H., 2013. Highly depleted harzburgite-dunite-chromitite complexes from the Neoproterozoic ophiolite, south Eastern Desert, Egypt: a possible recycled upper mantle lithosphere. Precambrian Research 233, 173-192.

Arai, S., Kadoshima, K., Moeishita, T., 2006. Widespread arc-related melting in the mantle section of the northern Oman ophiolite as inferred from detrital chromian spinels. Journal of the Geological Society of London 163, 869-879.

Dai, J., Wang, C., Polat, A., Santosh, M., Li, Y., Ge, Y., 2013. Rapid forearc spreading between 130 and 120 Ma: evidence from geochronology and geochemistry of the Xigaze ophiolite, southern Tibet. Lithos 172-173, 1-16.

Dilek, Y., Furnes, H., 2011. Ophiolite genesis and global tectonics: geochemical and tectonic fingerprinting of ancient oceanic lithosphere. Geological Society of American Bulletin 123, 387-411.

Giannakopoulou, P.P., Petrounias, P., Tsikouras, B., Kalaitzidis, S., Rogkala, A., Hatzipanagiotou, K., Tombros, S.F., 2018. Using Factor Analysis to Determine the Interrelationships between the Engineering Properties of Aggregates from Igneous Rocks in Greece. Minerals 8, 580.

McDonough, W.F., Sun, S.S., 1995. The composition of the Earth. Chemical Geology 120, 223-253.

Meschede, M., 1986. A method of discriminating between different types of mid-ocean ridge basalts and continental tholeiites with the Nb-Zr-Y diagram. Chemical Geology 56, 207-218.

Michailidis, K.M., 1990. Zoned chromites with high Mn-contents in the Fe-Ni-Cr-laterite ore deposits from the Edessa area in

Northern Greece. Mineralium Deposita 25, 190–197.
Pearce, J.A., 1996. A user's guide to basalt discrimination diagrams. In: Wyman, D.A. (Ed.), Trace element Geochemistry of Volcanic Rocks: Applications for Massive Sulphide Exploration Geological Association of Canada, 12. Short Course Notes, 79-113.
Pe-Piper, G.; Piper, D.J.W., 2002. The Igneous Rocks of Greece: The Anatomy of an Orogen; Gebrueder Borntraeger: Berlin/ Stuttgart, Germany.
Rogkala, A., Petrounias, P., Tsikouras, B., Giannakopoulou, P. P., & Hatzipanagiotou, K., 2019. Mineralogical Evidence for Partial Melting and Melt-Rock Interaction Processes in the Mantle Peridotites of Edessa Ophiolite (North Greece). Minerals 9(2), 120.
Rogkala, A., Petrounias, P., Tsikouras, B., Hatzipanagiotou, K., 2017. New Occurrence of Pyroxenites in the Veria-Naousa Ophiolite (North Greece): Implications on Their Origin and Petrogenetic Evolution. Geosciences 7(4), 92.
Saccani, E., Photiades, A., Santato, A., Zeda, O., 2008. New evidence for supra-subduction zone ophiolites in the Vardar zone of northern Greece: implications for the tectonomagmatic evolution of the Vardar oceanic basin. Ofioliti 33, 65–85.
Shervais, J.W., 1982. Ti-V plots and the petrogenesis of modern and ophiolitic lavas. Earth and Planetary Science Letters 59 (1), 101-118.
Singh, A.K., Nayak, R., Khogenkumar, S., Subramanyam, K.S.V., Thakur, S.S., Singh, R.K.B., Satyanarayanan, M., 2016. Genesis and tectonic implications of cumulate pyroxenites and tectonite peridotites from the Nagaland-Manipur ophiolites, Northeast India: constraints from mineralogical and geochemical characteristics. Geological Journal DOI: 10.1002/gj.2769.
Uysal, I., Kaliwoda, M., Karsli, O., Tarkian, M., Sadiklar, M.B., Ottley, C.J., 2007. Compositional variations as a result of partial melting and melt-peridotites interaction in an upper mantle section from the Ortaca area, southwestern Turkey. Canadian Mineralogist 45, 1791-1813.
Vougioukalakis, G., 2002. Petrological, Geochemical and Volcanological Study of the Almopias Pliocene Volcanic Formations and their Correlation with the Geothermal Manifestations in the area. PhD thesis, Aristotle Univ. of Thessaloniki, Thessaloniki, 303pp.
Winchester, J.A., Floyd, P.A., 1977. Geochemical discrimination of different magma series and their differentiation products using immobile elements. Chemical Geology 20, 325-343.

17th INTERNATIONAL CONGRESS of the Geological Society of Greece

BULLETIN OF THE GEOLOGICAL SOCIETY OF GREECE, SP. PUBL.

EXTENDED ABSTRACT 271

Shallow Depth P-wave Velocity Profiling Using Seismic Interferometry: The CORSSA Site

Roumelioti Z.[1], Katsaitis N.[1]
(1) Department of Geology, University of Patras, Patras, Greece, zroumelioti@upatras.gr

Abstract
We apply the method of seismic interferometry by deconvolution to analyze vertical accelerometer array data from the CORSSA site in Greece and determine P-wave velocities (VP) at shallow depths. We show that in the case of the CORSSA site, the method is able to overcome the challenges of resolving the much faster P-wave travel times and provide statistically robust mean velocity values for different depth ranges. Thus, we propose a V_P velocity model for the studied site to complement the previously proposed V_S models. We also compare the interferometry inferred V_P/V_S values with independent results and find them to be realistic and consistent with empirical relationships based on rich data sets from different parts of the world. Within the nearly 10 years that the studied dataset spans, we observe a significant temporal variation of V_P, mostly in the shallower depth ranges studied, which appears to be longer in duration than the seasonal variation previously reported for V_S at this site. However, the lack of temporal continuity in our dataset does not allow a detailed analysis of this variation.

Background and objectives
Changes in the ratio of P-wave to S-wave velocity, V_P/V_S, in soft sediments often reveal variations in fluid content, sediment compaction, material composition, and stress conditions. Monitoring these changes is critical for both geotechnical and geophysical applications. Historically, the method of seismic interferometry by deconvolution has been applied to horizontal recordings of vertical accelerometer array data sets to monitor temporal variations of V_S at shallow depths (e.g., Nakata and Snieder, 2011; Chandra et al., 2016; Gueguen, 2016; Roumelioti et al., 2020, Qin et al., 2022). The vertical component is usually not exploited in the specific method, primarily because the much faster travel times of P-waves are difficult to resolve.
The CORSSA vertical accelerometer array (e.g., Kassaras et al., 2016) was installed in the coastal area of the city of Aigio (northern Peloponnese, western Gulf of Corinth) a few years after the catastrophic 1995 M6.5 Aigio earthquake. The primary goal of this infrastructure was to collect strong motion records to be used in studies of site effects and soil response. To understand the changes in the seismic wavefield as it propagates from the bedrock to the ground surface, four stations were installed inside boreholes at different depths (14, 31, 57 and 178 m) and one station was installed on the surface inside a lightweight protective structure. The infrastructure operated in trigger mode for several years, although with several interruptions due to technical problems, and its data for the period 2022-2012 have been organized and published as a database (http://corssa.gr/; Kassaras et al., 2016).
The CORSSA dataset has been analyzed by seismic interferometry by deconvolution with respect to the horizontal recordings and associated Vs (Roumelioti et al., 2018), revealing a seasonal variation of V_S in shallow layers that decreases with depth and becomes undetectable below ~30m. In this work, we extend the analysis to the vertical components of the earthquake records in the CORSSA database, with the aim of determining the V_P profile for the CORSSA site and investigating the V_P values with respect to previously published V_S in terms of their ratio, V_P/V_S, and its change with depth.

Methods and Data
Seismic interferometry by deconvolution on an array of sensors comprises the division of the spectral representation of one trace at one receiver by that of another. Assuming that the distance between a specific earthquake source and the array is many times larger than the array inter-station distances, the spectral division is expected to remove any source-specific imprints and common path propagation effects, yielding the transfer function of the medium between the two involved stations, which resembles a pulse signal. This transfer function is the inverse Fourier transform of:

$$D_{j-i}(\omega) = \frac{A_j(\omega)A_i^*(\omega)}{|A_i(\omega)|^2+\varepsilon} \quad (1)$$

where $A_j(\omega)$ and $A_i(\omega)$ represent the Fourier transforms of the recordings at the *j*-th and *i*-th (reference) receivers, respectively, and ε the water-level parameter, introduced to stabilize the deconvolution at very low denominator values (Clayton and Wiggins, 1976). By measuring the travel times of the resulting pulses and knowing the exact distances between stations in the array, it is possible to compute wave velocities in the between the two stations propagating medium.
For this study, the seismic interferometry by deconvolution was applied to the vertical components of recordings from four CORSSA borehole stations, using the surface station as a reference. In total, we analyzed records of 709 earthquakes at each

station. Some characteristics of the dataset, such as the distribution of magnitudes (local magnitude, M_L) in magnitude bins, the distribution of magnitude with epicentral distance, and the distribution of peak ground acceleration (PGA) with distance, are shown graphically in Figure 1.

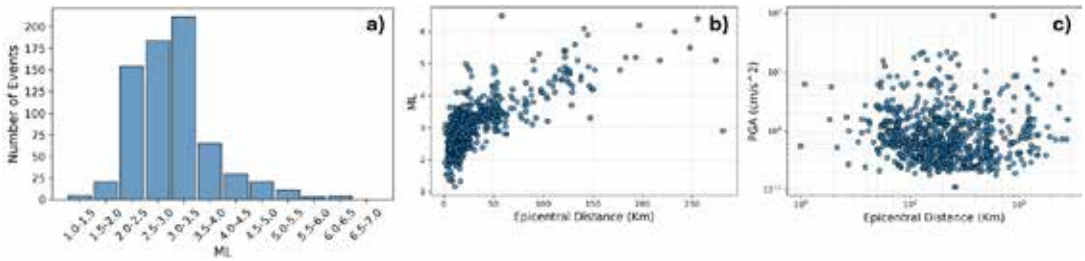

Figure 1. Brief description of the processed dataset: a) Distribution of earthquake records in the dataset in magnitude (M_L) bins, b) M_L occurrences and c) PGA (east-west component of the surface CORSSA station) with respect to the epicentral distance of the earthquakes from the CORSSA site.

We set ε=10% and resampled the inverse Fourier transform of $D_{i-i}(\omega)\,D_{i-i}(\omega)$ with a step 100 times smaller than the original. In this way, we artificially densified the pulse-like transfer functions to improve the accuracy of the picking of the travel time of the pulse (e.g., Roumelioti et al., 2020; Qin et al., 2023). Figure 2 shows a sample output from the application of the described method to the vertical recordings of a M_L3.5 earthquake at 14 km distance. The subplots show the results of the interferometry at different depth intervals and include an upward propagating pulse. We use the top of this pulse as a characteristic point to follow its propagation and measure its travel times from one sensor depth to the other. At the 14m subplot in Figure 2, two pulses appear, one on the negative side of the time axis and one on its positive side. This means that there is significant wave energy that has been reflected at the surface and propagated downward, but it does not affect our results, which are based solely on time measurements on the negative side. In recordings richer in low frequencies, or as V_P increases, the two pulses may move closer together and become inseparable, making it impossible to measure V_P.

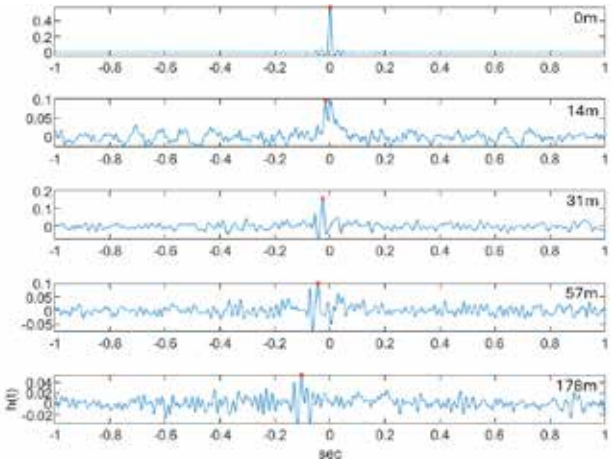

Figure 2. Example output of the interferometry by deconvolution on the vertical components of a record (29/12/2011, 15:19UTM, M_L3.5, R14km) at the CORSSA site. Each subplot shows the deconvolution of a waveform at the depth marked on the top right with respect to the waveform at the surface. A propagating pulse appears on the negative side of the x-axis and its top is marked (red dot) as a characteristic point to measure time differences (i.e., travel times).

V_P from seismic interferometry by deconvolution

We have applied seismic interferometry by deconvolution to resolve P-wave velocities in the depth intervals 0-14 m, 0-31 m, 0-57 m, 0-178 m, 14-31 m, 31-57 m, and 57-178 m. As noted above, there are inherent difficulties in applying the method to the much faster P-waves. The first is the sampling rate commonly used for ground acceleration monitoring, which is low for resolving very small changes in the propagation time of the impulse response of soft soils. In our case (sampling rate of 200 s/s), we limit this restriction to some extent by resampling the interferometric result at a higher rate, allowing a more accurate measurement of the travel times. The second major difficulty is the very high velocities of the P-waves, even in soft sediments, which in combination with the often small distances between the stations result

in extremely short travel times that cannot be resolved. A third difficulty is that the wavelengths of interest change as we attempt to define velocities at different depth intervals, and not all recordings have the necessary frequency content to provide an unambiguous time reading. As a result, the efficiency of the method at a particular location and depth interval may not always be known a priori, but only through trial and error. Furthermore, even if the method is successful but V_P increases with time, it may fail above a certain level of increase.

For all of the above reasons, in our application at the CORSSA site although we had many stable results, we also had numerous "outliers", which we define in the following. To isolate and work with the most populated concentrations of resulting V_P values, we applied a two-step interquartile range (IQR) outlier removal. First, we removed V_P values that were outside 3 times the IQR (Q3-Q1) of the overall distribution. These "extreme" outliers were also manually checked and were found to be related to poor quality waveforms or to the events with the richest low-frequency signal, resulting in broad pulses with an almost flat top (i.e., the area where we usually expect a sharp peak to be used for travel time measurement). In the second step, we performed a standard removal of values outside 1.5 times the IQR. The procedure is shown graphically in Figure 3 for the example case of the 0-14m depth interval. The IQR, i.e., the area where 75% of the computed values are concentrated, is shown in purple and the lighter color marks the 1.5×IQR area. Everything that falls within these two areas is included in the subsequent analysis, and values outside these areas are considered outliers. Figure 3 also marks the mean of the finally considered values ± 1 standard deviation (s.d.).

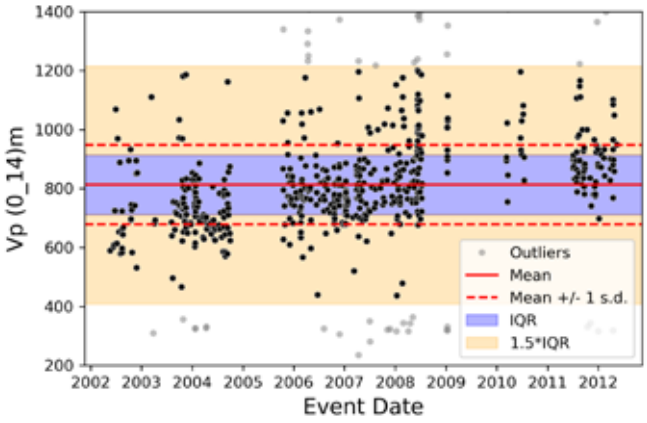

Figure 3. Graphical description of the outlier removal procedure for the example case of V_P estimates for the depth interval 0-14m. Gray points, lying beyond 1.5 times the interquartile range (IQR) (orange shaded area), are considered as outliers and are not being used in the estimate of the mean V_P value.

The results of the interferometry by deconvolution for all depth intervals examined are summarized in Table 1. More specifically, Table 1 lists percentage of final data points and outliers with respect to the initial dataset of 709 earthquake records for each depth interval, the mean V_P ± 1 s.d. and the corresponding information for the two horizontal components (from Roumelioti et al., 2018), east-west (V_{Se}) and north-south (V_{Sn}), for comparison. The agreement of the results of the two V_S is remarkable, as well as the amount of data finally considered for V_P despite the difficulties mentioned above. The depth interval with the largest number of outliers, for both V_P and V_S computations is the 0-178m interval. This is a rather unsurprising result considering the very weak character of most of the waveforms in the dataset (Kassaras et al., 2016) (Figure 1c). An interesting finding was the high mean V_P in the 14-31m depth interval, quite higher than the underlying examined "layer", most likely indicating an increased presence of groundwater.

Table 1. Mean V_P and V_P/V_S values inferred from interferometry for the CORRSA site and percentages of determined values and outliers with respect to the starting dataset. Depth intervals are defined by the downhole sensors' installation depths. V_S values for the two horizontal components of Roumelioti et al. (2018) are included for comparison.

Depth Interval (m)	Data/Outliers (%) for V_P	V_P (± 1s.d.) (m/sec)	Data/Outliers (%) for V_{Se}	V_{Se} (± 1s.d.) (m/sec)	Data/Outliers (%) for V_{Sn}	V_{Sn} (± 1s.d.) (m/sec)	V_P/V_{Se}	V_P/V_{Sn}
0-14	76/24	813 (135)	97/3	208 (7)	97/3	214 (8)	3.9	3.8
0-31	93/7	1135 (107)	99/1	240 (6)	98/2	240 (6)	4.7	4.7
0-57	77/23	1224 (96)	96/4	268 (4)	94/6	268 (4)	4.6	4.6
0-178	67/33	1710 (59)	63/37	430 (4)	61/39	424 (15)	4.0	4.0
14-31	76/24	1754 (233)	93/7	277 (7)	86/14	271 (11)	6.3	6.5
31-57	81/19	1382 (46)	91/9	308 (3)	93/7	314 (4)	4.5	4.4
57-178	87/13	2140 (32)	71/29	602 (5)	60/40	583 (11)	3.6	3.7

Figures 4 and 5 show the results graphically, Figure 4 for interferometry results with respect to the surface station and Figure 5 for pairs where both stations were in boreholes. Each row of the subplots corresponds to a different depth interval (i.e., station pair in the interferometry), while the columns from left to right include: the V_P values derived in this study, the V_{Se} and V_{Sn} values computed by Roumelioti et al. (2018) using the same method. In all subplots, the mean velocity ± 1 s.d. (i.e., the values included in Table 1) is also marked. Although our dataset is not continuous in time, it is clear that there is a temporal variation in both V_P and V_S values that increases in amplitude with depth. Although the left column in Figure 4 may suggest some seasonal variation, it is certainly not as clear as for V_S, and the temporal discontinuity of the dataset examined, as well as the variability of V_P make any identification even more difficult. It is possible that the temporal variation of V_P is longer in period than an expected seasonal one. This can be seen very clearly in the upper left subplot of Figure 4, where V_P values in 2003-2004 are mostly clustered around 700m/s, whereas in 2006-2008 they are around 800m/s. Reasons for such slower changes could be, for example, multi-year changes in groundwater, or sudden compaction of sediments after shaking caused even by relatively distant strong earthquakes.

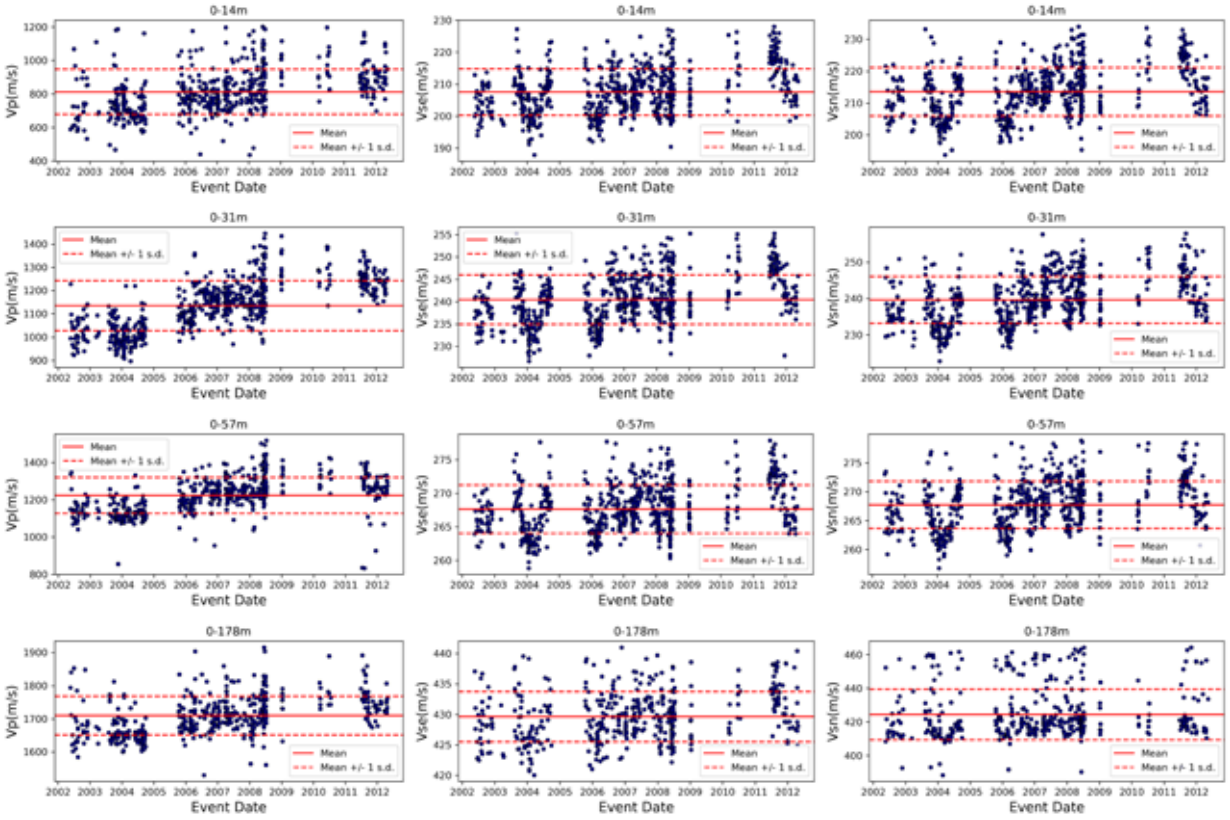

Figure 4. Velocity variation with time for depth intervals noted at the top of each subplot (0-14m, 0-31m, 0-57m, 0-178m from top to bottom. The left column contains the V_P values, the middle the V_S in the east-west component (V_{Se}) and the right column the V_S in the north-south component (V_{Sn}). V_S values are taken from Roumelioti et al. (2018).

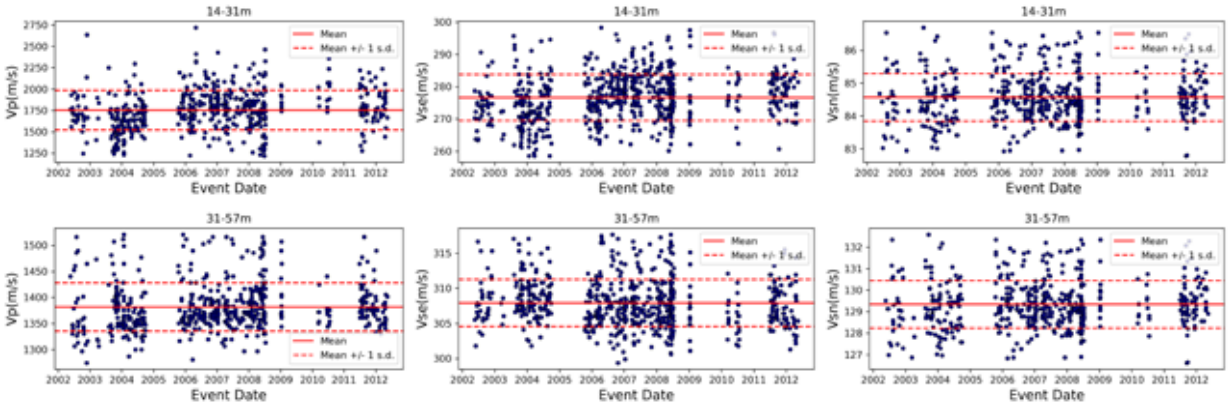

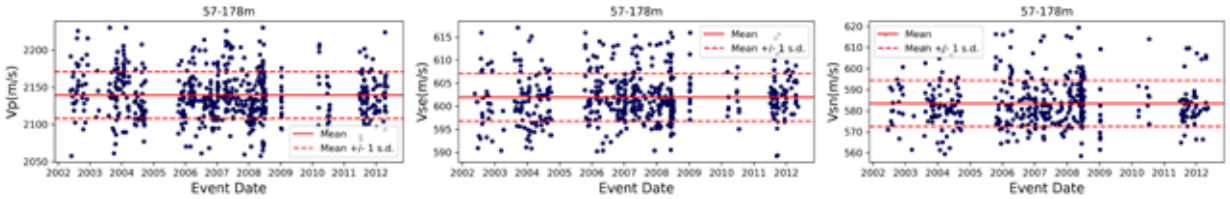

Figure 5. As in Figure 5, but for the intermediate depth intervals (from top to bottom) of 14-31m, 31-57m, and 57-178m.

V_P profile at the CORSSA site

The mean VP values derived for the depth intervals 0-14m, 14-31m, 31-57m and 57-178m are plotted in Figure 6 in the form of a velocity profile, along with previously proposed VS profiles (CORSSA, 2002; Roumelioti et al., 2018). Although the applied method provides well-constrained mean VP values directly at the site and from actual ground motio data, a shortcoming is that the interferometric "layer" thicknesses in Figure 6 have no physical or geological meaning and are defined by the depths of the sensors in the accelerometer array.

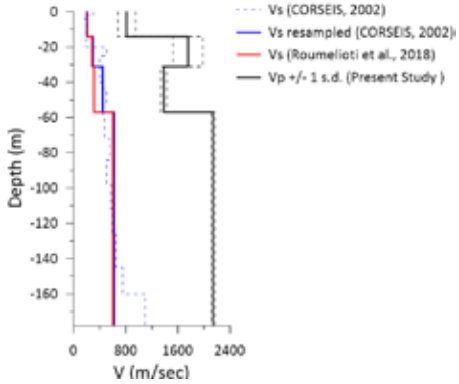

Figure 6. Seismic wave velocity profiles at CORSSA. The V_P profile is a result of this study and "layers" thicknesses are enforced by the depths of the borehole array sensors. The V_S profiles are from Roumelioti et al. (2018) and include the information from the European project "CORSEIS" (2002) as originally provided and resampled at the depth intervals of the CORSSA array.

V_P/V_S ratio

The last two columns in Table 1 show the V_P/V_S using the mean velocity values for each depth interval examined. The results using the mean V_S values in the two horizontal components show insignificant differences. V_P/V_S has values <4 in the shallowest (0-14m) and deepest (57-178m) depth ranges and well >4 in the 14-31m and 31-57m intervals. Figure 6 shows how these values compare to previously published V_P-V_S relations. We chose to compare the CORSSA values to the empirical relation of Brocher (2005), who has incorporated many northern California profiles that are more representative of younger tectonic terranes such as the one examined in this study. We also compare our values with two relations proposed in a more recent study by Nagashima and Kawase (2021), which is based on a very large number of KiK-net and K-NET station sites in Japan. Nagashima and Kawase (2021) found an abrupt increase in V_P around 4m depth and attributed it to the transition from unsaturated to saturated soil formations. As a result, they proposed two different V_P-V_S relationships. The CORSSA values for the three deepest ranges investigated compare well with the Brocher (2005) relation and the saturated soil version of Nagashima and Kawase (2021). The 0-14m appears to be more compatible with the unsaturated version of the Nagashima and Kawase (2021) relationship, suggesting that the top 14m at CORSSA is mostly unsaturated. This is also supported by the absolute value of the mean V_P for this layer, ~ 800m/s, which is much lower than the speed of P-waves in water (1200 to >1400 m/s, also depending on the salinity).

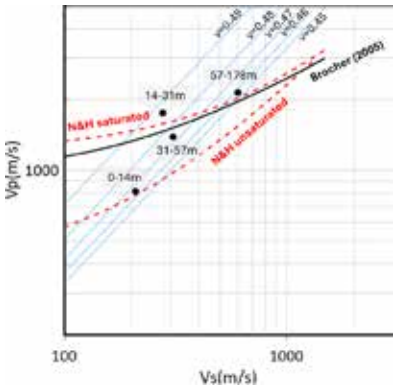

Figure 6. Mean V_P versus mean V_S for the examined depth intervals at the CORSSA site. Blue straight lines mark the V_P, V_S relation for Poisson's ratios (v) of 0.45-0.49. Previously published pertinent relations are also shown for comparison; black curve for Brocher (2005) and red dashed curves for Nagashima and Kawase (2021; N&H) for saturated and unsaturated soils.

Conclusions/Discussion

We applied the method of seismic interferometry by deconvolution to the vertical components of a dataset of 709 earthquake records at the CORSSA borehole array. We examined the four borehole stations of the array (at depths of 14, 31, 57 and 178m) with respect to the surface station, as well as station pairs at 14-31m, 31-57m, and 57-178m, and computed V_P velocities for the corresponding depth intervals. Due to the high velocities of the P-waves, the short distances examined and the weak character of most of the waveforms in the dataset, the results included several unrealistically high or low V_P values, many of which were removed as outliers using a two-step interquartile outlier removal approach. The outliers for the V_P computation were in the range of 7-33% of the initial number of data points, which is considered rather small considering the previously mentioned difficulties in measuring V_P. Based on the final data points, we computed the mean $V_P \pm 1$ s.d. for each depth interval examined and we provided a V_P velocity model for the site of the CORSSA infrastructure. We used our V_P values and the V_S values of Roumelioti et al. (2018) to compute V_P/V_S ratios for the different depth intervals examined, but also to demonstrate that continuous monitoring of this quantity is feasible with the applied method.

Acknowledgements

The study was carried out in the framework of the research project "UNMASK", supported by the Hellenic Foundation for Research and Innovation (H.F.R.I.) under the "2nd Call for H.F.R.I. Research Projects to support Faculty Members & Researchers" (Project Number: 2724).

References

Brocher, T.M., 2005. Empirical relations between elastic wave speeds and density in the earth's crust. Bull. seism. Soc. Am. 95, 2081–2092.

Chandra, J., Guéguen, Ph., Bonilla, L.F., 2016. PGA-PGV/VS considered as a stress-strain proxy for predicting nolinear soil response. Soil Dynamics and Earthquake Engineering 85, 146-160.

Clayton, R.W., Wiggins, R.A., 1976. Source shape estimation and deconvolution of teleseismic bodywaves. The Geophys. J. of the Royal Astronomy Soc. 47, 151-177.

CORSSA, 2002. Project Final Report, available in hard copy from the Research Unit of Soil Dynamics and Earthquake Engineering of the Department of Civil Engineering of the Aristotle University of Thessaloniki (personal communication with M. Manakou).

Guéguen, Ph., 2016. Predicting nonlinear site response using spectral acceleration VS PGV/VS30: A case history using the Volvi-Test site. Pure Appl. Geophys. 173(6), 2047-2063.

Kassaras, I., Roumelioti, Z., Ktenidou, O.-J., Pitilakis, K., Voulgaris, N., Makropoulos, K., 2016. Accelerometric data and web portal for the vertical Corinth Gulf soft soil array (CORSSA). Bulletin of the Geological Society of Greece, 50(2), 1081–1090.

Nagashima, F., Kawase, H., 2021. The relationship between V_S, V_P, density and depth based on PS-logging data at K-NET and KiK-net sites. Geophys. J. Int. 225, 1467 – 1491.

Nakata, N., Snieder, R., 2012. Estimating near-surface shear wave velocities in Japan by applying seismic interferometry to KiK-net data. J. Geophys. Res. 117 B01308, 1-13.

Qin, L., Steidl, J.H., Qiu, H., Nakata, N., Ben-Zion, Y., 2022. Monitoring Seasonal Shear Wave Velocity Changes in the Top 6 m at Garner Valley in Southern California with Borehole Data. Geophys. Res. Lett. 49.

Roumelioti, Z., Hollender, F., Gueguen, Ph., 2018. Shear wave velocity variations at the CORSSA (Central Greece) vertical array. 16th European Conference on Earthquake Engineering, Thessaloniki, Greece, p. 12.

Roumelioti, Z., Hollender, F., Guéguen, P., 2020. Rainfall-induced variation of seismic waves velocity in soil and implications for soil response: What the Argonet (Cephalonia, Greece) vertical array data reveal. Bull. Seismol. Soc. Am. 110, 441–451.

17th INTERNATIONAL CONGRESS of the Geological Society of Greece

BULLETIN OF THE GEOLOGICAL SOCIETY OF GREECE, SP. PUBL.

EXTENDED ABSTRACT 272

Establishing the soil geochemical mapping in Lesvos Island, Greece

Roussos A.[1], Kelepertzis E.[1], Kypritidou Z.[1], Aivatzidis, E.[1], Drougas C.[1], Vassilakis, E.[1], Voudouris, P.[1], Zouros N.[2]

(1) Department of Geology and Geoenvironment, National and Kapodistrian University of Athens, Panepistimioupolis, Zografou, 15784, Athens, Greece

(2) Geography Department, University of the Aegean, Mytilene, 81100, Lesvos, Greece

Research Highlights

- Effect of different lithological types on the chemical composition of the soil.
- Application of multivariate analysis and G.I.S. techniques to determine controlling factors on soil geochemistry.

Abstract

Geochemical mapping is commonly applied by geoscientists to document the spatial distribution of elemental concentration levels in materials occurring at the Earth's surface, such as soil. Here, we present the applied methodology for establishing the soil geochemical mapping in the unique island of Lesvos that exhibits a complex geological structure with different rocks occurring on island surface. A total of 74 surface (0-20 cm depth) soil samples were collected from 66 locations on a 5 km x 5 km grid extending across the whole island. Preliminary results in terms of distribution of major and trace element concentrations and interpretations based on geology and mineralization will be presented.

Introduction / Background and Objectives

Geochemical mapping is a technique rooted in mineral exploration but has now found worldwide application in environmental studies. Geochemical mapping has a crucial role, nowadays, not only for mineral exploration, but also for studies about environment and human health (Kirkwood et al., 2016). Officially, International Geochemical Mapping Project was accepted by UNESCO/IUGS just in 1988 and technical – regional committees, which include scientists and organizations from all over the world, coordinated the project with aim to resolve scientific and technical issues. For example, many surveys have a huge number of samples that have been analyzed for different groups of elements by a variety of analytical methods, with uncertain quality control (Darnley, 1990). Another problem is the sampling density and the map scale that should be followed, but these depend on the objectives of each project (Demetriades et al., 2022). By definition the geochemical maps are based on the concentrations of chemical elements from samples of surface media such as soil, water or stream sediments (e.g. Salminen et al., 1998).

In this project, Lesvos Island is the study area and soil samples were collected in order to produce geochemical maps of elements across the whole island. The samples were collected during July 2024 and the aim was to contribute new knowledge in terms of the geochemical characterization of the island. The density of soil sampling followed a 5 km x 5 km grid in order to produce a comprehensive geochemical mapping of the island's soils.

The diverse geological formations that occur on the island, the various types of mineralizations found in the northeastern Aegean, but also the limited research on the geochemistry of the island's soils, motivated us to carry out this research. The main objective is the accomplishment of the soil geochemical mapping in terms of major and trace elements with the aim to determine the effect of local geology on soil geochemistry. On the island of Lesvos, geological mapping has been carried out previously (Hecht, 1972; Katsikatsos et al., 1986; Thomaidou, 2009), but extensive geochemical mapping of soils on the island has not been carried out.

Description of the study area

Lesbos is the third largest island in Greece, covering an area of 1,630 km² and is located in the northeastern part of the Aegean Sea, very close to the Anatolian coast. Regarding the geomorphology of Lesbos, two large, enclosed bays dominate the southern part of the island: Kalloni Bay and Geras Bay, which are clearly related to the tectonic evolution of the broader northern Aegean area and especially to the neotectonic activity. Two large mountain masses, Mount Lepetymnos (968 m) at the northern part and Mount Olympus (967 m) at the southern part of Lesbos, between the two bays, stand out on the overall mountainous island of Lesbos. In general, the topography of Lesbos is varied, showing abrupt changes and is quite pronounced in other areas as well, such as the Amali Peninsula (527 m) and especially in the western part, where Mount Ordymnos (589 m) dominates, creating a very impressive landscape with steep transitions toward the island's western coast (Thomaidou, 2009).

Lesbos Island, located in the northeastern Aegean Sea, is known for its unique geological features, diverse

rock formations, and significant tectonic activity. The island's geology offers a fascinating glimpse into the Earth's geological processes, particularly with respect to its volcanic history, the presence of numerous mineral deposits, and its tectonic setting along the boundary of the Eurasian and African plates (Apostolopoulos et al., 2009).

Lesbos has a rich volcanic history. Volcanic activity is responsible for much of the island's landscape, with lava flows, volcanic ash deposits, and geothermal activity still visible in several locations. The island's most famous volcanic area is near Molyvos, where extensive basaltic lava flows have been found. Sigri, on the western part of the island, is another significant volcanic site, with large volcanic deposits and fossilized lava formations (Georgiadis, 2001).

Obviously, the geological structure and composition of Lesvos played a key role in the geomorphology of the island. The western and northern parts are mostly covered by volcanic rocks and there are the important volcanic centers of the island. This is one more element that contributes to the morphology, with the existence of large calderas (e.g. the caldera of Vatoussa), but also the presence of important dykes (e.g. the dome of Ypsilos) that characteristically elevate the morphology of the island, creating large differences in altitude with rounded mountain ranges without vegetation (Papadopoulos et al., 1991).

On the contrary, the south-east part of Lesvos, i.e. the areas of Mount Olympus, the village of Agiasos up to the town of Plomari, as well as the area around the Gulf of Gera and the peninsula of Amalis, have a mountainous landscape but smoothed by erosion and with significant vegetation cover (Papadopoulos et al., 1991).

However, it is mainly neotectonic activity that has played a decisive role in shaping the morphology of Lesbos, as it is responsible for the large depressions of height and the strong transitions that occur (Apostolopoulos et al., 2009), as Turkey's microplate moves to the SW and pushes the Aegean area, forcing it to make an expansion in the same direction. The wider tectonic field in the NE Aegean region is dominated by the action of large clockwise horizontal displacement faults, on which the region is mainly moving and which, together with normal-moving fault surfaces, form the lacy-looking Asia Minor coastline (Georgiadis, 2001).

At Western Lesbos volcanic rocks dominate, mainly basalts and andesites, along with pyroclastic deposits (tuffs and tephra). Central and Eastern Lesbos are characterized by the occurrence of predominantly sedimentary rocks, including limestone, marl, conglomerates and sandstones. Also, at specific regions, north and at the center of the island, metamorphic rocks are observed, such as schists and gneisses. In the western region of the island, Sigri, fossil-rich sedimentary rocks are observed (Papanikolaou, 2005) and of course geothermal deposits, such as silica, appeared in some regions of the island linked to geothermal springs (Georgiadis, 2001).

The rest of Lesvos, i.e. the northern, western and central parts of the island around the Gulf of Kalloni, is occupied by Neogene volcanic formations (Figure 2) and other mineral deposits covering the pre-alpine and alpine rocks universally. Exceptions are the small outcrops of alpine and pre-alpine rocks in the north-western edge of Lesvos in the areas of Sigri and Gavathas and some isolated micro-outcrops of the same rocks in the area of Eressos. These small occurrences are exposed beneath the surrounding Neogene volcanic formations in the form of island (Thomaidou, 2009).

Lesbos Island's mineral deposits are mostly associated with its volcanic history and hydrothermal activity. Although the island is not renowned for large-scale mining operations, there are localized mineral occurrences worth noting. For example, silica was deposited through hydrothermal processes during and after volcanic activity in the Miocene epoch and was found in hydrothermal veins and as silicified material in the Petrified Forest. The fossilized trees in the Petrified Forest are a result of extensive silicification, making silica the most visually striking mineral deposit on the island. Sulfide minerals, such as Chalcopyrite (CuFeS□) and Galena (PbS) are scattered and often localized to hydrothermal zones near volcanic centers. Clay Minerals, such as Kaolinite and Montmorillonite formed through the hydrothermal alteration of volcanic rocks and found in areas with extensive weathering and hydrothermal influence. Also, there have been occasional reports of minor occurrences of Gold (Au) associated with hydrothermal quartz veins, though in trace amounts, and Copper (Cu) linked to chalcopyrite in volcanic and hydrothermal systems.

The island's land use is characterized by extensive olive cultivation, significant forested areas, agricultural zones, and protected natural habitats (Figure 1). The most esteemed olives are harvested between Plomari and Agiasos from November to December. Lesbos features diverse forested regions, including pine and oak forests, as well as Mediterranean maquis vegetation. The island's varied habitats support a rich array of plant species, contributing to its impressive biodiversity. Beyond olive groves, Lesbos maintains areas dedicated to vineyards, pastures, and other agricultural activities. Livestock farming, particularly sheep and goats, is also prevalent, supporting the production of traditional cheeses.

Also, recognizing its ecological significance, several areas of Lesbos are designated under the Natura 2000 network, aiming to preserve valuable and endangered species and habitats. Notable protected regions include:

- Kalloni Bay: A vital wetland area supporting diverse bird species.

- Gera Bay – Mount Olympus: An area encompassing significant ecological elements.
- Western Lesbian Peninsula: A region with unique ecological features.

These protected areas underscore Lesbos's commitment to conserving its unique natural environment.

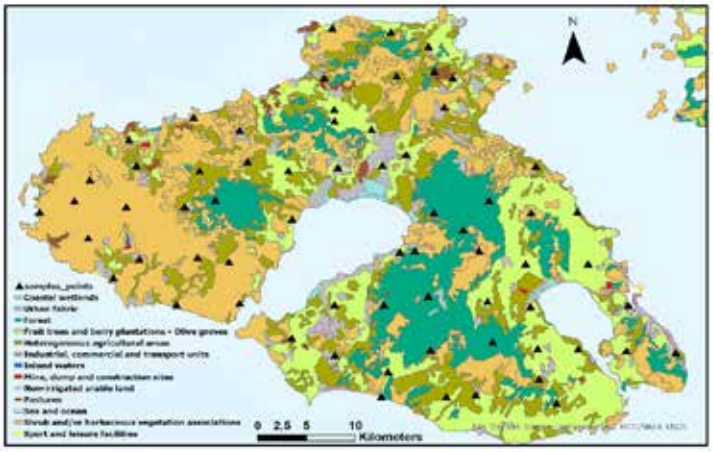

Figure 1: Land use map of the study area in Lesvos Island, showing sampling points on the Corine Land Cover (CLC) map (Heymann et al., 1994).

Sampling and Analysis

A total number of 74 soil samples (0 – 20 cm depth), from 66 locations, were collected from all over the island (Figure 2). The sampling procedure was common for the collection of 66 soil samples, as well as for the 8 randomly selected duplicate samples. All soil samples were collected at distance at least 200 m from main roads and away from tree roots, recent crops and rubble. To collect the soil sample, it was necessary to create a square with a side of 20 cm and digging to a depth of 10-20 cm (Demetriades et al., 2022). Approximately 1.5 - 2 kg of sample was collected, and the duplicate samples were spaced 3 m apart from each other (Demetriades et al., 2022). After daily collection of soil samples, the bags of these samples were left open in order to release the soil moisture. Upon return to the laboratory, they were placed in a drying oven at 40°C for 48 hours to remove the volatile components of the soil.

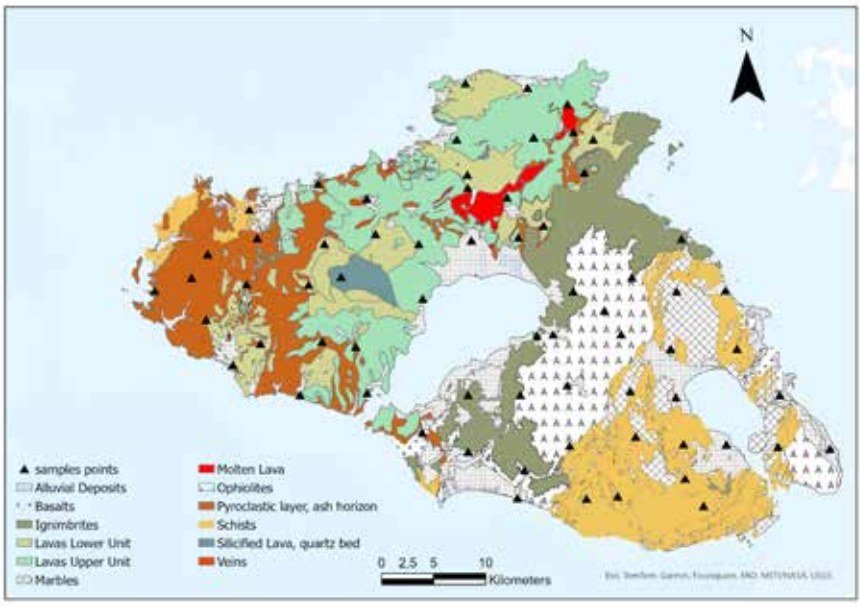

Figure 2: Geology (Hecht, 1972) and sampling points of the soil samples in Lesvos Island.

Sample preparation included disaggregation, during which each soil sample was disaggregated in a porcelain mortar

and sieved through a 2 mm sieve. Between the samples, the mortar and sieve were thoroughly cleaned with air and acetone. A portion of the 2mm fraction of the soil samples was mechanically pulverized in an automatic agate mortar to obtain a particle size of <0.063 mm. Initially, the soil samples were homogenized and divided in four quarters. Two of the diagonal quarters of the soil sample were selected to be pulverized. This step is repeated (3 times in total) to obtain approximately 100 ml of soil sample of less than 200 μm in size. Between the samples, the mortar was also cleaned with 30 ml of cristobalite to avoid cross contamination. The mortar and the tools used (spoon, beakers, brushes) were thoroughly cleaned with air and acetone (where necessary) after the end of the powdering of each sample.

The analysis will be carried out with aqua regia for soils and the samples will be analyzed by ICP-MS for trace elements (e.g. As, Cd, Zn, Pb, Cu, Cr, Ni) and by ICP-OES for major elements (e.g. K, Na, Ca, Fe, Al, Mg).

Results and Discussion

The analytical data will be processed in terms of quality control and the elemental concentrations will be compared with the island's geology.

Acknowledgements

Geochemical analyses and fieldwork were supported by the Natural History of the Lesvos Petrified Forest and the Special Account for Research Grants, NKUA (MSc programme: Earth Sciences and Environment, Department of Geology & Geoenvironment, National and Kapodistrian University of Athens).

References

Apostolopoulos, G., & Dimitriadis, A., 2009. Geology of the Aegean Sea: Contributions to the tectonic evolution of the eastern Mediterranean. Springer.

Darnley, A.G., 1990. International geochemical mapping: a new global project. Journal Geochemical Exploration 39. 1–13.

Demetriades, A., Johnson, C.C., Smith, D.B., Ladenberger, A., Adánez Sanjuan, P., Argyraki, A., Stouraiti, C., Patrice de Caritat, Knights K.V., Rincón G.P., Simubali, G.N., 2022. International Union of Geological Sciences Manual of Standard Methods for Establishing the Global Geochemical Reference Network. The International Union of Geological Sciences (IUGS).

Georgiadis, S., 2001. Volcanic and Geothermal Features of Lesbos Island. Hellenic Geological Society, Athens.

Hecht, J., 1972. Geological map "Plomari-Mytilini" sheet, scale 1:50.000. I.G.M.E.

Heymann, Y., Steenmans, Ch, Croissille, G., Bossard, M., 1994. Corine Land Cover. Technical Guide, EUR12585. Office for Official Publications of the European Communities, Luxembourg.

Katsikatsos, G., Migiros, G., Triantaphyllis, M. and Mettos, A., 1986. Geological structure of the internal Hellenides (E. Thessaly - SW. Macedonia, Euboea - Attica - Northern Cyclades Islands and Lesvos). I.G.M.E. Geological and Geophysical Research. Special Issue, 191-212.

Kirkwood, C., Cave, M., Beamish, D., Grebby, S., Ferreira, A., 2016. A machine learning approach to geochemical mapping. Journal of Geochemical Exploration 167. 49–61.

Papadopoulos, G., & Papanikolaou, D. (1991). The Geology of the Island of Lesbos. Bulletin of the Geological Society of Greece, 25(2), 287–297.

Papanikolaou, D., 2005. Pleistocene Fossils and Stratigraphy of Lesbos Island. Journal of the Geological Society, 162(2), 253-265. .

Salminen, R., Tarvainen, T., Demetriades, A., Duris, M., Fordyce, F., Gregorauskiene, V., Kahelin, H., Kivisilla, J., Klaver, G., Klein, H., 1998. FOREGS Geochemical Mapping Field Manual.

Thomaidou, E., 2009. The geological structure of the island of Lesvos.

17th INTERNATIONAL CONGRESS of the Geological Society of Greece

BULLETIN OF THE GEOLOGICAL SOCIETY OF GREECE, SP. PUBL.

EXTENDED ABSTRACT 273

Pluto is lost!

Rozi A.[1] , Papadimitriou Z.[2]

(1) 3rd Junior High-school of Glyfada , Athens, Greece, rosi_corina@yahoo.gr (2) 3rd Junior High-school of Glyfada , Athens, Greece

Abstract

This paper examines the integration of drama and science as an innovative approach to teaching scientific concepts, focusing on the educational theatrical production *Pluto is Lost!*, created and performed by students at the 3rd Junior High School of Glyfada, Athens, Greece. The initiative aimed to introduce students to the Solar System and environmental science—subjects often overlooked in the Greek compulsory school curriculum—while fostering creativity, teamwork, and critical thinking. The project was implemented within the framework of the "Learning Science Through Theatre" program, which promotes interdisciplinary learning by merging science education with artistic expression.

Through a project-based learning model, students engaged in five phases: defining goals, designing, executing tasks, presenting results, and evaluating outcomes. They humanized astronomical and environmental concepts by creating a storyline where celestial bodies and Earth's ecosystems were personified, and the dynamics of the Solar System and environmental sustainability were explored through imaginative narratives. The embodied learning process enabled students to express scientific ideas through gestures, movements, and emotional engagement, enhancing comprehension and retention.

The production also addressed contemporary challenges, such as climate change, environmental conservation, and societal issues, connecting science to real-world contexts. Dissemination efforts included performances in collaboration with local institutions and recognition through multiple awards, including the "Learning Science Through Theatre" award for best theatrical and musical performance, the EPI2 award from the Athens Science Festival, and presentations at COSPAR 2022 (Athens, Greece) with the latter receiving a full grant.

The study concludes that combining science and theatre effectively engages students, promotes scientific literacy, and encourages creative exploration of complex topics. This initiative highlights the potential of arts-based methods in science education, offering a replicable model for fostering interdisciplinary learning and inspiring passion for STEAM fields.

Figure 1. Asteroids Dancing

Acknowledgements

The authors would like to express their gratitude to Mr. Menelaos Sotiriou, Dr. Zacharoula Smyrnaiou, and Science View for their invaluable support and guidance throughout this project.

References

Aikenhead G. (2006) *Science education for everyday life: Evidence-based practice* (New York and London, Teachers' College Press).

Alexopoulos I., Sotiriou S., Smyrnaiou Z., Sotiriou M., Bogner F (2016) *Developing an Engaging Science Classroom* Available online at https://www.researchgate.net/publication/312176004_Developing_an_Engaging_Science_Classroom (accessed 11 July

2022).

Braund M. (2010) *Talk in science: Forgotten corner of the constructivist classroom?,* in: D. Mogari, A. Mji, F. Mundalamo, U. Ogbonnaya (Eds) *Proceedings of the ISTE international conference on mathematics, science and technology education: towards effective teaching and meaningful learning in mathematics, science and technology education*. Mopani Camp, Kruger National Park, South Africa, 18–21 October 2010 (Pretoria, University of South Africa (UNISA) Press), 287–301.

Braund, M. (2013) *Drama and learning science: An empty space?* Available online at https://www.researchgate.net/publication/260410840_Drama_and_learning_science_An_empty_space (accessed 11 July 2022)

Brinder, K., Anuj, S.(2004) *S & T Communication through pupperty – A case study (India)* Available online at https://www.academia.edu/48647908/S_and_T_Communication_Through_Puppetry_a_Case_Study_India_(accessed 11 July 2022)

Musacchio, G, Lanza, T, D'Addezio(2015) *An Experience of Science Theatre to Introduce Earth Interior and Natural Hazards to Children* Available online at https://www.ccsenet.org/journal/index.php/jel/article/view/43677 (accessed 11 July 2022)

Ødegaard, M. (2003) Dramatic science. A critical review of drama in science education, *Studies inScience Education*, 39(1), 75–101.

Smyrnaiou, Z., Georgakopoulou, E., Sotiriou, M., Sotiriou, S. (2018). Constructing Scientific Notions: Students' Conceptual Change through a Re-sponsible Research and Innovation Initiative. Co-Create ! - Co-creation of curricula, tools and educational scenarios for building softcompetences for personal development and employability (Multi-conference on Responsible Research and Innovation in Science, Innovation and Society m-rrisis 2018). Tartu, Estonia, 17-19 Septembre

Smyrnaiou Z., Georgakopoulou E., Sotiriou M., Sotiriou S. (2017). The Learning Science Through Theatre initiative in the context of Responsible Research and Innovation. Proceedings of The 10th International Multi-Conference on Society, Cybernetics and Informatics: IMSCI 2017

Toonders, W., Verhoeff, R.P., Zwart, H.A.E.(2016) *Performing the future: on the use of drama in philosophy courses for science students* Available online at https://repository.ubn.ru.nl/handle/2066/161707 (accessed 11 July 2022)

17th INTERNATIONAL CONGRESS of the Geological Society of Greece

BULLETIN OF THE GEOLOGICAL SOCIETY OF GREECE, SP. PUBL.

EXTENDED ABSTRACT 274

Rheological behaviour along the Hellenic Subduction Zone and the Adria-Eurasia continental collision

Russo D.[1,2], Caputo R.[1,2]

(1) Department of Physiscs and Earth Sciences, University of Ferrara, Ferrara, Italy, davide.russo@unife.it (2) Centro Interuniversitario per La Sismotettonica Tridimensionale, CRUST-UR Ferrara, Italy

Based on the approach and workflow of the recently proposed 3D thermo-rheological model of the broader Aegean Region (Maggini et al., 2023), the present work focuses on the rheological properties corresponding to both the slab interface of the Hellenic Subduction Zone (HSZ) and the basal thrust of the Adriatic-Eurasian Continental Collision Zone (CCZ). For the purpose of this note, the geometry of the interfaces (Figure 1) was mainly reconstructed on the basis of the results of Bocchini et al. (2018), especially for the HSZ sector, and Halpaap et al. (2018) for the continental collision zone. For the Montenegro sector of the CCZ, the results of Schmitz et al. (2020) were also considered.

The aforementioned 3D model is based on a simplified approach: two main rheological behaviours have been assumed to occur at depth within the study area, namely the brittle and the ductile, described by the constitutive equations for frictional sliding (e.g. Sibson, 1977; Scholz, 1988; Ranalli, 1995) and power-law creep (e.g. Brace and Kohlstedt, 1980; Sibson, 1983; Ranalli, 1995) deformational mechanisms, respectively.

The calculations required to reproduce the thermo-rheological features of the considered area have been performed through purposely written MATLAB scripts (Maggini, 2020; Maggini and Caputo, 2020a; 2020b; 2021). The first output obtained is a number of 1D rheological profiles or “strength envelopes” (e.g. Sibson, 1977; Goetze and Evans, 1979; Brace and Kohlstedt, 1980; Scholz, 1988), which reconstruct the vertical rheological behaviour and the geothermal gradient of the investigated rock volumes in correspondence of the nodes of a regular horizontal grid (115 x 115 pixels). Among the input parameters, a considerable influence was attributed to the heat flow; derived merging and smoothing, applying a Gaussian filter in order to remove outliers, local-scale (e.g. Fytikas and Kolios, 1979; Taktikos, 2001) and regional scale (e.g. Hurter and Haenel, 2002; Cloetingh et al., 2010) measurements. The adopted strain rate was based on weighted and averaged available maps mainly derived from GPS measurements (e.g. Kahle et al., 1998; Hollenstein et al., 2008; Floyd et al., 2010; Kreemer et al., 2014; Chousianitis et al., 2015; England et al., 2016). Considering the results of Byerlee (1968) a standard value (0.6) was attributed to the internal friction coefficient; however, in correspondence of major the seismogenic sources (from GreDaSS 2.0; Caputo and Pavlides, 2013) this value was reduced to 0.5. This choice was motivated by the presence of well-defined shear zones in these crustal volumes, characterized by wearing processes that cause a significant reduction in the friction coefficient values (e.g. Viti et al., 2018; Collettini et al., 2019). For the frictional sliding equation, the Skempton coefficient (e.g. Skempton, 1954; Wang, 2000) was taken equal to 0.4, basically assuming, as a first approximation, a hydrostatic fluid pressure (e.g. Ranalli and Murphy, 1987; Ranalli, 1995). Both the upper and lower plates were modelled considering four vertical litho-mechanical layers (i.e. sedimentary cover, upper crust, lower crust and upper mantle), each one associated to a representative lithology and the related thermo-rheological parameters given by the considered constitutive equations (see Maggini, 2020 for a more detailed description and references).

The thickness of the considered layers was reconstructed from the depth of the top of the crystalline basement, the Moho discontinuity and the Lithosphere-Asthenosphere Boundary (LAB). The first two were strongly influenced by the work of Makris et al. (2013), while the LAB from the work of Sodoudi et al. (2006).

The selected pixel size for the 3D model is 10 x 10 km with vertical steps each 100 m. All the input parameters, have been accordingly averaged using standard GIS tools. In order to provide the 3D cover for the Aegean Region, the 1D logs were then interpolated to reconstruct a pseudo 3D model.

Following the general results of Maggini et al. (2023), and for the purpose of the present note, we examined a 500 m thick volume on each side of the modelled plate boundary (Figure 1), in both the continental-continental and oceanic-continental lithosphere domains, north and south of the Cephalonia Transform Fault Zone, respectively. In particular, we analysed the rheological behaviour of the lowermost part of the upper plate (i.e. Eurasian or Aegean) and the uppermost part of the lower plate (i.e. African or Nubian in the oceanic subduction zone and Adriatic block in the continental collision zone). Although in principle four different combinations, or “rheological contrasts”, of brittle *versus* ductile and upper *versus* lower plate could occur, the results emphasise the predominance of three conditions, each one uniformly and regularly covering wide sectors of the investigated interface zones (Figure 2).

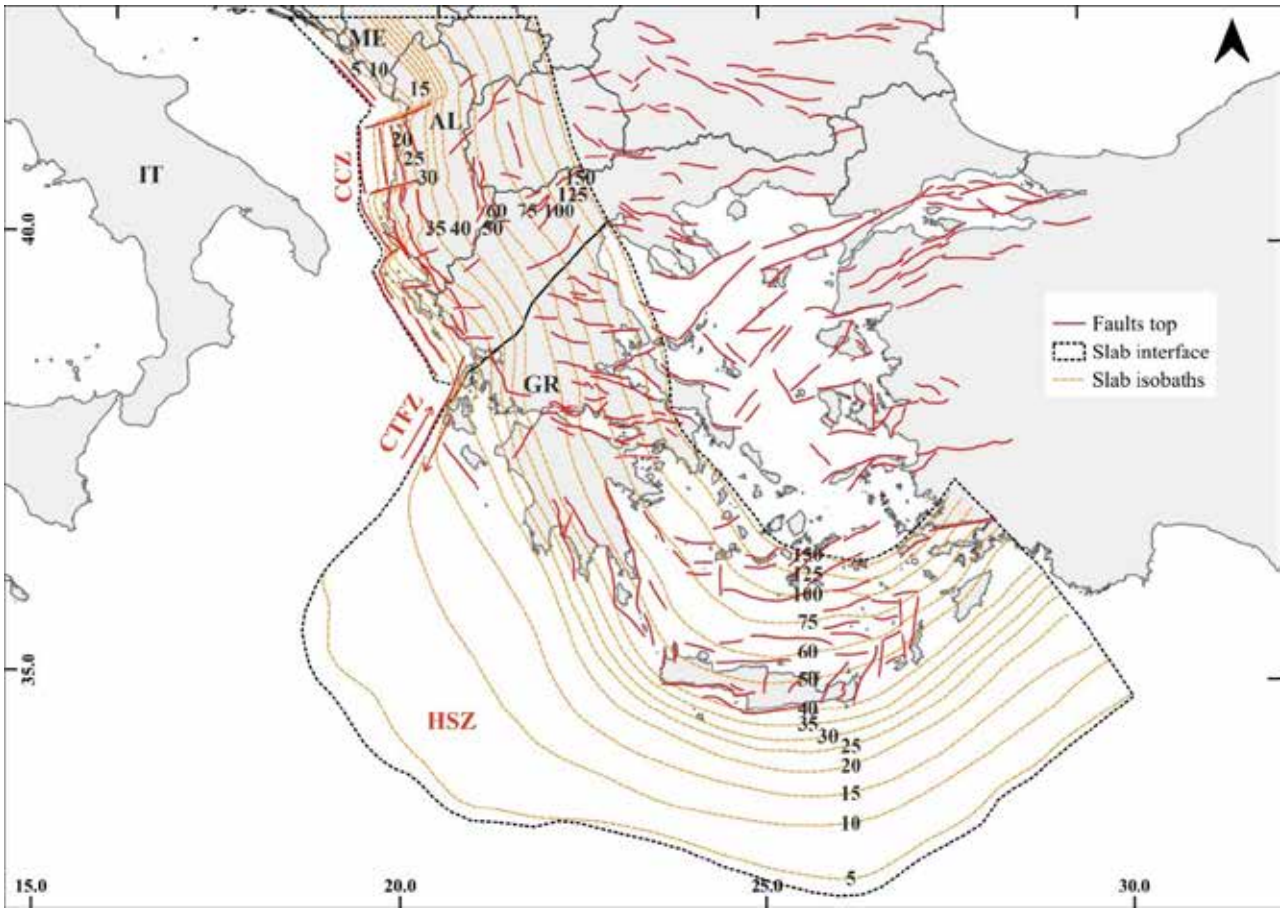

Figure 1. Modelled geometries of the Hellenic Subduction Zone (HSZ) and the Adria-Eurasia Continental Collision Zone (CCZ) based on Bocchini et al. (2018) and Halpaap et al. (2018). Black dotted polygons represent the projection of the slab interface; black solid line is the separation between continental collision and oceanic subduction domains. CTFZ = Cephalonia Transform Fault Zone. Slab isobaths expressed in km (orange dashed). Red solid represents the seismogenic sources top lines from GreDaSS 3.0 (Caputo et al., 2025; submitted to this congress).

Based on these results, five different 'rheological zones' were reconstructed in the continental collision area and in the vicinity of the basal thrust. The first emphasises a predominant brittle behaviour in both the Adria microplate and the European plate (Figure 2, blue) and extends down to a depth of ca. 25 km, except in the Montenegro sector where its limit is shallower at ca. 15 km. The second modelled zone, developing down to a depth of ca. 30 km (25 km in Montenegro), exhibits brittle behaviour in the upper plate and ductile behaviour in the lower one (Figure 2, green). The same brittle-on-ductile conditions have been recognised between 40 and 75 km-depth, but geometrically separated by an interposed sector, between 30 and 40 km, characterised by a ductile-on-ductile behaviour (Figure 2, magenta). Finally, at depths greater than 75 km, the conditions in the investigated area show again a ductile-on-ductile setting.

As concerns the HSZ, only three major sectors have been recognised along the interface; the outermost and shallower one (Figure 2), roughly at the base of the sedimentary accretionary wedge, shows a predominant brittle behaviour both above and below the slab interface. This condition persists down to a depth of ca. 50 km, although this limit is not homogeneous, being at ca. 45 km in the western sector of the HSZ, at ca. 50 km in the central sector and at ca. 40 km on the eastern side (Figure 2). The second zone, modelled continuously to a depth of about 100 km, is characterised by a predominance of brittle behaviour at the base of the overlying plate facing a ductile behaviour at the top of the lower plate (Figure 2, green). Deeper than 100 km, the interpolate shear zone shows predominant ductile properties on both sides of the interface (Figure 2, magenta). Finally, in a small sector of the HSZ at a depth of 35 and 40 km in correspondence of Aetolo-Akarnania and northern Peloponnesus, the results of the rheological model show that the interface is characterised by predominantly ductile behaviour in the upper plate and brittle characteristics in the lower plate (Figure 2, yellow).

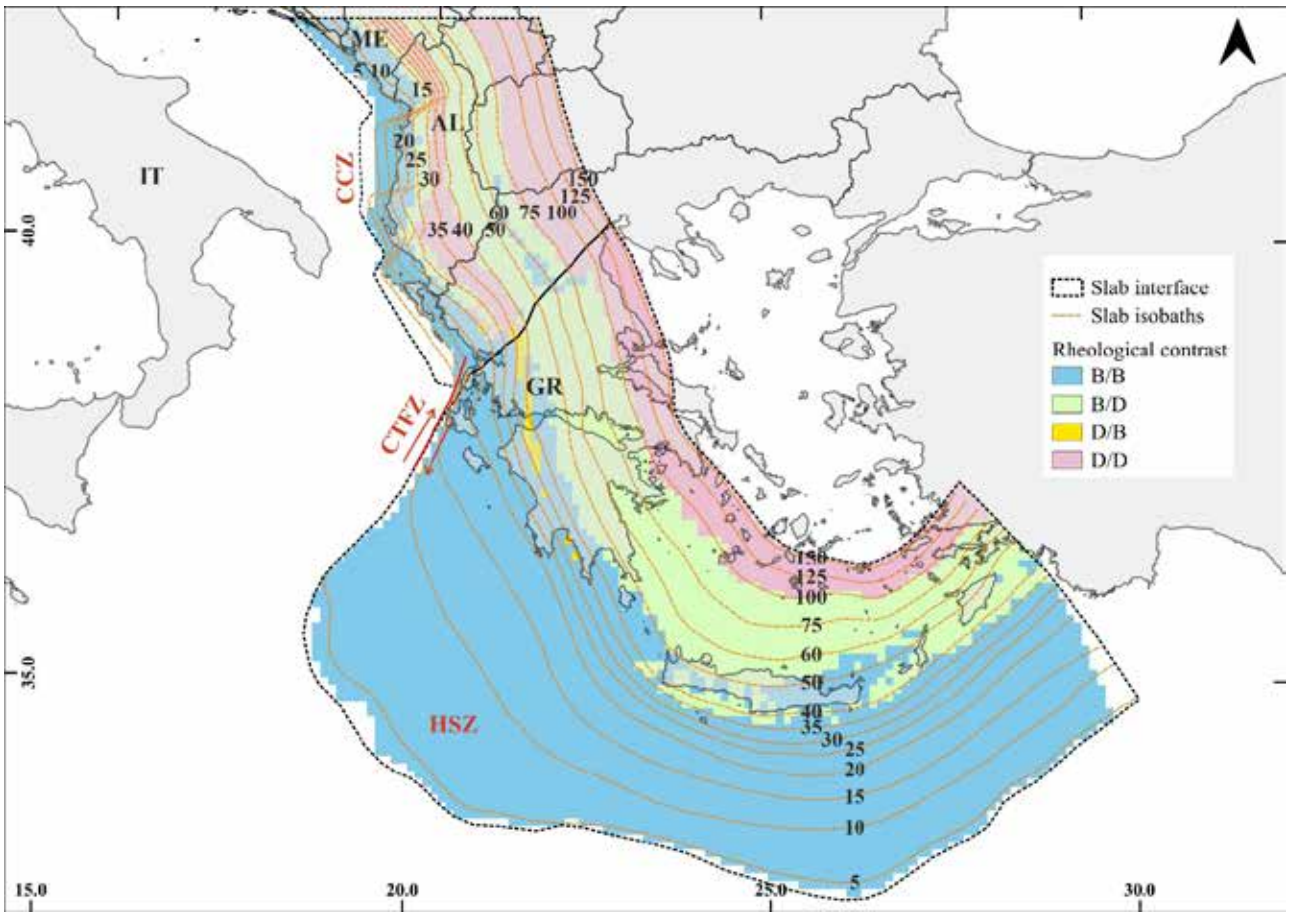

Figure 2. Same as Figure 1; coloured areas represent the recognised rheological behaviours (B/B = brittle/brittle; B/D = brittle/ductile; D/B = ductile/brittle; D/D = ductile/ductile) in correspondence of the slab interface (orange dashed).

Based on these results and considering both the overall geometry of the interplate surface and the associated seismicity (Bocchini et al. 2018), as a preliminary major conclusion the possible maximum down-dip extension of the seismogenic portion (i.e. the Wadati-Benioff zone) along the Hellenic subduction could be constrained at ca. 100 km-depth. Indeed, at greater depths, where at least 1 km-thick rock volume embedding the interplate shear zone has been modelled to behave ductilely, seismogenesis is not expected to occur. Accordingly, deeper recorded seismicity should likely occur within the subducting slab and not along the plate interface. These latter considerations are supported by literature; in Meier et al. (2004), for example, the relocated interplate seismicity plotted on the reconstructed profile across the Aegean generally does not exceed 60 km-depth, with only a few events between 80 km and 100 km. Halpaap et al. (2018), who tomographically imaged the Hellenic Wadati-Benioff zone, identified earthquake clusters characterised by inter-slab seismicity between 40 km and 60 km, while in Bocchini et al. (2018), the interface seismicity is imaged at depths systematically shallower than 100 km.
As a final comment, it should be noted that geometrical models of the interface surface slightly differing from the selected one used in the performed exercise would not likely impact on the overall obtained results especially in terms of the distribution of the contrast in terms of rheological contrast between upper and lower plate.

References

Bocchini, G. M., Brüstle, A., Becker, D., Meier, T., van Keken, P. E., Ruscic, M., Papadopoulos, G. A., Rische, M., Friederich, W., 2018. Tearing, segmentation, and backstepping of subduction in the Aegean: New insights from seismicity. Tectonophysics, 734–735, 96–118.

Brace, W. F., Kohlstedt, D. L., 1980. Limits on lithospheric stress imposed by laboratory experiments. Journal of Geophysical Research: Solid Earth, 85(B11), 6248–6252.

Byerlee, J. D, 1968. Brittle-ductile transition in rocks. Journal of Geophysical Research (1896-1977), 73(14), 4741–4750.

Caputo, R., Pavlides, S., 2013. The Greek Database of Seismogenic Sources (GreDaSS), version 2.0. 0: A compilation of potential

seismogenic sources (Mw> 5.5) in the Aegean Region.
Caputo, R., Koukouvelas, I., Papathanassiou, G., Russo, D., Taftsoglou, M., Tarabusi, G., Valkaniotis, S., 2025. The Greek Database of Seismogenic Sources (GreDaSS) version 3.0. A compilation of potential seismogenic sources (Mw> 5.5) in the Aegean Region. 17th International Congress of the Geological Society of Greece**,** Mytilene, Greece, (this volume)**.**
Cloetingh, S., van Wees, J. D., Ziegler, P. A., Lenkey, L., Beekman, F., Tesauro, M., Förster, A., Norden, B., Kaban, M., Hardebol, N., Bonté, D., Genter, A., Guillou-Frottier, L., Ter Voorde, M., Sokoutis, D., Willingshofer, E., Cornu, T., Worum, G., 2010. Lithosphere tectonics and thermo-mechanical properties: An integrated modelling approach for Enhanced Geothermal Systems exploration in Europe. Earth-Science Reviews, 102(3), 159–206.
Collettini, C., Tesei, T., Scuderi, M. M., Carpenter, B. M., Viti, C., 2019. Beyond Byerlee friction, weak faults and implications for slip behavior. Earth and Planetary Science Letters, 519, 245–263.
Floyd, M. A., Billiris, H., Paradissis, D., Veis, G., Avallone, A., Briole, P., McClusky, S., Nocquet, J.-M., Palamartchouk, K., Parsons, B., England, P. C., 2010. A new velocity field for Greece: Implications for the kinematics and dynamics of the Aegean. Journal of Geophysical Research: Solid Earth, 115(B10).
Fytikas, M. D., Kolios, N. P., 1979. Preliminary Heat Flow Map of Greece, in V. Čermák & L. Rybach (Eds.), Terrestrial Heat Flow in Europe, 197–205. Springer Berlin Heidelberg.
Goetze, C., Evans, B., 1979. Stress and temperature in the bending lithosphere as constrained by experimental rock mechanics. Geophysical Journal International, 59(3), 463–478.
Halpaap, F., Rondenay, S., Ottemöller, L., 2018. Seismicity, Deformation, and Metamorphism in the Western Hellenic Subduction Zone: New Constraints From Tomography. Journal of Geophysical Research: Solid Earth, 123(4), 3000–3026.
Hollenstein, Ch., Müller, M. D., Geiger, A., Kahle, H.-G., 2008. Crustal motion and deformation in Greece from a decade of GPS measurements, 1993–2003. Tectonophysics, 449(1), 17–40.
Hurter, S., Haenel, R. (Eds.), 2002. *Atlas of geothermal resources in Europe*. European Commission Office for Official Publications of the European Communities.
Kahle, H.-G., Cocard, M., Peter, Y., Geiger, A., Reilinger, R., Barka, A., Veis, G., 2000. GPS-derived strain rate field within the boundary zones of the Eurasian, African, and Arabian Plates. Journal of Geophysical Research: Solid Earth, 105(B10), 23353–23370.
Maggini, M., 2020. 3D rheological modelling in the Aegean Region and its importance for the seismotectonics of the area. PhD Thesis, University of Ferrara, Italy, 268 pp.
Maggini, M., Caputo, R., 2020a. Rheological behaviour in continental and oceanic subduction: Inferences for the seismotectonics of the Aegean Region. Turkish Journal of Earth Sciences, 29(3), 381–405.
Maggini, M., Caputo, R., 2020b. Sensitivity analysis for crustal rheological profiles: Examples from the Aegean region. Annals of Geophysics, 63(3), GT334–GT334.
Maggini, M., Caputo, R., 2021. Seismological data versus rheological modelling: Comparisons across the Aegean Region for improving the seismic hazard assessment. Journal of Structural Geology, 145, 104312.
Maggini, M., Russo, D., Caputo, R., 2023. A 3D rheological model for the Aegean Region: Mechanical layering and seismotectonic implications. Journal of Structural Geology, 175, 104956.
Makris, J., Papoulia, J., Yegorova, T., 2013. A 3-D density model of Greece constrained by gravity and seismic data. Geophysical Journal International, 194(1), 1–17.
Meier, T., Dietrich, K., Stöckhert, B., Harjes, H.-P., 2004. One-dimensional models of shear wave velocity for the eastern Mediterranean obtained from the inversion of Rayleigh wave phase velocities and tectonic implications. Geophysical Journal International, 156(1), 45–58.
Ranalli, G., 1995. Rheology of the Earth. Springer Science & Business Media.
Ranalli, G., Murphy, D. C., 1987. Rheological stratification of the lithosphere. Tectonophysics, 132(4), 281–295.
Scholz, C. H., 1988. The brittle-plastic transition and the depth of seismic faulting. Geologische Rundschau, 77(1), 319–328.
Sibson, R. H., 1977. Fault rocks and fault mechanisms. Journal of the Geological Society, 133(3), 191–213.
Sibson, R. H., 1983. Continental fault structure and the shallow earthquake source. Journal of the Geological Society, 140(5), 741–767.
Sodoudi, F., Kind, R., Hatzfeld, D., Priestley, K., Hanka, W., Wylegalla, K., Stavrakakis, G., Vafidis, A., Harjes, H.-P., Bohnhoff, M., 2006. Lithospheric structure of the Aegean obtained from P and S receiver functions. Journal of Geophysical Research: Solid Earth, 111(B12), 1-23.
Taktikos, S., 2001. Heat flow–Underground temperatures of Greece. Institute of Geology and Mineral Exploration.
Viti, C., Collettini, C., Tesei, T., Tarling, M. S., Smith, S. A. F. , 2018. Deformation Processes, Textural Evolution and Weakening in Retrograde Serpentinites. Minerals, 8(6), 241, 1-20.
Wang, H., 2000. Theory of linear poroelasticity with applications to geomechanics and hydrogeology (Vol. 2). Princeton university press.

17th INTERNATIONAL CONGRESS of the Geological Society of Greece

BULLETIN OF THE GEOLOGICAL SOCIETY OF GREECE, SP. PUBL.

EXTENDED ABSTRACT 275

Marine geological-geophysical data may contribute to the understanding of the early 2025 seismic activity in the Santorini-Amorgos Zone

Sakellariou D.[1], Morfis I.[1], Livanos I.[1], Varesis A.[1], Petrakis S.[1], Kapsimalis V.[1]
(1) Institute of Oceanography, Hellenic Centre for Marine Research, Anavyssos, Greece, sakell@hcmr.gr

Introduction

The late 2024 earthquake activity below the Caldera of Santorini and the early 2025 seismic crisis between Santorini and Amorgos, in particular below Anydros Ridge, renewed the interest on the tectonic / volcanic / magmatic structure and the active geodynamic processes that control the evolution of the area. Here below we re-evaluate existing data along with new marine geological-geophysical data obtained in February 2025 with the aim to contribute to the understanding of the processes that led to the recent earthquake activity and their relationship with the long-term deformation of Santorini-Amorgos Zone.

The Santorini-Amorgos Zone is a complex morphological feature (Fig. 1) composed of seven NE-SW trending, spindle-shaped or elongated basins: Anydros, Anafi, Amorgos South, Amorgos North, Kinairos, Astypalea North and Astypalea South Basins. Two uplifted, shallow ridges, Anydros and Astypalea, separate the aforementioned basins. Two more, smaller ridges, Akrotiri and Anafi, occur south and southwest of Santorini (Tsampouraki-Kraounaki et al. (2021). Akrotiri Ridge marks the SW-ward prolongation of the southern part of Thera where the metamorphic alpine basement outcrops. Anafi Ridge extends WSW of Anafi Island.

Mascle & Martin (1990) proposed NE-SW strike-slip faulting in the area and Papadopoulos & Pavlides (1992) characterized Amorgos Fault as oblique-normal with significant right-lateral component. Piper & Perissoratis (2003) and Piper et al (2007) have suggested that the NE-SW faulting, the narrow basement ridges and the basin inversions in the area are evidence of strike-slip regime. Sakellariou et al. (2010) proposed that both Thera and Kolumbo volcanic centers occur within the NE-SW-trending Anydros graben, which constitutes a negative flower structure related to a 40 km long, possibly dextral, strike-slip zone, the Kameni-Kolumbo strike-slip, which can be extended SW-wards to the Christiana volcanic island. Sakellariou & Tsampouraki-Kraounaki (2019) and Tsampouraki-Kraounaki et al. (2021) suggest that the NE-SW-trending Santorini-Amorgos Shear Zone undergoes dextral transtensional deformation accommodated by NE-SW strike-slip to oblique faults and E-W normal step-over faults (Fig. 2). This is compatible with the microseismicity data observed by Bohnhoff et al. (2006), the results of Papadimitriou et al. (2015) on the seismic activity in the caldera of Santorini and the dextral transtensional movement of 4.5 mm yr-1 between Amorgos and Astypalea islands observed by Briole et al. (2021). Nomikou et al. (2016, 2018), Hooft et al. (2017) and others propose normal NE-SW trending faulting as the main deformation mechanism that forms the geomorphological features of the area with secondary, steep faults probably indicating strike-slip component. Finally, Tzanis et al (2020) studied the kinematic regime of the Santorini area by using gravity, magnetotelluric and DGPS data and suggested that Santorini-Amorgos area is characterized by NW-SE dextral strike slip faults and NE-SW normal to sinistral faults.

Data

Swath bathymetry, airgun seismic profiles, deep-towed side scan and chirp subbottom profiles and sediment cores have been collected during various cruises of HCMR's research vessel AEGAEO in the broader area around Santorini, between Santorini, Anafi, Astypalea, Amorgos, Kinairos and Kos (Fig. 1). New swath bathymetry data and high resolution sparker subbottom profiles were collected during the recent cruise of R/V AEGAEO (12-17 Febr. 2025) in the area around Anydros Island (Fig. 3) and between Santorini and Kolumbo.

Results & Discussion

Seismic profiles studied and interpreted by Tsampouraki-Krounaki et al. (2021) show that the northwestern steep flank of Akrotiri Ridge is controlled by the NE-SW striking, NW-dipping Akrotiri Fault (AF) (Fig. 2). The possible prolongation of AF to the NE coincides with the southeastern wall of Santorini Caldera as well as with the boundary between the alpine basement (that outcrops in Athinios and Profitis Ilias Mt.) to the South and the volcanic formations to the North. The Profile 1 of Fig. 6 shows a schematic NW-SE cross section across the Caldera with the NW-dipping inferred prolongation of AF. The recent earthquake activity in the Caldera occurred at shallow depths below the Nea and Palaia Kameni Islands and Fira, along the NE-SW striking "Kameni Line". "Kameni Line" strikes parallel to the prolongation of AF. It is proposed here that the "Kameni Line" represents the linear distribution of earthquake epicenters that, at depth, occur on the NW-dipping, steep Akrotiri Fault. If so, Akrotiri Fault may be considered as the southern boundary of the volcanic activity that has shaped Santorini throughout Quaternary.

Geodetic data obtained during the seismic activity showed fast movement of the northern part of Santorini toward

NE (unpublished data of EPPO Seismic Hazard Committee, M. Foumelis courtesy). That motion occurred roughly in the first half of February 2025, it affected mainly the northern part of Thera and the island of Therasia while the southeastern part of Thera remained almost unaffected. In other words, the NE-ward movement affected mostly the volcanic part of Santorini on the hanging-wall of Akrotiri Fault, while the foot-wall of the fault (the basement) remained more or less stable.

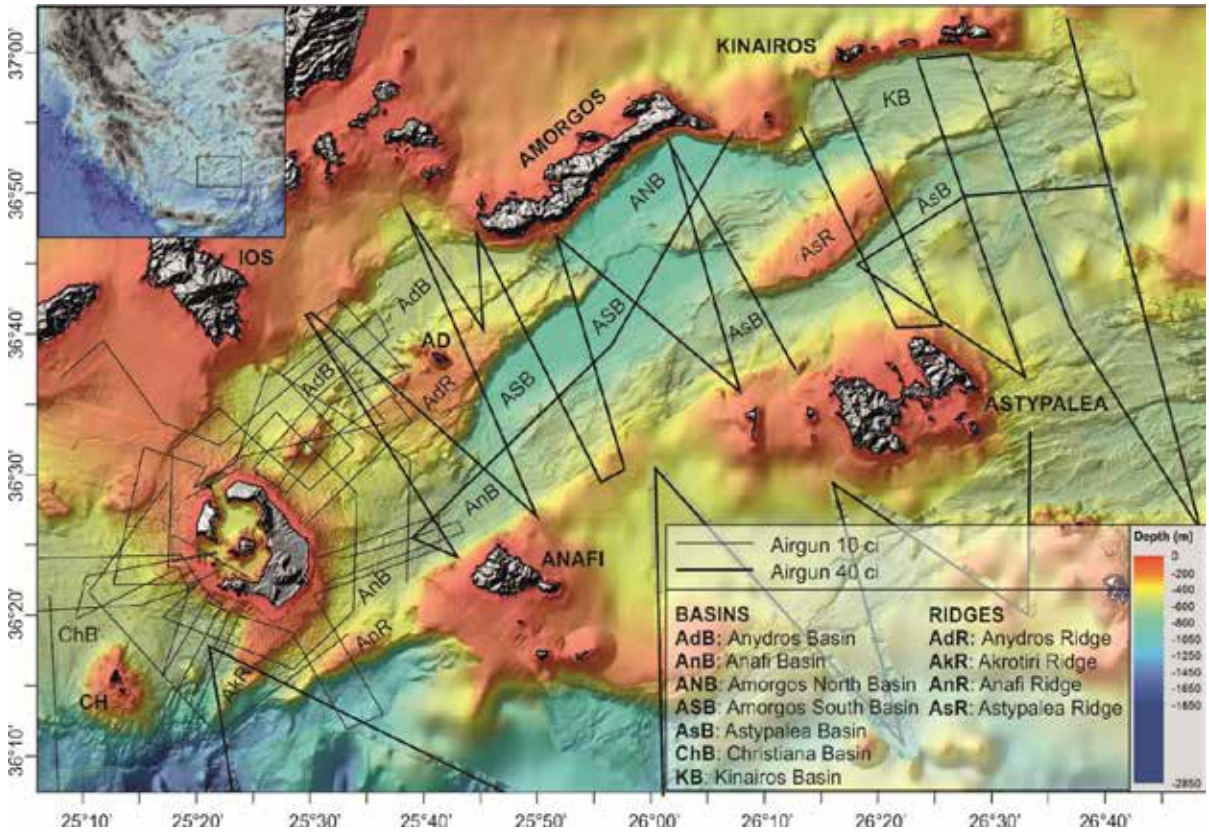

Figure 1. Shaded relief map of the Santorini-Amorgos Zone modified after Tsampouraki-Kraounaki et al (2021).

Anydros Ridge is a shallow, positive, SW-NE trending morphological feature that has been uplifted between the 400 m deep Anydros Basin to the NW from the 700 m Amorgos South Basin to the SE (Fig. 2, 3). It displays a rather complicate shape controlled by SW-NE and E-W striking faults. Morphological and seismic/subbottom profiling data indicate a mean, gentle, NW-ward tilting of Anydros Ridge seafloor by 0.5°-1.5° (Fig. 4, 5). Astypalea Ridge along with Amorgos and the Kinairos-Levitha Islands display similar, NW- / N-ward tilting, with steep, high SW- / S-ward facing slopes and gently sloping northwestern / northern flanks (Fig. 2, 3). Several faults crosscut the top of Anydros Ridge, they have led to local subsidence and the creation of small depressions filled with sedimentary deposits with up to 80 msecs thickness on top of the alpine basement of the ridge (Fig. 4, 5). Two geometrical unconformities U1 and U2 within the seismic stratigraphy of the sedimented depressions display gentle NW-ward dip direction, following the tilting of the ridge.

Geodetic data obtained during the seismic activity showed significant NW-ward tilting of Anydros Island (unpublished data of EPPO Seismic Hazard Committee, M. Foumelis courtesy) roughly in the first half of February 2025. The sense of the tilting of Anydros Island coincides with the tilting of the entire Anydros Ridge as described above.

The mostly linear and steep SE slope of the ridge has developed along the SE-dipping Anydros Ridge South Fault Zone (AdRSFZ). The NW limit of the ridge is rather irregular and less well defined and is largely controlled by multiple segments of the NW-dipping Anydros Ridge North Fault Zone (AdRNFZ) (Fig. 2, 3).

The sparker subbottom profile of Fig. 4 provides a high-resolution imaging of the shallow sub-seafloor structure across Anydros Ridge and at short distance southwest of Anydros Island. Three NW-dipping fault splays of AdRNFZ offset the seafloor (Fig. 4B). The northern one displays minimum cumulative offset of 50 msecs, extends further to the NE and outcrops on Anydros island (Fig. 3). On site measurements of the geometric and kinematic data on Anydros (unpublished data of EPPO Seismic Hazard Committee, D. Galanakis courtesy) show a steep, NW-dipping oblique normal fault with significant dextral horizontal component.

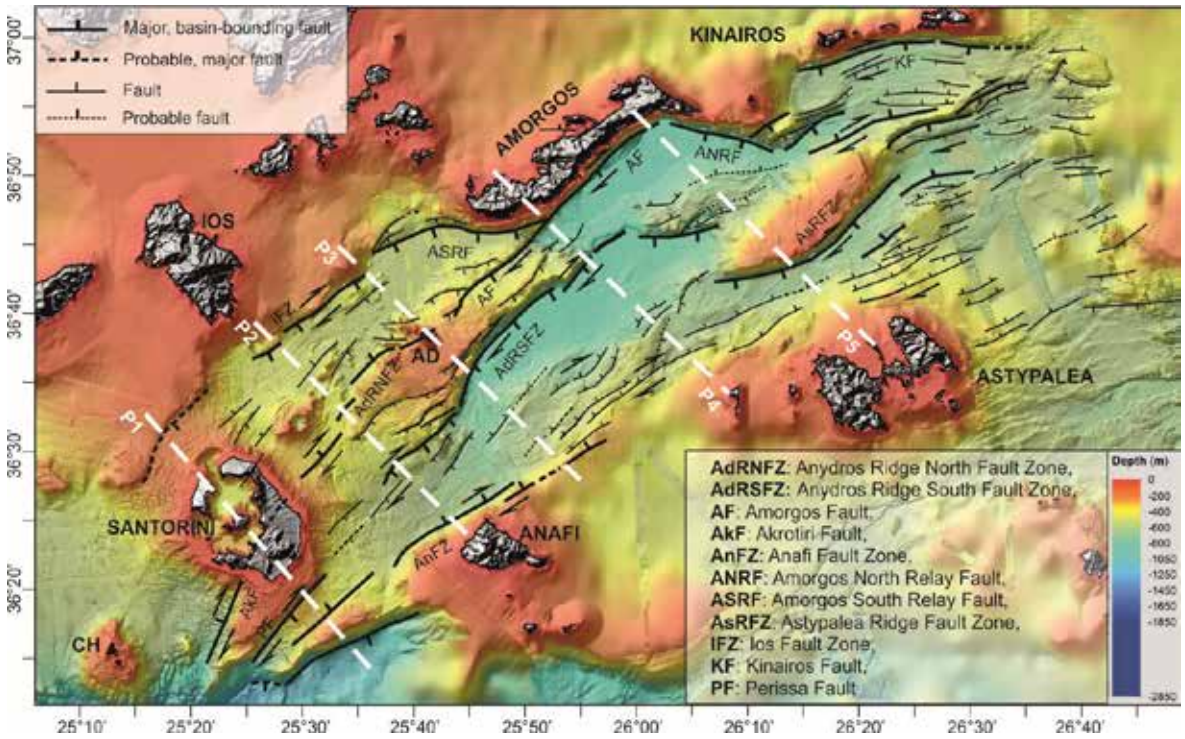

Figure 2. Shaded relief map and fault network of the Santorini-Amorgos Zone modified after Tsampouraki-Kraounaki et al (2021). White dashed lines P1 – P5 indicate the location of the geological profiles shown on Figure 6.

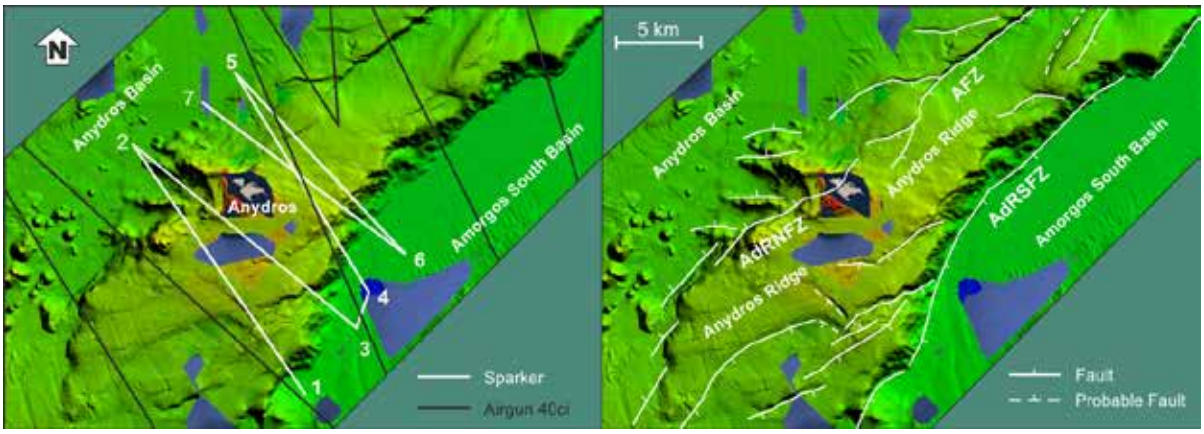

Figure 3. Shaded relief map, airgun and sparker profiles (left map) and fault network (right map) of Anydros Ridge.

The trace of the NW-dipping AdRNFZ terminates at a short distance north-northeast of Anydros Island. Further to the NE the structure of Anydros Ridge is controlled by the SE dipping Amorgos Fault Zone (AFZ). The sparker subbottom profile of Fig. 5 provides a high-resolution imaging of the shallow sub-seafloor structure across Anydros Ridge and at a few kilometers distance northeast of Anydros Island. Fig. 5B and C shows the SE-dipping fault splays of AFZ that offset the seafloor and unconformity U2 by up to 50 msecs or less.

The northeastern termination of the NW-dipping AdRNFZ and the southwestern termination of the SE-dipping AFZ are only a couple of kilometers apart (Fig. 3). The reversal of the tectonic polarity between them is not well understood.

Re-exploitation of the pre-2025 data along with the analysis of the new swath bathymetry and seismic profiling data provide insights into the geological and tectonic structure of the Santorini-Amorgos Zone. The five profiles shown on Fig. 6 aim to provide a schematic visualization of the here proposed structure of the upper crust at up to 10 km depth. Under the light of the new knowledge and information derived from the multiple datasets obtained during the recent seismic activity, they may be used as a first draft scheme that may certainly need corrections or improvements and can contribute to the understanding of the longterm processes that controlled the evolution of Santorini-Amorgos Zone and the processes that led to the 2025 seismic activity.

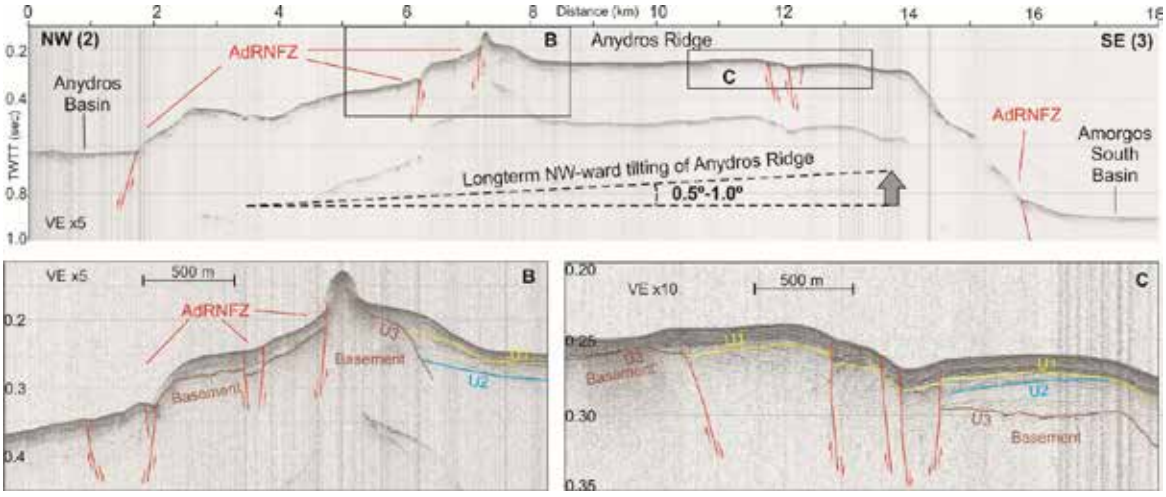

Figure 4. Sparker Subbottom Profile 2-3 across Anydros Ridge. See Figure 3 for location.

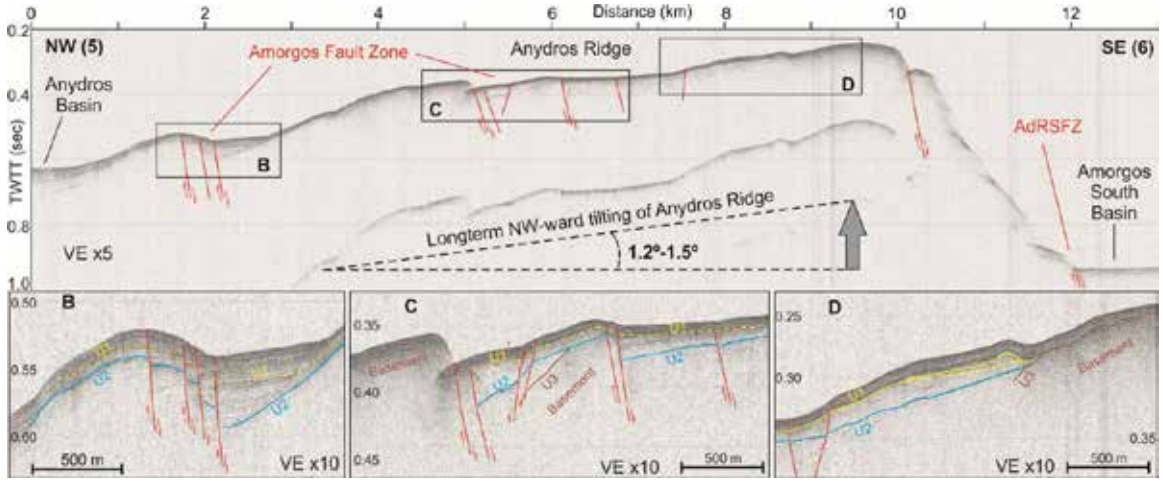

Figure 5. Sparker Subbottom Profile 5-6 across Anydros Ridge. See Figure 3 for location.

Profile 1 (Fig. 6), across Therasia, Caldera/Kameni, Thera, Anafi Basin and Anafi Ridge, proposes that magmatic and volcanic activity of Santorini is confined between Ios FZ and Akrotiri FZ. The latter marks the boundary between the alpine basement and the volcanic formations of Santorini. The late 2024 – early 2025 earthquake activity in the Caldera occurred at shallow depths below the Nea and Palaia Kameni Islands and Fira, along the NE-SW striking "Kameni Line". It is possible that the earthquakes were triggered by magma flow on the NW-dipping Akrotiri Fault.
Profile 2 (Fig. 6), across Anydros Basin, Anydros Ridge and Anafi Basin, proposes that magmatic and volcanic activity of the Kolumbo volcanic chain is confined below Anydros Basin, between Ios FZ and AdRNFZ.
Profile 3 (Fig. 6), across Anydros Basin, Anydros Ridge, Anydros Island, Amorgos South Basin and Anafi Basin, shows the transtensional Anydros and Amorgos South Basins separated by the uplifted Anydros Ridge. Anydros Basin displays symmetrical geometry while Amorgos South Basin exhibits enhanced subsidence along its NW margin. The eastern termination of Anafi Basin displays SE-ward asymmetry. Preliminary location of the earthquake hypocenters indicates that the 2025 seismic activity occurred predominantly below Anydros Ridge between AdRNFZ and AdRSFZ.
Profile 4 (Fig. 6), across Amorgos Island, Amorgos North Basin, Amorgos South Basin and Astypalea Basin, displays NW-ward asymmetry of the Amorgos North and South Basins and SE-ward asymmetry of the Astypalea Basin.
Profile 5 (Fig. 6), across Amorgos Island, Amorgos North Basin, Astypalea Ridge, Astpalea Basin and Astypalea Island, displays NW-ward asymmetry of the Amorgos North Basin and NW-ward tilting of Astypalea Ridge.
All major faults drawn on the above profiles are considered as oblique normal faults with significant component of dextral lateral slip. It is proposed here that lateral slip on some of the faults may exceed vertical slip.
The entire Santorini-Amorgos Zone is considered here as a transtensional feature or dextral oblique rift that has evolved during Quaternary.

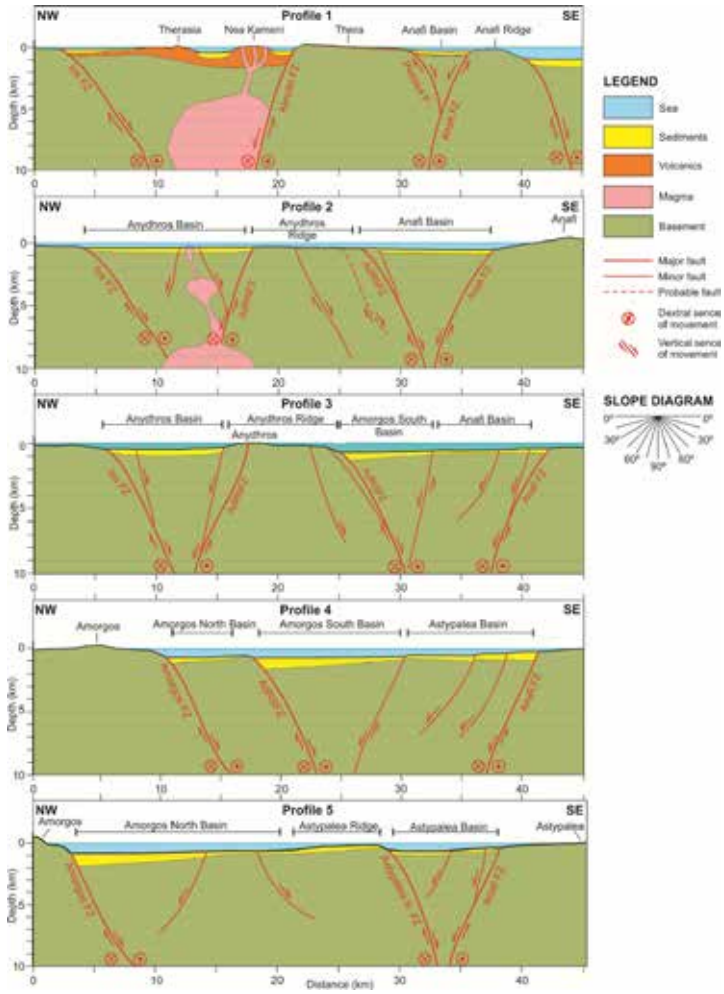

Figure 6. Schematic cross-sections across the Santorini-Amorgos Zone. The location of the five profiles is shown on the map of Figure 2. No vertical exaggeration. Abbreviations and names shown on the profiles are as in Fig. 1 & 2.

Conclusions

Re-exploitation of the pre-2025 data along with the analysis of the recently collected swath bathymetry and seismic profiles provide the following conclusions on the geological and tectonic structure of the Santorini-Amorgos Zone that can contribute to the understanding of the longterm processes controlling its evolution and the processes that led to the 2025 seismic activity:

- The “Kameni Line” represents the linear distribution of earthquake epicenters that, at depth, are probably associated with the NW-dipping, steep Akrotiri Fault.
- The geodetically observed NE-ward movement of Santorini that occurred in the first half of February 2025 affected the hanging-wall of Akrotiri Fault, while the foot-wall of the fault (the basement) remained more or less stable.
- The significant NW-ward tilting of Anydros Island observed on geodetic data during the seismic activity coincides with the long-term tilting of the entire Anydros Ridge observed on swath bathymetry and seismic profiling data.
- The NW-dipping Anydros Ridge North Fault Zone (AdRNFZ) controls the NW flank of Anydros Ridge and crosscuts the island of Anydros. Geometric and kinematic data of this fault measured on Anydros show a steep, NW-dipping oblique normal fault with significant dextral horizontal component.
- The trace of NW-dipping AdRNFZ is followed laterally towards northeast by the trace of the SE-dipping Amorgos Fault Zone (AFZ). The reversal of the tectonic polarity between these two fault zones is not well understood.
- Earthquake activity and ground deformation observed during the early 2025 seismic crisis are compatible with the long-term deformation of Santorini-Amorgos Zone.

Acknowledgements

This work uses swath bathymetry and seismic profiling data acquired during several cruises of R/V AEGAEO between 2001 and 2017 and funded partly by THERA (2006) and Eurofleets2 LGT-AMORGOS-56 international projects and partly by national (HCMR) funds. The February 2025 cruise of R/V ARGAEO was implemented within the “Athena vs. Egeladus” project funded by the Hellenic Foundation for Research & Innovation (HFRI). The authors are grateful to the colleagues and technicians who contributed to the acquisition of the data during all mentioned cruise. The crew and the captain of R/V AEGAEO are particularly acknowledged for their continuous support and smooth collaboration.

References

Bohnhoff, M., Rische, M., Meier, T., Becker, D., Stavrakakis, G., Harjes, H., 2006. Microseismic activity in the Hellenic Volcanic Arc, Greece , with emphasis on the seismotectonic setting of the Santorini – Amorgos zone. Tectonophysics **2006**, 423, 17–33

Briole, P., Ganas, A., Elias, P., Dimitrov, D., 2012. The GPS velocity field of the Aegean. New observations, contribution of the earthquakes, crustal blocks model. Geophysical Journal International, ggab089, https://doi.org/10.1093/gji/ggab089

Hooft, E.E.E., Nomikou, P., Toomey, D.R., Lampridou, D., Getz, C., Christopoulou, M.-E., O’Hara, D., Arnoux, G.M., Bodmer, M., Gray, M., Heath, B.A., VanderBeek, B.P., 2017. Backarc tectonism, volcanism, and mass wasting shape seafloor morphology in the Santorini-Christiana-Amorgos region of the Hellenic Volcanic Arc. Tectonophysics, 712-713, 396-414.

Mascle, J., Martin, L., 1990. Shallow structure and recent evolution of the Aegean Sea: A synthesis based on continuous reflection profiles. Mar. Geol., 94, 271–299

Nomikou, P., Hűbscher, C., Ruhnau, M., Bejelou, K., 2016. Tectono-stratigraphic evolution through successive extensional events of the Anydros Basin, hosting Kolumbo volcanic field at the Aegean Sea, Greece. Tectonophysics**,** 671, 202–217, doi:10.1016/j.tecto.2016.01.021.

Nomikou, P., Hübscher, C., Papanikolaou, D., Farangitakis, G.P., Ruhnau, M., Lampridou, D., 2018. Expanding extension, subsidence and lateral segmentation within the Santorini - Amorgos basins during Quaternary: Implications for the 1956 Amorgos events, central - south Aegean Sea, Greece. Tectonophysics, 722, 138–153

Papadimitriou, P., Kapetanidis, V., Karakonstantis, A., Kaviris, G., Voulgaris, N., Makropoulos, K., 2015. The Santorini Volcanic Complex: A detailed multi-parameter seismological approach with emphasis on the 2011 – 2012 unrest period. J. Geodyn.**,** 85, 32–57

Papadopoulos, G.A., Pavlides, S.B., 1992. The large 1956 earthquake in the South Aegean: Macroseismic field configuration, faulting, and neotectonics of Amorgos Island. Earth Planet. Sci. Lett.**,** 113, 383–396

Piper, D.J.W., Perissoratis, C., 2003. Quaternary neotectonics of the South Aegean arc. Mar. Geol., 198, 259–288

Piper, D.J.W., Pe-Piper, G., Perissoratis, C., Anastasakis, G., 2007. Distribution and chronology of submarine volcanic rocks around Santorini and their relationship to faulting. Geol. Soc. Lond. Spec. Publ.**,** 291, 99–111

Sakellariou, D., Sigurdsson, H., Alexandri, M., Carey, S., Rousakis, G., Nomikou, P., Georgiou, P., Ballas, D., 2010. Active tectonics in the hellenic volcanic arc: the Kolumbo submarine volcanic zone. Bull. Geol. Soc. Greece**,** 43, 1056–1063.

Sakellariou, D., Tsampouraki-Kraounaki, K., 2019. Plio-Quaternary extension and strike-slip tectonics in the Aegean. In: J. Duarte (Ed.): Transform Plate Boundaries and Fracture Zones, Chapter 14, **2018**, p. 339-374, https://doi.org/10.1016/B978-0-12-812064-4.00014-1, ELSEVIER, 2019.

Tsampouraki-Kraounaki, K., Sakellariou, D., Rousakis, G., Morfis, I., Panagiotopoulos, I., Livanos, I., Manta, K., Paraschos, F., Papatheodorou, G., 2021. The Santorini-Amorgos Shear Zone: Evidence for Dextral Transtension in the South Aegean Back-Arc Region, Greece. Geosciences 2021, 11, 216, https://doi.org/10.3390/geosciences11050216

Tzanis, A., Chailas, S., Sakkas, V., Lagios, E., 2020. Tectonic deformation in the Santorini volcanic complex (Greece) as inferred by joint analysis of gravity, magnetotelluric and DGPS observations. Geophys. J. Int.**,** 220, 461–489

17th INTERNATIONAL CONGRESS
of the Geological Society of Greece

BULLETIN OF THE GEOLOGICAL SOCIETY OF GREECE, SP. PUBL.

EXTENDED ABSTRACT 276

Airborne and marine survey of the 8th June 2023 earthquake-triggered coastal collapse at Mylos Gialtron, North Evia: Contribution to the understanding of coastal zone vulnerability

Sakellariou D., Morfis I., Vandarakis D., Livanos I., Kourliaftis I.
Institute of Oceanography, Hellenic Centre for Marine Research, 19013 Anavyssos, Greece, sakell@hcmr.gr

Introduction

An earthquake with magnitude Mw:4.9 occurred on June 8th 2023, 10 km southwest of Atalanti, at 9 km depth (https://bbnet.gein.noa.gr/HL/seismicity/mts , 2023-06-08, 12:33:53.52, Lat: 38.5635°, Long.:22.9209°) (Fig. 1A). The tremor was felt in North Evia and triggered a landslide on the coastal zone of Mylos Gialtron (Fig. 1B). A 20 m long by 10 m wide part of the sandy beach in front of Mylos collapsed into the sea and created local turbulence of the seawater.
One week after the earthquake, on June 15th 2023, the Inst. Of Oceanography of HCMR undertook airborne mapping and documentation of the coastal collapse at Mylos Gialtron with a drone. Two weeks after the earthquake, on June 22nd and 23rd, a marine survey was implemented using a multibeam echosounder on board the research vessel Alkyon of HCMR. The results of the airborne and marine surveys on the coastal slide at Mylos Gialtron are presented here below and provide insights into the vulnerability of the Greek shoreline to co-seismic and non-seismic coastal slides.

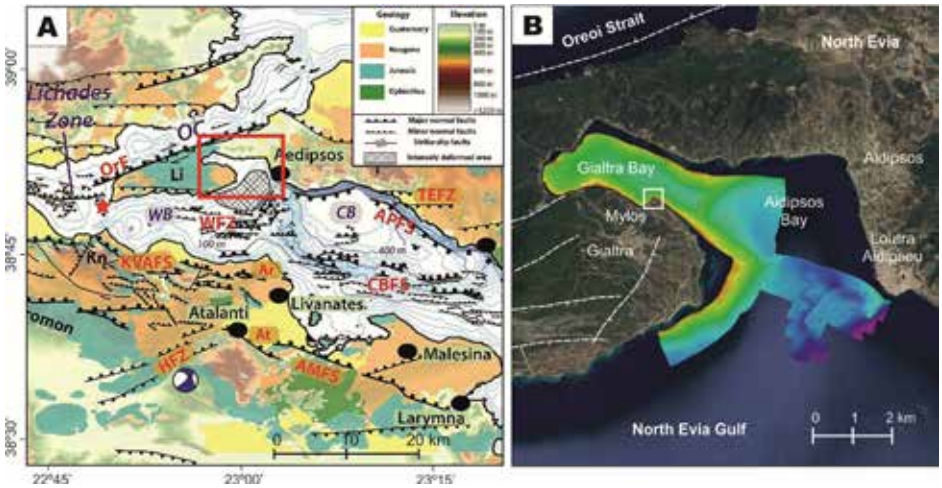

Figure 1. A: Geological and tectonic map of the broader North Evia Gulf (modified after Caroir et al., 2024). Red box: Fig. 1B. Blue-white beachball: Epicenter and moment tensor solution of the 8th June 2023 earthquake. B: Google Earth image with location of Mylos Gialtron (white box) and swath bathymetry coverage during the survey on board R/V Alkyon. White dashed lines: Faults after Galanakis et al. (1998) and Caroir et al. (2024).

Tectonic and Geographic Setting

Active neotectonics of the broader area of Eastern Central Greece, North Evia Gulf, North Evia and Oreoi Strait is dominated by E-W, SW-NE and NW-SE striking normal, oblique and dextral/sinistral strike-slip faults (Galanakis et al., 1998; Kranis, 2007; Sakellariou et al., 2007; Ganas et al., 2016; Caroir et al., 2024 and references therein). The two nodal planes observed by the moment tensor solution (https://bbnet.gein.noa.gr/HL/seismicity/mts) of the 8 June 2023 Mw 4.9 earthquake are compatible with the local tectonic pattern (Fig. 1A).
The sandy beach of Mylos (windmill) is located in North Evia, north of the village of Gialtra and west of Loutra Aidipsou, roughly 30 km north of the epicenter of the 8th June 2023 earthquake. It is a small, flat, triangular cape on the southern shoreline of Gialtra Bay that has been formed by the deposition of alluvial deposits due to the local coastal marine currents. The onshore area adjacent to Mylos is built mostly of carbonates and schists and displays rough relief.

Methods

In this study, a DJI Matrice 210 RTK Unmanned Aerial Vehicle (UAV) was used for the airborne mapping of the coastal

and shore morphology and the documentation of the shallow coastal collapse (Casella et al., 2020; Papakonstantinou et al., 2016). The UAV was equipped with a Zenmuse X5S sensor and RTK technology. Six (6) Ground Control Points (GCPs) were implemented to achieve geolocation accuracy of ±2 cm. The flight plan consisted in nine (9) N-S and eight (8) E-W oriented tracks (Fig. 2 A) (Trajkovski et al., 2020; Zhou et al., 2024). In total, 185 photos were taken from 120m Above Ground Level (AGL), the front and side overlap were at 80% and the Ground Sampling Distance (GSD) was at 2.69 cm/pixel. The achieved Root Mean Square Error (RMSE) of accuracy of the resulted Orthomosaic, Digital Surface Model (DSM) and Digital Terrain Model (DTM) was about 0.012 m (Fig. 2B). The Pix4d mapping software was used for the construction of the maps. The total area covered was 377 X 319 m and the coordinate system used was GCS_GGRS_1987. Based on the height of the drone flight the DSM and Orthomosaic resolution was fixed at 2.69cm/pixel. Noise and surface filters were implemented to eliminate potential errors during the processing. The Inverse Distance Weighting Method was used for the construction of the DSM (and DTM) raster.

A Teledyne/RESON SEABAT T50-R, 200 – 400 kHz multibeam echosounder hull-mounted on HCMR's Research vessel Alkyon was used for the acquisition of swath bathymetry data in the Aidipsos and Gialtra Bay. T50-R multibeam echosounder emits up to 1024 beams arranged in iso-distance or iso-angle mode at 165° across the vessel's track and offers maximum swath equal to up to 5 times the current water depth. A Sea Bird Electronics SeaCat 19 Profiler CTD (Conductivity – Temperature – Depth) was used for the sound velocity profile of the water column during the survey. The resulted swath bathymetry of 13.5 km^2 in Gialtra and Aidipsos Bays has been processed at 1 m spatial resolution.

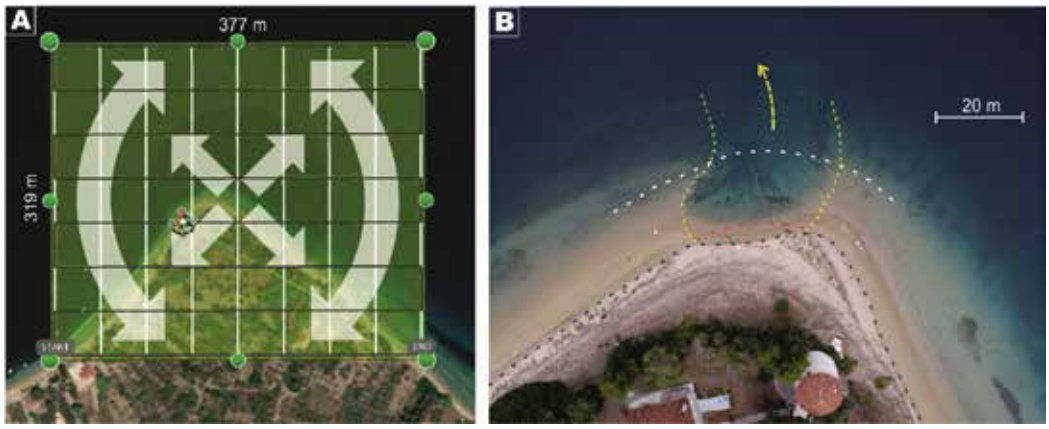

Figure 2. A: Flight plan of the drone over the area of Mylos Gialtron. B: Airphoto of the coastal collapse at the tip of Mylos Gialtron sandy beach taken from the drone on June 15, 2023. Blue dashed line: post-earthquake shoreline. Red dashed line: pre-earthquake shoreline. White dashed line: pre-earthquake 4 m depth contour (approximately).

Results

The swath bathymetry data showed that Gialtra Bay is a flat, 35-40 m shallow embayment with a large number of a few meters high mounds of probable biogenic origin (Fig. 3). The up to 50% steep littoral slope connects the southern, narrow coastal zone with the flat bottom of the Bay. The northern side displays gentler slope value. A 30 m shallow, NE-SW trending sediment ridge (Barrier in Fig. 3) separates the shallow seafloor of Gialtra Bay to the East from the deeper Aidipsos Bay. The latter is characterized by rather flat seafloor that deepens smoothly to 55 m depth towards the center. Aidipsos Bay is open to the South to the North Evia Gulf. A prominent, >5 m deep valley incises the 50 m shallow, flat seabed between Gialtra and Loutra Aidipsou and connects the 55 m deep seafloor of Aidipsos Bay with the 440 m deep Central Basin of the North Evia Gulf.

Three areas with slope failures have been identified on the seafloor (Fig. 3). An amphitheatric scar occurs east of Gialtra at depths between 20 and 30 m and marks a submarine landslide that took place not very long ago, possibly not earlier than 5-6 kyrs before present, when the area was already drowned by the last sea-level rise. Multiple evidence of recent coastal slides and mass transport deposits have been observed off the shoreline of Mylos Gialtron (Fig. 4 & 5) and will be described below. Finally, evidence of composite on- and offshore slope failure and rock falls have been found at the southwestern part of Gialtra Bay coastal zone (Fig. 6).

The Mylos Gialtron coastal collapse(s)

The airborne DTM and orthophotomosaic of Mylos Gialtron provide a precise documentation of the onshore coastal plain, the sandy beach and the shallow seafloor up to roughly 9 to 10 m depth (Fig. 4). The western slope is steeper than the eastern one and show evidence of slope failures at shallow depth. The scar created by the coastal collapse

of 8th June 2023 at the northern tip of the shoreline has been mapped in detail up to the depth of 4.5 m (Fig. 4 & 2B). The airphoto of Fig. 2B shows the coastal zone at the tip of Mylos Gialtron one week after the earthquake-triggered collapse of 8th June 2023. A 20 m long by up to 10 m wide part of the sandy beach and its offshore continuation are missing because they collapsed northwards and slid downslope leaving behind an amphitheatric scar. The dashed red line shows the shoreline prior to the collapse. The white dashed line shows the approximate location of the 4 m depth contour prior to the collapse. Note that the 4 m depth contour is less than 20 m away from the shoreline indicating a minimum mean coastal slope value of 25%. The two yellow dashed lines mark the edges and the yellow arrow shows the direction of the slide.

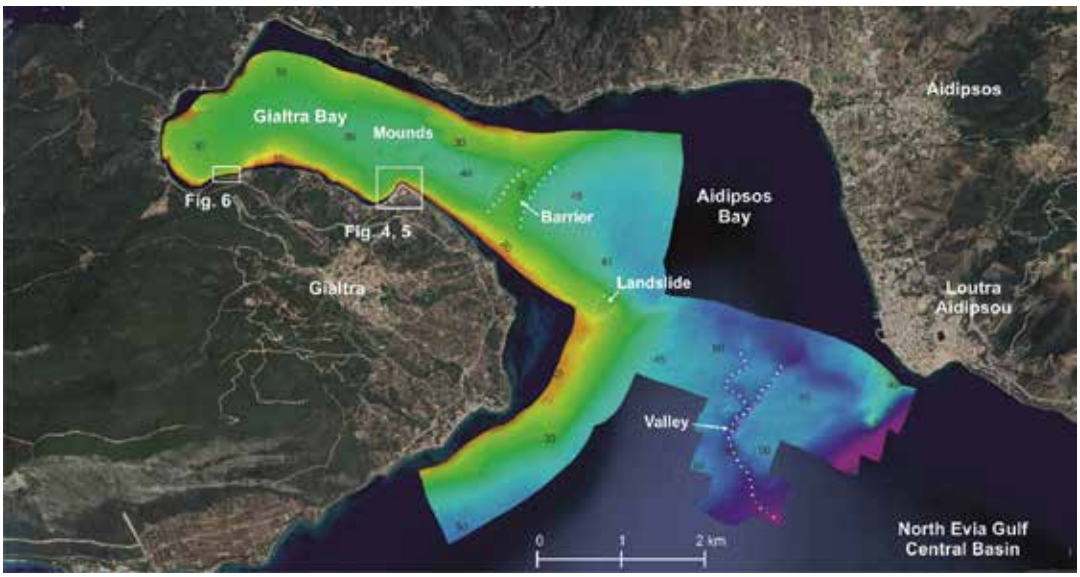

Figure 3. Swath bathymetry of the Aidipsos and Gialtra Bay acquired on board R/V Alkyon on June 22-23, 2023.

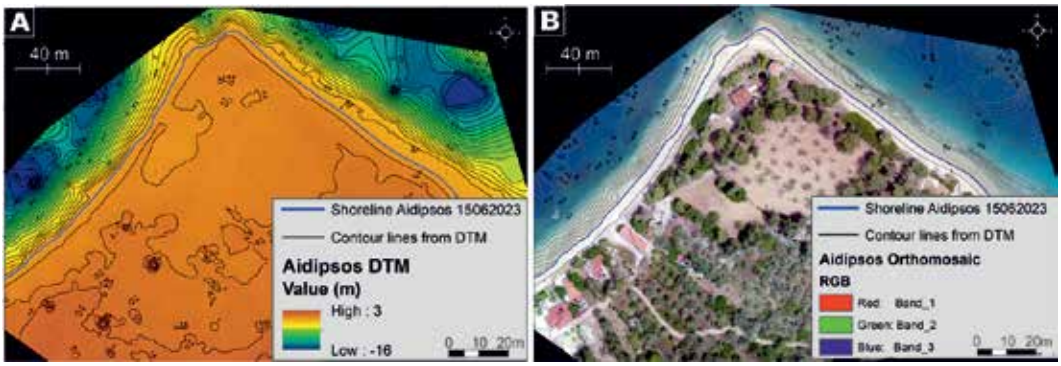

Figure 4. DTM (A) and Orthophotomosaic (B) derived from the airborne survey at Mylos Gialtron on June 15, 2023.

The swath bathymetry acquired with R/V Alkyon complemented the airborne mapping of the seafloor off Mylos Gialtron. Thanks to the crew of R/V Alkyon, the vessel navigated at very short distance from the shoreline during the marine survey in order to achieve sufficient complementarity, without gaps between the airborne and the marine coverage.

Multiple shallow slope failures are evident off the western shoreline of Mylos (Fig. 5A). The toe of the slope deposits reaches 30 m depth. No scar has been identified on the airborne and marine data indicating that these failures may have taken place at least some tens of years ago, sufficient time for the dynamic coastal zone environment to heal the failure scars.

The coastal scar at the northern tip of the sandy beach continues downslope toward north-northwest (Fig. 5B). A 15 m wide and 3-4 m deep gully incises the slope down to roughly 15-20 m depth and is followed by the depositional lobe. The lobe widens to reach a diameter of at least 50 to 60 m and extends up to the 30 m depth contour. Assuming a mean thickness of 2 m for the depositional lobe, the estimated volume of the slide is calculated to >7,000 m^3. Local witnesses reported extensive turbulence of the seawater in front of the sandy beach when the collapse took place. This indicates that the collapse and the slide evolved abruptly and at high velocity, however, no tsunami was reported.

At least one more, older, depositional lobe is evident on the seafloor. The white dashed line on the map of Fig. 5A outlines the morphological expression of an older lobe that is located further off the slide deposits of 8th June 2023. This older lobe extends off the 35 m depth contour, at roughly 150-200 m distance from the shoreline and has the shape of a wide, flat mound with its highest surface 2-3 m higher than the surrounding seafloor. The shape and orientation of this depositional lobe strongly indicates that it is the result of a coastal slide similar to but two times larger than the one of June 2023. Local witnesses reported to the survey team that a coastal collapse similar to the one of 8th June 2023 occurred at the time of the 9th July 1980, M:6.3 Almyros earthquake. It has not been possible to verify this information, however it is reasonable to assume that the older slide may have been triggered by an earthquake in the recent past.

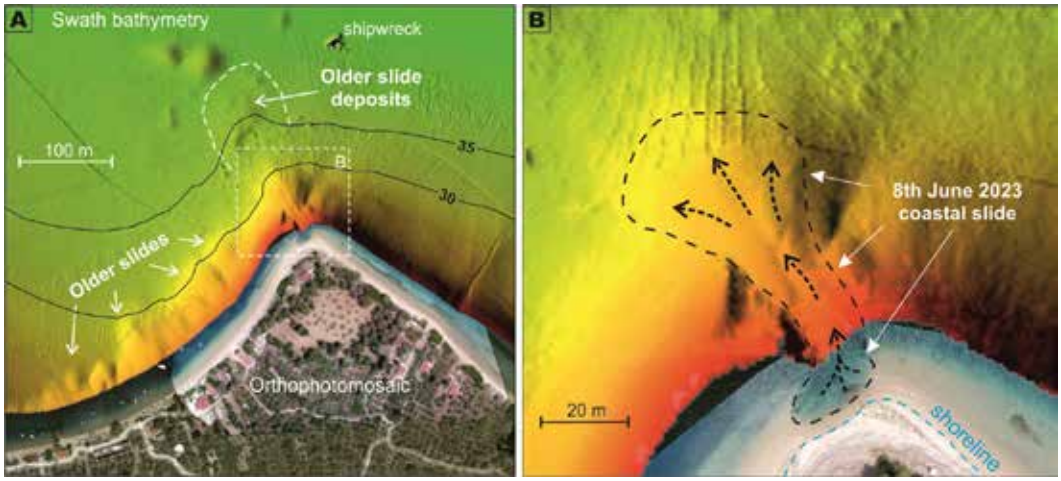

Figure 5. A: Orthophotomosaic and shaded bathymetry of the coastal and offshore Mylos Gialtron area. White arrows point to landslide deposits before the 8th of June 2023. Black thin lines are depth contours B: Detail of previous image showing the 8th June 2023 co-seismic coastal collapse and slide deposits off the sandy beach of Mylos Gialtron.

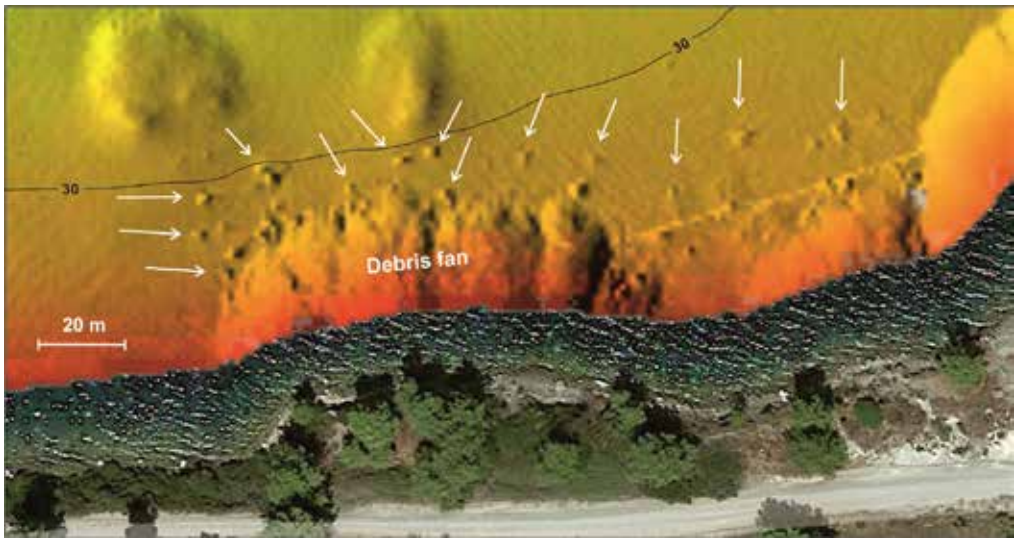

Figure 6. Shaded swath bathymetry off the southern shoreline of Gialtra Bay (see Fig. 3 for location) showing a submarine debris fan and multiple boulders (arrows) fallen from the nearby onshore rocky cliff. Thin black line: 30 m depth contour.

Evidence of coastal slope failure has been found on the seafloor at the southwestern margin of Gialtra Bay (Fig. 6). The shaded relief of the seafloor shows a 100 m wide submarine fan. The fan has evolved off and parallel to the convex-shaped shoreline and is incised by several small gullies. The foot of the debris fan is at 25-28 m depth and is surrounded by multiple, small positive features (pointed with arrows on Fig. 6). Based on their shape, dimensions and context they are interpreted as rock boulders with diameter up to roughly 2 meters. Both the debris fan and the boulders may have derived from a landslide on the nearby onshore, north-facing, mountain flank. The available data

provide no constraints on the possible age of the landslide that is responsible for the creation of the debris fan and the rock falls.

Discussion

The co-seismic coastal collapse and submarine landslide of 8th June 2023 is probably the first one in Greece that has been documented right after its occurrence with the use of airborne and marine survey techniques. The results presented above highlight two main critical factors that favor the development of slide events in the coastal zone once a proper triggering mechanism (e.g. earthquake) is activated (Fig. 7A & B).

The first factor is the presence of a coastal sedimentary prism built and thickened by fast accumulation of non-coherent sediments, e.g. the loose deposits that accumulate along the shoreline and build the sandy beaches and the dynamically changing, on- and offshore coastal zone. The second factor is the presence of a relatively steep slope on the seafloor at short distance off the shoreline. In the case of Mylos Gialtron the submarine slope starts at 10-15 m off the shoreline and displays dipping value >25% basinwards. Certainly, the initial, driving factor for the collapse is the magnitude of the seismic acceleration that will or will not destabilize the non-coherent coastal deposits.

The schematic drawing shown on Fig. 7 visualizes in a simplified way the main factors described above as well as the evolution of the coastal collapse to a submarine landslide. Fig. 7A shows the structure of the coastal zone before the event. The red, dashed line marks the sliding plane of the imminent slide. The area highlighted in yellow indicates the sedimentary material (evacuation zone) to be involved into the coastal collapse and slide. The red line in Fig. 7B marks the slide scar and the red half arrow points the pathway of the sliding mass. The yellow lobe on the deep seafloor visualizes the deposition lobe of the landslide.

The structural and morphological characteristics as presented above for Mylos Gialtron and visualized in Fig. 7 are fairly common along the Greek shoreline. Large or smaller segments of the coastal zone of the Ionian Islands, the Gulf of Corinth, the islands of the Hellenic Arc (Crete, Kasos, Karpathos, Rhodes), the eastern Peloponnese to the Argolikos Gulf and Myrtoon Sea, the coast of Evia to the Aegean Sea and the North Evia Gulf, the Sporadhes Islands are some of the areas along the Greek coastline that (a) display structural and morphological characteristics similar to the ones described above and (b) are characterized by frequent, high earthquake activity.

These areas need to be systematically surveyed with the aim to document precisely the structure and morphology of the coastal zone, estimate and understand their vulnerability to coastal landslides similar to or even larger than the recent one at Mylos Gialtron and design measures for the mitigation of their impact on the coastal societies.

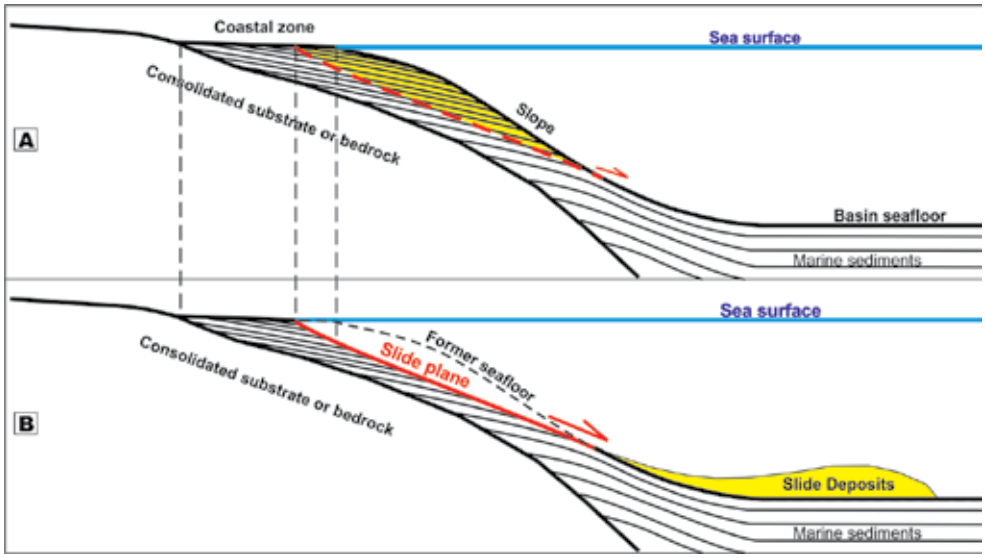

Figure 7. Schematic visualization of the coastal collapse and submarine landslide of 8th June 2023 at the sandy beach of Mylos Gialtron. See text for description.

Conclusions

The coastal collapse at Mylos Gialtron, southern shoreline of Gialtra Bay in North Evia was triggered by the Mw:4.9 magnitude earthquake of June 8th 2023, 10 km southwest of Atalanti. Airborne orthophotomosaic, digital terrain and surface models (DTM, DSM) of the coastal zone combined with swath bathymetry mapping of Gialtra and Aidipsos Bays provided detailed documentation of the coastal collapse and showed that it evolved as submarine landslide.

Gialtra Bay is characterized by flat, 35-40 m shallow seafloor with an up to 50% steep southern slope and gentler sloping northern margin. It is separated from the deeper Aidipsos Bay by a 30 m shallow, NE-SW trending sediment ridge. Aidipsos Bay displays rather flat, up to 55 m deep seafloor and is open to the South to the North Evia Gulf. A prominent, submarine valley incises the 50 m shallow, flat seabed between Gialtra and Loutra Aidipsou and connects Aidipsos Bay with the 440 m deep Central Basin of the North Evia Gulf.

A 20 m long by up to 10 m wide part of the sandy beach at Mylos Gialtron and its offshore continuation collapsed and slid downslope, toward the 35-40 m deep flat seafloor of Gialtra Bay, leaving behind an amphitheatric scar. The sliding mass created a 15 m wide by 3-4 m deep gully on the slope down to roughly 15-20 m depth. The gully is followed by the 50 to 60 m in diameter depositional lobe that extends up to the 30 m depth contour. Assuming a mean thickness of 2 m for the depositional lobe, the estimated total volume of the slide is calculated to >7,000 m^3.

One more, older, larger depositional lobe is found on the seafloor. It extends beyond the 35 m depth contour, at roughly 150-200 m distance from the shoreline and has the shape of a wide, 2-3 m high, flat mound. The shape and orientation of this depositional lobe strongly indicates that it is the result of a coastal slide similar to but two times larger than the one of June 2023. According to local witnesses, a coastal collapse at the same spot was triggered by the 9th July 1980, M:6.3 Almyros earthquake, 43 years before the recent coastal collapse. This collapse may be associated with the older slide.

Further evidence of extensive on/offshore landslide, debris flow and rock falls has been found at the southwestern margin of Gialtra Bay. According to the bathymetric and morphological data this slope failure is relatively recent, however no precise age constraints are available.

Certain, larger or smaller segments of Greece's coastal zone (e.g. Ionian Islands, Gulf of Corinth, Hellenic Arc islands, Eastern Peloponnese etc.) display structural and morphological characteristics similar to the ones of Mylos Gialtron coastal zone and are characterized by frequent, moderate to high earthquake activity. These areas need to be systematically surveyed with the aim to understand their vulnerability to coastal landslides similar to or even larger than the recent one at Mylos Gialtron and design measures for the mitigation of their impact on the coastal societies. Detailed geological mapping along the broader, on- /offshore coastal zones is of outmost importance for the understanding of their morphology and sedimentary structure and the assessment of coastal landslide vulnerability.

Acknowledgements

The implementation of this two-phase survey has been possible thanks to the internal funding by the Institute of Oceanography of the Hellenic Centre for Marine Research and the assistance of the Major of Istiaia-Aidipsos Municipality and the Master of Aidipsos Harbor. Our colleagues M. Moschides and N. Nicolis, captain and engineer of R/V Alkyon, are greatly acknowledged for their continuous support and assistance during the marine survey.

References

Caroir, F., Chanier, F., Gaullier, V., Sakellariou, D., Bailleul, J., Maillard, A., Paquet, F., Watremez, L., Averbuch, O., Graveleau, F., Ferriere, J., 2024. Late Quaternary deformation in the western extension of the North Anatolian Fault (North Evia, Greece): Insights from very high-resolution seismic data (WATER surveys). Tectonophysics 870 (2024) 230138.

Casella, E., Drechsel, J., Winter, C., Benninghoff, M., Rovere, A. (2020). Accuracy of sand beach topography surveying by drones and photogrammetry. In Geo-Marine Letters (Vol. 40, Issue 2). Geo-Marine Letters. doi: 10.1007/s00367-020-00638-8

Galanakis, D., Pavlides, S., Moundrakis, D. [1998] Recent brittle tectonic in Almyros-Pagasiticos, Maliakos, N. Euboea and Pilio. Bulletin of the Geological Society of Greece, 32, 263-273.

Ganas, A., Mouzakiotis, E., Moshou, A., Karastathis, V., 2016. Left-lateral shear inside the North Gulf of Evia Rift, Central Greece, evidenced by relocated earthquake sequences and moment tensor inversion. Tectonophysics 682, 237–248. https://doi. org/10.1016/j.tecto.2016.05.031.

Kranis, H., 2007. Neotectonic Basin evolution in Central-Eastern mainland Greece: an overview. Bull. Geol. Soc. Greece 37, 1–14. https://doi.org/10.12681/bgsg.16621.

Papakonstantinou, A., Topouzelis, K., Pavlogeorgatos, G. (2016). Coastline zones identification and 3D coastal mapping using UAV spatial data. In ISPRS International Journal of Geo-Information (Vol. 5, Issue 6). doi: 10.3390/ijgi5060075

Sakellariou, D., Rousakis, G., Kaberi, H., Kapsimalis, V., Georgiou, P., Kanellopoulos, Th., Lykousis, V., 2007. Tectono-sedimentary structure and late Quaternary evolution of the North Evia Gulf basin, Central Greece: preliminary results. Bull. Geol. Soc. Greece 40, 1–12. https://doi.org/10.12681/bgsg.16644.

Trajkovski, K. K., Grigillo, D., Petrovič, D. (2020). Optimization of UAV flight missions in steep terrain. Remote Sensing, 12(8), 1–20.

Zhou, X., Zhu, Q., Zhang, Q., & Du, Y. (2024). The full-field displacement intelligent measurement of retaining structures using UAV and 3D reconstruction. Measurement, 227, 114311.

17th INTERNATIONAL CONGRESS of the Geological Society of Greece

BULLETIN OF THE GEOLOGICAL SOCIETY OF GREECE, SP. PUBL.

EXTENDED ABSTRACT 277

Continuous GNSS Geodetic Networks. A Powerful Tool for Monitoring and Understanding Complex Volcanic Environments: The Case of Santorini Volcano During the Seismic Crisis of 2024-2025

Sakkas V.[1], Pikridas C.[2], Ganas, A.[3], Anastasiou D.[4], Elias P.[5], Bitharis S.[2], Chousianitis K.[3], Raptakis K.[4], Kapetanidis V.[1], Kaviris G.[1], Liadopoulos S.[3], Voulgaris N.[1], Alexopoulos J.[1], Lagios E.[1]

(1) National and Kapodistrian University of Athens, Laboratory of Geophysics, Laboratory of Seismology, Greece (vsakkas@geol.uoa.gr)

(2) Aristotle University of Thessaloniki, School of Rural and Surveying Engineering, Thessaloniki, Greece

(3) National Observatory of Athens, Institute of Geodynamics, Athens, Greece

(4) National Technical University of Athens, School of Rural, Surveying and Geoinformatics Engineering, Athens, Greecde

(5) University of Patras, Department of Geology, Patra, Greece

Abstract

Late summer of 2024 an unusual raise of the seismic activity was observed inside the Caldera of Santorini Volcanic Complex. This was the first time since the 2011-2012 unrest period that increased seismicity was recorded inside the Santorini Caldera. Together with the raise of the seismicity, daily GNSS data from a permanent station in Imerovigli (station SANT) as well as two other operating stations in Santorini, exhibited change on the kinematic behavior of the Island. The typical SE directional motion of the SANT station (with respect to ITRF2014) observed the last decade was altered to a strong ENE motion. Moreover, increased uplift started taking place in the SANT station with a rate of almost 80mm/yr, an order of amplitude higher than the typical of 2-3 mm/yr of the last years. This kinematic motion could be explained by volcanic activity inside the caldera, modeled as a typical Mogi point source.

However, at the end of January 2025, almost 6 months after the initiation of the activity inside the caldera, there was an abrupt migration of the seismicity NE of Santorini, in the marine area between Thira and Amorgos Islands. During a period of almost a month (February 2025) intense seismic activity was recorded in the marine area around the islet of Anydros, located ~25km NE of Thira. Several seismic events of M>3 were recorded almost every day, during that period, with the larger event to be of M5.3. This intense seismicity was accompanied by strong ground deformation on the broad area of South Aegean. As was expected, the most intense ground deformation was observed in Thira Island and in Anydros Islet. However, the type of motion in SANT cGNSS station was of completely different type compare to the previous period (while the seismicity was located inside the Caldera). The SANT station showed a strong North motional component and intense subsidence. It has to be noticed that the daily amplitude of the ground deformation reached values up to 10mm/day during the peak of the seismic crisis (10-15 of February). Moreover, GNSS data from the surrounding islands, as is Ios and Naxos to the North of Thira exhibited changes in their kinematic behavior, highlighting the intense activity that was taking place in the marine area of Anydros Islet.

The strong ground deformation decreased around the end of February 2025, almost a month after its initiation. Since then, it appears that the rate of ground deformation has significantly decreased in both horizontal and vertical component. The decrease of ground displacement coincided with the decrease in the seismicity, that has been expressed not only with smaller number of events per day, but also and of smaller amplitude, with the events of ~M3 to be less than the previous one month long period.

A major issue during this crisis was the identification of the seismic activity; it was of volcanic or tectonic character / origin? In the complex environment of South Aegean, where the Santorini Volcanic complex is located, there is not an easy or unique answer to such issues. Major tectonic zones, as is the Amorgos area (with a history of strong earthquakes), volcanic centers as is the Kameni Islet and the submarine Kolubo volcano, create an extremely complex geological environment that requires a multidisciplinary approach in order to comprehend it. To better understand, explain and monitor the ongoing processes in the broad area of south Aegean the geodetic and seismological academic and research community of Greece took action establishing a dense network of continuous GNSS stations, as well as seismological stations. In this common effort several institutes from abroad also collaborate and joint efforts with the Greek institutes. The main scope of this effort is to achieve a better spatial coverage of the area, with permanent operating stations, and be able not only to monitor the daily progress of the deformation and seismological crisis but also to foresee its evolution. As result of this joint effort, it was the establishment, and/or

re-start of more the 20 permanent GNSS stations in the broad area of South Aegean Sea. The new GNSS stations that were established in the island of Thira, Thirasia, Ios, Amorgos, Anafi, Sikinos, and in the islets of Anydros and Christiana, together with the existing stations in the surrounding islands that were operated by other private entities (Hellenic Cadastre HEPOS, Metrica SA, JGC SA, TreeCompany SA,), together with new sites that were established by other international institutes in collaboration with the Greek ones (ie, CNRS - École Normale Supérieure - PSL, France, INGV, Instituto Nazionale di Geofisica e Vulcanologia, Italy) and with the support of Earthquake Planning and Protection Organization of Greece (EPPO) will provide on a continuous base all the necessary data in order to monitor this vital area of Greece, will help to better protect the local community and will also provide valuable insight on the geological processes that are taking place in the complex environment of Santorini Volcano, the broad area of South Aegean, as well as along the Hellenic Volcanic Arc. The daily GNSS data from all the operating stations are processed on a near real-time basis, using advanced algorithms, from all the participating institutions providing solutions and information not only for scientific use but also for operational use on the framework of the civil protection actions.

Acknowledgements
The authors would like to acknowledge the organization efforts of Dr. S. Lalexos on behalf of Earthquake Planning and Protection Organization of Greece. Daily GNSS raw (RINEX) data were contributed by: (1) The “Institute for the Study and Monitoring of Santorini Volcano” IMOSAV providing data from several GNSS stations in Thira, Thirasia and Nea Kameni (https://ismosav.gr/en/home/); (2) The Hellenic Positioning System (HEPOS) provides data from five stations in the south Aegean free of charge by the Hellenic Cadastre (www.ktimatologio.gr); (3) METRICA S.A. provides GNSS data from several stations located in the broad area of South Aegean (https://gr-sbc.nrtk.eu); (4) JGC Geoinformation Systems S.A. offers data from one permanent station in Thira (https://www.jgc.gr/jgc-net/) (5) TreeCompany and its GNSS network URANUS provides data from one station in Thira (https://uranus.gr/). Also, the authors acknowledge the contribution of Dr. P. Briole (from CNRS France) in order to establish new GNSS stations in the South Aegean area, as well as the establishment of GNSS sites from INGV (Instituto Nazionale di Geofisica e Vulcanologia, Italy).

17th INTERNATIONAL CONGRESS of the Geological Society of Greece

BULLETIN OF THE GEOLOGICAL SOCIETY OF GREECE, SP. PUBL.

EXTENDED ABSTRACT 278

Ground Deformation in Nisyros Volcano (Greece) Determined by GPS and SAR Interferometric Techniques

Sakkas V.[1], Tzanis A.[1], Lagios E.[1]
(1) Geophysics Laboratory, Department of Geology and Geoenvironment, National and Kapodistrian University of Athens, Greece, vsakkas@geol.uoa.gr

Introduction

The southeastern part of the Hellenic Volcanic Arc (HVA), including Kos, Yali and Nisyros islands, is geodynamically very active (Figure 1). Intense seismic activity occurred on Nisyros Island during 1996-1998, accompanied with strong ground deformation and temperature increase of the fumaroles. Nisyros Island lies above a basement of Mesozoic limestone (Geotermica Italiana 1983; 1984). The exposed rocks are Quaternary volcanics. The evolution of Nisyros Volcano during the past 160,000 years, together with the succession of calc-alkaline lavas and pyroclastic rocks, has been studied in detail by various authors (ie Hardimann 1999; Tibaldi et al. 2008).
Major fault systems have been identified within the volcanic edifices of the Kos-Yali-Nisyros Volcanic Field (Figure 1) on the basis of structural and geological investigations (ie Papanikolaou and Nomikou 2001; Nomikou and Papanikolaou 2011). The caldera's rim and its accompanying cone-shaped local faults are entirely volcanic structures, which are a result of the collapsing of the caldera after the last Plinian eruptions.

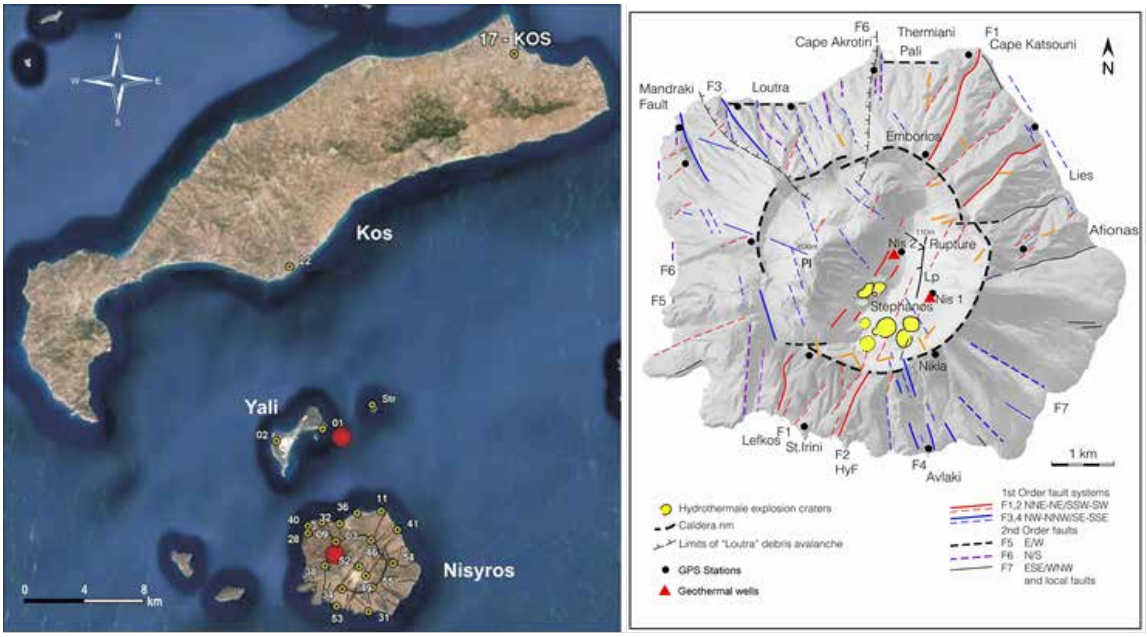

Figure 1. Left part: Distribution of stations of the GPS network of the Kos-Yali-Nisyros Volcanic Field. Solid red circles represent the two modelled Mogi point sources. Str stands for the station established on Strongyli Islet). Right part: Fault pattern of major faulting systems (F1 to F7), location of hydrothermal explosion craters and other significant features superimposed on a digital elevation model of Nisyros Island. Abbreviations of locations; PI: Prophitis Elias, Lp: Lakki Plain.

Earthquakes have been described throughout historical times as has been reported in detail since 1830 (Gorceix 1873a, b and c; Stiros and Vougioukalakis 1996). Their origin may be a result of regional tectonic processes, magma ascent, degassing phenomena of deep crustal magma and steam explosions within the hydrothermal system. The Mandraki Fault (Figure 1) that comprises a branch of the F3 fault system was reactivated in 1996 (Lagios et al. 2005) and caused damage to buildings and other structures within Mandraki (Ioannidis 1998). Tectonic processes expressed by the latest seismicity indicate tensional fracturing (Makris and Chonia 1999) which could reduce the lithostatic pressure and trigger explosive volcanic phenomena, such as those reported in 1871 and 1873 by Gorceix (1873a). The most recent seismic activity in the area was in 2017 with a strong earthquake (Mw6.2; Jul. 20, 2017) taking place NE of Kos Island (Ganas et al., 2019). Moreover, increased seismicity occurred during Jun-August 2021, in the marine area SW of Nisyros. Both these bursts of seismicity were of tectonic character and have not been

associated with volcanic activity.
Efforts for studying the ground deformation on Nisyros started after the outbreak of the seismic activity in 1996 and have involved GPS observations and SAR interferometric analysis (e.g. Lagios et al. 2005;). This study presents the ground deformation on Nisyros up to 2023 and addresses its evolution during the years 2002-2023 on the basis of combined GPS/GNSS and advanced SAR interferometric techniques.

GPS/GNSS Measurements

A geodetic GPS network (Figure1) was established in the broader area of Nisyros in June 1997 in order to study ground deformation. It initially consisted of 21 stations and included a local reference station (17-Kos) at the northeastern part of Kos Island (Lagios et al. 2005). Another station (benchmark) was installed on Strongyli Islet in 2013. Moreover, a continuous operating GNSS station was established in Mandraki in November 2016, as well two more continuous station were established in 2023 in Nikia and Yali. Campaign measurements were performed in periodic times, with the last measuring period to be December 2023. All campaigns were made in the static mode using tripods cantered above the permanently installed benchmark at a given station. Post-processing was performed using the Bernese GNSS Software, versions 5.2 (Dach et al. 2015), together with post-computed satellite orbits (available through the International GNSS Service) to improve the error estimation. Accuracies of 2 to 5mm and 4 to 8 mm were achieved for the horizontal and vertical components, respectively.
The GPS measurements during the active period (1997-1999) showed that the amplitude of the horizontal deformation ranged from 20 to 60 mm. The maximum horizontal displacement occurred between 1997 and 1998 during the peaking (1997) and subsequent high level (1998) of seismic activity. The period 1999-2002 Nisyros entered a different mode of deformation with a clear westward in-crease of the horizontal component in almost all its western part for the period 2001-2002. Vertical deformation in the sense of a general uplift of the whole island occurred over almost the entire active period of observation up to 2002, and in particular the majority of stations exhibited uplifts of 40 to 60 mm between 1997 and 1998. Greater values of uplift were measured at stations installed on the western uplifted side of the activated Mandraki Fault.
The GPS network on Nisyros after 2002 was remeasured in August 2012, which was a decade after its establishment. Through this decade (2002-2012), there was no significant seismic activity in the broader area, nor was there any other type of volcanic activity as would be detected via temperature increase in the fumaroles. It may thus be assumed that the ground deformation that occurred in the island was of an almost linear character without any strong fluctuations. After 2012, the network was re-measured more often, in total eight times up to 2023, deducing a more accurate velocity field of the area (Figure 2).

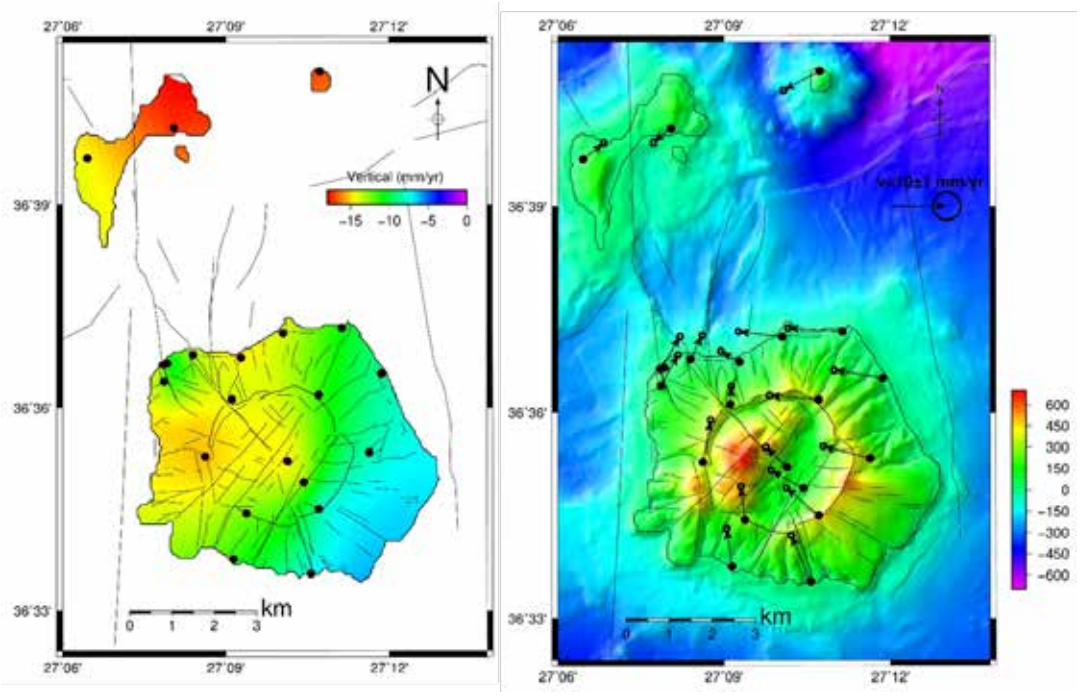

Figure 2. Vertical (left panel) and horizontal (right panel) deformation on Yali-Nisyros for the period 2002-2023 (relative to ITRF2014 reference frame, subtracting the regional motion of the area).

As can be seen on the velocity map for the period 2002-2023 (Figure 2), the most prominent aspect of ground deformation is the subsidence that took place in Nisyros and Yali during this ,ore than 20 years period. The subsidence reached values of more than 10mm/yr in the northern part of Nisyros, but with smaller values (~3-5 mm/yr.) in the southern and eastern parts. The horizontal velocity vectors of the stations located on the NE had motion to the SW, while the stations on the NW exhibited motion to the ENE. The amplitudes of the horizontal velocity vectors are slightly higher for the stations at the northeastern part (~9 mm/yr.) as compared to the northwestern part (~5 mm/yr.). The two GPS stations located in Lakki Plain also subsided. Generally, it should be noticed that the stations located outside the caldera's rim had exhibited stronger deformation as compared to those located inside the rim for both horizontal and vertical components. The nearly opposite direction of horizontal motion that is observed for the stations located at the eastern and western parts of Nisyros may be due to the strong subsidence which had taken place at its northern and central parts during this period, thus forcing the facing eastern and western flanks of the island to 'collapse' towards its centre which produced the observed westward and eastward horizontal motions, respectively.
Significant subsidence (~8 mm/yr.) had also occurred in Yali islet. The horizontal velocity components of the two stations, located on the extreme eastern and western parts, have similar amplitudes (~8 mm/yr.) and clearly point towards the central area of the islet. It is concluded that strong subsidence likely occurred in the region between Yali and Nisyros which caused the two edges of the islet to converge toward this area, consistent with the deformational pattern observed at those two stations.

SAR Interferometry

Conventional Synthetic Aperture Radar (SAR) Interferometry (InSAR) and GPS measurements are the most widely used techniques to measure the ground deformation in volcanoes. For the period 2003-2010 ASAR ENVISAT images were processed in ascending and descending orbital geometry using the SqueeSAR™ Technique. Based on this technique Line of Sight (LOS) velocity maps were produced (Figure 3).

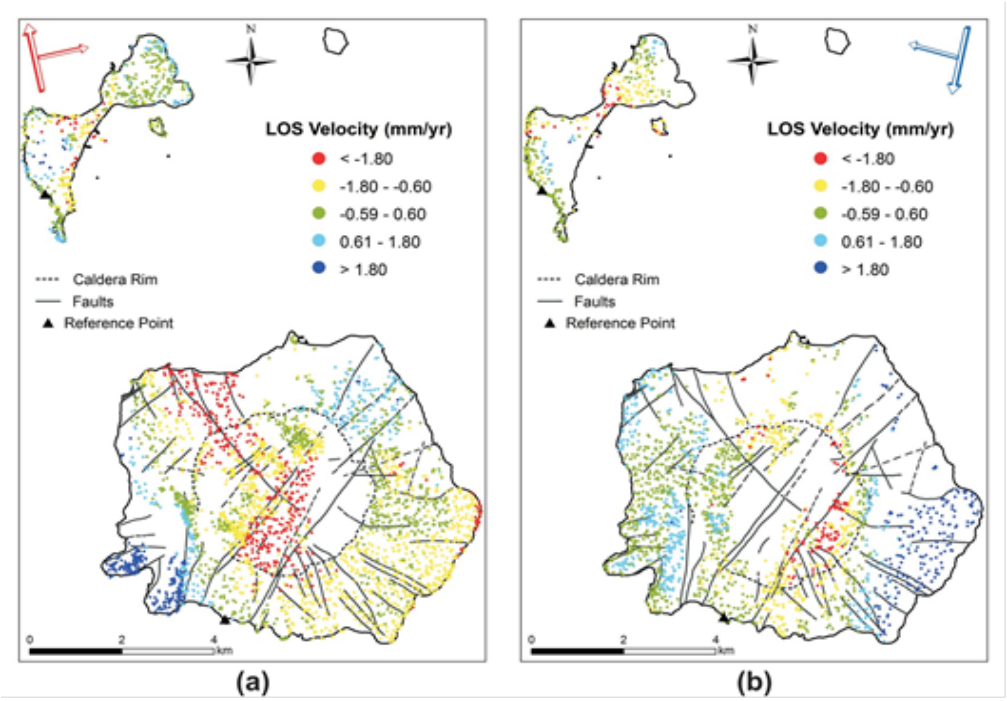

Figure 3. LOS Velocity Field deduced from the SqueeSARTM for Ascending (left panel), and Descending (right panel) orbital geometries, for the period 2003-2010. Red and blue arrows indicate the orbit and acquisition directions for the ascending and the descending data sets, respectively.

Greater negative LOS velocities (~2.5 mm/yr) are observed along the F3 faulting system and between F1 and F2 faulting zones inside the caldera in the ascending image. These values are not observed in the descending image. The western part of Nisyros and west of the caldera's rim show similar velocities for both images, ranging from relatively stable to slightly positive values (~1.5 mm/yr). The greatest LOS velocities (1.8 to 3.0 mm/yr) are observed in the ascending image near the two small peninsulas at the extreme southwestern part, bounded by F1 and F6 faulting systems. The southeastern part of Nisyros shows small negative LOS velocities (~-1.5 mm/yr) in the ascending

image and positive values (up to 2 mm/yr) in the descending image, indicating an eastward component of ground deformation during 2003-2010. The northeastern part of Nisyros has positive LOS velocities (0.6 to 1.8 mm/yr) on both images, with an inconsistent pattern of ground deformation in the northern part due to dense vegetation. The Yali islet shows no consistent deformation pattern between acquisition geometries, except in the northeastern part with relatively stable to small negative LOS velocities. Differential motion between the northeastern and southwestern parts may be due to differing geological characteristics: obsidian in the northeast and pumices in the southwest.
For the period 2018-2022 interferometric results were obtained by the European Ground Motion Service (EGMS, https://egms.land.copernicus.eu/). The data of Ascending and Descending orbital geometries were initially calibrated using the permanent station in Mandraki, and then decomposed on East-West and Vertical component (Figure 4).
To perform the calibration of the InSAR data in the island the velocity vector of the continuous operating GNSS station NISY has been taken into consideration. Initially, the GNSS velocity vector was estimated for the time period that the EGMS product covered, and it was projected into the LOS direction, for both ascending and descending orbital geometries. As a second step, from the EGMS products the LOS velocity vector in both geometries for the “Data Points” located close to GNSS station were compared to the GNSS projected LOS vector, and the difference between the GNSS LOS projected vector and the InSAR LOS vector was estimated. Finally, the difference was “added” to the rest of the “Data Points” to obtain the GNSS calibrated LOS velocity fields. The new calibrated LOS velocity maps on both geometries were combined in order to decompose the LOS vector into the Vertical and the East-West components.

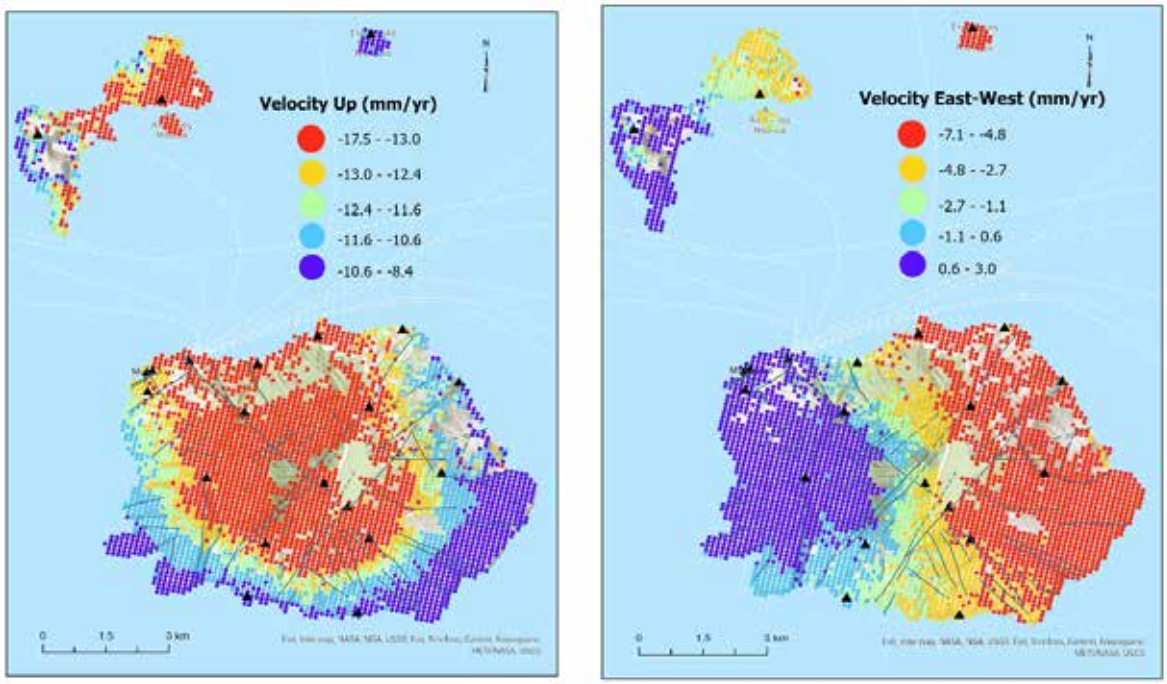

Figure 4. Vertical (left panel) and East-West (right panel) velocity field calibrated using the continuous GNSS station in Mandraki area.

The local calibrated and decomposed EGMS interferometric product show small velocities values for both components, indicative of linear type of deformation. The vertical velocity field highlights and confirm the velocity field deduced by the GPS technique, showing intense subsiding motion in the central and northern part of island (up to -17 mm/yr), but smaller subsidence in the southern Nisyros. The East-West component also clearly depicts the diametrical opposition between the eastern and western part of Nisyros and Yali. The western part exhibits positive velocity values, consistent to eastward motion, while the eastern flanks show negative velocities, indicative of westward motions. A feature that rises observing the East-West velocity field is that changes on the sign of motion coincide with the main tectonic zones that cross-cut the island.

Discussion

During the “unrest” period from 1996 to 2000, strong ground non-linear deformation was observed, which was explained using a model that included two MOGI Point Sources: one offshore and one inland. Interferometric results

(SqueeSAR™) for the subsequent period from 2003 to 2010 showed linear deformation along major faulting zones that cross-cut the island. This deformation included a significant vertical component (subsidence) mainly in the central and northern parts, and a considerable horizontal component in the eastern, western, and southeastern parts. Differential GPS measurements for the period from 2002 to 2023, and interferometric products for the period 2018-2022 indicated intense subsidence at all stations, with a horizontal component pointing towards the central part of Nisyros. The observed deformation may be explained as a result of combined volcanic and tectonic activity, including a decrease in pressure in the possible magma chambers beneath and offshore of Nisyros Island, and possible tectonic motions along the trough offshore north of Nisyros and south of Yali Islet. Notably, there was an absence of any significant shallow seismic activity during the period from 2002 to 2023 in the vicinity of Nisyros.

Acknowledgements

SqueeSAR™ processing was performed by TRE company. Part of this research was supported by the project “Provision of services regarding the implementation of an integrated solution for the continuous and necessary microseismic monitoring of the island of Nisyros, with emphasis on the area of Agia Irini, highlighting the parameters required for geothermal projects” funded by the Public Power Corporation Renewables SA (PPCR) (Special Account for Research Grants of NKUA, project).

References

Ganas A., Elias P., Kapetanidis V., Valkaniotis S., Briole P., Kassaras I., Argyrakis P., Barberopoulou A., Moshou A., 2019. The July 20, 2017 M6.6 Kos Earthquake: Seismic and Geodetic Evidence for an Active North-Dipping Normal Fault at the Western End of the Gulf of Gökova (SE Aegean Sea) (2019), 176 (10), pp. 4177 – 4211.

Geotermica Italiana. 1984. Nisyros 2 geothermal well. PPC EEC report: 1-44.

Geothermica Italiana. 1983. Nisyros 1 geothermal well. PPC EEC report:1-106.

Gorceix MH, 1873a. Sur d’´etat du volcan de Nisyros au mois de mars 1873. C.R. Acad. Sci. (Paris) 77: 597–601

Gorceix MH, 1873b.Sur la r´ecente ´eruption de Nisyros. C.R. Acad. Sci. (Paris) 77: 1039

Gorceix MH, 1873c. Sur l’´eruption boueuse de Nisyros. C.R. Acad. Sci. (Paris) 77: 1474–1477

Hardimann JC, 1999. Deep sea tephra from Nisyros Island, Eastern Aegean Sea, Greece. In Firth, C.R. & McGuire W.J. (eds.) Volcanoes in the Quaternary. Geol. Soc. (London), Spec. Publ. 161: 69-88.

Ioannidis K.,1998. Nisyros Island: Observed damages to buildings in Mandraki. Newsletter, European Center for Prevention & Forecast Earthquakes 2: 33–353

Lagios E, Sakkas V, Parcharidis I, Dietrich V., 2005. Ground deformation of Nisyros Volcano (Greece) for the period 1995-2002: Results from DInSAR and DGPS observations. Bull. Volcanology 68: 201-214

Makris J, Chonia T., 1999. Active and Passive Seismic studies of Nisyros Volcano, East Aegean Sea. In: Jacob BAW, Bean CJ, Jacob STF (eds), Active and Passive Seismic Techniques Reviewed, Proc. 1999 CCSS Workshop Dublin, Ireland: pp 9–12

Nomikou P, Papanikolaou D., 2011. Extension of active fault zones on Nisyros Volcano across the Yali-Nisyros Channel based on onshore and offshore data. Mar. Geophys. Res. 32: 181-192

Papanikolaou D, Nomikou P., 2001. Tectonic structure and volcanic centres at the eastern edge of the Aegean Volcanic Arc around Nisyros Island. Bull. Geol. Soc. Greece XXXIV: 1289–296

Stiros SC, Vougioukalakis G., 1996. The 1970 Yali (SE edge of the Aegean Volcanic Arc) earthquake swarm: Surface faulting associated with a small earthquake. Ann. Tecton. X: 20–30

Tibaldi A, Pasquare, FA, Papanikolaou D, Nomikou P.,2008. Tectonics of Nisyros Island, Greece, by field and offshore data, and analogue modelling. J. Structural Geol. 30: 1489-1506

17th INTERNATIONAL CONGRESS of the Geological Society of Greece

BULLETIN OF THE GEOLOGICAL SOCIETY OF GREECE, SP. PUBL.

EXTENDED ABSTRACT 279

Comparison of dermal bioaccessibility of Cu, Pb, and Hg between modern and ancient cosmetics

Samothraki M-I.[1], Kypritidou Z.[1], Argyraki A.[1]

(1) Department of Geology and Geoenvironment, National and Kapodistrian University of Athens, Panepistimiopolis, Zographou, 15784, Athens, Greece

Introduction

This research highlights the severe health risk that the ancient populations faced by applying raw minerals as cosmetics on a daily basis, following the risk assessment methodology used in modern cosmetics.

In each century, facial cosmetics fulfilled a specific purpose. Since ancient times, the use of cosmetics has been a way of making a statement, an element of culture, as well as an example of scientific development in the field of health. Both men and women in ancient Egypt, Greece and Rome (14th century BCE) used cosmetics not only during religious rituals, but as a daily-care routine to show their social status and prestige. Black-coloured eyeliners were the most common facial cosmetics, which were produced by grinding galena or stibnite (Murube J., 2013, Perez-Arantegui J., 2021). Green, grey, white, red and bluish eyeshadows were prepared by malachite, galena, cerussite, and chryssocolla powders, respectively (Murube J., 2013). Red ochre, cinnabar and minium were used to blush their cheeks. Cerussite and white marl were often used as skin whiteners.

It is reported that cerussite and cinnabar were used until the 16th century BCE by royalty as skin whiteners, lipsticks, and blush (McMullen & Dell'Acqua, 2023; Welcomme *et al*., 2006). However, these natural cosmetics consist of highly toxic elements such as Pb, Sb, Cu, As and Hg, causing serious health effects in ancient populations (Olson K., 2009). Anemia, neurological disorders, kidney failure, liver damage, miscarriage and cancer, are some of the health impacts induced upon ingestion or inhalation of mineral dust containing the above elements. However, references regarding the effects of dermal exposure to these elements (except for exema) and their bioaccessibility through the skin, are scarce.

The aim of this study was the comparison of the potential dermal bioaccessibility of Pb, Cu and Hg contained in ore minerals (such as those used in antiquity) and modern cosmetics. The specific objectives of the study were the determination of: (a) the pseudo-total and sweat extractable elemental concentration, (b) the bioaccessible metal content, and (c) the examination of the systematic exposure and hazard from these elements, in both minerals and cosmetics.

Materials and Methods

Four minerals and the respective commercial cosmetics were selected and studied for their dermal bioaccessible content of toxic elements. The selected minerals include galena, cerussite, malachite, and cinnabar, which were used as eyeliner, foundation, eyeshadow, and blush respectively. By analogy to these minerals, the respective modern cosmetics include foundation, blush, eyeliner, and eyeshadow, purchased from local stores (Table 1). The mineralogical composition of the samples (minerals and cosmetics) was examined through X-ray Diffraction spectroscopy in randomly oriented mounts, from 3-65^{o} 2-theta, with a scanning rate 1^{o}/min (Cuka radiation, 40kV, 40mA, SIEMENS D5000).

Table 1. The associated minerals and cosmetics, and the respective analyzed element of the current study

Mineral	Modern cosmetics	Associated element
Galena	Eyeliner	Pb
Cerussite	Foundation	Pb
Malachite	Eyeshadow	Cu
Cinnabar	Blush	Hg

The pseudo-total elemental composition of minerals and cosmetics was identified by aqua regia digestion. Specifically, about 0.1g of mineral or 1g of cosmetic powders were digested in 1:3.5 HNO3:HCl mixture, for 2hrs in a sandbath (~110^{o}C) following the procedure as described by Irfan *et al.* (2022). The dermal bioaccessible elemental concentrations were determined by extracting the solids with an artificial sweat solution. The extraction solution was composed of 0.5% NaCl, 0.1% urea and 0.1% lactic acid according to EN 1811:2023. The pH 6.5 was adjusted by drops of NH_3. About 0.4g of solid was dispersed in 40ml solution following the assumption that the solid/sweat ratio that is deposited on the face daily is 1mg/0.1ml per skin surface area (Anselm et al., 2022). The suspensions were mixed for 2 hours in the thermal chamber under the constant temperature of 37 Celsius (similar to the human body). Then, followed centrifugation for 5 minutes. Due to the high concentrations level, the aqua regia samples were diluted by 1: 10 ml ratio of sample and 2% HNO_3, whereas, dermal samples were diluted by 1:10 ml ratio of dermal sample and half of the amount of sweat solution with 2% HNO_3. Each sample (mineral and cosmetic) was analyzed in dublicates, and the mean and relative percent difference were calculated. Blanks were also included in each analytical batch. The

extracted solutions were stored at 4°C prior to analysis with F-AAS and ICP-MS, for Pb, Cu, and Hg.
The dermal bioaccessibility of Pb, Cu, and Hg (D_{dermal}, %) from each mineral and/or cosmetic was calculated by dividing the sweat extracted concentration (C_{sweat}, mg/kg) with the pseudo-total concentration (C_{AR}, mg/kg) obtained by aqua regia digestion (Eq 1):

$$D_{dermal}(\%) = \frac{C_{sweat}}{C_{AR}} \times 100 \qquad \text{(Eq. 1)}$$

The systematic exposure dose (SED, mg/kg bw/d) of each element from minerals and cosmetics was calculated according to the European Scientific Committee on Consumer Safety (SCCS, 2023) (Eq. 2):

$$SED = \frac{E_{prod}}{BW} \times \frac{C}{100} \times \frac{D_{abs}}{100} \qquad \text{(Eq. 2)}$$

where E_{prod} is the effective exposure per product (mg/kg/d), BW is the body weight of the consumer (60 kg), C is the elemental concentration (%wt) in the product, and Dabs is the dermal absorption factor (%). E_{prod} values were 0.005 for galena/eyeliner, 0.51 for cerussite/foundation, 0.02 for malachite/eyeshadow and cinnabar/blush, and 0.4 for orpiment/waxing cream respectively (SCCS, 2023).
The risk to human health by application of minerals and modern cosmetics onto the skin on a daily basis, was assessed by calculating the Hazard Quotent (HQ) for each element as (Eq. 3):

$$HQ = \frac{SED}{RfD} \qquad \text{(Eq. 3)}$$

Where RfD is the reference dermal dose for each element. The established RfD for Pb, Cu, and Hg are $1.6*10^{-4}$, $5*10^{-1}$, and $2.3*10^{-4}$ mg/kg bw (Irfan *et al.*, 2022). The sum of HQ for minerals and cosmetics defines the Hazard Index (HI), with an accepted value less than one, when no hazard is induced.

Results & Discussion

The mineralogical analysis of minerals revealed that cerussite and malachite were free of impurities, whereas cinnabar contained minor quartz and galena traces of wurtzite (Fig. 1a). The examined cosmetics (blush, foundation, eyeshadow) consisted mainly of talc, kaolinite and micas. Blush contained also chlorite, smectite and anorthite, whereas the foundation contained zincite and anatase (Fig. 1b).
The pseudo-total elemental concentrations in minerals range from 11.3% wt Hg in cinnabar to 47%wt Pb in cerussite (Fig. 2a), exceeding by far the EU limits for metals in cosmetics (2 mg/kg Pb and 0.1 mg/kg Hg). The respective concentrations in cosmetics range from 6.4 mg/kg Hg in blush to 134 mg/kg Pb in eyeliner, also exceeding the regulatory values.

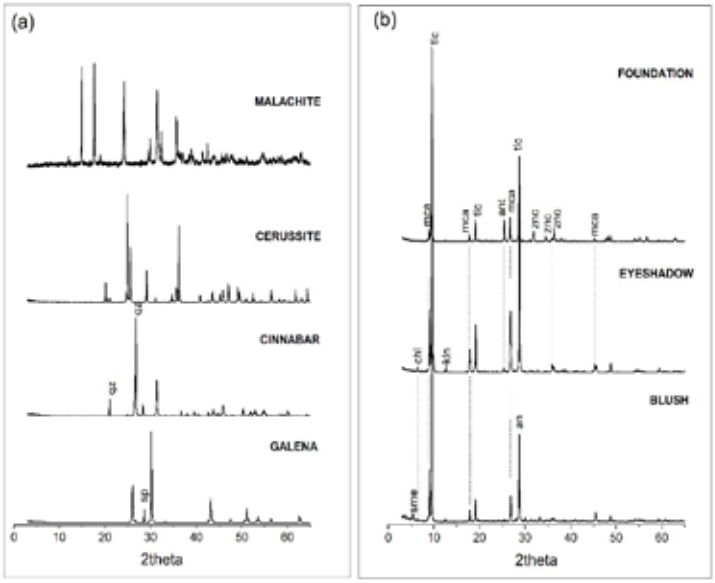

Figure 1. XRD patterns of minerals and cosmetics. The non-annotated peaks in (a) are assigned to the corresponding main mineral phases (i.e. galena, cerussite, cinnabar and malachite). Mineral symbols after IMA (Warr, 2021) (anorthite (an), anatase (ant), chlorite (chl), kaolinite (kln), mica (mca), talc (tlc), quartz (qz), smectite (sme), sphalerite (sp), zincite (znc))

The elemental concentrations extracted by the artificial sweat are much lower in minerals, showing a relative stability to dissolution (Fig. 2b). Particularly, the sweat-extracted concentrations range from 78 mg/kg Hg in cinnabar to 2299 mg/kg Pb in cerussite. The dermal bioaccessibility of minerals is less than 2%. The respective sweat-extracted concentrations in cosmetics range between 0.5 mg/kg Hg in blush and 108 mg/kg Pb in eyeliner. However, the dermal bioaccessibility of the elements is high, following the order: Cu (eyeshadow, 100%)> Pb (eyeliner, 81%)>Pb (foundation, 67%)>Hg (blush, 7%). This shows that, although the sweat extracted concentrations in cosmetics are much lower compared to minerals, they are readily bioaccessible. This is explained by the fact that these elements are bound onto the clay surfaces of cosmetics (smectite, micas) and are easily exchanged by sodium (the major cation in sweat solution).

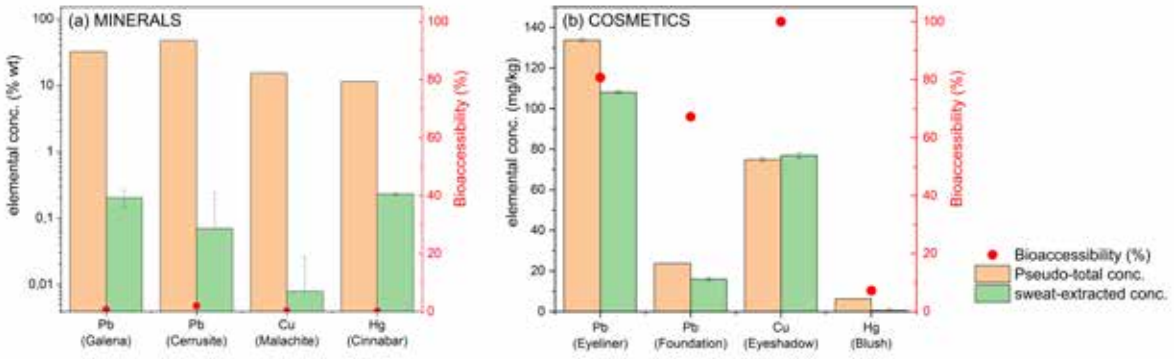

Figure 2. Pseudo-total and sweat extracted concentrations of Pb, Cu, Hg and As from (a) minerals and (b) cosmetics, and their bioaccesibilities

The exposure of consumers to various ingredients contained in cosmetics is assessed based on the systematic exposure dose (SED) as established by SCCS (2023). The SED values for Pb, Cu and Hg were calculated for both minerals and cosmetics, by examining two bioaccessibility scenarios. The first (worst case) scenario assumed that 100% of the pseudo-total concentration of each element is bioaccessible (D_{abs}=100%), whereas the second scenario assumed that only the sweat-extracted elemental concentrations are bioaccessible (D_{abs}=D_{dermal}%). The obtained SED values are given in Table 2.

Table 2. SED values (mg/kg bw/d) as calculated for each element contained in minerals and cosmetics for the two bioaccessibility scenarios

Element	Mineral	D_{abs}=100%	D_{abs}=D_{dermal}%
Pb	Galena	$2,68*10^{-2}$	$1,68*10^{-4}$
Pb	Cerussite	$9,61*10^{-1}$	$1,95*10^{-2}$
Cu	Malachite	$1,57*10^{-1}$	$2,32*10^{-4}$
Hg	Cinnabar	$5,09*10^{-2}$	$2,62*10^{-5}$

Element	Cosmetic	D_{abs}=100%	D_{abs}=D_{dermal}%
Pb	Eyeliner	$1,12*10^{-5}$	$9,00*10^{-6}$
Pb	Foundation	$2,02*10^{-4}$	$1,36*10^{-4}$
Cu	Eyeshadow	$2,49*10^{-5}$	$2,57*10^{-5}$
Hg	Blush	$2,13*10^{-6}$	$1,67*10^{-7}$

As expected, the SED values elements in minerals are much higher than those in cosmetics. The 100% bioaccessibility scenario gives the highest SED values especially for minerals. However, these cosmetics (ancient and modern ones) are applied together onto the face skin on a daily basis, therefore a cumulative systematic exposure should also be calculated. The cumulative SED value ranged from 0.02 to 1.2 mg/kg bw/d in minerals, and $1.7*10^{-4}$ to $2.4*10^{-4}$ mg/kg

bw/d in cosmetics. It is evident that the ancient populations were systematically exposed in high metal concentrations compared to today on a daily basis by applying the raw minerals onto their faces.

The Hazard Quotent and the Hazard Index (HI) for minerals and cosmetics were also calculated for each element in each bioaccessibility scenario. Specifically, at the 100% bioaccessibility scenario the HI for minerals is 2700, whereas for cosmetics 0.16. Additionally, when the dermal bioaccessibility is considered as the exposure scenario, the HI for minerals is 6.22 and for cosmetics 0.05. In either case the HI values of minerals is much higher than 1, implying that the high hazard due to application of ancient cosmetics.

In the 100% bioaccessibility scenario, Hg is the most hazardous element, contributing 63.7% and 89.8% to the total hazard in ancient and modern cosmetics respectively (Fig. 3). On the contrary, when dermal bioaccessibility is considered, Pb is the more hazardous element, contributing over 70% in total HI. This shows that, although Hg is more toxic and carcinogenous, it is less hazardous due to its lower penetration through the skin. It is documented that, among the mercuric substances, cinnabar is insoluble in water with low oral bioaccessibility (~0.2%) (Liu et al., 2009). Moreover, studies on dermal contact between cinnabar-rich sands and workers, showed that Hg was not bioaccessible through skin (Cegolon et al., 2022). However, Pb has high bioaccessibility, explaining the various health effects induced during ancient times. Among lead compounds, lead released from cerussite is more bioavailable than from galena, due to its higher solubility. Considering that cerussite is more easily dissolved and applied as a foundation in a larger surface area, the expected health impacts are more severe, compared to the other elements.

Figure 3. Contribution of each element to the total HI obtained by applying minerals and modern cosmetics, in the two bioaccessibility scenarios

Conclusions

Minerals have been extensively used as cosmetics from ancient times since the 16th century BCE, due to their variety of colours, such as galena, cerussite, cinnabar and malachite. However, these phases are primary ore minerals for the extraction of Pb, Cu and Hg, elements of high toxicity for living organisms. Although numerous in vitro and in vivo toxicological studies have been carried out regarding the bioaccessibility of these elements, most of them involve artificial organic compounds (mostly present in commercial products) with different physicochemical properties compared to natural mineral phases. Moreover, these studies refer to bioaccessibility due to inhalation and/or ingestion of these compounds, which is much higher compared to the penetration through skin. In this study we tried to assess the bioaccessibility of elements contained in ancient cosmetics following the risk assessment procedure of modern cosmetics. The results indicate that the ancient populations were exposed to severe health risk due to the application of raw minerals onto their skin on a daily basis.

References

Anselm, O.H., Davidson, C.M., Oyeyiola, A.O., Oluseyi, T.O., 2022. Effects of Artificial Sweat Formulation and Extraction Temperature on Estimation of the Dermal Bioaccessibility of Potentially Toxic Elements in a Contaminated Soil from an E-Waste Recycling Site. Geosciences 12, 31.

Cegolon, L., Mastrangelo, G., Covelli, S., Petranich, E., Pavoni, E., Filon, F.L., 2022. Occupational exposure to mercury from cinnabar enriched sand in workers of Grado Beach, Gulf of Trieste (North-eastern Italy, upper Adriatic Sea). Marine Pollution Bulletin 184, 114057

European Committee for Standardization, 2023. EN 1811:2023 Reference test method for release of nickel from all post assemblies which are inserted into pierced parts of the human body and articles intended to come into direct and prolonged contact with the skin, p.29

Irfan, M., Shafeeq, A., Siddiq, U., Bashir, F., Ahmad, T., Athar, M., Butt, M.T., Ullah, S., Mukhtar, A., Hussien, M., Lam, A.S., 2022. A mechanistic approach for toxicity and risk assessment of heavy metals, hydroquinone and microorganisms in cosmetic creams. Journal of Hazardous Materials 433, 128806

Liu, J., Shi, J-Z., Yu, L-M., Goyer, R.A., Waalkes, P., 2008. Mercury in traditional medicines: Is cinnabar toxicologically similar to common mercurial? Exp Biol Med (Maywood) 233(7), 810–817

Murube, J., 2013. Ocular cosmetics in Ancient Times. The Ocular Surface, 11 (1), 2-7.

Olson, K., 2009. Cosmetics in Roman Antiquity: Substance, Remedy, Poison. The Classical World 102, 3, 291-310

Perez-Arantegui, J. 2021. Not only wall paintings—pigments for cosmetics. Archaeological and Anthropological Sciences 13, 189

SCCS (Scientific Committee on Consumer Safety), 2023. The SCCS notes of guidance for the testing of cosmetic ingredients and their safety evaluation, 12th revision, p.199

Warr L.N. 2021. IMA-CNMNC approved mineral symbols. Mineralogical Magazine 85, 291–320

17th INTERNATIONAL CONGRESS
of the Geological Society of Greece

BULLETIN OF THE GEOLOGICAL SOCIETY OF GREECE, SP. PUBL.

EXTENDED ABSTRACT 280

Result of an inventory program (SAMY) of boreholes of various uses and their contribution to the water balances of groundwater systems.

P. Sabatakakis[1], M. Theodoropoulou, M. Tzima, C. Christidis.
[1]Hellenic Survey of Geology and Mineral Exploration (H.S.G.M.E) 1 Spirou Loui St., 13677 Acharne, Greece, psampatakakis@eagme.gr

Research Highlights

This project constitutes the first systematic documentation of Greece's water resources, with a focus on both qualitative and quantitative groundwater characteristics.
The project data, combined with the Daniel storm in the Thessaly Region, demonstrated its contribution to aquifer management in the affected area and to mitigating the impacts of severe weather.

Introduction

Water is a heritage that must be protected. Both internationally and in Greece, the pressures on water resources are increasing, because of the growing demand from various users for sufficient quantity and quality of water.
Boreholes constitute a critical parameter in the management of water resources, particularly groundwater. The large number of boreholes as well as uncontrolled abstractions have created and accumulated several problems of mismanagement, either in the form of salinization of coastal aquifers or depletion of aquifers. The extensive operation of boreholes in Greece, many of which remain undeclared, significantly affects water balance calculations, the quantitative assessment of groundwater systems, and the evaluation of water usage and needs.
The SAMY Project is carried out by the Hellenic Survey of Geology and Mineral Exploration (H.S.G.M.E.). Project main activities in Greek Territory are: (a) borehole inventory by recording drilling technical data and on-line measurements, (b) database production based to all recorded data and (c) groundwater abstraction related to groundwater resources in ground water bodies. During fieldwork, data recording includes geographical coordinates, operational status, and technical borehole characteristics (depth, drill hole diameter, casing diameter, and pump type). Also, borehole usage such as irrigation, drinking water, stock farming are basic features of recording data with details of pumping.
Based on inventory data final reports are drawn up for all Ground Water Systems in the field including also geomorphological, geological, hydrogeological conditions, land use area, statistics with processing of all recording raw data, drawing water estimation and aquifer water balance.
The result of the inventory program with the systematic counting of boreholes in all the Ground Water Systems (GWS) and the recording of the extractable quantities of water, contributed to the effective implementation of the Water Framework Directive 60/2000, but also to the formulation, implementation and control of policies (water saving, programs of measures, etc.) concerning the rational management of water resources.
The annual volume of groundwater which is used from an aquifer system is one of the two basic factors of the 'equation' required to achieve its rational exploitation in each case. The other factor concerns the recording and mapping of the hydrogeological and hydrological characteristics of a groundwater table, some of which require a "one-time" recording and mapping, such as geological and hydrolithological structures. The establishment of such an information platform, alongside the development of an institutional mechanism for continuous data updating, is essential for effective groundwater management.

Materials and Methods

This study represents the first systematic documentation of water resources in Greece. The program created an extensive database far beyond that of the hydrogeological management of the country's groundwater systems, such as: irrigation needs in different areas for the same crops, energy costs for the same pumping quantities but from different depths in the various rural areas, etc.
A total of 108,092 boreholes of various uses were inventoried and the information collected for this project is:

- geographical and topographic data of the project location
- data of the owner and user of the project
- data of the use of the project (duration, water supplies, type of use)
- hydrological data (average precipitation of at least 20 years, and evapotranspiration), utilizing the information of the 3rd Community Support Framework (CSF) Program of the H.S.G.M.E, which was implemented in all water compartments simultaneously during the period 2006-2012)

- on-site data of the technical characteristics of the boreholes, in particular with regard to the depth of borehole and extraction, duration of extraction / year, yields / hour
- physicochemical data of water (conductivity, temperature, pH)

The high density of collected data, particularly in plains with a significant number of boreholes, facilitated both precise estimations of annual and peak-period water consumption and the detailed analysis of specific hydrogeological parameters. The detailed mapping whose information may be useful beyond hydrogeology.

The methodology for processing large-scale aquifer data included: (a) aquifer system delineation based on Management Plan boundaries, (b) assessment of infiltration and evapotranspiration parameters, and (c) analysis of meteorological data spanning at least 20 years.

For the compilation of the maps, the same methodology was followed in terms of processing the measurements in "non-pumping" conditions and not in dynamic conditions. This is because, as is known, for example, both the level and the conductivity can vary significantly in pumping conditions, resulting in the mapping presenting irregular local variations.

The collection of annual groundwater consumption data and withdrawal rates facilitated not only the total volume estimation but also the assessment of the groundwater systems' overall transfer capacity during the same period. The Project provided important hydrogeological information regarding the supply capacities of a groundwater system or a large part of it is under universal intensive exploitation, as occurs during the period when irrigation is at its peak. During this period and in whatever groundwater systems the inventory work was in progress, it became possible to capture the dynamic salinization conditions in coastal groundwater systems with an "open" hydraulic front to the sea, as well as the overall dynamic retreat of the hydrostatic level.

Results and discussion

The project's results support the General Directorate of Water of the Ministry of Environment & Energy in strengthening national water policy, ensuring both water quality and quantity while aligning with EU Directives (60/2000/EC, 118/2006/EC, and 91/676/EEC).

The total number of recorded boreholes is 108,092. Also, the technical reports include statistical analysis and processing to draw conclusions on all basic parameters as they arise from the registration of the inventory forms, the recording of all parameters on thematic maps and the assessment of the water balance components with the characterization of the Ground Water System (G.W.S.) as Surplus or Deficit. From the preparation of the Technical Reports, it emerged that the large G.W.S. that concentrate the largest number of active boreholes are characterized as deficient.

Figure 1. The total of boreholes in Greece by SAMY Project.

SAMY and DANIEL storm

Following the devastating DANIEL storm, the SAMY Project played a key role in identifying water points within the flooded areas and monitoring underground aquifers in the Thessaly Region. During the SAMY Project, more than 21,894 boreholes have been recorded in Thessaly Region.

Based on the boundaries of the flooded areas of the DANIEL storm (as produced by the Copernicus program - 11/09/2023) and the data of the SAMY, the following results emerge:

- Within the boundaries of the flooded areas, 4,452 boreholes are located, which correspond to approximately 20% of the total boreholes in Region Thessaly.
- More specifically, within the flooded areas, the rate of 87.1% (3,876 boreholes) are active and main use for irrigation, 12.1% (539 boreholes) are inactive/unexploded, 0.5% (22 boreholes) for domestic water 0.3% (15 boreholes) for livestock water and 297 abandoned boreholes have been inventoried.
-

Table 1. Number of boreholes in Thessaly Region

Municipality	Boreholes	Flood zone	Boreholes
Sofades	1,160	Larisa- Stefanovikeio	843
Palama	1,060		
Larisa	383	Trikala – Karditsa - Palamas	3,617
Trikaion	345		
Farsala	299		
Kileler	281		
Farkadonas	186		
Tirnavos	183		
Tempi	181		
Dokomos	173		
Riga Feraioy	61		
Mouzaki	120		
Karditsa	20		

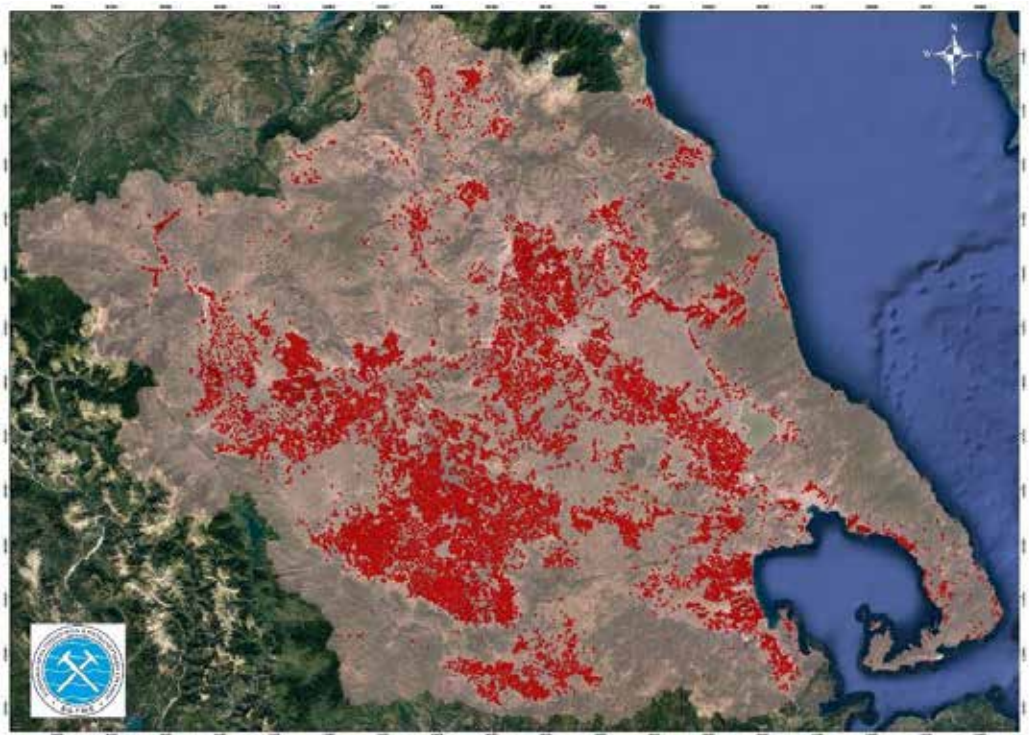

Figure 2. Boreholes in Thessaly aquifer

The functionality of the boreholes located within the flooded areas may have been affected to a very large extent due to the reverse infiltration of water and the subsequent deposition of fine clay material (mud) within the permanent piping of the boreholes, resulting in the non-functionality of the filter pipes and submersible pumping units due to blockage (clogging). Extensive damage is also expected to the accompanying facilities such as sheds, electrical supply panels, pumping units, etc.

Table 2. Number of each use and operational function of boreholes in Thessaly Region

Operational function	Boreholes	Main Use	Boreholes
Active	3,921	Irrigation	3,876
Unexploited	297	Domestic water	22
Inactive	242	Livestock uses	15
		Industrial use	8

Also, from the total available quantities in the entire Water District of Thessaly, it emerged that approximately 90% is used to cover irrigation needs, 6.7% for livestock farming, 1.6% for water supply and 1.7% for industrial and other use.

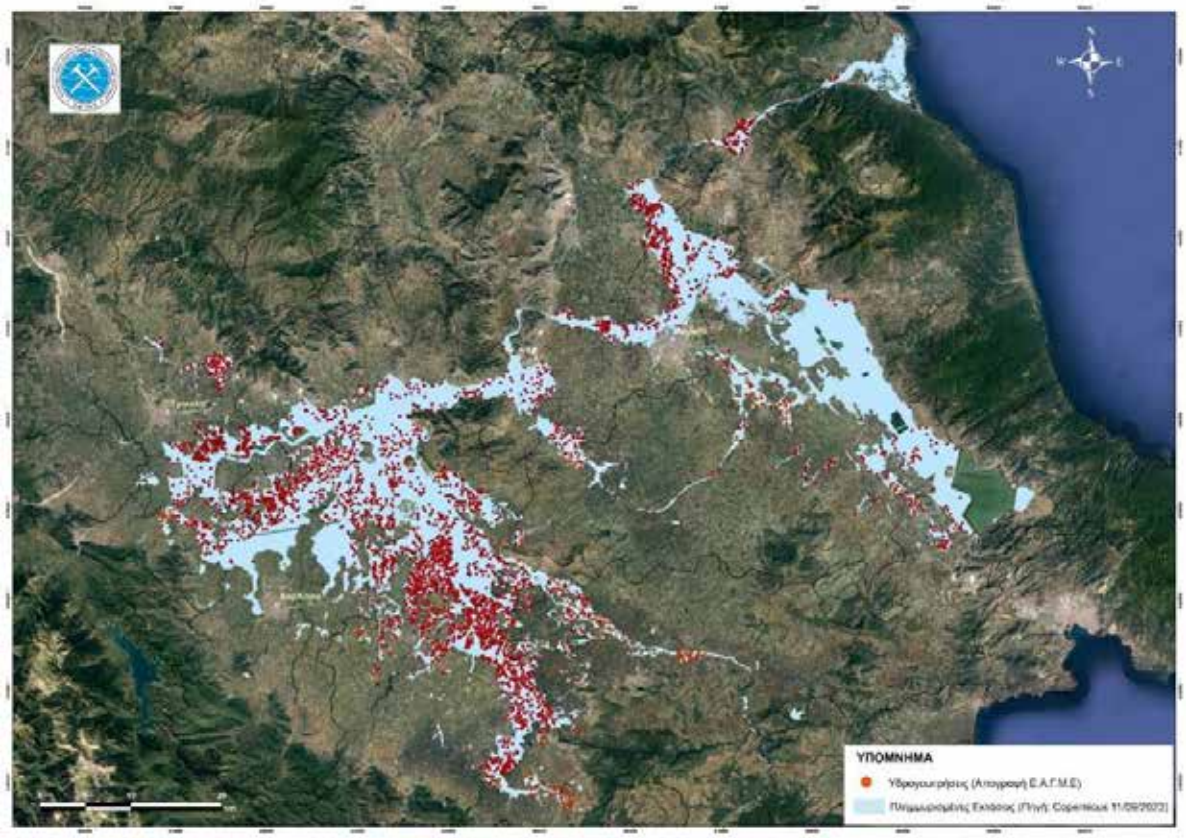

Figure 3. Borehole distribution and flooded areas in the Thessaly Region

Conclusions

This study presents an overview of Greece's water resources. The SAMY Project is a key tool in the effective management of water abstraction and the protection of groundwater systems from over-pumping. The volume of water abstraction is an important parameter for the calculation of water balances, helping to assess the status of Groundwater Systems and the pressures they are exposed to take appropriate measures, as well as to achieve the goal of their rational management. For the first time, we integrate temporal and spatial groundwater data with geological, hydrogeological, land use, and other relevant information to provide a comprehensive analysis. Our key findings are:

- Rational management of the country's water resources and thereby ensuring sustainable development,

benefiting the entire population of the country. This will significantly contribute to the correct decision-making on water resources management by the competent decision-making centers.

- Achieving social consensus and citizen support, allowing them to understand the importance of the entire project by helping to collect data, as well as the benefits that will arise with a direct impact on productive and social life.
- Informing local communities, through a mechanism that will promote dialogue, to learn about the possibilities of the Aquifer System from which they are supplied and thus have knowledge about the possibilities of its exploitation, or even the need to contain and protect the reserves. In both cases there is a social benefit for the integrated and sustainable management of water systems.
- Approval of a strategic plan for the exploitation of the country's water resources by implementing specific actions, to ensure the needs of society and the economy for sustainable water, while at the same time raising awareness among citizens and making them stakeholders in the rational management of available water resources.
- Provision of the National Water Abstraction Register with points/data that will result from the implementation of this project in accordance with Directives 60/2000/EC, 118/2006/EC & 676/91/EEC.

Finally, the continuous update and integration of groundwater data are fundamental for sustainable management in Greece. Furthermore, establishing a Strategic Water Policy will be crucial in addressing future demands and mitigating climate change impacts. The establishment and operation of an Entity, that will utilize the experience and data of the SAMY Project. Also, it ensures the continuation of the flow of this information is the only way for the rational management of water resources.

Acknowledgements

We acknowledge the Hellenic Survey of Geology and Mineral Exploration (H.S.G.M.E.) for their invaluable support in providing data and technical information essential to this research.

References

Copernicus, (2024). Copernicus program - 11/09/2023 data.

H.S.G.M.E., (2024). Results from the hydro-census work and water balance calculation of all groundwater system in Greece. Technical Report. (in Greek).

H.S.G.M.E., (2024). 3rd Community Support Framework (CSF) Program for the period 2006-2012.

Ministry of Environment and Energy (2024). Watershed Management Plans (WMP). Available online: https://wfdver.ypeka.gr/el/management-plans-gr/2revision-approved-management-plans-gr/

17th INTERNATIONAL CONGRESS of the Geological Society of Greece

BULLETIN OF THE GEOLOGICAL SOCIETY OF GREECE, SP. PUBL.

EXTENDED ABSTRACT 281

The 2025 Santorini Swarm: Spatiotemporal Distribution and Coulomb Stress Changes. Preliminary Results

Sardeli E.[1], Pavlou K.[1], Karakonstantis A.[1,2], Athanasopoulos A.[1], Pappas S.[1], Vallianatos F.[1,3]

(1) Section of Geophysics-Geothermics, Department of Geology and Geoenvironment, National and Kapodistrian University of Athens, 15784 Athens, Greece, eirsard@geol.uoa.gr

(2) University of Patras, Patra, Greece

(3) Institute of Physics of Earth's Interior and Geohazards, UNESCO Chair on Solid Earth Physics and Geohazards Risk Reduction, Hellenic Mediterranean University Research & Innovation Center, 73133 Chania, Greece

Introduction

Santorini Island is located in the central part of the Hellenic Volcanic Arc, which lies in the back-arc region of the Hellenic subduction zone. The majority of identified faults in Santorini exhibit a SW-NE orientation (Heiken & McCoy, 1984). Similarly, Santorini's main volcanic centers, including the Christiana Islands and the submarine volcano Columbo (located 7 km northeast of Santorini), are aligned along two seismic fault lines: the Kameni Line and the Columbo Line. These lines intersect the caldera in a northwest-southeast direction. Santorini is predominantly composed of volcanic rocks, except for a pre-volcanic substratum in the southeastern region, consisting of Mesozoic and Cenozoic metamorphic limestones and schists (Nicholls, 1971; Druitt et al., 1989).

The most significant eruption of the Santorini volcano, known as the Minoan eruption, occurred approximately in 1600 BC. In 1650, Santorini Island suffered significantly from the explosive eruption of the Columbo submarine volcano, The last recorded eruption occurred in 1950. The most intense seismic activity in this region has been observed along the NE–SW trending Santorini–Columbo volcano-tectonic line (Druitt et al., 1999).

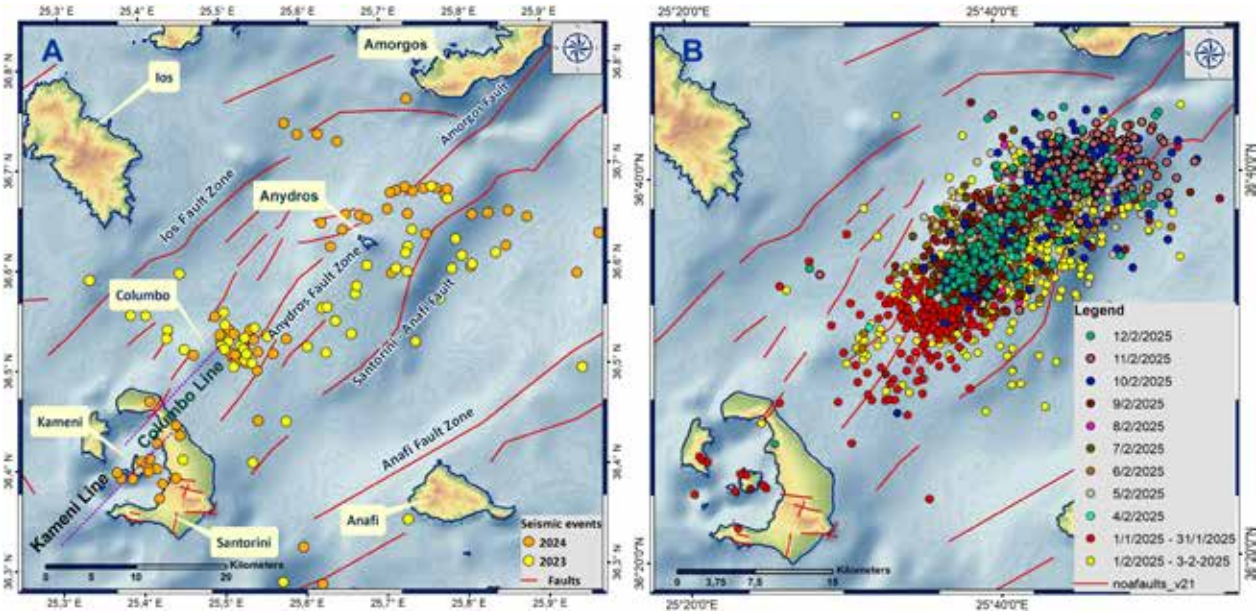

Figure 1. (A) Seismicity in the broader area of Santorini Island during the period 2023-2024. (B) Spatiotemporal distribution of the earthquake swarm during the first period of temporal distribution.

Since January 2025, weak to moderate earthquakes have occurred north – east of Santorini (Figure 1A). However, in early 2025, Santorini Island experienced a significant seismic swarm, recording over 4,000 earthquakes (Figure 1B). The largest earthquake had a local magnitude of M_L 5.3 on February 10, 2025. This seismic activity initiated in the caldera area of Santorini and progressively migrated northeast, offshore the island, between Santorini and Amorgos. In this study, we examine the spatiotemporal distribution and the computed Coulomb stress changes resulting from each earthquake of moment magnitude $M_w \geq 4.7$ that occurred during the 2025 Santorini - Amorgos swarm. Additionally, we determined the Coulomb stress changes at each focus of the following significant earthquakes, defined as those of moment magnitude $M_w \geq 4.7$. Finally, a modified Wadati method was used to determine the average V_p/V_s ratio for the Santorini-Amorgos area.

Seismic Data and Methodology

To investigate the spatiotemporal distribution and the computed Coulomb stress changes during the 2025 Santorini earthquake swarm, we used data such as the earthquake catalog from January 1, 2025, to February 28, 2025, and the available CMT (Centroid Moment Tensor) focal mechanism solutions from the National Observatory of Athens (https://bbnet.gein.noa.gr/HL/seismicity/mts). The earthquakes that were selected for the period from February 3rd to 18th have a moment magnitude M_w greater than or equal to 4.7 (Table 1).

Numerous studies on major earthquakes have demonstrated a strong correlation between positive Coulomb stress changes and the spatial evolution of seismic events (King et al., 1994; Vallianatos & Pavlou, 2021). Research has shown that Coulomb failure stress changes (ΔCFS) triggered by large earthquakes can either accelerate or delay the occurrence of subsequent seismic events. Additionally, these Coulomb stress changes can influence and control their temporal and spatial distribution (Stein, 1999; Kilb et al., 2002). Specifically, a positive ΔCFS transfer to a receiver fault brings it closer to failure, whereas a negative ΔCFS indicates a delay in failure.

The calculation of Coulomb Failure Stress changes (ΔCFS) under undrained rock conditions is based on the Coulomb failure criterion, which quantifies the proximity to failure. It is expressed by the following equation (Scholz, 2019):

$$\Delta CFS = \Delta_T - \mu' \Delta_\sigma$$

where Δ_T represents the changes in static shear stress, Δ_σ denotes the changes in effective normal stress, and $\mu\mu$' is the coefficient of friction (Cocco, 2002).

The ΔCFS changes were calculated using the Coulomb 3.3 software (Toda et al., 2011) in an elastic half-space, assuming a uniform slip on the rupture planar surfaces that imposes an "ideal" stress redistribution around the seismic faults. The software was used to model the Coulomb failure stress changes (ΔCFS) with a mean friction coefficient of μ' = 0.4. Additionally, the empirical relations of Wells and Coppersmith (1994) were employed to determine the width and length of the subsurface faults for each modeled earthquake (Lin & Stein, 2004; Toda et al., 2005).

Table 1. The most significant 2025 Santorini seismic events

No	Date -Time	Latitude	Longitude	Depth	Mw	Strike	Dip	Rake
1	3/2/2025 9:29	36.5854	25,7364	13,7	4,8	41	52	-117
2	3/2/2025 12:17	36,6389	25,7478	10,5	4,8	50	55	-86
3	3/2/2025 20:19	36,6289	25,6975	13,9	4,8	14	78	-161
4	4/2/2025 2:46	36,6197	25,7066	14,3	4,7	44	51	-97
5	4/2/2025 13:04	36,6167	25,727	5,0	5,0	44	48	-98
6	5/2/2025 19:09	36,6582	25,7213	11,2	5,0	45	48	-80
7	7/2/2025 7:16	36,5664	25,7278	7,0	4,7	19	56	-127
8	8/2/2025 9:00	36,5799	25,7439	5,0	4,7	35	55	-118
9	9/2/2025 19:05	36,6454	25,6544	11,2	5,1	26	62	-133
10	10/2/2025 11:23	36,6602	25,8546	10,0	4,7	15	79	-172
11	10/2/2025 20:16	36,6538	25,7456	5,0	5,2	207	66	-154
12	10/2/2025 22:37	36,6255	25,787	10,0	4,9	50	45	-92
13	11/2/2025 5:58	36,6952	25,8178	5,0	4,7	192	79	179
14	12/2/2025 8:29	36,4071	25,9418	5,0	4,8	221	85	-164
15	12/2/2025 9:15	36,5977	25,6425	8,8	4,7	247	37	-57
16	17/2/2025 7:49	36,599	25,7047	5,1	4,8	233	43	-82
17	18/2/2025 4:46	36,6199	25,8577	5,0	4,9	39	46	-110

Furthermore, the present study used the best-located hypocentral solutions (~1600 earthquakes) to improve hypocentre depth estimates. This subset of events was recorded in stations with both P- and S-wave arrival time picks at epicentral distances <200 km. An average $V_p/V_s V_p/V_s$ ratio was determined for the Santorini-Amorgos area using a modified Wadati method (Chatelain, 1978). This method is based on the differences in body wave arrival times P_i and P_j and S_i and S_j for an event k recorded by two stations (i, j) at hypocentral distances x_i and x_j, respectively, $DT_p = P_i - P_j = (x_i - x_j)/V_p$ and $DT_s = S_i - S_j = (x_i - x_j)/V_s$. Thus, $DT_s/DT_p = V_p/V_s$, and a plot of versus DT_p indicates a V_p/V_s ratio of 1.76 for the broader region (Figure 2). Konstantinou et al. (2013) estimated the Vp/Vs ratio between February 2011 and June 2012 at Santorini caldera. The average Vp/Vs ratio was 1.54 ± 0.17, much lower than the regional background value of 1.77. This led the authors to conclude that the involvement of gases was the

main factor that influenced the evolution of that swarm. On the contrary, Andinisari et al. (2021) estimated that Vp/Vs ratios varied from 1.74 to 1.91 during the 2011 to 2019 time period.

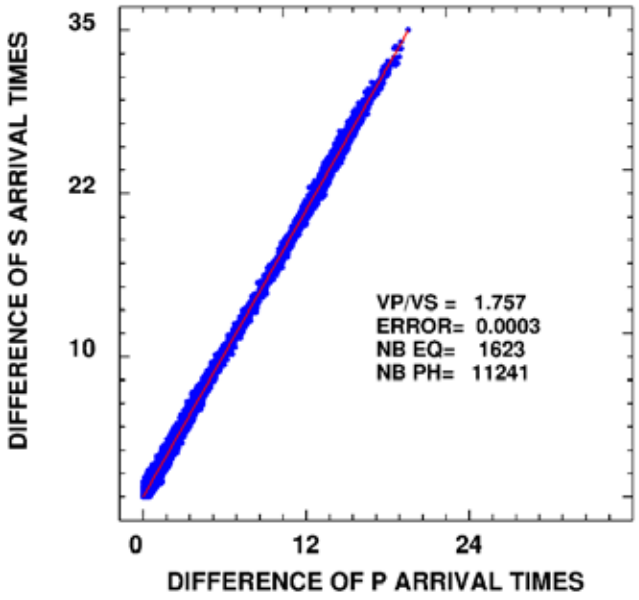

Figure 2: Vp/Vs ratio in the Santorini-Amorgos area using a modified Wadati diagram.

In the same study, the authors estimated the Vp/Vs ratio between 1.77 and 1.86 in the area to the NE, between Santorini and Amorgos, near the region that was activated in this period that we have examined.

Results and Discussion

The seismic swarm began with small seismic events in January 2025. However, on February 3, 2025, three earthquakes of magnitude M_w 4.8 occurred. In the following days, specifically until February 18, 2025, another 15 seismic events of a magnitude M_w greater than 4.7 took place in the Santorini-Amorgos area. Hence, to understand the evolution of the earthquake sequence, the co-seismic static Coulomb stress changes for each of these earthquakes, which occurred at depths ranging from 5 to 15 km (Table 1), were calculated.

Figure 3 depicts the first two significant earthquakes on February 3, 2025, at 9:25 and 12:17, both of a magnitude M_w 4.8 and at depths 13.7 km and 10.5 km, respectively. The spatial distribution of the ΔCFS reveals a stress decrease towards the NW and SE and a stress increase towards the NE and SW. Earthquakes that occurred up to February 18, 2025, are represented by white dots, and their spatial distribution follows the fault strike with a significant concentration in positive lobes. Cross-section AB, which illustrates the seismic events in the seismically activated area, shows that the subsequent events following the mainshock occur in regions with positive values of Coulomb stress changes (red lobe). These positive values indicate that the transfer of Coulomb stress changes due to the occurrence of the first strong event may have triggered the following events.

Additionally, the ΔCFS values at the hypocenters of the following seismic events were estimated. The results indicate a stress increase of +1.425 bar from the earthquake on February 4, 2025, at 13:04 to February 17, 2025, +0.314 bar from the earthquake on February 4, 2025, at 13:04 to February 10, 2025, at 20:16, +0.196 bar from the earthquake on February 4, 2025 at 13:04 to February 7, 2025, and +0.173 bar from the earthquake on February 9, 2025 to February 12, 2025 at 9:15. It is worth noting that while the co-seismic Coulomb stress changes were modeled assuming pure double-couple (DC) sources, recent studies (Zahradnik et al., 2025) have shown that several events within the 2025 Santorini–Amorgos swarm exhibit significant non-double-couple components. These components may locally alter the stress field beyond what is captured by DC-only modeling.

The spatial distribution of the static Coulomb stress changes for earthquakes with a magnitude greater than or equal to M_w 4.7 reveals a stress increase towards NE and SW. The migration of seismicity in the Santorini-Amorgos region closely aligns with the Coulomb stress transfer results, confirming that stress redistribution played a crucial role in triggering subsequent earthquakes. The initial scattered seismicity in late January intensified in early February, with a clear NE migration until February 5. This pattern corresponds to areas of increased Coulomb Failure Stress (ΔCFS), indicating that the stress changes induced by earlier earthquakes facilitated the activation of nearby faults.

The return of seismicity to the broader Anydros region after February 6 and the secondary NE shift on February 10–11 further support the influence of stress transfer on the sequence's evolution. These findings underscore the strong correlation between seismic migration and Coulomb stress changes, highlighting the importance of stress redistribution in controlling the evolution of the sequence.

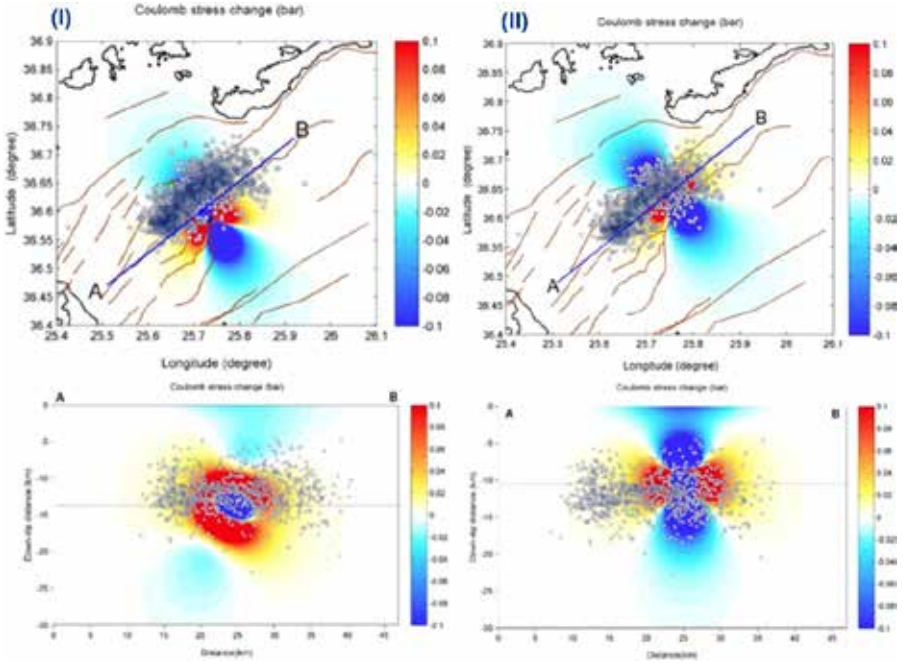

Figure 3: Coseismic Coulomb stress change distributions resulting from (I) the M_w 4.8 earthquake on February 3, 2025, at 9:29 and (II) the M_w 4.8 earthquake on February 3, 2025, at 12:17, with centroid depths of 13.7 km and 10.5 km, respectively. The white circles represent the hypocenters of the swarm until February 18, 2025. Cross-sections AB illustrate the changes in Coulomb stress (ΔCFS) relative to depth related to these seismic events.

Acknowledgements

The research work of S.E was supported by the Hellenic Foundation for Research and Innovation (HFRI) under the 5th Call for HFRI PhD Fellowships (Fellowship Number: 20518).

References

Andinisari, R., K.I. Konstantinou, and P. Ranjan (2021). Seismicity along the Santorini-Amorgos zone and its relationship with active tectonics and fluid distribution, Physics of the Earth and Planetary Interiors, 312, 106660, https://doi.org/10.1016/j.pepi.2021.106660

Cocco, M. 2002. Pore pressure and poroelasticity effects in Coulomb stress analysis of earthquake interactions. Journal of Geophysical Research, 107(B2), 2030. DOI: 10.1029/2000JB000138

Druitt T. H., Davies M. S., et al., 1999. The Santorini Volcano. (Geological Society Special Memoir, 19), Geological Society Pub House, London. ISBN 1 86239 048 7

Druitt, T. H., Mellors, R.A., Pyle, D.M., and Sparks, R.S.J., 1989. "Explosive volcanism on Santorini, Greece." GEOLOGICAL MAGAZINE, Vol. 126, No. 2, p. 95-126. DOI:10.1017/S0016756800006270. [Journal Article]

Heiken, G., McCoy, F., 1984. Caldera Development during the Minoan Eruption, Thira, Cyclades, Greece. Journal of Geophysical Research, 89, 8441-8462. https://doi.org/10.1029/JB089iB10p08441

Kilb, D., Gomberg, J., Bodin, P., 2002. Triggering of earthquake aftershocks by dynamic stresses. Nature 408,570–574. DOI: 10.1038/35046046

King, G. C., Stein, R. S., Lin, J., 1994. Static stress changes and the triggering of earthquakes: Bulletin of the Seismological Society of America, 84(3),935-953. https://doi.org/10.1785/BSSA0840030935

Konstantinou, K.I., Evangelidis, C.P., Liang, W.-T., Melis, N.S., Kalogeras, I., 2013. Seismicity, Vp/Vs and shear wave anisotropy variations during the 2011 unrest at Santorini caldera, southern Aegean. J. Volcanol. Geotherm. Res. 267, 57–67. https://doi.org/10.1016/j.jvolgeores.2013.10.001

Lin, J., & Stein, R. S., 2004. Stress triggering in thrust and subduction earthquakes and stress interaction between the southern San Andreas and nearby thrust and strike-slip faults: STRESS TRIGGERING AND FAULT INTERACTION. Journal of Geophysical Research: Solid Earth, 109(B2). https://doi.org/10.1029/2003JB002607

Nicholls, I. A., 1971. Petrology of Santorini Volcano, Cyclades, Greece. J. Petrol. 12 (1), 67–119. https://doi.org/10.1093/petrology/12.1.67

Scholz, C.H., 2019. The Mechanics of Earthquakes and Faulting (3rd ed.). Cambridge University Press. https://doi.org/10.1017/9781316681473

Stein, R. S., 1999. The role of stress transfer in earthquake occurrence. Nature, 402(6762), 605-609. https://doi.org/10.1038/45144

Toda, S., 2005. Forecasting the evolution of seismicity in southern California: Animations built on earthquake stress transfer. Journal of Geophysical Research, 110(B5), B05S16. https://doi.org/10.1029/2004JB003415

Toda, S., Stein, R.S., Sevilgen, V., Lin, J., (2011). Coulomb 3.3 Graphic□rich deformation and stress□change software for earthquake, tectonic, and volcano research and teaching□user guide. U.S. Geological Survey Open□File Report 2011□1060, 63.

Vallianatos, F., Pavlou, K., 2021. Scaling properties of the Mw7.0 Samos (Greece), 2020 aftershock sequence. Acta Geophysica, 69(3), 1067–1084. https://doi.org/10.1007/s11600-021-00579-5

Wells, D.L., & Coppersmith, K.J., 1994. New empirical relationships among magnitude, rupture length, rupture width rupture area, and surface displacement. Bull Seismol Soc Am 84(4), 974–1002. https://doi.org/10.1785/BSSA0840040974

Zahradnik, J., Sokos, E., Roumelioti, Z., & Turhan, F. (2025). Positive isotropic components of the 2025 Santorini-Amorgos earthquakes. https://doi.org/10.31223/X5RD9S

17th INTERNATIONAL CONGRESS of the Geological Society of Greece

BULLETIN OF THE GEOLOGICAL SOCIETY OF GREECE, SP. PUBL.

EXTENDED ABSTRACT 282

Stabilisation of volcanic rock slopes in traditional settlements. The case of Petra, Lesvos Island

Saroglou C. [1], Kallimogiannis V.[2], Tsirogianni A.[3], Klironomou G.[4]
(1) National Technical University Athens, Greece, saroglou@central.ntua.gr (2) Civil Engineer, MSc, PhD NTUA (3) Civil Engineer, MSc, (4) Civil Engineer.

Introduction

Rock slope instabilities pose a significant problem to cultural heritage sites in Greece (Saroglou, 2012a and Saroglou *et al*., 2012b). The paper presents the assessment of rock slope stability of the volcanic rock cliff in the village of Petra in Lesvos Island, on which the Church of the Koimisi of Theotokos is founded (Figure 1). The rock cliff has almost vertical slopes with height up to 40 m and is formed by an andesitic rockmass, fractured by four discontinuity sets. The predominant kinematic instability is wedge or toppling failures of medium-sized rock blocks. The problem of potential rock instability of the volcanic slope in Petra has been investigated in the past (Apostolopoulos & Koukis, 1979) and rock fall episodes have occurred mainly triggered by intense rainfall. Due to the weathering and deterioration of the andesitic rockmass, the risk of rock instability has increased in the last two decades and it was deemed necessary to protect the foundation of the monument as well as the surrounding settlement and visitors from potential rockfalls. Stabilisation measures were proposed to minimize the risk of rockfalls and protect the foundation of the Church.
Similar problems of rock instabilities have been identified in many sites in Greece (Saroglou, 2019) but also near the study area at Mythimna Castle (Marinos *et al*, 2002). Saroglou (2012a) has studied the engineering geological behaviour of the volcanic formations in the northern part of Lesvos Island and highlighted the controlling factors of different types of slope instabilities, including landslides and rockfalls. The properties of the volcanic formations and their long-term behaviour in slopes are strongly controlled by the degree of weathering and the mineralogy of clay components when totally weathered (Irfan, 1999).

Figure 1. Volcanic rock cliff of Church of the Koimisi of Theotokos, Lesvos Island

Geological setting

Geologically the northern part of Lesvos Island consists of 400 m thick Neogene volcanic formations, formed by the Upper Miocene to the Middle Pliocene volcanic activity in the northeast Aegean Sea. These formations can be further distinguished in an upper lava unit and lower lava unit of Stypsi (Pe-Piper,1978). The upper lava unit consists of rhyodacitic, latitic and latiandesitic lavas, which are strong and hard formations, usually highly fractured, characterized by the magmatic pseudolayering, and intensely altered at places (kaolinitized) due to hydrothermal

activity. Two fault zones exist in the wider area, the main one with a WNW-ESE strike forming the tectonic graben of Petra and the secondary one with a NE-SW strike. As a result of compressive strains, the structure of rhyodacitic and latiandesitic lavas is characterized by two perpendicular joint systems which are vertical and intersect the pseudo bedding of lavas, thus forming orthogonal rock blocks. The rock cliff consists of rhyodacitic and latiandesitic lavas of the upper lava unit.

Rockmass conditions

The rock slopes surrounding the cliff were divided into eight distinct areas and the kinematic analysis of each area was analysed separately according to the discontinuity geometry and properties and the prevailing mechanism of failure (Figure 2). The volcanic rock appears massive in most places but locally is intensely fractured with a dense discontinuity network which forms wedges and rock pillars. The rockmass of the southern cliff appears extensively fractured and highly weathered, resulting in cavities. Due to the inaccessibility of the cliff, the rock slopes were mapped with UAV and LiDAR survey producing a point cloud and digital terrain model was created for the entire study site (Figure 3).

Figure 2. Plan view of the study site with designated slope areas

The discontinuity geometry was assessed using Discontinuity Set Extractor (Riquelme, 2015) which processes the point cloud data and then classifies points into planes (discontinuities) with similar orientation (dip/dip direction). The rockmass is intersected by three main discontinuity sets, as presented in Figure 4. The joint spacing was calculated as less than 1m (ranging from 0.3 to 0.7m), thus most blocks have a maximum volume of 0.5m^3.

Kinematic stability and rockfall analysis

Based on the mechanism of kinematic analysis (planar sliding, wedge sliding or toppling) in each area of the cliff, stability analysis was carried out for all the slope sections to define the factor of safety against each type of failure and determine the appropriate stabilisation measures. The analysis was performed in static conditions, with presence of water pressure in joints and under seismic loading.

The principal failure type is rockfall due to toppling, mainly in areas where large cavities are formed by the combined effect of weathering of the volcanic rock and the presence of discontinuities. Secondly, there are planar and wedge sliding failures in specific slope areas. The slope angle ranges between 55° and 88° and the steepest slopes are found in Areas 3,4 and 7, while the slope height ranges from 7 to 18m, with the highest slopes found in Areas 1, 3 and 4.

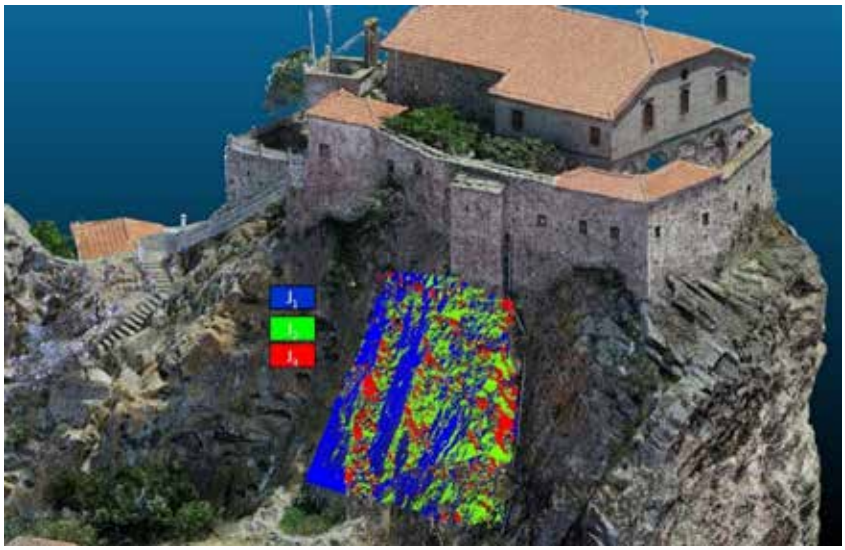

Figure 3. Digital terrain model and discontinuity mapping in the south side of the cliff

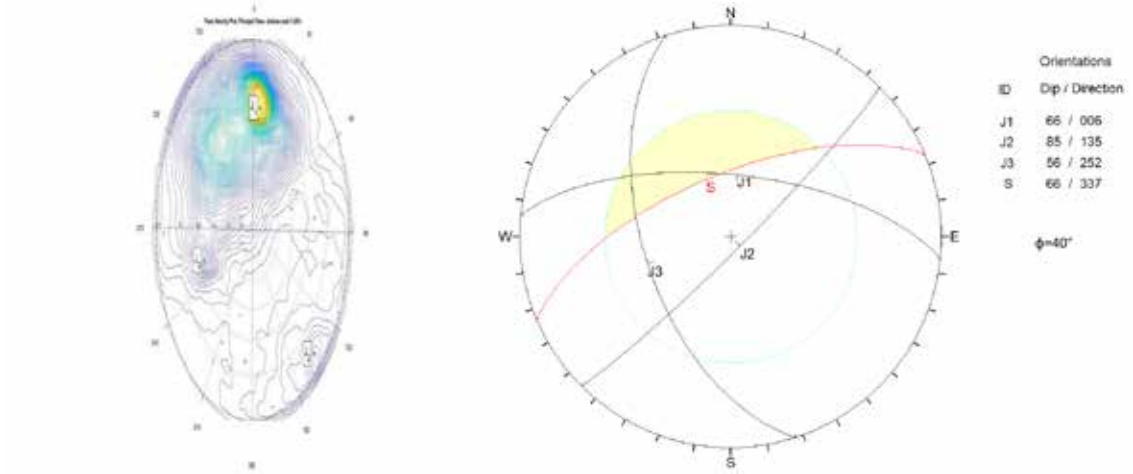

Figure 4. a) discontinuity pole density (from DSE), b) Stereographic plots with main sets in south cliff side.

In Area 1 (south side), toppling failure prevails due to a discontinuity set with NE-SW strike, as presented in Figure 4. In Area 2, planar sliding could occur along a discontinuity set with NW-SE strike. In Area 3, potential wedges are formed by the intersection of discontinuity sets of NW-SE and WE strike. In Areas 4 and 5, no systematic presence of discontinuity sets was observed. In Area 6, toppling failure prevails due to a discontinuity set with NNW-SSE strike, while in Area 7 toppling failure prevails due to a discontinuity set with N-S strike. In Area 8, planar sliding could occur along a discontinuity set with N-S direction and wedge failures could occur with a conjugate joint system. The determined factors of safety were not acceptable in many cases and therefore installation of rock bolts was considered necessary.

Rockfall analyses were performed for certain slope sections under different loading conditions. The critical locations of potential detached blocks were selected based on in-situ observations and the 3D terrain model of the slope and were used in the rockfall analysis performed in RocFall (Rocscience Ltd). The normal and tangential coefficients of restitution for the andesitic slope surfaces were taken equal to 0.45 and 0.85, respectively, based on experience from previous studies (Saroglou et al.,2012). The height of block detachment was defined in the range of 17 to 29 m above the slope base, with a maximum of 29 m in Area 1 (Figure 5a). The analysis shows that Areas 1, 4 and 5 are the most critical sections due to impact of falling rocks on houses and on the street which is around the cliff. In Area 1, the majority of falling blocks impact the houses with a maximum kinetic energy of 110 kJ. In Area 4 certain blocks reach the houses with a maximum kinetic energy of 160 kJ (Figure 5b). In Area 5 most falling blocks reach directly the residential zone with a maximum kinetic energy of 90 kJ and significant bouncing heights. On the contrary, there

are areas that are considered as lower risk, such as Area 2, where falling blocks stop at a plateau located near the base of the slope and Area 3 where most rocks reach the base of the slope with a maximum kinetic energy of 80kJ.

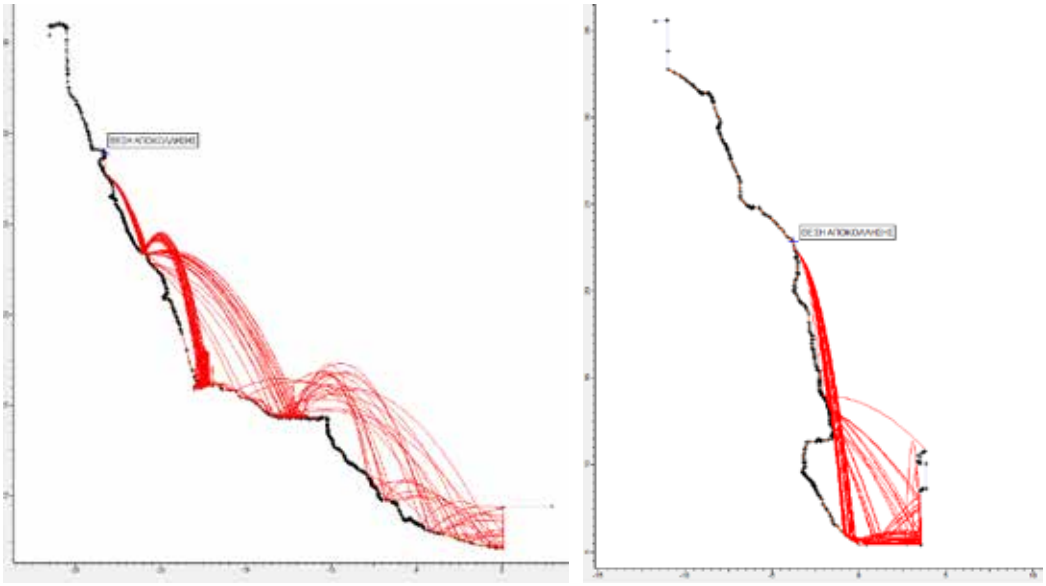

Figure 5. a) Rockfall analysis in Area 1 (south cliff) and b) in Area 4 (north cliff)

Stabilisation measures

Based on the stability analyses it was considered necessary that active support measures (rock bolts, anchored wire mesh) are installed to minimise the risk of rock blocks falling from the upper parts of the slopes, instead of installing passive measures (rockfall barriers). The option of installing rockfall barriers on the slope was not acceptable to due to achieve the minimum impact on the cultural heritage site.

The proposed rock stabilization works aimed to enhance the overall stability and reduce the risk of further rock falls. The stabilization measures are summarised below, and an example is presented in Figure 6.

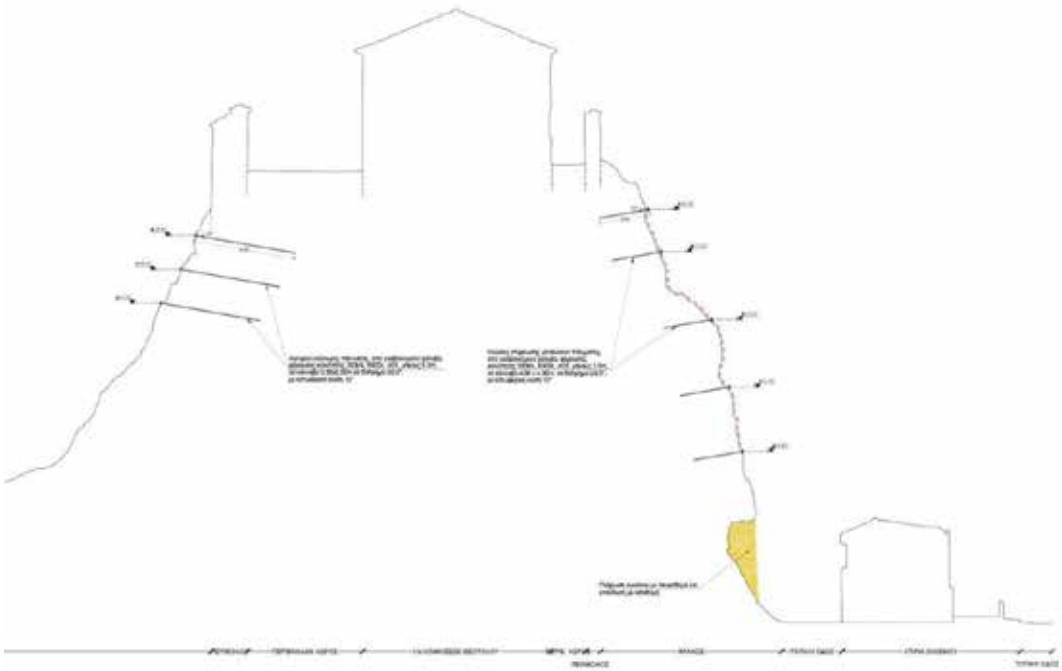

Figure 6. Section with proposed stabilisation measures in Area 1 (south) and Area 4 (north)

The main measures were:
1. Installation of spot bolts for anchoring individual relatively small rock blocks and pattern bolting for anchoring of larger blocks. The aim of this measure was to support potentially unstable blocks and improve the stability conditions of the upper part of the cliff below the foundation of the Church.
2. Installation of a steel wire rope net, anchored with fully grouted bolts in order to control further loosening of the rock mass in areas where it is fractured.
3. Filling of voids in specific locations with sprayed concrete or reinforced concrete, depending on their location, geometry and size. The intention was to minimise the enlargement of voids due to weathering and support the overhangs of rocks.

Conclusions

The stabilisation of steep rock slopes in areas where human activities are impacted is a very challenging task. The case of Church of the Koimisi of Theotokos in Petra is such an example, which demonstrates the difficulty to stabilise a rock slope in inhabited area, while at the same time respecting the cultural heritage character of the monument.
In this study, a methodology was presented which is based on identifying the engineering geological behavior of the volcanic rock formations and determining the prevailing failure mechanisms in different sections of the slope to propose the appropriate stabilisation measures. The advantage of technologies, such as UAV and LiDAR and use of software for automatic detection of discontinuities was demonstrated to enhance the assessment of kinematic stability analysis and protection of the monument.

Acknowledgements

The authors acknowledge the support of the Ministry of Culture for funding the present research and would like to thank Emeritus Prof. C. Spyrakos for the collaboration.

References

Andronopoulos B. and Koukis G. 1979. Geological, Microtectonic and Geotechnical Study in the NW part of the Lesbos Island. Unpublished report, Institute of Geological and Mining Research, Engineering Geology Investigations No. 8, 41 p., Athens.

Irfan, T.Y., 1999. Characterization of weathered volcanic rocks in Hong Kong. Quaternary Journal Engineering Geololgy, 32, 317–348.

Marinos P., Kavvadas M., Tsiambaos G., Saroglou H., 2002. Rock slope stabilization in Mythimna castle, Lesvos Island, Greece. 1st European conference on landslides, Balkema, ed: Rybar Stemberk & Wagner, Prague, p. 635-639.

Pe-Piper G, 1978. The Cenozoic volcanic rocks of Lesvos Island. Ph.D.Thesis. University of Patras.

Riquelme AJ, Abellan A, Tomas R., 2015. Discontinuity spacing analysis in rock masses using 3D point clouds. Engineering Geology, 195,185–195.

Rocscience Ltd. 2022. Rocfall user's manual.

Saroglou, H. 2012a. Engineering geological behaviour of volcanic formations. References to instability phenomena and town planning in Lesvos Island, Greece. Bulletin of the Geological Society of Greece, 46, 108-122.

Saroglou H., Marinos V., Marinos P., Tsiambaos G., 2012b. Rockfall hazard and risk assessment: an example from a high promontory at the historical site of Monemvasia, Greece. Natural Hazards and Earth System Sciences, 12, 1823–1836.

Saroglou C., 2019. GIS-based rockfall susceptibility in Greece. Geosciences, 9, 163.

17th INTERNATIONAL CONGRESS of the Geological Society of Greece

BULLETIN OF THE GEOLOGICAL SOCIETY OF GREECE, SP. PUBL.

EXTENDED ABSTRACT 283

Mapping pyroclastic formations at the Lesvos Petrified Forest, Greece the Akrocheiras hill pyroclastic sequence

Savvelos L.[1, 2] and Zouros N.[1, 2]
(1) Natural History Museum of the Lesvos Petrified Forest
(2) Department of Geography, University of the Aegean, Greece

Introduction

The Lesvos Petrified Forest is a unique natural monument located in western Lesvos. It is the geological heritage treasure with international significance of the Lesvos Island UNESCO Global Geopark. It is also included in the 100 first Geological Heritage sites of the International Union of Geological Sciences (IUGS). The Lesvos Petrified Forest includes massive assemblages of silicified tree trunks located in situ within the Sigri pyroclastic formation of Lower Miocene (Velitzelos and Zouros 1997, 1998, Pe-Piper et al. 2019, Zouros 2021).The Natural History Museum of the Lesvos Petrified Forest is conducting scientific research, excavation and conservation works in the Lesvos Petrified Forest during the last 30 years. Excavations in the Lesvos Petrified Forest reveled a large number of standing and lying silicified tree trunks, root systems, brunches, leaves and cones that belong to conifer and angiosperm tree species. The composition of the forest ecosystem represents subtropical climatic conditions (Velitzelos and Zouros 1997, 1998, Pe-Piper et al. 2019).

Silicification of the Lesvos Petrified Forest is related with the volcanic activity in Lesvos during Lower Miocene (Pe-Piper et al. 2019b, 2024). The perfect preservation of the fossils is due to the circulation of hydrothermal fluids rich in silicon dioxide SiO_2, (Pe-Piper et al. 2019b).

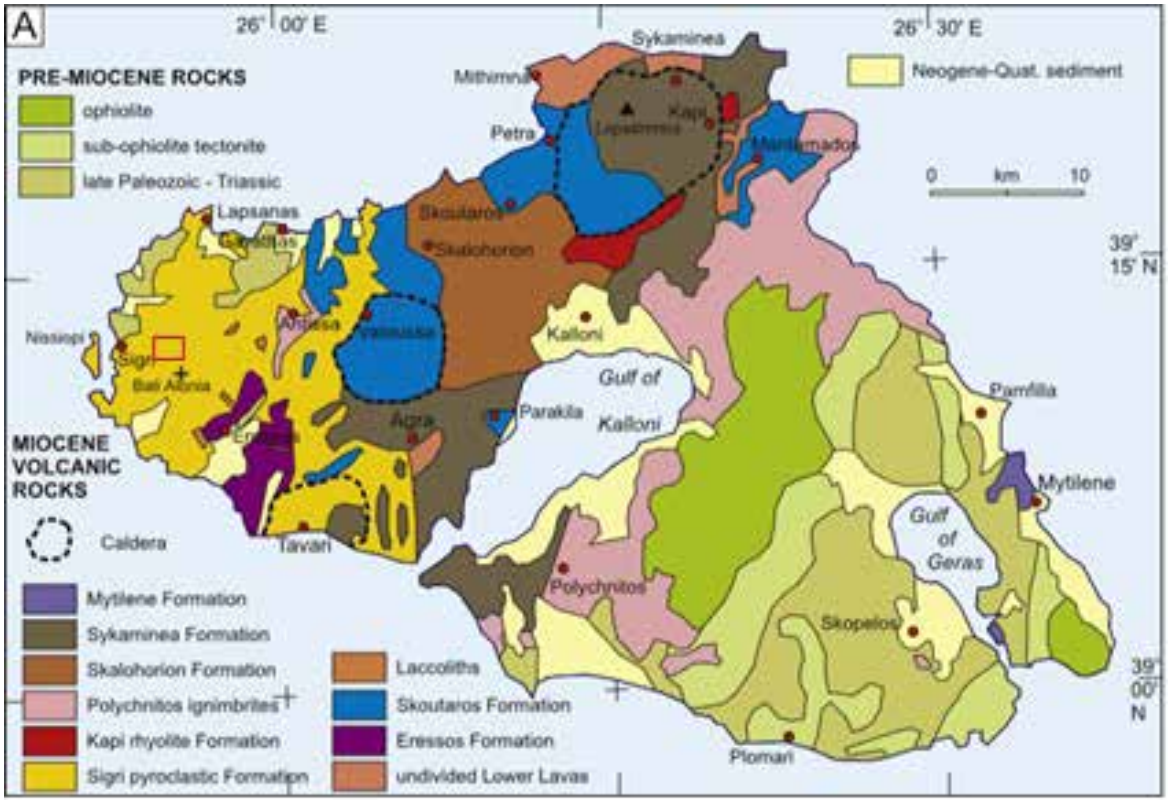

Figure 1: Geological Map of Lesvos Based on Hecht (1972-1976), modified by Pe-Piper (1992). Red rectangle indicating the study area of current research

Since 2014 extensive rescue excavation works were carried out by the Natural History Museum of the Lesvos Petrified Forest due to the construction of the Kalloni - Sigri, road crossing the protected area of the Lesvos Petrified Forest. As a result large amounts of new data in a number of significant fossil sites were collected (Zouros et al. 2015, Zouros 2021, Pe-Piper et al. 2019b, 2024).

As several significant fossil sites are located on the northern flanks of the Akrocheiras hill, a detailed mapping project in the area of Akrocheiras hill was carried out, in order to archive a better understanding of the stratigraphy of the pyroclastic sequence. Therefore the main objective of the current study is the identification and mapping of successive fossiliferous horizons associated with different volcanic eruptions that led to the preservation of the fossilized forests

Study Area

The protected area of the Petrified Forest of Lesvos spans at the western peninsula of the island covering 15.000 ha. Throughout the area, silicified trunks can be found at various depths. Akrocheiras hill lies in the center of the protected area, 7 km east of Sigri village (Fig. 2), reaching an altitude of 370 meters above sea level and covering an area of approximately 1.2 km². Recent rescue excavations conducted in the area along the Kalloni-Sigri road uncovered thousands of petrified trunks along the road, which were showcased and preserved in situ through the efforts and acts of the Natural History Museum of the Lesvos Petrified Forest. Additionally, hundreds of fossils were uncovered and preserved on the hilltop, due to rescue excavations for the re-construction of the Sigri windmill farm, where the longest fallen petrified trunks were excavated, along with a large number of standing in-situ and lying silicified tree trunks.

The study area is entirely covered by the Sigri pyroclastic formation (Figure 1), featuring a variety of volcanic deposits that covered and preserved fossiliferous horizons (Pe-Piper et al., 2019b). The Sigri pyroclastic formation is several hundred meters thick and consists of tuffs and coarse-grained volcanic materials. Stratigraphically, it overlies the Gavathas and Eresos formations and underlies the younger Skoutaros formation (Pe-Piper et al., 2019b).

Following the deposition of this formation, the intrusion of the Moni Ipsilou dome occurred, dated to approximately 17.9 million years ago. The Sigri pyroclastic formation in several sites is covered by recent deposits.

This description highlights the geological complexity and significance of the area, particularly in the context of preserving the fossilized forest and understanding its volcanic history.

Methodology

To achieve the identification of successive fossiliferous horizons associated with different volcanic eruptions and the evaluation of volcanic episodes that preserved fossilized forests, detailed mapping was conducted in the study area (Fig. 5). The mapping included fossil sites with standing in-situ petrified tree trunks, root systems, and fallen petrified tree trunks in direct contact with pyroclastic material, as well as occurrences of volcanic sequence of pyroclastic formations marking the onset of deposition from a volcanic eruption (Fig. 5).

The standing petrified tree trunks (Fig. 2, Fig. 4), being fossilized in their original position, serve as significant evidence to define a fossiliferous horizon. When the root system of the trunk is a marker of the original layer where a dense subtropical forest once thrived.

The fallen petrified trunks are displaced from their original position by pyroclastic flows. The composition of the clasts and orientation of the fallen trunks provide significant information on the origin of the pyroclastic flows involved in the silicification of the trees.

Coarse-grained horizons of volcanic conglomerates with clasts of diameter <2m are found throughout the area(Fig. 3a). These usually contain polygenetic volcanic pebbles, consisting of flows—volcanic conglomerates or debris flows —and appear to have been formed by water-driven flows that filled a complex network of paleo-river channels of that time (Pe-Piper et al., 2019b). This formation was created during a relatively calm period, meaning it was not driven by eruptions, unlike the tuffs found in the area. This feature provides insights into how the region's morphology developed between eruptions.

Therefore, the fine-grained pyroclastic horizons, the tuffs, whose creation and deposition are processes closely linked to the various volcanic eruptions, are expected to appear in the field as stratigraphically overlying on the previously formed substrate of the area—in this case, the debris flow. Thus the fine-grained formations simultaneously act as markers of deposition from a volcanic eruption.

Vitric tuff (Figure 3b) is a volcanic tuff primarily composed of fragments of volcanic glass that have undergone alteration (Pe-Piper et al., 2019b). It forms during an eruption and the rapid cooling of magma (Sparks & Walker, 1977; Pe-Piper et al., 1980). The binding material of the tuff consists of volcanic ash and contains fragments of pumice and small pieces of lava ejected during the eruption (pumice-lithic lapilli) (Pe-Piper et al., 2019b). It is deposited from the air (Sparks & Walker, 1977) directly onto already formed substrate of the area and serves as a strong indicator of the onset of deposits from a volcanic eruption.

Lithic tuff is pyroclastic sediment (Figure 3c). It consists of a primary binding material (matrix) made of volcanic ash with a grain size of ~2 mm and fragments of andesitic-dacitic lava <64 mm, which are shattered from pre-existing surrounding rocks and spread during the eruption (Pe-Piper et al., 2019a).

Figure 2 a, b, c, d: Standing in situ petrified trunks at the north and south flanks of Akrocheiras

Its deposition is closely linked to the volcanic eruption. It usually exhibits variability in the distribution of clasts due to the varying intensity of the eruption that caused its deposition (Pe-Piper et al., 2019a). Additionally, the deposition of this formation usually in the most cases succeeds that of Vitric tuff. In many cases though, in the field the two formations are found together, with lithic tuff being the base and vitric tuff overlying on top, directly on the already formed substrate (Pe-Piper et al., 2019a). Consequently, lithic tuff also serves as an important indicator for the onset of deposits from a volcanic eruption.

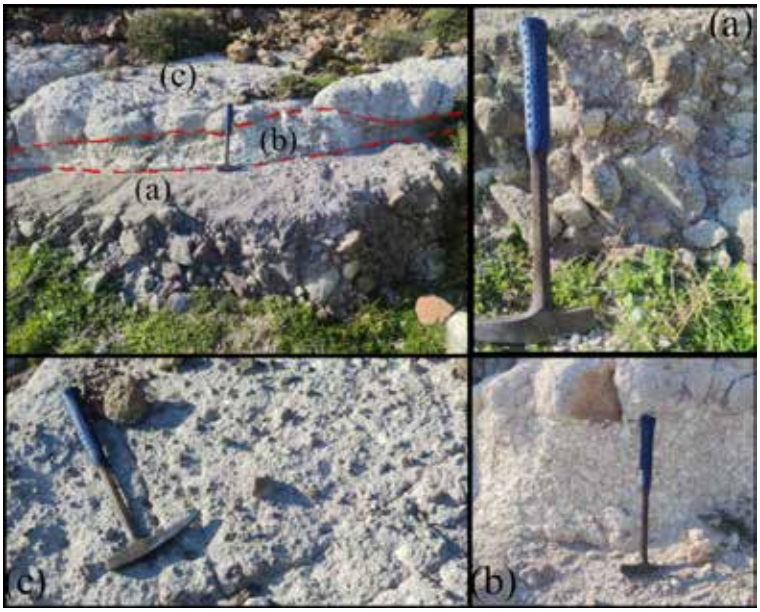

Figure 3: Appearance of the main sequence marking the deposition of a new volcanic eruption, where: a: Coarse-grained pyroclastic flow (Debris flow). b: Vitric tuff, deposited directly from the air; the vitric tuff forms during the eruption due to the rapid cooling of magma and serves as a critical marker indicating the onset of a new volcanic sequence. c: Lithic tuff, a pyroclastic sediment containing volcanic tuff and andesitic-dacitic clasts.

The formations mentioned above (debris flow, vitric tuff, lithic tuff) constitute a representative stratigraphic volcanic sequence (Figure 3), which is observed in the field and marks the onset of deposits from a volcanic eruption. The identification of locations where the whole sequence or parts of it appear is crucial for understanding and evaluating

the fossiliferous horizons and volcanic episodes hosted by Akrocheiras.
The occurrence of the primary volcanic sequence or parts of it containing vitric and lithic tuff, and the extent to which it repeats upstream on the slopes of Akrocheiras is the key element distinguishing fossiliferous horizons from one another, as well as different volcanic episodes.
The main and primary indicator is vitric tuff, as mentioned earlier, since it forms during the rapid cooling of magma during a volcanic eruption. It is deposited from the air directly onto the already formed topography of the ground surface, which supports a subtropical forest. Therefore, it is expected that the vitric tuff horizons represent the main fossiliferous horizons.
In the field, petrified trunks and root systems that protrude directly from vitric tuff (Fig. 4) are encountered, and in such cases, the recognition of the fossiliferous horizon is facilitated. However, even in cases where the formation is found without the presence of fossils, this does not mean that fossils are absent, they simply do not happen to be visible at the specific location.

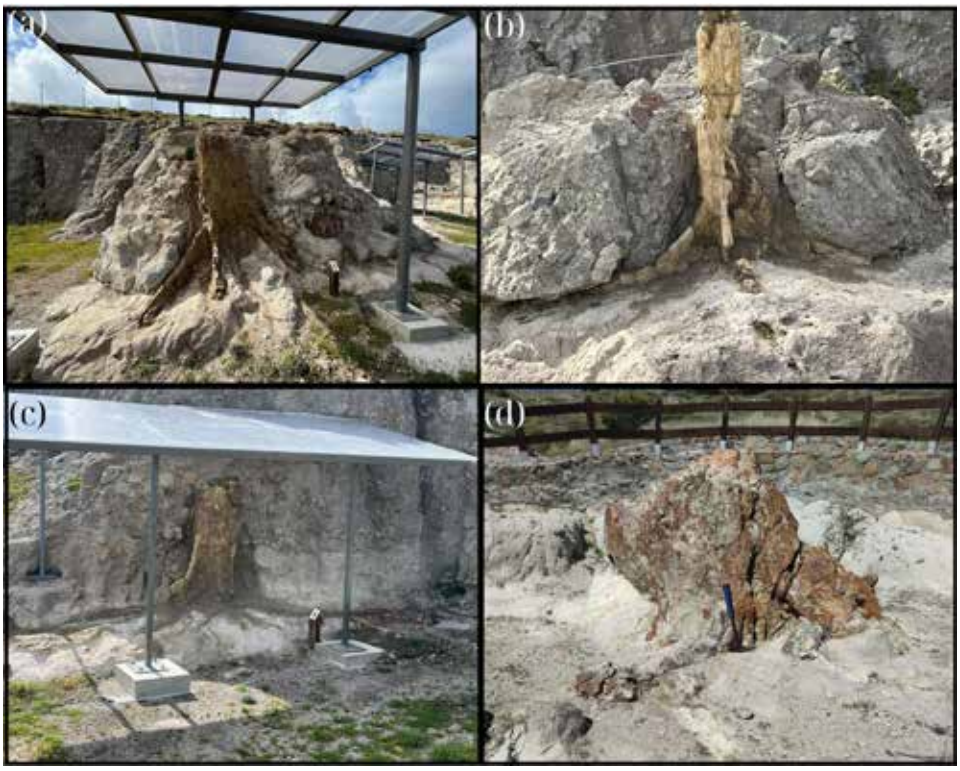

Figure 4 a, b, c, d: Standing in situ petrified trunks at the broader area of Akrocheiras illustrated with their roots systems spreading in the air fall vitric tuff and a, b, c also covered by coarse-grained volcanic conglomerates.

Results

The primary objective of this study is the identification and evaluation of successive fossiliferous horizons associated with different volcanic eruptions, as well as the assessment of volcanic episodes that preserved fossilized forests.
By combining the locations of standing petrified trunks that display their root systems, along with the occurrences of the entire volcanic sequence or parts of it featuring vitric tuff or lithic tuff, the following map is produced (Figure 5).
Documented locations (Figure 5) indicate that the Akrocheiras hill hosts at least 11 successive fossiliferous horizons associated with different volcanic eruptions. This represents the minimum number that can be established based on the evidence and their respective locations.

Conclusions-Discussion

Akrocheiras hill is covered by the Quaternary deposits and low vegetation, which makes the mapping effort very challenging. Detailed mapping curried out in Akrocheiras hill provide evidence for the presence of at least 11 successive pyroclastic horizons representing successive volcanic eruptions.
If we consider that only in the “Ioannis Toumpelekis Park”, at the northeastern edge of the Akrocheiras Hill, where the soil horizon has been removed and the volcanic formations are fully exposed, at least 8 fossiliferous horizons have been documented, it becomes evident that the Akrocheiras hill hosts dozens of petrified forests.

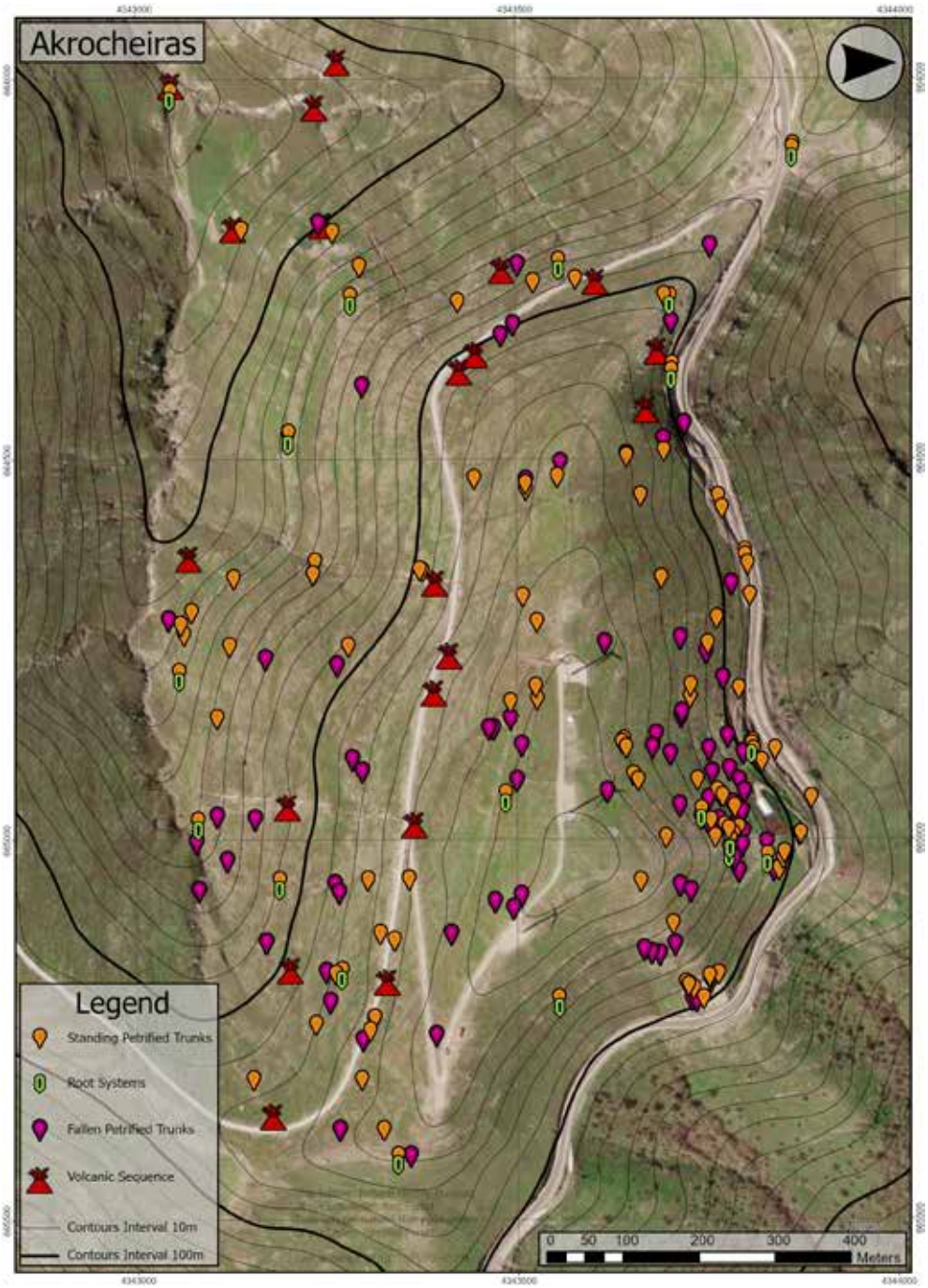

Figure 5: Result of the mapping of the plant fossils (standing, petrified tree trunks, lying petrified tree trunks , root systems) and volcanic horizon contacts conducted in the Akrocheiras area, within the protected area of the Lesvos Petrified Forest.

Additionally, the fact that the volcanic sequence in the northern part of the hill, along with the significantly higher density of fossil concentrations (see Figure 6), are phenomena that require further scientific investigation. These are possibly directly linked to the geomorphology of the area during the deposition of the Sigri pyroclastic formation. Finally, the primary objective of this study is a topic that requires much more research. This initial approach and estimation open a significant scientific discussion regarding the minimum number of successive fossiliferous horizons associated with different volcanic eruptions and the assessment of volcanic episodes that preserved fossilized forests, initially for the Akrocheiras hill and, by extension, for the broader recognized area of the Petrified Forest of Lesvos.

References

Pe-Piper, G., 1980: Geochemistry of Miocene Shoshonites, Lesbos, Greece. Contributions to Mineralogy and Petrology 72, 387-396.

Pe-Piper, G., Piper, D. J.W., Zouros, N.C., Anastasakis, G., 2019: Age, Stratigraphy, Sedimentology and Tectonic Setting of the Sigri Pyroclastic Formation and its Fossil Forests, Early Miocene, Lesbos, Greece. Basin Reasearch 31, 1178-1197.

Pe-Piper, G., Imperial, A., Piper, D. J.W., Zouros, N.C., Anastasakis, G., 2019: Nature of the hydrothermal alteration of the Miocene Sigri Petrified Forest and host pyroclastic rocks, western Lesbos, Greece. Journal of Volcanology and Geothermal Research 369, 172-187.

Pe-Piper, G., Piper, D. J.W., Anastasakis, G., Zouros, N.C., Lyras, G., 2024: Variability in mineralization of the petrified forests in the UNESCO Global Geopark of Lesvos, Greece. Marine and Petroleum Geology 167, Article 106990.

Sparks, R.S.J. & Walker, G.P.L., 1977: The Significance of Vitric-Enriched Air-Fall Ashes Associated With Crystal-Enriched Ignimbrites. Journal of Volcanology and Geothermal Reasearch 2 329-341.

Velitzelos, E., & Zouros, N. (1998). New results on the petrified forest of Lesvos. *Bulletin of theGeological Society of Greece*, *32*(2), 133–142.

Zouros, N.C., 2021. The Miocene petrified forest of Lesvos, Greece: Research and geoconservation activities. Conservation Research 4 (2), 635–649.

Zouros,N., Soulakellis,N.,Valiakos,I., Bentana,K., Theodorou,E., Zgournios,E., Antonakis,E. and Lamprakopoulos,A. 2022: Enhancement and promotion of the new fossiliferous sites along the new Kalloni Sigri road.-An example of good practice in geoconservation in Lesvos Isl. UNESCO Global Geopark Greece. Bulletin of Geological Society of Greece Sp. Publ. 10, pp. 849-850.

17th INTERNATIONAL CONGRESS of the Geological Society of Greece

BULLETIN OF THE GEOLOGICAL SOCIETY OF GREECE, SP. PUBL.

EXTENDED ABSTRACT 284

Mapping petrified tree trunks and pyroclastic formations at the Lesvos Petrified Forest, Greece, case study of the Bali Alonia area

Savvelos L.1, 2 and Zouros N.1, 2
(1) Natural History Museum of the Lesvos Petrified Forest
(2) Department of Geography, University of the Aegean, Greece

Introduction / Background

The Lesvos Petrified Forest constitutes a distinctive natural monument situated in the western region of Lesvos. It represents a geological heritage asset of considerable international importance within the Lesvos Island UNESCO Global Geopark. Additionally, it is recognized among the first 100 Geological Heritage sites designated by the International Union of Geological Sciences (IUGS). The Lesvos Petrified Forest encompasses extensive assemblages of silicified tree trunks that remain in situ within the Sigri pyroclastic formation, dating back to the Lower Miocene epoch (Velitzelos & Zouros 1997, 1998; Pe-Piper et al. 2019; Zouros 2021). The Natural History Museum of the Lesvos Petrified Forest has been engaged in scientific research, excavation, and conservation efforts within the Lesvos Petrified Forest for the past 30 years. Excavations conducted in the Lesvos Petrified Forest have unveiled a substantial quantity of both standing and fallen silicified tree trunks, root systems, branches, leaves, and cones attributable to coniferous and angiosperm tree species. The composition of the forest ecosystem reflects subtropical climatic conditions (Velitzelos & Zouros 1997, 1998; Pe-Piper et al. 2019).

The silicification process of the Lesvos Petrified Forest is intricately associated with the volcanic activity that transpired in Lesvos during the Lower Miocene epoch (Pe-Piper et al. 2024). The exceptional preservation of the fossils is attributed to the circulation of hydrothermal fluids that were enriched in silicon dioxide (SiO2) (Pe-Piper et al. 2019).

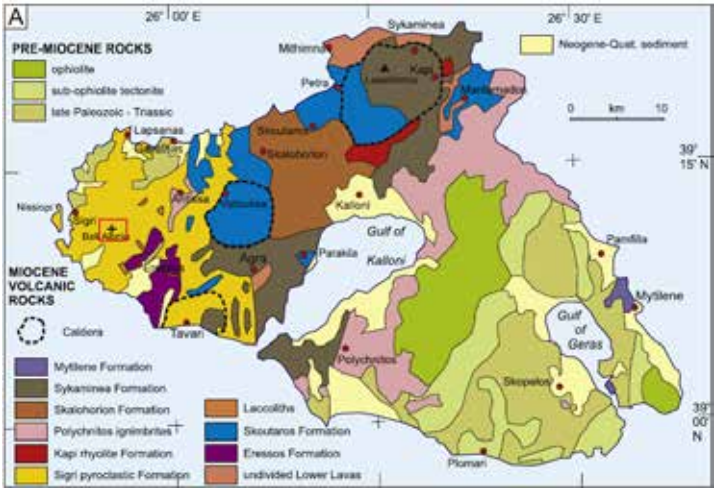

Figure 1: Geological Map of Lesvos Based on Hecht (1972-1976), modified by Pe-Piper (1992). Red rectangle indicating the study area, Bali Alonia broader area.

Since 2014, extensive rescue excavation initiatives have been conducted by the Natural History Museum of the Lesvos Petrified Forest in response to the construction of the Kalloni - Sigri road, which crosses the designated protected area of the Lesvos Petrified Forest. Therefore, a considerable amount of new information has been collected from various notable fossil locations (Zouros 2021; Pe-Piper et al. 2024).

Due to the presence of several prominent fossil sites inside the fenced area of “Bali Alonia Park”, an extensive mapping initiative was conducted within this region to meticulously identify and document fossil-bearing locations. Consequently, the primary aim of the present investigation is the identification and cartographic representation of standing tree trunks, fallen tree trunks, root systems, as well as vitric and lithic tuffs. By determining the precise locations of these fossils, we can more effectively safeguard and analyze the Petrified Forest. The mapping effort has also facilitated an enhanced comprehension of the stratigraphy associated with the pyroclastic formations.

Study Area

The Petrified Forest of Lesvos spans an area on the western edge of the island of Lesvos. Within this area, with the efforts of the Natural History Museum, accessible parks have been established where visitors can view the in situ petrified tree trunks. Approximately 10 km away from the settlement of Sigri lays the area of Bali Alonia (Fig. 2). Historically, this is where the first petrified tree trunks were protected and showcased. Subsequently, a section of the area was fenced and protected, leading to the creation of the first park of the Petrified Forest, named the Main Fossil area or the Bali Alonia Park. Fossilized in situ trunks can be found both within the fenced section and in the broader area of Bali Alonia

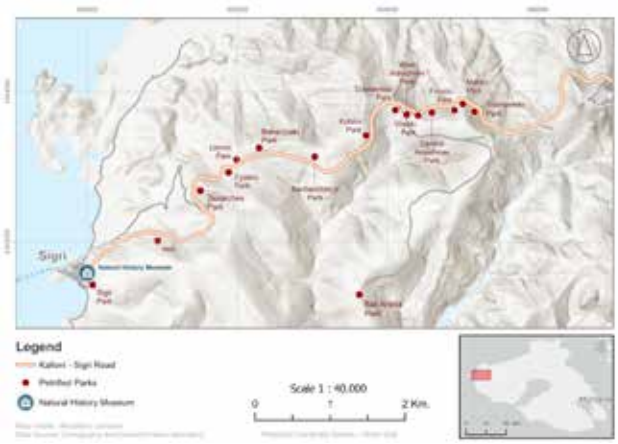

Fig 2: Regional map indicating locations of significant fossil parks along the Kalloni-Sigri road, also the main fossil area petrified forest park Bali Alonia.

For the purposes of this specific study, the broader area, covering approximately 7 km², was designated as the study area (Fig. 1). From the lowest point at an elevation of ~60 meters to the highest point of the study area at ~300 meters above sea level, standing tree trunks, fallen tree trunks, root systems and vitric and lithic tuffs are distributed.

The geographical region under investigation is comprehensively enveloped by the pyroclastic formation of Sigri (Fig. 1), which is distinguished by a diverse array of volcanic deposits that have effectively covered and preserved petrified forests in different strata (Pe-Piper et al. 2018). The Sigri pyroclastic formation exhibits a thickness of several hundred meters and is composed of tuffs alongside coarse-grained volcanic materials. From a stratigraphic perspective, it is situated above the Gavathas and Eresos formations while being positioned beneath the more recent Skoutaros formation.

Subsequent to the deposition of this geological formation, the intrusion of the Moni Ipsilou dome transpired, with a temporal attribution of approximately 17.9 million years ago. The majority of the Sigri pyroclastic formation is obscured by more recent deposits, with only the coarse-grained materials, lava flows, and volcanic domes emerging above these overlying layers. In select regions, tuffs are also present, exhibiting formations characterized by grain sizes of less than 2 mm (Pe-Piper et al. 2018).This exposition emphasizes the intricate geological attributes and importance of the region, especially concerning the conservation of the petrified forest**s** and the comprehension of its volcanic past.

Coarse-grained materials characterized by clasts with a diameter of less than 2 meters are prevalent throughout the region. These formations are typically distributed, consisting of overcompressed flows—specifically volcanic conglomerates or debris flows (Fig. 5a)—and appear to have originated from water-induced flows that infiltrated a complex network of paleo-river channels from that period (Pe-Piper et al. 2018). This formation emerged during a relatively tranquil epoch, between volcanic episodes, indicating that it was not a result of volcanic eruptions, in contrast to the tuffs present in the vicinity. This characteristic offers valuable insights into the morphological evolution of the region between volcanic events.

Consequently, the finely textured pyroclastic materials known as tuffs, whose formation and deposition are definitely associated with volcanic eruptions, are anticipated to be found in the field as stratigraphically overlying layers on top

the pre-existing substrate of the region—in this instance, the debris flow or volcanic conglomerate. Therefore these layers concurrently function as indicators of deposition resulting from a volcanic episode.
Vitric tuff is a type of volcanic tuff that is predominantly contains volcanic glass fragments that have experienced alteration (Fig. 5b) (Pe-Piper et al. 2019). It is generated during an eruption and the quick cooling of magma (Sparks & Walker 1988; Pe-Piper et al. 1980). The matrix of the tuff comprises volcanic ash and includes fragments of pumice and small lava pieces expelled during the eruption (pumice-lithic lapilli) (Pe-Piper et al. 2018). It is deposited as air fall formation (Sparks & Walker 1977) directly onto the pre-existing substrate of the region and serves as a main indicator of the initiation of deposits resulting from a volcanic eruption.

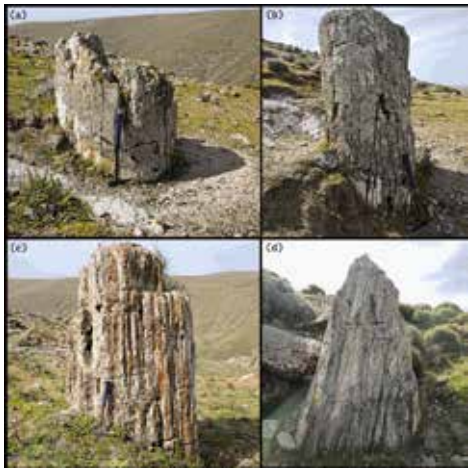

Figure 3 a,b,c,d: Standing in situ petrified trunks stable in their original position. . a: 663,737.98E 4,340,605.91N m, b: 663,709.15E 4,340,596.20N m, c: 663,617.72E 4,340,502.68N m, d: 663,692.56E 4,340,621.39N m,

Lithic tuff is classified as pyroclastic sediment. It comprises a primary binding material (matrix) consisting of volcanic ash with a grain size of approximately 2 mm, along with fragments of andesitic-dacitic lava measuring less than 64 mm, which are fragmented from pre-existing surrounding rocks and disseminated during the eruption (Fig. 5c) (Pe-Piper et al. 2018). The process of its deposition is intricately associated with volcanic eruptions. Typically, it displays variability in clasts distribution, a consequence of the differing intensities of the eruptions responsible for its deposition (Pe-Piper et al. 2018). Moreover, the deposition of this formation generally follows, on top, that of Vitric tuff. Nevertheless, in numerous instances, both formations are observed in situ, with Lithic tuff acting as the substrate and Vitric tuff overlaying it directly upon the pre-existing substrate (Pe-Piper et al. 2018). Consequently, lithic tuff serves as a significant indicator of the initiation of deposits resulting from a volcanic eruption.
This description highlights the geological complexity and significance of the area, particularly in the context of preserving the fossilized forest and understanding its volcanic history.

Methodology

The research encompassed a thorough cartographic endeavor within the specified study region, employing a methodical field survey methodology. The principal objective was to precisely identify and document fossiliferous sites, including both upright and fallen petrified tree trunks. To achieve this, we also delineated the stratigraphy of the pyroclastic deposits, with particular focus on the tuff horizons (both vitric and lithic tuff).
Field investigations were executed utilizing the FieldMove Clino Version 3.0.6 application, which afforded precise geospatial coordinates and enabled real-time data recording. In advance of data acquisition, the application underwent calibration in accordance with the manufacturer's specifications to guarantee measurement precision and dependability. Special attention was directed towards mapping regions where tuffs were exposed, particularly along the stream valleys that define the study area.
Subsequent to the identification of each relevant site, positional data was systematically documented through the

FieldMove Clino application, along with further site-specific observations recorded manually. These observations encompassed geological and geomorphological attributes. Data points were collected at locations deliberately selected during the mapping process to maximize spatial resolution and reliability.
The KMZ file format was chosen for its intuitive usability and compatibility with ArcGIS Pro, coupled with its ability to include location-specific images, thus considerably improving the data processing and interpretative phases. Data accuracy and consistency assessments were conducted to ensure the quality of the gathered dataset.
The standing petrified tree trunks (Fig. 3, Fig. 4), being fossilized in their original position, serve as significant evidence to define a fossiliferous horizon. The root systems of these trunks are markers of the original layers where a dense

Figure 4 a, b, c, d: Standing in situ petrified trunks at the broader area of Akrocheiras illustrated with their roots systems spreading in the air fall vitric tuff and a, b, c also covered by coarse-grained volcanic conglomerates. a: 663,805.18E 4,341,410.44N m located in the Park Bali Alonia, b: 663 770,269E 4,343,366,122N m, c: 663 777,896E 4,343,388,585N m, d: 664,396.99E 4,343,703.54N m. Trunks b, c, located at the Park Kotsini and d located at the Park Vrysaki.

Figure 5: Appearance of the main sequence marking the deposition of a new volcanic eruption, where: a: Coarse-grained pyroclastic flow (Debris flow). b: Vitric tuff, deposited directly from the air; the vitric tuff forms during the eruption due to the rapid cooling of magma and serves as a critical marker indicating the onset of a new volcanic sequence. c: Lithic tuff, a pyroclastic sediment containing volcanic tuff and andesitic-dacitic clasts. Coordinates of the locality: 664,134.57E 4,341,600.77N m

Figure 4 illustrates the distinctive geological formations of the Bali Alonia region previously discussed (debris flow, vitric tuff, lithic tuff) that have been observed in situ and signify the commencement of deposits resulting from volcanic activity. The discernment of sites where the interrelationship among the pyroclastic layers is evident is essential for comprehensively understanding and assessing the fossiliferous stratas and volcanic episodes present in the broader area of Bali Alonia.

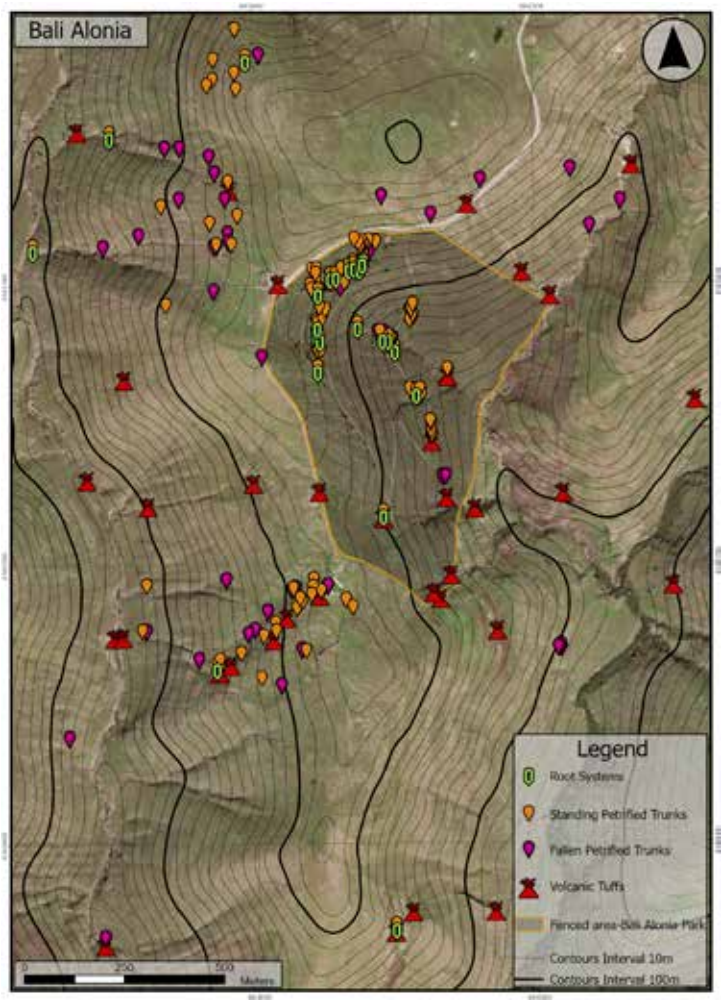

Figure 6: Result of the mapping of the plant fossils (standing, petrified tree trunks, lying petrified tree trunks , root systems) and volcanic horizon contacts conducted in the Bali Alonia area, within the protected area of the Lesvos Petrified Forest.

Results

The principal aim of this research is to identify and delineate standing tree trunks, fallen tree trunks, root systems, also vitric and lithic tuffs, which are instrumental in pinpointing successive fossiliferous horizons linked to distinct volcanic eruptions. By integrating the geographical coordinates of upright petrified trunks that exhibit their root systems, in conjunction with the occurrences of vitric tuff or lithic tuff, the resultant map was generated (Fig. 6).

The recorded locations (Fig. 6) suggest that the Bali Alonia region contains multiple successive fossiliferous horizons corresponding to various volcanic eruptions.

Discussion

Bali Alonia broader area is characterized by its coverage of quaternary deposits and sparse vegetation, which complicates the mapping endeavors significantly. Comprehensive mapping conducted on Bali Alonia region has furnished substantial evidence for the existence of multiple successive pyroclastic layers that

signify a series of volcanic eruptions.
The excavation activities undertaken by the Natural History Museum of the Lesvos Petrified Forest have resulted in the removal of quaternary deposits and soil profiles, thereby fully exposing the volcanic formations at the excavation sites along the Kalloni Sigri thoroughfare. It is noteworthy that within the confines of "Ioannis Toumpelekis Park" located at the northeastern periphery of Akrocheiras Hill, a minimum of 8 fossiliferous layers have been documented. This finding underscores the notion that the study area is home to numerous successive fossiliferous horizons.
Empirical observations reveal that petrified tree trunks that have fallen are predominantly located at lower elevations, embedded within debris flow deposits, while standing trunks with visible root systems are typically found protruding from tuff layers at higher altitudes. This observed distribution implies that the occurrence of fallen trunks within debris flow deposits does not directly correlate with volcanic eruptions. Rather, these trunks likely represent fragments of previously standing trees that were displaced and subsequently deposited during debris flow events. These flows, influenced by hydrological factors during non-eruptive intervals, transported tree remnants alongside volcanic materials, embedding them within coarse-grained deposits. The consistent vertical and spatial arrangement of standing trunks above fallen trunks is recurrently observed along Bali Alonia broader Area. Consequently, the distribution of fallen trunks in these instances is indicative of prolonged natural transport mechanisms rather than direct volcanism; however, this pattern does not universally apply across the entirety of the study area, as in other locations the distribution of fallen trunks is directly associated with volcanic activity.
Furthermore, the instant correlation of the petrified trunks hosted in the fenced area, the Bali Alonia Park at the West side of the hill, with the numerous trunks at the East of the hill (Fig. 6), it is a subject that demands furthermore research. These occurrences are potentially directly associated with the geomorphological characteristics of the region during the deposition of the Sigri pyroclastic formation and of course will provide very important additional information to the main objective of the current study.
Ultimately, the principal aim of this research represents a subject that warrants extensive further investigation. This preliminary analysis and assessment catalyze a substantial academic discourse concerning the distribution of petrified tree trunks and volcanic tuffs, which contribute to the identification of successive fossiliferous horizons correlated with diverse volcanic eruptions and the evaluation of volcanic episodes that have preserved fossilized forests, initially focusing on Akrocheiras hill and subsequently extending to the broader recognized expanse of the Petrified Forest of Lesvos.

References

Pe-Piper, G. (1980). Geochemistry of Miocene shoshonites, Lesbos, Greece. *Contributions to Mineralogy and Petrology, 72*(4), 387–396. https://doi.org/10.1007/BF00371346

Pe-Piper, G., Piper, D. J. W., Zouros, N. C., & Anastasakis, G. (2019). Age, stratigraphy, sedimentology and tectonic setting of the Sigri Pyroclastic Formation and its fossil forests, Early Miocene, Lesbos, Greece. *Basin Research, 31*(6), 1178–1197. https://doi.org/10.1111/bre.12365.

Pe-Piper, G., Imperial, A., Piper, D. J. W., Zouros, N. C., & Anastasakis, G. (2019). Nature of the hydrothermal alteration of the Miocene Sigri Petrified Forest and host pyroclastic rocks, western Lesbos, Greece. *Journal of Volcanology and Geothermal Research, 369*, 172–187. https://doi.org/10.1016/j.jvolgeores.2018.11.018.

Pe-Piper, G., Piper, D. J. W., Anastasakis, G., Zouros, N. C., & Lyras, G. (2024). Variability in mineralization of the petrified forests in the UNESCO Global Geopark of Lesvos, Greece. *Marine and Petroleum Geology, 167*, Article 106990. https://doi.org/10.1016/j.marpetgeo.2024.106990

Sparks, R. S. J., & Walker, G. P. L. (1977). The significance of vitric-enriched air-fall ashes associated with crystal-enriched ignimbrites. *Journal of Volcanology and Geothermal Research, 2*(4), 329–341. https://doi.org/10.1016/0377-0273(77)90019-1

Velitzelos, E., & Zouros, N.C. 1998. New results on the petrified forest of Lesvos. *Bulletin of theGeological Society of Greece*, *32*(2), 133–142.

Zouros, N. C. (2021). The Miocene petrified forest of Lesvos, Greece: Research and geoconservation activities. *Geoconservation Research, 4*(2), 635–649. https://doi.org/10.30486/gcr.2021.1927340.1090

17th INTERNATIONAL CONGRESS of the Geological Society of Greece

BULLETIN OF THE GEOLOGICAL SOCIETY OF GREECE, SP. PUBL.

EXTENDED ABSTRACT 285

Travertine deposits of Greece, a mineralogical and geochemical study

Schifano V.[1], Li Vigni L.[1], Randazzo L.[1,2], Brusca L.[2], Bellomo S.[2], Calabrese S.[1,2], D'Alessandro W[2]

(1) Department of Earth and Marine Sciences, University of Palermo, Palermo, Italy, vanessa.schifano@community.unipa.it; (2) National Institute of Geophysics and Volcanology, Palermo, Italy

Research Highlights

- Greek travertines are dominated by calcite with aragonite, hydromagnesite, hematite and clay minerals;
- Chemical composition of travertines shows high concentrations of some potentially toxic elements (e.g. As, Ba, Cu, Cr, Ni, Pb, V).

Introduction

Travertine, also known as *Lapis Tiburtinus* by ancient Romans, is a type of "chemically precipitated continental limestone" which consists of calcite or aragonite minerals. (Pentecost, 2005). The precipitation of carbonate minerals occurs primarily through the degassing of carbon dioxide from a groundwater source, resulting in calcium carbonate supersaturation (Pentecost, 2005). The occurrence of travertine deposits has been observed around both cold springs (i.e. tufa or meteogene travertine) and warm-hot springs (i.e. travertine or thermogene travertine), suggesting two distinct origins of travertine. The distinction between these two types of deposit can be determined based on features of parent waters and on the source of CO_2 (e.g. Pentecost and Viles, 1994; Ford and Pedley, 1996). Meteogene travertines are formed from parent waters that are characterized by lower temperature and neutral pH values (7-8). CO_2 has a meteoric and/or biogenic origin and shows carbon isotope compositions that range mostly from about -11 to 0 ‰, reflecting the depleted ^{13}C of soil CO_2 (Deines, 1980). On the other hand, thermogene travertines form from parent waters with high temperatures and lower pH values. The CO_2 in this case has mostly a geogenic source, with a $\delta^{13}C$ range of -4 to +8 ‰ (Pentecost and Viles, 1994), resulting from the interaction between host rocks and deep CO_2-rich fluids, such as mantle fluids or metamorphic decarbonation reactions (Ohmoto and Rye, 1979). In addition, while meteogene travertines display low deposition rates (<10 mmol cm^{-2} a^{-1}), thermogene travertine show very high deposition rate of hundreds of mmol cm^{-2} a^{-1} (D'Alessandro *et al.*, 2007).

An increased interest in studying travertine deposits is driven by their potential applications in paleoclimatic and paleoenvironmental studies, as well as in hydrogeological studies, rock and oil exploitation. Thermogenic travertine deposits also allow for the evaluation of any endogenic processes. Additionally, travertine deposits facilitate the estimation of paleo CO_2 fluxes associated with their deposition (Mancini *et al.*, 2019).

Travertine deposits are widespread in Greece, with the most studied being found in Northern Euboea and Eastern Central Greece. These areas are characterised by a high geothermal gradient, which leads to the presence of several thermal springs. In some of these thermal springs are depositing thermogene travertine, as a result of the cooling and degassing of thermal waters, leading to the rapid precipitation of calcium carbonate (Kanellopoulos *et al.*, 2017 and references therein).

In this research, we present data about the mineralogical and geochemical compositions of 39 travertine samples collected along the whole Hellenic territory from thermal, cold–gas-rich, acidic and hyperalkaline springs, in order to better investigate the possible differences between different type of parent waters.

Methods

Thirty-nine travertine samples were collected along the whole Hellenic territory (Fig.1 and Table 1) from a variety of springs, including thermal, cold–gas-rich, acidic and hyperalkaline springs. Samples were analysed for their mineralogical and geochemical composition. Information on the physico-chemical parameters and the chemical composition of the parent waters were taken from (Li Vigni *et al.*, 2022, 2023).

Samples were, firstly, pulverised in an agate mortar and then, subdivided in two aliquots. The first aliquot was used for the investigation of mineralogical composition by X-ray powder diffraction (XRPD). The XRPD analysis was being carried out at the laboratories of the Department of Earth and Marine Sciences of the University of Palermo, using a PANanalytical X'PERT PRO diffractometer. The second aliquot was mineralized to obtain the chemical composition of the samples. About 100 mg of dried sample were dissolved in a polypropylene bottle with a solution of 1 mL of ultrapure HCl (37%), 0.5 mL of ultrapure HNO_3 (65%) and 50 mL of milliQ water. The obtained solutions were analysed for major cations (Ca, K, Mg, Na, P, S, Si) by Inductively Coupled Plasma Optical Emission Spectrometry

(ICP-OES; Jobin Yvon Ultima 2), whilst 26 trace elements (Li, Be, B, Al, Ti, V, Cr, Mn, Fe, Co, Ni, Cu, Zn, As, Se, Rb, Sr, Mo, Cd, Sn, Sb, Cs, Ba, Tl, Pb, and U) were analysed by Inductively Coupled Plasma Mass Spectrometry (ICP-MS; Agilent 7800). Results are expressed as μg g^{-1} of solid. Pre-treatment procedures were carried out at the laboratories of the Department of Earth and Marine Sciences of the University of Palermo, and analysis were carried out at laboratories of the Istituto Nazionale di Geofisica e Vulcanologia (INGV-Palermo).

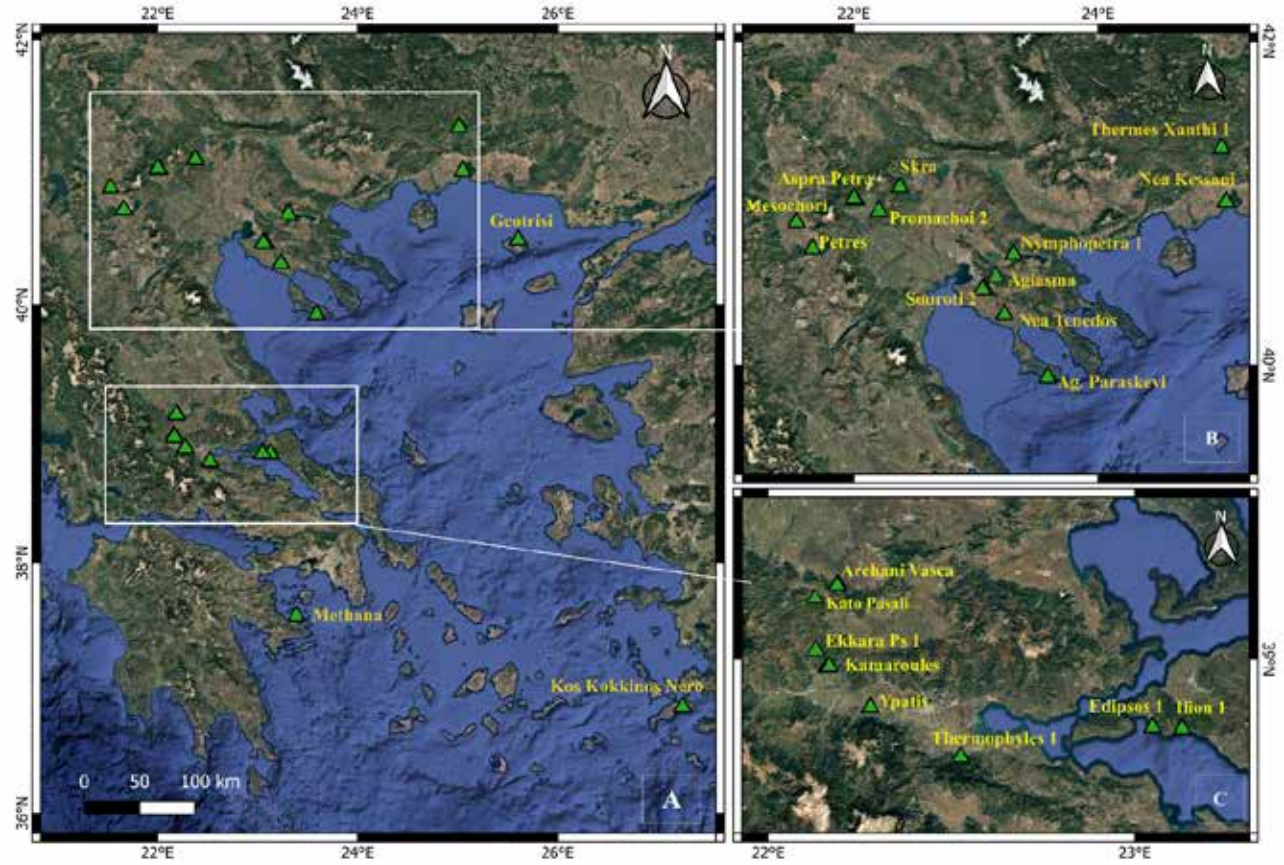

Figure 1. Geographic distribution of sampling sites of travertine deposits. Map was created using the QGIS software, version 3.28.6. Basemap by ESRI maps.

Table 1. Identification number and geographical coordinates of travertine samples. Type of parent waters are also indicated.

ID	Name	Type waters	Date	Latitude	Longitude
GR 01	Mesochori	Thermal	22/05/2016	40.89119	21.53241
GR 02	Geotrisi	Thermal	23/05/2016	40.49705	25.603
GR 03	Archani Vasca	Hyperalkaline	05/10/2017	38.98339	22.16155
GR 04	Skra	Gas-rich cold	03/03/2020	41.10575	22.37831
GR 05	Ekkara Ps	Hyperalkaline	05/09/2017	39.15805	22.18965
GR 06	Ekkara Ps 2	Hyperalkaline	05/09/2017	39.15805	22.18965
GR 07	Nea Kessani	Thermal	18/05/2016	41.01707	25.05148
GR 08	Pareskevi	Thermal	28/05/2016	39.92402	23.59009
GR 09	Kos Kokkino Ner	Acidic	30/09/2016	36.85501	27.24797
GR 10	Ypatis	Thermal	07/10/2016	38.89774	22.2789
GR 11	Kamaroules	Hyperalkaline	07/10/2016	38.98465	22.16633
GR 12	Geotrisi	Thermal	20/03/2017	40.49705	25.603
GR 13	Thermes Xanthi 1	Thermal	22/03/2017	41.34762	25.01361
GR 14	Thermes Xanthi 2	Thermal	22/03/2017	41.34762	25.01361

GR 15	Thermes Xanthi 3	Thermal	22/03/2017	41.34762	25.01361
GR 16	Nymphopetra 1	Thermal	23/03/2017	40.69157	23.30884
GR 17	Nymphopetra 2	Thermal	23/03/2017	40.69157	23.30884
GR 18	Nymphopetra 3	Thermal	23/03/2017	40.69157	23.30884
GR 19	Kato Pasali	Hyperalkaline	09/05/2017	39.15659	22.18749
GR 20	Archani 159	Hyperalkaline	10/05/2017	38.98319	22.16115
GR 21	Archani 160 fuori	Hyperalkaline	10/05/2017	38.98317	22.16124
GR 22	Archani 160	Hyperalkaline	10/05/2017	38.98317	22.16124
GR 23	Thermopyles 1	Thermal	11/05/2017	38.79254	22.52572
GR 24	Thermopyles 2	Thermal	11/05/2017	38.79254	22.52572
GR 25	Thermopyles 3	Thermal	11/05/2017	38.79254	22.52572
GR 26	Ilion 1	Thermal	23/06/2018	38.85212	23.12909
GR 27	Ilion 2	Thermal	23/06/2018	38.85212	23.12909
GR 28	Promachoi 1	Thermal	14/10/2018	41.02973	22.0195
GR 29	Promachoi 2	Thermal	14/10/2018	41.02973	22.0195
GR 30	Promachoi 3	Thermal	14/10/2018	41.02973	22.0195
GR 31	Aspra Petra	Gas-rich cold	27/07/2021	41.03720	22.00308
GR 32	Petres	Gas-rich cold	30/04/2023	40.72604	21.66508
GR 33	Nea Tenedos	Thermal	03/05/2023	40.3178	23.2343
GR 34	Agiasma	Gas-rich cold	03/05/2023	40.47342	23.0551
GR 35	Souroti	Gas-rich cold	03/05/2023	40.4733	23.07653
GR 36	Methana	Thermal	/	37.57744	23.38702
GR 37	Edipsos	Thermal	/	38.85514	23.04845
GR 38	Edipsos	Thermal	/	38.85514	23.04845
GR 39	Archani incrostazioni	Hyperalkaline	10/05/2017	38.98339	22.16155

Results

X-ray diffraction analyses were carried out on 13 travertine samples. The analysis revealed that the main mineral phases show close similarities. The samples are predominantly composed of calcite (Fig. 2), with a very low percentage of aragonite in few samples. Traces of halite and hydromagnesite were also found. Further investigations are underway to verify their presence. Moreover, traces of hematite were found in travertine samples of Mesochori (GR01) and Giotrisi (GR02), whereas traces of clay minerals were found in Archani (GR20).

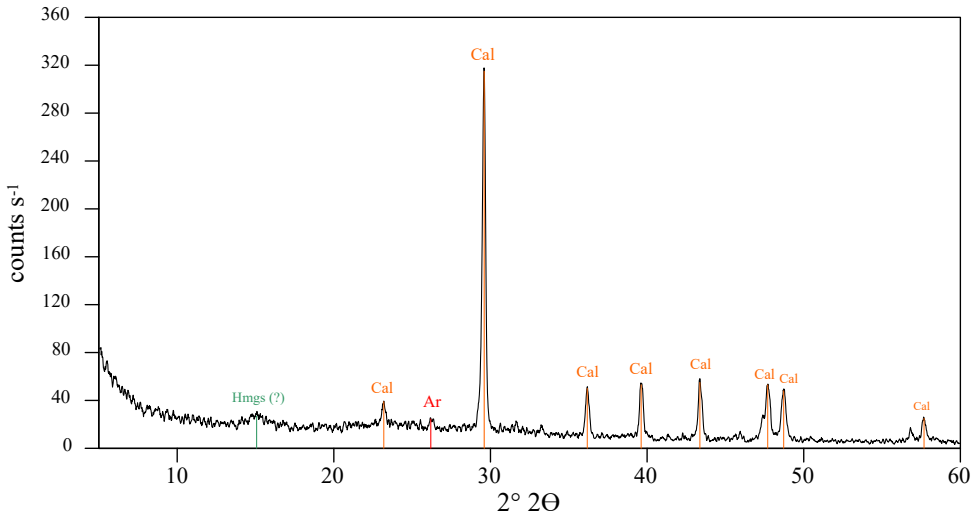

Figure 2. X-ray diffractogram of the travertine sample of Nea Kessani. Hmgs = Hydromagnesite; Cal = Calcite; Ar = Aragonite.

The results of the geochemical analyses are summarised in the boxplot in figure 3, which shows a wide range of concentration, generally, exceeding three orders of magnitude. Calcium is the dominant cation in all the samples,

with concentrations ranging from 94,800 μg g^{-1} to 462,000 μg g^{-1}. The elements can be categorized, based on their median concentrations, into minor elements (Mg, S, Na, Fe, Sr, Si), which show a median values between 1% and 0.1%, and into trace elements (Mn, Ba, P, B, Zn, As, Li, Ti, Ni, Cr, Cu, V, Pb, Rb, Co, Be, U, Cs, Sb, Mo, Se, Cd, Sn, Tl) with median concentrations below to 0.1%.

Thermogene travertine samples of Thermopyles (GR23, GR24, GR25), Ilion (GR26, GR27) and Edipsos (GR37, GR38) have been compared with literature data (Kanellopoulous et al., 2017), showing a similar composition. Elements such as Fe (Thermopyles up to 265 μg g^{-1}, Ilion up to 285,800 μg g^{-1}, Edipsos up to 9280 μg g^{-1}) and As (Thermopyles up to 156 μg g^{-1}, Ilion up to 15,360 μg g^{-1}, Edipsos up to 90.6 μg g^{-1}) displayed concentrations within the range reported by the same authors. According to them, the lithogeochemistry of these ore-bearing travertines reflects the geochemical composition of the parent hydrothermal fluids, which are enriched in Fe and As, particularly in the case of Ilion. The presence of metal(loid)s in thermogenic travertine can be attributed to a primary magmatic source and to reduced and low-sulfidation state of the hydrothermal fluids (Kanellopoulous *et al.*, 2017). However, other travertine samples exhibit enrichment in some metal(loid)s, including Mesochori (GR01), Giotrisi (GR02, GR12) and Skra (GR04).

All these trace elements may be incorporated in the mineral structure of the carbonates substituting for Ca or precipitate as constituents of secondary minerals or be adsorbed onto the surface of the forming crystals or amorphous phases. Therefore, further studies are required to ascertain both the origin and water-rock interaction processes, such as the precipitation of secondary minerals, that took place.

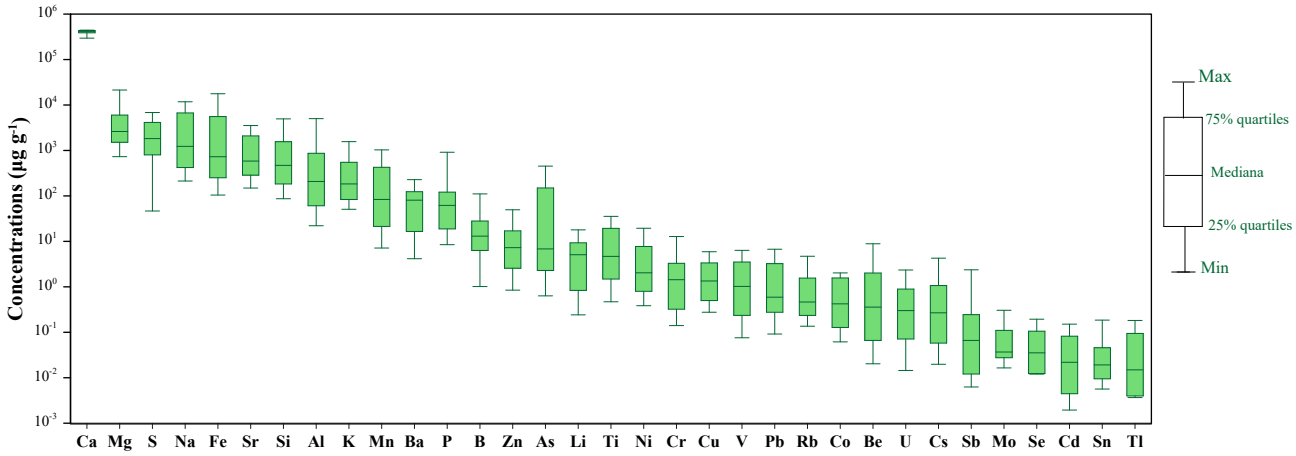

Figure 3. Boxplot of major ions and trace elements of collected travertine samples.

Conclusions

Despite the widespread presence of travertine in Greece, few studies can be found in the scientific literature. Their geochemical and mineralogical characterization may provide important information on water-rock interaction processes, dissolution and precipitation patterns, the origin of CO_2 and the genesis of travertines themselves. These preliminary data show both their mineralogical phases associated dominantly with calcite although traces of aragonite, hydromagnesite, hematite and clay minerals are sometimes found. From a geochemical perspective, calcium is the predominant element. Nonetheless, their chemical composition comprises a large number of trace metals, including some potentially toxic elements (e.g. As, Ba, Cu, Cr, Ni, Pb, V) and some strategical industrial elements like Li and B. Further steps of this preliminary study will be to investigate the relationship between travertine samples and their parent waters in order to better understand water-rock interaction processes.

References

D'Alessandro, W., Giammanco, S., Bellomo, S., Parello, F., 2007. Geochemistry and mineralogy of travertine deposits of the SW flank of Mt. Etna (Italy): Relationships with past volcanic and degassing activity. Journal of Volcanology and Geothermal Research, 165, 64–70.

Deines, P., 1980. The isotopic composition of reduced carbon, in: Fritz, P., and Fontes, J.C. (Eds.), Environmental Isotope Geochemistry, 329-407.

Ford, T.D., Pedley, H.M., 1996. A review of tufa and travertine deposits of the world. Earth-Science Reviews 41, 117–175.

Kanellopoulos, C., Mitropoulos, P., Valsami-Jones, E., Voudouris, P., 2017. A new terrestrial active mineralizing hydrothermal system associated with ore-bearing travertines in Greece (northern Euboea Island and Sperchios area). Journal of

Geochemical Exploration, 179, 9-24https://doi.org/10.1016/j.gexplo.2017.05.003

Li Vigni, L., Daskalopoulou, K., Calabrese, S., Parello, F., Brugnone, F., D'Alessandro, W., 2022. Geochemical characterization of the thermo-mineral waters of Greece. Environmental Geochemistry and Health, 44, 2111-2133. https://doi.org/10.1007/s10653-021-01001-1

Li Vigni, L., Daskalopoulou, K., Calabrese, S., Kyriakopoulos, K., Bellomo, S., Brusca, L., Brugnone, F., D'Alessandro, W., 2023. Characterization of trace elements in thermal and mineral waters of Greece. Environmental Science and Pollution Research, 30, 78376–78393. https://doi.org/10.1007/s11356-023-27829-x

Mancini, A., Frondini, F., Capezzuoli, E., Galvez Mejia, E., Lezzi, G., Matarazzi, D., Brogi, A., Swennen, R., 2019. Evaluating the geogenic CO_2 flux from geothermal areas by analysing quaternary travertine masses. New data from western central Italy and review of previous CO_2 flux data. Quaternary Science Reviews, 215, 132-143. https://doi.org/10.1016/j.quascirev.2019.04.030.

Ohmoto, H. and Rye, R.O. 1979. Isotopes of sulfur and carbon, in: Barnes, H.L. (Eds.), Geochemistry of Hydrothermal Ore Deposits, 509-567.

Pentecost, A., Viles, H., 1994. A review and reassessment of travertine classification. Géographie Physique et Quaternaire, 48, 305–314

Pentecost, A., 2005. Travertine, Springer, Berlin.

17th INTERNATIONAL CONGRESS of the Geological Society of Greece

BULLETIN OF THE GEOLOGICAL SOCIETY OF GREECE, SP. PUBL.

EXTENDED ABSTRACT 286

The Upper Devonian sequence of the Noravank and Ertych geosites in Armenia: stratigraphy and geotouristic potential

Serobyan V.[1], Danelian T.[2], Grigoryan A.[1]

(1) Institute of Geological Sciences of the National Academy of Sciences of the Republic of Armenia, 24A, Marshal Baghramyan Avenue, Yerevan 0019, Republic of Armenia, (2) University of Lille, CNRS, UMR 8198- Evo-Eco-Paleo, F-59000 Lille, France

Introduction / Background

Upper Devonian sequences crop out in the southern part of central Armenia (Fig. 1). They are relatively thick and rich in fossils, especially brachiopods, a fact that has been acknowledged since mid-19th century, at the time of the first geological expeditions in the region by Hermann Abich, considered as “the Father of Caucasian Geology”. Interest on these sequences and their brachiopods was revived after the end of World War II, when at the time of the Soviet Union, extensive stratigraphic and mapping efforts were conducted by the Institute of Geological Sciences of the National Academy of Sciences of the Republic of Armenia. The rich brachiopod fauna was studied by Abrahamyan (1957); it allowed her to recognize a number of stratigraphically succeeding brachiopod assemblages that served as a foundation for the stratigraphic understanding and mapping of the Upper Devonian and Lower Carboniferous sequences of Armenia (Arakelyan, 1964). Following this phase of extensive mapping the sequences were considered as relatively well known. In the framework of the preparation of the IGCP n° 491 meeting (*Devonian Vertebrates of the Continental Margins*), held at Yerevan in May 2005, some identifiable conodonts and chondrichthyan microremains were found in limestones processed by Araiyk Grigoryan (Ginter *et al.*, 2011). However, comprehensive and systematic studies of these Upper Devonian sequences in Armenia, with deployment of modern approaches and techniques, only began in earnest with the launch of the co-tutorial PhD work of Vahram Serobyan, which focused on a revision of the taxonomy and biostratigraphy of the Brachiopods recovered from the Frasnian and lower Famennian sequences of Armenia (Serobyan, 2021).
Previous studies conducted in Armenia and Nakhichevan would suggest that some of the Upper Devonian outcrops could include sedimentary sequences deposited during the late Frasnian and early Famennian interval; however, detailed stratigraphic studies were missing. The Frasnian–Famennian transitional interval bears a particular significance for the evolution of marine ecosystems, since the diversity of the marine biosphere was affected profoundly during the Kelwasser mass extinction event. Although the study of Serobyan (2021) was mainly focused on the brachiopods, it allowed to clarify stratigraphic relationships of the Noravank section, which takes its name from the presence of the famous Noravank monastery constructed on top of the Upper Devonian sequence (Fig. 2). This section was correlated with the better-exposed Ertych section (Fig. 1). The correlations established by Serobyan (2021) were based not only on revised brachiopod assemblages, but also on lithostratigraphy. His PhD study confirmed the interest of these sequences as potentially containing the transition between the Frasnian and the Famennian stages, with the possibility of documenting a regional record of the Kelwasser mass extinction in the Lesser Caucasus. This latter part is currently one of the objectives of the ongoing GREATPAL project (*Deciphering the Global vs Regional record of Environmental chAnges in The PALeozoic mountains of Armenia*), funded by the Higher Education and Science Committee of Armenia. We here present recent biostratigraphic results obtained in the framework of this project and discuss the potential of these sections to become geotouristic destinations in Armenia, especially the Noravank geosite, given that the Noravank monastery is one of the most visited touristic attractions in Armenia.

Stratigraphic and palaeogeographic setting

The Upper Devonian sedimentary sequences in Armenia are over 1,000 m-thick; they represent the earliest part of the depositionary history of the Paleozoic sediments that are present in the region. These sedimentary sequences accumulated in a tropical shallow-water platform that was positioned on the northern margin of Gondwana, facing the Paleotethys to the North. This part of Gondwana was individualized afterwards, during the Triassic, as the South-Armenian Block, after it started migrating northwards as a result of the opening of Neotethys further to its South.
In Armenia, the known Frasnian–Famennian sequences crop out essentially on the flanks of a deep valley that has been formed along the Gnishik river, where the Noravank monastery is located, and on the southern bank of the Arpa river, ca. 8.5 Km east of the village of Areni, near the ruins of the ancient village Ertych (Fig. 1). Both sections display a similar lithostratigraphic succession (Fig. 3) and can be subdivided into four lithostratigraphic intervals. The lower and upper parts of the sections are represented by two distinct carbonate intervals that are composed essentially of marly/sandy limestones. The older (lower) carbonate interval is rich in brachiopods characteristic of the *Ripidiorhynchus gnishikensis–Angustisulcispirifer arakelyani* assemblage zone, which have been directly correlated with the latest early

to late Frasnian interval, based on conodonts characteristic of the *transitans* to late *rhenana* conodont zones (Serobyan *et al.*, 2023). It is stratigraphically overlain by an interval dominated by black shales that are intercalated by relatively thin sandstone beds. They are in their turn overlain by thick mature sandstones, in which we may find occasionally some intercalations of shales. Finally, the younger (upper) limestone interval is also rich in brachiopods characteristic of the *Aramazdospirifer orbelianus–Tornitospirifer armenicus* brachiopod assemblage. Conodonts identified by Ginter et al. (2011) in this limestone interval correspond to the lower Famennian *Palmatolepis crepida* conodont zone.

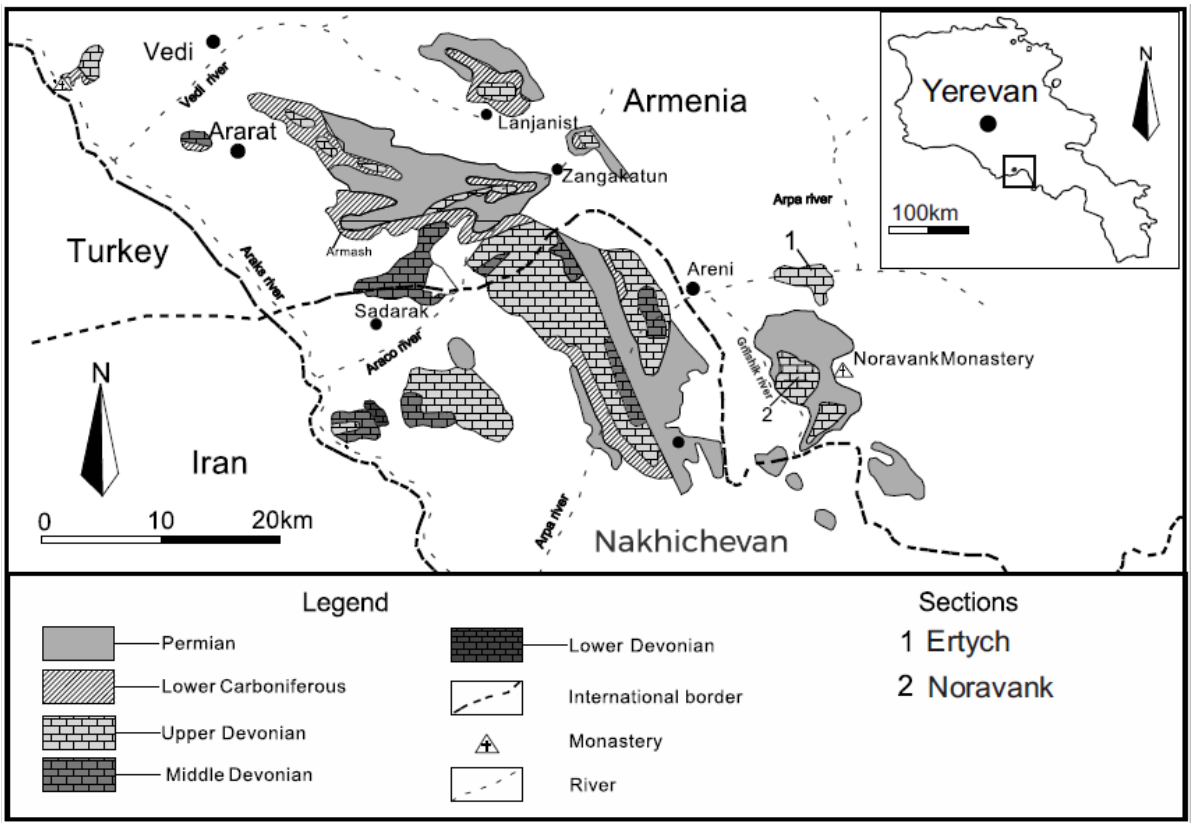

Figure 1. Schematic geological map of the Middle-Upper Palaeozoic sequences in the Lesser Caucasus (Central Armenia and Nakhichevan), with localization of the Noravank and Ertych sections discussed in this study.

Stratigraphy: recent palynological results and correlations

The Upper Devonian sequences of Armenia are indeed rich in fossils; more particularly, they contain a diverse and well-preserved brachiopod fauna (Serobyan *et al*., 2023). However, they also contain chondrichtyan microremains and conodonts (Ginter *et al*., 2011), tentaculitides (Vinn *et al*., 2025), rare bryozoans (Ernst *et al*., 2024), corals and trilobites (unpublished data). However, since terrigenous siliciclastic sediments, devoid of any carbonate beds, are intercalated between the lower and the upper limestones, the critical Frasnian–Famennian transitional interval has largely remained unzoned. Nevertheless, major biostratigraphic progress has recently been achieved for this interval thanks to the initiation of palynological studies. Indeed, Khachatryan *et al.* (2025) discovered abundant and diverse palynomorphs from the entire terrigenous interval. These authors document for the first time miospore assemblages recovered from eleven samples of the Ertych section. The presence of the miospore species *Teichertospora torquata*, found present in most of the examined samples, suggests that the entire terrigenous siliciclastic interval should be attributed to the *torquata-gracilis* miospore zone, indicating a late Frasnian to early Famennian age. Interestingly, this terrigenous interval contains also the species *Acinosporites lindlarensis*, which corresponds to the spores of the herbaceous lycophyte *Leclerquia*, for which it is well established that it went extinct at the end of the Frasnian. Thus, the miospore record suggests that the age of the black shales and mature sandstones should be limited only to the late Frasnian. In addition, acritarchs, prasinophytes and chitinozoans are also found in the same samples, which establishes that these terrigenous sediments were accumulated in a marine depositional environment (Yeghiazaryan *et al*., 2025).

Geotouristic potential: where history meets palaeontology, stratigraphy and the topic of mass extinctions

Noravank has an immense historical and touristic significance for Armenia. The geosite hosts a monastery that is

composed of a church built initially during the 9th and 10th century. The existing church was re-built during the 12th, 13th and 14th centuries to become the mausoleum of the Orbelian royal family, as it represents one of the most notable monasteries constructed by the Orbelian dynasty.

Figure 2. Left: Field photograph of the Noravank section. Right: the Noravank monastery.

The area surrounding the Noravank geosite has been studied since the 19th century by Abich (1858). Born and educated in Germany, he spent most of the time of his life in Russia. He travelled for 30 years different regions of the Lesser Caucasus and more particularly in the current and historic Armenia.

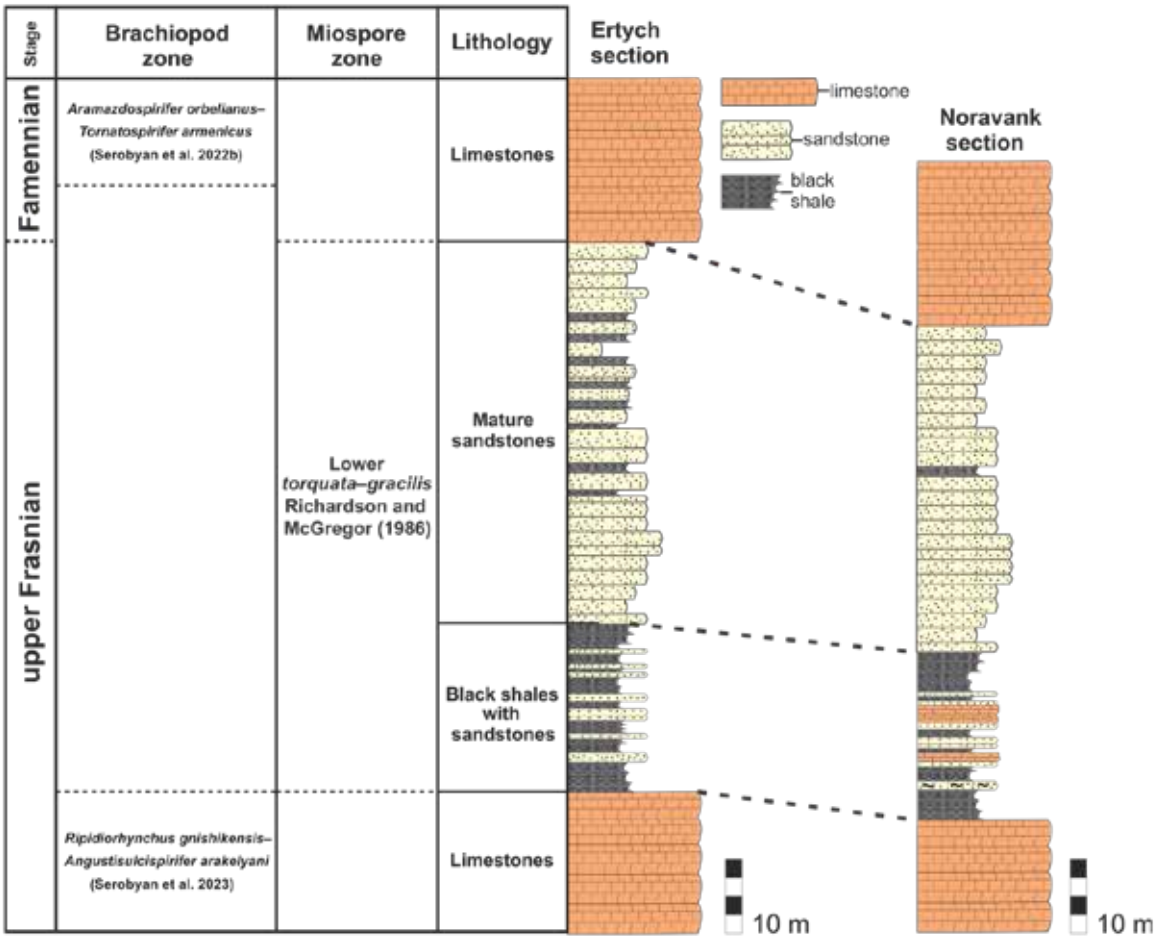

Figure 3. Lithostratigraphic columns and biochronostratigraphic framework of the Upper Frasnian–lower Fammenian sedimentary sequences of the Ertych and Noravank sections.

At Noravank, he found a new brachiopod species, which he dedicated to the Orbelian dynasty, one of the most prominent in medieval Armenia; he named it *Spirifer orbelianus* Abich, 1858. The Orbelian family has had a long-lasting political influence in Armenia and this has been materialized in numerous inscriptions found in different constructions throughout southern Armenia, namely the Vayotz Dzor and Syunik regions. Although Abich did not explicitly mention where exactly he had found the holotype of this species, we believe that it was found in the lower Famennian marly limestones cropping out just below the Noravank monastery (see Serobyan *et al.*, 2022, for more details). During his PhD, V. Serobyan re-examined new specimens of this species (Fig. 4), which he collected from the type locality (the Noravank section). He studied the internal structure of this brachiopod species based on numerous serial thin sections. He found out that this species should be assigned to a new genus, which he introduced under the genus name *Aramazdospirifer*, in honor of Aramazd, the chief god in pre-Christian Armenian mythology. It is obvious that all these palaeontological and stratigraphic elements are of great potential interest for a touristic visit. The Noravank, but also Ertych geosites, may be considered as open-air geological museums for tourists interested in geoeducation.

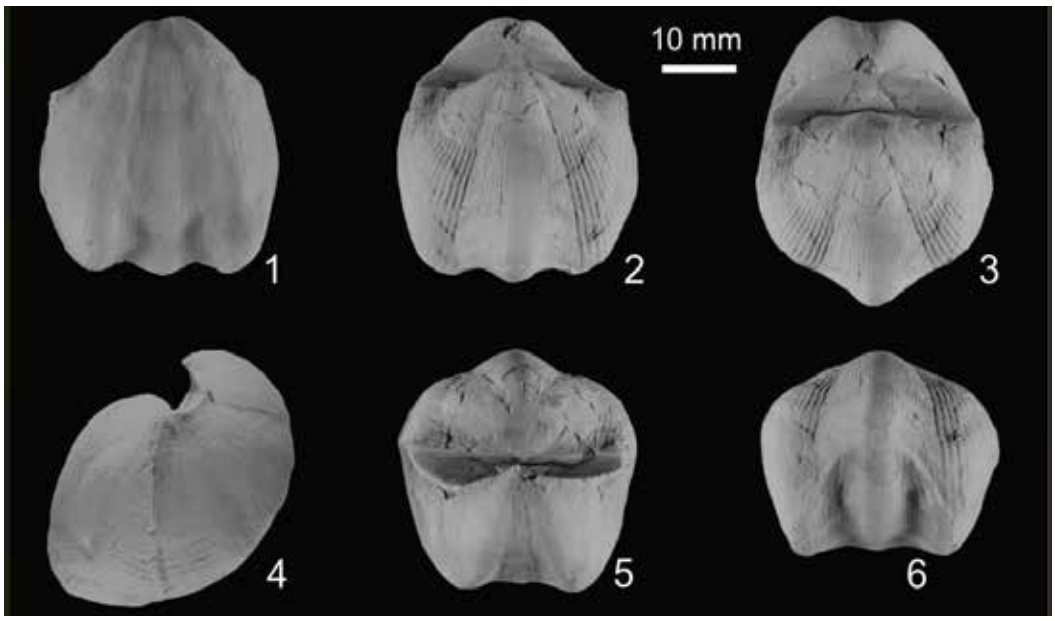

Fig. 4: Microphotographs of a single specimen of *Aramazdospirifer orbelianus* (Abich, 1858) collected from the lower Famennian limestones of the Noravank section. ventral (1), dorsal (2), posterodorsal (3), lateral (4), posterior (5) and anterior (6) views (deposited at the Institute of Geological Science, Yerevan, collection n° IGSNASRAGM 3897/AB97/48; neotype).

Acknowledgements

The research of this extended abstract was supported by the Higher Education and Science Committee of the Ministry of Education, Science, Culture, and Sports of the Republic of Armenia (Research project 22RL-016).

References

Abich, H., 1858, Vergleichende geologische Grundzüge der Kaukasischen, Armenischen und Nordpersischen Gebirge: Prodromus einer Geologie der Kaukasischen Länder: Mémoires de l'Académie impériale des Sciences de Saint-Pétersbourg, 6ème série, Sciences mathémathiques et physiques, v. 7, p. 359–534.

Abrahamyan, M.S., 1957, Brakhiopody verkhnefamenskikh i etrenskikh otlozheniy yugo-zapadnoy Armenii: Yerevan, Izdatelstvo Akademii Nauk Armyanskoy SSR, 142 p. [in Russian]

Arakelyan, R.A., 1964, Devon, *in* Mkrtchian, S.S., Vardaniants, L.A., Gabrielian, A.A., Maghakian, I.G., and Paffenholz, C.N., eds., Geologiya Armyanskoy SSR: Yerevan, Akademiya Nauk Armyanskoy SSR, v. 2, p. 46–96. [in Russian]

Ernst., A., Serobyan, V., Danelian, T., 2024. Biostratigraphic, palaeoenvironmental and palaeobiogeographic implications of bryozoan fauna from the Upper Devonian sequences of Armenia. Geobios 85, 10–18.

Ginter, M., Hairapetian, V., and Grigorian, A, 2011, Chondrichthyan microfossils from the Famennian and Tournaisian of Armenia: Acta Geologica Polonica, v. 61, p.153–173.

Khachatryan S., Cascales-Miñana B., Danelian T., Breuer P., Steemans P., Grigoryan A., Gabrielyan I., Hairapetian V., Regnier S.,

Kroeck D.M., Serobyan V. 2025. First palynological evidence from the Upper Devonian of Armenia (northern Gondwanan margin): biostratigraphic implications. Palaeoworld v. 34, 100879.

Serobyan, V., 2021. Upper Devonian brachiopods and sedimentary sequences from Armenia; biodiversity, stratigraphy and paleobiogeography. Co-tutorial Ph.D. Thesis, University of Lille and Institute fo Geological Sciences of Armenia, Lille/ Yerevan, 280 p.

Serobyan, V., Danelian, T., Crônier, C., Grigoryan, A., Mottequin, B. 2022a. *Aramazdospirifer*, a new cyrtospiriferid genus (Brachiopoda) from the lower Famennian (Upper Devonian) of the Gondwanan South-Armenian Block. Comptes Rendus PalEvol v. 21, 145–156.

Serobyan, V., Danelian, T., Hairapetian, V., Grigoryan, A., Crônier, C., Randon, C., Mottequin, B., 2023. Frasnian (Upper Devonian)
brachiopods from Armenia: Biostratigraphic & Palaeobiogeographic Implications. Rivista Italiana di Paleontologia e Stratigrafia
v. 129, 373-409.

Vinn, O., Hambardzumyan, T., Temereva, E., Grigoryan, A., Tsatryan, M., Harutyunyan, L., Asatryan, K., Serobyan, V., 2025. Fossilized soft tissues in tentaculitids from the Upper Devonian of Armenia: Towards solving the mystery of their phylogenetic affinities. Palaeoworld 34, 100888.

Yeghiazaryan, M., Kroeck D.M., Danelian T., Grigoryan A., Regnier S., Serobyan V. 2025. Acritarchs and prasinophytes from the Upper Devonian of Armenia: biostratigraphical and palaeobiogeographical implications. Palynology, https://doi.org/10 .1080/01916122.2024.2445040

17th INTERNATIONAL CONGRESS of the Geological Society of Greece

BULLETIN OF THE GEOLOGICAL SOCIETY OF GREECE, SP. PUBL.

EXTENDED ABSTRACT 287

Marble as an educational fabric interweaving cultural and geological heritage, the case study of ancient Philippi site rock art, Kavala, Greece

Sideridis A.[1], Koutsoumpis E.[1], Mytakidou K.[2], Boumpouka M.[3], Anevlavi V.[4], Rousopoulos P.[5]
(1) Krinides Gymnasium, Kavala, Greece, alkisside@sch.gr (2) 4th Gymnasium of Kavala, Kavala, Greece (3) 1st elementary school of Nea Peramos, Kavala, Greece (4) Austrian Archaeological Institute, Austrian Academy of Sciences, Vienna, Austria (5) Kupa Ceramics, Kavala, Greece

Introduction

The educational system is dealing with ever-changing classrooms in constant need of contemporary teaching methodologies. Due to technological advancements and changes in the perception of the world, students are not efficiently responding to traditional teaching methods. Most prefectures in Greece combine both interesting Geology and Archaeology and these make up for great educational tools, especially when combined with alternative teaching methods and an interdisciplinary approach. As detailed below, the paradigm of the ancient Philippi site will be presented.

Geology of Ancient Philippi site

The area around the Philippi site belongs to the Rhodope massif and, more specifically, to the lower tectonic unit (Pangaion unit). The latter consists of marbles, gneisses, schists and amphibolites of upper greenschist-lower amphibolite metamorphic facies (Eleftheriadis and Koroneos, 2003; Papanikolaou and Panagopoulos, 1981) and later underwent retrograde greenschist metamorphism (Mposkos and Liati, 1993). NE of the archaeological site (Figure 1A, B, C), small occurrences of the Philippi middle Oligocene granitoid intrude in marbles and gneisses of the Pangeon unit (Tranos et al., 2009), inducing local contact metamorphism. The Philippi Plain comprises quaternary sediments. Local geo-materials such as clay, granite and coarse-grained marble were used in the ancient Philippi site. Marbles from Thasos and ophicalcite from Larissa have also been used.

Historical background

Philippi's inclusion on the UNESCO World Heritage list in 2016 underscores the site's cultural and archaeological significance (Delev, 2018). These monuments, comprising relief images, etchings, inscriptions, and niches, have historically been documented on the acropolis slopes (Figure 1C, D). The predominant depiction among these carvings is a youthful huntress, commonly identified as Artemis/Diana (Figure 1D), which suggests an emphasis on themes of popular religion from the Roman era (Graml et al., 2024). The origins of these carvings, however, extend beyond the Roman period. Some are attributed to the Thracian Hedones tribe, dating from the Late Bronze Age to the Early Iron Age (Dimitriadis, 2008). Despite the rise of Christianity in the region, many of these pagan carvings persisted, reflecting the endurance of earlier religious traditions (Abrahamsen, 1988).

Educational methods and results

Regarding the subject of Geology-Geography in public Greek schools, this is only being taught sparsely in primary schools and for two years in middle school, a time not sufficient to ingrain basic geoscience concepts with the current educational form. Considering the needs of a classroom consisting of Generation Z and Alpha students (born between 2012-2018) the following methods have been adapted: a) Interdisciplinary education (subjects of technology, arts, history), b) Education Through Art and Storytelling, c) Nature-Culture Trails and d) Working groups and reverse classroom (Politis, 2019). This methodology is based on the environmental projects of the Philippi Centre of Environmental and Sustainability Education and was modified to meet the needs of the students. A trail was planned leading to the site. Along the way, students were introduced to the local geology, identifying lithologies and understanding their physical properties and potential uses. Reaching the site and the rock art monuments, students either etched or photographed the carvings and listened to stories related to rock art. Moreover, they tried to identify the lithologies within the Philippi site and discuss rock-provenance and uses. In the classroom, students working in teams tried to interpret the carvings and produce their own rock art on pieces of clay, inspired by their everyday life. The questionnaire results demonstrate that students were able to better grasp the geological and local history and make links between the local geology and other disciplines such as technology, commerce, and architecture. More importantly, they developed their environmental consciousness through the environmental trail and interaction with nature. Art proved to be an effective method for increasing student engagement while nurturing fine motor skills.

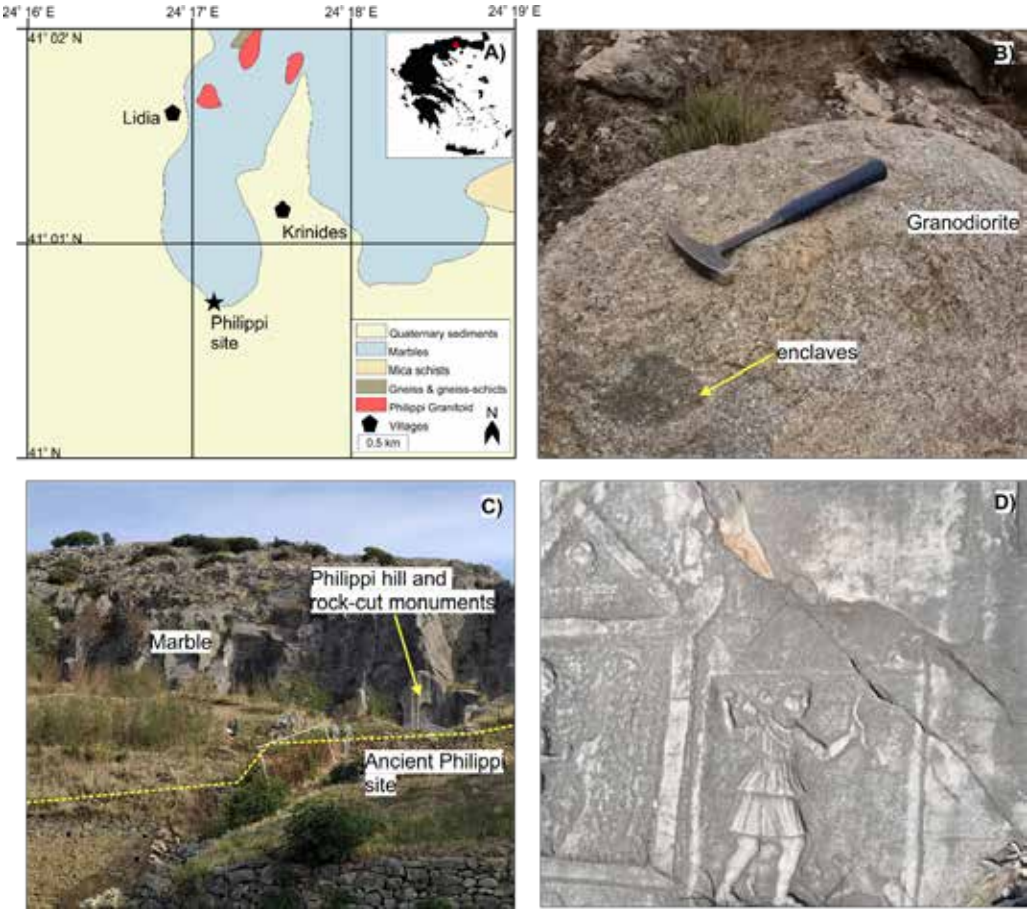

Figure 1 A) Simplified geological map of the studied area; B) Granodiorite occurrence adjacent to the site of Philippi; C) 'Contact' between the natural environment and the ancient Philippi site; D) relief image of hunting Artemis.

Conclusions

To conclude teaching of geosciences can make use of the following methods: a) Interdisciplinary education, b) Education Through Art and Storytelling, c) Nature-Cultural Trails and d) Working groups and reverse classroom. Better engagement, interdisciplinary and syllogistic reasoning, introduction to sustainability and differentiated expression through art are a few of the outcomes. The adapted plan is especially feasible for schools in the Greek countryside that have archaeological sites in their vicinities.

References

Abrahamsen, V., 1988. Christianity and the Rock Reliefs at Philippi. Biblic Archaeol 51, 46–56. https://doi.org/10.2307/3210038

Delev, P., 2018. The History of Philippi. Classical Rev 68, 543–545. https://doi.org/10.1017/S0009840X18001439

Dimitriadis, G., 2008. Hellenic Rock Art-State of Art, Open Questions and New Paradigms. Man India 88, 449–458.

Eleftheriadis, G., Koroneos, A., 2003. Geochemistry and Petrogenesis of Post-Collision Pangeon Granitoids in Central Macedonia, Northern Greece. Geochemistry 63, 364–389. https://doi.org/10.1078/0009-2819-00024

Graml, C., Diosono, F., Hunziker, M., 2024. Rock-Cut Monuments at Macedonian Philippi – Taking Image Analysis to the Religioscape. Open Archaeology 10. https://doi.org/10.1515/opar-2024-0018

Mposkos, E., Liati, A., 1993. Metamorphic evolution of metapelites in the high-pressure terrane of the Rhodope Zone, northern Greece. The Canadian Mineralogist 31, 401–424. https://doi.org/10.3749/1499-1276-31.2.401

Papanikolaou, D., Panagopoulos, A., 1981. Observations on the structural style of the Southern Rhodope. Geologica Balcanica 11, 12–22.

Politis, I., 2019. The Value of the "Environmental Trail" as a Holistic Experiential Approach in Reenforcing the Educational Role for the Environment and Sustainability of Nature Centres Through the Beliefs of their Staff - Problems and Adversities. Hellenic Open University, Athens.

Tranos, M.D., Eleftheriadis, G.E., Kilias, A.A., 2009. Philippi granitoid as a proxy for the Oligocene and Miocene crustal deformation in the Rhodope Massif (Eastern Macedonia, Greece). Geotectonic Research 96, 69–85. https://doi.org/10.1127/1864-5658/09/96-0069

17th INTERNATIONAL CONGRESS of the Geological Society of Greece

BULLETIN OF THE GEOLOGICAL SOCIETY OF GREECE, SP. PUBL.

EXTENDED ABSTRACT 288

First record of pockmarks in the North Aegean Trough

Sklavounaki P.[1], Tzafaridi V.[1], Hasiotis T.[1], Missias S.[2], Paleokrassas A.[2]
(1) Department of Marine Sciences, University of the Aegean, Mytilene, Greece, mar21053@marine.aegean.gr, (2) Akti Engineering, Piraeus, Greece

Research Highlights

Discovery of small depressions in the North Aegean Trough that probably contribute to the Limnos oil seep cluster

Introduction

Pockmarks are crater-like depressions of the seafloor where underlying fluids in the sediment pores escape to the water column. They have been discovered in numerous environments all around the world: in shallow areas, along continental margins, and in deep environments (Judd and Hovland, 2007), even in lakes (i.e., Toker and Tur, 2021). The records of pockmarks in Greece are numerous as well (Papatheodorou *et al.*, 1993), mostly found in shallow areas, like the pockmark fields in Patra and Corinth gulfs (Christodoulou *et al.*, 2003). During a marine survey for the laying of a power cable between Thrace and Limnos Island, numerous small depressions resembling pockmarks were discovered along a narrow corridor in the North Aegean Trough (NAT) (Figure 1a,b). NAT is a main geotectonic and morphological feature in the North Aegean Sea. It has a complex bathymetry containing three main basins (Limnos, Athos and Sporades). The tipping point of the most important fault system that characterizes the region, the dextral strike-slip fault known as the North Anatolian Fault (NAF), is differentiating the SW part of the NAT (Sporades and Athos basins) from the NE part of the NAT (Limnos basin) (Sakellariou *et al.*, 2016). The basins have small dimensions and steep slopes, and they are isolated and separated from each other by bathymetric highs (Roussakis *et al.*, 2004). The bathymetric high between Athos and Limnos Basins is the area under consideration for this study. Recently, Jatiault *et al.* (2024) discovered numerous oil seeps in the wider NAT region probably related to leakage from the broader fault system (Figure 1b). The western part of NAT (to the west of north Limnos), including the survey area, was mapped by Papanikolaou *et al.* (2002), however, pockmarks were not discerned. Thus, the objective of this study is to describe the distribution, morphology, size and density of the observed depressions and examine their potential relation with the oil seeps reported by Jatiault *et al.* (2024).

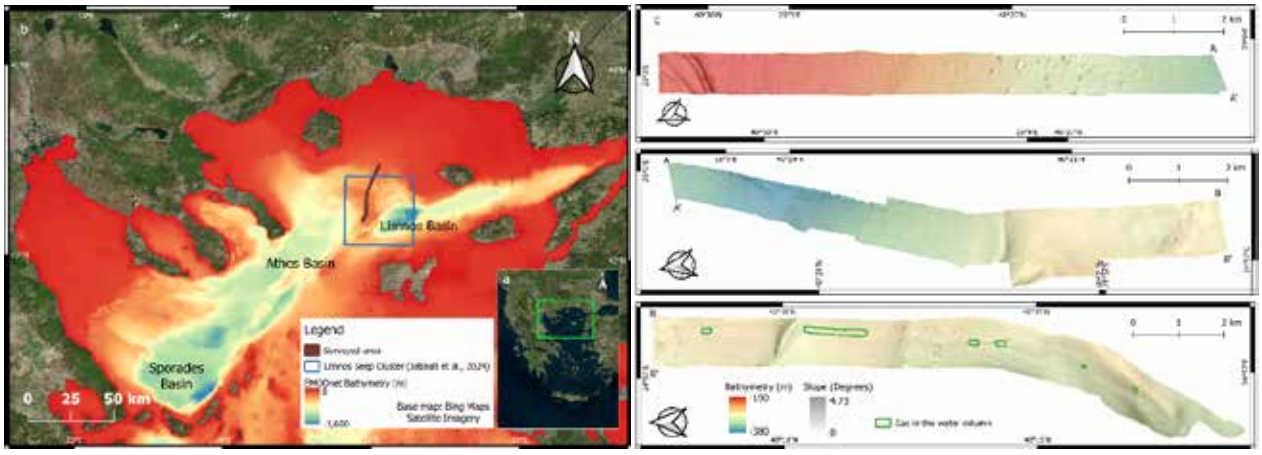

Figure 1. (a) Location of the broader study area (in green), (b) general bathymetric map of the North Aegean and location of the surveyed area (brown line) and of the Limnos seep cluster (blue box) studied by Jatiault *et al.* (2024), (c) bathymetry of the surveyed area overlaid by slope (selected layer transparency: 40%), clipped to 3 subregions for better visualization.

Methods

The survey was conducted during June 2024, along a corridor that was pre-selected by the Independent Power Transmission Operator (IPTO) of Greece, to pass along a bathymetric high in-between Limnos and Athos basins, so as to limit the depth of cable laying and burial. The distance between the survey lines was approximately 250 m. For bathymetry an R2Sonic 2026 (170-450 kHz) multibeam echosounder (MBES) was used. A Valeport Midas profiler was utilized for sound velocity profiles. Data acquisition was performed using the NaviScan and R2Sonic controller software packages. For the morphological survey, an EdgeTech 2050 Side Scan Sonar (SSS) was deployed, able to

scan simultaneously the seafloor with a lower (230 kHz) and a higher frequency (540 kHz). A Sonardyne Ranger-2 USBL system was used for the towfish position. Survey speed was maintained at approximately 3-4 knots. Subbottom profiler records and sediment cores were also collected but are not presented in this study. MBES processing was performed utilizing EIVA, whilst for the SSS data processing and analysis and the production of high-resolution georeferenced sonar mosaics (pixel size of 0.25 m), the Chesapeake Technology SonarWiz software was used. QGIS was used for (i) mapping purposes (bathymetry cell size of 1 m), (ii) the descriptive measurements of the depressions, (iii) slope extraction and (iv) the creation of shaded relief imagery.

Results

Water depths in the study area range between 194 and 373 m. The northernmost part of the surveyed area is relatively shallow but gradually towards the south, the depth increases, reaching its maximum value (Figure 1c) with the deepest region occupying only a small part of the corridor. After this area and towards the southernmost part of the surveyed area, the depth is maintained at approximately 260 m. Slopes gradients are mild, not exceeding ~4.5°.

Throughout the surveyed area, numerous depressions were easily observed. Most of the pockmarks appear in the northern and southern parts of the surveyed zone, whilst along the deepest part depressions rarely occur. A total of 136 depressions were recognized and mapped (Table 1). Although relatively small (average spatial extent of ~1830 m^2) and shallow (1-3 m deep) they appear in a variety of shapes, and they were categorized following the definitions of Judd and Hovland, (2007) for pockmark morphologies. 90 resemble “asymmetrical pockmarks”, lacking a well-defined rim, something that made their recognition difficult in the bathymetric maps. 40 were categorized as “well-defined circular”, and 6 appeared as “composite pockmarks”, implying merging of two or more smaller depressions.

Table 1. Summary of pockmarks’ main characteristics.

	Minimum	Maximum	Average
Occurrence water depth (m)	197	370	282.4
Pockmark depth (m)	1	3	1.3
Perimeter (m)	15.8	675.8	149.9
Area (m^2)	16.6	21414.9	1831.2

The SSS records revealed a uniformly low reflectivity seabed, which indicates the presence of fine-grained sediments. Abundant crossing longitudinal marks suggest intense trawling fishing creating sharp scars on the soft seabed. Upon comparing the pockmarks detected in the bathymetric data with the SSS observations, it was evident that numerous depressions observed in the bathymetrical survey were not observed in the morphological survey, and SSS navigation errors produced discrepancies in the pockmark positions. Thus, unlike the bathymetric data, the SSS images discerned only 104 pockmarks, 28 in both SSS frequencies, 53 only in the low frequency, 11 only in the high frequency, whilst for 12 only low-frequency data were available, thus they could not be compared with the higher frequency information that was missing. Also, along specific areas towards the southern part of the surveyed area, anomalous reflections were recognized in the water column of the SSS records, probably due to fluid seepage (Figure 1c).

Jatiault *et al.*, (2024) studying Sentinel-1 data, reported oil seepage on topographic highs located west of Limnos trough and close to the NAF that coincides with the area under consideration. Fluid leakage was attributed to upward fluid migration through the local fault zone that displaces the shallow sedimentary structure.

Discussion and Conclusions

The study area is located within a topographic high of NAT, separating Limnos and Athos basins and has depths that do not exceed 370 m. The observed pockmarks are so far the deepest observed in the Greek maritime region, even if they have small dimensions. It must be mentioned that since the surveyed corridor spreads only for 1.1-1.2 km, pockmarks are obviously expected to occur in the wider area. This is also supported by the fact that the Limnos oil seep cluster (Jatiault *et al.*, 2024) extends over ~40 km, in water depths ranging from 140 to 1200 m. Leakage in the water column is fueled through faults from deeper sedimentary strata, however, fluid seepage may also take place through pockmarks, and this process might have likewise contributed to their formation. Yet, the fact that leaking fluids in the water column, as observed in the SSS images, were not detected over the entirety of the pockmark field, possibly indicates that seeping activity through pockmarks is sporadic, and that probably only some of the observed pockmarks contribute to the fluid leakage in lower concentrations. Although the wider area is characterized by relatively high sedimentation rates (Roussakis *et al.*, 2004) the topographic high where pockmarks occur probably corresponds to an area of lower sediment accumulation rates, thus ensuring the more stable conditions also needed for pockmark formation (Judd and Hovland, 2007). Finally, at least the surficial sediments are fine-grained, as observed in SSS images, a fact that contributes to the variety of pockmark morphologies that can be found in certain fields (Judd and Hovland, 2007).

References

Christodoulou, D., Papatheodorou, G., Ferentinos, G., Masson, M., 2003. Active seepage in two contrasting pockmark fields in the Patras and Corinth gulfs, Greece. Geo-Mar Letters 23, 194-199.

Jatiault, R., Henry, P., Loncke, L., Sadaoui, M., Sakellariou, D., 2024. Natural oil seep systems in the Aegean Sea. Marine and Petroleum Geology 163, 106754.

Judd, A., Hovland, M., 2007. Seabed Fluid Flow: The Impact on Geology, Biology, and the Marine Environment, 1st ed. Cambridge University Press.

Papanikolaou, D., Alexandri, M., Nomikou, P., Ballas, D., 2002. Morphotectonic structure of the western part of the North Aegean Basin based on swath bathymetry. Marine Geology 190, 465-492.

Papatheodorou, G., Hasiotis, T., Ferentinos, G., 1993. Gas charged sediments in the Aegean and Ionian Seas, Greece. Marine Geology 112, 171-184.

Roussakis, G., Karageorgis, A.P., Conispoliatis, N., Lykousis, V., 2004. Last glacial–Holocene sediment sequences in N. Aegean basins: structure, accumulation rates and clay mineral distribution. Geo-Mar Letters 24, 97-111.

Sakellariou, D., Rousakis, G., Vougioukalakis, G., Ioakim, C., Panagiotopoulos, I., Morfis, I., Zimianitis, E., Athanasoulis, K., Tsampouraki-Kraounaki, K., Mpardis, D., Karageorgis, A.P., 2016. Deformation pattern in the western North Aegean trough: preliminary results. Bulletin of the Geological Society of Greece 50 (1), 124-133.

Toker, M., Tur, H., 2021. Shallow seismic characteristics and distribution of gas in lacustrine sediments at Lake Erçek, Eastern Anatolia, Turkey, from high-resolution seismic data. Environmental Earth Sciences 80, 727.

17th INTERNATIONAL CONGRESS of the Geological Society of Greece

BULLETIN OF THE GEOLOGICAL SOCIETY OF GREECE, SP. PUBL.

EXTENDED ABSTRACT 289

Mineralogical and petrographic characterization of different limestones used as raw materials in cement production

Skontovolou L.[1], Lampropoulou P.[1], Baskoutas I.[2], Raptopoulou C.[2], Giannakopoulou P.P.[1], Rogkala A.[1], Kareli A.[1], Savvatis P.[1], Petrounias P.[1]

(1) Department of Geology, University of Patras, 265 04 Patras, Greece, loukiaskontovolou@gmail.com (2) Titan Cement Company S.A., Drepano Plant, Patras, Greece

Introduction

Nowadays, global environmental regulations require industrial production to align according to principles of sustainable development. In cement industry it consists of priority, since optimizing raw material use and energy efficiency are crucial for reducing environmental impact. Limestone is a key raw material in cement production, primarily serving as a source of calcium carbonate (CaCO□) for clinker formation. Its mineralogical composition and structural characteristics significantly influence both grinding efficiency and thermal behavior during calcination (Nuhu et al., 2020).

This preliminary study focuses on the petrographic characteristics of different limestone types and their effects on the critical stages of grinding, calcination and clinker formation. A deeper understanding of these variations enables a more targeted selection and design of the initial raw material mixture, improving grinding and calcination efficiency as well as ensuring a stable, high-quality clinker product. Such improvements can lead to reduced production costs, lower energy consumption, and enhanced process control, all contributing to a more sustainable cement manufacturing process.

Materials and methods

This study consists of part of a project in progress in cooperation with TITAN Cement Company S.A. (Drepano plant, Patras, Greece). Under this project rrepresentative limestone samples were collected from the quarries of the company in Drepano, Achaia. These samples, were delivered from TITAN to the Department of Geology, University of Patras, in order to be studied regarding their mineralogical and petrographic characteristics.

The characterization of the samples was conducted by the following techniques and methodology:

- XRD (X-ray diffraction)

The mineralogical analyses of the studied samples were carried out by an X-ray diffractometer, Bruker D8 Advance type, equipped with a copper cathode with nickel filter and fast, high-resolution detector (Lynxye). The scan area was in the range of 2–70o 2θ, with a resolution step of 0.3 s / 0.015o. Before the analyses, the powdered samples placed in the special container and flattened by a glass in order to ensure uniform surface. Identification of these phases was done using DIFFRACplus EVA12® software (Bruker-AXS) and the accompany ICDD Powder Diffraction, PDF- 2 2006, EVA database, which compares the data to a database of known crystal phases. The semi-quantitative analysis was performed using the TOPAS 4.0® software (TOPAS MC Inc., Oakland, CA, USA), based on the Rietveld method. Finally, ccorrections of the semi-quantitative results were performed by chemical analyses.

- Petrographic microscope

A Leitz Ortholux polarized light petrographic microscope was used for the petrographic study of the samples, while thin sections of representative samples were prepared for observation.

- SEM (Scanning electron microscope)

A JEOL 6300 SEM was used to observe the microstructure and perform microanalyses. The microscope is equipped with an X-ray Energy Dispersive Spectrometer (EDS), which was utilized for elemental analysis. The analyses were performed on carbon-coated thin sections.

Results and discussion

Mineralogical study

During the analyses of limestone samples using XRD, the amount of calcite ranges from 88% (sample 3) to 97% (sample 4), (Figure 1, Table 1). Additionally, small amounts of quartz (max of 8% in sample 3) were detected, along with low amounts of clay minerals and opaque in the detection limit of technique (max 4% in sample 3), (Figure 1, Table 1)

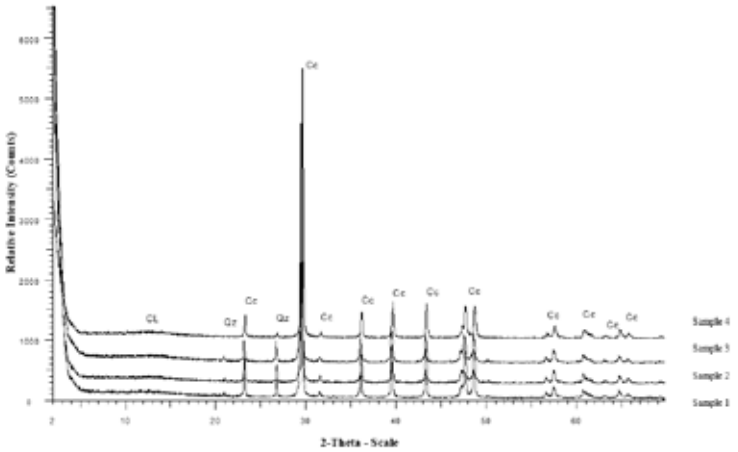

Figure 1. X-ray diffractogram of limestone samples.
Abbreviations: Cc: Calcite, CL: Clay, Qz: Quartz.

Table 1. Qualitative and semi-quantitative phase analysis results obtained through Rietveld refinement, with corrections based on chemical analyses, for the analyzed limestone samples. GOF Good of Fitness (GOF) is 1.25 and error is below 1%.

Mineral phases / Samples		Sample 1	Sample 2	Sample 3	Sample 4
Calcite	**$CaCO_3$**	91%	93%	88%	97%
Quartz	**SiO_2**	6%	4%	8%	2%
Clay/Opaque	**Al-Si minerals/ Fe oxides or hydroxides**	3%	3%	4%	tr*

Abbreviation: tr: traces

Overall, considering the results and the potential impact of impurities in the primary limestone material, such as silicate, clay minerals and opaque, sample 4 exhibits the purest calcite composition in contrasts to sample 3, which contains the highest percentage of quartz and opaque minerals (such as oxides and hydroxides, see Table 1), is the least favorable raw material for cement.

Petrographic study

Examination of the samples under a petrographic microscope proves that these are sedimentary rocks classified as biochemical limestones.

Figure 2. The analyzed limestone samples (Sample 1, Sample 2, Sample 3, Sample 4).

Sample 1 shows micritic to microsparitic and locally oolitic texture (Figure 3). Carbonate veins with sparitic material

are sometimes partially oriented. Also, porosity is low in the form of mostly individual pores. The shape of the crystals is hypidiomorphic to anhedral. Minerals that prevail in this sample are calcite with accompanying minerals of quartz, muscovite or other clay minerals and opaque (as iron oxides/hydroxides) in low percentages.

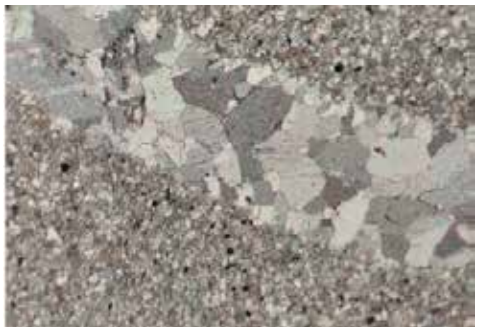

Figure 3. Microstructure in the polarizing microscope of sample 1 (Nicols vertical with magnificence 100x). Sparitic vein with isometrical calcite crystals developed in a mainly micritic microstructure.

Sample 2 exhibits micritic to locally oolitic texture. Moreover, sparitic veins and microveinlets filled with hypidiomorphic to adhedral grains occur (Figure 4). Porosity is low and sometimes capillary channels (i.e. microcracks) appear. The primary mineral in this sample is calcite, and it coexists with minor amounts of quartz, muscovite and plagioclase.

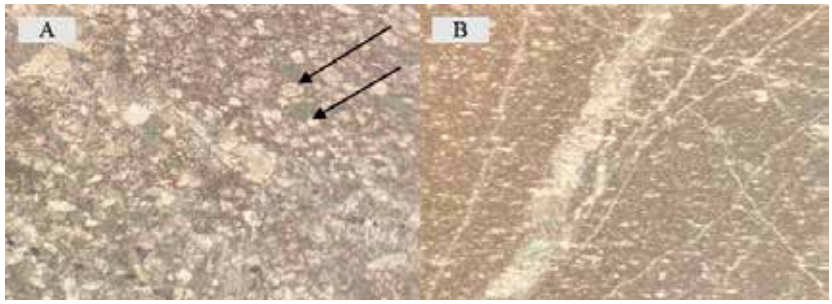

Figure 4. Microstructure in the polarizing microscope of sample 2 (Nicols vertical with magnificence 100x). A. Locally oolitic texture (spheroidal shaped grains). B. Micro veinlets filled with carbonate material of sparitic texture within a micritic main mass.

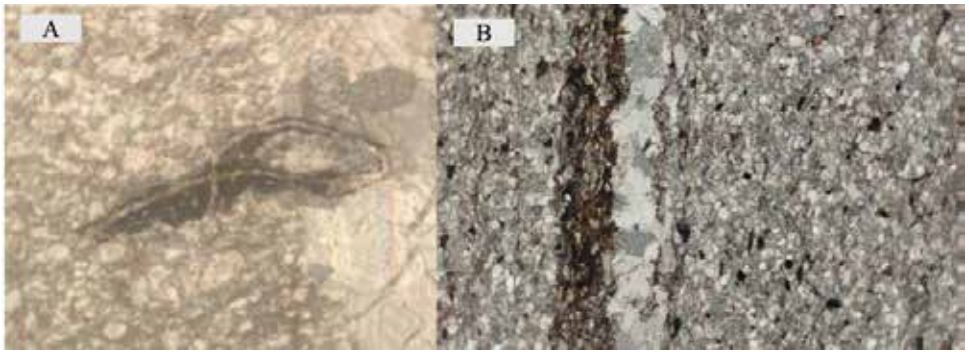

Figure 6. Microstructure in the polarizing microscope of sample 3 (Nicols vertical with magnificence 100x). A. Presence of fossil material. B. Sparite vein composed of calcite and opaque minerals. Polarization colors range from brown and red-brown to black, corresponding to calcite, clay minerals, and opaque phases. Gray coloration is associated with silicate minerals, including quartz and feldspars.

Sample 3 is characterized by micritic texture, locally oolitic, with the presence of scattered veins (Figure 5). The

porosity forms capillary-shaped or even larger channels. The presence of opaque minerals, partially in an oriented distribution, is common. The primary minerals of this sample are calcite, while feldspars, microcrystalline quartz and muscovite appear more often than in the other samples. Opaque, most iron oxides and some fossils are observed too (Fiure 6).

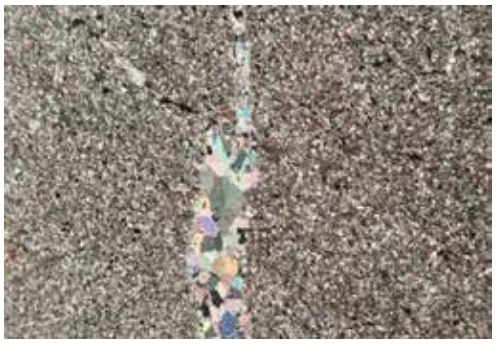

Figure 5. Microstructure in the polarizing microscope of sample 3 (Nicols vertical with magnificence 100x). Presence of sparitic vein in a micritic mass with calcite.

Sample 4 appears a more homogeneous mineral composition and microstructure compared to the others. Specifically, it is appeared fine-grained with a micritic to locally oolitic texture and low porosity. The mineralogical composition consists of calcite and low amounts of quartz. However, micro-areas filled with carbonate material and veins of various sizes and orientations were identified.

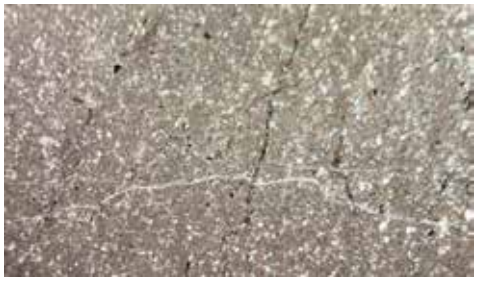

Figure 7. Microstructure in the polarizing microscope of sample 4 (Nicols vertical with magnificence 100x). Homogeneous microstructure with micritic texture.

Influence of petrographic characteristics of limestone to the grinding and calcination processes

Grinding and calcination are critical processes in cement production and are significantly influenced by the physical and mineralogical characteristics of raw materials (Soltan & Serry, 2011). Understanding these characteristics is essential for the optimizing processes in cement production regarding the energy cost, environmental impact in accompany with the quality of final product. The main mineralogical and petrographic features of the limestones, along with their potential effects on the two crucial parameters mentioned above, are summarized in the table below (Sousa, 2021).

The desired characteristics for grinding are:

- **Micritic texture**: It is the fine-grained texture of the calcite material, which facilitates the milling process, as the smaller and uniform crystal sizes require less milling time.
- **Reduced number of veins:** Micro micritic veins contribute less to the inhomogeneity of the structure than the larger ones or/ with the occurrence of veins filled with sparite (He et al., 2022).
- **Homogeneous structure and mineralogical composition:** A uniform distribution of fine-grained structure and minerals are expected to promote the efficient of grinding. Moreover, homogeneity would positively influence some crucial parameters such as hardness and plasticity. Minor amounts of quartz, opaque minerals, feldspars, and soft phyllosilicates are not expected to affect significantly the process.

Likewise, for calcination:

- **Micritic texture – microcrystalline:** Having a fine-grained and microcrystalline texture facilitates uniform heating and consistent sintering performance.
- **Reduced number of veins:** The reduced presence of veins limits the possibility of uneven heating and the occurrence of failures in the material during the firing process (He et al., 2022).
- **Homogeneous structure and mineralogical composition:** The stable structure and uniformity in mineral composition ensure isomeric heating and predictable reactions, which is critical to creating high-quality end products.
- **Fossils:** The presence of fossils of a non-calcic composition is not desirable because it can affect the thermal behavior of the material and lead to inhomogeneities or to the formation of undesirable by-products during firing.
- **Porous in the form of channels:** Having pores in the form of channels can favor heating as it facilitates air circulation, improving calcination efficiency (Freire-Gormaly et al., 2015).
- **Impurities of other minerals:** Low percentages of quartz and opaque minerals could have a positive or neutral effect during

the firing process (Sandström et al., 2024).

Based on the above characteristics, the analyzed samples are categorized and presented in Table 2. In particular, the sample 4 presents the smallest grain size, the most suitable mineralogical composition and high homogeneity of microstructure. Micro veinlets, porosity or even fossils are sometimes present in the microstructure but they do not alter significantly the prevalence of the micritic texture.

Sample 1 exhibits the desired characteristics in terms of grain size, mineralogical composition and homogeneity, although it falls slightly short compared to sample 4. The micritic texture is satisfactorily developed. It has high porosity and a small percentage of veins, but the presence of fossils is more rare compared to that in sample 4.

Sample 2 has a relatively fine grain size but exhibits significant heterogeneity, which may cause issues during processing. The predominance of sparitic texture makes it less desirable, as its involvement in the formation of new phases is expected to be delayed. Its relatively high porosity may contribute to improved combustion efficiency.

Sample 3 has characteristics that place it lower in the overall evaluation. Even it exhibits the lowest porosity and contains few fossils, it is the most heterogeneous in terms of grain size and mineralogical composition. Although it displays veins less frequently than the other samples, the larger grain size of its mass may prolong the heating time or potentially cause inhomogeneity during calcination.

Table 2. Summary table including the most favorable characteristics for cement production observed for each limestone sample.

Grain Size	Mineralogical Composition	Homogeneity	Micrite-Sparite	Veins	Porosity	Fossils
Samples	4, 1, 2, 3	4, 1, 2, 3	4, 1, 3, 2	4, 1, 3, 2	3, 1, 4, 2	3, 4, 2, 1

Conclusions

- Sample 4 is the purest compositionally with the most homogenous structure of predominantly micritic character, while porosity channels and veins of carbonate material are present in its structure.
- Sample 3 is the most mineralogically inhomogeneous with microsparitic main texture. In addition, it presents the highest percentage of quartz, opaque minerals and porosity in the form of channels.
- Samples 1 and 2 appear an intermediate mineralogical composition compared to the above, low porosity in the form of isolated pores and microsparitic-micritic oolitic texture.
- Sample 4 is considered as the most favorable material, as it gathers the most desirable characteristics. It is followed by samples 1, 2 and 3 in terms of suitability.

Although no significant differences were observed in the suitability of the different limestone types for cement production, variations in their grinding and calcination behavior could impact energy consumption, cost, and time during production, as well as clinker phase formation. More homogeneous raw materials, in terms of texture and mineral composition, are expected to facilitate grinding and reduce energy and time consumption. These characteristics also promote sintering, enabling more efficient phase formation.

Despite their general suitability, micro-scale differences in the limestones may influence the final material properties and should be considered. Ongoing experiments on clinker production from different raw materials and grinding processes will further optimize raw material mixtures and process parameters, with results to be presented in a future work.

Acknowledgements

Special thanks to TITAN Cement Company S.A., Drepano plant, Patras, Greece for our collaboration, support and funding of this project.

References

Freire-Gormaly et al., 2015. Pore Structure Characterization of Limestones.

He, J., Li, T., Zheng, B., Mao, T., Wu, Y., Li, S., & Li, X. 2022. Effect of calcite veins on the mechanical behavior and fracture propagation of carboniferous limestone. Engineering Geology, 300, 106592.

Nuhu, S., Ladan, S., Muhammad, A. U., Cao, A. F., 2020. Effects and control of chemical composition of clinker for cement production. International Journal of Control Science and Engineering, 10(1), 16-21.

Sandström, K., Carlborg, M., Eriksson, M., Broström, M., 2024. Characterization of Limestone Surface Impurities and Resulting Quicklime Quality. Minerals 14(6), 608.

Soltan, A. M. M., & Serry, M. A., 2011. Impact of limestone microstructure on calcination activation energy. Advances in Applied Ceramics 110(7), 409-416.

Sousa, L., Menningen, J., López-Doncel, R., Siegesmund, S., 2021. Petrophysical properties of limestones: influence on behaviour under different environmental conditions and applications. Environmental Earth Sciences 80(24), 814.

17th INTERNATIONAL CONGRESS of the Geological Society of Greece

BULLETIN OF THE GEOLOGICAL SOCIETY OF GREECE, SP. PUBL.

EXTENDED ABSTRACT 290

The role of the epikarst zone in the influx of water and the manifestation of humidity at the Holy Monastery of Kleiston, Mount Parnitha, Attica, Greece

Skourtsos E[1], Filis, C.[1], Vassilakis, E.[1], Konsolaki, A.[1], Kotsi E.[1], Lekkas, E.[1]
(1) National and Kapodistrian University of Athens, Department of Geology and Geoenvironment, Athens, Greece
eskourt@geol.uoa.gr

Introduction

The epikarst zone represents an essential facet of karst landscapes, positioned at the boundary between the soil and the underlying bedrock. This area, distinguished by its high porosity, plays a significant role in the hydrology and ecology of karst systems.

Originally defined by Mangin (1974), the term “epikarst” has undergone a nuanced evolution in its interpretation. Williams (1983) characterized it as “subcutaneous”, highlighting its importance as the karst morphology of the rock layer directly beneath the soil. As noted by Bakalowicz (2004), the epikarst can be envisioned as the “skin” of the karst system, implying its function as a protective and interactive layer that governs water infiltration, drainage, and the overarching dynamics of the karst environment.

At the Holy Monastery of Kleiston which is situated on Mount Parnitha in Attica, localized points of water and humidity intrusion manifest in several buildings and functional spaces, particularly during the winter months and following rainfall of considerable intensity and/or prolonged duration, as well as snowfalls. The issues of humidity display greater persistence, even becoming evident in the summer months. The localized sites of water and humidity intrusion include the following:

- The Catholicon of the Holy Monastery of Kleiston (Holy Monastery of the Dormition of the Theotokos).
- The storage facility of the Holy Monastery of Kleiston, located within a cavern (to the north of the Catholicon).
- The building of the cells situated immediately before the entrance to the Catholicon (to the south of the Catholicon).
- The edifice housing the old cells of the Fathers, in addition to various common areas (the reception hall, the dining room, the kitchens, etc.) (to the east of the Catholicon).
- The Church of the Holy Cross.

This work outlines the epikarst in the region of the Holy Monastery of Kleiston, and analyzes its role in the aforementioned phenomena of water and humidity intrusion.

Morphology and Geological Setting

The Holy Monastery of Kleiston is situated within the gorge of the Giannoulas stream, which divides the mountainous mass of Strati to the west from the peaks of Korifoula, Koromilia, and Alogorachi to the east. The gorge has an average orientation from north to south and features steep slopes primarily composed of carbonate rocks. These steep to nearly vertical slopes attain heights of up to 400 m. The Monastery is founded on the edge of a narrow “terrace” on the western slope of the valley, at an elevation of 450 m, rising approximately 80 m above the valley floor.

The region of Monastery is composed of geological formations belonging to the Sub-Pelagonian or unmetamorphosed Pelagonian Unit (Dounas, 1971; Katsikatsos et al., 1986). Specifically, it comprises clastic and volcanic rocks from the Upper Paleozoic to the Lower Triassic (P-Ti.tf), as well as limestones and dolomites dated Lower Triassic to Lower Jurassic (Ti-Ji.k,d).

The lower stratigraphically volcanosedimentary formation exhibits an elongated outcrop that originates to the north of the Monastery, passes west of it, and is observable along the road leading to it. This consists of keratophyres and keratophyric tuffs, sandstones, and argillaceous schists. The thickness of the formation varies from 10 m near the Church of the Holy Cross and reaches 50 to 60 m to the north and south of the Monastery.

The carbonate rocks consist of platy to thick-bedded, locally massive limestones dolomitic limestones and dolomites. The upper strata are mainly thin-bedded to platy carbonates with intercalations and nodules of chert.

To the north-northwest of the Monastery, the appearance of the volcanosedimentary formation is obscured by debris and scree (H.cs,sc) composed of breccias and carbonate blocks of various sizes. This formation originates from the overlying limestones, where carbonate fragments were dislodged from their original positions-potentially due to erosion-and subsequently rolled downstream.

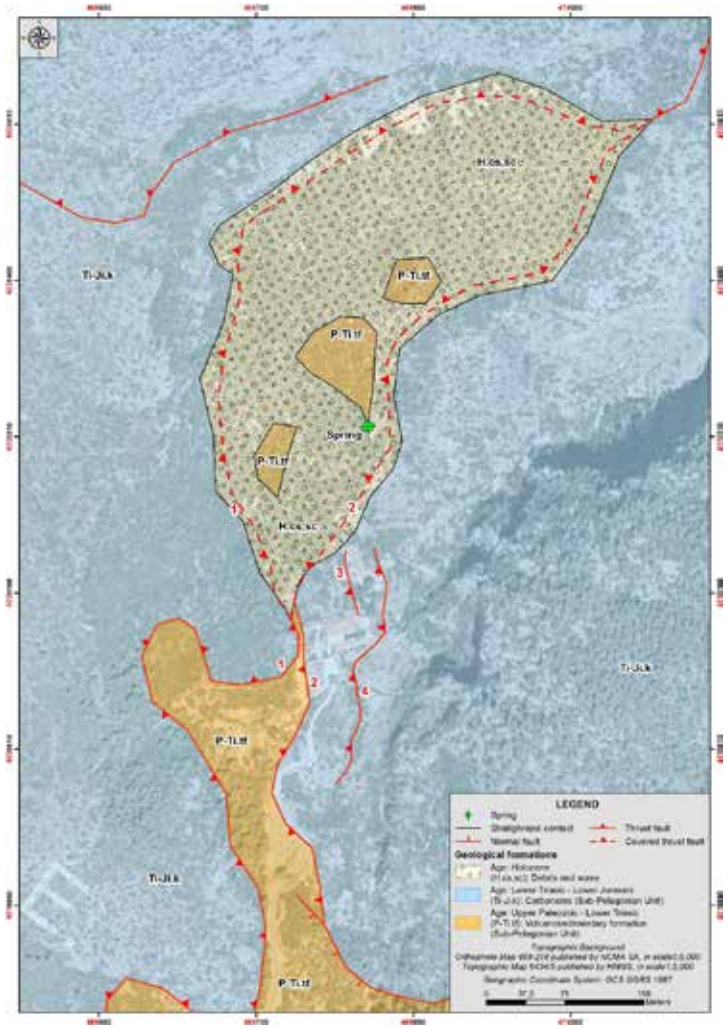

Figure 1. Geological map of the area of the Holy Monastery of Kleiston.

The formations of the Sub-Pelagonian Unit are in contact with one another via reverse faulting (thrusts) and steep normal faults, resulting in the lower clastic formations being thrust upon and overlain by the carbonate rocks. This deformation can be attributed to at least two tectonic episodes, one during the Middle Jurassic to Lower Cretaceous and another during the Middle Eocene to Lower Miocene. Subsequently, steeply dipping normal to oblique-normal faults led to the fragmentation of the earlier structures, constituting a third tectonic episode, which remains active in the broader region to this day (e.g., the Fili earthquake).

Through detailed mapping in the vicinity of the Holy Monastery of Kleiston, the following tectonic contacts were identified:

- Upper thrust (No 1, Figure 1 & Figure 2), which places the carbonate rocks above the volcanosedimentary rocks. This tectonic contact is characterized by a gentle slope, generally dipping towards the south-southwest, as the elevation of the contact gradually decreases in that direction.
- Lower thrust (No 2, Figure 1 & Figure 2), which positions the volcanosedimentary formation upon the carbonate rocks. The trace of this fault is sub-parallel to the upper thrust. The lithologies of the overlying volcanosedimentary formation along the tectonic contact are markedly faulted, brecciated and schistose.

Within the footwall of the lower thrust and within the carbonate rocks, successive tectonic surfaces can be observed, many of which have developed along or sub-parallel to the bedding of the carbonates. These are sub-horizontal to gently and moderately dipping surfaces, occasionally flat but also slightly undulating, anastomosed surfaces that primarily incline towards the north-northwest and southwest, though locally they may trend in other directions.

In the vicinity of the Monastery, two primary low-angle fault surfaces can be observed:

- An upper low-angle fault surface (No 3, Figure 1, Figure 2 & Figure 3, left), located at the main foundation level of the Monastery, which is the minor of the two.

- A lower and larger low-angle fault surface (No 4, Figure 1, Figure 2 & Figure 3, right), situated at lower elevation than the main foundation level of the Monastery.
-

Figure 2. UAV image showing the synthetic depiction of the tectonic contacts at the Holy Monastery of Kleiston. 1: Upper thrust which places the carbonate rocks above the volcanosedimentary rocks. 2: Lower thrust which positions the volcanosedimentary formation upon the carbonate rocks. 3: Upper low-angle fault surface located at the main foundation level of the Monastery. 4: Lower low-angle fault surface situated at lower elevation than the main foundation level of the Monastery. 5: Carbonate fragment.

Figure 3. View of the upper low-angle fault surface (No 3, Figure 1 & Figure 2) which forms the roof of the Catholicon (left). View of the lower low-angle fault surface (No 4, Figure 1 & Figure 2), situated at lower elevation than the main foundation level of the Monastery, where minor caves and undermining have formed (right).

The measurements conducted on the discontinuities at the Holy Monastery of Kleiston revealed two principal systems, with average strike of north-northwest to south-southeast and northeast to southwest, inclined primarily towards the northeast and southeast, respectively. Other secondary systems of discontinuities include northeast-southwest and northwest-southeast, which dip towards the north to north-northwest and southwest, respectively.
Overall, the discontinuities are represented by planar, curved, and open joints, as well as fractures or faults. When classified as open, the gaps range from 1 to 2 centimeters up to 0.30 m. They are frequently infilled with reddish soil and carbonate breccias. Along the open joints, root systems from trees and shrubs that have flourished in the area have penetrated. The depth of this penetration is not easily discoverable but exceeds 2 to 3 m, and in certain instances, it has been found to surpass 5 to 7 m. This phenomenon is evidenced by the presence of roots extending all the way to the Catholicon and the storage rooms.

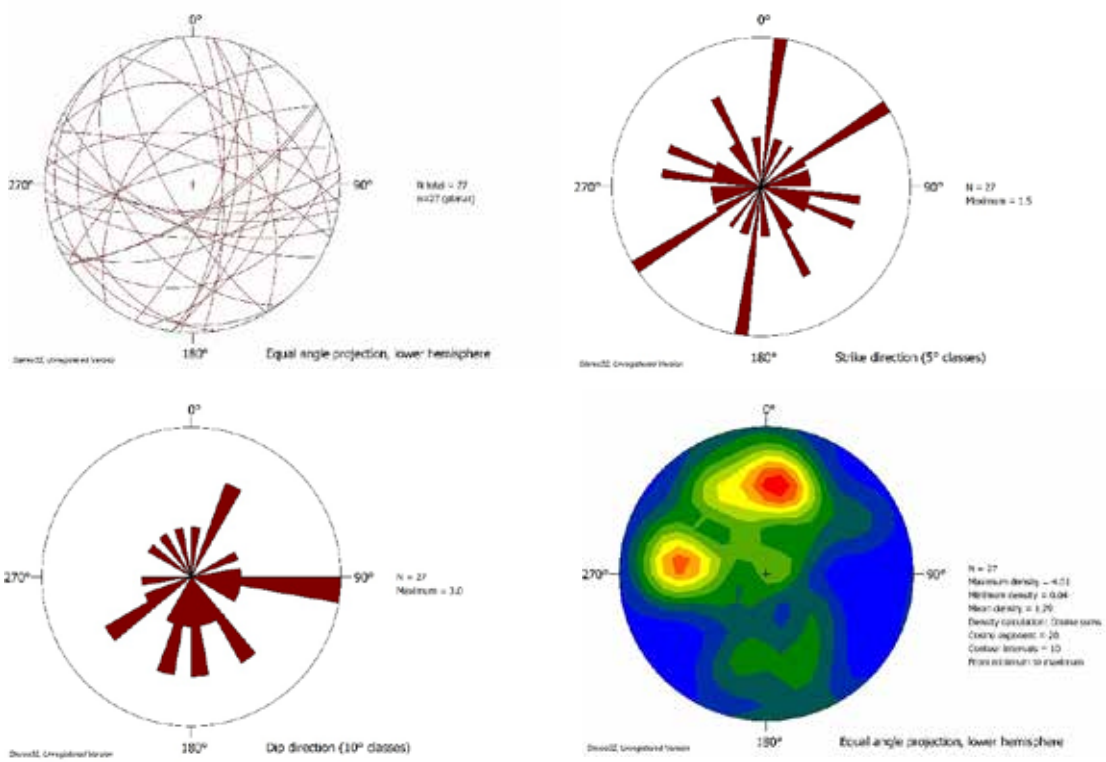

Figure 4. Stereographic projection (up, left), rose diagrams of direction (up, right) and dip direction (down, left) of maximum inclination, and pole density chart (down, right) for all measured discontinuities in the vicinity of the Holy Monastery of Kleiston.

Hydrogeological Conditions

The geological formations within the Holy Monastery of Kleiston fall into the following categories, according to the standards of the International Association of Hydrogeologists (Struckmeier & Margat, 1995; Nikas et al., 2010):

- Debris and scree (H.cs,sc): They develop local and thin aquifers with high yield or extensive aquifers with moderate yield (Subclass 1b).
- Carbonate formation of the Lower Triassic to Lower Jurassic (Ti-Ji.k,d): This formation generates extensive aquifers with high yield (Subclass 2a).
- Volcanosedimentary formation of the Upper Paleozoic to Lower Triassic (P-Ti.tf): This formation develops aquifers of little practical significance or non-aquifer formations (Subclass 3b).

The Holy Monastery of Kleiston is supplied by a spring located 150 m to its north. Improvement work has been performed in the spring, which operates year-round. This spring discharges from the weathered mantle of the volcanosedimentary formation, which is likely fed upstream by the overlying carbonate formations.

In the underlying carbonate formation, a deep karst aquifer of significant capacity has developed. This carbonate formation appears to be highly fragmented and fissured, displaying two primary systems of joints, alongside additional secondary systems that exhibit pronounced karstification.

Epikarst zone

The surface layer of the lower carbonates is characterized by the development of an extensive epikarst zone of high permeability, resulting from significant secondary porosity, with thickness exceeding 10 m in certain locations. The epikarst zone forms a locally saturated zone or an aquifer near the surface, occurring almost exclusively during the winter months when precipitation levels are elevated.

The recharge of the epikarst zone, upstream from the Holy Monastery of Kleiston, occurs through:

- Direct inputs from precipitation.
- Contribution from the overlying granular aquifer developed in the debris and scree, due to hydraulic communication. Notably, upstream there is localized lateral recharge to the granular aquifer from the upper karst aquifer, facilitated by the fractured volcanosedimentary formation at the base of the upper nappe.

The groundwater of the epikarst zone partially infiltrates the underlying rapid flow karst system developed within the

lower carbonates and partially discharges into fronts of epikarst springs that manifest at both the upper and lower fault surfaces of the lower carbonate rocks.
The front of the epikarst springs that emerges at the upper low-angle fault surface discharges in the area encompassing the Catholicon of the Holy Monastery as well as the adjacent buildings and functional spaces, including:

- The cell building located immediately prior to the entrance of the Catholicon (south of the Catholicon).
- The storage facility situated within a cave (north of the Catholicon).
- The small cave (north of the Catholicon).
- The building of the old cells of the Fathers and other common areas (east of the Catholicon).

1.

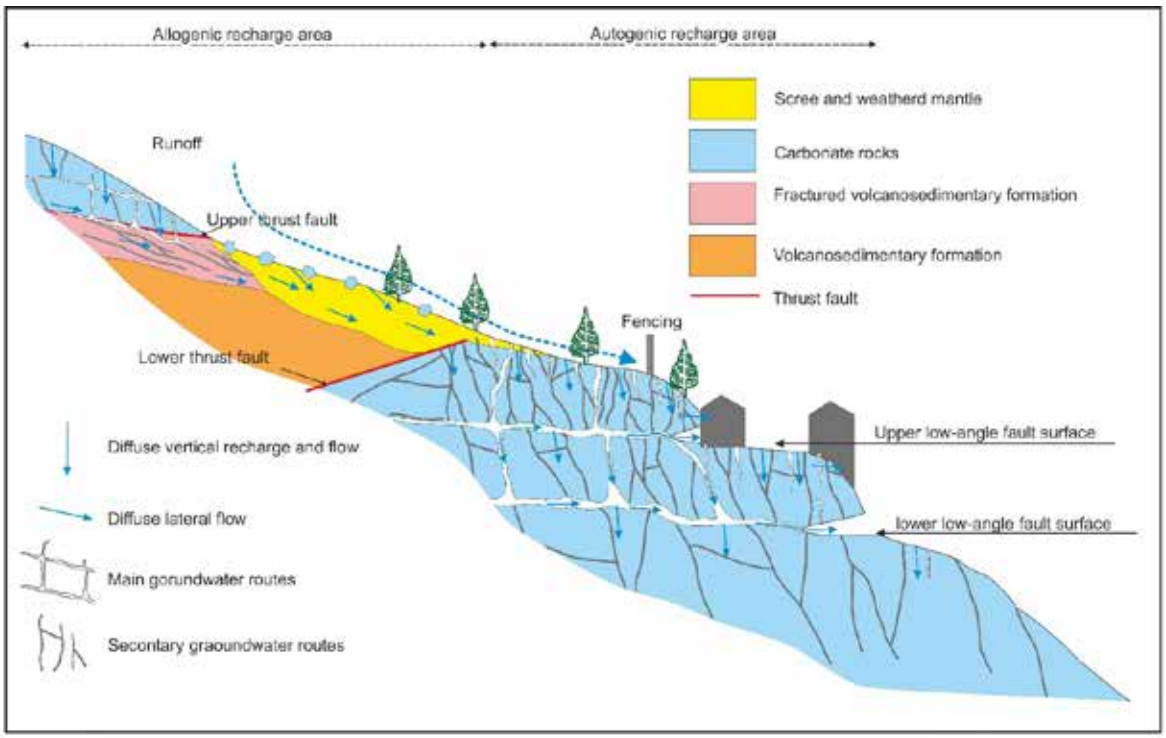

Figure 5. Sketch of the geological and hydrogeological conditions in the vicinity of the Holy Monastery of Kleiston. The various hydrogeological units and the main tectonic elements of the area, the main and secondary routes of the groundwater and the location of the main building infrastructure of the monastery are distinguished.

The front of the epikarst springs that appear at the lower low-angle fault surface discharges into minor caves beneath the foundation of several retaining walls along the northeastern and southeastern perimeter of the Monastery as well as the building containing the old cells of the Fathers and other communal spaces.
The building housing the old cells of the Fathers and other communal spaces is situated between the two discharge fronts of the epikarst springs, yet it is primarily influenced by the upper front and secondarily by the lower front, particularly following prolonged and continuous periods of intense rainfall and snowfall.
Given that the thickness of the overlying carbonate formation upstream of the Catholicon of the Monastery does not exceed 5-6 meters, this facilitates the direct infiltration of rainwater. This is further exacerbated by the significantly fractured and fissured nature of the rock mass, which is compounded by the presence of trees whose root systems have penetrated the rock's discontinuities, leading to further enlargement of these openings. Water intrusion thus extends into the interior of the Catholicon and the adjacent buildings and functional spaces.
In the vicinity of the Church of the Holy Cross, both the upper and lower carbonate series are observed in very close proximity, in places not exceeding 5 meters apart, resulting in highly deformed of the volcanosedimentary formation, which is entirely fissured.
The upper nappe of the carbonates upon the practically impermeable volcanosedimentary formation dips southeast, resulting in this carbonate formation discharging at a front of springs on the artificially constructed slope west of the Sanctuary of the Church. As water flows downstream, the path leading to Gkoura, which runs behind the Sanctuary, transforms into a small and ephemeral stream, with quantities of water infiltrating the interior of the Church through the foundation base (floor).

Discussion - Conclusions

The epikarst zone in the vicinity of the Holy Monastery of Kleiston constitutes a surface horizon of the lower carbonate formations, approximately 10 meters in thickness, characterized by high porosity and permeability. This significant porosity arises not only from the dissolution of carbonate rocks by CO_2-rich water but also from the presence of two main systems and at least two smaller groups of fractures and joints, as well as the existence of two low-angle fault surfaces. The lower of the two fault surfaces governs the base of the epikarst zone.

The epikarst is recharged by precipitation and laterally through the scree and the weathered mantle of the volcanosedimentary formation. These two formations, in turn, are fed by the upper carbonates. These conditions indicate that the recharge of the epikarst is dual in nature, both allogenic and autogenic.

During the wet season, rainwater and meltwater infiltrate the epikarst zone through discontinuities and percolate deeper into the horizons of the carbonate rocks. However, a portion of the infiltrating water remains within the voids and fractures of the epikarst zone, forming an epikarst aquifer where the presence of two low-angle fault surfaces enables the lateral flow of groundwater and the discharge of the epikarst aquifer into springs within caves observed along those two fault surfaces.

This discharge is the cause of water influx and the manifestation of moisture within many of the buildings of the Holy Monastery of Kleiston. The presence of vegetation cover in the epikarst zone helps retain soil moisture, minimizing evaporation and enhancing humidity in the areas surrounding the Monastery.

This study highlights the overall importance of the epikarst zone in the collection and flow of water infiltrating karst formations, particularly emphasizing its critical role in the hydrogeological conditions of the area surrounding the Holy Monastery of Kleiston. Its impact on water influx and the manifestation of humidity is complex and is influenced by morphological, lithostratigraphic, tectonic, and climatic factors.

Acknowledgements

The research team extends its most heartfelt gratitude to the Monks of the Holy Monastery of Kleiston, particularly to the Abbess Mariam, for the time they dedicated and their invaluable assistance during the fieldwork both within and beyond the Monastery. Additionally, we express our appreciation to Mayor Mr. Christos Pappous, the elected officials, and the staff of the Municipality of Fili for their collaboration and the generous provision of support.

References

Bakalowicz, M., 2004. The epikarst. The skin of karst. In: Jones, W.K., Culver, D.C. & Herman, J.S. (Eds.). Epikarst. Special Publication 9. Charles Town, WV: Karst Waters Institute: 16-22.

Dounas, A., 1971. The geology between Megara and the Red area. PhD thesis. Athens. Geological and Geophysical Research, 15/2, 250p.

Katsikatsos, G., Mettos, A., Vidakis, M., Dounas, A.,1986. Geological map of Greece, sheet “Athens – Elefsis”, scale 1:50,000, I.G.M.E. Publications, Athens.

Mangin, A., 1975. Contribution a` l’e´tude hydrodynamique des aquiferes karstiques, Ph.D. Thesis, Univ. de Dijon, Dijon, France, 124p.

Nikas, K, Antonakos, A, Kallergis, G, Kounis, G., 2010. International Hydrogeological Map of Europe: Sheet D6 “Athina”. Proceedings of the 12th International Congress, Patras, 2010 Bulletin of the Geological Society of Greece, Volume XLIII No 4, pages 1821-1830.

Struckmeier, W.F., Margat, J., 1995. Hydrogeological maps: a guide and a standard legend (Vol. 17). Hannover: Heise.

Williams, P.W., 1983. The role of the subcutaneous zone in karst hydrology, J. Hydrol., 61, 45-67.

17th INTERNATIONAL CONGRESS of the Geological Society of Greece

BULLETIN OF THE GEOLOGICAL SOCIETY OF GREECE, SP. PUBL.

EXTENDED ABSTRACT 291

Composition and physicochemical properties of muds from the Evros river delta, Thrace district (Northern Greece) and their potential use in pelotherapy

Sofianska E.[1], Athanassoulis K.[1], Tarenides D.[1], Gkagka M.[1]
(1) Hellenic Survey of Geology and Mineral Exploration, 1 S. Louis st., 13677, Acharnes, Athens, Greece, esofianska@eagme.gr

Abstract
Mud samples from the Evros river deltaic sediments (ERDS) Thrace district (Northern Greece) were analyzed by several physicochemical techniques: grain size distribution, X-ray diffraction, optical microscopy, chemical composition (major and trace elements), cation exchange capacity (CEC) and plasticity index (PI), at an effort to evaluate their potential use in pelotherapy. Results showed that in terms of granulometry ERDS are characterized as loam-silts and silts, with silt-clay fractions varying from 69.8% to 97.72%. Non clay minerals include quartz, feldspars, amphiboles, calcite, sphene, rutile, magnetite, ilmenite, hematite, and pyrite. Main clay minerals present are illite (15-20 wt%), kaolinite (14-18 wt%), smectite (4-9 wt%), micas (6-8 wt%), and chlorite (5-7 wt%), and constituting 49 to 59 wt% of the mud samples. Among the analyzed potentially toxic elements (PTEs) average values of V, Cr, Ni, Cu, Zn, As and Pb exceed the Earth's crust content. Cation exchange capacity and PI range from 19.32 to 23.22 meq/100g and 18 to 32%, respectively. The measured properties of the studied Evros muds are comparable to those of peloids commonly used in SPA centers and, therefore, render them potentially suitable for pelotherapy. However, a sieving process of the muds is recommended to enhance the silt-clay size fraction particles and consequently to further improve the CEC and PI values, which are the more favorable properties for peloids in pelotherapy.
Key words: Clay minerals, physicochemical properties, pelotherapy, Evros river muds, Greece.

Introduction
Mud therapy or pelotherapy is the topical application of thermal muds (peloids) on the human body for medical or cosmetic purposes, and it is known since ancient times (Veniale et al., 2007). These applications are carried out either at natural sites or in thermal centers (SPAs) for the treatment of muscle, bone, skin pathologies, or for beauty therapy (Rebelo et al., 2010, Barthoumi et al., 2018). Peloids are defined as "matured muds composed of a complex mixture of fine-grained geological materials, mineral water or sea/lake water and very often organic compounds from biological metabolic activity" (Gomes et al., 2013, Maraver et al., 2021).
The growing interest in human health and welfare has increased the scientific investigation on the selection of potentially suitable materials for the formulation of thermal muds to be used in pelotherapy. To this direction a five years research project (2018-2023) has been performed by the Hellenic Survey of Geology and Mineral Exploration (HSGME) on many areas of Greece to localize natural occurrences of suitable muds for pelotherapy (Sofianska et al., 2019, 2022). Natural occurrences of thermal muds, which are empirically used for therapeutic, aesthetic, and pharmaceutical purposes exist in Greece (Kamitsou et al., 2017, Sofianska et al., 2019).
The suitability of a geologic material for pelotherapy can be defined on the basis of its mineralogy and chemistry, along with some physical and technological properties like granulometry, CEC, pH, organic matter content, adsorption capacity, plasticity, rheological and thermal behavior (Carretero et al., 2014).
With regard to chemical composition of muds in pelotherapy it is important to know the concentration of elements either beneficial (Ca, Mg, Na, K, Fe among others) or PTEs (Hg, As, Cu, Cr, Pb, Zn, Co, Sb, Ba, V, U) since both pass through the skin of the patient during treatment (Veniale et al., 2007, Carretero et al., 2014).
In the present investigation the texture, mineralogy, chemistry and some physicochemical characteristics of representative mud samples from the Evros river deltaic sediments (Thrace district, Northern Greece) were studied, at an effort to evaluate their potential use as raw material for peloids in pelotherapy.

Materials and methods
Mud samples collected in June of 2020 from the Evros river delta shore were used in this investigation. Four samples were collected from the sea bottom offshore and one from a river lagoon (AL-DE-05). The sampling points were randomly distributed, and their spatial site was recorded using a handhold positioning system (GPS). Collection of mud samples was carried out using a plastic pipe (3 m long and 2.5" ⌀) pressed on the bottom deposits. The raw material was collected in plastic boxes. Besides, depth, temperature and pH of water column were measured in each

sampling point. Mud samples collected were dried for 7 days and stored in polyethylene bags for further analytical work. Portions of the samples were used for grain size, mineralogical and geochemical analyses, as well as for the evaluation of physicochemical properties. Grain size distribution was performed in two stage processes. Firstly, the samples were wet sieved to separate the coarser particles (>74μm) in accordance with the ASTM D422-63. The fractions <74 μm were measured by means of a Laser granulometer Microtrac S 3500.

Optical microscopy and X-ray powder diffraction (XRD) analysis were used for the study of the mineralogical composition of the samples. Bulk samples and the separated clay fraction (<2 μm) in oriented, glycolized and heated to 550°C were X-rayed using a X'Pert PRO X-ray diffractometer equipped with graphite-filtered CuKα radiation.

Semiquantitative mineralogical composition of ERDS was found by analysis of the XRD patterns using the X'Pert PRO program.

The chemical composition of the samples (major and minor elements) was determined by X-ray fluorescence analysis (XRF), using the S4 PIONEER equipment of the BRUKER AXS. The concentration of PTEs were found by Inductively coupled plasma mass spectrometry (ICP-MS) using the PE SCIEX ELAN 6100 equipment.

Cation exchange capacity (CEC) was estimated by using the barium chloride solution method (ISO 11260:1994).

Plasticity index was calculated using Atteberg limit in the Casagrande test.

Chemical results were compared with the composition of the Earth's upper crust (Rudnick and Gao, 2003) and with peloids applied in pelotherapy in Spain (Carretero et al., 2014), Turkey (Karakaya et al., 2010) and Slovenia (Glavas et al., 2017).

All the analytical work was conducted at the Laboratories of the Hellenic Survey of Geology and Mineral Exploration (HSGME).

Results and discussion

In Table 1 the coordinates of the mud samples sites, along with some physicochemical parameters of sea water column are given.

Table 1. Coordinates of mud sampling sites and physicochemical parameters of water column.

Sample	X	Y	Depth of sea water	T °C of sea water	pH of sea water
AL-DE-01	670273,61	4517556,74	1.5	28.7	8.6
AL-DE-02	671573,00	4514546,00	2.0	28.3	8.6
AL-DE-03	670426,07	4518083,25	1.0	28.7	8.6
AL-DE-04	669227,00	4519268,00	2.0	28.2	8.6
AL-DE-05 lagoon	670731,06	4518477,55	0.1	34.1	8.4

Textural analyses showed that the ERDS are composed of 17.61 (2.28-30.19%) sand, 76.86% (64.92-92.86%) silt and 5.54% (4.89-5.92%) clay, with the silt and clay average fractions exceeding 82.49% (Table 2) and they are plotted in the silt and silt loam fields (Curtis, 2005) of the ternary discrimination diagram (Fig. 1).

In terms of granulometry best peloids should contain a high percentage of the clay fraction or a high silt and clay fraction as stated for the Spanish peloids (Carretero et al., 2014) and the Turkish thermal muds (Karakaya et al., 2010). Large clay fraction content creates a pleasant sensation, when applied to the skin and enhances ion exchange capacity through mud/skin interface (Veniale et al. 2004, 2007, Rebelo et al., 2010). Therefore, a sieving process to remove sand fraction is needed to improve the granulometry of the studied samples and their quality as raw material for peloid formulation.

Optical microscope study showed a polymineralic composition of the samples, including mainly detrital grains of quartz, feldspars, amphiboles, calcite, chlorite, mica, epidote, with minor amounts of sphene and rutile. Opaque minerals include magnetite, ilmenite, hematite and pyrite (single microcrystals and framboids). Calcite is present in the form of detrital grains, as well as biogenic in fossil shells. Non clay minerals match to 41-51wt%.

X-ray diffraction analyses showed that the clay minerals present are mainly illite (17.6 wt%), kaolinite (16.2 wt%), smectite (6.8 wt%), mica (7.4), chlorite (5.8%), and in one sample interstratified chlorite-smectite (3 wt%) (Table 2). The clay mineral content (mainly smectite) is relevant to therapy and of great importance, determining properties like high water absorption, CEC and specific heat (Cara et al., 2000).

Regarding the chemical composition of the studied muds, only TiO_2, MnO, MgO and F_2O_3 were found increased compared to the Earth's crust (Table 3, Fig. 2). Among the analyzed PTEs (values in mg/kg) (Table 3) V (98-125),

Cr (100-180), Ni (55-93), Cu (38-59), Zn (84-160), Pb (38-92) and As (6-13) were found to exceed significantly the composition of the Earth's upper crust (Rudnick and Gao, 2003). However, many examples of peloids applied in pelotherapy are referred to contain similar or even higher levels of these elements (Quintela et al., 2012, Carretero et al., 2014). Clayey materials selected for peloid applications must be safe. Therefore, elements like Cd, Pb and As known to be toxic to human and environmentally hazardous must be absent. European directives and USA regulations state that heavy metal concentrations in cosmetic products must be avoided if they exceed 10 mg/kg in case of Pb, 3 mg/kg for Cd and As (Rebelo et al., 2010). Besides, Mo, Ni, V, Cr and Cu, been reported to have less toxicity than previously mentioned elements must be limited in pharmaceutical formulations (Berthoumi et al., 2019). It is worth noting that the bioavailability and the potential enter of the PTEs in to the patient's body is more important than their concentration in the peloid constituents (Carreretero et al., 2014).

The analyzed SO_3 content of the Evros area muds was found varying between 1.04% and 2.01 wt% and comes most probably from pyrite. Sulfur content could influence therapeutic action as sulfur shows a keratolytic effect, analgetic influence on the pain receptors and inhibition of the immune response and has a bactericidal and antifungal effect (Baricz et al., 2021).

The CEC is controlled by the clay size fraction content, the kind of clay minerals, and the presence of organic matter (Baricz et al.,2021). The CEC of the muds studied are relatively low, ranging from 19.32 to 23.33meq/100g (average 21.54), and reflecting the clay minerals contents. Enhance CEC values in the studied muds are most probably related to both higher content of smectite and organic matter (Table 2).

Table 2. Main physical and chemical characteristics of the Evros area muds

Sample	Particle size (%)			CEC meq/100g	Clay mineral content (%)						Non clay min. (%)	LL (%)	PI (%)	Org. matt. (%)
	Sand	Silt	Clay		Ilt	Kln	Sme	Chl	Chl/ Smc	Mca				
AL-DE-01	11.82	82.45	5.73	20.47	19	18	7	5	-	8	43	57	30	6.31
AL-DE-02	24.17	70.52	5.31	19.32	15	14	4	6	3	8	50	43	18	4.56
AL-DE-03	2.28	91.86	5.86	23.22	20	18	8	5	-	6	43	63	32	7.76
AL-DE-04	19.56	74.52	5.92	21.41	15	15	6	6	-	7	51	51	24	6.78
AL-DE-05	30.19	64.92	4.89	23.76	19	16	9	7	-	8	41	51	23	9.09
Average	17.60	76.85	5.54	21.63	17.6	16.2	6.8	5.8	0.8	7.4	45.6	53	25	6.9

Ilt – Illite, Kln – Kaolinite, Sme – Smectite, Chl – Chlorite, Mca – Mica.

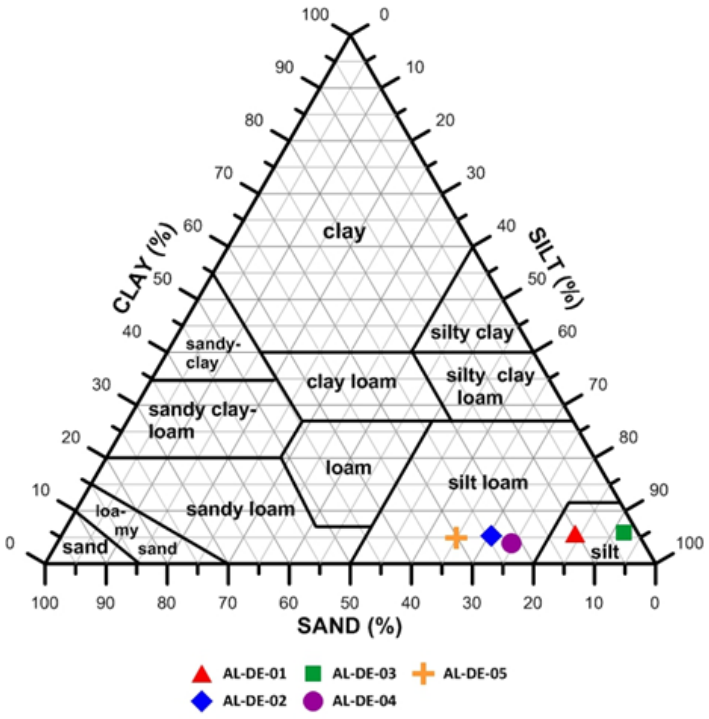

Figure 1. Ternary discrimination diagram of the studied muds.

Table 3. Chemical composition of the ERDS (major and minor elements as oxides, trace elements in mg/kg), upper continental crust, range of variability of Spanish (Carretero et al., 2010), Turkish peloids (Karakaya et al., 2010) and Sečovlje healing saline mud (Glavas et al., 2017).

Element	AL-DE-01	AL-DE-02	AL-DE-03	AL-DE-04	AL-DE-05	Average.	UCC	Spanish peloids range	Turkish peloids range	1*
wt%										
SiO_2	53.18	57.97	52.30	55.13	48.79	53.53	65.89	18.41 - 51.12	28.56 - 50.79	38.68
TiO_2	0.74	0.62	0.71	0.65	0.65	0.66	0.50	0.22 - 0.55	0.35 - 0.66	0.46
Al_2O_3	15.59	15.55	15.39	14.68	14.42	15.03	15.17	3.58 - 12.24	6.24 - 13.34	8.27
MnO	0.06	0.07	0.08	0.08	0.19	0.10	0.07	0.02 - 0.61	0.05 - 0.19	0.05
MgO	3.43	3.26	3.52	3.02	3.72	3.38	2.20	0.98 - 22.35	1.65 - 9.95	3.30
CaO	1.61	2.11	1.71	2.43	2.74	2.22	4.19	2.27 - 26.48	5.9 - 29.69	12.30
Na_2O	3.16	2.74	3.35	3.43	3.82	3.33	3.89	0.3 - 4.34	0.53 - 3.39	4.21
K_2O	2.85	2.97	2.79	2.72	2.77	2.81	3.39	0.57 - 2.57	0.97 - 2.93	1.84
P_2O_5	0.14	0.18	0.15	0.16	0.18	0.17	0.20	-	0.06 - 0.2	0.07
Fe_2O^3T	5.63	5.21	6.12	5.35	5.63	5.38	4.49	1.7 - 5.24	3.1 - 5.49	3.69
SO_3^T	1.75	1.04	1.22	1.65	2.01	1.49		0.15 - 5.92	0.15 - 1.82	
LOI	11.61	8.21	12.7	10.67	15.12	11.67		13.95 - 53.84	18.3 - 27.1	
mg/kg										
V	105	98	125	115	125	113.6	107	31.6 - 90.9	55 - 95	
Cr	120	180	145	110	110	133.0	85	14.6 - 68.2	61.6 - 547.4	85
Co	15	13	16	14	19	15.4	17	4 - 16.8	9.1 - 54.5	11
Ni	67	93	74	55	72	72.2	44	3.4 - 50.8	27 - 671	64
Cu	59	40	52	38	46	47.0	25	11.5 - 52.3	12.4 - 32.2	29
Zn	115	84	155	92	160	121.2	71	33.1 - 160.4	33 - 56	78
As	13	6	11	12	11	10.6	1.5	4.4 - 29.6	5.1 - 62.6	9
Se	<1	<1	<1	<1	<1	<1	0.05	<1 - 1.6	<0.5 - 0.7	
Rb	32	38	42	24	38	34.8	112	35.5 - 120.5	38.7 - 175.1	
Sr	3	31	39	24	52	29.8	350	87.3 - 1879	214.3 - 1540.4	530
Mo	1	3	2	2	1	1.8	1.5	<1 - 4.4	0.2 - 1.2	4
Cd	<1	<1	<1	<1	<1	<1	0.098	<10	0.1 - 0.2	0
Ba	97	67	95	46	110	83	550	147.7 - 799	110 - 1153	138
Pb	65	39	81	38	92	63	17	10.9 - 37.5	6.9 - 38.2	23
U	2	1	1	1	3	1.6	2.8	<1.20 - 18.4	1 - 6.3	
Bi	2	1	1	1	1	1.2				0.3
Ag	2	1	1	1	1	1.2	50	<6	<0.1 - 0.1	0.1

UCC Upper Continental Crust (Rudnick and Gao 2003) 1* Average composition of Sečovlje healing saline mud (Glavas et al., 2017).

Similar CEC values are, however, referred for Spanish peloids (Pozo et al., 2013). As stated by Matike et al. (2011) at high CEC values (>15 meq/100g) ions exchange from the skin to the clay minerals mixture and release of ions to the skin can occur during application of peloid, facilitating skin cleansing and providing a refreshing sensation. CEC of clay mineral particles is significantly affecting ion exchange between peloid and the skin of the patient and thus contributes to a cleansing process (Tateo et al., 2009).

The liquid limit measured values and the plasticity indices found are varying between 43 and 63 (average 53) and 18 to 32% (average 25), respectively (Table 2), classifying the muds into the high plasticity clays in the Casagrande chart (Fig. 3) (except the AL-DE-02 sample). The liquid limit values >50% reflect the relative smectite content of the studied muds.

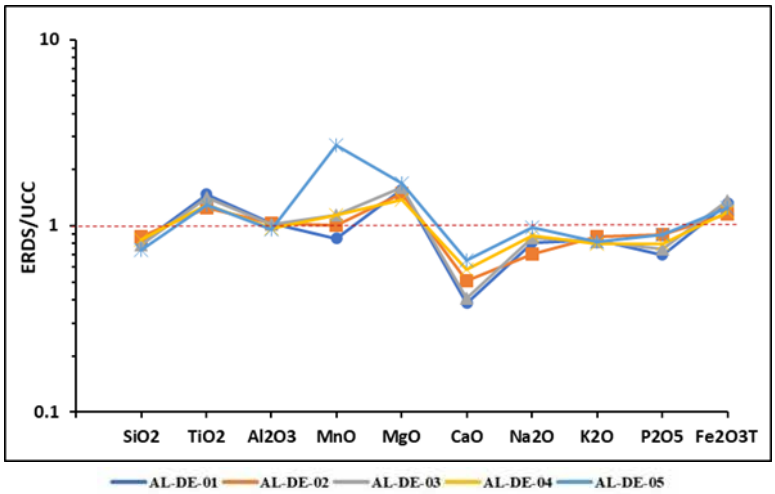

Figure 2. Earth's upper crust normalized composition of the Evros area muds.

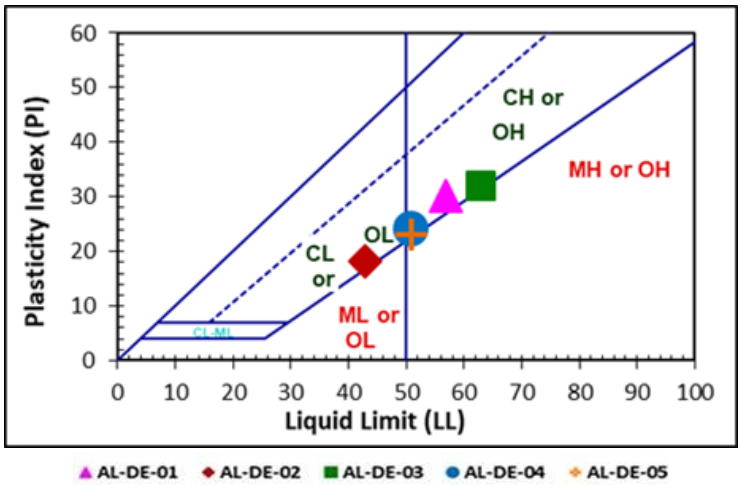

Figure 3. Projection of plasticity indices (PI) and liquid limits (LL)%values of the Evros delta muds in the Casagrande chart (C-clay, M-silt, O- organic, L- Low plasticity, H-High plasticity).

Conclusions

Mud samples from the Evros delta area were characterized in terms of different physicochemical (granulometry, mineralogy geochemistry, CEC and plasticity) properties.

Particle size, clay mineral content, CEC and PI found render the investigated mud samples from the Evros river delta potentially suitable for use as peloids in pelotherapy. Potentially toxic elements (PTEs) concentrations, although were found exceeding the Earth's crust composition, are considered acceptable because their concentrations are within the ranges referred for peloids applied in pelotherapy.

A sieving process is recommended to enhance the clay-size fraction particles of them and consequently improve their CEC and plasticity. Moreover, a further investigation is needed to study the technical properties of a derivative peloid formed from the mixture of the Evros muds with a medical mineralized water or sea water, after a maturation process.

Acknowledgements

This work was financed by the Project: Characterization of muds and volcanic rocks for therapeutic uses, H.S.G.M.E., N.S.R.F. (National Strategic Reference Framework) 2014-2020 / Operational Programme «Competitiveness and Entrepreneurship» / Project "ACTIONS FOR THE RATIONALE AND SUSTAINABLE USE OF GEOTHERMAL ENERGY" Athens 2023.

Thanks are also due to the anonymous reviewer who helped to improve the present manuscript.

References

American Society for Testing and Material ASTM D422 – 63, 1997 (second edition). Standard Test Method for Particle-Size Analysis of Soils, In: Annual book of ASTM Standards: Soil and rock, p. 1026.

Baricz A, Levei EA, Șenilă M, Pînzaru SC, Aluaş M, Vulpoi A, Filip C, Tripon C, Dădârlat D, Buda DM, Dulf FV, Pintea A, Cristea A, Muntean V, Keresztes ZG, Alexe M, Banciu HL., 2021. Comprehensive mineralogical and physicochemical characterization of recent sapropels from Romanian saline lakes for potential use in pelotherapy. Sci Rep. 2021 Sep 20;11(1):18633. doi: 10.1038/s41598-021-97904-1. PMID: 34545115; PMCID: PMC8452724.

Barhoumi, T., Bekri-Abbes, I., Srasra, E., 2019. Physicochemical characteristics and suitability of curative pastes made of Tunisian clay minerals and thermal waters for use in pelotherapy. C. R. Chimie 22, 126–131.

Cara, S., Carcangiu, G., Padalino, G., Palomba, M., Tamanini, M., 2000. The bentonites in pelotherapy: Chemical, mineralogical and technological properties of materials from Sardinia deposits (Italy). Applied Clay Science, 16, 117–124.

Carretero, M., Pozo, M., Martín-Rubí, J., Pozo, E., Maraver, F., 2010. Mobility of elements in interaction between artificial sweat and peloids used in Spanish spas. Applied Clay Science, 48, 506–515.

Carretero, M. I., Pozo, M., Legido, J. L., Fernández-González, M. V., Delgado, R., Gómez, I., Armijo, F., Maraver, F., 2014. Assessment of three Spanish clays for their use in pelotherapy. Applied Clay Science, 99, 131–143.

Curtis, J.O., 2005. Electromagnetic Poser Attenuation in Soils. ERDC/EL TR-05-5. Vicksburg, MS: U.S. Army Engineer Research and Development Center.

Glavas, N., Mourelle, M.L., Gómez, C.P., Legido, J.L., Smuc, N.R., Dolenec, M., Kovac, N., 2017. The mineralogical, geochemical, and thermophysical characterization of healing saline mud for use in pelotherapy. Appl. Clay Sci. 135, 119–128.

Gomes, C., Carretero, M. I., Pozo, M., Maraver, F., Cantista, P., Armijo, F., Legido, J., Texeira, F., Rautureau, M., Delgado, R., 2013. Peloids and pelotherapy: Historical evolution, classification and glossary. Applied Clay Science, 75-76, 28–38.

ISO 11260, 1994. Soil quality – Determination of effective cation exchange capacity and base saturation level using barium chloride solution.

Kamitsou, M.D., Sygouni, V., Kanellopoulou, D.G., Gardikis, K., Koutsoukos, K.P.G., 2018. Physicochemical characterization of sterilized muds for pharmaceutics/cosmetics applications. Environ. Geochem. Health 40, 1449–1464.

Karakaya, M.C., Karakaya, N., Sarıoğlan, S., Koral, M., 2010. Some properties of thermal muds of some spas in Turkey. Applied Clay Science, 48, 531–537.

Li, YH.A., 2009. A compendium of geochemistry. Princeton: Princeton University Press.

Maraver, F., Armijo F., Fernández-Toran, M.A., Armijo, O., Ejeda J.M., Vazquez, I., Corvillo I., Torres-Piles, S., 2021. Peloids as thermotherapeutic agents. International Journal of Environmental Research and Public Health, 18 (4), 1-17.

Matike, D. M. E., Ekosse, G. I. E., Ngole, V. M., 2011. Physico-chemical properties of clayey soils used traditionally for cosmetics in Eastern Cape, South Africa. International Journal of the Physical Sciences, 6(33), 7557–7566.

Pozo, M, Carretero, M.I, Maraver, F, Pozo, E, Gómez, I, Armijo, F, Martín-Rubí, JA, 2013. Composition and physico-chemical properties of peloids used in Spanish spas: a comparative study. Applied Clay Science, 83–84, 270–279.

Quintela, A., Terroso, D., Da Silva, E. F., Rocha, F., 2012. Certification and quality criteria of peloids used for therapeutic purposes. Clay Minerals, 47, 441–451.

Rebelo, M., Viseras C., Lopez Galindo, A., Rocha F., Fereira da Silva, E., 2011. Characterization of Portugese geological materials to be used in medical hydrology. Applied Clay Science 51, 258-66.

Rizo, O.D., Rudnikas, A.G., Rodrigues, K.D., Padila, D.B., 2000. Assessment of historical heavy metal content in healing muds from San Diego (Cuba) using nuclear analytical techniques. Nucleaus 53, 19-23.

Rudnick, R. & Gao, S., 2003. Composition of the Continental Crust. Treatise on Geochemistry, 3, 1–64.

Sofianska E., Athanassoulis, K., Tarenides, D., Gaga M., 2022. Assessment of marl samples from Kefalonia Island (western Greece) for their potential use in pelotherapy. 16th International Congress of the Geological Society of Greece, 17-19 October, 2022 - Patras, Greece, Bulletin of the Geological Society of Greece, Sp. Publ., Ext. Abs. ID 106.

Sofianska E., Athanassoulis, K., Tarenides, D., Xirokostas, N., Gaga M., 2019. Textural, Mineralogical and Geochemical Assessment of the Pikrolimni Lake Sediments (Kilkis district, Northern Greece) and suitability for use in pelotherapy, Bulletin of the Geological Society of Greece 55 (1), 170. DOI: 10.12681/bgsg.21080.

Tateo, F., Ravaglioli, A., Andreoli, C., Bonina, F., Coiro, V., Degetto, S., Giaretta, A., Menconi Orsini, A., Puglia, C., Summa, V., 2009. The in-vitro percutaneous migration of chemical elements from a thermal mud for healing use. Applied Clay Science, 44, 83–94.

Veniale, F Battero, A., Jobstraibizer, P.G., Setti M., 2007. Thermal muds: Perspectives of innovations. Applied clay science, 36, 141-147.

Veniale, F., Barberis, E., Carcangiu, G., Morandi, N., Setti, M., Tamanini, M., Tessier, D., 2004. Formulation of muds for pelotherapy: Effects of “maturation” by different mineral waters. Applied Clay Science, 25, 135–148.

17th INTERNATIONAL CONGRESS
of the Geological Society of Greece

BULLETIN OF THE GEOLOGICAL SOCIETY OF GREECE, SP. PUBL.

EXTENDED ABSTRACT 292

REE distribution in the b1 bauxite strata of the Parnassos–Giona Unit, Greece

Sofis N.[1], Ntouros E.[1], Kalaitzidis S.[1*]
(1) Laboratory of Economic Geology, Department of Geology, University of Patras, Rio, Greece, skalait@upatras.gr

Research Highlights

The REE distribution in b1 bauxite strata of the Parnassos-Giona Unit points to variable forming conditions
The content of REE is moderate and strongly depended on the lithologies
REE bearing minerals were identified for the first time in b1 bauxite strata

Introduction

The Mesozoic carbonate sequence of Parnassos-Giona Unit extends over the mountainous areas of Oiti, Giona, Parnassos and Helicon. The neritic carbonate sedimentation began at the Upper Triassic and ceased at the beginning of Paleocene. The Unit hosts three major karstic-type bauxite strata namely b1, b2, b3, which were deposited between Middle Jurassic and Upper Cretaceous times (Papastamatiou, 1960; Celet 1962). The allochthonous karst-type bauxite deposits of the Parnassos-Giona Unit are part of the Mediterranean bauxite zone, and have been the subject of research by numerous researchers (e.g. Valeton 1972; Bárdossy 1982; Valeton *et al*. 1987).
The lower bauxite strata (b1) hasn't been studied extensively in the past decades, as it occurs sporadically (mainly in the east and northeast parts of the Parnassos-Giona Unit), with limited quantities and low grade in terms of Al.
In this study, seven sampling sites were examined in order to assess their main mineralogical, geochemical and mineral-chemical characteristics, with emphasis on the REE distribution. The aim of this study is to investigate the REE mode of occurrence in the bauxite samples in the lower bauxite strata of the Parnassos-Giona Unit (Fig. 1).

Figure 1: The PL2 section, in which the overlying Upper Jurassic limestones and the b1 bauxite strata are outcropping.

Methods

The main objective of this study is the assessment of the geochemical distribution of rare earth elements in the studied geological sites. In order to achieve this, geochemical analysis was applied on representative bauxite samples and transitional lithologies (in total 39 samples), including X-Ray Fluorescence (XRF) and Inductively Coupled Plasma Mass Spectrometry (ICP-MS), as well as Scanning Electron Microscopy to determine mineralogical chemistry. Furthermore, X-Ray Diffraction was applied to the total amount of samples to determine the mineralogical assemblage of each sample (Fig. 2A). Optical observation was performed using optical microscope of polarized white light for describing the petrographic characteristics and main morphological features.

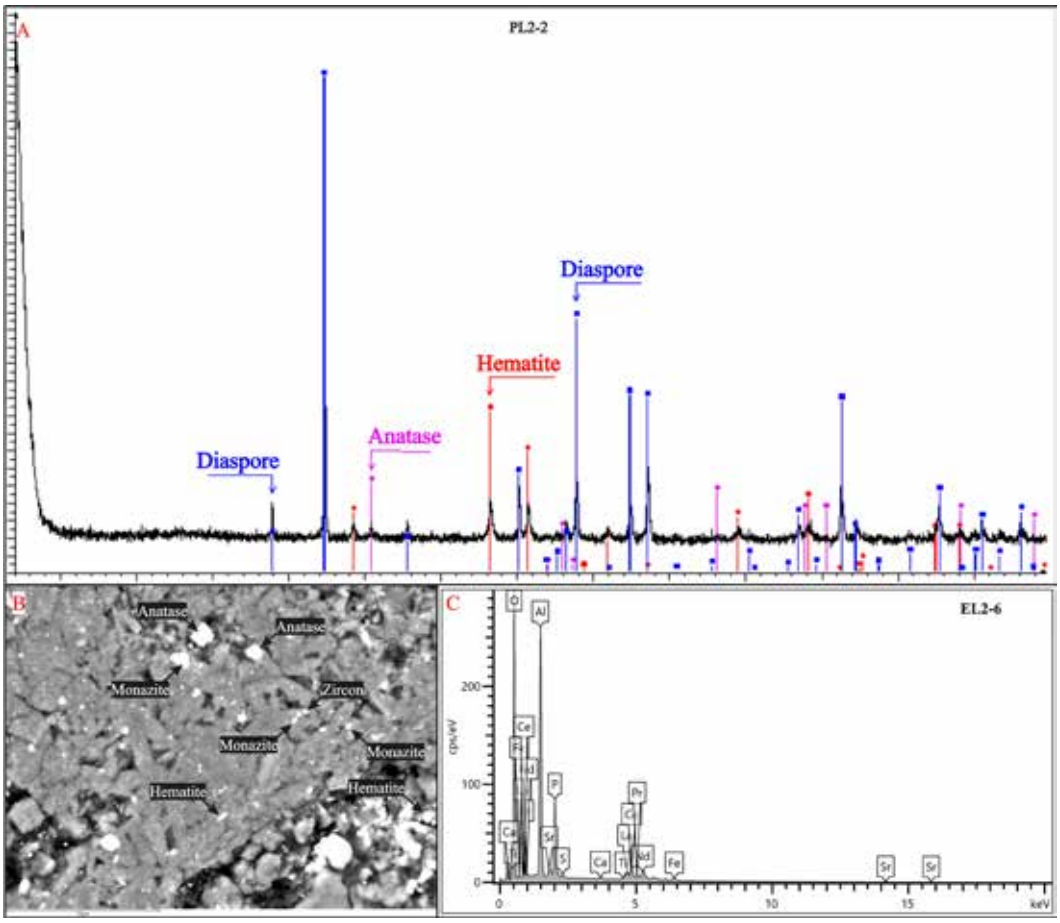

Figure 2: A) Evaluated PL2-2 X ray diffractogram, B) Back Scattered Electron image of the EL2-6 bauxite sample showing the presence of REE bearing mineral monazite, C) scanning electron microscopy (SEM) spectrum of monazite in sample EL2-6 bauxite sample.

Results

The geochemical data reveal an average Al_2O_3 content of 42.73 wt.-% in the bauxite samples, 58.08 wt.-% of CaO in the limestone samples, and 35.86 wt.-% of Fe_2O_3 in the bauxite samples and transitional lithologies. The SiO_2 and TiO_2 average value the studied lithologies are 6.77 and 2.24 wt.-%, respectively. The mean value of the ΣREE in bauxite samples is 565.4 mg/kg, while the ΣLREE and the ΣHREE are 433.06 mg/kg and 132.33 mg/kg respectively. The SEM analysis provided the mineral chemistry of the representative bauxite samples, as well as the presence of REE-bearing and REE minerals, e.g. cerianite and monazite (Fig. 2B and 2C).

Discussion

According to REE/Chondrite normalized patterns of the studied bauxite samples per sampling site, a positive anomaly is observed for Ce, Er, and Tm, while Eu, Dy and Ho show a negative one. Furthermore, the ratio Eu/Eu* ranges from 0.56 to 0.69, whereas the Ce/Ce* fluctuates from 0.41 to 7.43.

Variations on the total content of the REE depending on the lithological facies were observed. Generally, the bauxite samples seem to be more enriched (ΣREE = 565.4 mg/kg) than the transitional lithologies (ΣREE = 404.97 mg/kg). The Eu/Eu* fluctuates from 0.56 to 0.69, which based on published data regarding the parental rocks of the bauxites of the Parnassos-Giona region (Mameli et al., 2007; Mongelli et al., 2014; Mondillo et al., 2022) indicates that igneous rocks with intermediate to basic affinity were the parental rocks of the b1 bauxite.

According to Ellahi et al. (2016), positive La/Y anomalies indicate alkaline conditions during bauxitization, whereas the negative ones acidic. At the PR1, PR2, PL2, EL2, EL3A and EL4 profiles alkaline conditions prevailed, whereas at EL3 acidic ones. The positive Ce/Ce* anomaly indicates oxic conditions during bauxitization, whereas the negative ones show reduced conditions. At PR1, PR2, EL2, EL3A and EL4 bauxite profiles, most probably oxic conditions prevailed, while at PL2 and EL3 reduced ones.

Conclusions

The lower bauxitic strata b1 at Parnassos-Giona Unit shows a relative enrichment in rare earth elements, which seem to concentrate at the pure bauxite samples in comparison to the transitional lithologies. In most sampling sites alkaline and oxic conditions prevailed during the bauxitic mud deposition. Most probably, igneous rocks with intermediate to basic affinity were the parental rocks of the b1 lenses confirming previous studies in the area.

References

Bardossy, G., 1982. Karst Bauxites, Bauxite Deposits on Carbonate Rocks, Developments in Economic Geology, Elsevier, Amsterdam, Vol. 14, 441 p.

Celet, P. 1962. Contribution a l' etude geologique du Parnaasse-Kiona et d' une partie des regions meridionales de la Grece continentale. Ann. Geol. Pays Hellen. 7, 1-358

Ellahi, S.S.; Taghipour, B.; Zarasvandi, A.; Bird, M.I.; Somarin, A.K., 2016. Mineralogy, geochemistry and stable isotope. studies of the dopolan bauxite deposit, Zagros Mountain, Iran. Minerals, 6, 11.

Mameli, P., Mongelli, G., Oggiano, G., Dinelli, E., 2007. Geological, geochemical and mineralogical features of some bauxite deposits from Nurra (western Sardinia, Italy): Insights on conditions of formation and parental affinity. Int. J. Earth Sci., 96 (5), 887-902.

Mondillo, N., Di Nuzzo, M., Kalaitzidis, S., Boni, M., Santoro, L., Balassone, G., 2022. Petrographic and geochemical features of the B3 bauxite horizon (Cenomanian-Turonian) in the Parnassos-Ghiona area: A contribution towards the genesis of the Greek karst bauxites. Ore Geology Reviews, 143, 104759.

Mongelli, G., Boni, M., Buccione, R., Sinisi, R., 2014. Geochemistry of the Apulian karst bauxites (southern Italy): chemical fractionation and parental affinities. Ore Geol. Rev. 63, 9-21.

Papastamatiou, J., 1960. La géologie de la région montagneuse du Parnasse Kiona Oeta. Bull. Soc. Géol. Fr., (7), 11, 398-409, Paris.

Valeton, I., 1972. Bauxites. Elsevier Publishing Company, Amsterdam, 226 pp.

Valeton, I., Biermann, M., Reche, R., Rosenberg, F., 1987. Genesis of nickel laterites and bauxites in Greece during the Jurassic and Cretaceous, and their relation to ultrabasic parent rocks. Ore Geol. Rev., 2, 359-404.

17th INTERNATIONAL CONGRESS of the Geological Society of Greece

BULLETIN OF THE GEOLOGICAL SOCIETY OF GREECE, SP. PUBL.

EXTENDED ABSTRACT 293

Plio-Quaternary tectonics and evolution of Southeastern Lesvos Island and Lesvos Basin, Greece: Transtensional deformation and relationship with the July 2017 earthquake activity

Sotiropoulou S.[1,2], Kalaitzis M.[1,2], Skourtsos E.[1], Sakellariou D.[2], Kranis H.[1]

1 Department of Geology & Geoenvironment, National and Kapodistrian University of Athens, 15784, Zografou, Greece

2 Institute of Oceanography, Hellenic Centre for Marine Research, 19013, Anavyssos, Greece

Introduction

The Aegean domain is regarded as a distinct, deforming microplate situated between the converging Eurasian (to the north) and African (to the south) tectonic plates, alongside the westward advancing Anatolian block (to the east) and Apulia (to the west) (Le Pichon & Angelier, 1979, 1981; Dewey & Şengör, 1979; Mascle & Martin, 1990; Armijo et al. 1996, 1999;). It is delineated to the north by the dextral, NE-SW strike-slip North Anatolian Fault (NAF), to the west by the NNE-SSW striking dextral strike-slip Kefallonia Fault, and to the southeast by the sinistral strike-slip fault zones of Strabo and Pliny. The region is characterized by a south-southwest directional extension, with a velocity of 40-50 mm per year relative to Eurasia, and experiences intricate extensional and strike-slip deformation influenced by the retreat of the Hellenic Subduction and the pressure exerted by the movement of the Anatolian Block along the NAF and its southern branches.

The present study concentrates on the northeastern margin of the North Aegean Sea, specifically on the southern part of Lesvos Island, encompassing the area that stretches from the eastern edge of the Gulf of Kalloni to the region further east of Vatera. The objective of this research is to provide insights into how the fault patterns of the study area are connected to the Lesvos Basin through geological mapping, conducting geological and structural observations, and integrating these findings with recent onshore data, particularly elucidating their significance in relation to the seismicity of the larger region.

Methodology

The present study employed a multifaceted approach to interpret the tectonic regime and fault network of the study area. A thorough examination of existing literature and research findings served as a foundational element in the development of this study's methodologies and framework. Between 2019 and 2021, a series of extensive field campaigns were conducted to comprehensively map the fault network governing the region. These expeditions enabled the possession of crucial geometric and kinematic data necessary for decoding the tectonic characteristics of the area. To supplement the field data, high-resolution topographic maps were utilized to establish the hydrographic network and identify potential fault zones of significance. The integration of geospatial techniques facilitated a more nuanced understanding of the tectonic landscape.

Tectonic Setting of NE Aegean and Lesvos Island

Most of the research conducted in the broader region predominantly relies on geological and geophysical data, focusing on earthquake mechanisms (e.g. Koukouvelas et al., 2002; Kiratzi et al., 2018, Papadimitriou et al., 2018). Seismic activity dates back to ancient time highlighted by a significant seismic event of magnitude 7.0 in 1867 along the Agia Paraskevi – Kalloni dextral strike – slip fault zone (Poumelioti and Kiratzi 2010; Chatzipetros et al., 2013). This activity persists today (Papazachos et al. 1997; Papazachos and Papazachou 2003; Taymaz et al. 1991, 2007), with a notable seismic event occurring in June 2017 featuring a mainshock of magnitude 6.3, characterized by a WNW-ESE normal fault, dipping 45º to the SSE. It was followed by two main aftershocks of magnitudes 5.2 and 5.0 on two NW-SE sub – vertical faults showing strike – slip motion (Nomikou et al., 2021; Papadimitriou et al., 2017; Kiratzi 2018).

The main fault structures in Lesvos can be categorized into three groups based on their strike. These consist of (i) NNE-SSW striking faults, which are mainly characterized as clockwise strike – slip faults, such as the Agia Paraskevi Fault Zone (APFZ), (ii) WNW-ESE striking faults which are represented mostly of normal faults with significant counterclockwise strike – slip component., (iii) E-W striking which is usually represented by normal faults, which act as "relay ramps" connecting the aforementioned strike-slip faults (Chatzipetros et al., 2013; Papadimitriou et al., 2018).

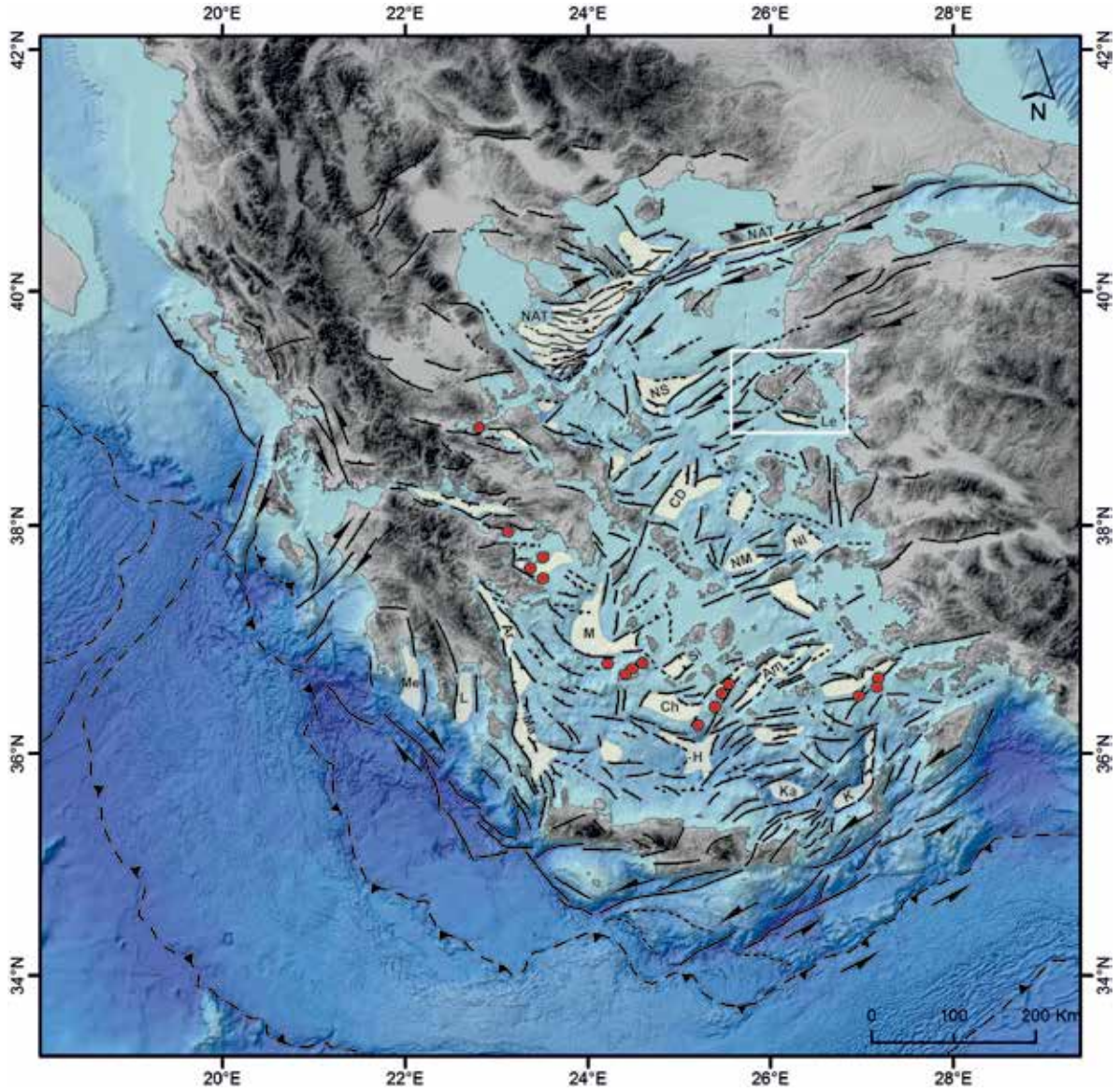

Figure 1. Active fault network and distribution of Plio-Quaternary basins in the Aegean. Red dots show the main volcanoes of the Volcanic Arc. Yellow areas indicate Plio-Quaternary basins with sediment thickness >500 m. Black lines show active faults, dashed black lines indicate possible/inferred faults. Ticks on the faults mark the hangingwall. Half arrows show the sense of strike-slip motion. Basins: Am; Amorgos, Ar: Argolikos, CD: Cavo Doro, Ch: Christiana, H: Heraklion, K: Karpathos, Ka: Kamilonisi, L; Lakonikos, Le: Lesvos, M: Myrtoon, Me: Messiniakos, NAT: North Aegean Trough, NI: North Ikarian, NM: North Mykonos, NS: North Skyros, Si: Sikinos (Sakellariou & Tsampouraki – Kraounaki, 2019). The white box marks the island of Lesvos and the broader study area.

Geology and fault geometry of the SE Lesvos

The principal geological structure within the study area is the asymmetrical Vatera Basin, characterized by its triangular shape, bordered to the north by a series of hills that rise to altitudes of up to 350 meters, and to the south by the coastline. At the base of the southern slopes of this hill range lies the Vrisa Fault (VFZ), extending approximately 13 km from the Gulf of Kalloni to the west, passing south of the village of Polichnitos, north of the settlement of Vrisa, and reaching eastward to the settlement of Drota, while its trace terminates at the coastline, with a likely offshore extension further eastward. Vacchi et al. (2012) refer to this fault as the Vatera Fault, while Chatzipetros et al. (2013) and Papadimitriou et al. (2018) identify it as the Plomari-Polichnitos Fault. The fault exhibits a WNW-ESE strike with high-angle dips to the NNW. Kinematically, it displays counterclockwise strike-slip motion with a notable normal slip component, although normal characteristics were also observed through slickensides identified in its central segment. The thickness of the damage zone exceeds 1 m.

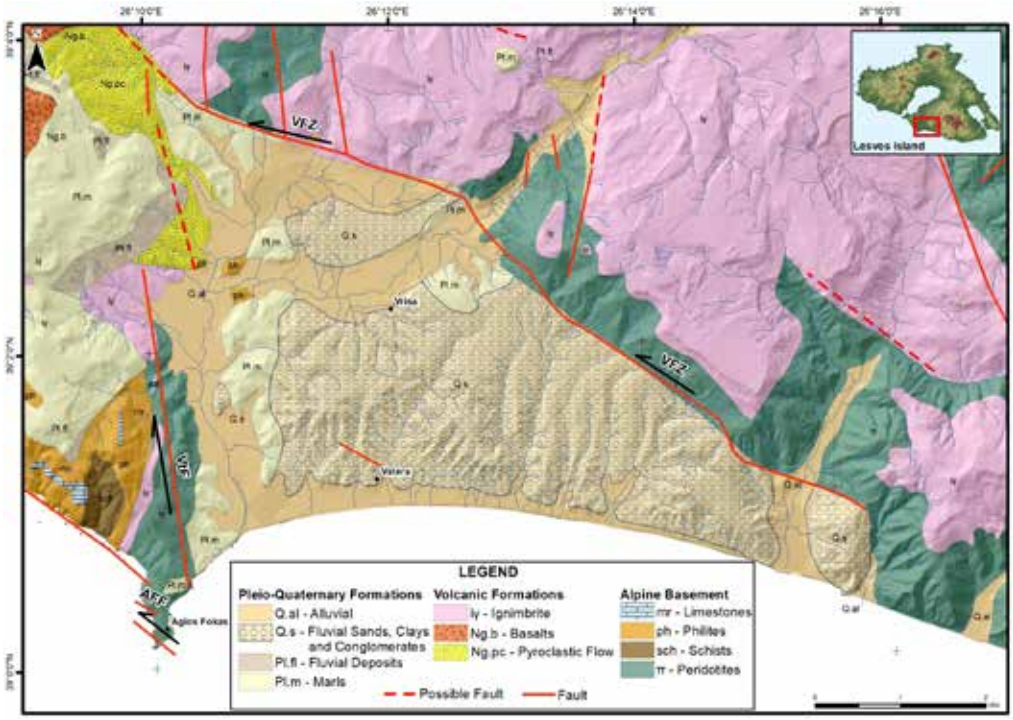

Figure 2. Geological and tectonic map of the study area, based on IGME maps (POLYCHNITOS and PLOMARI Sheets), showing the major fault zones described in this study. AFF: Agios Fokas Fault, VtF: Vatera Fault, VFZ: Vrisa Fault Zone.

The hill range constitutes the footwall of the fault and is composed of ophiolitic rocks, upon which beds of ignimbrites have been deposited. Above the fault block lies a thick sequence of Pleistocene fluvial conglomerates that comprises the central and eastern parts of the basin; beneath this, a Pliocene sequence primarily consisting of alternating marls and conglomerates, is distinguished in the western part. The size of the gravels in the upper sequence decreases from east to west, indicating a source of sediments from the northeast. The lower marly sequence exhibits eastern dips, while the overlying conglomeratic sequence dips southwest, although near the fault, it tends to tilt towards it.
During the June 2017 earthquake, surface ruptures were observed along the fault on the dirt roadway intersecting it. These ruptures measured 50 m in length and 1 cm in width without accompanying displacements. Additionally, large fragments of the fractured ophiolitic rock detached from the fault scarp and tumbled downward, while pre-existing ruptures within the fault's damage zone were widened (Mavroulis et al., 2018).

Figure 3. Fault scarps with the striations of the AFF (left image) and VFZ (right image). The geometry of the slickensides in AFF is 01º/122º and for VFZ is 112º/30º in a fault which dips towards SW.

Agios Fokas Fault Zone (AFFZ) is situated in the central south-southwestern region of the study area and predominantly extends parallel to the coastline, with its most notable onshore manifestation found at the eponymous cape. The AFFZ follows a NW-SE orientation, almost parallel to the VFZ, is a steep fault and consists of numerous

fault segments arranged in an en-échelon pattern. The footwall of the fault is built by old alpine formations, such as phyllites, crystalline limestones, green schists and metabasalts, on which Miocene volcanic rocks and finally Pliocene marls of the lower series of the Vatera basin have been deposited. Kinematical this fault zone is mainly characterized by strike-slip motion as indicated by the slickenlines observed on its fault surfaces. However, the presence of beachrocks above sea level on its footwall may suggest uplift attributable to this fault zone, potentially implying the coexistence of a normal component of shear. These kinematic features match those on the VFZ.
The faults situated in the NNW-SSE/N-S strike tend to play a subordinate role in the main fault zones outlined above (VFZ and AFFZ), serving as the structural connections between them. Notably, the steep Vatera Fault Zone (VtFZ), located in the central portion of the study area, is characterized by an almost N-S to NNW-SSE orientation, with a primary dip to the ENE. This fault zone extends from the VFZ to the north, terminating at the cape of Agios Fokas to the south. The existence of VtFZ is corroborated by the presence of distinct successive fault scarps arranged in an en échelon pattern, as well as geomorphological observations. In kinematic terms, VtFZ predominantly exhibits a clockwise component of slip, although its normal component holds substantial importance, as it significantly influences the hydrographic network of the region, causing it to shift towards the southwest and forming an asymmetry in its drainage basin. This asymmetry arises from the pronounced elevation of the western footwall of VtFZ relative to the eastern hanging wall. This relative vertical motion is further substantiated by the presence of Pleistocene conglomerates exclusively in the eastern part of the Vatera Basin.

Levos Basin

South of the study area, geomorphological analysis of the offshore morphology south of the Lesvos Island and seismic analysis results, highlight the existence of a depression, which is called the Lesvos Basin (LB) formed in Pliocene (Mascle & Martin, 1990). It is an asymmetric depression of about 700 m deep and of NW-SE strike which is characterized by a thick sedimentation (Sakellariou & Tsampouraki – Kraounaki, 2019). The results from a series of transverse Parasound profiles in the N-S direction, showed that the eastern part of LB is WNW-ESE basin, running parallel to the southeastern Lesvos coastline, with a length of more than 30km, maximum depth of 703m and its axis located at 5-6 km from the coast. Its northern margin is controlled by a WNW-ESE marginal fault of the Lesvos Basin with steep slopes forming a steep submarine escarpment more than 600 m height (Mascle & Martin, 1990; Sakellariou & Tsampouraki – Kraounaki, 2019; Nomikou et al., 2021). The eastern segment of the fault, located south of the town of Plomari, exhibits a WNW-ESE strike and is situated in the southeastern extension of the VFZ. Further west, south of the Vatera coastline, the marginal fault shifts slightly in strike, transitioning to a nearly E-W orientation. The earthquake of June 2017, along with its seismic aftershocks, aligns in a WNW-ESE direction within the LB, and it has been proposed that it resulted from the activation of the marginal fault associated with the basin, which corresponds to its eastern segment (Papadimitriou et al., 2018).
South of Agios Fokas Cape an abrupt change of the bathymetry of the LB is observed with a shallow-water platform around 300–400 m depth formed westwards. The change from the main basin occurs along a N-S boundary zone (Nomikou et al., 2021). According to the authors, a similar structure is evident in the eastern margin of the basin, where it has been proposed by them that this zone corresponds to a sinistral strike-slip fault. The western zone is in the submarine extension of the VtFZ. Thus, it can be suggested that this zone is also tectonically shaped by a strike-slip fault.

Discussion and conclusions

Various studies, (e.g. Sakellariou & Tsampouraki-Kraounaki, 2019; Beniest et al.,2016), indicate that certain faults in NE Aegean form transtensional and transpressional structures, especially where faults change strike. The Plio-Quaternary basins formed in a transtensional regime—such as releasing bends and pull-apart basins, or at the junction of NE-SW dextral and NW-SE sinistral strike-slip faults—are entirely controlled by those faults.
We have established that the VFZ is a NW-SE to NNW-SSE, sinistral strike-slip fault zone that exhibits a notable normal component. The kinematic characteristics of this fault align with the proposed models for the Northern Aegean, which support for this type of slip across all faults of similar strike (Sakellariou & Tsampouraki-Kraounaki, 2019). The characteristics of the VFZ are also corroborated by the tilting of conglomerates in the eastern part of the VB, indicating local extension. Furthermore, the VFZ is regarded as the onshore extension of the offshore eastern segment of the marginal fault of the LB (Vacchi et al., 2012; Papadimitriou et al., 2018), as both faults share comparable strike and dip orientations, as well as analogous kinematic behaviors.
The data presented above indicates the following possible scenario of basin evolution in the study area.
In Pliocene, a large basin was formed in the area of Southern Lesvos Island and the present LB. It was characterized by the deposition of (lacustrine?) marls and was bounded to the north-northeast by the VFZ and to the west by the NE-SW striking prolongation of the dextral Agia Paraskevi – Kalloni FZ (APFZ).

In Early Quaternary, enhanced uplift and erosion of the footwall of VFZ led to deposition of massive fluvial conglomerate deposits in the hanging wall of the fault, on VFZ hanging wall and possibly further east and south. At the same time two new faults initiate: the WNW-ESE striking Lesvos Fault (LF) and the NNW-SSE striking Vatera Fault (VtF). The latter marks the new western margin of the basin while the former leads to enhanced subsidence of its hanging wall (Lesvos Basin). Initiation of the Agios Fokas Fault (AFF) may also have taken place in Early Quaternary.
In Late Quaternary, activity on Lesvos Fault leads to uplift of the area of Vatera (Vatera Basin, conglomerate deposits) and enhanced subsidence of Lesvos Basin. The latter is bounded to the west by the offshore possible prolongation of Vatera Fault (VtF).
From Late Quaternary until present day, the morphology of the study area has changed a lot. The most important change concerns the uplift of the study area, which is now exposed to the surface conditions on land. The main reason for this relative uplift was the intense activity of the now offshore, normal, LF, which causes uplift of the NNE onshore part of the LB, and further subsides its NW part.

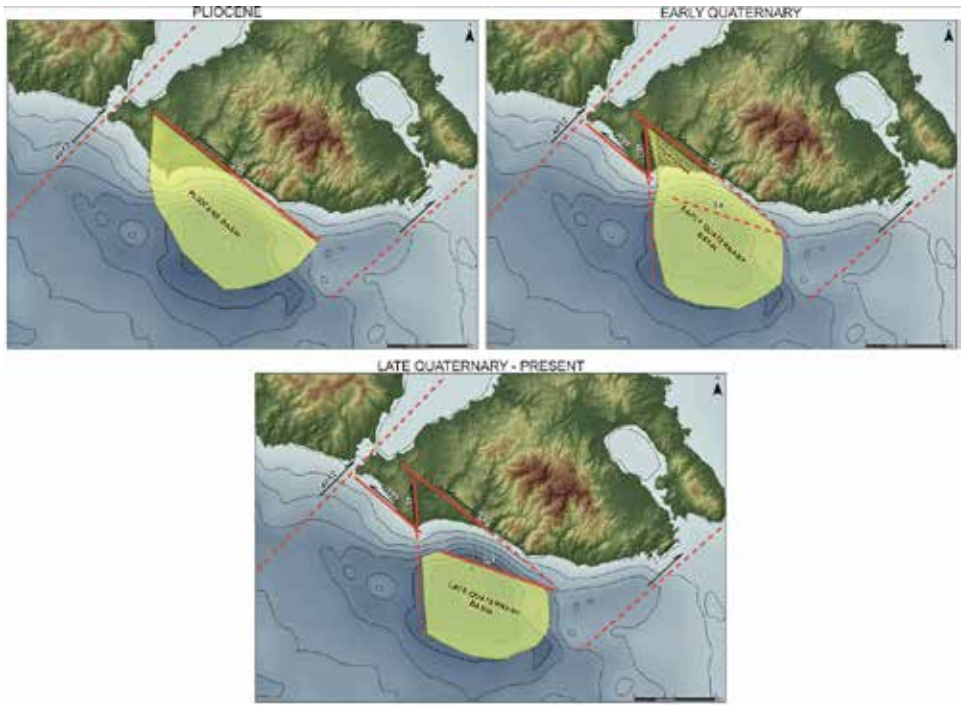

Figure 4. Proposed paleogeographic evolution of the basin in the study area. APFZ: Agia Paraskevi Fault Zone, VFZ: Vrisa Fault Zone, AFF: Agios Fokas Fault, VtF: Vatera Fault.

As regards the offshore LF, although the so far acquired data show a predominant normal slip character, it is considered quite possible for it to simulate the kinematic characteristics of almost all the fault zones mentioned in this study and act both as a normal and a strike – slip fault, which from the Pliocene until the present day, has greatly shifted the morphology of the study area.
The activity of the above structure is confirmed by the recent earthquake of June 2017 (Mw 6.3), with the seismic sequence taking place within the basin, in the hanging wall of the boundary fault (Kiratzi et al., 2018; Papadimitriou et al, 2018) and the focal mechanisms showing normal sense of shear (Kiratzi et al., 2018; Papadimitriou et al., 2018). According to the morphological data provided, this newly formed, offshore basin is probably delimited to the west by the offshore prolongation of the VtFZ, as the direction of both zones is similar.
In conclusion, it is noteworthy that both the VFZ and the AFFZ are regarded as segments or splays of the LF, collectively forming a comprehensive fault zone that governs the entire southern boundary of Lesvos Island and significantly contributes to the geological evolution of its southern region. It is evident that the strike orientations and kinematic characteristics of the mentioned fault zones, both onshore and offshore, align perfectly with the findings from prior research conducted in the North Aegean. Therefore, the kinematics of the fault network in the study area oscillates between strike-slip and extension, epitomizing a distinctly transtensional regime. This observation parallels the broader deformation occurring in the North Aegean region, attributable to the North Anatolian Fault and its extension into the Aegean Sea through its associated strands.

References

Armijo, R., Meyer, B., King, G. C. P., Rigo, A. & Papanastassiou, D. 1996. Quaternary evolution of the Corinth rift and its implications for the Late Cenozoic evolution of the Aegean. Geophysical Journal International 126:11-53.

Armijo, R., Meyer, B., Hubert, A., Barka, A., 1999. Westward propagation of the north Anatolian into the northern Aegean: timing and kinematics. Geology 27 (3), 267–270.

Beniest, A., Brun, J.P., Gorini, C., Crombez, V., Deschamps, R., Hamon, Y., Smit, J., 2016. Interaction between trench retreat and Anatolian escape as recorded by neogene basins in the northern Aegean Sea. Mar. Pet. Geol. 77, 30–42. https://doi.org/10.1016/j.marpetgeo.2016.05.011

Chatzipetros, A., Kiratzi, A., Sboras, S., Zouros, N., Pavlides, S., 2013. Active faulting in the north-eastern Aegean Sea Islands. Tectonophysics 597–598, 106–122. https://doi.org/10.1016/j.tecto.2012.11.026

Dewey, J. F. & Şengör, A. M. C. 1979. Aegean and surrounding regions: Complex multiplate and continuum tectonics in a convergent zone. Geological Society of America Bulletin 90:84-92.

Hecht, J., 1972. Geological map of Greece 1:50000, Sheet Plomari - Mytilene. I.G.M.E.

Hecht, J., 1974b. Geological map of Greece 1:50000, sheet Polychnitos. I.G.M.E.

Nomikou, P., Papanikolaou, D., Lampridou, D., 2021. The active tectonic structures along the southern margin of Lesvos Island, related to the seismic activity of July 2017, Aegean Sea, Greece. Geo-Mar Lett 41, 49 https://doi.org/10.1007/s00367-021-00723-6

Katsikatsos, G., Migiros, G., Triantaphyllis, M., Mettos, A., 1986. Geological structure of the internal Hellenides (East Thessaly - Southwest Macedonia, Eubea - Attica - Northern Cyclades islands and Lesvos). Geol. Geophys. Res. 191–212.

Kiratzi, A., 2018. The 12 June 2017 Mw 6.3 Lesvos Island (Aegean Sea) earthquake: Slip model and directivity estimated with finite-fault inversion. Tectonophysics 724–725, 1–10. https://doi.org/10.1016/j.tecto.2018.01.003

Koukouvelas, I.K., Aydin, A., 2002. Fault structure and related basins of the North Aegean Sea and its surroundings. Tectonics 21. https://doi.org/10.1029/2001TC901037.

Le Pichon, X., Angelier, J., 1979. The Hellenic arc and trench system: a key to the neotectonic evolution of the eastern Mediterranean area. Tectonophysics 60, 1–42.

Le Pichon, X., Angelier, J., 1981. The Aegean Sea. Philosophical Transactions of the Royal Society of London 300, 357–372.

Mascle, J., Martin, L., 1990. Shallow structure and recent evolution of the Aegean Sea: A synthesis based on continuous reflection profiles. Mar. Geol. 94, 271–299. https://doi.org/10.1016/0025-3227(90)90060-W

Papadimitriou, P., Kassaras, I., Kaviris, G., Tselentis, G.A., Voulgaris, N., Lekkas, E., Chouliaras, G., Evangelidis, C., Pavlou, K., Kapetanidis, V., Karakonstantis, A., Kazantzidou-Firtinidou, D., Fountoulakis, I., Millas, C., Spingos, I., Aspiotis, T., Moumoulidou, A., Skourtsos, E., Antoniou, V., Andreadakis, E., Mavroulis, S., Kleanthi, M., 2018. The 12th June 2017 Mw = 6.3 Lesvos earthquake from detailed seismological observations. J. Geodyn. 115, 23–42. https://doi.org/10.1016/j.jog.2018.01.009

Papazachos, B. C., Kiratzi, A. A., & Karacostas, B. G., 1997. Toward a homogeneous moment-magnitude determination for earthquakes in Greece and the surrounding area. Bulletin of the Seismological Society of America, 87(2), 474–483.

Pe-Piper, G., Piper, D.J.W., 1992. Geochemical variation with time in the Cenozoic high-k volcanic rocks of the island of Lesbos, Greece: significance for shoshonite petrogenesis. J. Volcanol. Geotherm. Res. 53, 371–387. https://doi.org/10.1016/0377-0273(92)90092-R

Pe-Piper, G., Piper, D.J.W., Zouros, N., Anastasakis, G., 2019. Age, stratigraphy, sedimentology and tectonic setting of the Sigri Pyroclastic Formation and its fossil forests, Early Miocene, Lesbos, Greece. Basin Res. 31, 1178–1197. https://doi.org/10.1111/bre.12365

Sakellariou, D., Tsampouraki-Kraounaki, K., 2019. Plio-quaternary extension and strike-slip tectonics in the aegean, Transform Plate Boundaries and Fracture Zones. Elsevier Inc. https://doi.org/10.1016/B978-0-12-812064-4.00014-1

Taymaz, T., Jackson, J., McKenzie, D., 1991. Active tectonics of the north and central Aegean Sea. Geophys. J. Int. 106, 433–490. https://doi.org/10.1111/j.1365-246X.1991.tb03906.x

Vacchi, M., Rovere, A., Zouros, N., Desruelles, S., Caron, V., Firpo, M., 2012. Spatial distribution of sea-level markers on Lesvos Island (NE Aegean Sea): Evidence of differential relative sea-level changes and the neotectonic implications. Geomorphology 159–160, 50–62. https://doi.org/10.1016/j.geomorph.2012.03.004

17th INTERNATIONAL CONGRESS of the Geological Society of Greece

BULLETIN OF THE GEOLOGICAL SOCIETY OF GREECE, SP. PUBL.

EXTENDED ABSTRACT 294

Discovering the geoheritage of Skiathos Island (Northern Sporades, Greece)

Soultanis K.[1], Soukis K.[1], Triantaphyllou M.V.[1]
(1) National and Kapodistrian University of Athens, Athens Greece, kimonasofficial@gmail.com

This paper attempts to probe and highlight the geoenvironmental attractions of Skiathos Island and to propose friendly geo-routes and accessible geo-locations that could appeal to visitors.

Skiathos Island belongs to the Northern Sporades located in north Aegean, Greece. It has an irregular, NE-SW elongated shape, stretching approximately 12 km in length and 6 km in width, with a hilly and undulating terrain. The highest peak, Mount Karafiltzanaka (433 m), and other smaller hills form a central spine running through the island, gradually sloping towards the coast. The island's northern part is steeper and more mountainous, with cliffs dropping sharply into the sea, while the southern part has gentler slopes and is more developed, with sandy beaches and natural harbors. The presence of weathered rock formations and thin soil layers supports dense pine forests and small seasonal streams that contribute to its lush, green environment. Skiathos features a well-developed coastal zone with numerous bays, peninsulas, small capes, and sandy shores formed by sediment transport and coastal processes.

Skiathos is situated in the back-arc area of the Hellenic Arc and comprises rocks belonging to the Pelagonian domain, a continental lithospheric block considered part of the Cimmerian ribbon continent, affected by the Late Jurassic - Early Cretaceous closure of the Vardar Ocean and the early Cenozoic Alpine deformation. The lower part includes late Paleozoic augen gneisses, para- and orthogneisses, amphibolites, and schists, occupying the central and western part, overlain by a Triassic-Jurassic marble and late Jurassic calc phyllites and slates, observed at the eastern and northern parts. The upper part is made of a transgressive late Cretaceous limestone observed at the central and northern parts of the island. (Ferentinos 1973; Jacobshagen and Wallbrecher 1986; Mountrakis 1986; Papanikolaou 2021)

We have identified and classified several key locations across the island, comprising distinct geosites that combine natural geoscientific monuments with aesthetic, naturalistic, cultural, historical, touristic and educational values (Figure 1). All included geosites have been assessed based on the criteria applied by Skentos (2012). The outcome of this assessment enabled the development of sustainable geo-routes (e.g., Spyrou et al., 2002; Triantaphyllou et al., 2023).

Figure 1. Geo-routes and geo-locations of Skiathos Island and the surrounding islets (Basemap: Esri Worldmap Imagery).

These sites exhibit significant geomorphological, mineralogical, tectonic, and historical interest. While primarily of local significance, they serve as an essential introduction for visitors and residents to engage with the island's diverse geoenvironment.

Beyond their scientific and educational value, these locations play a crucial role in advocating for the preservation of Skiathos' rich geological heritage. Some of these geosites form well-defined geo-routes, accessible by foot or vehicle, allowing visitors to immerse themselves in the island's breathtaking landscapes while exploring its geological diversity (Figure 2a-c). Others, more secluded and reachable only by sea, offer a unique opportunity to experience the island's untouched, rugged terrain, making them ideal destinations for daily excursions to remote and pristine coastal areas.

Figure 2a-c. a) Augen gneisses of the prealpine Pelagonian basement. b) Crenulation cleavage in the Late Jurassic calc phyllites. c) View of the narrow canal of the Strofilia lagoon.

References

Jacobshagen, V. and Wallbrecher, E., 1984. Pre-Neogene nappe structure and metamorphism of the North Sporades and the southern Pelion peninsula. Geological Society, London, Special Publications, 17(1), pp.591-602.

Manda, A.K., Horsman, E., 2015. Fracturesis Jointitis: Causes, Symptoms, and Treatment in Groundwater Communities. Groundwater 53(6), pp.836-840.

Ferentinos, G. C. 1973. The geology-petrology of the island of Skiathos. Bull. Geol. Soc. Greece, 10, 323-358.

Mountrakis, D., 1986. The Pelagonian zone in Greece: A polyphase-deformed fragment of the Cimmerian continent and its role in the geotectonic evolution of the eastern Mediterranean. The Journal of Geology, 94(3), pp.335-347.

Papanikolaou, D.I., 2021. Regional Geology Reviews The geology of Greece. Springer Nature.

Skentos, A. 2012. Geosites of Greece: Record, Schematic, Geological Regime and Geotouristic Assessment; National and Kapodistrian University of Athens: Athens, Greece.

Spyrou, E., Triantaphyllou, M.V., Tsourou, T., Vassilakis, E., Asimakopoulos, C., Konsolaki, A., Markakis, D., Marketou-Galari, D. and Skentos, A., 2022. Assessment of geological heritage sites and their significance for geotouristic exploitation: The case of Lefkas, Meganisi, Kefalonia and Ithaki Islands, Ionian Sea, Greece. Geosciences, 12(2), p.55.

Triantaphyllou, M.V., Firkasis, N., Tsourou, T.; Vassilakis, E., Spyrou, E., Koukousioura, O., Oikonomou, A., Skentos, A., 2023. "Geo-Archaeo-Routes" on the Island of Lemnos: The "Nalture" Experience as a Holistic Geotouristic Approach within the Geoethical Perspective», Geosciences 13, 143.

17th INTERNATIONAL CONGRESS of the Geological Society of Greece

BULLETIN OF THE GEOLOGICAL SOCIETY OF GREECE, SP. PUBL.

EXTENDED ABSTRACT 295

Cyclone Daniel's Impact: A Study of Geohazards in Meteora, Greece

Natalia Spanou[1]
(1) Hellenic Survey of Geology and Mineral Exploration (HSGME), Athens, Greece

Research Highlights

- Extreme weather events, such as Cyclone Daniel, significantly impact slope stability and increase the occurrence of geohazards, such as landslides, erosion, and flood-induced deposition of eroded materials.
- Understanding the mechanisms of geohazards can enhance risk mitigation strategies for affected communities.
- Evaluation of existing landslide susceptibility maps highlights the need for improved predictive tools in vulnerable regions.
-

Introduction/ Background

Cyclone Daniel, a severe weather event in September 2023, triggered extensive flooding, landslides, and associated phenomena across Central Greece. This event provides a unique case study for examining the link between extreme weather and the occurrence of geohazards. This analysis specifically focuses on the Meteora municipality, particularly the Municipal Units of Kleinovos, Kastania, and Aspropotamos, an area heavily impacted by landslide phenomena.

Detailed data on the geohazards that occurred in Meteora, meticulously collected through in-situ investigations, are analyzed. These data include the location, size, and characteristics of the geohazards. By examining these data, researchers aim to understand how the intensity of the cyclone and precipitation patterns affected slope stability in this region.

Existing landslide susceptibility maps for Greece are evaluated for the Meteora region. By comparing these maps with the actual landslide distribution, their effectiveness for the municipality is assessed, revealing areas that require adjustments.

Objectives

This study aims to achieve the following key objectives:

- Decipher Triggering Mechanisms: Identify specific meteorological factors associated with Cyclone Daniel that contributed to geohazards occurrences within the Meteora municipality.
- Inform Mitigation Strategies: Develop recommendations for improved geohazards risk mitigation strategies specific to Meteora, with potential applicability to other vulnerable municipalities.
- Validate Susceptibility Maps: Assess the accuracy of existing susceptibility maps in predicting landslide locations during the extreme weather event.
-

Methods

The detailed data on geohazard occurrences in Meteora, triggered by Cyclone Daniel, have been subjected to meticulous in-situ investigation and subsequent analysis. The dataset includes information on the location, dimensions, and characteristics of these phenomena. A total of 114 geohazard events were documented within the municipal boundaries of Meteora (Fig.1). These phenomena encompass a variety of processes, including rotational and translational slides, as well as soil and debris flows. Erosion in stream beds is also a common occurrence. Additionally, the accumulation of transported materials from the high sediment supply of the streams is another notable phenomenon (Spanou, 2024; Spanou, 2025a; Spanou 2025b).

The objective of this analysis is to assess the impact of the cyclone's intensity and precipitation patterns on slope stability within the region (Fig. 2). Additionally, recommendations for improved geohazard risk mitigation strategies specific to Meteora—with potential applicability to other vulnerable municipalities—are developed. Furthermore, the effectiveness of existing landslide susceptibility maps for the Meteora region has been evaluated. A comparison of these maps with the actual landslide distribution allows for an estimation of their accuracy for the municipality and identifies areas that may require adjustments (Apostolidis *et al.*, 2023).

Results

This study aimed to elucidate the mechanisms that precipitate geohazards in the Meteora municipality, which was significantly impacted by Cyclone Daniel. The specific meteorological factors triggering geohazard events within the municipality have been identified. Additionally, recommendations for enhanced geohazard risk mitigation strategies—tailored to Meteora and potentially applicable to other vulnerable municipalities—have been put forth. Finally, the accuracy of existing susceptibility maps in predicting landslide locations during extreme weather events was assessed (Spanou *et al.*, 2024).

Conclusions

Following the study, the most effective protection and mitigation measures were identified as follows:

- Surface and Subsurface Water Management: Implementation of surface water settlement projects and underground water drainage systems.
- Landslide-Specific Approaches: Adopting a case-by-case approach for selecting appropriate support works for landslides.
- Risk Demarcation: Conducting detailed demarcation studies to accurately identify and delineate areas already affected or at risk.
- Infrastructure Maintenance: Ensuring ongoing maintenance and repair of infrastructure along the road network—encompassing technical components, bridges, and other structures—to guarantee continued functionality and safety.

These measures provide a comprehensive framework for mitigating geohazard risks and enhancing public safety in vulnerable regions.

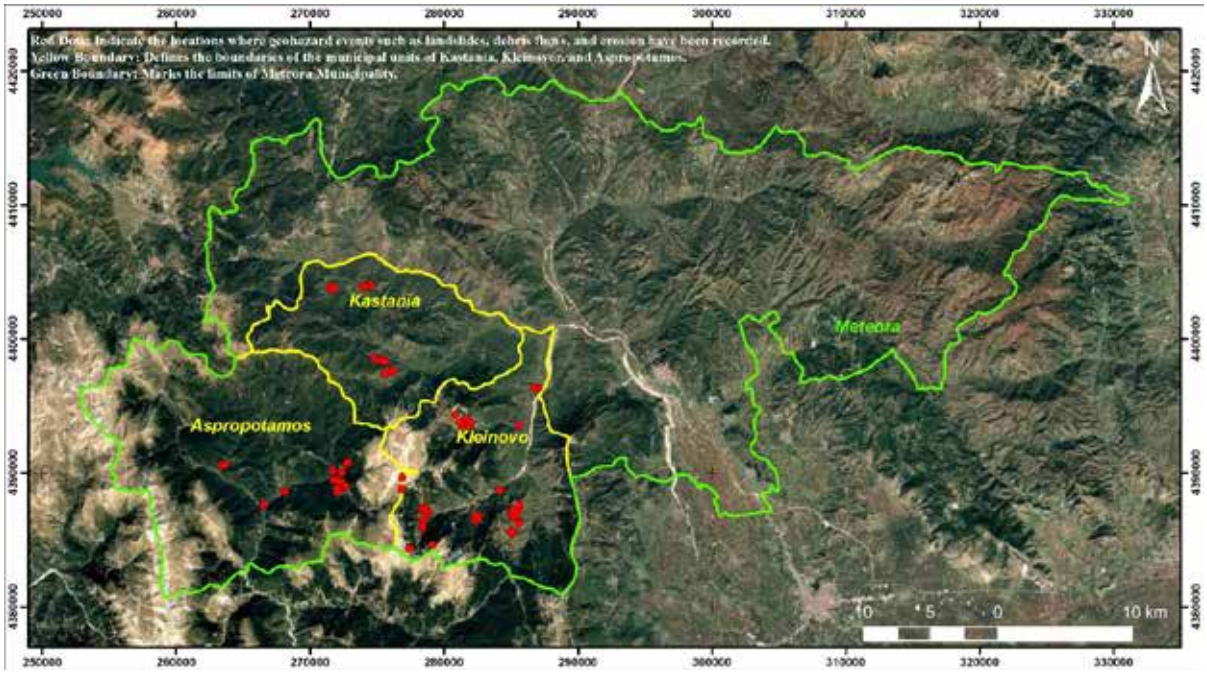

Figure 1. A total of 114 geohazard events were recorded in Meteora Municipality following Cyclone Daniel.

Figure 2. A few of the impacts of geohazards triggered by Cyclone Daniel in the Meteora Municipality.

References

Apostolidis, E., Spanou, N., Kavoura, K., Panagiotidou, F., Ieronymakis, V., Kokkali, P. 2023. Assessment of Landslide Susceptibility in Greece. Unpublished Report HSGME, T – 3273, Athens.

Spanou, N., 2024. Geotechnical Survey of Landslide Phenomena in the Municipal Communities of Krania, Kallirroi, Katafyto, and Chaliki of the Aspropotamos Municipal Unit of Meteora Municipality, Trikala Prefecture. Unpublished Report HSGME, T – 3296, Athens.

Spanou, N., Kavoura, K., Nikolaou, N., 2024. Cyclone Daniel's scars: a landslide analysis in Meteora, Greece. EUROENGEO 2024 - 4th European Regional Conference of IAEG, Dubrovnik, Croatia.

Spanou, N., 2025a. Geotechnical Survey of Landslide Phenomena in the Municipal Communities of Kastania, Amarantos, Ampelochori, and Matoneri of the Kastania Municipal Unit of Meteora Municipality, Trikala Prefecture. Unpublished Report HSGME, T – 3297, Athens.

Spanou, N., 2025b. Geotechnical Survey of Landslide Phenomena in the Municipal Communities of Ampelia, Kleino, Aidona, and Chrysomilia of the Kleinovo Municipal Unit of Meteora Municipality, Trikala Prefecture. Unpublished Report HSGME, T – 3298, Athens.

17th INTERNATIONAL CONGRESS of the Geological Society of Greece

BULLETIN OF THE GEOLOGICAL SOCIETY OF GREECE, SP. PUBL.

EXTENDED ABSTRACT 296

Combining Ground and UAV Mapping for GIS-Based Assessment of Flash Flood Impact Severity: Application of the FFISS to the 2009 and 2020 Evia (Greece) Floods

Nafsika Ioanna Spyrou [1], Michalis Diakakis [2], Spyridon Mavroulis [1], Georgios Deligiannakis [3], Emmanuel Andreadakis [1], Christos Filis [1], Evelina Kotsi [1], Zacharias Antoniadis [1], Maria Melaki [1], Marilia Gogou [1], Katerina-Navsika Katsetsiadou [1], Eirini-Spyridoula Stanota [1], Emmanuel Skourtsos [1], Emmanuel Vassilakis [2], and Efthymios Lekkas [1]

1 Department of Dynamic, Tectonic, Applied Geology, Faculty of Geology and Geoenvironment, School of Sci-ences, National and Kapodistrian University of Athens, 15784 Athens, Greece; nspyrou@geol.uoa.gr (N.I.S.); smavroulis@geol.uoa.gr (S.M.); eandreadk@geol.uoa.gr (E.A.); chfilis@geol.uoa.gr (.C.F.); ekotsi@geol.uoa.gr (E.K.); zaxarias@gmail.com (A.Z.); mariamelaki@gmail.com (M.M.); mgogou@geol.uoa.gr (M.G.); knavsi-ka@geol.uoa.gr (K.N.K.); estanota@geol.uoa.gr (E-S.S.); eskourt@geol.uoa.gr (E.S.); elekkas@geol.uoa.gr (E.L)
2 Department of Geography and Climatology, Faculty of Geology and Geoenvironment, School of Sciences, National and Kapodistrian University of Athens, 15784 Athens, Greece; diakakism@geol.uoa.gr (M.D.); evassilak@geol.uoa.gr (E.V.)
3 Department of Natural Resources Management and Agricultural Engineering, Agricultural University of Athens, 10447Athens, Greece; gdeligian@aua.gr (G.D.)

1. ntroduction

Flash floods are among the most destructive natural hazards, causing loss of life, infrastructure damage, and environmental harm, impacts expected to worsen with climate change, especially in the Mediterranean. Their sudden and localized nature makes systematic assessment difficult, particularly in urban and large-scale events (Merz et al., 2010; Petersen, 2001; Diakakis et al., 2017). The variability of impacts across different areas hinders the development of a standardized evaluation method. Existing approaches often target specific sectors, limiting a holistic understanding. A simple, multi-criteria system is needed to assess flash flood severity across events. (Marchi et al. 2023; Gourley et al., 2013; Boudou et al., 2016; Sîli et al., 2020). Lack of systematic impact data limits flood risk identification, relying on history and local knowledge. This weakens future predictions and mitigation efforts due to poor understanding of flood impacts. Using the Flash Flood Impact Severity Scale (FFISS), the study compares 2009 and 2020 floods to analyze severity patterns and improve preparedness (Schroeder et al., 2026; Boudou, 2016; Calianno et al., 2013; Diakakis et al., 2020).

2. Study area and flood events

The Lilas River catchment covers 249 km² in Evia Island (Greece), within two municipalities (Figure 1). It includes Vassiliko and nearby settlements, with a total population of about 16,500 residents (Hellenic Statistical Authority, 2021). Most of the area is forested, while the mid and lower sections support significant agriculture. The fertile Lilas Plain near the outlet has held historic agricultural and strategic importance. The Lilas catchment collects water from the southern and southwestern slopes of Mount Dirfi (1,743 m a.s.l.) and the surrounding Messapios mountains. Initially, the terrain is steep and rugged, but as the elevation decreases, the slopes become more gradual. Covering an area of 259.19 km², the drainage network is denser in the upper reaches, while in the lower elevations, the floodplain and main river channel have experienced flooding in the past (Figure 2).

2.1. The 2009 Flood

The 2009 flood in central Evia was triggered by intense rainfall, with 376.8 mm recorded in 18 hours at Steni. It caused major damage to infrastructure, homes, and vegetation, including roof collapse and severe erosion. Sediment deposition altered the river's flow, uprooted vegetation worsened flooding, and vehicles were swept away. The event underscored the need for better flood management, infrastructure upgrades, and ecosystem restoration (Meteo, n.d.).

2.2. The 2020 Flood

On August 8, 2020, a persistent storm system brought extreme rainfall to central Evia, with 300 mm recorded at Steni. The flood devastated the Lilas catchment resulting in damage to homes, roads, bridges, and farms and five fatalities. Infrastructure failures disrupted emergency response, while erosion reshaped riverbanks and reduced water capacity. The event revealed the need for resilient infrastructure, ecological restoration, and better flood preparedness (Lekkas et al., 2020; Mavroulis et al., 2021).

Figure 1. Map of the Evia Island in the eastern part of Mainland Greece. The red frame indicates the study area affected by flash floods in 2009 and 2020.

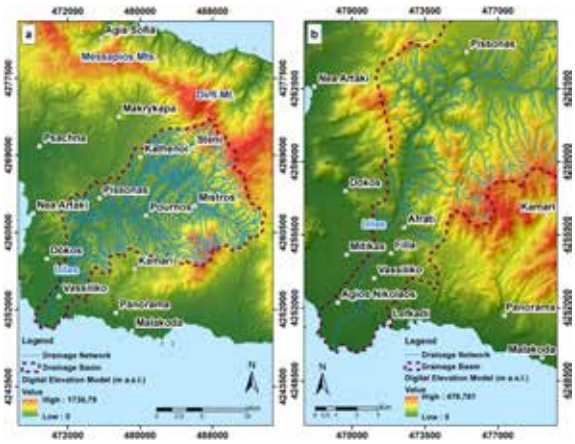

Figure 2. (a) Map showing the flood-affected Lilas catchment along with its drainage network and the elevation reaching over 1,730 m a.s.l. in the wider mountainous area comprising Messapios and Dirfi Mts located north of Lilas. (b) Map illustrating the lower part of the Lilas catchment, which was mainly affected by the 2009 and 2020 flash floods.

3. Methodology

3.1. Flash Flood Impact Data Collection

Flood impact data were gathered from official reports and media sources, alongside field surveys by the authors. These surveys used drones (DJI Mavic 2) and on-ground methods to capture high-resolution images and videos. UAS technology helped assess damage in areas too large or inaccessible for traditional methods. Geo-tagged data documented the location, type, and scale of damage with high spatial accuracy. Combining aerial and ground surveys ensured a complete picture of both widespread and localized impacts. Using the Unique Flood Impact Elements (UFIEs) enabled structured analysis, supporting better flood response and long-term planning (Spyrou et al., 2020; Spyrou et al., 2025; Andreadakis et al., 2020).

3.2. FFISS application

Flood impact data from both events were added in a GIS geo-database, with each entry (UFIE) mapped as a point and described by type, severity, and damage using FFISS (Diakakis et al. 2020). FFISS includes four impact categories:

(i) Built environment – damage to structures and infrastructure, from minor flooding to collapse or dam failure.

(ii) Mobile objects – displacement of items from lightweight to large vehicles.

(iii) Natural environment – effects on geomorphology, vegetation, agriculture, and pollution, from debris to severe contamination.

(iv) Population – from minor disruptions to fatalities. The scale consists of ten classes (Class I–X) to differentiate flood impact severity and avoid saturation seen in other models. It was developed through a global review of flash flood impacts, ensuring comprehensive coverage of diverse effects (Musson & Cecić, 2012; Diakakis et al., 2020).

3.3. Data processing and uncertainties

Only UFIEs with precise locations were used. Data lacking exact coordinates were excluded from analysis. Field data were GPS-logged with 3 m accuracy, while official records were mapped using building centroids or multiple points if needed. Visible pollution signs marked contamination, and with a 100 m grid, minor placement errors were acceptable unless exceeding cell size. (Diakakis et al., 2020; Spyrou et al., 2025).

4. Results

4.1. Application of the FFISS scale in the study area

According to the FFISS scale, the impacts of the 2009 Lilas River flood were systematically recorded and mapped across several affected areas, including Vassiliko, Afrati, and critical road networks. The transportation infrastructure experienced a range of damage severity, from road inundation and asphalt degradation to embankment erosion. Notably, partial and complete bridge failures led to the temporary isolation of entire communities during the peak of the flooding event (Figure 3). Varying levels of impact severity were recorded in the built environment, particularly at the level of individual buildings. In many inundated areas, flooding affected gardens, yards, pilotis, ground floors, and basements of both residential and commercial properties, significantly disrupting daily life. Structural damages ranged from collapsed fences to partial building failures, necessitating urgent search, rescue, and evacuation operations (Figure 4). The impact severity on mobile objects ranged from minor incidents, such as lightweight items and flower pots being displaced, to more significant cases like large waste bins carried by floodwaters. The severity escalated considerably with the displacement of vehicles, including cars and trucks swept into the sea, posing

serious risks to human life, particularly if occupants were present during the event (Figure 5). Finally, the observed impact severity in the natural environment included the uprooting and transport of low vegetation to riverbeds, roads, bridges, and residential areas, along with the flooding of higher ground plants. Severity increased with the uprooting of trees over 3 meters and significant geomorphological changes, such as soil erosion and deposition exceeding 3 meters in depth, which altered the morphology of the riverbed and delta (Figure 6).

Figure 3. Different flash flood impact severity classes on transportation. (a, b) Inundation of road surface in Vassiliko village (a) and Afrati settlement (b) (Class I). (c, d) Damages to the asphalt surface and levees scoured on the road Afrati – Pissonas (c) and in the Afrati settlement (d) (Class V). (e, f, g) Bridges suffered from structural damages and partial collapses in Vassiliko (e), Filla (f) and Afrati (g) (Class VII). (h) Bridge suffered from complete collapse in the settlement of Mistros (Class VIII).

Figure 4. Different flash flood impact severity classes on buildings. (a, b) Garden and pilotis had flooded in Lefkadi beach (Class I). (c) Yard walls and fences suffered from structural damages including total collapse in Vassiliko (Class IV). (d) House suffered from structural damages including failure of supporting elements in Vassiliko (Class VI).

Figure 5. Different flash flood impact severity classes on mobile objects. (a) Very light and small objects were transported at the beach of Agios Nikolaos (Class I). (b) Flower pots transported by floodwaters at Agios Nikolaos beach (Class II). (c) Large trash bins were carried away by floodwaters at Agios Nikolaos beach (Class III). (d, e, f), Cars were carried away during the flood in Vassiliko (Class IV). (g, h) Large tracks were transported by floodwaters in Afrati (Class VIII).

Figure 6. Different impact severity classes on the natural environment including (a, b) low vegetation uprooted and transported in the riverbed in Vassiliko (a) and on the bridge of Afrati (b) (Class II), (c) higher ground plants are affected by the flood in Vassiliko village (Class III), (d) tree smaller than 3 meters uprooted and carried away in the riverbed in Vassiliko (Class V), (e) large tree over 3 meters uprooted and destroyed on the riverbank in the village of Vassiliko (Class VI), (f, g) deposited material with a thickness of less than 3 meters in the riverbed downstream of Vassiliko village (f) and upstream of Afrati settlement (g) (Class VI), (h, i) eroded material with a thickness of more than 3 meters on the riverbank along the street of Afrati - Pissonas (h) and in Afrati (i) (Class VII).

Overall, 886 unique flood impact elements (UFIEs) were identified. We identified 187 and 699 UFIEs for the 2009 and the 2020 events, respectively. The frequency distribution across severity classes, highlighting key trends in the built and natural environments for the years 2009 and 2020. In the built environment, 2020 exhibited the highest frequency in Class III, with 104 events, indicating a notable concentration of lower-impact occurrences, while 2009 showed a peak in Class V with 15 events, reflecting more severe impacts. In the natural environment, both years recorded the highest frequency in Class IV. However, 2020 had a significantly higher count (116 events) compared to 2009 (57 events). This consistent dominance of Class IV, despite differing magnitudes, reveals a recurring vulnerability in the natural environment over time. Also, the highest frequency of severity for mobile objects was observed in Class IV, with 27 recorded events, indicating a notable concentration of impacts within this

class. Similarly, the human population sector showed the highest frequency in Class III, with 48 events, reflecting a moderate level of impact during the 2020 flood. No impact data were recorded for either sector in 2009, likely due to the absence of precise georeferenced information during that period.

4.2. Comparison of flood impact severity between 2009 and 2020

A comparison of impact severity between the two events shows both similarities and differences, influenced by environmental factors, land use changes, and discharge magnitude. In the built environment near the Lilas delta, the 2020 event showed lower severity than the 2009 one, largely due to post-2009 riverbed widening and the removal of damaged structures. However, in areas like Vassiliko, Filla, and Afrati, 2020 recorded higher severity, driven by greater discharge, erosion, and resulting structural damage to bridges. These findings underline the role of river morphology and infrastructure changes in shaping flood impact severity (Figures 7, 8).

Figure 7. Depiction of the morphological changes and the riverbed widening from the 2020 flood.

Figure 8. Illustration of the riverbed and estuary morphology of the Lilas River before the 2009 flood (above), as well as the destroyed buildings during the 2009 flood due to the widening of the riverbed (below).

The 2020 flood event resulted in a marked increase in impact severity in the area extending from Agios Nikolaos to Afrati and along the Afrati-Pissonas road. Elevated water levels and increased discharge significantly affected the river's geomorphology, leading to substantial sediment deposition within the riverbed and pronounced erosion along the riverbanks, phenomena not observed during the 2009 flood, which was characterized by lower discharge levels. This contrast in hydrological intensity and geomorphological outcomes is illustrated in Figure 9. Furthermore, no impact data concerning mobile objects or the human population were recorded during the 2009 event, although the absence of fatalities implies a lower severity level. Consequently, all relevant data and observations pertain exclusively to the 2020 flood. Notably, near the Afrati Bridge, high severity was recorded due to the floodwaters sweeping away heavy trucks and bulldozers from a nearby business (Figure 10).

Figure 9. A downstream view of the Vassiliko bridge, illustrating the estimated maximum water levels during the 2009 and 2020 flood events (indicated by white and yellow lines), based on high-water marks identified during post-flood surveys. The blue arrow indicates the river flow direction.

Figure 10. Illustration of the Afrati Bridge featuring bulldozers and large trucks that were carried away by the floodwaters. The yellow arrow indicates the river flow direction.

Across the entire impacted region and within all sectors of flood impact, the 2020 flood event was characterized by high-severity classifications in areas upstream of Agios Nikolaos, extending toward the settlement of Pissonas. In contrast, the 2009 flood exhibited lower-intensity classifications overall, with the notable exception of the Lilas River delta. This variation is primarily attributed to the fact that, in 2009, the built environment in the delta area suffered extensive damage, as several structures that

existed at the time were destroyed, thereby elevating the severity levels. By 2020, these structures had been removed, leading to a notable reduction in impact severity.

In addition, elevated severity classes (Classes V to VIII) were recorded in 2020 along the stretch from Agios Nikolaos to Afrati, due to extensive geomorphological alterations, significant damage to the built environment, particularly bridges, and the displacement of large mobile objects. Conversely, in 2009, no impact severity was documented in the areas of Agios Nikolaos and Lefkandi. Downstream of Pissonas, higher severity classifications (Class VIII) were also recorded in 2020 compared to 2009, mainly due to pronounced geomorphological changes and widespread vegetation disturbance caused by increased surface runoff. As for the Lilas River delta, severity classifications in 2020 were generally lower (Classes II–V) than those recorded in 2009 (Classes V–VIII) (Figure 11).

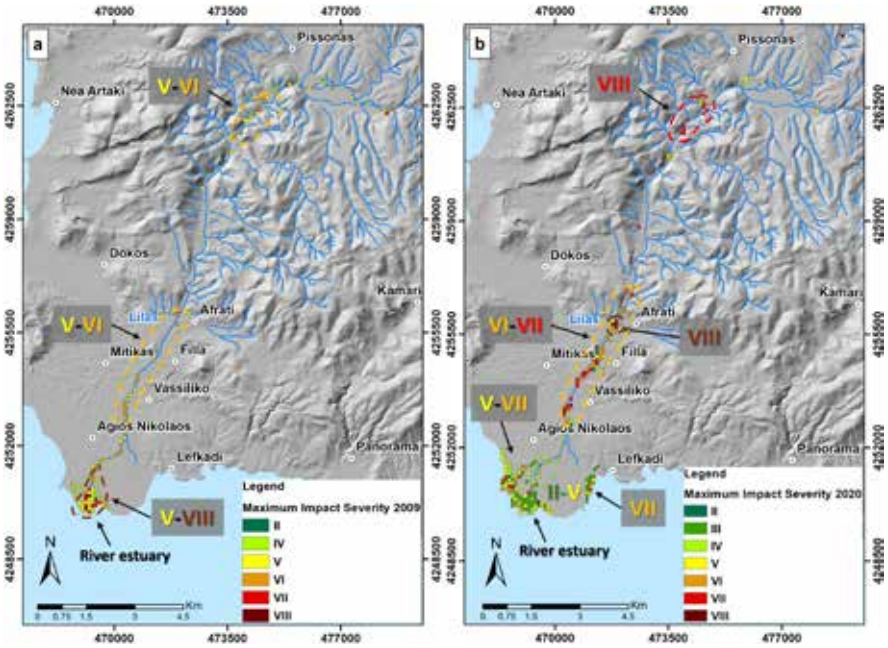

Figure 11. Comparison of maximum flash flood impact severity in the affected area of 2009 (a) and 2020 (b). The zones of impact concentration are divided as follows: at the estuary of the Lilas River, upstream of the Vassiliko bridge and downstream of Filla, in Afrati, and along the road Afrati-Pissonas.

5. Conclusions

This study applied the FFISS scale with four categories (built environment, natural environment, mobile objects, and population) and ten severity classes to assess two flood events in 2009 and 2020. Advanced technologies, including drones and ground-based observations, were used to capture high-resolution imagery and data across the affected areas. The FFISS scale allowed for a detailed comparison of both events, revealing a range of severity from classes II to VIII. While the 2009 flood had higher severity near the Lilas River delta, the 2020 flood impacted a wider area, including regions near the Vassiliko bridge and Pissonas. The 2020 flood was more intense, with increased discharge, higher flow velocities, and severe impacts such as sediment deposition, bank erosion, and bridge collapse. In 2009, riverbed widening near the delta affected the built environment, increasing the severity, but the absence of these structures in 2020 reduced impacts. The study demonstrated that the FFISS scale is useful even without geo-referenced data, as seen in the 2009 flood's movable objects and population sectors. The 2020 flood, however, involved significant displacement of large vehicles and fatalities, highlighting increased risks. The findings suggest that riverbed widening and flood mitigation measures, including hydraulic structures and retention measures upstream, are essential to reduce future flood risks.

References

Andreadakis, E.; Dakakis, M.; Vassilakis, E.; Deligiannakis, G.; Antoniadis, A.; Andriopoulos, P.; Spyrou, N-I.; Nikolopoulos, E. Unmanned aerial systems-aided post-flood peak discharge estimation in ephemeral streams. Journal of Remote Sensing. 2020, 12, 24, 4183. https://doi.org/10.3390/rs12244183

Boudou, M. Approche multidisciplinaire pour la caractérisation d'inondations remarquables: Enseignements tirés de neuf évènements en France (1910-2010). Environnement et Société. Université Paul-Valéry Montpellier III 2016.

Boudou, M.; Lang, M.; Vinet, F.; Coeur, D. Comparative hazard analysis of processes leading to remarkable flash floods (France, 1930–1999). J. Hydrol. 2016, 541, 533–552. https://doi.org/10.1016/j.jhydrol.2016.05.032

Calianno, M.; Ruin, I.; Gourley, J.J. Supplementing flash flood reports with impact classifications. J. Hydrol. 2013, 477, 1–16. https://doi.

org/10.1016/j.jhydrol.2012.09.036

Diakakis, M;Andreadakis, E.; Nikolopoulos, E.I.; Spyrou, N.I., Gogou, M.E.; Deligiannakis, G.; Katsetsiadou, N.K.;Antoniadia, Z.; Melaki, M.; Georgakopoulos, A.; Tsaprouni, K.; kalogiros, J.; Lekkas, E. An integrated approach of ground and aerial observations in flash flood disaster investigations. The case of the 2017 Mandra flash flood in Greece. International Journal of Disaster Risk Reduction, Elsevier 2019, 33, 290-309. https://doi.org/10.1016/j.ijdrr.2018.10.015

Diakakis, M.; Deligiannakis, G.; Antoniadis, Z.; Melaki, M.; Katsetsiadou, N.K.; Andreadakis, E.; Spyrou, N.I., Gogou, M. Proposal of a flash flood impact severity scale for the classification and mapping of flash flood impacts. Journal of Hydrology 2020, 590, 125452, ISSN 0022-1694. https://doi.org/10.1016/j.jhydrol.2020.125452

Gourley, J.J.; Hong, Y.; Flamig, Z.L.; Arthur, A.; Clark, R.; Calianno, M.; Ruin, I.; Ortel, T.; Wieczorek, M.E.; Kirstetter, P.E.; Clark, E.; Krajewski, W.F. A unified flash flood database across the United States. Bull. Am. Meteorol. Soc. 2013, 94, 799–805. https://doi.org/10.1175/BAMS-D-12-00198.1

Lekkas, E.; Spyrou, N.I.; Kotsi, E.; Filis, C.; Diakakis, M.; Cartalis, C.; Vassilakis, E.; Mavrakou, T.; Sartabakos, P.; Gogou, G.; Katsetsiadou, K.N.; Barsaki, V.; Lagouvardos, K.; Kotroni, V.; Karagiannidis, A.; Dafnis, S.; Parcharidis, I.; Karavias, A.; Bafi, D.; Gougoustamos, I. (2020). The August 9, 2020 Evia (Central Greece) Flood. Preliminary Report: National and Kapodistrian University of Athens 2020, ISSN 2653-9454. https://edcm.edu.gr/images/docs/newsletters/Newsletter_19_2020_Evia_flood.pdf.

Marchi, L.; Borga, M.; Preciso, E.; Gaume; E. Characterisation of selected extreme flash floods in Europe and implications for flood risk management. J. Hydrol. 2010, 394, 118–133. https://doi.org/10.1016/j.jhydrol.2010.07.017

Mavroulis, S.; Mavrouli, M.; Lekkas, E. Geological and hydrometeorological hazards and related disasters amid COVID-19 pandemic in Greece: Post-disaster trends and factors affecting the COVID-19 evolution in affected areas. Safety Science 2021, 138, 105236. ISSN 0925-7535. https://doi.org/10.1016/j.ssci.2021.105236

Meteo, n.d. Available online: https://www.meteo.gr/gmap.cfm (last accessed on 12 December 2024).

Merz, B.; Kreibich, H.; Schwarze, R.; Thieken, A. Review article “assessment of economic flood damage”. Nat. Hazards Earth Syst. Sci. 2010, 10, 1697–1724. https://doi.org/10.5194/nhess-10-1697-2010

Merz, B.; Kreibich, H.; Schwarze, R.; Thieken, A. Review article “assessment of economic flood damage”. Nat. Hazards Earth Syst. Sci. 2010, 10, 1697–1724. https://doi.org/10.5194/nhess-10-1697-2010

Musson, R.; Cecić, I. Intensity and Intensity Scales, in: Bormann, P. (Ed.). New Manual of Seismological Observatory Practice 2. IASPEI, GFZ German Research Centre for Geosciences, Potsdam 2012, 1–41. https://doi.org/10.2312/GFZ.NMSOP-2

Hellenic Statistical Authority (HAS), 2021. Available online: https://unece.org/fileadmin/DAM/stats/documents/ece/ces/ge.41/2000/files/Greece/Presentation%20of%20the%20census%202001.pdf (last accessed on 12 December 2024).

Petersen, M.S. Impacts of Flash Floods. In: Gruntfest, E., Handmer, J. (eds) Coping with Flash Floods. NATO Science Series, Springer 2001, 77. https://doi.org/10.1007/978-94-010-0918-8_2

Spyrou, N.I.; Stanota, E.S.; Diakakis, M.; Andreadakis, E.; Lekkas, E.; Vassilakis, E. Estimation of Flow Velocity During Flash Floods with the synergy of Unmanned Aerial Systems (UAS) data and Ground Observations: The Case of 2017 Mandra Flash Flood, Greece. EGU 2020 International Conference 4-8 May, Vienna 2020. https://doi.org/10.5194/egusphere-egu2020-17845

Spyrou, N. I., Diakakis, M., Mavroulis, S., Deligiannakis, G., Andreadakis, E., Filis, C., Kotsi, E., Antoniadis, Z., Melaki, M., Gogou, M., Katsetsiadou, K.-N., Stanota, E.-S., Skourtsos, E., Vassilakis, E., & Lekkas, E. (2025). Integrating Ground and UAV Mapping for GIS-Based Application of the Flash Flood Impact Severity Scale (FFISS) for the 2009 and 2020 Evia (Greece) Flash Floods. Applied Sciences, 15(3), 1100. https://doi.org/10.3390/app15031100

Schroeder, A.J.; Gourley, J.J.; Hardy, J.; Henderson, J.J.; Parhi, P.; Rahmani, V.; Reed, K.A.; Schumacher, R.S.; Smith, B.K.; Taraldsen, M.J. The development of a flash flood severity index. J. Hydrol. 2016, 541, 523–532. https://doi.org/10.1016/j. jhydrol.2016.04.005

Sîli, N.; Apostu, I.; Faur, F. Floods and their effects on agricultural productivity. Research Journal of Agricultural Science 2020, 52, 4.

Meteo, n.d. Available online: https://www.meteo.gr/gmap.cfm (last accessed on 12 December 2024).

17th INTERNATIONAL CONGRESS of the Geological Society of Greece

BULLETIN OF THE GEOLOGICAL SOCIETY OF GREECE, SP. PUBL.

EXTENDED ABSTRACT 297

Evaluating Airborne LiDAR and RGB Imagery for Accurate Shoreline Detection

Panagiotis Stamatis[1*], Michaela Doukari[1], Kostas Topouzelis[1]

(1) Department of Marine Sciences, School of the Environment, University of the Aegean, University Hill, 81100 Mytilene, Greece.

** Correspondence: p.stamatis@aegean.gr*

Abstract

Understanding and monitoring shoreline changes is critical for effective coastal zone management, particularly in regions experiencing dynamic erosion and accretion. This study evaluates the effectiveness of airborne LiDAR and RGB imagery acquired via Unmanned Aerial Systems (UAS) for accurate shoreline detection, focusing on Gavathas Beach, Lesvos Island, Greece. Both technologies were utilized to generate high-resolution Digital Elevation Models (DEMs) and orthophotographs, enabling precise delineation of the shoreline. The LiDAR data, collected using the YellowScan VX-15 system mounted on a DJI Matrice 600 Pro, provided dense 3D point clouds with centimeter-level accuracy. Simultaneously, RGB imagery was captured using a Sony Alpha 6000 camera synchronized with the LiDAR system. The RGB-derived orthophotographs facilitated visual interpretation and supported the identification of shoreline features under varying environmental conditions.

Digital Shoreline Analysis System (DSAS) was employed to quantify shoreline changes by comparing the extracted shorelines with reference data collected using a Differential GPS (DGPS) system. The results demonstrated that LiDAR-derived shorelines exhibited superior accuracy, with mean deviations of less than 0.5 meters from the reference data. RGB-derived shorelines showed slightly higher deviations due to challenges in image contrast and environmental lighting conditions but remained within acceptable thresholds for practical applications. This comparative analysis highlights the potential of integrating airborne LiDAR and RGB imagery for efficient and reliable shoreline mapping. The findings emphasize the advantages of LiDAR for its high spatial resolution and robust performance in complex coastal environments, while RGB imagery offers a cost-effective and operationally flexible alternative for areas with clear land-water boundaries. These insights contribute to the optimization of coastal monitoring practices and inform future applications of remote sensing technologies in shoreline management.

Keywords: LiDAR, UAV, 3D point cloud, Erosion, Remote Sensing

Introduction

Coastline mapping is an essential practice for understanding and managing coastal dynamics. Coastal zones worldwide are subject to significant changes due to natural and anthropogenic factors, including sediment transport, sea-level rise, and human intervention (Boak and Turner 2005). Monitoring these changes is critical for mitigating the risks associated with coastal erosion, flooding, and habitat loss (Klemas 2011). Traditional methods of monitoring, such as aerial photography and satellite imagery, have provided valuable insights into large-scale patterns but often lack the spatial resolution required for detailed shoreline mapping (Ford 2013; Kaichang Di, Jue Wang, Ruijin Ma et al. 2003). Measurement sensors deployed along coastlines, such as geodetic instruments and soil pressure gauges, also offer systematic data but are constrained by limited coverage and resource-intensive operations (El-Raey et al. 1999).

Over recent decades, advancements in remote sensing technologies have transformed coastal monitoring practices. Unmanned Aerial Systems (UAS) equipped with LiDAR sensors and RGB cameras now enable high-resolution, cost-effective data collection in dynamic and inaccessible coastal environments. Airborne LiDAR, in particular, is recognized for its ability to produce detailed Digital Elevation Models (DEMs) with high vertical and horizontal accuracy, making it an indispensable tool for analyzing complex topographies (Fiedler et al. 2021; Wozencraft and Millar 2005). For example, Wozencraft and Millar (2005) emphasized the critical role of LiDAR in capturing high-resolution elevation data for developing accurate DEMs, which significantly enhance shoreline delineation and coastal management practices.

Complementary to LiDAR, RGB imagery offers a more affordable and operationally flexible approach to shoreline mapping, particularly in areas with clear visual contrast between land and water. Gómez-Gutiérrez et al. (2024) demonstrated the effectiveness of combining RGB photogrammetry with LiDAR to generate accurate 3D models, even in the absence of ground control points (GCPs) (Lin et al. 2019). This integration highlights the growing potential of combining LiDAR and RGB technologies for coastal applications, as it balances precision and cost-efficiency.

In this study, we leverage the capabilities of airborne LiDAR and RGB imagery to evaluate their performance in shoreline mapping at Gavathas Beach, Lesvos Island, Greece. This site, characterized by its diverse coastal features—including sandy beaches, rocky outcrops, and vegetated dunes—offers a robust testing ground for these technologies. By employing Differential GPS (DGPS) as ground-truth data, we assess the accuracy of LiDAR- and RGB-derived shorelines and provide a comparative analysis of their strengths and limitations. The findings aim to contribute to the optimization of remote sensing methods for coastal monitoring and to inform sustainable coastal management strategies.

Materials and Methods

Study Area

The study area is Gavathas Beach, situated on the northwest coast of Lesvos Island, Greece. This location was selected for its diverse coastal morphology, characterized by a gently sloping sandy shoreline bordered by rocky outcrops and vegetated dunes. Gavathas Beach experiences minimal tidal variation, with a microtidal range typically less than 0.5 meters, providing stable conditions for data collection. The wave energy is generally low to moderate, influenced by the northwest orientation of the beach, which shelters it from prevailing winds and swells. This relatively undisturbed environment, with limited human activity, was ideal for uninterrupted data collection and minimized interference with the deployed equipment. The study focused on a 200-meter segment of the eastern beach, where the combination of sandy and rocky sections offered a valuable testing ground for evaluating the performance of airborne LiDAR and RGB imagery in shoreline mapping. The data collection was conducted on June 8, 2023, under clear skies and light winds, ensuring optimal conditions for aerial surveys.

Field data

The data collection process involved the coordinated use of airborne LiDAR and RGB imagery systems. A DJI Matrice 600 Pro Unmanned Aerial System (UAS) was employed as the platform for both sensors. The YellowScan VX-15 LiDAR system was mounted on the UAS to capture high-resolution 3D point clouds, providing detailed elevation data with centimeter-level accuracy. This system integrates a LiDAR sensor with advanced GNSS and IMU systems, ensuring precise georeferencing of the collected data. The TopCON Hiper VR GNSS system was utilized to achieve precise georeferencing and real-time measurement capabilities. Supporting multiple GNSS constellations (GPS, GLONASS, Galileo, BeiDou), it provided exceptional accuracy, reaching up to 8 mm in horizontal and 15 mm in vertical measurements under optimal conditions. This system ensured the reliable alignment of the airborne LiDAR data. Ground control points (GCPs) were established using the Hiper VR rover, which also measured the reference coastline for subsequent shoreline change analysis. Simultaneously, a Sony Alpha 6000 camera was mounted and synchronized with the LiDAR system to capture high-resolution RGB imagery. The camera underwent professional calibration to ensure optimal alignment with the LiDAR system, enabling seamless integration of image and elevation data during post-processing. The RGB images were used to create orthophotographs, which provided additional context for shoreline delineation. The data acquisition was conducted early in the morning to ensure stable environmental conditions and minimize potential disturbances. Ground control points (GCPs) were established using a Differential GPS (DGPS) system to provide accurate georeferencing for both LiDAR and RGB datasets. The UAV followed a pre-programmed flight path, capturing overlapping data to ensure complete coverage of the study area. This coordinated approach ensured the collection of high-quality datasets for subsequent analysis of shoreline changes.

Methodological framework

The methodological framework for this study integrates data acquisition, processing, and analysis to evaluate the accuracy of shoreline delineation using airborne LiDAR and RGB imagery, as shown in **figure 1**. The workflow began with field data collection, as described above, followed by pre-processing of the datasets. LiDAR data were first georeferenced and processed using Applanix's POSPac Mobile Mapping Suite to correct trajectory data and align the LiDAR point clouds accurately. The refined point clouds were imported into YellowScan's CloudStation software for visualization, noise filtering, and delineation of the study area. Key processes included the removal of redundant points, outliers, and the selection of the region of interest for analysis. The data were then exported in LAS format for compatibility with GIS software and further processing. The RGB imagery underwent a structured photogrammetric workflow using Agisoft Metashape. The process started with image alignment, where overlapping images were analyzed to generate a sparse point cloud. This was followed by the creation of a dense point cloud, which provided high-resolution 3D spatial data. An orthophotograph was subsequently generated, ensuring accurate representation of the study area. Ground control points were used to enhance the spatial accuracy of the outputs, and the resulting orthophotographs were exported in GeoTIFF format for integration into GIS platforms.

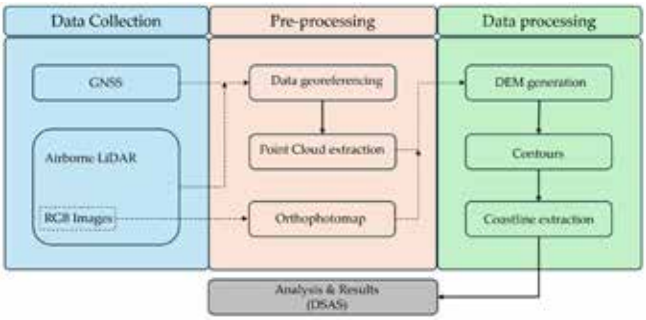

Figure 1. Methodology flowchart.

The data processing workflow involved generating high-resolution Digital Elevation Models (DEMs), extracting elevation contours, and analyzing shoreline changes using the Digital Shoreline Analysis System (DSAS). Initially, LAS files derived from LiDAR pre-processing were imported into ArcGIS Pro for further analysis. These georeferenced point clouds were visualized using the LAS Dataset Layer tool, enabling a detailed overlay of elevation data on basemaps of the study area. The creation of DEMs utilized the LAS Dataset to Raster tool in ArcGIS Pro, which transformed the elevation points into a continuous raster format. The interpolation method was configured to Binning (Natural Neighbor), and a cell size of 0.5 meters was selected to balance high resolution with computational efficiency. The Z-values from the LAS files represented elevation data, and the resulting raster was exported as a GeoTIFF file, capturing the intricate topography of the coastal zone. From these DEMs, elevation contours were extracted using the Contour tool in ArcGIS Pro. Contours provided a vectorized representation of elevation data, simplifying the interpretation of topographic variations. The contour interval was set to 0.5 meters, reflecting fine-scale changes in coastal morphology, and the base contour value was aligned with the minimum elevation within the DEM. The resulting contours were saved in ESRI Shapefile format, ensuring compatibility with spatial analysis tools. These contours served as a critical reference for shoreline delineation by identifying the contour line closest to the mean sea level (MSL). The integration of DEMs and contours enabled a comprehensive examination of the coastal environment, providing precise inputs for shoreline extraction and subsequent DSAS analysis. This systematic approach ensured that the spatial data maintained high accuracy and reliability, supporting detailed assessments of coastal dynamics and morphological changes.

The Digital Shoreline Analysis System (DSAS) was utilized within ArcGIS to quantify shoreline changes and assess accuracy. Baselines were manually digitized landward of the shorelines to serve as references. Transects were generated perpendicular to the baselines at regular intervals to measure deviations between LiDAR, RGB-derived shorelines, and the DGPS reference data. Metrics such as Net Shoreline Movement (NSM) and End Point Rate (EPR) were computed to evaluate temporal and spatial changes. Visual outputs, including charts and maps, were created to illustrate deviations and shoreline dynamics.

Results

For the evaluation of different mapping technologies, this study utilized data from airborne LiDAR and RGB imagery, which were processed to generate high-resolution Digital Elevation Models (DEMs) and elevation contours. These data were georeferenced using a GNSS base station, a GPS rover, and ground control points strategically placed within the study area to ensure accuracy. Additionally, on the day of data acquisition, the shoreline was recorded using DGPS as a reference line, serving as the benchmark for validating results from the airborne sensors. Table 1 summarizes the detected shorelines from DGPS, RGB imagery, and airborne LiDAR, focusing on their ability to delineate features such as the Instantaneous Shoreline, Intermediate Shoreline, and Wave Runup.

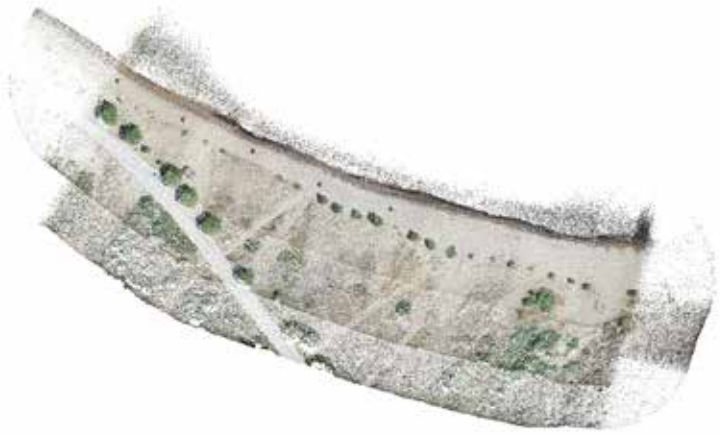

Figure 2. Results of airborne LiDAR: Colorized point cloud.

Airborne LiDAR showcased outstanding capability in shoreline mapping, delivering high spatial resolution and accuracy across extensive coastal areas. The method excelled in identifying key shoreline features, including the instantaneous shoreline, wave runup, and intermediate shoreline, with minimal deviations. Its deployment on a UAV platform enabled rapid data acquisition with consistent coverage, even in complex and dynamic coastal environments. The coastline derived from LiDAR data demonstrated

a mean deviation of just 0.5 meters when compared to the DGPS reference, emphasizing its precision. Moreover, the wave runup and intermediate shoreline were accurately captured, reflecting the system's ability to resolve fine-scale topographic variations. **Figure 2** highlights the outcomes of LiDAR data processing, showcasing the raw point cloud colored with aerial RGB imagery and **figure 3** shows the corresponding Digital Elevation Model (DEM) with extracted contours on the right, which were used to delineate the final shoreline.

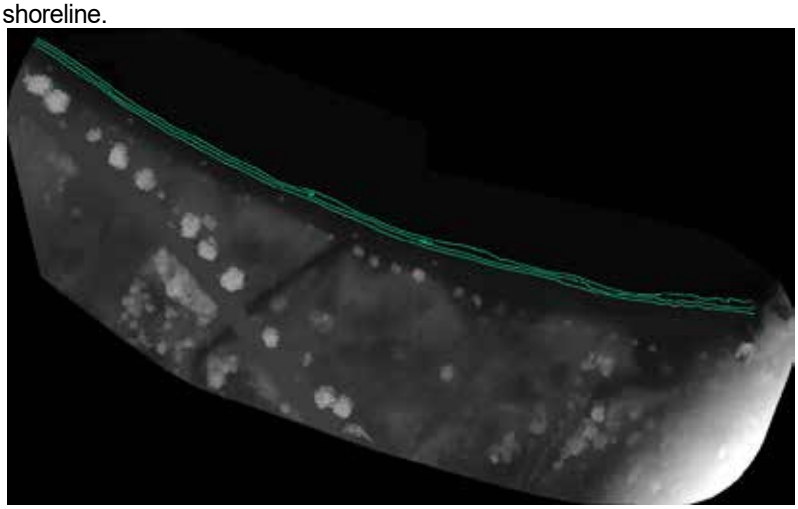

Figure 3. Results of airborne LiDAR: Digital Elevation Model (DEM) and elevation contours.

The RGB imagery captured by the mounted Sony Alpha 6000 camera on the UAV proved effective in generating a high-resolution orthophotomap, providing a visual reference for shoreline extraction, as shown in **figure 4**. However, this method was more prone to errors influenced by lighting conditions and image contrast. The approach performed best in areas with distinct land-water boundaries, where photogrammetric techniques delivered accurate results. Nevertheless, the shoreline derived from the RGB orthophotomap exhibited a larger deviation from the DGPS reference, with a mean offset of approximately 1.5 meters. This discrepancy was primarily attributed to difficulties in identifying clear shoreline boundaries in regions with low contrast. **Figure 5** presents the Digital Elevation Model (DEM) and the extracted elevation contours are shown, which were employed for precise coastline delineation.

Figure 4. RGB imagery results: Orthophotomap.

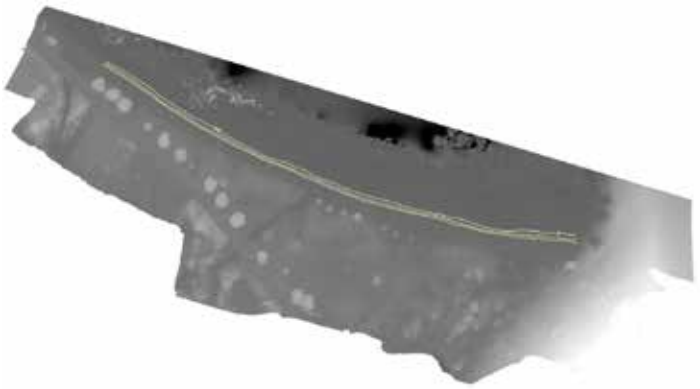

Figure 5. RGB imagery results: Digital Elevation Model (DEM) and elevation contours.

The analysis results demonstrate that airborne LiDAR provides superior accuracy and precision in delineating coastal features compared to the RGB imagery. LiDAR data achieved a mean deviation of only 0.5 meters from the DGPS reference coastline, showcasing its exceptional capability in capturing fine-scale topographic details. This accuracy is particularly evident in the identification of critical shoreline features, such as the instantaneous shoreline, wave runup, and intermediate shoreline. The ability of the LiDAR system to generate high-resolution Digital Elevation Models (DEMs) and extract detailed elevation contours further highlights its effectiveness in coastal monitoring. In contrast, the RGB-derived orthophotomap, while offering valuable visual context, exhibited a larger deviation from the DGPS reference. The mean offset of approximately 1.5 meters was primarily attributed to limitations in photogrammetric processing, especially in areas with low contrast or ambiguous land-water boundaries.

These challenges were particularly evident in vegetated or shadowed regions, where the RGB imagery struggled to distinguish the shoreline accurately. Despite these limitations, the RGB orthophotomap proved to be a cost-effective and operationally flexible alternative for areas with well-defined shoreline features. In **figure 6**, we can observe the coastlines detected using the RGB sensor (on the left) and airborne LiDAR (on the right).

Figure 6. Results of coastline detection: (Left) Coastlines from Orthophotomap; (Right) Coastlines from airborne LiDAR.

The DSAS analysis revealed consistent trends between the LiDAR and RGB-derived shorelines, with LiDAR consistently outperforming RGB in terms of accuracy. The transects generated across the study area showed that the maximum deviation between the LiDAR and RGB-derived shorelines reached up to 2.1 meters in areas with complex coastal features, such as rocky outcrops or densely vegetated dunes. However, in regions with clear visual contrast between land and water, the RGB orthophotomap aligned closely with the LiDAR data, demonstrating its potential for efficient shoreline mapping in less challenging environments. **Figure 7** illustrates the results of the DSAS analysis. The baseline and transects used for measuring deviations between the LiDAR- and RGB-derived shorelines are displayed, providing an overview of the study area. **Figure 8** demonstrates a close-up section that highlights the alignment of the shorelines, clearly showing the areas where deviations are most pronounced. The LiDAR data precision in capturing subtle elevation changes is evident in its ability to detect features such as the wave runup and intermediate shoreline, which are less distinct in the RGB-derived data.

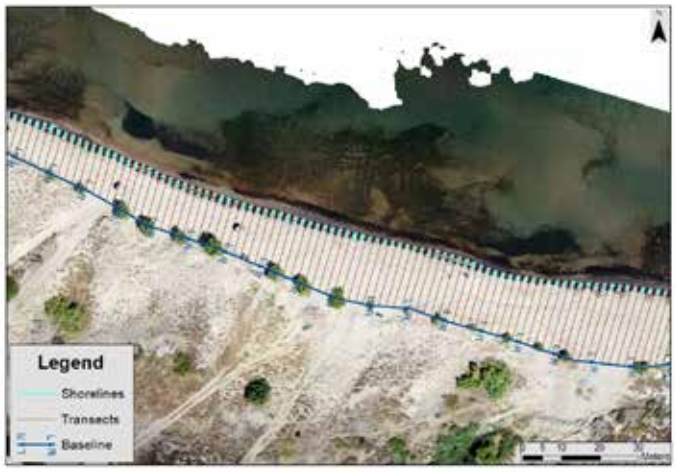

Figure 7. Results of the DSAS analysis: The entire study area, showing the baseline, transects, and shorelines.

In addition to accuracy, the efficiency of data collection and processing was another significant advantage of the airborne LiDAR system. The LiDAR system required only 7 minutes of flight time and approximately 30 minutes of preparation to complete the survey, compared to the longer photogrammetric processing time required for the RGB data. Moreover, LiDAR's elevated perspective and dense point cloud generation minimized the influence of environmental factors, such as lighting conditions or vegetation movement, which significantly impacted the RGB results.

Figure 8. Results of the DSAS analysis: A portion of the study area, highlighting the difference between the shorelines.

While both methods have their strengths, the comparative analysis underscores the superior performance of airborne LiDAR in terms of accuracy, efficiency, and versatility. However, the RGB orthophotomap remains a valuable tool for providing supplementary visual information and serves as a practical alternative for mapping in areas where LiDAR deployment may be constrained by budget or logistical challenges. These findings contribute to the ongoing development of integrated approaches for coastal monitoring, combining the strengths of both technologies to optimize shoreline detection and analysis.

Conclusions

The outcomes of this study confirm the efficacy and unique characteristics of airborne LiDAR and RGB imaging in coastal mapping applications. Airborne LiDAR demonstrated unparalleled accuracy and spatial coverage, closely aligning with the reference coastline captured via DGPS. Its ability to precisely capture dynamic shoreline features, such as the instantaneous shoreline, wave runup, and intermediate shoreline, highlights its suitability for complex coastal environments. The dense 3D point clouds generated by the LiDAR system enabled the creation of high-resolution Digital Elevation Models (DEMs) and detailed elevation contours, which are essential for understanding subtle topographic variations and monitoring morphological changes over time.

In contrast, RGB imaging, while a cost-effective and flexible alternative, exhibited greater sensitivity to environmental factors, including lighting conditions and surface contrast. These challenges resulted in slightly lower precision, with deviations from the reference coastline averaging 1.5 meters. Nevertheless, RGB orthophotomaps provided valuable visual context, particularly in areas with distinct land-water boundaries, and offered an operationally efficient method for shoreline delineation in less dynamic environments.

This comparative analysis underscores the importance of selecting the appropriate technology based on specific project needs. Airborne LiDAR excels in applications requiring high accuracy, extensive spatial coverage, and the ability to capture fine-scale details in dynamic coastal settings. Meanwhile, RGB imaging serves as a practical alternative for budget-constrained projects or areas where logistical challenges limit the deployment of LiDAR systems.

The integration of Differential GPS (DGPS) data as ground truth further validated the performance of both methods, providing a reliable benchmark for assessing their accuracy. Additionally, the use of the Digital Shoreline Analysis System (DSAS) enabled a comprehensive evaluation of shoreline changes, quantifying spatial discrepancies and providing insights into the dynamic processes shaping coastal environments. The ability to combine LiDAR and RGB data into an integrated analysis framework enhances our understanding of shoreline dynamics and supports the development of more robust coastal monitoring practices.

The broader implications of this research highlight the growing need for innovative and hybrid approaches to coastal management. As demonstrated, the complementary strengths of airborne LiDAR and RGB imaging can significantly improve the precision and reliability of coastal assessments. By leveraging these technologies in tandem, researchers and policymakers can better address the challenges posed by coastal erosion, sea-level rise, and other environmental changes.

This study contributes to the advancement of coastal monitoring methodologies by offering a detailed comparative framework for evaluating remote sensing technologies. The findings emphasize the importance of tailoring the choice of technology to the specific requirements of each project, ensuring the optimal balance between accuracy, cost, and operational feasibility. As environmental changes accelerate, integrating cutting-edge remote sensing tools will be crucial for sustainable coastal development and the implementation of effective erosion mitigation strategies.

Acknowledgments: We would like to express our gratitude to Professor Christos-Nikolaos Anagnostopoulos from the Department of Cultural Technology and Communication at the University of the Aegean for providing the Terrestrial Laser Scanner (TLS) used in this study. We also extend our thanks to the team from the Cartography & Geoinformatics Laboratory at the Department of Geography, University of the Aegean,

for their valuable assistance in the TLS data collection process. Special thanks go to Argyris Moustakas and Apostolos Papakonstantinou for their significant contributions during the fieldwork operations.

References

Boak, Elizabeth H., and Ian L. Turner. 2005. “Shoreline Definition and Detection: A Review.” Journal of Coastal Research 21(4): 688–703.

El-Raey, M., S. H. Sharaf El-Din, A. A. Khafagy, and A. I. Abozed. 1999. “Remote Sensing of Beach Erosion /Accretion Patterns along Damietta-Port Said Shoreline, Egypt.” International Journal of Remote Sensing 20(6): 1087–1106.

Fiedler, Julia W. et al. 2021. “Enhanced Surf Zone and Wave Runup Observations with Hovering Drone-Mounted Lidar.” Journal of Atmospheric and Oceanic Technology 38(11): 1967–78.

Ford, Murray. 2013. “Shoreline Changes Interpreted from Multi-Temporal Aerial Photographs and High Resolution Satellite Images: Wotje Atoll, Marshall Islands.” Remote Sensing of Environment 135: 130–40.

Kaichang Di, Jue Wang, Ruijin Ma, Ron Li et al. 2003. “Automatic Shoreline Extraction from Highresolution IKONOS Satellite Imagery.” ASPRS 2003 Annual Conference Proceedings 130(May): 1–4.

Klemas, Victor. 2011. “Remote Sensing Techniques for Studying Coastal Ecosystems: An Overview.” Journal of Coastal Research 27(1): 2–17.

Lin, Yi Chun et al. 2019. “Evaluation of UAV LiDAR for Mapping Coastal Environments.” Remote Sensing 11(24): 1–32.

Wozencraft, Jennifer, and David Millar. 2005. “Airborne Lidar and Integrated Technologies for Coastal Mapping and Nautical Charting.” Marine Technology Society Journal 39(3): 27–35.

17th INTERNATIONAL CONGRESS of the Geological Society of Greece

BULLETIN OF THE GEOLOGICAL SOCIETY OF GREECE, SP. PUBL.

EXTENDED ABSTRACT 298

Domestic Rainwater Harvesting Tanks´ Sizing under Climate Change Conditions in Nisyros Island

Stavropoulos T., Feloni E.

Department of Surveying and Geoinformatics Engineering, University of West Attica, 28 Ag. Spiridonos, 12243 Egaleo, Athens, Greece; tstavropoulos@uniwa.gr; efeloni@uniwa.gr

Introduction

The Mediterranean region has long been recognized as a climate change hotspot by numerous studies and researchers (e.g., Giorgi, 2006; Zittis et al., 2022). Arid and semi-arid areas, such as the Greek islands (Pnevmatikos and Katsoulis, 2006), face heightened challenges due to their unique climatic conditions (Köppen, 1936), which make them particularly susceptible to extreme heat, droughts, and water scarcity. Additionally, the growing influx of tourists, even on smaller islands like those in the Aegean Sea, further strains local water resources. This evolving reality underscores the urgent need for stakeholders to implement cost-effective strategies to ensure water security. In this context, the present study examines the performance of a rainwater harvesting system (RWHS) on Nisyros, a small island in the southeastern Aegean Sea, Greece, with a population of 1,048. Nisyros is renowned for its unique geological history and volcanic origin and is currently a candidate for UNESCO Global Geopark designation (Nomikou et al., 2023).

Aligned with Sustainable Development Goals 9 and 11, enhancing resilience in local communities and ensuring sustainable water management solutions are critical for the years ahead (UNDESA, 2024). Rainwater harvesting (RWH) is explored as a viable domestic-scale approach to supplement water needs for non-potable uses, reducing reliance on conventional freshwater sources. RWH is an economically feasible and relatively simple method to implement (Farreny et al., 2011) and has been widely utilized for centuries, dating back to ancient civilizations (Valdez et al., 2016). Depending on the level of treatment, RWHS can provide both potable and non-potable water for household and agricultural applications (Londra et al., 2015).

Methodology

This study employs a daily water balance model to evaluate the efficiency of an urban RWHS (Figure 1) using rooftop collection. The model is designed to determine the optimal rainwater tank dimensions necessary to store the collected rainwater while meeting a targeted percentage of household water demand, excluding drinking water. In this study, the household water consumption was determined to be 150 liters per capita per day. This value represents the average prescribed limits according to Government Gazette Issue B 174/1991, which sets a minimum consumption of 100 liters per day per person and a maximum of 200 liters per day per person. Additionally, according to the official data from ELSTAT (2011), most households consist of 1 to 3 members (Ncap). Therefore, scenarios are applied for Ncap = 1, Ncap = 2, and Ncap = 3.

The simulation tracks the daily water balance in the tank, considering both inflow from rainfall and outflow for domestic use, providing insights into the system's overall efficiency.

Daily rainfall data from the National Meteorological Service station on Nisyros were used for the available period from 2017 to 2023, spanning six hydrological years. This timeframe aligns with the German standard DIN 1989-1 (2002), which recommends a minimum of 5 to 10 years of rainfall data for RWHS dimensioning. The rainfall station was selected based on data availability, completeness, and geographic relevance, ensuring accuracy in tank sizing calculations.

The water balance equation applied in this study is:

$$S_t = S_{t-1} + R_t - D_t, 0 \leq S_{t-1} \leq V_{tank}$$

where: St is the stored volume at the end of t day (m^3); St-1 is the stored volume at the beginning of t day (m^3); Rt is the daily harvested (added) rainwater volume at the end of t day (m^3); Dt is the daily water demand at the end of t day (m^3); and Vtank the capacity of the rainwater harvesting tank (m^3).

To enhance the accuracy of the system's spatial assessment, mapping tools such as ArcGIS and Google Earth Pro were utilized to calculate the available rooftop catchment area of buildings (Durgasrilakshmi et al., 2018). This approach ensures that the estimated collection areas reflect real-world conditions.

Additionally, future climate projections were incorporated to assess RWHS performance under climate change conditions. Two Representative Concentration Pathways (RCPs) were examined: RCP 4.5 (moderate emissions scenario) and RCP 8.5 (high emissions scenario). Future rainfall data for the period 2026–2060 were obtained from the DEAR Clima database (DEAR-Clima-2024).

Three main scenarios were investigated, varying in household size and catchment area:

- A single-person household with a rainwater collection area of 20–120 m².
- A two-person household with a rainwater collection area of 20–120 m².
- A three-person household with a rainwater collection area of 20–120 m².

These scenarios provide a comprehensive evaluation of RWHS effectiveness under different household and climate conditions, offering valuable insights for sustainable water management on Nisyros.

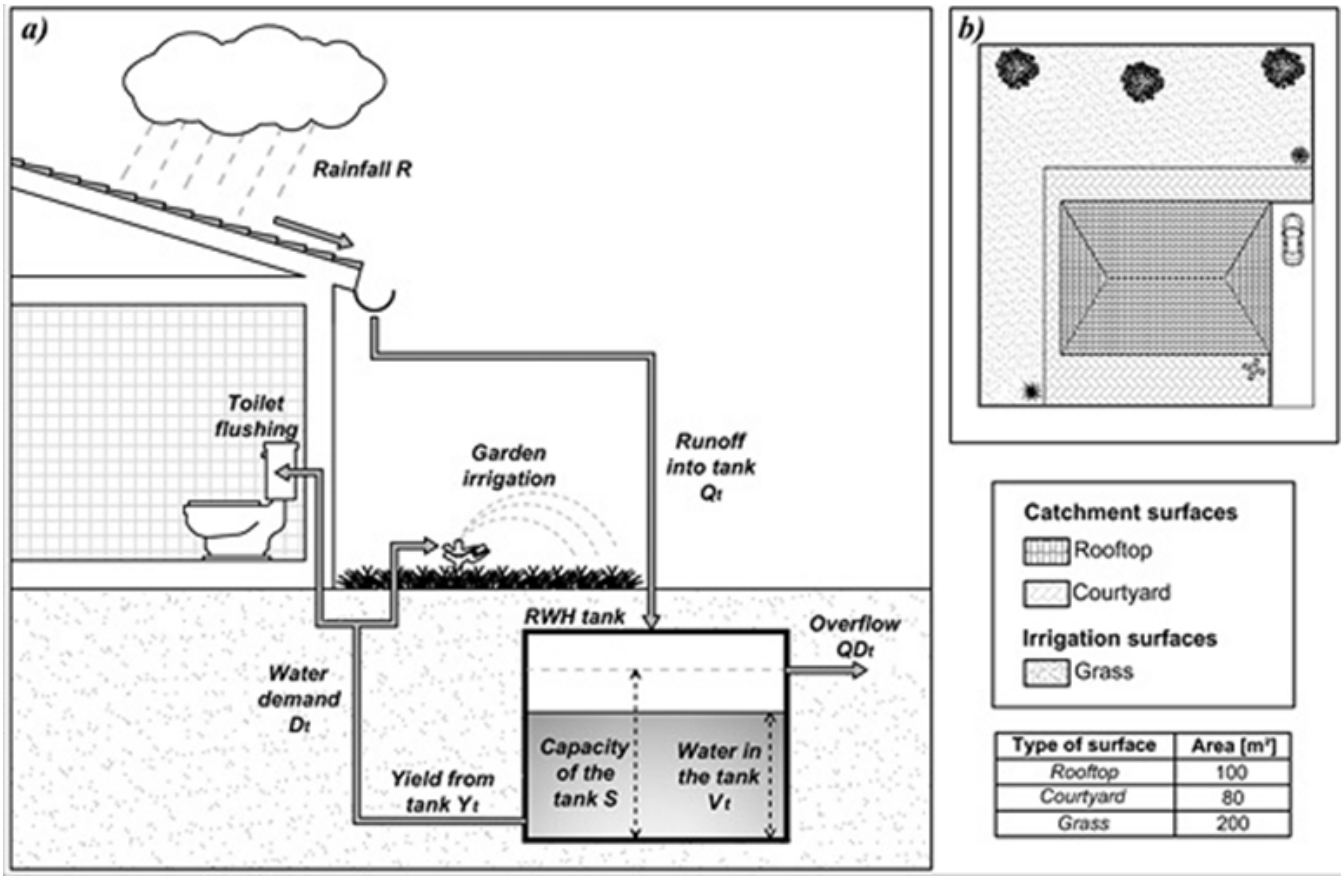

Figure 1: RWHS scheme (Source: Liuzzo et al., 2016)

Results

A. Results for historical timeseries

Figure 2 illustrates the results for the first scenario (single-person household), showing that system reliability ranges from 38% to 100%. The smallest rainwater collection area that ensures 100% reliability is 40m², with a tank capacity of 30m³. Additionally, the smallest tank volume that achieves full reliability is 5m³ when paired with a 60m² collection area. In general, for collection areas between 60 and 120m², the system consistently reaches 100% reliability for a single-person household, with tank volumes (Vtank) varying from 5 to 30m³. Notably, a significant shift in system performance is observed for collection areas between 20 and 40m², while at 20m², full reliability is not attained.

For the second scenario (Figure 3), which considers a two-person household, system reliability ranges from 14% to 100%. Compared to the first scenario, minimum efficiency is notably reduced due to the increased water demand. A sharp transition in system efficiency occurs for collection areas between 20 and 100m². Full reliability is achieved for households with collection areas of 100m² and 120m², with tank capacities between 10 and 30m³. The table below details the combinations of tank volume and collection area that ensure full reliability.

In the third scenario (Figure 4), representing a household with three members, reliability values range from 6% to 82%. Unlike the previous cases, full reliability is not achieved under any configuration. Additionally, a pronounced shift in system reliability is observed across collection areas ranging from 20 to 120m².

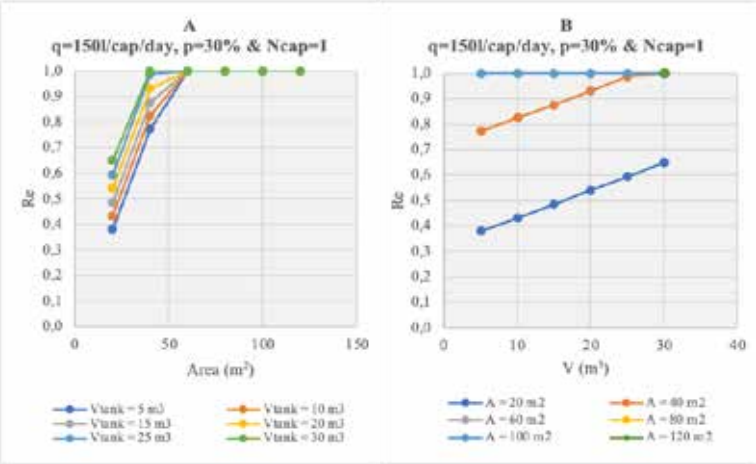

Figure 2. Reliability of demand coverage by the studied rainwater harvesting system for an average daily demand of q=150 l/cap/day, a demand coverage percentage of p=30%, and Ncap=1, with water collection areas ranging from 20 to 120 m². A: Reliability as a function of collection area range. B: Reliability as a function of tank volume.

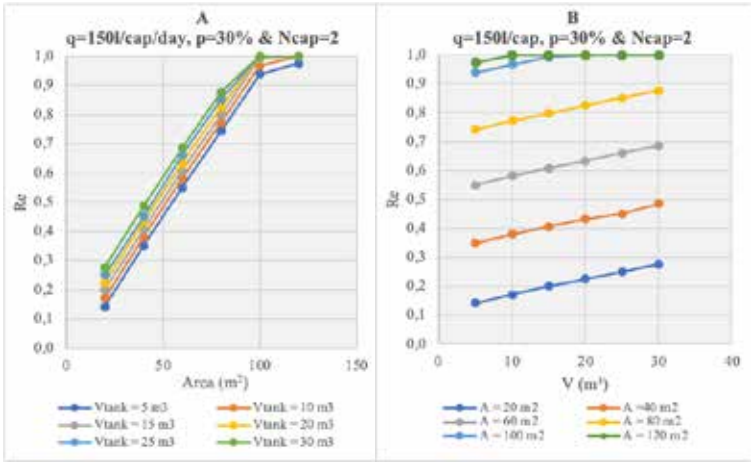

Figure 3. Reliability of demand coverage by the studied rainwater harvesting system for an average daily demand of q=150 l/cap/day, a demand coverage percentage of p=30%, and Ncap=2, with water collection areas ranging from 20 to 120 m². A: Reliability as a function of collection area range. B: Reliability as a function of tank volume.

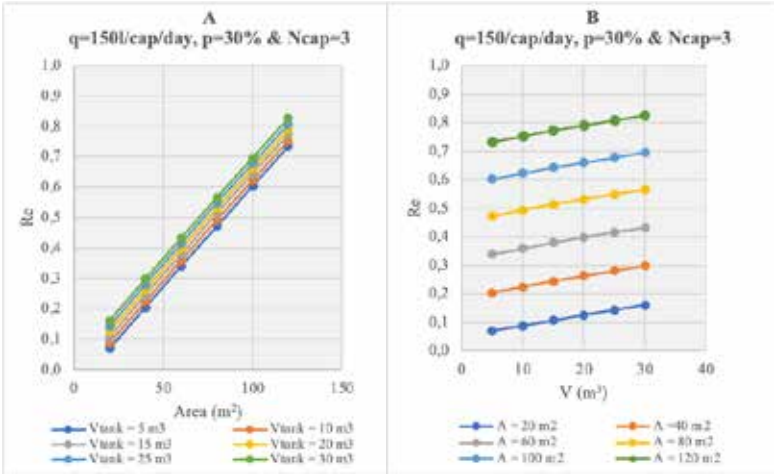

Figure 4. Reliability of demand coverage by the studied rainwater harvesting system for an average daily demand of q=150 l/cap/day, a demand coverage percentage of p=30%, and Ncap=3, with water collection areas ranging from 20 to 120 m². A: Reliability as a function of collection area range. B: Reliability as a function of tank volume.

B. Results for future climatic scenarios

In most scenarios involving a two-person household, the system successfully meets the target of supplying 30% of the total water demand. The water collection area (A) is identified as a critical factor, with smaller collection areas leading to lower reliability. Regarding the rainwater tank volume (Vtank), increasing the storage capacity results in only a marginal improvement in system reliability.

For households with three members, full reliability is achieved in certain cases under the RCP 4.5 climate scenario. However, under the RCP 8.5 scenario, a slight decline in reliability is observed compared to RCP 4.5, which is in accordance with the negative trends of rainfall patterns, indicating a potential impact of future climate conditions on system performance.

Table 1: Combinations of minimum rainwater collection areas and rainwater tank volumes for full system efficiency under the scenario Ncap=2.

	A (m^2)	Vtank (m^3)
Historic Time Series	100	20
RCP 4.5	60	5
RCP 8.5	60	5

Table 2: Combinations of minimum rainwater collection areas and rainwater tank volumes for full system efficiency under the scenario Ncap=3.

	A (m^2)	Vtank (m^3)
Historic Time Series	-	-
RCP 4.5	80	5
RCP 8.5	80	10

Conclusions

The study demonstrated that the reliability of the rainwater harvesting system is highly sensitive to both the collection surface area and tank volume. For the historical rainfall time series (2017–2023), reliability increased with larger collection areas and storage capacities. A single-person household achieved full reliability with a 40m² collection surface and a 30m³ tank, while the smallest volume ensuring 100% reliability was 5m³ with a 60m² surface. In the two-person household scenario, full reliability was reached at 100m² with a 20m³ tank, with the minimum tank volume ensuring complete reliability being 10m³ for a 120m² surface. However, for three-member households, full reliability was not achieved due to higher water demands. Regarding future climate projections (2026–2060), the system generally showed improved reliability under the RCP 4.5 and RCP 8.5 scenarios compared to historical data, except for the SMHI-RCA4_IPSL-IPSL-CM5A-MR dataset, which exhibited lower reliability. The system's reliability appears to improve, likely due to an increase in daily rainfall values within the upper 20% of the distribution, as observed in future scenarios compared to historical data. Most projections also indicate a reduction in wet days, though the duration of the longest drought periods does not appear to be significantly affected. Although RCP 8.5 led to a slight decline in system performance compared to RCP 4.5, it still outperformed the historical series. However, due to the limited timespan of the available historical data, the reliability of these estimates remains uncertain. For two-member households, full reliability was first achieved with a 60m² collection surface and a 5m³ tank in both RCP scenarios, while in the three-person household scenario, full reliability was obtained at 80m² with a 5m³ tank under RCP 4.5 and at 80m² with a 10m³ tank under RCP 8.5. Further research could provide valuable insights by assessing the system's performance under a broader range of climate projections and exploring the relationship between reliability and changing water consumption.

References

Data Extraction Application for Regional Climate (DEAR-Clima); Web Application Tool. Available online: http://meteo3.geo.auth.gr:3838/ (accessed on 5 February 2024).

DIN 1989-1, 2002. Rainwater harvesting systems. German Institute for Standardisation.

Durgasrilakshmi Hari et al., (2018). Assessment of rainwater harvesting potential using GIS. IOP Conf. Ser.: Mater. Sci. Eng.

Farreny, R.; Gabarrell Durany, X.; Rieradevall, J., 2011. Cost-Efficiency of Rainwater Harvesting Strategies in Dense Mediterranean Neighbourhoods. Resour. Conserv. Recycl. 55, 686–694

Giorgi, F. (2006) Climate change hot-spots. Geophysical Research Letters, 33.

Köppen, W. (1936) Das Geographische System der Klimate.In: W. K ¨oppen and R. Geiger (eds), Handbuch derKlimatologie 3. Berlin: Gebrueder Borntaeger, 46 pp

Liuzzo, L.; Notaro, V.; Freni, G. A Reliability, 2016. Analysis of a Rainfall Harvesting System in Southern Italy. Water, 8, 18.

Londra P.A., Theoharis A.T., Baltas E. and Tsihrintzis V.A. (2015), Optimal sizing of sainwater harvesting tanks for domestic use in Greece, Water Resources Management, 29, 4357-4377.

Nomikou, P.; Panousis, D.; Nikoli, E.; Antoniou, V.; Emmanouloudis, D.; Pehlivanides, G.; Agiomavritis, M.; Nastos, P.; Cieslak-Jones, E.; Batis, A., 2023. Nisyros Aspiring UNESCO Global Geopark: Crucial Steps for Promoting the Volcanic Landscape's Unique Geodiversity. Geosciences 2023, 13, 70.

Pnevmatikos, J.D. and Katsoulis, B.D. (2006), The changing rainfall regime in Greece and its impact on climatological means. Met. Apps, 13: 331-345

UNDESA, 2024. The Sustainable Development Goals Report 2024 – June 2024. New York, USA: UN DESA. © UN DESA. https://unstats.un.org/sdgs/report/2024/.

Valdez C.M., Adler I., Barrett M., Ochoa R. and Pérez A. (2016), The water-energy-carbon nexus: optimizing rainwater harvesting in mexico city, Environmental Processes, 3, 307-323.

Zittis, G., Almazroui, M., Alpert, P., Ciais, P., Cramer, W., Dahdal, Y. et al. (2022) Climate change and weather extremes in the Eastern Mediterranean and Middle East. Reviews of Geophysics, 60,

17th INTERNATIONAL CONGRESS of the Geological Society of Greece

BULLETIN OF THE GEOLOGICAL SOCIETY OF GREECE, SP. PUBL.

EXTENDED ABSTRACT 299

Numerical modeling of fault genesis in the Santorini-Amorgos basin: an interplay of tectonic forces and magmatism

M Stavropoulou[1] G. Soukis K,[1] Kranis H.[1] Skourtsos Em.[1] Exadaktylos[2]

(1) National and Kapodistrian University of Athens, Athens, Greece, mstavrop@geol.uoa.gr, (2) National Technical University of Athens, Athens, Greece

Research Highlights

The structure and evolution of the Santorini-Amogos basin can be reproduced by applying a plane-strain numerical model.

The Santorini-Amorgos basin (SE Cycladic plateau) is the stage of a complex interaction between active faulting and magmatism, causing the January- March 2025 swarm-type earthquake sequence.

Introduction

The Aegean Sea (Greece), in its present configuration, was formed as a response to the retreat of the Hellenic subduction zone, a retreat that was accelerated since the Middle Miocene, leading to the exhumation of lower and middle crustal rocks that were previously subducted to great depths (Jolivet and Brun, 2010; Ring et al., 2010). Active faulting is restricted along narrow zones with strike-slip and oblique-normal sense of motion, where shallow-intermediate depth seismicity also manifests (Kokkalas et al., 2006).

The Attic Cycladic Crystalline Complex (ACCC, Figure 1) is one such area where the central part is generally aseismic, and major active faults and earthquake activity are located along the north and especially the southern margin, where the modern volcanic arc has been established since the Pliocene (Pe-Piper and Piper 2002 and references therein; Papanikolaou 2021). At the southeastern margin, the Santorini – Amorgos basin is characterized by NE-SW faults creating a complex horst and graben pattern with sediments exceeding 1000m thickness (Figure 2a-b, Nomikou et al., 2016, 2018; Sakellariou and Tsampouraki 2019; Tsampouraki et al., 2021). From January to March 2025, swarm-type earthquakes of magnitudes in the range 1≤M≤5.2 were recorded, having epicenters at depths mainly from 15 km up to 4 km concentrated along a narrow zone extending offshore Santorini near the Columbo volcanic center towards NE, south of Amorgos island (Figure 2c, seismicity catalog of the National Observatory of Athens available in http://www.gein.noa.gr). Whether this sequence could result just from tectonic forces or the combined effect of tectonic forces and magmatic activity is debated.

In this paper, we investigate the structural evolution of the region by virtue of a numerical model, starting from a pure continuum brittle crust due to combined tectonic forces and magmatism. Given that the studied region of the south Cyclades plateau is a major volcanic center and driven from knowledge of hydraulic fracturing processes in deep reservoirs, we examine the hypothesis that the swarm-type of earthquakes is that of magma injections in chambers or dykes lying along this narrow zone.

Geological Framework

The Hellenides represent a segment of the Alpine-Himalayan orogeny, characterized by the convergence between the Eurasian and African plates since the Jurassic (Jolivet and Brun, 2010; Papanikolaou 2021). The Attic-Cycladic Crystalline Complex (ACCC) in the central Aegean comprises scattered relics of the Upper Cycladic Nappe (UCN), which overlies the Cycladic Blueschist unit (CBU), the Cycladic Basement (CB), and the Basal Unit. The lower units experienced Eocene-Oligocene high-pressure metamorphism and then were exhumed to the surface first synorogenically within the subduction zone and then post-orogenically during the Neogene through low-angle crustal-scale detachment systems (Figure 1), rooting in the brittle-ductile transition, as a result of subduction zone retreat (Jolivet and Brun 2010; Jolivet et al., 2010; Ring et al., 2010; Grasemann et al., 2012). The southeastern part of the Cycladic plateau was exhumed from the top-to-SE Santorini Detachment system (Schneider et al., 2018; Grasemann et al., 2022; Laskari et al., 2024; Roche et al., 2024). High-angle faults that succeeded the low-angle faulting further contributed to the exhumation of the metamorphic rocks since the Pliocene and facilitated the ascent of melts that formed, among others, the Santorini volcanic center with the adjacent Christiana and Columbo volcanoes (Kokkalas et al., 2006; Kokkalas and Aydin 2013). The Santorini – Amorgos Fault Zone comprises NE-SW faults with NW-SE direction of extension and a significant dextral sense of motion in the same area where the 1956 Amorgos >7Mw earthquake took place (Nomikou et al., 2018; Sakellariou and Tsampouraki 2019; Tsampouraki et al., 2021).

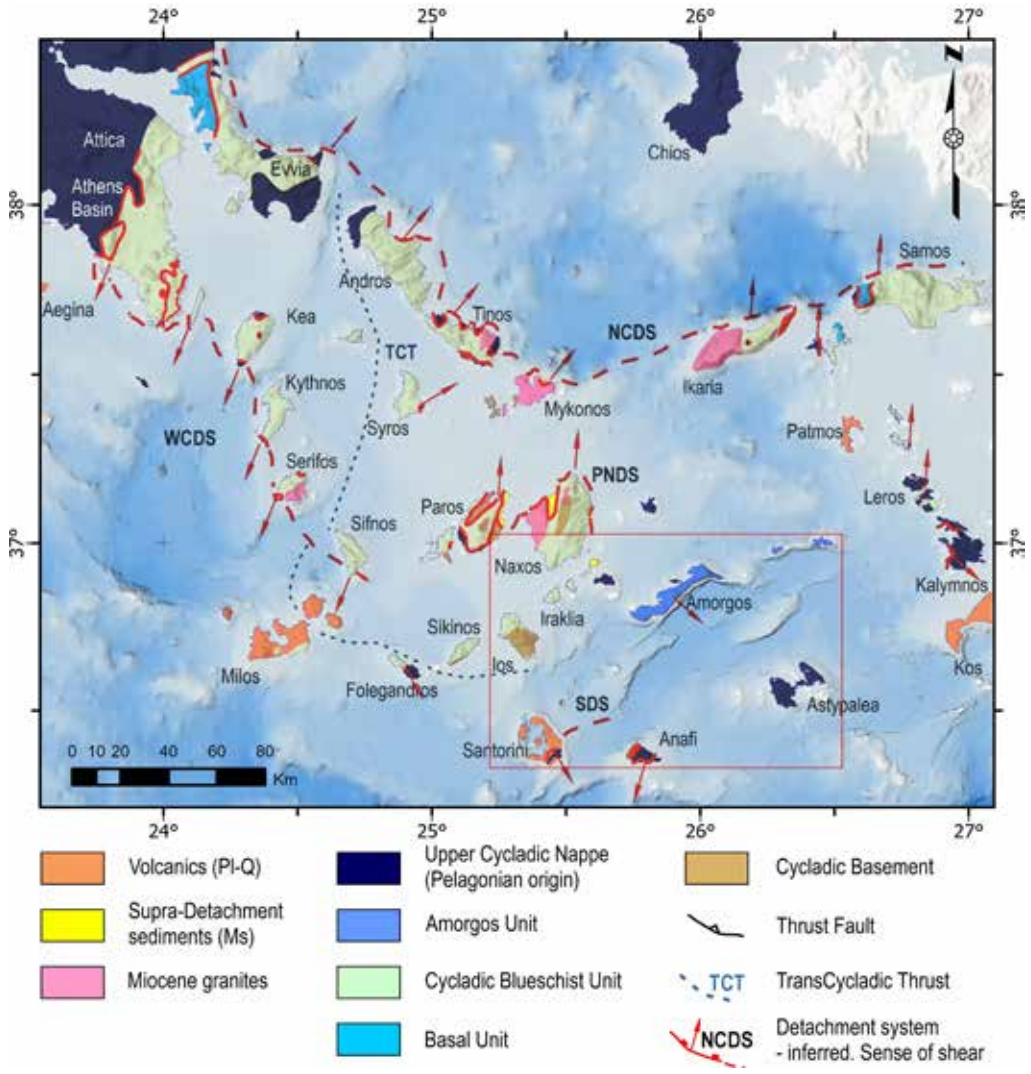

Figure 1. Geotectonic map of the Attic-Cycladic Crystalline Complex (modified after Laskari et al., 2024 and references therein). (Rectangle indicates the study area shown in detail in Figure 2a).

Model Parameters

As mentioned, the first objective is to reproduce the structural features of the Santorini-Amorgos basin associated with the NW-SE extension direction, and the second is to introduce magmatic activity. The sedimentation in the basin is ignored for simplification reasons. To this purpose, a plane strain numerical model corresponding to the NW-SE section of Figure 2a-b was constructed (Figure 3). The model comprises two regions above and below a mechanical decoupling zone 1-2-3 dipping SE (detachment zone) between the upper and the lower crust, corresponding to the brittle-ductile transition for silicate-dominated rocks. The upper region (A) corresponds to the upper crust and is occupied by brittle material, whereas the lower (K) corresponds to the lower crust and is occupied by ductile material. The rock material of the upper crust (A) is modeled as an elastoplastic (e-p) Mohr-Coulomb material, whereas the material of the lower crust (K) is considered a rigid body (r-b).

Simulations were performed with FLAC, a large-strain finite difference software, and an explicit time-marching solution of the full equations of motion (including inertia terms). The finite difference grid is shown in Figure 3. The top surface is stress-free, whereas we assume H_M=10km; thus, the depth of the upper crust at the right end of the model is approximately $2H_M$. Each simulation was conducted in two stages: an initial stage to establish initial equilibrium under the influence of gravitational body forces and boundary restraints, followed by a stage during which the kinematic or static boundary conditions were applied. The extensional loading of the continuum model was simulated by imposing a constant displacement velocity *v* along the right-vertical boundary and the segment 2-3 of the detachment zone.

In the sequel, we assume the formation of a magmatic chamber due to the injection of magma in the weakest region between the two half-grabens between points 1 and 2 of the model. We assume a hemispherical shape of the chamber with the center at the detachment zone and its apex at a depth of 5 km, given that the dip angle of the detachment zone is δ_M=12°. To obtain new shear bands after a few simulation steps, we have applied constant pressure *p/E=1/1000* where E denotes Young's modulus of the upper crust. We do not consider infiltration of magma in the crust; hence, all new cracks are not propagating due to hydraulic fracturing but due to stresses created by the constant applied pressure. This is a reasonable assumption, provided that the viscosity of the fluids is large, and the cracks are tortuous.

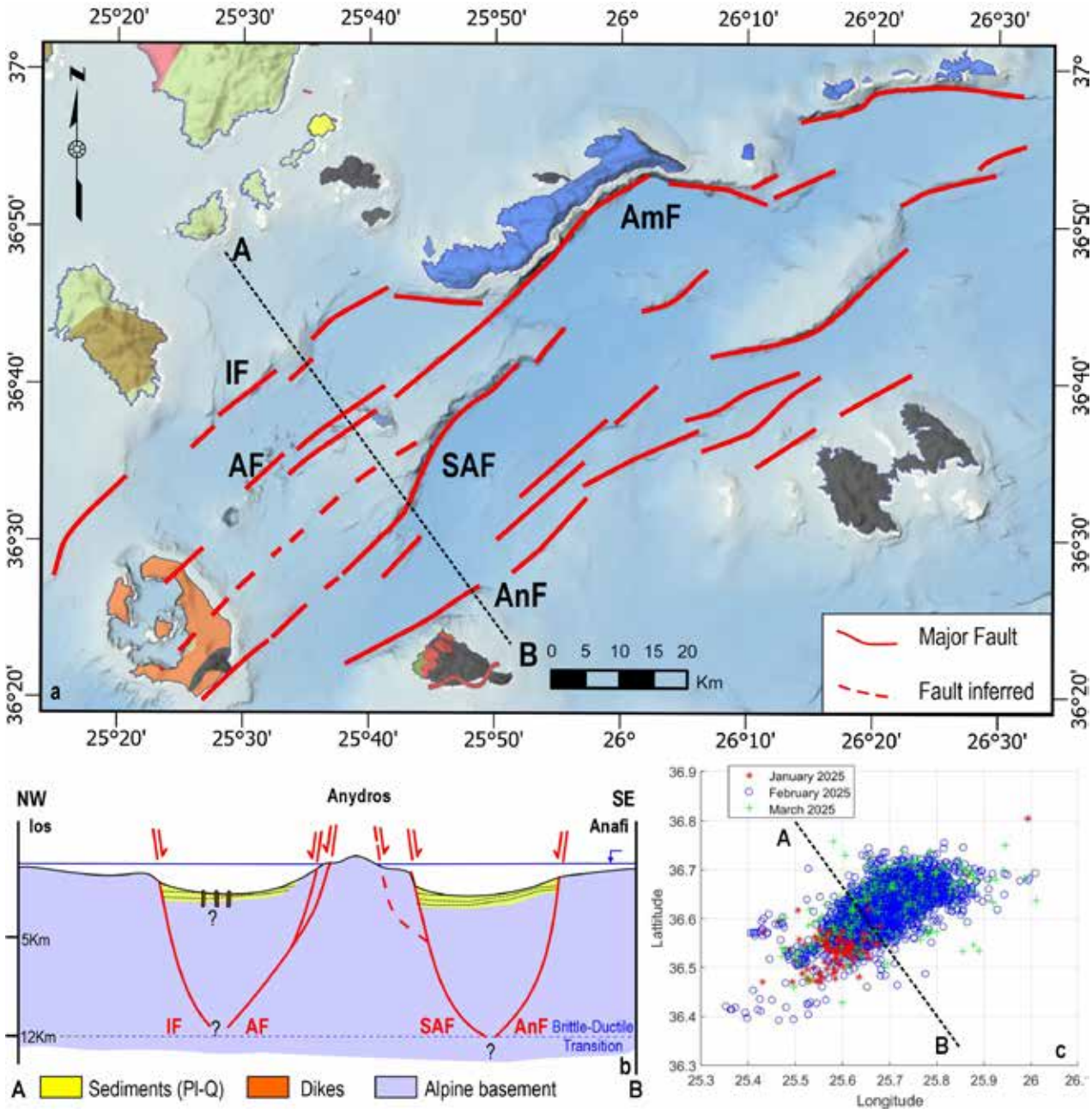

Figure 2a-c. a) Detail of Figure 1 showing the Santorini-Amorgos basin and the main faults (compiled after Nomikou et al., 2018; Sakellariou and Tsampouraki 2019; Tsampouraki et al., 2021), IF: Ios Fault, AF: Anydros Fault, SAF: South Anydros Fault, AnF: Anafi Fault b) Schematic NW-SE cross-section AB (not to scale) c) Projection of the swarm-type earthquake sequence of January-March 2025 (Seismic catalog. of the National Observatory of Athens http://www.gein.noa.gr)

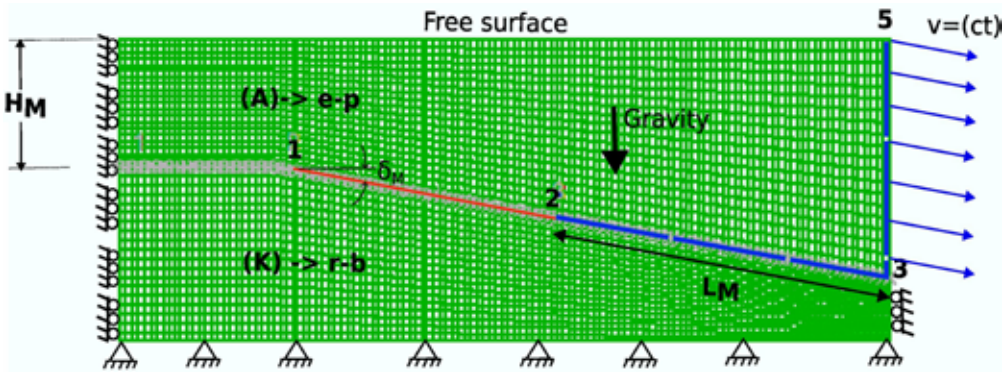

Figure 3. Vertical section of the discretized model and boundary conditions, along the AB cross-section of Figure 2a.

Results

The first stage of the simulation depicts the obtained structural configuration without the interference of magmatic activity. In this first stage, a decoupling zone is assumed at a depth of ~10-12 kilometers. Seismic reflection surveys in the Cycladic plateau estimate the upper and lower crust boundary at ~15 Km (Sachpazi et al., 1997). Since the area is adjacent to the Santorini volcanic center, e.g., within the volcanic arc domain, the geothermal gradient is probably elevated, and it is reasonable to assume that it is close to ~25-30°C/Km. Accordingly, at 10-12 Km depth, the temperature is ~300°C, roughly corresponding to the brittle-ductile transition zone. This zone corresponds to the level of the crust where deformation is localized.

Figure 4a depicts the contours of the maximum shear strain rate after a certain amount of sliding along the detachment zone. These contours indicate strain localization in shear bands (faults). Inside the band, the stress is lower than immediately outside. This stress drop at a newly formed shear band (fault) segment during the upward propagation of the normal fault creates an earthquake. Four sets of contours are formed in the final configuration, e.g., four fault zones, creating alternating horst and graben structures. Our model predicts that the southeast-dipping faults are the main faults and the northwest dipping are antithetic. The dip of the main fault (South Anydros Fault, SAF) of the right half-graben is greater (~70°) compared to the dip values of the rest of the normal faults (Ios Fault IF →60°, Anydros Fault AF →50°, Anafi Fault AnF→50°). It is also evident from the subsidence profile of the surface that the antithetic fault AnF has reached the surface like the rest of the faults.

Figure 4b shows the results of the second stage, where the effect of magmatic activity on the structural configuration obtained in the first stage is depicted. The application of pressure causes the creation of new faults starting at the chamber wall and propagating upwards. These could correspond to earthquakes clustering at 4-6Km depth. Some shallow faults are created due to the bending of the surface. New radially propagating faults are confined in the ridge between Anydros Fault (AF) and the main fault of South Anydros Fault (SAF). Shear strain also accumulates at the base of the fault zones, along the detachment zone, which could correspond to the second group of earthquakes clustering around 12Km depth.

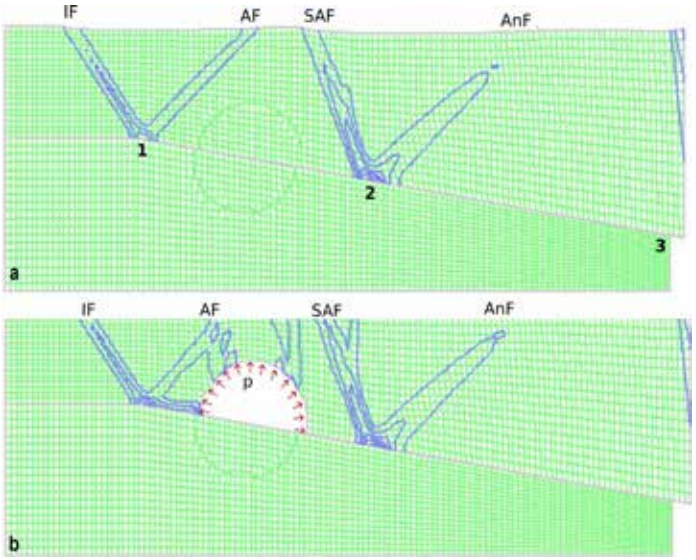

Figure 4a-b. a) Final graben structure of the modeled region at the end of the first simulation phase b) Second simulation phase: applied constant pressure at the wall of the magmatic chamber leads to initiation and propagation of shear bands in the ridge between AF and SAF faults.

Conclusions

- The application of a plane strain numerical model can simulate the structural configuration of the Santorini Amorgos basin and the January-March 2025 swarm-type earthquakes.
- The proposed model is based on the localization of deformation and differential sliding along a decoupling zone at a depth of 10-12Km, corresponding to the brittle-ductile transition.
- The complex geometry of the basin with alternating horst and graben segments results from successive NE-SW faults perpendicular to the local direction of extension.
- The shallow part of the structural configuration obtained from the first step of the simulation is at least in accordance with shallow seismic reflection data in the region.
- The injection of magma strike increases shear strain and creates new faults starting at the magma chamber wall and propagating upwards. The occurrences of new faults are confined in the Anydros ridge, between the AF and SAF.
- The Santorini-Amorgos basin is in the stage of a complex interaction between active faulting and magmatism, causing the January- March 2025 swarm-type earthquake sequence.

Acknowledgements

Field work was supported by grants from the National and Kapodistrian University of Athens ELKE to K. Soukis, H. Kranis and Em Skourtsos.

References

Grasemann, B., Schneider, D.A., Stockli, D.F., and Iglseder, C. 2012. Miocene bivergent crustal extension in the Aegean: Evidence from the western Cyclades (Greece). Lithosphere, 4(1), 23-39.

Grasemann, B., Schneider, D.A., Soukis, K., Roche, V. and Hubmann, B., 2022. Paleogeographic position of the central Dodecanese Islands, southeastern Greece: The push-pull of Pelagonia. Bulletin, 134(5-6), pp.1506-1528.

Jolivet, L., and Brun, J.P. 2010. Cenozoic geodynamic evolution of the Aegean. Int. J. Earth Sci., (Geol. Rundsch.), 99(1), 109–138.

Jolivet, L., Lecomte, E., Huet, B., Denèle, Y., Lacombe, O., Labrousse, L., Le Pourhiet, L., Mehl, C. 2010. The North Cycladic detachment system. Earth Planet. Sci. Lett., 289, 87–104.

Kokkalas, S., Xypolias, P., Koukouvelas, I., and Doutsos, T., 2006, Postcollisional contractional and extensional deformation in the Aegean region. In: Dilek, Y., and Pavlides, S., (Eds.), Postcollisional tectonics and magmatism in the Mediterranean region and Asia: Geological Society of America Special Paper 409, p. 97–123.

Kokkalas, S. and Aydin, A., 2013. Is there a link between faulting and magmatism in the south-central Aegean Sea?. Geological Magazine, 150(2), pp.193-224.

Laskari, S., Soukis, K., Lozios, S. and Stockli, D.F., 2024. Switching from the top-NW backthrusting to top-SE post-orogenic deformation in the Aegean domain: Insights from the calcite microfabric and siliciclastic rocks of the Amorgos Unit (SE Cyclades, Greece). Journal of Structural Geology, 178, p.105011.

Nomikou, P., Hübscher, C., Ruhnau, M. and Bejelou, K., 2016. Tectono-stratigraphic evolution through successive extensional events of the Anydros Basin, hosting Kolumbo volcanic field at the Aegean Sea, Greece. Tectonophysics, 671, pp.202-217.

Nomikou, P., Hübscher, C., Papanikolaou, D., Farangitakis, G.P., Ruhnau, M. and Lampridou, D., 2018. Expanding extension, subsidence and lateral segmentation within the Santorini-Amorgos basins during Quaternary: Implications for the 1956 Amorgos events, central-south Aegean Sea, Greece. Tectonophysics, 722, pp.138-153.

Papanikolaou, D.I. 2021. The Geology of Greece. 345pp, Springer Nature.

Pe-Piper, G., and Piper, D.J.W. 2002. The igneous rocks of Greece. The anatomy of an orogen. Gebr. Borntraeger, Berlin, pp 1–573.

Ring, U., Glodny, J., Will, T., and Thomson, S. 2010. The Hellenic Subduction System: High-Pressure Metamorphism, Exhumation, Normal Faulting, and Large-Scale Extension. Ann. Rev. Earth Planet. Sci., 38(1), 45–76.

Roche, V., Grasemann, B., Schneider, D., Soukis, K. and Pichler, M., 2024. Cold tectonics of Kos, central Dodecanese: Oligocene bivergent extension of the Pelagonian domain. Tectonics, 43(12), p.e2024TC008355.

Sachpazi, M., Hirn, A., Nercessian, A., Avedik, F., Mc Bride, J., Loucoyannakis, M. and Nicolich, R.I.N.A.L.D.O., 1997. A first coincident normal-incidence and wide-angle approach to studying the extending Aegean crust. Tectonophysics, 270(3-4), pp.301-312.

Sakellariou, D., & Tsampouraki-Kraounaki, K. 2019. Plio-Quaternary Extension and Strike-Slip Tectonics in the Aegean. In: J. Duarte (ed). Transform Plate Boundaries and Fracture Zones, 339–374.

Schneider, D.A., Grasemann, B., Lion, A., Soukis, K., Draganits, E. 2018. Geodynamic significance of the Santorini Detachment System (Cyclades, Greece). Terra Nova 30, 414–422.

Tsampouraki-Kraounaki, K., Sakellariou, D., Rousakis, G., Morfis, I., Panagiotopoulos, I., Livanos, I., Manta, K., Paraschos, F. and Papatheodorou, G., 2021. The Santorini-Amorgos shear zone: Evidence for dextral transtension in the south Aegean back-arc region, Greece. Geosciences, 11(5), p.216.

17th INTERNATIONAL CONGRESS of the Geological Society of Greece

BULLETIN OF THE GEOLOGICAL SOCIETY OF GREECE, SP. PUBL.

EXTENDED ABSTRACT 300

Sedimentary, Metamorphic, and Igneous Rocks in Harmony: Unveiling the rocky microcosm of the Vikos-Aoos UNESCO Global Geopark

Stergiou C.L.[1], Papaioannou H.[2], Dimou G.V.[1], Peristeridou E.[1], Melfou M.[1], Stamatiadis A.G.[1], Melfos V.[1], Koukousioura O.[1], Kitsaki G.[2]

(1) School of Geology, Aristotle University of Thessaloniki (AUTH), 54124 Thessaloniki, Greece (2) Vikos-Aoos UNESCO Global Geopark - Development Agency of Epirus S.A. (EPIRUS S.A.), Ioannina, Greece

Research Highlights

Laboratory and field investigations held for a rock and mineral exhibition of the Vikos-Aoos UNESCO Global Geopark revealed new intersections between geoheritage and cultural heritage, indicating significant links between specific rocks, minerals and cultural features.

Introduction

Geodiversity forms the basis of geoheritage and geoconservation, representing the variety of geological, geomorphological, pedological, and hydrological features of Earth. Geoheritage refers to geodiversity elements deemed significant for conservation due to their cultural, scientific, and educational value (Wolniewicz, 2021). It supports the preservation of unique geological sites and provides essential resources like raw materials, water, and energy. Rocks, minerals, and fossils are key components, revealing the dynamic history of the Earth (Pereira, 2023). The growing connection between geoheritage and cultural heritage enhances the value of geoheritage sites by linking them to social identity, history, and art (Pijet-Migón & Migón, 2022). In Greece, this extraordinary geodiversity is exemplified by the Vikos-Aoos UNESCO Global Geopark, where ophiolites, igneous and metamorphic rocks, and fossil-rich sedimentary formations narrate the story of the evolving landscapes of the Earth. UNESCO Global Geoparks like Vikos-Aoos play a vital role in fostering education, conservation, and sustainable tourism, offering a platform to explore the deep connections between geology, culture, and society.

In this context, the Development Agency of Epirus S.A. (EPIRUS S.A.), the managing organization of the Vikos-Aoos UNESCO Global Geopark, organized the exhibition "The Rocks of the Vikos-Aoos UNESCO Global Geopark Under the Microscope: Aspects of Their Microcosm" to highlight the geoheritage of the region. The exhibition was curated by members of the School of Geology, Aristotle University of Thessaloniki, and was first presented in Ioannina from 7th to 10th June 2023, and later traveled to Konitsa and Aristi village in Zagori. The exhibition welcomed hundreds of visitors, which had the opportunity to explore the geology of the geopark and the intricate world hidden within its rocks, through large-scale photomicrographs taken under a petrographic microscope. The exhibition featured hands-on rock and mineral samples, and a microscope allowed attendees, especially younger visitors, to examine thin sections of rocks. Informational material and volunteers helped explain the mineral microcosm, complemented by maps and field photographs, encouraging further exploration of the geopark.

The research conducted for the preparation of the exhibition further expanded the existing knowledge on the mineralogy, petrology, and micropaleontology of the geopark, while also exploring new aspects where geoheritage and cultural heritage intersect. This has led to the development of new research fields and geoeducational potential. In this publication, we briefly present the exhibition and highlight two major findings from the ongoing research that link specific rock types and minerals to cultural aspects and processes and are related to the large spherical concretions of Gamila peak and the Oxya ophiolites.

Geology of the Vikos-Aoos Geopark

The Vikos-Aoos UNESCO Global Geopark, located in the Pindos mountain range in NW Greece, spans 1200 sq. km and presents a geological history that exceeds 200 million years. Rock units belonging to the Ionian Unit, the Pindos Unit and the ophiolitic nappe of Pindos Unit build up the geopark. The Ionian Zone encompasses extensive formations of carbonate rocks and flysch (Figure 1). Upper Jurassic-Lower Cretaceous dolomites and limestones of Vigla Formation, "Senonian limestones" with rudist fossils, and Paleocene-Eocene limestones rich in planktonic microfossils constitute a continuous, collectively over 2200 m thick, calcareous marine stratigraphy, deeply exposed within the Vikos and Aoos Gorges through karstification (Perrier *et al.,* 1968). Overlying the Paleocene-Eocene limestones the Oligocene to Lower Miocene flysch formation is found, including an 1,800 m thick, turbiditic sequence of sandstones and marlstones, which dominates the eastern Zagori region and parts of Konitsa (Perrier *et al.,* 1968, Figure 1).

Pindos Unit underpins almost half of the regional geology covering the eastern part of the geopark (Figure 1). It is represented by Upper Cretaceous limestones and the overlying Paleocene to Eocene flysch formation (Mavridis & Manakos, 1987). The flysch, over 1250 m thick, consists of silty marlstones, fine-grained sandstones, limestones and conglomerates with ophiolitic clasts. Ophiolitic rocks are found obducted on the Pindos flysch and constitute fragments of the old Tethyan oceanic sediments,

crust and upper mantle that were obducted on Pindos Unit forming a now appearing fragmented ophiolitic nappe. The ophiolite components date back to the Lower Jurassic, and consist of ultramafic to mafic igneous rocks that have undergone extensive serpentinization. These include harzburgite, dunite, pyroxenite, gabbro, and diabase veins (i.e. igneous rocks), alongside large occurrences of serpentinite (i.e. metamorphic rocks, Mavridis & Manakos, 1987). The thickness of the ophiolitic thrust sheets reaches 1000 m at their most prominent and complex exposure found at Mount Smolikas (Figure 1). Locally, small outcrops of Jurassic schists, red cherts and limestones intercalated with cherts occur, representing Tethyan deep sea and hemipelagic sedimentation respectively (Mavridis & Manakos, 1987). These outcrops are typically less than 100 m thick and are often bounded by tectonic contacts (Figure 1). This complex geology combined with faulting and folding, documents the tectonic evolution of the region, which transitioned from passive margin sedimentation to compressional orogenesis during the Alpine orogeny.

The Pleistocene-Quaternary deposits include glacial moraines, prominent in the Tymfi and Smolikas mountains, and Holocene alluvial sediments along the Voidomatis, Aoos, and Sarantaporos rivers (Perrier *et al.,* 1968, Figure 1). Glacial deposits often loosely cemented and landslide-prone, contrast with the sands, clays, cobbles, and angular fragments of alluvial terraces elevated above current river flows (Perrier *et al.,* 1968, Figure 1).

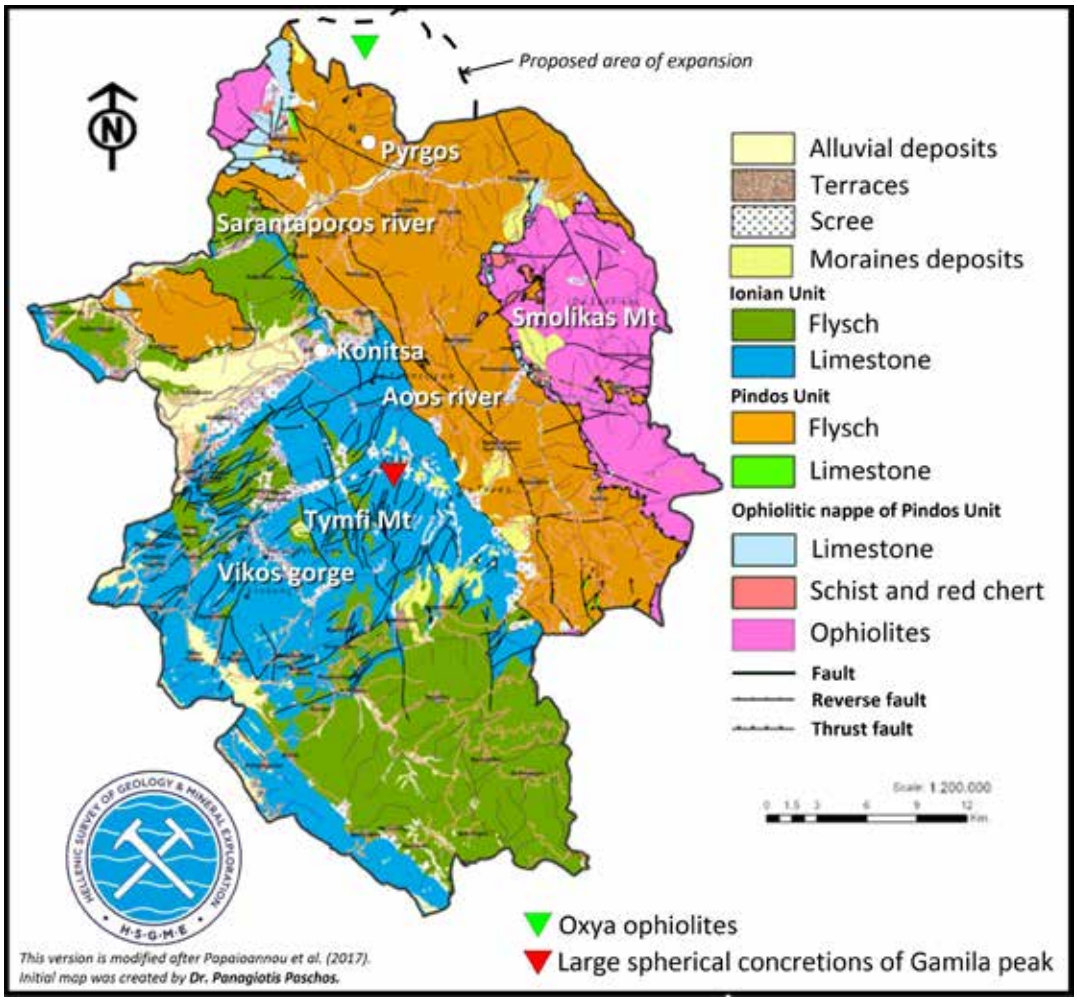

Figure 1. Simplified geological map of the Vikos-Aoos UNESCO Global Geopark. Main rock units and faults are shown. The Ionian limestone sequence is presented unified for clarity (modified after Papaioannou *et al.* (2017), initial map was created by Dr. Panagiotis Paschos).

Methods

Forty one samples were collected from primary outcrops and secondary sources, such as alluvial deposits, representing all the rock units of Vikos-Aoos Geopark, as well as special geological features (e.g. concretions, ore minerals, calcite masses). Rock samples were collected from outcrops close to the 51 recognized geosites and to the additional 30 sites of special

geological interest, which represent the geodiversity and geoheritage of the geopark. The collection sites were documented photographically using appropriate scales, and GPS data were collected for future reference. Thirty one of these samples were selected to be studied under the microscope. Thus, twenty six thin sections and 5 polished sections were produced and studied under a ZEISS Axioskop 40 dual reflected-transmitted light polarizing microscope coupled with a Canon Powershot A640 digital camera at the Department of Mineralogy-Petrology-Economic Geology, School of Geology, Faculty of Sciences, Aristotle University of Thessaloniki. The acquired micro-photographs were saved and logged. The digital enhancement of the micro-photographs and the preparation of the exhibition materials were carried out using the software Adobe Photoshop and Adobe Illustrator. For the exhibition needs twenty one micro-photographs were printed on 70 cm X 50 cm foam boards to cover the needs of the photographic exhibition. Following the exhibition, EPIRUS S.A. decided to publish a special volume dedicated to the mineral microcosm of the Vikos-Aoos UGGp in an effort to extend the impact of the exhibition and to ensure that the educative content and the aesthetics captured in the photographs will continue to inspire and engage audiences and forward the education on geoheritage and cultural heritage intersections (see Figure 4 below).

The Oxya ophiolites

The ophiolitic occurrence (N40.243086°, E20.804622°) at Oxya village, Konitsa, lies just outside the northern periphery of the geopark in a proposed area of expansion, and is one of the 30 designated sites of special geological interest (Figures 1, 2a). It is part of the ophiolitic cover of Pindos Unit, which appears thrusted on the flysch of Pindos Unit. These outcrops were first studied and reported back in the 1950s by Marinos *et al.* (1957) during the post-World War II efforts to support the economic development for Epirus. The ophiolitic assemblage includes gabbros and diabases intruding into basalts and pillow lavas, surrounded by serpentinites and scattered serpentinized dunites. Within the diabases, disseminations and minor stockworks of metallic mineralization occur, comprising pyrite, magnetite, and minor pyrrhotite, chalcopyrite, galena and ilmenite. In contrast, the pillow lavas host mainly pyrite and minor magnetite (Figure 2b,c), which, in surface samples, is heavily oxidized to form yellowish brown to red encrustations of goethite and hematite (Figure 2b).

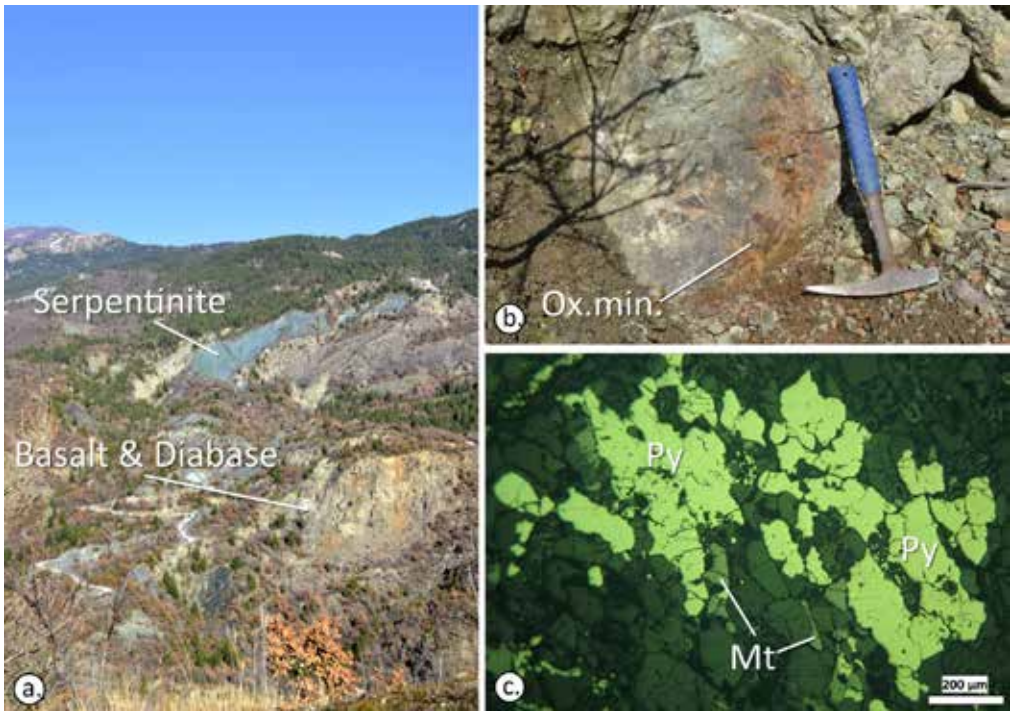

Figure 2. a. Field photograph of the Oxya ophiolites, characteristic outcrops of serpentinite, basalt and diabase are highlighted. Rocky cliffs appear yellowish brown due to the extent encrustations of goethite and hematite. b. Oxidized mineralization (Ox.min.) in diabase. c. Photomicrograph under plane reflected light (Nichols //) of the pyrite (Py) and magnetite (Mt) mineralization hosted in basalt.

Local reports support that pieces of the oxidized pyrite mineralization collected as ochre have historically been utilized as pigments for coloring by the famous Chioniadites painters, demonstrating an intersection of geological and cultural significance. Chioniades village is located NW of the Oxya ophiolites at 1150 m on the eastern slopes of Mount Grammos, and is where the Chioniadites School of painters had thrived between 18th and 20th centuries. Religious and popular creations of this school of painters are found from Albania and Epirus to Macedonia and Thessaly (Tsiodoulos, 2009). The artistic tradition of the village dates back to 1747 as is documented by the signed depiction of Saint George in the church of Koimisi Theotokou at Vourbiani

village, attributed to Konstas of Chionades (Tsiodoulos, 2009). The Chioniadites School of painters does not exhibit any characteristic painting style but follows the aesthetic standards of each time period (Stergiou 2024). Anastasios Papakostas-Marinas (1856) and his sons Christodoulos (1857-1932) and Thomas (1864-1930), are among the last and most famous painters of the Chioniadites School of painters (Stergiou 2024).

South of the Chioniades and Oxya villages, near Pyrgos village, another smaller ophiolitic outcrop (N40.164892°, E20.785197°) is found thrusted on the flysch of Pindos Unit (Figure 1). There, the local tradition narrates the extraction of a hard stone, locally called "gretzia," derived from the local term "grentzos" (meaning rough, coarse, uneven on the surface), which in turn comes from the Italian greggio/grezzo (meaning raw, unprocessed, unshaped) for the production of millstones. Hard, fine grained volcanic rocks like diabase or basalt have been traditionally used across Greece for the production of millstones (Melfos *et al.,* 2014), and this could also be the case at Pyrgos village.

The Large Spherical Concretions of Gamila Peak

The Gamila Peak spherical concretions (N39.97753°, E20.79079°), is another remarkable geological feature of the Vikos-Aoos Geopark, first described by Telbisz *et al.* (2019). Found at approximately 2,100 m a.s.l. along the trail to Gamila Peak (2,497 m a.s.l., Figure 1), these formations are observed in limestone boulders or as individual concretions within collapsed rocky scraps. The Paleocene-Eocene limestone formation of the Ionian Zone is the host rock of the concretions. The concretions exhibit spherical to elongated elliptical shapes, ranging usually from 0.1 to 1 m in diameter, and exhibit distinctive concentric layering (Figure 3a). Locally, large concretions form discontinuous layers reaching or exceeding 20 m in length (Figure 3b). The concentric layers that build up the concretions, alternate between fine-grained carbonate material and varying amounts of siliceous and carbonate cement, and contain abundant bioclastic material (Figure 4). The mixed cement suggests a diagenetic process involving early, incomplete carbonate cementation coupled with substantial SiO_2 precipitation in the intergranular spaces. The silicification likely resulted from the dissolution of siliceous bioclasts, though contributions from external SiO_2-enriched fluids cannot be excluded. The microscopic study revealed that the concretions retain embedded microfossils of *Nummulites*, *Alveolina* and orthophragmines. The size of the microfossils in some cases exceeds 3 mm in length (Figure 4). These microorganisms, part of the Large Benthic Foraminifera group, lived in shallow marine environments during the Middle Eocene (47 to 41 My ago), in depths up to 40 m according to the total recorded assemblage. Their presence, along with the intricate mineralogical composition of the concretions, underscores the complex diagenetic and paleoenvironmental history preserved within this extraordinary natural feature. A smaller outcrop of spherical concretions is found at the northern foundation (N39.862341°, E20.775298°) of the Noutsos (or Kokkoris) arch-stone bridge near Kipoi village, Zagori. Mapping and documentation of all outcrops with such concretions on Mount Tymfi is essential for reconstructing the paleoenvironment and understanding its geological history.

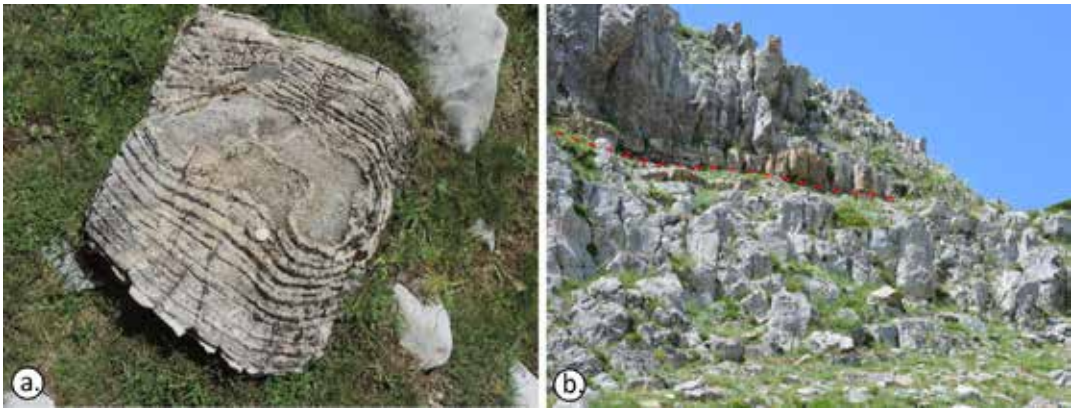

Figure 3. Field photographs of the large spherical concretions appearing as a fragmented boulder (a) and a discontinuous layer (red dashed line) of such large spherical concretions at a cliff close to Gamila peak, Mount Tymfi.

Recent field research at the villages of Megalo Papigo, Zagori, held by Christos L. Stergiou and Haritakis Papaioannou, documented another case of intersection between the geoheritage and cultural heritage of the Vikos-Aoos Geopark. Concentric concretions, texturally identically to those found near the Gamila peak but of smaller size (<40 cm in width) have been documented being embedded as stone carvings on traditional house facades that were mainly built along the 19th century (Figure 5a,b). These stone carvings are called hologlyphs and typically depict relief representations of anthropomorphic or dragon-like heads and were often embedded in churches, houses, fountains, and bridges in the Epirus region. They served a protective and apotropaic role, supported by three main characteristics: their grotesque appearance, the expression of the eyes, and the locations where they were placed (Tsoupi, 2006).

Figure 4. Sample layout from the upcoming special volume of the Vikos-Aoos UNESCO Global Geopark, showcasing rocks and minerals under the microscope alongside stories highlighting the intersection of geoheritage and cultural heritage. This example presents the geological significance and mineralogical composition of spherical concretions through macro-photographs and photomicrographs.

Figure 5. Photographs of the apotropaic hologlyphs installed on the facade of a traditional house at Megalo Papigo village build at 1876. Both are made of small spherical concretions. a. A roaring dragon-like. b. An anthropomorphic figure with a critical and stern gaze.

Conclusions

The Vikos-Aoos UNESCO Global Geopark, nestled in the geologically diverse terrain of the Pindos Mountains, exemplifies the intricate interplay between geology, culture, and nature. This research has highlighted key geological features within the geopark, such as the ophiolitic occurrences in Oxya and Pyrgos, the Gamila Peak

spherical concretions, and their connections to cultural heritage. The Oxya ophiolitic outcrops, part of Pindos Unit, host metallic mineralization, which were historically used by the Chioniadites painters as pigments. Similarly, the "gretzia" stone from Pyrgos village, likely derived from local diabases or basalts, showcases the traditional use of volcanic rocks for millstone production.

The spherical concretions at Gamila Peak, with their concentric layers and microfossil inclusions, offer insights into the Paleocene-Eocene shallow marine habitats and diagenetic processes that shaped the region. These concretions not only reveal vital biostratigraphic and paleoenvironmental data but also intersect with cultural heritage through their use as decorative carvings in traditional architecture. The hologlyphs embedded in house facades and other structures across the region serve as powerful symbols of the protective and artistic traditions of Zagori and Epirus. By uncovering these connections between geoheritage and cultural heritage, this ongoing research deepens our understanding of the geological and cultural history and enhances the geotourism and educational potential of the Vikos-Aoos Geopark.

Acknowledgements

Eleni Tsirigoti is acknowledged for handling the graphic production of the exhibition and the handbook under development. Region of Epirus, Municipality of Konitsa and the Ioannis Saralis Foundation are thanked for supporting the exhibitions held at Ioannina, Konitsa and Aristi, Zagori, respectively. The Development Agency of Epirus S.A. (EPIRUS S.A.) funded the thin and polished sections preparation of the collected rock samples, and covered the printing costs for the photographs and the informative material of the exhibition. Furthermore, EPIRUS S.A. is acknowledged for undertaking the publication of the album on the minerals and rocks of the geopark.

References

Marinos, G., Andronopoylos, B., Melidonis, N. 1957. Geology and mineral deposits of Epirus. Institute of Geology and Subsurface Research.

Mavridis, A., Manakos, K. 1987. Geological map sheet Konitsa, 1:50.000. Institute of Geology and Mineral Exlporation, Athens.

Melfos V., Papacharalampou C., Voudouris P.Ch., Kaiafa A., Voudouris, K. 2014. Raw materials used for the millstones production in ancient Greece: Examples from Macedonia and Thrace, in: Kalavrouziotis, I.K., Angelakis, A.N. (Eds.), Proceedings of the 4th IWA Regional Symposium on Water, Wastewater and Environment: Traditions and Culture, 773-783.

Papaioannou, H., Paschos, P., Nikolaou, E., Kitsaki, G. 2017. Vikos-Aoos Geopark. Visitor's Guide. Region of Epirus. Epirus SA – Development Agency, Ioannina, pp. 120.

Pereira, D. 2023. The value of Natural stones to Gain in the Cultural and Geological Diversity of our global Heritage. Heritage 6(6), 4542-4556.

Perrier, R., Koukouzas, K., Bizon, J.J., Bizon, G. 1968. Geological map sheet Doliana, 1:50.000. Institute of Geology and Mineral Exlporation, Athens.

Pijet-Migón E., Migón, P. 2022. Geoheritage and Cultural Heritage - A Review of Recurrent and Interlinked Themes. Geosciences 12, 98.

Stergiou, G. 2024. Conservation and restoration of a double-sided ecclesiastical banner from Saint Nicholas church, Molista, Ioannina, Greece, in: Karydis, C., Oikonomou, A., Kouloumpi, E., Vasilev, I., Stanev, S. (Eds.), The 2nd International Meeting for Conservation & Documentation of Ecclesiastical Artefacts (IMCDEA), Balkan Heritage Foundation, Sofia, Bulgaria, pp. 197-201.

Telbisz, T., Stergiou, C.L., Mindszenty, A., Chatzipetros, A. 2019. Karst features and related social processes in the region of the Vikos gorge and Tymphi mountain (Northern Pindos National Park, Greece). Acta Carsologica 48(1), 29-42.

Tsiodoulos, S. 2009. The Painted Decoration of the Houses in Zagori, Late 18th– early 20thCentury: A Historical and Cultural Approach, 1st edition. Rizareio Idryma.

Tsoupi, M. 2006. Epirotic Stone Carvings: Art and Society - Tracing in Zagori, 1st ediiton. Gefyra publications.

Ziogas, T.V. 2013. Place Names & Settlements of the Stone Mason Villages of Konitsa, 1st edition. Self publication.

Wolniewicz, P. 2021. Beyond geodiversity sites: exploring the educational potential of widespread geological features (rocks, minerals and fossils). Geoheritage 13(2), 34.